TURBULENCE AND AIR UPTAKE AT SPILLWAY RAMP AERATORS

By

AZAM RAZA KHAN
B.Sc (Honours) 1984
N.W.F.P University of Engg & Tech
PESHAWAR PAKISTAN

A thesis submitted to the University of Glasgow in fulfilment of the requirement for the Degree of Doctor of Philosophy
September 1991

Department of Civil Engineering
University of Glasgow
GLASGOW
UNITED KINGDOM

TEXT CUT OFF IN THE ORIGINAL

*In the Name of '**ALLAH**' "Most Gracious, Most Merciful"*

"Proclaim ! And thy Lord is most Bountiful"

"He Who taught (the use of) the Pen,"

"Taught man that which he knew not."

ACKNOWLEDGEMENTS

This work reported in this thesis was carried out in the Department of Civil Engineering University of Glasgow.

The author wishes to express his special thanks and appreciation to his supervisor Dr. D.A. Ervine, for his valuable guidance, advice and constant encouragement throughout this work.

The author would like to express his gratitude to Mr.W.Thomson (technician) for his assistance in the design and construction of the experimental apparatus especially the Laser carriage system.

The author would like to thank Mr. A.Burnett, superintendent, for his procurement of material and photography. The author would also express his gratitude to the remainder of Glasgow University technical staff especially R.McCaskie, A.Gray, Ken Ryan, Ian Dickson and A.Yuill for their help.

The author is also grateful to Professor Muir Wood (Cormack Professor and Head of the Department) and Professor Green (previous Head of Department) for allowing the use of the Glasgow University facilities.

Many thanks to Dr. J.G.Herbertson for his help and useful discussions during the course.

The author is grateful to his fellow researchers, Dr W.Withers, Dr. H.K.Jasem, Manuel Lorena, Paul Addison, M.Khan, M.Imran, M.Choudary, Mr Tanveer, Maj Iftakhar, M.Ashraf and Z.Khan for their helpful discussion and constant encouragement.

The author is grateful to the Government of Pakistan, Ministry of Science and Technology for the financial support during the course.

Finally, my thanks are reserved for my mother, my father, my wife, my son Saad and my daughter Aysha for their patience and constant encouragement throughout my studies.

ABSTRACT

The work in this thesis is a physical model study of air slot ramp aerators designed to eliminate cavitation in open channel spillway chute flows. The experimental work involves the use of a Laser system to measure the turbulent flow structure on a spillway, ramp and jet system, and then to relate the turbulent flow structure to the rate of air entrainment in the aerator.

Even though aerator model studies have been carried out for decades, this appears to be the first time that turbulence has been measured in detail, having regard both to the ability of a ramp to generate turbulence and also to the decay of turbulence in the aerator jet downstream of the ramp.

An expression is found for air entrainment in the models tested at Glasgow University. It is also valid for a range of previous prototype measurements, and is valid for a range of other previous model studies. The result are also translated into a computer program for designing such structures.

The model used was a rectangular cross–section perspex flume, sloping at 45^{0}, incorporating a range of ramps at different angles. A range of flow depths, flow velocities, and boundary roughness values were tested and the measurements were taken by a Laser Doppler Anemometer.

The results of this work provide a clearer understanding of the physical processes which occur in aerator ramp. This includesa clear demonstration of the ability of the ramp to generate additional turbulence in the flow, increasing turbulence values by about 30% above normal boundary layer values.

This thesis also shows the link between turbulence generated and air entrained into the underside of the nappe. The rate of air entrainment is shown to increase with increasing vertical turbulent velocity w', it is shown to decrease

with distance along jet length, especially for non–dimensional jet lengths ($L/h_3 > 10$), and it is shown to decrease with increasing cavity underpressure $\Delta h/h$.

The final empirical relationship for air entrainment also includes a scale effect term, based on the proposition that a vertical turbulent velocity w' of 0.3 m/s is required to instigate air entrainment into the underside of such aerator jets.

At the end of the thesis the author propose a new relationship for air entrainment at aerators, $q_a = C_2\ C_3\ (u_* - 0.18)\ L$, which appears to be accurate to ± 10% for prototype structures, and ± 20% for model studies data.

A computer program is presented for steady state flow behaviour upstream of an aerator, the jet trajectory, the air supply system and air entrainment at the underside of the jet.

TABLE OF CONTENTS

NOTATION

Symbol	Meaning
A_1	area of total head tube
A_2	area of shock chamber
A_d	area of air supply duct
Ag	specific constant for gas
b	width of the open channel
C	air concentration
d,D	diameter of nozzle or orifice
E	Young's modulus and specific energy
F	force on bubble
F(f)	frequency response
f	frequency
fd	natural frequency of transducer
fo	natural frequency of instrument
g	gravitational acceleration
H	total available head
h	depth of flow
h_3	depth of flow at section 3
h_s	height of offset
h_r	height of ramp
$\triangle h$	pressure difference in meters of water
K_d	total head loss coefficient in air supply system
k_s	roughness coefficient
l_r	length of the ramp

L	Length of jet in aerator
L	jet fall height
L_B	jet break-up length
Lo	length of upstream nozzle
L_1	total length of total head tube
L_2	length of shock chamber
L_{gr}	length of channel from gate to aerator ramp
ℓ	eddy length and distance from outlet
N	total number of time intervals
P	pressure
$\triangle p$	pressure underneath of water jet
Q_a	air flow rate
Q_w	water flow rate
q	unit discharge
R	radius of curvature of jet surface undulations
R_j	radius of jet
r	radial distance from jet centre line
r_j	distance from jet centre line to turbulence probe
T	time period
Tu	turbulence intensity
t	time
u	point velocity in longitudinal direction
$\bar{u}$	mean velocity in longitudinal direction
u,v,w	velocity components in x,y,z direction
u',v',w'	turbulent velocity components in x,y,z directions
U	jet velocity in longitudinal direction
U_{br}	bubble rise velocity
Ue	minimum entrainment velocity
u_*	shear velocity

V	velocity in radial direction
Ve	entrainment velocity
X,Y,Z	cartesian coordinates
X	longitudinal distance from outlet
Y_g	gate opening at enterence pressure box
Z	diaphragm deflection
Z , z	distance up from channel bed

Dimensionless numbers

Fr	Froude number	$[U/\sqrt{(gD)}]$
Re	Reynolds number	$[UD/\nu]$
We	Weber number	$[U/\sqrt{(\sigma/\rho D)}]$
Oh	Ohnesorge number	$[W_e/R_e]$

Greek symbols

α	jet convergence angle
α_e	entrainment coefficient
β	air/water ratio
δ_1, δ_2	inner and outer jet spread angle in atmosphere
δ_0	amplitude of initial surface disturbance
δ	boundary layer extent (and denotes partial differentiation)
ϵ	dynamic eddy viscosity and magnitude of surface disturbances
η	Poisson's ratio
θ	bed slope to the horizontal
μ	dynamic viscosity
ν	kinematic viscosity

ρ	density
ρ_d	density of diaphragm
σ	standard deviation and surface tension
τ	shear stress
Φ	angle of ramp
ω	vorticity

Subscript

1	section (1) 600mm upstream of the end of the ramp
2	section (2) 300mm upstream of the end of the ramp
3	section (3) at the end of the ramp
4	section (4) 300mm downstream of the end of the ramp
a	pertaining to air
i	denotes pool impact and submerged outlet conditions
o	denotes outlet section
r	restricted jet conditions
u	unrestricted jet conditions
w	pertaining to water

Superscript

–	mean component of quantity
~	denotes proportionality and fluctuating components
'	R.M.S. of fluctuating component

LIST OF FIGURES

CHAPTER. 1

INTRODUCTION TO AIR SLOT AERATORS

1.1 INTRODUCTION.

1.2 HYDRAULIC STRUCTURES WITH AIR SLOT AERATORS.

1.2.1 Basic Design Principles

1.2.2 Examples of Aeration Devices in Prototype Structures

1.3 PURPOSE OF RESEARCH.

1.1 INTRODUCTION

This thesis is a study of aeration devices used in high velocity spillway flows to entrain air and minimise the likelihood of cavitation damage to the spillway surface.

The concept is simple and is sketched in Fig 1.1. A ramp, or a slot, or a step–down on the spillway channel bed, or a combination of all three, is constructed on the channel bed, causing a rectangular jet to form, springing clear of the spillway surface as shown. Air from the atmosphere is allowed to enter the cavity formed between the jet and spillway surface, and enough turbulence is generated in the jet to allow air to be entrained into the underside of the jet. Air bubbles entrained, are transported downstream with the flow beyond the point of jet re–attachment with the spillway surface. The presence of air bubbles downstream, inhibits the process of cavitation damage, probably by gross reduction in the sonic velocity of the flow mixture.

Such devices have been in use for thirty years and in most cases have been very successful at reducing cavitation damage. The past decade has witnessed an increase in height of dams and in specific flow discharge rate down spillways. On many projects there are dam heights in excess of 200 m, with spillway discharge per unit width greater than $q = 270\ m^2/sec$. This implies velocities in the concrete spillway chute of the order of 50 m/sec with the attendant risk of cavitation damage. A world–wide trend to increase unit discharge capabilities, combined with long duration operation of the discharge structures, orignally planned as emergency devices, are contributing to the problems. Relief is sought by aeration of spillway chutes and outlet works.

Interest in this subject at the University of Glasgow is two–fold.

i) Dr Ervine has been involved with aeration in general for some years, concentrating on beneficial effects of aeration, as in siphon. spillways, but also on

harmful effects of aeration, as in blow—backs from dropshaft tunnel junctions. Following a visit to United States Bureau of Reclamation (USBR) in 1985 and 1988, Dr Ervine developed an interest in the mechanics of ramp aerators, and in particular, the effect of turbulence on the ramp aerator performance. This interest was sparked because of the apparently poor performance of an aerator at McPhee Dam (USA). The rectangular aerator jet formed at McPhee has a large length to thickness ratio (L/h), and apparently entrains significantly less air than would be expected from such a prototype structure. The relationship between model air entrainment and prototype measurement was also of considerable interest.

ii) The second point of interest comes from the author of this thesis, following a two year programme working at Tarbela Dam, Pakistan. Cavitation damage in the outlet chutes, necessitated the construction of ramp to provide aeration as shown in Fig 1.7. The aeration devices installed have been investigated in field measurements at Tarbela, with the design of the devices almost at the opposit end of the spectrum compared with McPhee Dam. First, the spillway chute was almost horizontal, the aspect ratio (width to jet thickness) was small compared with McPhee, the unit discharge ($q \simeq 266\ m^2/s$) were among the largest in the world, and the length of the aerator jets (L/h) were very short compared with McPhee.

Thus, both experiences of prototype performance outlined above, provided the necessary impetus for a more detailed experimental study at Glasgow. The results of the study were designed to provide insights into different behaviour patterns exhibited by various aerators, to provide data for a computer model also developed in this work, and to provide clearer scaling laws from model to prototype behaviour.

1.2 HYDRAULIC STRUCTURES WITH AIR SLOT AERATORS.

1.2.1 Basic Design Principles.

Aeration devices are known as air slot ramps. The purpose of an air slot ramp is to introduce air bubbles into the high velocity flow over the hydraulic structure to prevent cavitation erosion damage. All that is required is some means of getting a sufficient amount of air under the jet. Various design of air slots are sketched in Fig 1.2. These represent the main variations possible, including an offset, (step down in the channel bed), a deflector or ramp, and a groove (or slot), or any combination of all three as shown in Fig 1.2.

According to practical considerations, aerators should entrain as a large quantity of air as possible, so that air concentration is evenly distributed over spillway width and along the length of the channel. The aerator should be simple and economical in design, and it should also prevent any erosion damage to itself. The sudden discontinuity in the lower nappe with the solid surface creates an air/water interface along which high velocities entrain air. A groove can be added to a ramp and offset in order to improve condition for air entrainment. In fact the larger the area under the nappe, the more efficient the entrainment of air. Hence the best combination is ramp, offset, and groove as shown in Fig 1.2(g).

The efficiency of air supply system depends very much on its ability to minimize the sub–atmospheric pressure below the nappe. The lower the head loss through the air duct, the more air is entrained and the longer is the aerator jet length. Therefore, the air supply system should be designed for minimum head loss as shown in Fig 1.3. This graph shows that an aerator device with air vent, behaves in a similar manner to a pump with system loss curve, with the actual

behaviour shown where the two curves intersect. At that point a balance is reached between the air pumping ability of the jet and the air flow head losses through the vent system.

A range of air vent supply arrangements are shown in Fig 1.4. The most common arrangement being Fig 1.4(a). In this diagram, air is funnelled into a rectangular vent through a bellmouth type inlet. The air flow normally turns through a 90^0 smooth radiused bend, to exit in the cavity region under the aerator jet. This arrangement is usually built on both sides of the spillway to ensure a better distribution of air circulation under the aerator jet.

The remainder of the likely vent arrangement are shown in Fig 1.4 (b) to (e) and involve mostly side wall offset and slots to allow air flow to pass down the side and under the aerator jet.

A ramp is usually placed upstream of the aeration groove to prevent the groove from filling water. The ramp lifts the lower nappe of the flow prism causing the flow to follow a free trajectory. The trajectory taken by water is a function of the relative ramp height, the ramp angle, the flow velocity, and the pressure under the nappe. Several methods are available to determine the jet trajectory which will be discuss in detail in Section 2.5.3.

The cross sectional area of the air duct must be large enough to distribute the entrain air and not decrease the pressure under the nappe appreciably. If the drop in pressure becomes too large, sonic velocity will occur in the vent. When this occurs, the flow is said to be choked because the air flow will not increase as the pressure drops. The pressure ratio at which choking occurs is a function of the friction losses in the duct leading to the aeration groove. In general, problems with noise generation can be avoided if the pressure drop is less than or equal to one-tenth of the pressure from the critical pressure ratio. Further details on air vent design, choice of ramp angle, step heights and groove dimensions will be provided in Chapter 2, Section 2.6

1.2.2 EXAMPLES OF AERATION DEVICES IN PROTOTYPE STRUCTURES.

After 1960, various types of aeration devices have been employed in spillways and outlet works. The different types are based on grooves, offset, and deflectors, or a combination of all three as already discussed. In many cases, aeration devices were introduced after erosion damage had occured, while in others, they were incorporated in the orignal design.

First application of the aeration concept seems to have been at the outlet conduits at Grand Coulee Dam (1959–60). As for spillways, early references are for a tunnel spillway at Yellowtail Dam in United States, Sirikit in Thailand, and Bratsk spillway, a 100m high concrete dam in U.S.S.R.

(i) *Grand Coulee Dam Outlets.*

The Grand Coulee Dam outlets have a tapering cone at the end of a steel lined tunnel which reduces the tunnel diameter from 2.59m to 2.36m and creates a back pressure upstream. This is shown in Fig 1.5 . The outlet operates under heads of 61m to 76m. The concrete trough floor diverges 1 in 20.8 from the wall of the cone. According to the Wagner (1967), this abrupt change of direction was sufficient to induce extensive cavitation damage, requiring annual repairs. Cutting an aeration groove in the concrete as shown in Fig 1.5, was sufficent to provide air entrainment and to overcome cavitation problems. This was done in 1960, and no further cavitation damage has occured after 12,000 hours of operation.

(ii) *Yellowtail Dam Spillway.*

The spillway tunnel of Yellowtail Dam comprises a 55 degree inclined reach, followed by a nearly horizontal section which was utilized in diversion during construction. The spillway was designed for a maximum discharge capacity of 2600 m^3/sec. This is sketched in Fig 1.6. According to Colgate and Jabara (1971), the maximum velocity at full reservoir level was recorded as 49 m/sec. On June 26th, 1967, the flow was released for the first time from the spillway and was varied between June 26th, to July 28th, but never exceeded 510 m^3/sec. The observation of abnormal flow conditions at the flip bucket exit on July 14th, 1967, let to the assumption that some damage had occured in the tunnel. Afterward the spillway was operated at low discharges until shut down on July 28th.

The tunnel inspection showed that large quantities of the lime stone foundation rock have been removed, and other small damage occurred along the tunnel length. Major modification of the spillway included the construction of a groove in the concrete lining as shown in Fig 1.6. After repairs and modification in 1970, a test release of 450 m^3/sec was done over five days. Further inspection revealed no evidence of cavitation damage, and it was assumed that the aeration groove provided efficient protection.

(iii) *Tarbela dam Project.*

Tarbela Dam was constructed on the Upper Indus River of Pakistan in the period between 1965 and 1975. The dam is 3049 m long and 137 m high. The spillway has a capacity of 45340 m^3/sec at full reservoir level. On the right bank there are four tunnels, approximately 1.25 km long. The tunnels are curved

in alignment through the rock in the right abutment and during construction served as the river diversion works.

According to Karaki,S Stevens,M.A and Brisbane,T.E (1977), the prototype outlet works for tunnel 3 and 4 were field tested as the reservoir filled for the first time in 1974. After approximately 2 months of operation, some damage occured to the steel liners of radial gate chamber shown in Fig 1.7. After scale model studies at Colorado State University an air slot ramp as shown in Fig 1.7 and Fig 1.8 was installed on the floor of the chute at the end of steel liner. After repairs and installment of three ramps in the outlet works, a test was done at full reservoir level as shown in Plate (I) to (V). Plate I and II show the air flow measuring procedure at Tarbela in the prototype air vents. Plate III shows a pause in prototype testing for inspection of the outlet works for cavitation damage. Plate IV and V show the aerators and outlet works in full flow.

(iv) *McPhee Dam.*

McPhee is the main storage and regulation reservoir in the Dolores Project in southwest Colorado. The Dam is an earthfill structure 82.3m high and 396m wide at the crest. The chute spillway and stilling basin are located in the right abutment of the dam. The chute is 18.3m wide, 303m long and drops 90m in elevation from the maximum water surface to the stilling basin. The stilling basin is a combined hydraulic jump/flip bucket energy dissipator. At a flow of about 425 m^3/s the jump will wash out of the stilling basin and the flow will flip into a plunge pool downstream from the basin. Fig 1.9(a) shows the section through the spillway.

According to Frizell and Pugh (1988), the aeration device location was determined by the cavitation potential and the geometry of the spillway. The

ramp is 0.91m high and 7.8m long. A ramp without a slot in the chute floor was chosen since there was adequate freeboard available and a slot would require cutting into the chute floor, thus destroying the continuity of the reinforcing steel. Fig 1.9(b) shows the configuration of the aeration device.

The prototype tests consisted of measurements and observations at three spillway discharges, 28 m^3/s, 71 m^3/s, and 142 m^3/s. Quantities which were measured included air demand through the vents and pressure distribution on the downstream side of the ramp beneath the jet. The McPhee Dam aerator has large length to thickness ratio (L/h), and apparently entrains significantly less air then would be expected from such a prototype structure. This point is under consideration during this research program.

(v) *Other Prototype Aerators.*

Throughout this thesis reference is made not only Tarbela and McPhee aerators, but also a range of other prototype structures where field measurements are well documented. These include :–

(a) *Foz–do–Areia* aerators which are shown in detail in Fig 1.10. This is an open channel chute spillway in Brazil, South America, carrying discharges up to 104.8 m^3/s (per unit width), the spillway being 400m long and 70.6m wide. Model tests (Pinto 1982) revealed aerators were required at three separate locations along the spillway length, the chosen design being a ramp and step–down arrangement as shown in Fig 1.10. Each aerator had a slightly different design, and prototype field measurements were carried out at each aerator. The air vent design is the same principle as McPhee.

(b) *Emborcacao* aerators are shown in Fig 1.11. The chute spillway has a total width of 58.5m being split in two by central wall, and carrying a total maximum discharge of 48.3 m^3/s (per unit width). Aerators were required at two locations A and B as shown in Fig 1.11, the basic design composed of a ramp of slope Φ = 1/8 and 1/7.5. Air enters by side vents and flows into a deep groove, approximately 3m deep as shown. The air flow then passes through a narrower construction 500mm wide before being entrained into underside of the jet.

(c) *Colbun* aerators are shown in Fig 1.12. This is an open channel spillway of width varying from 50m to 71.1m, discharge up to 54.7 m^3/s (per unit width), and slopes varying from 1% to 51%. Two aeration ducts were required on the steep 51% slope, the design again composed of a ramp, step–down inthe channel bed together with side rectangular air vents. Prototype measurements were carried out at both vents.

(d) *The Amaluza* aerator duct is shown in Fig 1.13. The basic design is a concrete Ogee overflow, at bed slope 66.8^0 and carrying a design discgarge of 18.4 m^3/s (per unit width). An aerator duct (or slot) was cut in the concrete surface, approximately 2m x 2.1m, with a small ramp or nappe deflector as shown.

1.3 PURPOSE OF RESEARCH.

The ten major aims of this research were as follows:–

(i) To carry out a Physical model study of an air slot ramp aerator.

(ii) To vary key parameters such as ramp angle Φ, spillway boundary roughness k_s, depth of spillway flow h, velocity of spillway flow $\bar{u}$ and underpressure under the aerator jet ($\triangle p$).

(iii) To use Laser Doppler Velocimetry to measure the turbulent flow structure at an aerator device over the range of parameters mentioned in (ii).

(iv) To measure the air entrainment rate (Q_a) and the resulting aerator jet length (L) for the range of parameters mentioned in (ii).

(v) Having obtain a significant volume of experimental data, the first priority was to establish a link between the turbulent flow structure and the rate of air entrainment.

(vi) To compare experimental findings, especially the link between turbulence and air entrainment, to the performance of McPhee Dam (USA), Tarbela Dam (Pakistan), and other prototype aerators such as outlined in section 1.2.

(vii) To compare experimental findings with other physical scale model studies and to provide a new scaling law for air slot devices.

(viii) To carry out a more fundamental study of how jets behave in the atmosphere.

(ix) To write computer program for steady–state flows in chute spillways, incorporating an air slot ramp, jet trajectory calculations, simulation of air intake structure, underpressure under the jet, effect of turbulence on aerator jet behaviour and the amount of air entrained.

(x) To provide design guidelines for future aerators in the light of research findings.

It should be noted that one key area of aerator research was not attempted because of time constraints. That was, the behaviour of entrained air downstream of the aerator device, including diffusion–advection of the air bubbles in the flow, the decrease in air concentration near the solid boundary downstream of a device, and what distance apart to place such devices.

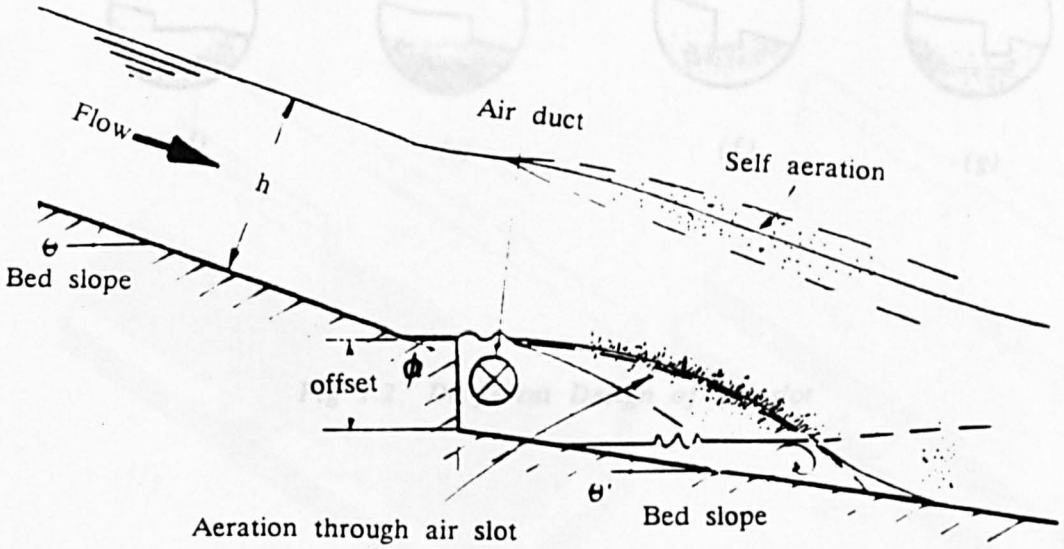

Fig 1.1 Sketch of air entrainment at air slot ramp

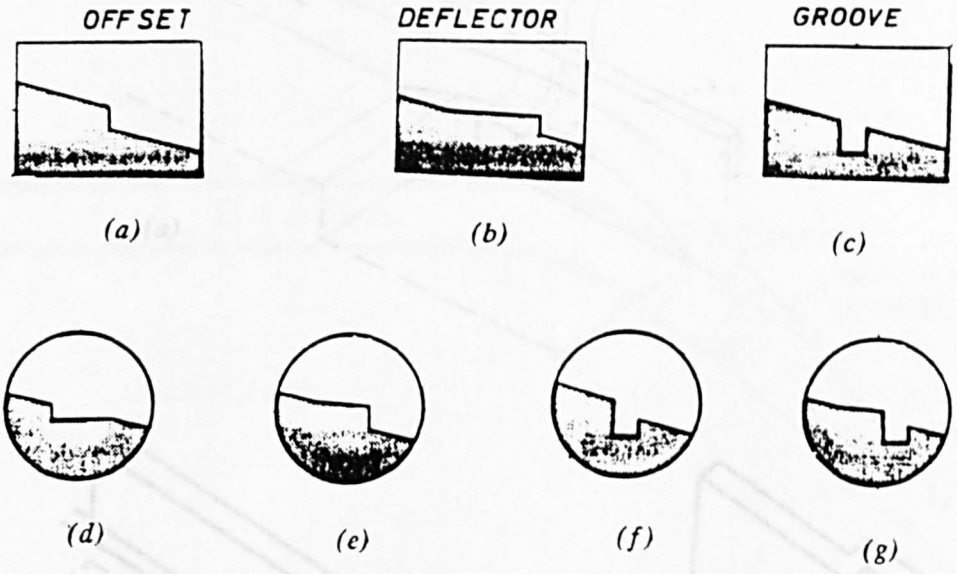

Fig 1.2 Different Design of air slot

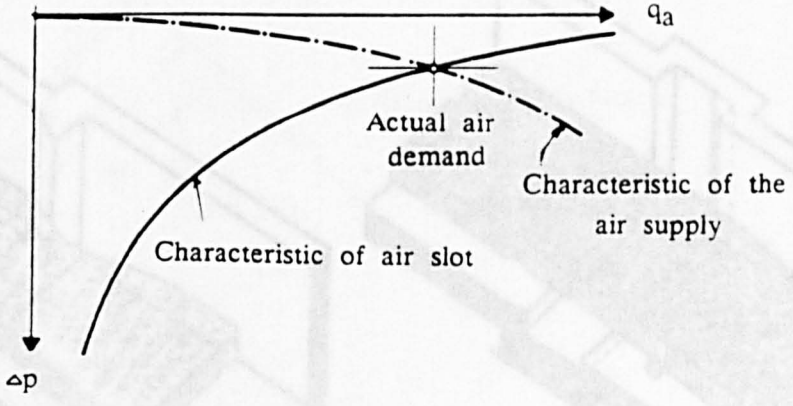

Fig 1.3 Interaction of the air supply & pumping device Characteristics

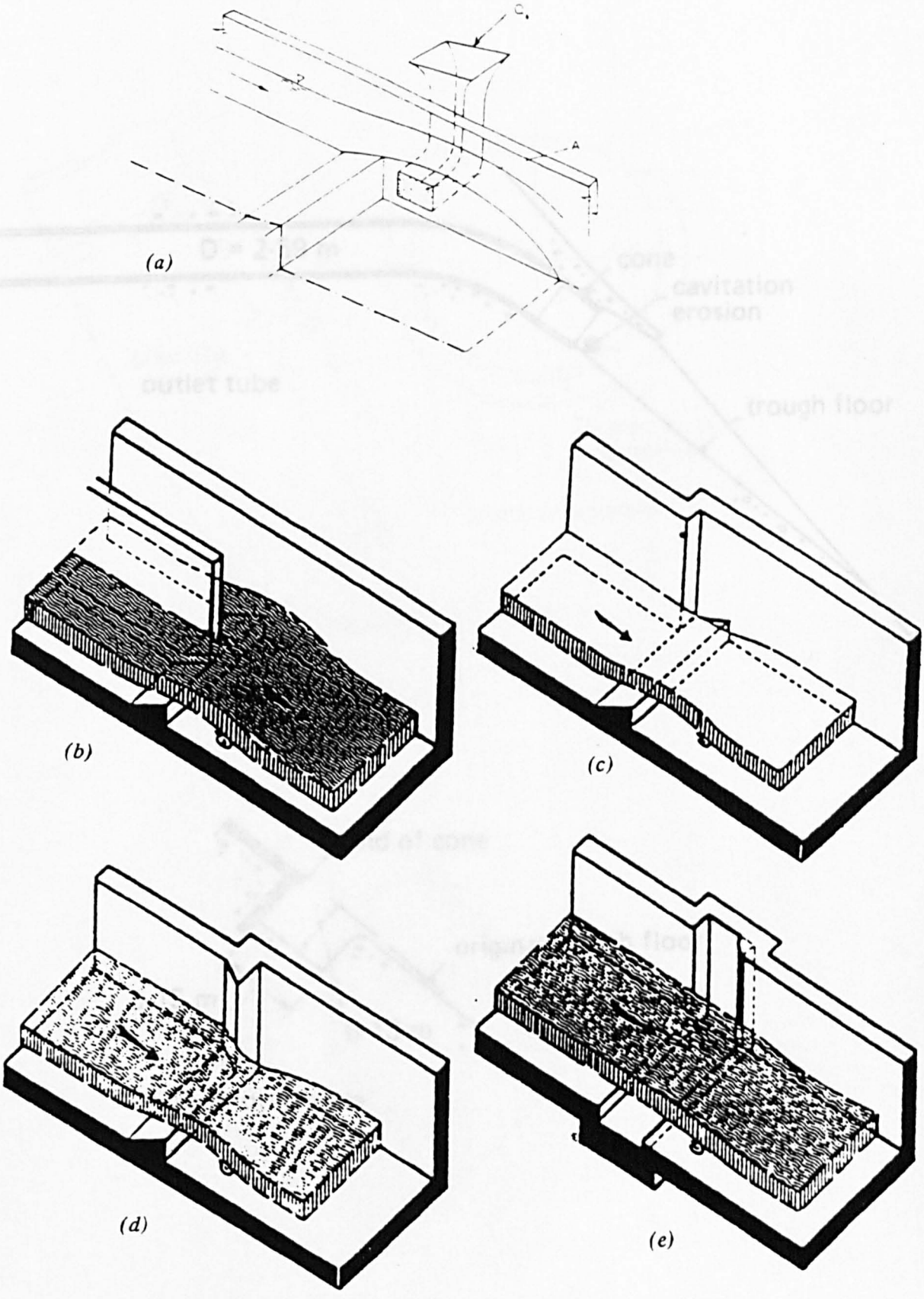

Fig 1.4 Air supply arrangements
(Low,H.S 1986)

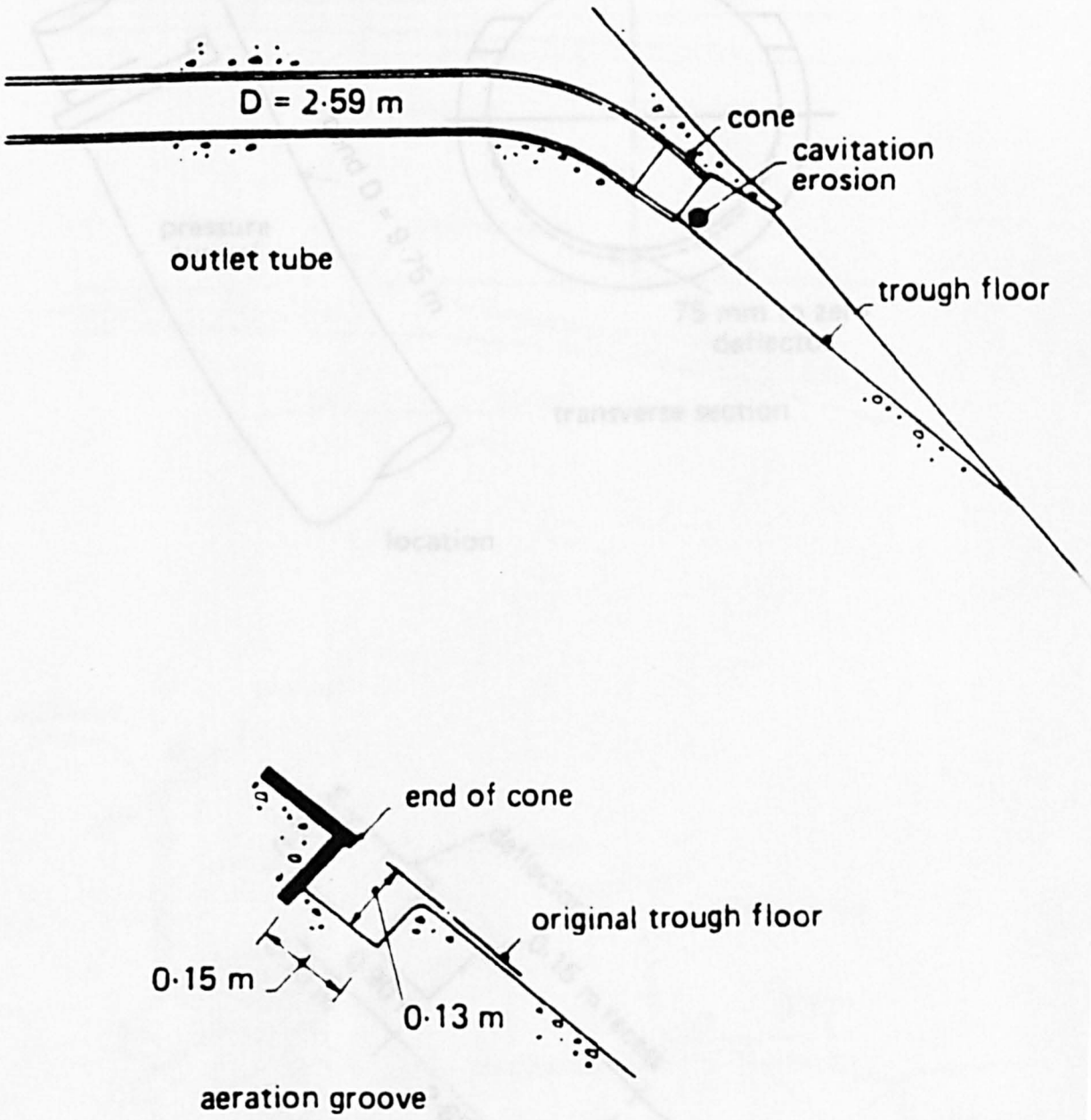

Fig 1.5 Details of Grand Coulee Dam outlet Structure
(Wagner, W.E)

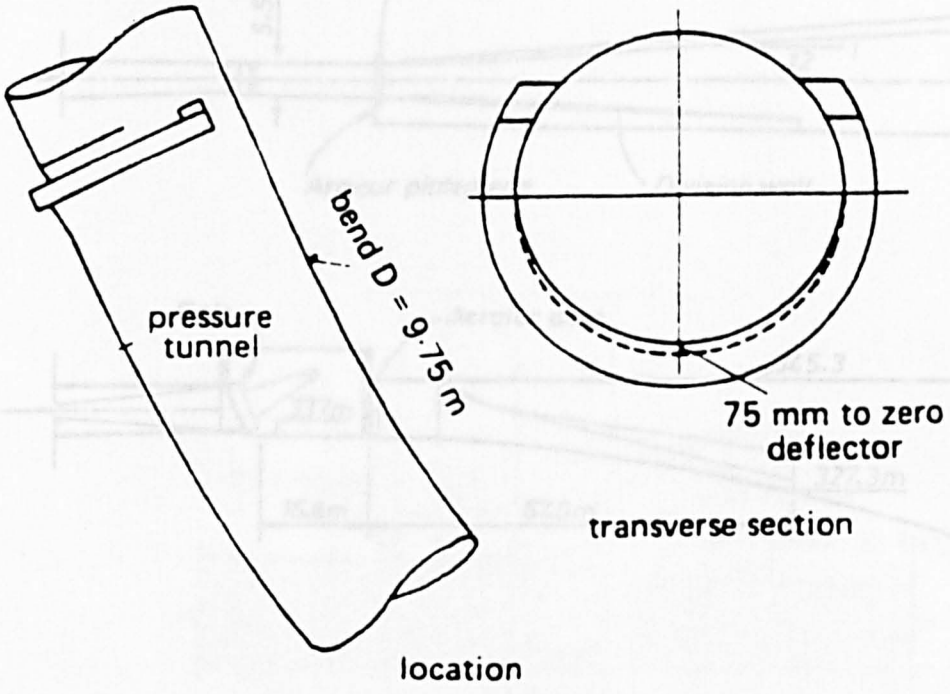

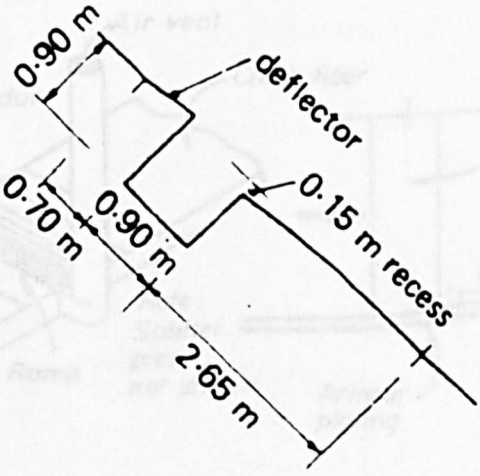

Fig 1.6 Details of Yellowtail Dam Spillway
(Colgate, D.M 1971)

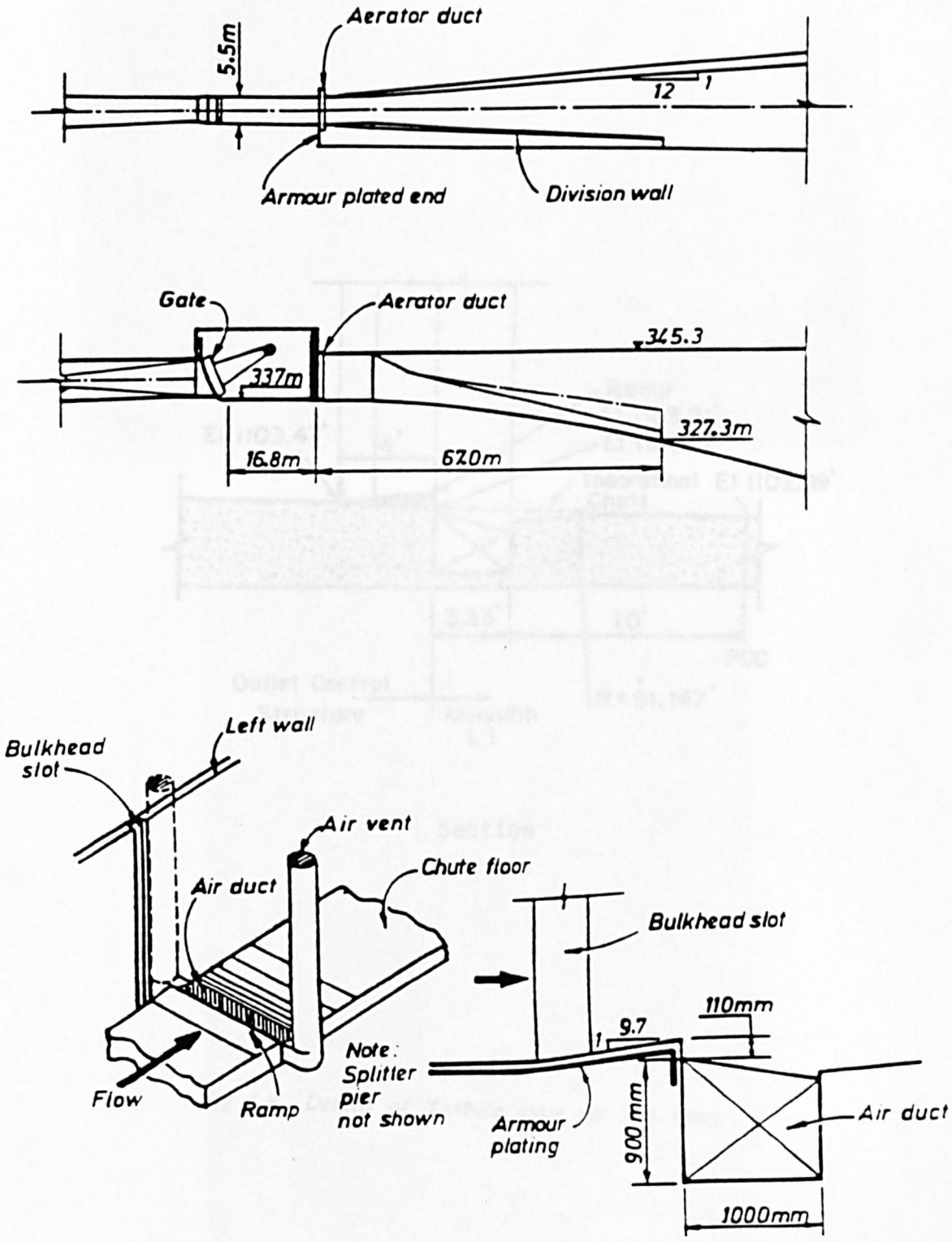

Fig 1.7 Details of Tarbela Dam outlet Works
(Karaki, S et al 1977)

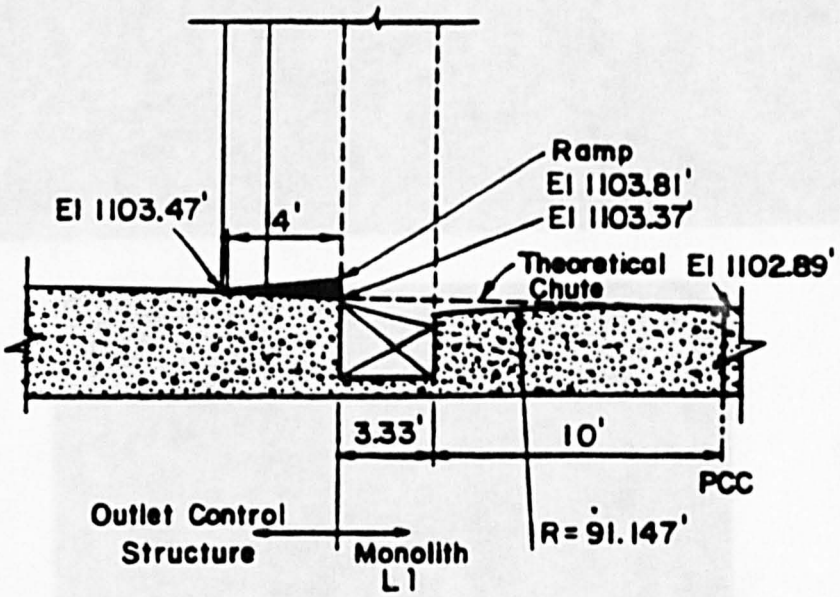

Fig 1.8 Details of Tarbela Dam air slot ramp

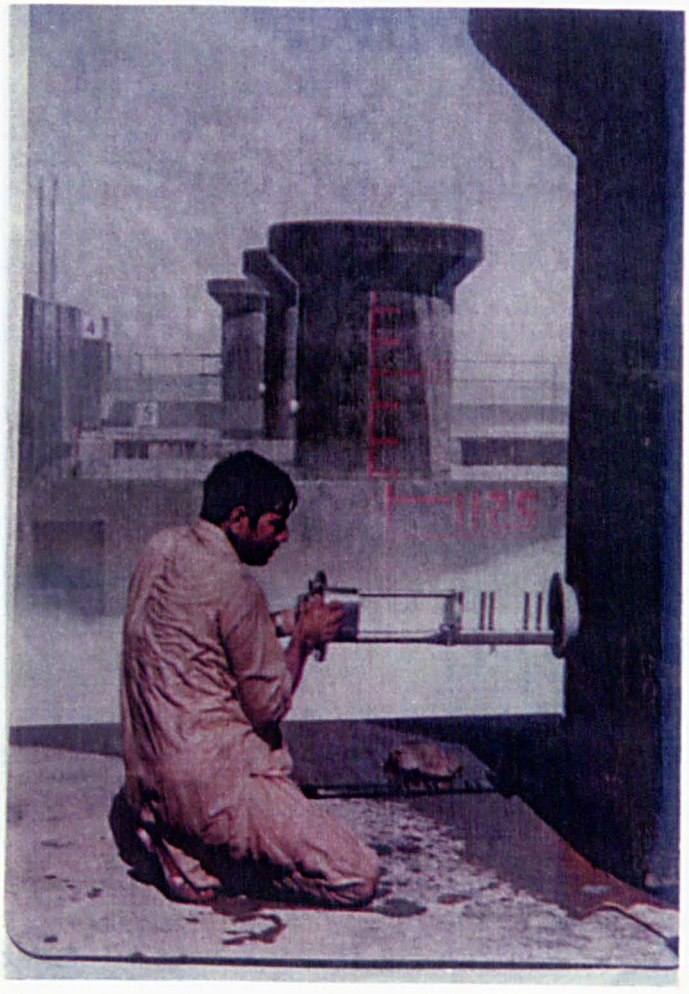

Plate I Air flow measurements at Tarbela Dam Project

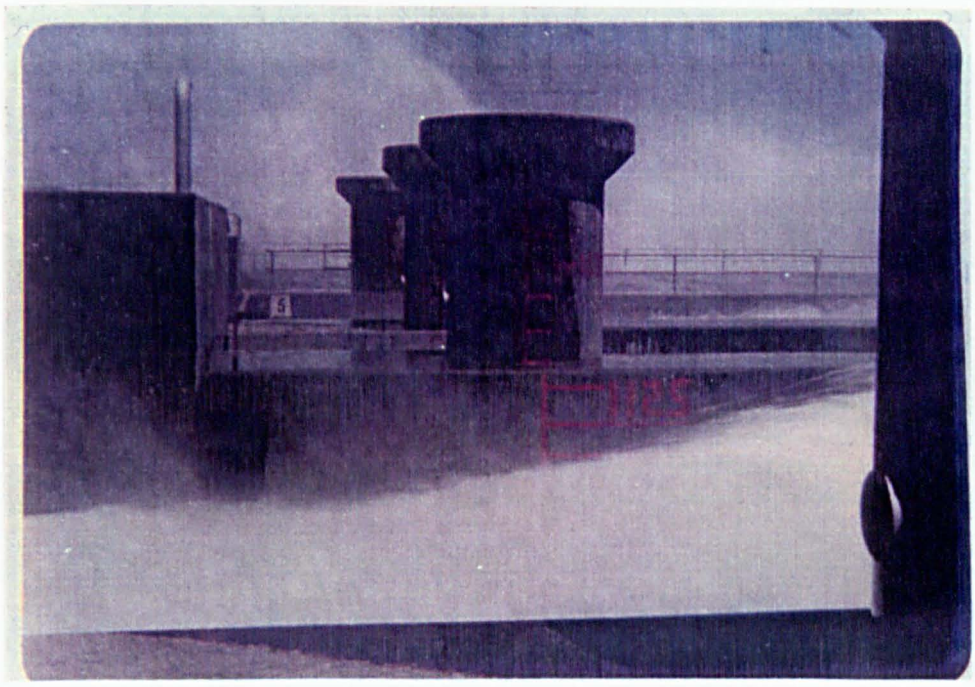

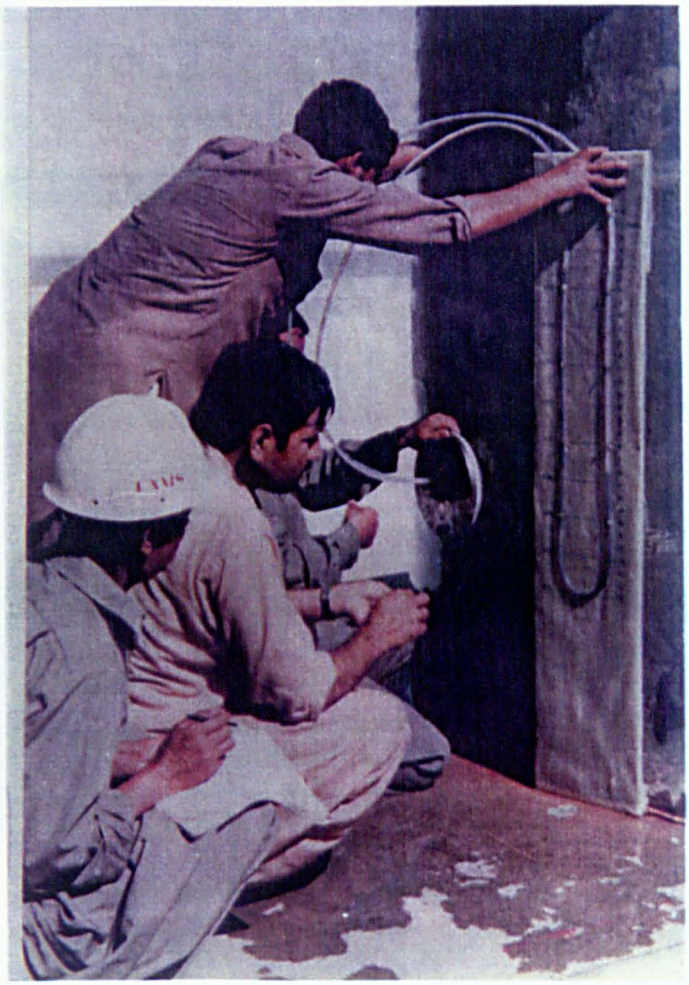

Plate II Air flow measurements at Tarbela Dam Project

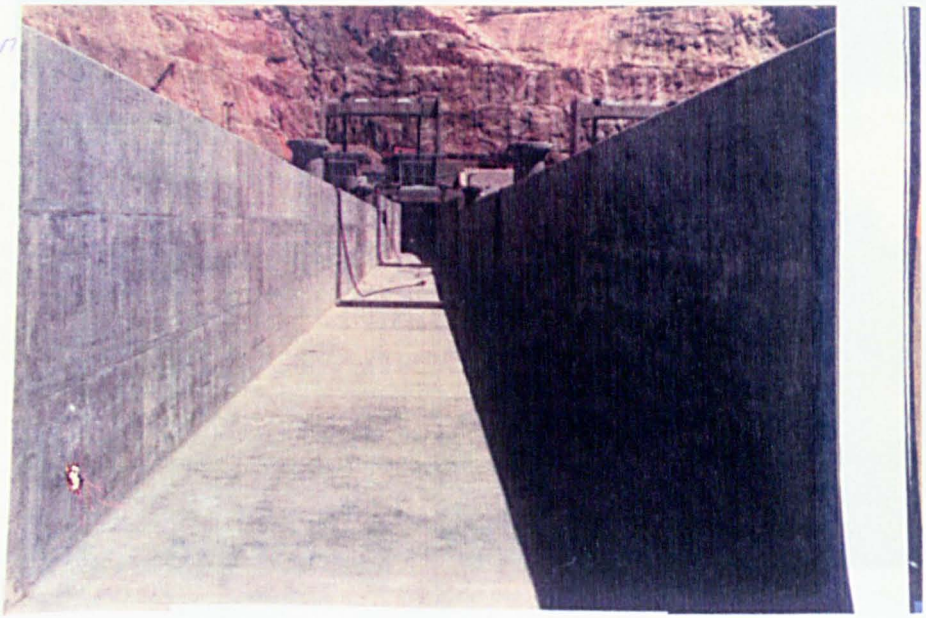

Plate III Inspection of the Outlet Works for Cavitation damage

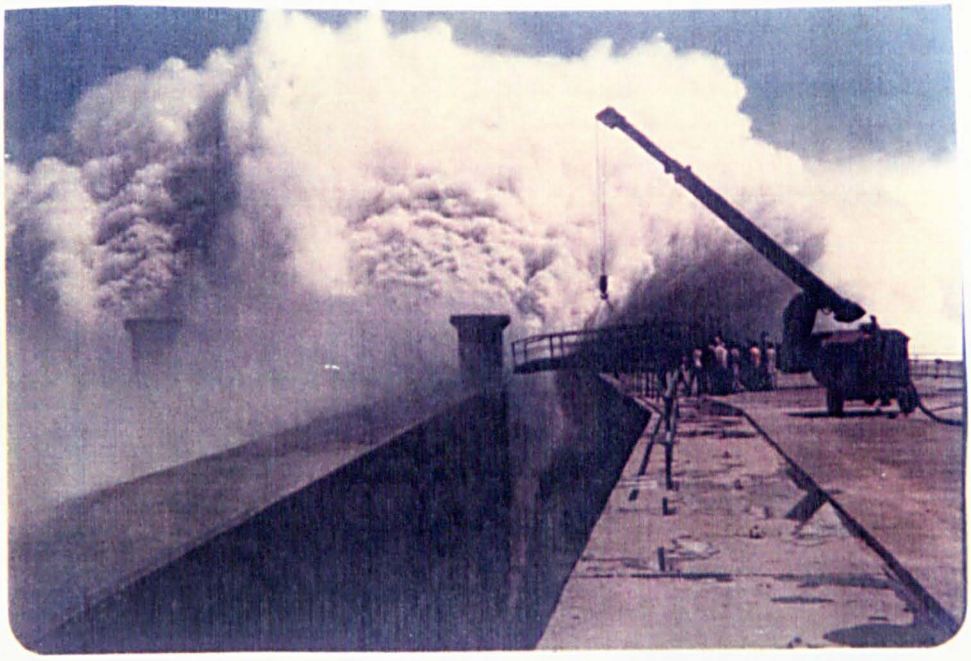

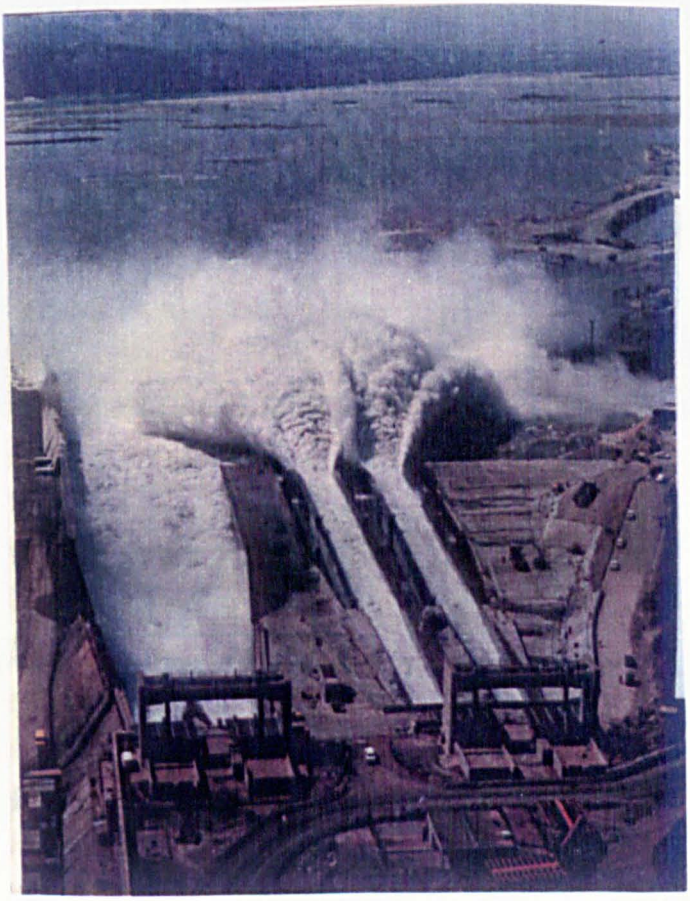

Plate IV Aerators and Outlet Works at Full Flow

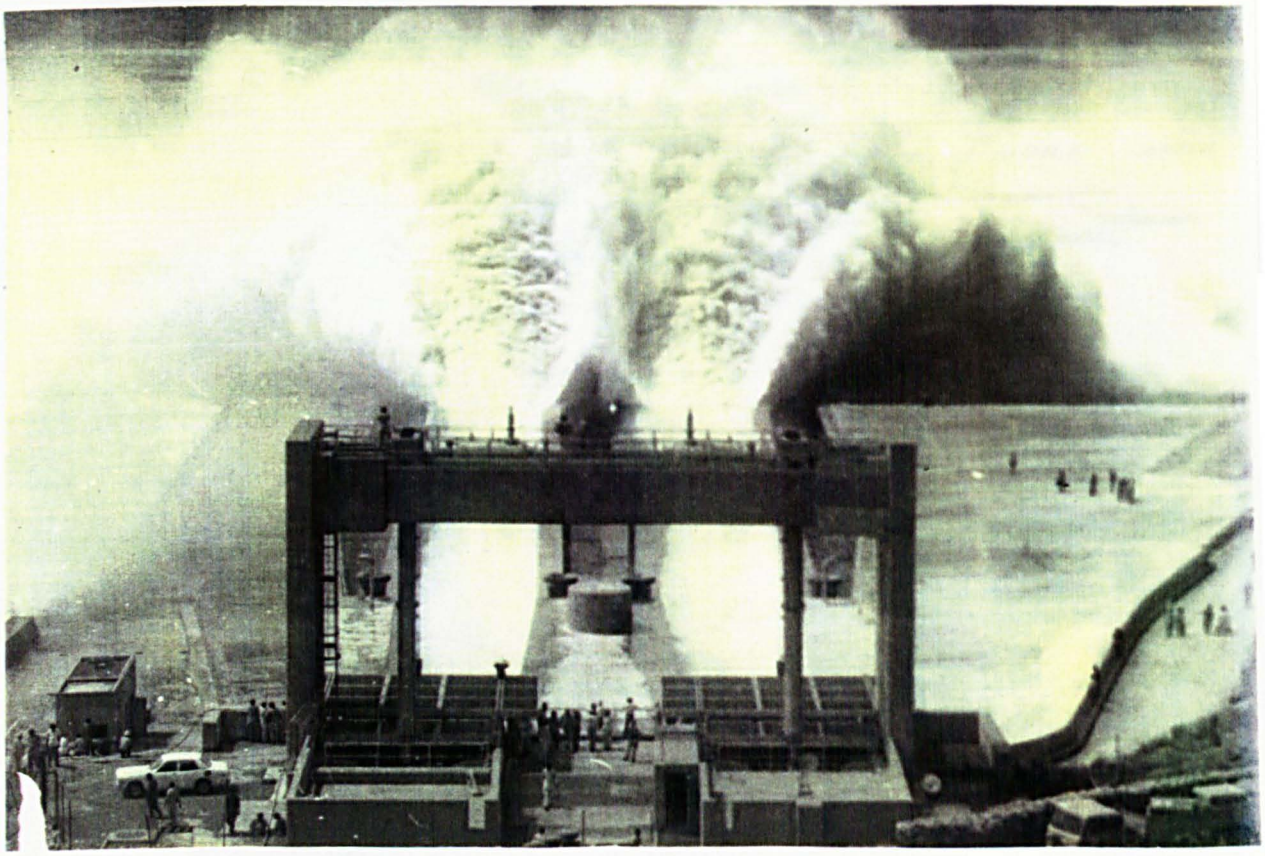

Plate V Aerator and Outlet Works at Full Flow

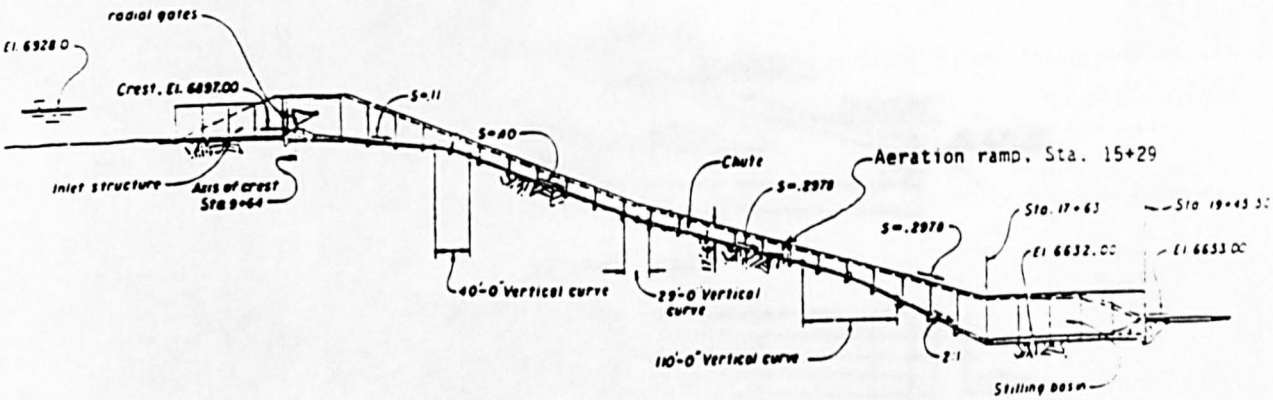

(a)

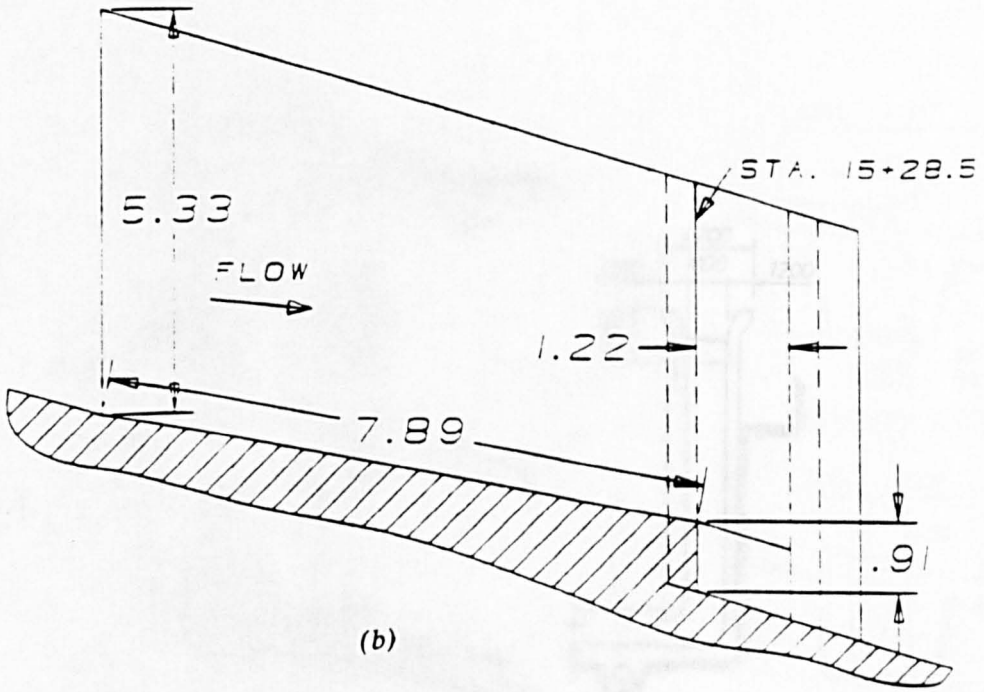

(b)

Fig 1.9 Details of McPhee Dam Spillway aerator
(Frizell & Pugh 1988)

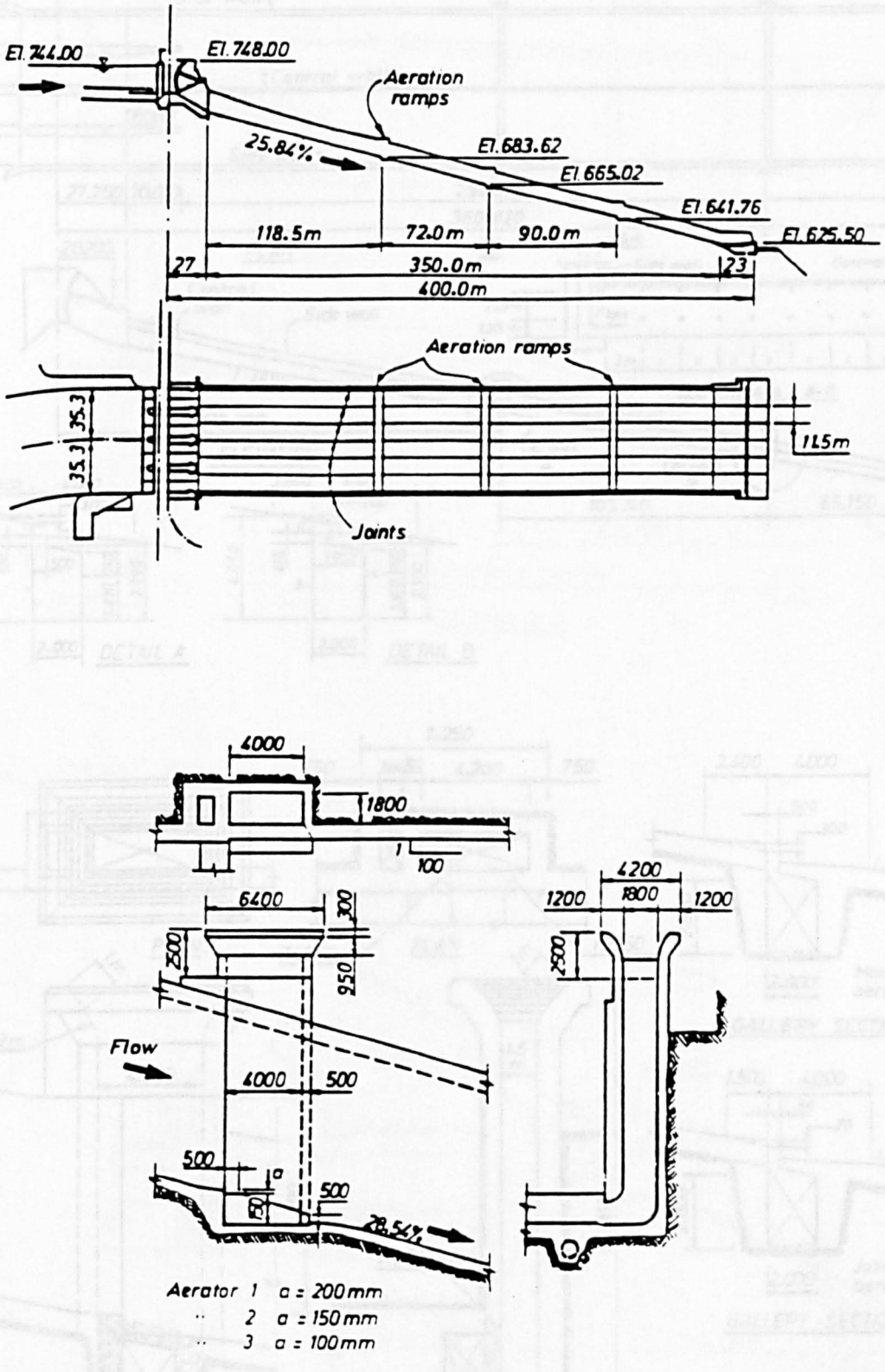

Fig 1.10 Details of Foz–do–Areia aerator geometry
(Pinto, N.L.des)

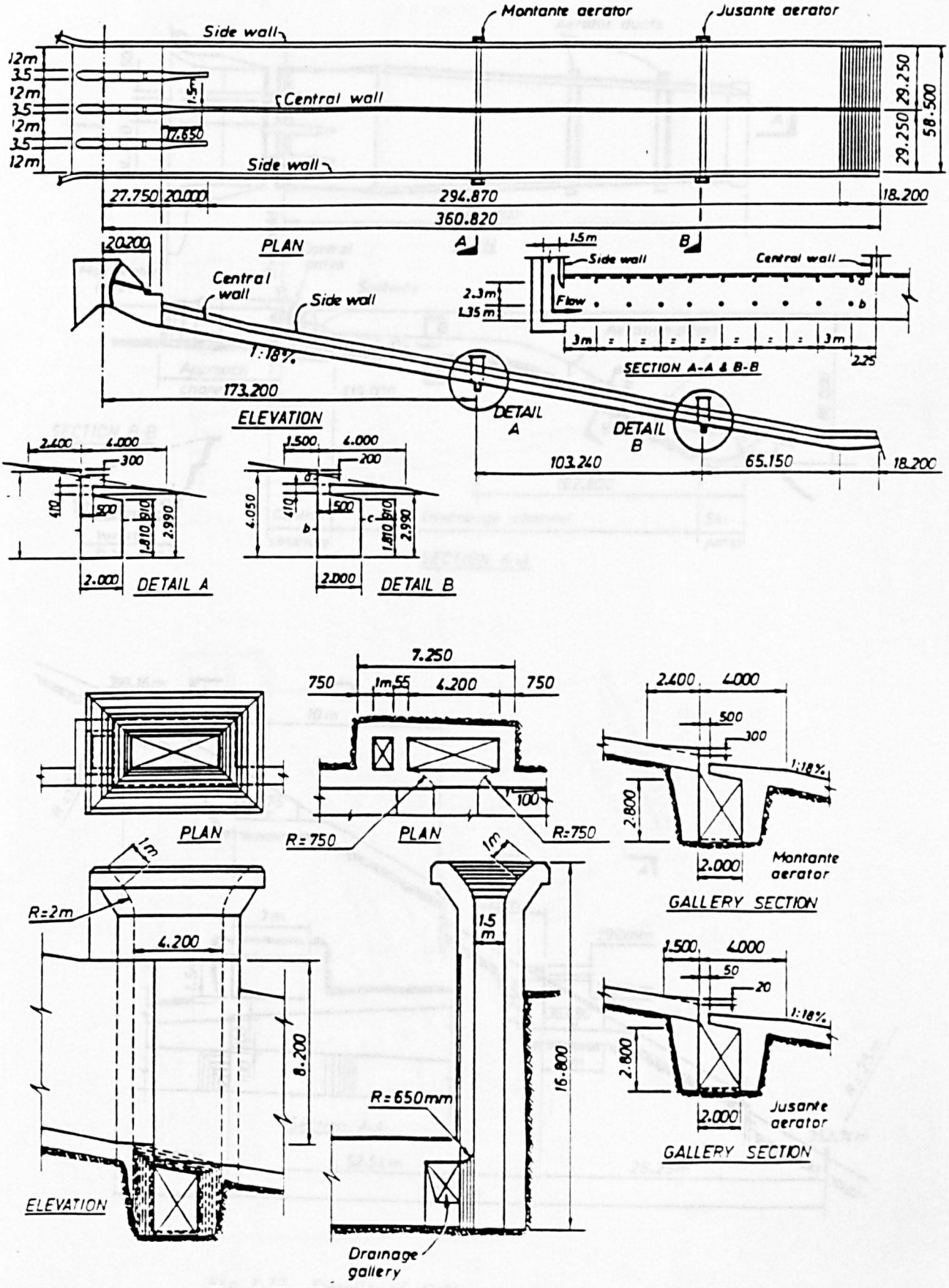

Fig 1.11 Details of Embrocacao aerator geometry
(Pinto, N.L.des)

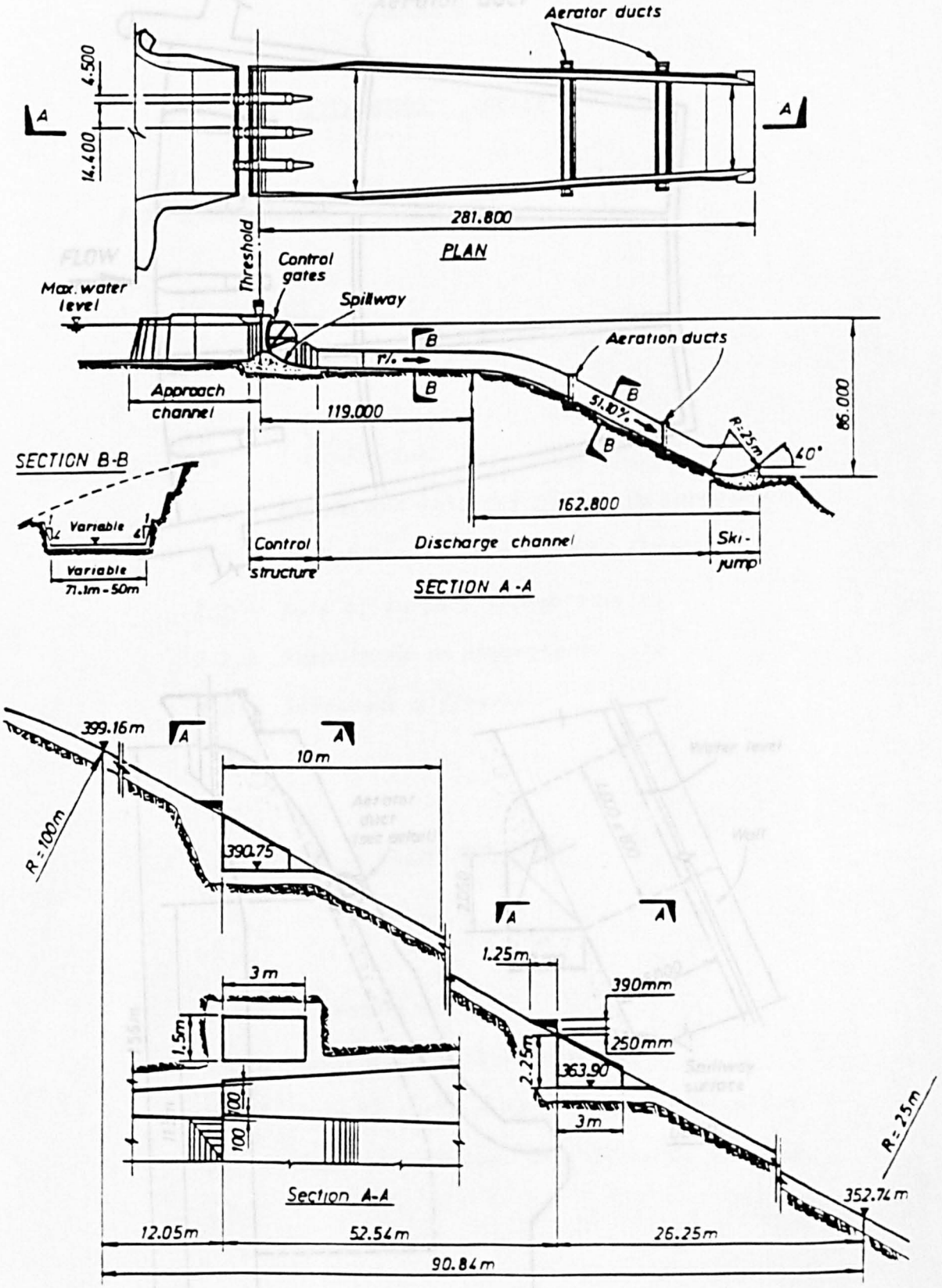

Fig 1.12 Details of Colbun aerator Spillway
(Pinto, N.L.des)

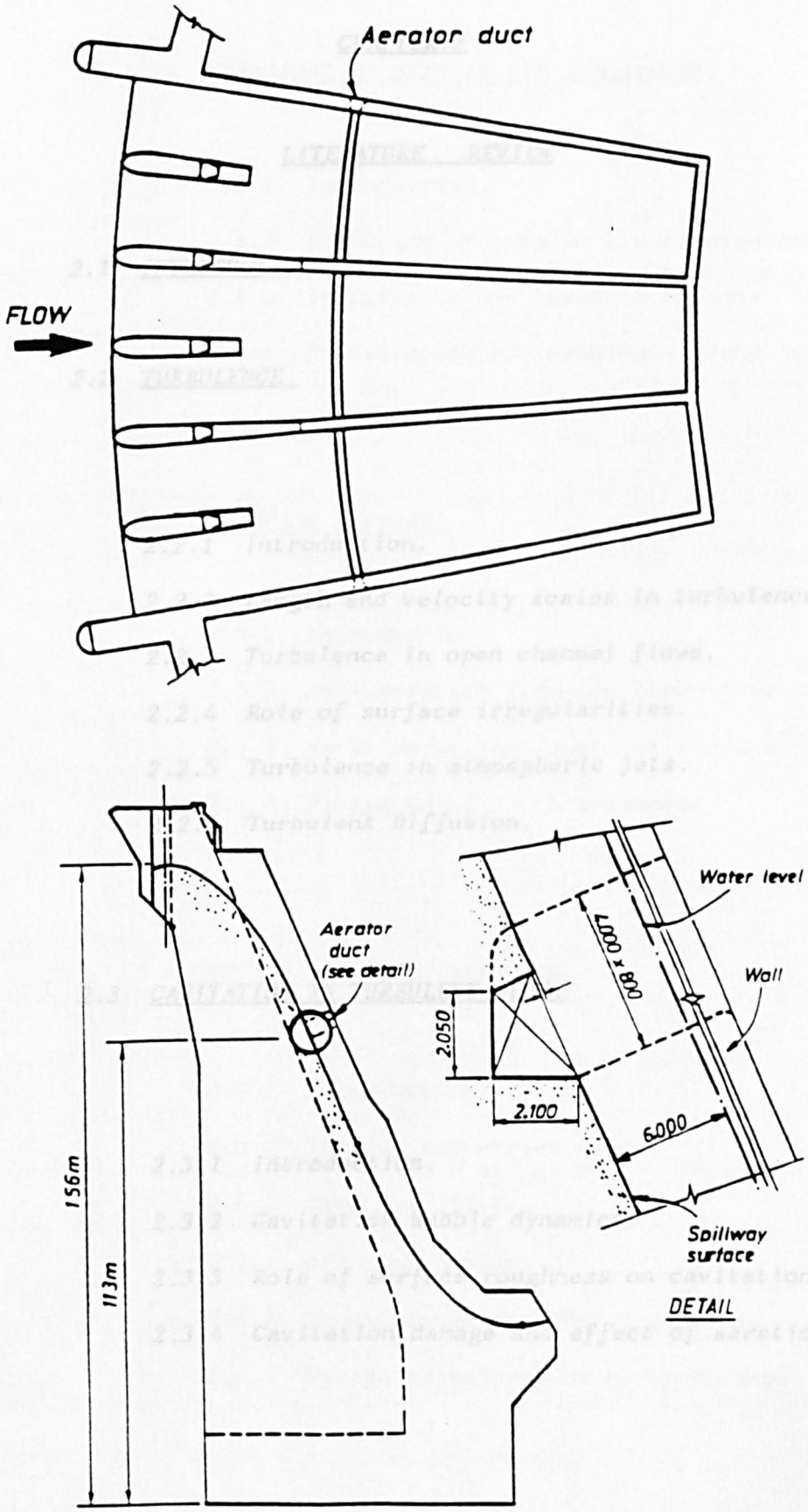

Fig 1.13 Details of Amaluza aerators Spillway

(Pinto, N.L.des)

CHAPTER.2

LITERATURE REVIEW

2.1 INTRODUCTION

2.2 TURBULENCE.

2.2.1 Introduction.

2.2.2 Length and velocity scales in turbulence.

2.2.3 Turbulence in open channel flows.

2.2.4 Role of surface irregularities.

2.2.5 Turbulence in atmospheric jets.

2.2.6 Turbulent Diffusion.

2.3 CAVITATION IN TURBULENT FLOW.

2.3.1 Introduction.

2.3.2 Cavitation bubble dynamics.

2.3.3 Role of surface roughness on cavitation.

2.3.4 Cavitation damage and effect of aeration.

2.4 BEHAVIOUR OF JETS IN THE ATMOSPHERE.

2.4.1 Introduction.

2.4.2 Diffusion of jets in the atmosphere.

2.4.3 Instability and break-up of jets.

2.4.4 Transmission of turbulence along aerator jets.

2.5 AERATION DEVICES.

2.5.1 Introduction.

2.5.2 Self aeration from the upper free surface.

2.5.3 Aeration at the lower jet surface.

2.5.4 Plunge point air entrainment.

2.6 DESIGN ASPECT OF AERATORS.

2.6.1 Introduction.

2.6.2 Typical geometries used.

2.6.3 Ramp and Offset.

2.6.4 Air vent design.

2.6.5 Longitudinal spacing of aerators.

2.6.6 Design procedure for aerator ramps.

2.7 SCALE EFFECTS IN AERATORS.

2.1 INTRODUCTION

Various flow phenomena associated with an air slot aerator are sketched in Fig 2.1. The effectiveness of such a device in eliminating cavitation damage is dependent on how much turbulence can be generated in the jet , how much air can be entrained into the underside of the jet and how much air can be kept in the region of the spillway solid boundries. The behaviour in Fig 2.1 represents a complex interplay between open channel flow turbulence structure, cavitation phenomena, jet behaviour in the atmosphere, air entrainment into jets as well as diffusion of air bubbles downstream. As well, there is a balance between the air pumping mechanism into the jet and the air vent losses (described in Chapter 1), producing an underpressure under the jet, which has the effect of shortening the jet length to the impact point and hence entraining less air.

This Chapter is not exactly a literature review. It is not intended as a review of every piece of research carried out in the field of aerators. It is more a series of five short essays, with each essay corresponding to a major flow phenomenon connected with the design of air slot aerators. The opening essays on turbulence and cavitation lead on to essays on the more practical aspects of jet behaviour in the atmosphere and aeration into jets, finally leading to an essay on the numerous model studies which have been done in the air slot research area.

It is hoped that by pulling together various strands of knowledge relating to this area, that a more fundamental understanding of aerators will be achieved, rather than simply reporting past modelling efforts.

2.2 TURBULENCE

2.2.1 *Introduction.*

The ordinary dictionary definition of turbulence as a state or condition of being violently disturbed is much too inclusive for use in technical considerations of this more common type of fluid motion. Perhaps the most generally accepted technical defination is one which Von.Karman (1936) quoted from Taylor G.I. " Turbulence is an irregular motion which in general makes its appearance in fluids, gaseous or liquid, when they flow past solid surfaces or even when neighbouring streams of the same fluid flow past or over one another." An essential feature of turbulence is the fact that the motion is random. It is continuous, however, in the sense that for very short time intervals there is a distinct correlation between velocity measured at a point and that measured at the same point a short time interval later or before. This feature is apparent in the velocity versus time plot in Fig 2.2. The lack of periodicity or the randomness is essential. Thus, vortex motions are not included in the technical definition of turbulence, although they are often be origin of turbulence. This is inspite of the fact that, qualitatively, turbulence is described as a hierarchy of eddies moving along with the mean motion.

Turbulent flows may be classified according to their homogeneity and isotropy as well as by the manner in which they occur. Even though some of the relevant terms have not, as yet, been defined here, its seems appropriate to introduce at this point such classifications of turbulent flows. Turbulence is defined as homogeneous when its scale and intensity are independent of co–ordinate position. It is further defined as being isotropic when these characteristic are independent of direction, thus the intensity of the turbulence fluctuations are same in all directions.

A useful way to consider the origin of turbulence, is to consider the transition between laminar and turbulent flows. Laminar pipe flow becomes turbulent at Reynolds number (based on mean velocity and diameter $\bar{u}\ D/\nu$) in the neighbourhood of 2000, unless great care is taken to avoid creating small disturbances that might trigger transition from laminar to turbulent flow. Early stages of transition can easily be seen in the smoke rising from a cigaratte. The turbulence can not maintain itself but depends on its environment to obtain energy. A common source of energy for turbulent velocity fluctuations is shear in the mean flow usually caused by flow over a solid boundary. If turbulence arises in an environment where there is no shear or maintenance mechanism, it decays. When the Reynolds Number decreases and the flow tends to become laminar again. Mathematically, the details of transition from laminar to turbulent flow are rather poorly understood. Much of the theory of instabilities in laminar flow is linearized theory and valid for very small disturbance. It cannot deal with large fluctuations in turbulent flow. On the other hand, almost all the theory of turbulent flow is asymptotic theory, fairly accurate at very high Reynolds number but inaccurate and incomplete, for Reynolds number at which the turbulence cannot maintain itself. A note worthy exception is the theory of the late stage of decay of wind tunnel turbulence by Batchelor (1959).

2.2.2 *Length and velocity scales in turbulence.*

One of the feature of turbulent flow is velocity fluctuations. The passage of successive turbulent eddies past a point in the flow will produce velocity fluctuations, in a given direction, as sketched in Fig. 2.2(a). The velocity at a given point will vary randomly with time. Reynolds (1894) inaugurated a statistical approach to analyse the random nature of the turbulent motions. This assumes that the flow can be divided into temporal mean and turbulent parts,

thus the velocity component in the mean flow or x direction is written :

$$u = \bar{u} + \tilde{u} \tag{2.1}$$

where $\tilde{u}$ = turbulent velocity fluctuation part.

$\bar{u}$ = mean velocity of flow.

The distribution of velocity fluctuation magnitudes has been found experimentally to follow the Gaussian or normal error curve closely. This is shown in Fig. 2.2(b). Since the standard deviation of such a distribution represents a suitable statistical measure, it is sometimes used in the definition of turbulence intensity. The root–mean–square (RMS) value of the turbulent velocity fluctuations (u') is given by :

$$u' = \left[\frac{\Sigma(\tilde{u}^2)}{n}\right]^{\frac{1}{2}} \tag{2.2}$$

where n = number of points

The ratio of this value to the mean flow velocity (i.e. the relative intensity), is termed the intensity (Tu) :

$$Tu = u'/\bar{u} \tag{2.3}$$

where u' = turbulent velocity fluctuations.

The fluctuating components are considered to vary differently in all three orthogonal directions as shown in Fig. 2.2(c). The RMS value is u' in the (x) direction, v' in the lateral (y) direction and w' in the vertical (z) direction.

When the turbulence is not isotropic, the mean value of all three components may be used, if they have been measured, as more appropriate to define the turbulence intensity.

Thus the three dimensional relative turbulence intensity becomes,

$$Tu = \frac{\sqrt{[(u'^2 + v'^2 + w'^2)/3]}}{\overline{u}} \qquad (2.4)$$

The source of the energy varies from flow to flow. In the case of jet flow it is the initial kinetic energy of the fluid. Whatever the source, the energy extraction can be ascribed to an interaction between the mean flow and large, fairly well–ordered elements of the turbulence. The smallest motions of the turbulence, with the largest shearing stresses, are responsible for the dissipation of turbulence energy and energy transfers within the turbulent flow are conceived to be a cascade of energy from the largest, energy–extracting scales of motion to the smallest, dissipating scales.

In isotropic turbulence where the mean square of the three fluctuation velocities to be equal to each other i.e $u' = v' = w'$. The source of energy in an open channel flow is the initial kinetic energy of the fluid. The kinetic energy per unit mass is given by:

$$E_k = \tfrac{1}{2}\, d/dt[\, u'^2 + v'^2 + w'^2] \qquad (2.5)$$

or

$$E_k = q^2/2 \qquad (2.6)$$

for isotropic turbulence

$$E_k = \frac{3\,(u'^2)}{2} \qquad (2.7)$$

There are usually three size of eddies available in a flow. The large eddies (which are relatively long lived) contain perhaps as much as 20% of the total kinetic energy. Medium size eddies make the main contribution to the

kinetic energy they are commonly called the " energy containing " eddies and their characteristic size is denoted by ℓ_e. Small eddies are of particular importance energetically, in that dissipation by viscous effects increases as the size of eddies diminishes. While the total energy of small eddies is not very great, they are continually being re–energized by momentum transfer from large eddies.

One of the features of well–developed turbulence is the hierarchy of scales, known as eddy length scales, with a transfer of kinetic energy from the largest to the smallest. The scale of the largest eddy motion may occupy the full depth of an open channel flow or half the diameter of a pipe flow. The scale of the smallest eddy motions, known as the Kolmogoroff micro scale, may involve tiny distances a fraction of a millimetre in diameter. At this end of the eddy length scale spectrum, turbulent energy is transferred to heat. An example of the variation of turbulent energy in each length scale is shown in Fig. 2.3(a) with energy transferred down the length scales, dissipation by viscosity and finally transfer into heat. The large variation in turbulent eddy lengths prompted Prandtl (1925) to devise a characteristic eddy length ℓ, which is akin to the mean free distance travelled by a lump of fluid before being embedded in an adjacent lump of fluid. In engineering type flows the eddy length is considered to vary in size linearly from a solid boundary. Davies (1972) shown that the eddy length ℓ, in pipe flow not far from the solid boundary is as;

$$\ell = 0.4\, y \tag{2.8}$$

where y = distance from solid boundary.

In an open channel the medium size eddy length ℓ_e varies with the turbulent velocity u' as;

$$\ell_e = (u')^3 / E_k \qquad (2.9)$$

where E_k = input kinectic energy

$E_k = 3(u'^2)/2.$ for isotropic turbulence.

thus,

$$\ell_e \propto 2(u')/3 \qquad (2.10)$$

2.2.3 *Turbulence in Open channel flows.*

Most of the work in this thesis is concerned with flow along and open channel spillway, a ramp and then a high velocity jet. It is important to have an appreciation of the nature of open channel flow turbulent structure.

To provide a realistic background for analysis of channel flows, consider the general features to be expected in turbulence near a fixed wall. The constraints applied by the wall influence the flow in opposing ways. The necessity that the tangential velocity drop to zero, coupled with the action of the turbulence, generates a very high velocity gradient. This provides a large direct dissipation and leads to further dissipation through the generation of turbulence. However, the requirement that the velocity vanish at the wall has a contrary effect: by suppressing turbulent activity very near the surface, it limits the extraction of energy from the mean flow. As the consequence of the mixed effects of the wall constraints, the turbulence structure varies profoundly across the channel. The most rapid changes occur very near the wall, the intensity reaches a peak and then falls away.

The Fig 2.4 indicates the several regions which can be distinguished in

a channel flow. The particular case considered is flow in round pipe, where the major changes are confined to the outer fifteen percent of the pipe radius. The pattern is similar for open channel flow an exaggerated scale has been used for the region very near the wall. In reality, region 1 and region 2 occupy only a very small fraction of the radius: for $R_e = 1 \times 10^5$, for example, $y_1/R \simeq 0.001$ and $y_2/R \simeq 0.01$. Despite their small extent, these inner layers influence the entire flow, since a significant fraction of the velocity variation occurs within them. Considering the regions as shown in Fig 2.4

1). The Viscous sublayer. Here the effective shear stress generated by turbulent mixing, $\tau_t = \rho\overline{uv}$ is negligible, since $v \simeq 0.0$. The variation in the mean velocity is determined by molecular viscosity, and is nearly linear, as in laminar flow. This region is also called the linear sublayer or laminar sublayer.

2). The Buffer layer. In this region the viscous and mixing stresses are of comparable magnitude. It is sometimes called the transition region, an appropriate description of its function.

3). The Fully turbulent layer. Here the flow is still dominated by the wall, but the turbulence develop sufficiently to render the viscous stress negligible. It also called the logarithmic layer because the mean velocity varies nearly logarithmically in this region.

4). The turbulent Core. In fully developed flow this is wholly turbulent but, unlike logarithmic layer, it is influenced by the constraints of the entire periphery of the pipe.

These four regions can be grouped in several ways. Region 1 and 2 comprise the viscous layer, the region in which molecular viscosity has a significant role in the generation of friction and in the extraction of energy from

the mean flow. A viscous layer of the kind described here will exist only when the wall roughness is small compared to the thickness of the layer; in practice, this description remains valid so long as the roughness elements do not project into the buffer region. Another significant grouping is the fully turbulent flow made up of regions 3 and 4. Here the largest scale of motion are independent of viscosity; they are responsible for friction generation and turbulence production, but not for dissipation, which take place in the smallest scales.

Having deduced some of the features to be expected, now consider the experimental results for pipe flow, based in measurements made by Laufer (1954). Fig 2.5(a) shows that how mean velocity $\bar{u}$ and the component intensities u', v' and w' vary between pipe wall and axis. The central part of the pipe and the thin wall layer are considered separately. For the former, the velocities are rendered dimensionless using u_c the maximum velocity at the centre of the pipe. In Fig 2.5(b), which relates to the layer where $y/R < 0.01$, the coordinates have been scaled in a less obvious way. It is argued that the wall stress τ_w and fluid viscosity μ and density ρ determine the flow in this region. From these quantities we can form the velocity and length scales can be form as:

$$u_* = \left|\frac{\tau_w}{\rho}\right|^{1/2} \quad \text{and} \quad y_f = \frac{\mu}{(\rho\tau_w)^{\frac{1}{2}}} = \frac{\nu}{u_*} \tag{2.11}$$

The first of these is called the friction velocity, or sometime the shear velocity, but its real significance is as a measure of the wall shear stress. If the postulate that τ_w, μ and ρ determine the wall layer flow is correct, the use of these scales will reduce all wall layers to the same form. Note that y_f decreases as the stress increases; thus the viscous layer becomes thinner as the flow velocity and wall stress rise.

In Fig 2.5(b) shows that the axial intensity u' is the largest over the entire flow. Its peak value is attained surprisingly near the wall, at $y/y_f \simeq 15$, which will shortly be seen to be well within the viscous layer.

On the basis of a phenomenological consideration Nezu (1986) proposed u'/u_* and w'/u_* as the universal functions in an open channel flow in the equilibrium region in which the turbulent energy production is approximately balance with the viscous dissipation.

$$\frac{u'}{u_*} = K_1 e^{-c_1 z/h} \tag{2.12}$$

$$\frac{w'}{u_*} = K_2 e^{-c_2 z/h} \tag{2.13}$$

where z/h is the non–dimensional open channel flow depth.

In these equations K_1, K_2, c_1 and c_2 are emperical constants. Nezu and Rodi (1986) found out experimentally the values of these constants as follows;

$K_1 = 2.26$

$K_2 = 1.23$

$c_1 = 0.88$

$c_2 = 0.67$

by subsituting these values

$$\frac{u'}{u_*} = 2.26\, e^{-0.88 z/h} \tag{2.14}$$

$$\frac{w'}{u_*} = 1.23\, e^{-0.67 z/h} \tag{2.15}$$

The variation of u'/u_* and w'/u_* is not linear with the depth of flow. This phenomenon could be easily understood by considering the Prandtl Mixing length theory. A German engineer Ludwing Prandtl (1925) introduced the concept

of mixing length that is, the average distance ℓ perpendicular to mean flow direction, in which a small particle moves from a faster layer to an adjacent slower layer and thus loses its extra momentum taking on the mean velocity of its surroundings. The idea is similar to the mean free path in molecular theory.

In practice the particle does not move a distance ℓ and suddenly changes its momentum, but loss of its momentum is gradual. But on the assumption that the change in velocity $\partial\bar{u}$ of the particle in moving distance ℓ in the z direction is $\ell\ (\partial\bar{u}/\partial z)$ and the average shear stress is

$$\tau_{xz} = -\rho\, u'w' \tag{2.16}$$

If the coefficient of proportionality being a number is absorbed into the ℓ term, then;

$$\tau_{xz} = \rho\, \ell^2\, [(\partial\bar{u}/\partial z)(\partial\bar{u}/\partial z)] \tag{2.17}$$

T.Von Karman (1930) introduced his so called "Similarity" hypothesis as:

$$\ell = K\, [(\partial\bar{u}/\partial z)/(\partial\bar{u}^2/\partial z^2)] \tag{2.18}$$

His analysis implies that ℓ is the ratio of the first to the second derivatives of mean velocity, where K was thought to be universal constant of 0.4, but in open channel with large Reynolds Number this relation is true for only h = 0 to h = 0.1 z as shown in Fig 2.3(b). Beyond h = 0.1 z, ℓ increases less rapidly, to a limit of about 0.088 z near the surface of flow. This is not to say that there are no larger or smaller eddies here: it means only that ℓ as defined in Equation (2.17) has this value, which is not intuitively unreasonable. At values of Reynolds number higher than 10^5, the curve remain the same as Re = 10^5 as shown in Fig 2.3(b).

2.2.4 *Role of Surface irregularities.*

In order to understand the role of roughness in the turbulent flow, consider the velocity distribution across the channel. The experimental trends as shown in Fig 2.6, shows that wall friction depends strongly on the roughness of the wall; indeed, for high Reynolds Numbers the friction is often determined the roughness alone. The factors effecting velocity in different cores are;

$$\text{a). } u \cong \tau_w, \mu, \rho, k, y \tag{2.19}$$

for the whole constant–stress layer, with k a length scale for the roughness elements;

$$\text{b). } du/dy \cong \tau_w, \rho, y \tag{2.20}$$

for fully turbulent part of the constant–stress layer; and

$$\text{c). } \Delta u \cong \tau_w, \rho, R, y \tag{2.21}$$

for the turbulent core.

Thus, so far as the fully turbulent part of the flow is concerned, the roughness merely alters the "slip" near the wall. A dimensionally homogeneous equation of the velocity with in the wall layer follows from Equation (2.19)

$$\frac{U}{u_*} = f\left|\frac{y}{y_f}, \frac{k}{y_f}\right| \tag{2.22}$$

for fully turbulent part, Equation (2.20) gives;

$$\frac{y}{u_*}\frac{dU}{dy} = \frac{y}{y_f}\frac{d(U/u_*)}{d(y/y_f)} = A \qquad (2.23)$$

where $A = 1/K$, A and K specify the rate at which turbulent mixing develops at point progressively further from the wall. Integrating Eq (2.23) gives;

$$\frac{U}{u_*} = A \ln\left|\frac{y}{y_f}\right| + f\left|\frac{k}{y_f}\right| \qquad (2.24)$$

the form of the additional function being detected by Eq (2.22). This result may equally well be written as;

$$\frac{U}{u_*} = A \ln\left|\frac{y}{k}\right| + g\left|\frac{k}{y_f}\right| \qquad (2.25)$$

The two roughness–characterizing functions are related by;

$$f\left|\frac{k}{y_f}\right| + A \ln\left|\frac{k}{y_f}\right| = g\left|\frac{k}{y_f}\right| \qquad (2.26)$$

In these generalizations of the smooth–wall logarithmic formulae the slip velocity across the viscous region is expressed as a function of the roughness. The general expression could be written as:

$$\frac{U}{u_*} = A \ln \left| \frac{y}{y_f} \right| + B \qquad (2.27)$$

Reynolds (1974) next consider the behaviour of the linked functions $f(k/y_f)$ and $g(k/y_f)$. The parameter k/y_f will increase when the scale of the roughness increases, or when the Reynolds Number rises with a corresponding decrease in y_f.

1). $k/y_f \rightarrow 0$. for an effectively smooth wall, the results are as;

$$f \left| \frac{k}{y_f} \right| \rightarrow B \qquad (2.28)$$

where B the smooth wall constant.

2). $k/y_f \rightarrow \infty$. for many forms of roughness, the friction become independent of viscosity in these circumtances, the wall being described as fully rough.

Concentrating on sand grain roughness which is often used as a standard, we see that it has little effect on the turbulent part of the flow as shown in Fig 2.7 (or on friction) when

$$\frac{k_s}{y_f} < 4 \qquad (2.29)$$

Limits of the same order exists for the roughness types. When these conditions are satisfied, the flow and surface are said to be hydraulically or aerodynamically smooth. Experimental results as shown in Fig 2.7 by Reynolds suggest that

$$\frac{k_s}{y_f} > 60 \qquad (2.30)$$

defines fully rough conditions. Looking at the effect of roughness more realistically, Reynolds realize that the drag of most roughness elements will have both viscous and inertial contributions. The effects on the flow are mixed: the roughness acts to entrain turbulent fluid and to promote turbulence near the surface; on the other hand, it carries the local effects of viscosity into the

on the surface of the protrusions. Ultimately, the inertial effect usually become dominated for the drag and for the outer flow.

2.2.5 *Turbulence in atmospheric jets.*

Having left the spillway ramp the high velocity flow in an aerator becomes a jet temporarily, until it reattaches with the spillway. The pressure on the upper side of the jet is atmospheric and the lower side is slightly sub atmospheric.

An important difference exists between jets in atmosphere and high velocity jets in a chute. For the jets in atmosphere, (ignoring resistance) the velocity gradient across the jet becomes negligible. As turbulence is generated by a velocity gradient, therefore no new turbulence will be generated in an atmospheric jet, and it will contain primarily decaying turbulence. Smaller eddies which existed in the flow will decay due to viscosity and also by the surface tension " skin " of the jet. No new smaller eddies will form. This means that eddy lengths will tend to become more uniform across a jet cross section and also, eddy lengths will become larger in the downstream direction due to gradual decay of smaller eddies. This further implies that as the largest eddy length contain less turbulent energy then at some distance downstream in the jet, the eddies will become too large and have too little energy to entrain air bubbles; which means that maximum air entrainment will occur near the start of the jet travel in the atmosphere. Thus air slot ramps which correlate quantities of air entrained linearly with jet length from the edge of the ramp, cannot be strictly accurate. Davies (1972) also showed that jet eddy lengths varies in the down stream direction (L) in the form;

$$\ell' = K (L)^{\frac{1}{2}} \qquad (2.31)$$

where L = jet length downstream from turbulence source

K = a constant

Such a phenomenon has significant implications for the turbulent energy spectrum as sketched in Fig 2.8, with significantly less turbulent energy in the micro length scales.

At the point of entry into the atmosphere the jet will contain some turbulence which will be more pronounced at the edges compared with the centre. Turbulence in the jet will immediately acts on surface tension of the jet to cause disturbance which grow in size in the axial direction. The internal fluid turbulence also spread rapidly towards the jet centre line. Because there is no turbulence generated along the jet length then existing turbulence after redistribution will be dissipated in the usual way of energy transfer down the eddy length scale. A graph showing growth of surface disturbances in the axial direction is shown from Davies (1972) in Fig 2.9.

The influence of air resistance at higher velocities magnifies the growth of jet surface disturbances. This is also true for the total trajectory length of the jet, as shown in Fig 2.10 from Novak (1984), indicating the physical reduction in jet trajectory due to air resistance. In the figure, considering flow leaving a flip bucket, it can be seen that the effect of air resistance is small whenever the exit velocity (u_0) is less than about 20 m/s, but as the velocity increases to 40 m/s the throw distance could be reduced by as much as 30% from the value given by projectile theory.

2.2.6 *Turbulent Diffusion.*

After the jump the spillway jet reattaches with the spillway bed and again become an aerated flow in an open channel. To estimate its mean air

concentration and transport process of air bubble downstream of aerator consider the turbulent diffusion and dispersion.

The transport process of turbulence in the downstream direction of a spillway chute is known as turbulent diffusion and dispersion. The two terms of turbulent diffusion and dispersion refer to the random scattering of particles in a flow by turbulent motion and scattering of particles by the combined effect of shear and transverse turbulent diffusion.

The complex mechansim of air entrainment is outlined in section 2.5.3 for the underside of a jet in steep chutes. Air bubbles, once entrained into the flow are diffused into the depth of the flow by turbulence, transfering momentum from faster layers to slower and air bubble from high concentration areas to lower. Bubbles are resisted in this process by the combination of an increasing pressure with depth as well as the natural buoyancy of the air bubbles. An equilibrium condition is considered to be set– up some distance downstream from the plunge point. At equilibrium condition the distribution of air bubble concentration with depth usually takes the form of an error function, erf y, given by;

$$\text{erf } y = \frac{2}{[\pi]^{\frac{1}{2}}} \int_0^{\infty} e^{-y^2} \, dy \qquad (2.32)$$

This will be discussed in more detail below.

Before the variation of air concentration with depth can be determined, it is useful to obtain estimates of the mean air concentration $\bar{c}$, or alternatively the mean ratio of air flow to water flow, $\bar{\beta}$. The two are related by

$$\bar{c} = \bar{\beta} \; / \; (\; 1 + \bar{\beta} \;) \qquad (2.33)$$

where β = air entrainment ratio (q_a/q_w)

And by dimensional analysis the mean air concentration should be related to the

parameters,

$$\bar{\beta},\ \bar{c} \ =\ f\ (\ Fr,\ Re,\ We,\ k/h,\ \theta,\ \rho_a/\rho_w\ ) \qquad (2.34)$$

where Fr = Froude Number $u/[gh]^{\frac{1}{2}}$

We = Weber Number $u/[\sigma/\rho h]^{\frac{1}{2}}$

Re = Renolds Number uD/ν

k/h = relative roughness

θ = bed slope

According to Haindl (1984) the simplest models for the mean air/water ratio $\bar{\beta}$ in a cross section in spillway chute flow are given in the form,

$$\bar{\beta} \ =\ K\ Fr^2 \qquad (2.35)$$

$$\bar{\beta} \ =\ K\ (\ u^2/gR\ ) \qquad (2.36)$$

where R is the hydraulic radius of the flow and K varies from 0.00355 to 0.0104 depending on the bed roughness. This realtionship has been modified by Yevjevich and Levin (1953) into the form,

$$\bar{\beta} \ =\ 0.175\ Fr^2\ \psi\ \alpha \qquad (2.37)$$

where ψ is a bed friction coefficient ($n\sqrt{g}\ /\ R^{1/6}$) (n = Mannings "n" value) and α a coriolis coefficient for aerated flow. As a rough guide it can be taken as unity.

Rao and Gangadharaiah (1971) produced a simple relationship for the mean air concentration in the form,

$$(1 - \bar{c}) = \frac{1}{(K\ Fr^{3/2} + 1)} \qquad (2.38)$$

which corresponds to $\bar{\beta} = K\ Fr^{3/2}$. In this case, the Froude Number is defined as the non aerated Froude Number of the spillway flow, $u/\sqrt{gh}$, and the value of K varied from 0.012 to 0.024 depending on the roughness at the channel bed floor. For smooth channels $K \simeq 0.012$ and for rougher channels $K \simeq 0.024$. Further work revealed the value of K to vary linearly with Mannings n value,

$$K = 1.35\ n \qquad (2.39)$$

Falvey (1979) proposed a relationship for the mean air concentration taking into account the influence of surface tension (Weber Number), and by assuming the turbulent stresses to scale with Froude Number. He proposed,

$$\bar{c} = 0.05\ Fr - \frac{(\sin\theta)^{\frac{1}{2}}\ We}{63\ Fr} \qquad (2.40)$$

where $Fr = u/[gh]^{\frac{1}{2}}$ for unaerated flow

θ = spillway bed slope

and $We = u/[\sigma/\rho h]^{\frac{1}{2}}$ for unaerated flow.

Falvey limited the use of Eq (2.39) to values of $\bar{c}$ less than 0.6.

After estimating the mean air concentration in the flow, we may now consider the variation of air concentration with depth. An air bubble in a turbulent spillway chute flow will have four main forces acting on it, namely inertial, drag, buoyancy and turbulent eddy transport forces. Consider an example sketched below in high velocity flows that inertial and drag forces are in balance, then the net rate of air bubble transport towards the wall will depend on the net

balance between turbulence transport force and the buoyancy force ($f_b \cos\theta$).

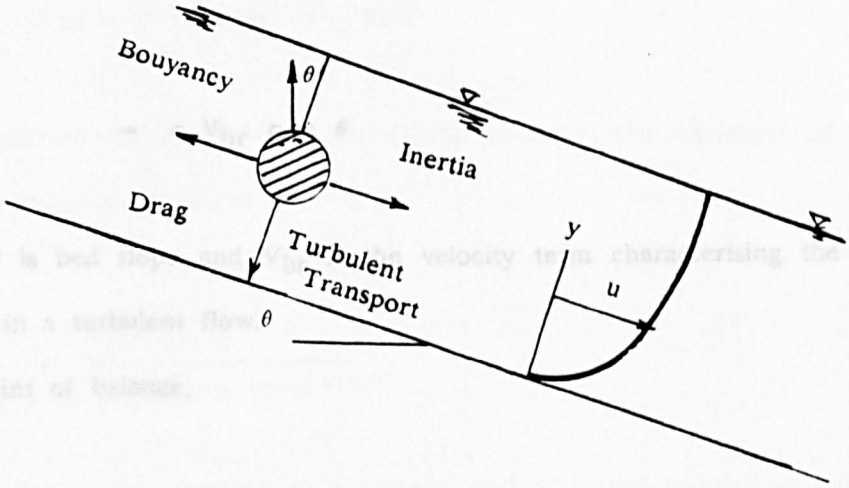

In effect it is more suitable to carry out the analysis considering the fluid as a pseudo– fluid of variable density $\rho(y)$ or variable air concentration c(y). Thus the net transfer of momentum per unit area is given by;

$$\tau = \rho \epsilon \, du/dy \qquad (2.41)$$

where τ = shear stress

ϵ = eddy diffusity

For the parallel case with air bubble concentration in the pseudo– fluid,

$$\tau = \rho \epsilon \, dc/dy \qquad (2.42)$$

or in terms of volumetric turbulent transport per unit area

$$\tau/\rho = \epsilon \, dc/dy \qquad (2.43)$$

For an equilibrium condition to exist, the downward volumetric transport rate per unit area should be balanced by the upward transport rate per unit area generated by bubble buoyancy, normal to the plane of flow.

$$= c V_{br} \cos \theta \qquad (2.44)$$

where θ is bed slope and V_{br} is the velocity term characterising the bubble rise velocity in a turbulent flow.

At a point of balance,

$$\epsilon \, dc/dy = c V_{br} \cos \theta \qquad (2.45)$$

This has been expressed in terms of pseudo–density in the form;

$$- \epsilon \frac{d}{dy} [\rho_w(1-c)] = \rho_w(1-c) V_{br} \cos\theta \qquad (2.46)$$

where density $\rho(y)$ replaces concentration c(y), and $\rho_w(1-c)$, where ρ_w is unaerated water density.

Wood (1983) produced same relationship as equation 2.46 for the variation of air concentration with depth. It was based on the conservation equation in the equilibrium flow regime,

$$-\epsilon \, d/dy \; [\rho_w(1-c)] = \rho_w(1-c) V_{br} \cos\theta \qquad (2.47)$$

where ϵ is the vertical eddy diffusivity (estimated by a constant value in the case), and V_{br} the equivalent for air bubbles of the fall velocity of sand grain in sediment studies,

Wood approximated V_{br} to,

$$V_{br} = K\, y_{90}\, c \tag{2.48}$$

$$y_{90} = y \text{ (where } c = 90\%) \tag{2.49}$$

Substitution of Eq (2.47) into Eq (2.48) revealed the variation of air bubble concentration with depth to be,

$$c = \frac{\beta}{\beta + e^{-\gamma \cos\theta\, y'^{2}}} \tag{2.50}$$

where β and γ are constant of integration and y' is the normalized depth y/y_{c90}. Wood outlines a method for solving Eq (2.49) by solving the empirical constants β and γ and determining the values of c at any depth from a knowledge of the mean air concentration $\bar{c}$.

2.3 *CAVITATION IN TURBULENT FLOW.*

2.3.1 *Introduction.*

A brief description of cavitation phenomena below is based on information contained in a comprehensive textbook by Knapp et al (1970) and surveys produced by different researchers such as Falvey (1990).

Cavitation is the name for a change of phase in water from liquid to vapour by the formation of small voids. If the voids are filled with water vapour than it is known as vaporous cavitation, or if the voids are filled with gases coming out of the solution then the process is called gaseous cavitation. Vaporous cavitation happens when the pressure locally is reduced to the vapour pressure of

water, which at 15 °C to 20 °C is around 2Kpa or 0.2 m head of water absolute. An understanding of the cavitation process can be obtained by examining the process of boiling. When water is heated the temprature increases which result in increase in its vapour pressure. When the vapour pressure equals the local pressure, boiling will occur. At the boiling point, water is changed into water vapour. This change first occurs at localized points within the water and it is observed as small bubbles. The temprature at which boiling occurs is a function of pressure. As pressure decreases, boiling will occur at lower and lower tempratures. Since the pressure is a function of elevation, boiling occurs at lower tempratures at higher elevations as shown in Fig 2.11.

The irregularities on the spillway surface will, in a high speed flow, cause small areas of flow separation where the pressure will be lowered locally. If the velocities are high enough the pressure may fall to below local vapour pressure of the water and vapour bubble will form. When these are carried downstream into high pressure region the bubble collapses, giving rise to high pressure pulses known as cavitation. Three main types of cavitation are, travelling cavitation, fixed cavitation, and vortex cavitation. In travelling cavitation the cavities form in area of low pressure, and travel with the flow and collapse in the region of high pressure. In fixed cavitation the flow separates from the body and forms a quasi−steady cavity attached to the boundary, and in vortex cavitation the cavitiesform in the core of fast rotating eddies.

The mechanism is still not fully understood, but is illustrated schematically below(overleaf). At the point of separation in the high velocity flow, eddies and vortices form with low pressure cores, with local pressures reaching as low as vapour pressure (−10m gauge).

When the cavitation bubbles move to an area of higher pressure they begin to collapse. The voids represent small pockets of great potential energy which, when they collapse near a solid boundary, water cannot enter the void as easily from the boundary side as from the other side. Therefore the collapse is

not symmetric, so water entering from one side forms a micro jet of such intensity that it can cause damage to stainless steel.

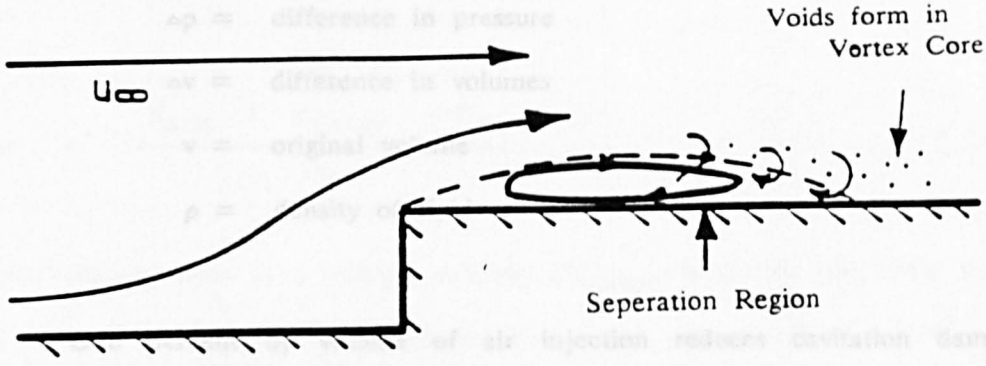

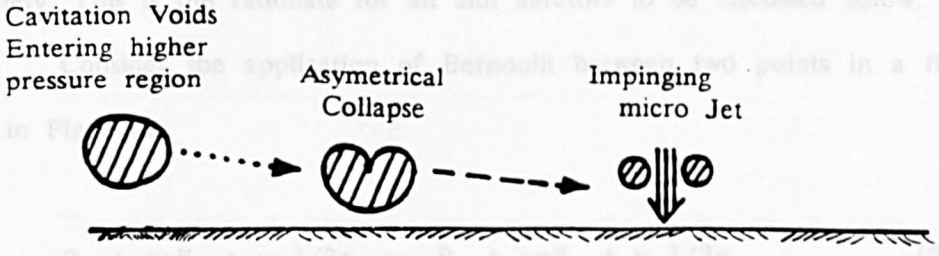

Numerical analyses and high speed photographs have shown that the cavity bubble collapse has similar characteristics to water hammer phenomena. The resulting dynamic pressures on the wall being similar in magnitude to water hammer pressures, and the micro jet velocities being of the order of 100 to 1000 m/s. The micro jet velocity impinging on the solid boundary (V) is closely related to sonic velocity C,

therefore,

$$V \propto C \propto \sqrt{K/\rho} \qquad (2.51)$$

where K = $\Delta p.v/\Delta v$ (Bulk Modulus)

Δp = difference in pressure

Δv = difference in volumes

v = original volume

ρ = density of fluid

One percent by volume of air injection reduces cavitation damage dramatically in a similar relation to the reduction in the velocity of sound. An air injection of 7% near the solid boundary removes the risk of cavitation completely. This is the rationale for air slot aerators to be discussed below.

Consider the application of Bernoulli between two points in a flow as shown in Fig 2.12

$$P_1 + \rho g Z_1 + v_1^2/2g = P_0 + \rho g Z_0 + v_0^2/2g \qquad (2.52)$$

where P_1 = instantaneous static pressure

P_0 = absolute static pressure

ρ = density of the liquid

v_0 = local velocity of fluid

If the absolute pressure falls below a critical value of vapour pressure P_v the flow will rapidly form cavities. An important requirement for dynamic similarity between different tests in the cavitation index of the flow defined as:

$$\sigma = \frac{(P_0 - P_v)}{\frac{1}{2}\rho V_0^2} \qquad (2.53)$$

where P_v is the vapour pressure of the liquid.

The cavitation index can also be written in terms of a head,

$$\sigma = \frac{H_{atm} + H_{gauge} - H_v}{V_0^2/2g} \qquad (2.54)$$

For open channel flow in a straight spillway, H_{gauge} is simply the static water head ($h\cos\theta$). On curved boundaries, centrifugal pressure H_r ($= hV_0^2/gR$) should also be included, where R is the radius of curvature, the + ve sign for a concave slope, and − ve for a convex slope.

$$\sigma = \frac{H_{atm} + H_{static} + H_r - H_v}{V_0^2/2g} \qquad (2.55)$$

The incipient cavitation index σ_i is the value of σ below which cavitation will occur in any particular geometry. The U.S.B.R has published some values of incipient cavitation number below which will cavitation occur, and are listed in the Table below.

Cavitation indices for chute spillways.

$\sigma_i > 1.7$	No cavitation
$0.58 < \sigma_i < 1.7$	Provide 1:5 chamfer
$0.36 < \sigma_i < 0.58$	Provide 1:10 chamfer
$0.25 < \sigma_i < 0.36$	Provide 1:20 chamfer
$\sigma_i < 0.25$	Provide aeration ramp
$\sigma_i < 0.12$	Revise concept

In spillway design where high velocities and low cavitation indices are to be expected it is necessary to compute the cavitation index at each point along the spillway and over a wide range of discharges up to the design discharge. An example of McPhee Dam has shown in Fig 2.13.

Inspection of Eq (2.55) reveals that the local velocity v_0 must increase to large values before cavitation is likely. Assumming H_{atm} in Eq (2.55) is 10.3 m, and H_{static} and H_r and H_v cancel each other out approximately, then for σ_i of 1.7 from above Table, the mean velocity v_0 is around 12m/s for cavitation. For a σ_i of 0.25, the mean flow velocity would require to be of the order of 28 m/s, this being a rough idea of the velocity of flow requiring an aerator ramp. The vapour head value H_v can be taken as low as 0.2 m but a more conservative approach is to take H_v as 1.5 m approximately. This is because tiny air bubbles come out of solution at heads around 8.5 m relative to the atmospheric, (or + 1.5 m absolute) and such bubbles can act as nucleii for cavitation.

2.3.2 *Cavitation bubble dynamics.*

Water does not spontaneously change from the liquid to the vapour state as either the temprature is raised or the pressure is decreased. Water which has been distilled and filtered many times can sustain extremely large negative pressures without cavitation. Cavitation and boiling are both observed to begin at the location of impurities in the flow or at minute cracks on a smooth boundary or at tiny air bubbles coming out of solution. It is not known if particles of dirt serve as nuclei for the vaporization. However, Katz (1984) observed that the appearance of visible cavitation in flowing water was always preceded by the occurrence of a swarm of microscopic bubbles in a small region of the flow field. The importance of the bubble as cavitation nuclei has been known for a long

time, and all of the theory for the formation of cavitation, has been built up around the existence of microscopic bubbles in the flow.

Spherical bubble stability was studied by Daily & Johnson (1956). The force balance on a hemispherical section of a bubble shown in Fig 2.14 containing water vapor and a gas is given by:

$$\pi r^2 (P_v + P_p) = 2 \pi r \epsilon + \pi r^2 P_0 \qquad (2.56)$$

or

$$P_v + P_p = 2\epsilon/r + P_0 \qquad (2.57)$$

where r = radius of bubble

P_0 = reference pressure (of fluid surrounding the bubble)

P_p = partial pressure of gas

P_v = vapour pressure of water

ϵ = interfacial surface tension

Assuming the gas bubble obeys the perfect gas law:

$$P_p = \frac{n_m R_u T_k}{v_g} = \frac{n_m R_u T_k}{\pi r^3} = \frac{m R_g T_k}{\pi r^3} \qquad (2.58)$$

where m = mass of gas in Kg

n_m = number of mole = m/M

M = mass of mole of gas, kg

R_g = engineering gas constant

R_u = Universal gas constant

T_k = temprature absolute in (kelvin^3)

v_g = volume of gas

Eq (2.57) becomes:

$$P_0 - P_v = A_g/r^3 - 2\epsilon/r \qquad (2.59)$$

where A_g is constant for a specific of gas, mass, and temperature,

i.e $A_g = mR_gT_k/\pi$

Eq (2.59) gives the solution of a family of curves for various quantities of air in the bubbles as shown in Fig 2.14. These curve represent the equilibrium condition for the vapour bubble containing air. The stability of the bubble can be investigated by examimining the full differential equation of the bubble as reported by Knapp (1955). The equation is:

$$\pi \left[r \frac{d^2r}{dt^2} + 1.5 \left| \frac{dr}{dt} \right|^2 \right] = -\left[P_0 - P_v + \frac{2\epsilon}{r} - \frac{A_g}{r^3} \right] \quad (2.60)$$

If the right side of the equation is positive, the bubble will grow. Conversely, if the right side of the equation is negative, the bubble will decrease in diameter. Thus, the right side of the equation represents a force that causes the bubble size to change. The bubble stability is determined by the algebric sign of the right side of the equation. The condition of neutral stability; (known as the locus of neutral stability) occurs when the right side of Eq (2.60) is equal to zero. This curve, shown on Fig 2.14, is defined by:

$$P_d = P_0 - P_v = -4/3 \left[\epsilon/r_c \right] \quad (2.61)$$

where:

P_d = difference between minimum fluid pressure and vapour pressure.

r_c = critical radius = $1.5 \left[m R_g T_k / \pi \epsilon \right]$

This theoretical development provides an insight into the mechanics of the formation of cavitation. For example, if a bubble with a small free gas content is convected into a low-pressure region, the bubble diameter will remain about constant. However, if the pressure decreases enough for the bubble dimensions to reach the critical radius, the bubble size will increase explosively as shown in Fig 2.14. The rapid expansion is only possible through vaporization of the water with

little contribution from the expansion of the gas. Therefore, the process is one of vaporous cavitation. Conversely, if a bubble containing a large free gas content is convected into a low–pressure region, the bubble diameter will continually expand without ever reaching a critical radius. In this case, the bubble expansion is primarily due to expansion of the gas. This non–explosive growth of the bubble in which vapour pressure is never reached is characteristic of gaseous cavitation.

2.3.3 *Role of Surface roughness on cavitation.*

Upon examining the flow surface of a hydraulic structure, the flow surface irregularities or the surface roughness can be characterized usually as one of the following two main categories.

1). Singular (isolated) roughnesses.

2). Uniform distributed roughnesses.

Singular roughnesses are irregularities in a surface that are large relative to the surface irregularities from where they protrude. A uniformly distributed roughness is a surface texture that does not contain singular roughnesses. Between these two extremes is a category of moderate height singular roughnesses in combination with a uniformly distributed roughness which has not been systematically studied. Sometimes, singular roughness are referred to as local asperities. Typical examples of these in hydraulic structures include:

a). Offset into–the–flow as shown in Fig (2.15a).

b). Offset away–from–the–flow, as shown in Fig (2.15c,d).

c). Voids or grooves, as shown in Fig (2.15e).

d). Protruding joints as shown in Fig (2.15g).

In all these cases, cavitation is formed by turbulence in the shear zone; the action is produced by the sudden change in flow direction at the irregularity. The location of the shear zone can be predicted from the shape of the roughness.

Depending upon the shape of roughness cavitation bubbles will collapse either within the flow or near the flow boundary.

Fig 2.15(f) depicts cavitation above a distributed roughness. Cavitation occurs within the flow because of turbulence generated by the roughness of the boundary. The cavitation location is not predictable; however, cavitation always occurs with in the body of the flow for distributed roughnesses.

The earliest studies of singular asperities concentrated on cavitation characterisitcs at misalignments. Investigation of into–the–flow offsets were presented as design curves by Colgate and Elder (1961) and are shown in Fig 2.16. Data were obtained in a test facility which was 102 mm high by 152 mm wide. The test section was located immediately downstream from a specially designed transition that produced an extremely thin boundary layer. For the larger offsets, the data are in error because blockage effects were not taken into account. The families of curve were corrected for blockage and expressed in a more compact form in by Colgate (1977). The condensed form was made possible by expressing the curves in terms of a cavitation index referenced to the plane of the offset, as in equation below:

$$\sigma_b = (P_n - P_v)/ \rho (V_{b/2})^2 \qquad (2.62)$$

where P_n = Pressure in free stream in plane of offset.

P_v = Vapour pressure of water.

V_b = Free stream velocity in plane of offset.

ρ = density of water.

The technique permitted all the characteristics of the sudden offsets to be drawn on a single plot as shown on Fig 2.17(a). For chamfers having length to height ratios less than 5:1, the cavitation characteristics are a function of the offset height. A similar plot, as shown in Fig 2.17(b) was made for rounding the

leading edge of the offset to an ellipse.

Jin et al (1980) also conducted studies of offsets and chamfers in a water tunnel. The test section was 200 mm by 200 mm and located immediately downstream of the convergent section. The boundary layer was extremely thin as with the tests by Colgate. Jin found that the incipient cavitation index, σ_i, for chamfers could be expressed according to following empirical relationship for $L_c/H > 5.0$:

$$\sigma_i = 1.8 \left[L_c/H \right]^{-0.7} \qquad (2.63)$$

where:

H = height of offset as shown in Fig 2.18

L_c = run of chamfer as shown in Fig 2.18

σ_i = incipient cavitation index

Zharov (1978) conducted experiments wherein the boundary layer thichness was 9 to 11 mm. Offset heights of 3, 6, 10 and 15 mm were tested. By using a cavitation index referenced to the height of the offset, as in Eq (2.62), investigations showed the index was independant of relative height and Reynolds Number. The Reynolds Number tested ranged from 10^3 to 10^6. A comparison of results, by the three investigators, shown on Fig 2.18 reveals that the experiments of Colgate & Jin agree closely and actually compliment each other. For small chamfer ($L_c/H \leqslant 1$), Zharov's results also agree with Colgate & Jin. However, for large chamfers, the cavitation characteristics differ. One reason for the difference in the results might be that Zharov tested with a significant boundary layer thickness. Another method of accounting for the velocity distribution within the boundary layer was based on the frozen streamline theory of Holl (1960). Holl proposed that the relationship between the cavitation index without a boundary layer was related to the cavitation index with a boundary layer by:

$$\sigma_k = \sigma_u \left[V_a/V_u \right]^2 \qquad (2.64)$$

where V_a = characteristic velocity

V_u = reference free stream velocity

σ_k = cavitation index based on average velocity over height of offset.

σ_u = cavitation index without a boundary layer

The characteristics velocity is the average velocity over the height of the offset and is defined as:

$$V_a = \left[\frac{1}{H} \int_0^H V_y^2 \, dy \right]^{\frac{1}{2}} \qquad (2.65)$$

where H = height of the offset

V_y = velocity at height y

V_a = characteristic velocity

y = vertical co-ordinate (distance from boundary)

for the one-fifth power law distribution of velocity, Eq (2.64) result in :

$$\sigma_k = 0.71 \, \sigma_u \, [H/\delta]^{0.4} \qquad (2.66)$$

where , δ equals to boundary layer thickness.

Clearly, Eq (2.66) demonstrates that the data of Zharov should lie below that of Colgate and Jin, when all three are compared using a cavitation index that is based on a thin boundary layer.

This approach, (by Holl), should permit tests with and without a boundary layer to be referenced to a common base. For example, the cavitation index with a thin boundary layer should be able to be predicted from Eq (2.66) using data taken from tests with a boundary layer. However, this approach has yielded only average results. Therefore, attempting to characterize the cavitation index only by some representative velocity within the boundary layer appears too simplistic.

Other studies of isolated asperities have used a better method to account for the velocity distribution in the boundary layer. Arndt et al (1979) concluded that cavitation index should be a function of the relative thickness of the boundary layer, the Reynolds Number of the flow, and a boundary layer shape factor. This is expressed as:

$$\sigma_i \propto f \{ H/\delta , R_h , S \} \tag{2.67}$$

where:

R_h = Reynolds Number based on height of offset and free stream velocity.

S = Boundary layer shape parameter.

The boundary layer shape parameter, S is defined as the ratio of the displacement thickness to the momentum thickness:

$$S = \delta_d / \delta_m \tag{2.68}$$

The displacement thickness δ_d, is defined as:

$$\delta_d = \int_0^{\delta} \left[1 - \frac{V_y}{V_b} \right] dy \tag{2.69}$$

The momentum thickness δ_m, is defined as:

$$\delta_d = \int_0^{\delta} \frac{V_y}{V_b} \left[1 - \frac{V_y}{V_b} \right] dy \tag{2.70}$$

where V_b equals free stream velocity in the plane of the offset.

2.3.4 *Cavitation damage and effect of aeration.*

Several mechanisms are usually involved in damage of hydraulic structures. For example, when cavitation forms because of a surface irregularity, surface damage will begin at the downstream end of the cloud of collapsing cavitation bubbles. After some time, an elongated hole will form in the concrete surface. As time progresses, the hole will get larger with high velocity flow impinging on the downstream end of the hole. This flow creates high pressure within the minute cracks around individual pieces of aggregate or within temperature cracks which form during the curing process. Pressure differentials between the impact zone and the surrounding area are created which can cause aggregate, or even chunks of concrete, to be broken from the surface and swept away by the flow. This damage process can be accurately regarded as erosion; whereas, the loss of material due to cavitation is not strictly erosion. Here, erosion is defined as an abrasion, dissolution, or transport process. As erosion from high velocity flow continues, reinforcing bars can become exposed. The bars may begin to vibrate which can lead to mechanical damage of the surface.

At the USBR. Glen Canyon Dam, concrete lumps were found attached to the end of the reinforcing steel as shown in plate 2.1. At this stage, high velocity flow acting on the lumps, rip reinforcement bars from the concrete even though the steel may be imbedded as deep as 150 mm. After the structure's lining has been penetrated, erosion can continue into the underlying foundation material. When damage penetrates the liner, the integrity of the structure is the first concern. As high velocity flows passes over a surface, a potential exists for the surface to be damaged by cavitation. Various factors that determine whether or not the surface will be damaged include:

a). cause of cavitation

b). location of damage

c). intensity of the cavitation

d). magnitude of the flow velocity

e). resistance of the surface to damage

f). air content of the water

g). length of time the surface is exposed

The resistance of a surface to damage depends upon several factors including the ultimate strength of the material, ductility, and homogeneity. It is not clear which strength characteristics of a material are significant when evaluating the surface resistance. With metals, surface deformation caused by the impact of collapsing bubbles produces tensile forces within the material. On concrete surfaces, tensile forces are also possibly the significant factor. Thus, tensile strength and not compressive nor shear strengths may be more important parameter. The properties of strength and ductility can be combined into one parameter known as resilience, Rao et al (1981). Resilience is defined as the area under the stress–strain curve of a material. Fig 2.19 shows a curve of relative damage developed for materials conventionally used in construction of hydraulic structures. Fig 2.19 shows that carbon steel was found to be damaged about 7 times faster than stainless steel: aluminum or copper is damaged about 25 times faster than stainless steel.

It is now well known that air bubble injection into a cavitation prove environment will spectacularly reduce the likelihood of cavitation damage. Estimates of around 7% air concentration are said to eliminate cavitation damage completely.

For low values of air concentration, damage has been found to vary inversely with the air concentration. Perterka (1955) conducted some air concentration tests between 8×10^{-6} and 20×10^{-6} parts of air per parts of water. At high air concentrations, of around 0.07 parts of air per parts of water, damage was found to be completely eliminated over a 2–hour test period in a

venturi–type test facility. In 1945, assumptions were that air injected under a water prism would " acts as a cushion between the high–velocity water and the tunnel lining", Bradley (1945). It was further reasoned that " the air would aid in relieving the subatmospheric pressure ". Neither axiom is correct.

Currently, two theories explain the mitigating effect of aeration on cavitation damage. One theory is based upon the presence of noncondensable gases in the vapor pocket that cushion or retard the collapse process. The second theory is based upon the change in sonic velocity of the fluid surrounding the collapsing vapor bubble due to the presence of undissolved air. Of the two current theories, about the effect of undissolved air in water, the theory regarding the change in the sonic velocity seems to be most valid. Studies have shown that the diffusion of undissolved gases into a vapor cavity proceeds at a very slow rate relative to the rate of vaporization. Because the vapour cavity growth time is short, it seems unlikely for sufficient gas to be present (in the vapor cavity) to significantly effect the rate of collapse of the cavity or the pressure generated by the collapse.

Whatever the real physical processes involved, it is now clear that aerators present the most economical method of removing cavitation probability, and their operation and design is the subject of this thesis.

2.4 *BEHAVIOUR OF JETS IN THE ATMOSPHERE*

2.4.1 *Introduction.*

It is clear from Fig 2.1 that the main function of an aerator ramp is to form a turbulent jet which springs clear of the spillway surface forming an almost atmospheric jet. The upper surface of the jet is at atmospheric pressure, although the under surface will be sub–atmospheric by virtue of the fact that air

is sucked into the cavity under the jet.

There are various aspects of jet behaviour which need to be considered in any fundamental review, especially aspects which relate to the type of jets occurring in aerator ramp designs.

(i) The jet trajectory, in the presence of turbulence, sub atmospheric pressures under the jet, and air resistance. This will be discussed in section 2.6.3 and in Chapter 7.

(ii) The ability of the jet to spread, to become unstable, break–up, and the ability to transmit turbulence along its length. These will be discussed in this section.

(iii) Aeration in aerator jets including free surface aeration on the upper surface, forced free surface aeration on the lower sub–atmospheric surface, and plunge point aeration at the jet reattachment point on the spillway surface. These will be the subject of section 2.5.

2.4.2 *Diffusion of jets in the atmosphere.*

When a high velocity jet enters the atmosphere (from a nozzle or orifice) it will invariably spread laterally, in a similar manner to a water jet entering a large body of water. The rate of spread of water jets in water is well established, Albertson et al (1948) and usually produces spreading angles of the order of 6^0 to 14^0 (10% to 25%) depending on the nature of the jet entering.

The rate of spread of water jets entering air is less well known and is complicated by the fact that gravity acts to contract the jet size due to acceleration. A study of jet spread was carried out by Withers (1991) and Ervine

(1987) with the results shown in graph in Fig 2.20. A long smooth tapered nozzle produced a half angle of jet spread less than 1%, whereas an orifice plate with no upstream flow strighteners produced spreads of around 4% to 5%. In all cases the rate of spread was found to be directly related to the turbulence level within the jet.

The physical mechanism of jet spreading is not well known and at least three ideas have been put forward, sketched below.

Ervine and Falvey (1987) argued that the spread of the outer edge of the jet is directly proportional to w'/u. This was backed up by turbulence measurements and photographs.

Hecker (1988) argued that the edge of this jet takes the form of eddies or waves which increase in size with increasing distance from the origin. This is similar to increasing eddy sizes in jet spreading in a body of water, Albertson (1948).

Hoyt (1977) argued that jet spreading is solely due to axial swirl which is caused by a helical instability the source of which is not clear. A Coriolis component ?.

In fact the spreading of a jet in the atmosphere is essentially a shearing process between water and air with the air remaining ambient, almost the reverse of the generation of sea waves where the air moves and the water is ambient. It is clear that surface waves will form and that internal jet turbulence will causes bulges in the jet surface, so it is possible that all three ideas sketched below have relevence.

In aerator jets, spread is likely to be significant because of high internal jets turbulence combined with large velocities of the jet (30 − 40 m/sec) producing significant "waves" of the Hecker variety.

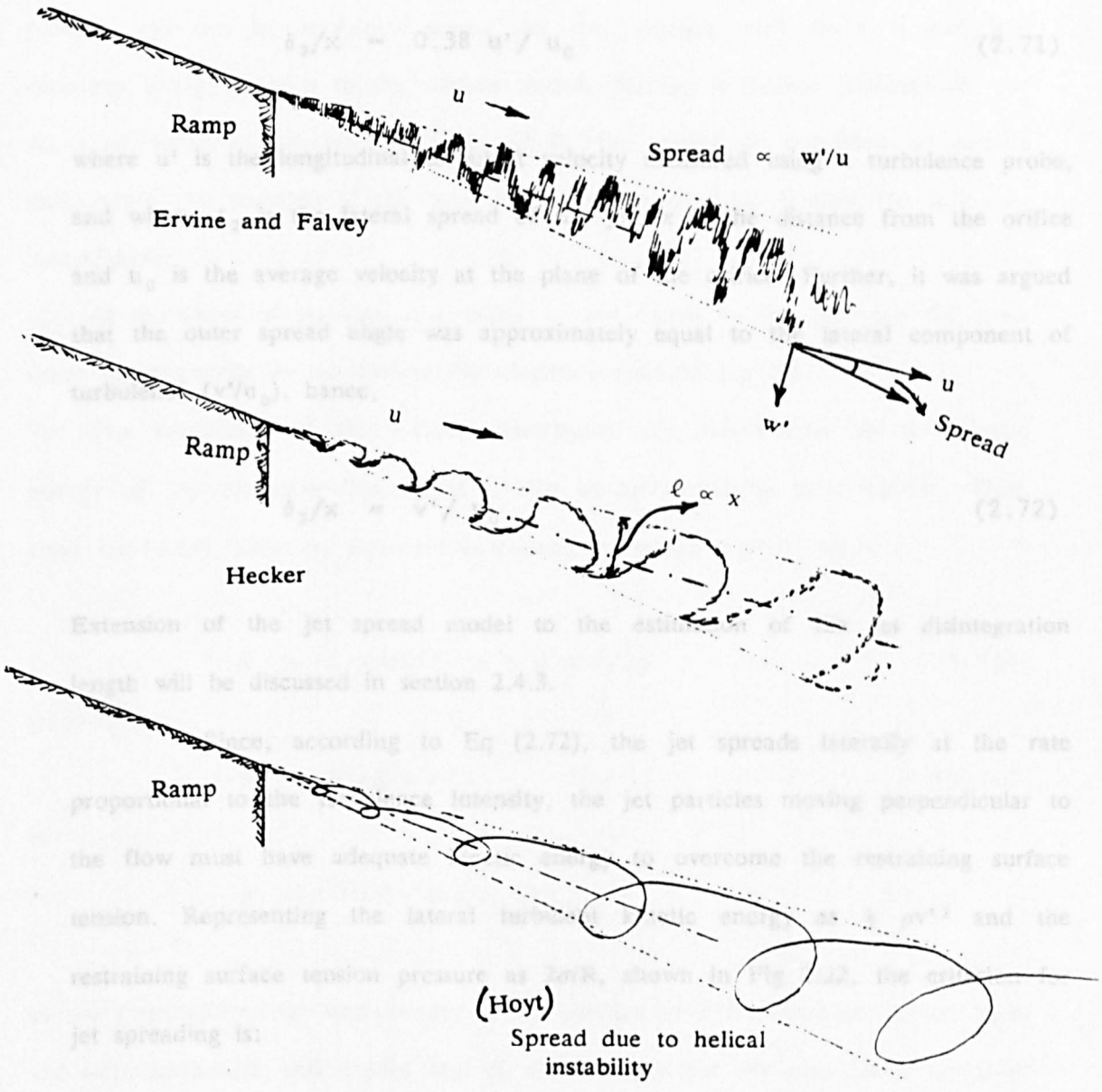

Ervine and Falvey (1987) have produced a simple model which might be applicable both for the conditions necessary for jet spread, and also the condition necessary for the onset of aeration (section 2.5). Their argument stemmed from previous work by Hunt (1984) and Sene (1984) and was based on large scale model experiments on jet spread and turbulence. Fig 2.21(a) shows the relation between the jet spread and the jet axial turbulence intensity at the orifice outlet and Fig 2.21(b) shows the simplified condition of the spreading turbulent jet. With limited data, the rate of jet spread was found to be:

$$\delta_2/x = 0.38\ u'/u_0 \qquad (2.71)$$

where u' is the longitudinal turbulent velocity measured using a turbulence probe, and where δ_2 is the lateral spread of the jet, x is the distance from the orifice and u_0 is the average velocity at the plane of the orifice. Further, it was argued that the outer spread angle was approximately equal to the lateral component of turbulence (v'/u_0). hance,

$$\delta_2/x \approx v'/u_0 \qquad (2.72)$$

Extension of the jet spread model to the estimation of the jet disintegration length will be discussed in section 2.4.3.

Since, according to Eq (2.72), the jet spreads laterally at the rate proportional to the turbulence intensity, the jet particles moving perpendicular to the flow must have adequate kinetic energy to overcome the restraining surface tension. Representing the lateral turbulent kinetic energy as $\frac{1}{2}\ \rho v'^2$ and the restraining surface tension pressure as $2\sigma/R$, shown in Fig 2.22, the criterion for jet spreading is:

$$\tfrac{1}{2}\ \rho v'^2 \geq 2\ \sigma/R \qquad (2.73)$$

or from Eq (2.71)

$$\tfrac{1}{2}\ \rho u'^2 \geq 13.8\ \sigma/R \qquad (2.74)$$

where R is the radius of curvature of jet surface undulations and is valid only for circular bulges on the jet surface. σ is the surface tension parameter.

Equation (2.73) is stipulated as a criterion for jet spreading and also

for the onset of free surface aeration. Water droplets will not be ejected and air bubbles will not be entrained across the free surface until there is sufficient turbulent energy relative to the surface tension forces. A further criterion for the onset of aeration concerns the value of R, the radius of curvature of surface undulations. An estimate of the value of R can be obtained making the following assumptions:

1) At the onset of aeration, the radius of the eddies in the jet have the same order of magnitude as the surface disturbance amplitude Fig 2.22.

2) The magnitude of the surface disturbance are proportional to the kinetic energy of the turbulent fluctuations $u'^2/2g$ as advocated by Sene (1984). Thus, from Eq (2.73), assuming isotropic turbulence meantime ($u' = v'$),

$$R \geq 4\,\delta/\rho u'^2 \simeq \epsilon \simeq u'^2/2g \qquad (2.75)$$

giving :

$$u'^4 \simeq 8\,\delta g/\rho \qquad (2.76)$$

or

$$u' \simeq 0.275 \text{ m/s at } 10^0 \text{ C}$$

as the criterion for the entrainment of air bubbles at a free surface. In an equal and opposite action, this should also be the criterion for the creation of drops of water or spray at the air–water interface provided droplets are of similar dimension to air bubble being entrained. Eq (2.76) may also be expressed in the form of jet velocity:

$$u = \frac{0.275}{u'/u} = \frac{0.275}{Tu} \qquad (2.77)$$

where u is the jet velocity at the onset of aeration or spray.

2.4.3 *Instability and break–up of jets.*

One of the curious feature of jets plunging through the atmosphere is that eventually they break– up and disintegrate. For low turbulence circular jets, break– up does not occur until $L/D_0 \simeq 300$, where L is the jet plunge length in the atmosphere and D_0 the jet diameter. For very turbulent circular jets the break– up length reduces to $L/D_0 \simeq 50$.

Rectangular aerators jets are also of high turbulence (Tu ≃ 10%) and are also liable to have short break– up lengths L/h ≃ 40 to 50, where h is the water depth. Fortunately, most aerator jets have L/h values less than 20, so jet break– up is not liable to be a significant problem at design discharges. Except for specific dams such as McPhee (Frizell & Pugh 1988) where the L/h values occassionally reach values of 30 – 60, complete jet disintegration should not occur.

Gradual jet disintegration is a complex process involving internal jet turbulence (Reynolds Number), jet surface tension (Weber Number), and air resistance from the ambient air. Photographs of the disintegration process from Hoyt and Taylor (1977) are shown in Fig 2.23. The first photograph shows behaviour in the first few diameters; the secound shows the jet sinuous nature further downstream and finally the jet break– up point at about 240 diameters downstream in this case. Hoyt and Taylor (1977) shows that the jet is finally destroyed by helical instabilities, but do not reveal where these instabilities come from.

In the discussion below, many authors have attempted to measure and predict the break– up length of a jet. Early work tended to concentrate on small scale laminar jets increasingly moving to larger scale, more turbulent jets.

Early work by Rayleigh (1892) on the stability of low velocity laminar jets, due to the growth of axisymmetric disturbance, resulted in equations for the break– up length dependent only on surface tension and inertial forces. Further

analysis was carried out by Weber (1931), who also took account of the effect of viscosity on the jet break–up characteristic. The dimensionless break up length was given by:

$$L_B/D = \ln (r/\delta_0) \left[(We) + 3(We^2/Re) \right] \quad (2.78)$$

where

L_B = jet break–up length

D = diameter of outlet

r = radius of the jet

δ_0 = amplitude of initial surface disturbance

We = Weber number $\{ \sqrt{(\rho u^2 D/\delta)} \}$

Re = Reynolds number (uD/ν)

The value of $\ln(r/\delta_0)$ had to be found experimentally. Weber reported a value of 12, based on data by Haenlein (1932), whereas Smith and Moss (1917) found a value of 13 to be more appropriate. For glycerol/water solutions, Grant and Middleman (1966) reported an average value of 13.4 for $\ln(r/\delta_0)$, in good agreement with earlier work. As a convenient means of representing experimental jet stability data, stability curves are commonly constructed. A schematic example is shown in Fig 2.24, which applies to a particular liquid and outlet configuration. Grant and Middleman proposed a similar expression for the linear break–up region as follows:

$$L_B/D = 19.5 (We + 3 We^2/Re)^{0.85} \quad (2.79)$$

They also proposed that the initial disturbance $\ln(r/\delta_0)$ is a variable and is more appropriately represented by the correlation.

$$\ln(r/\delta_0) = -2.66 \ln(We/Re) + 7.68 \quad (2.80)$$

where We/Re = (Oh) Ohnesorge or stability number.

This is important number in jet stability analysis as it represent the ratio of restraining or disturbing forces.

Various empirical correlations for break–up of small scale turbulent jets have been put forward. For instance, Grant and Middleman (1966) developed a relation for jets issuing horizontally from long smooth nozzles as follows:

$$L_B/D = 8.51\ (We)^{0.64} \qquad (2.81)$$

Chen and Davies (1964) produced a further correlation for this region. For fully developed turbulent flow issuing from horizontal pipes, the following relationship was given:

$$L_B/D = 1.15\ We + 30 \qquad (2.82)$$

Using the dimensional analysis approch, Baron (1949) also provided a relationship, this time including surface tension and viscosity, as follow:

$$L_B/D = 537\ \ We/(Re)^{\frac{1}{8}} \qquad (2.83)$$

This relationship has proved effective for high turbulence jets. Horeni (1956) investigated the break–up of a free rectangular jet of water in air. From experimental results the break–up length was found to be a function of Reynolds Number as follow:

$$L_B = 7.8\ Re^{0.319} \qquad (2.84)$$

This equation is not dimensionally correct and may be applicable only to the experimental range tested. Van de Sande and Smith (1976) developed a relatioship for free vertical jets from circular outlets where turbulent was fully developed,

$$L_B = 320\ U_j\ D^{1.5} \qquad (2.85)$$

where U_j = jet velocity at break up point.

Ervine, McKeogh and Elsewy (1980) argued that the turbulence level of the issuing jet was the main parameter causing perturbations on the jet surface and jet disintegration. As various turbulence levels can be attained at constant Reynolds Number, due to nozzle geometry, then relationships without this parameter would not be representative. Be careful alteration of flow conditions in the header tank, the above authors managed to determine break up lengths of low velocity, circular jets at various turbulence levels. The jets plunged near vertically into a receiving pool below. As expected, when the turbulence level was increased, holding other parameters constant, the break up length was substantially reduced. The break up length was related to outflow in a general form as follow:

$$L_B = C\ Q^x \qquad (2.86)$$

The constant C and exponent x were determined by relative turbulence intensity of issuing jet. Typical values of C and x for low to high turbulence are given below in Table (2.1).

TABLE 2.1

Jet turbulence level %	Break-up length = f (Q_w)
0.3	$L_B = 60\ Q_w^{0.39}$
3.0	$L_B = 17.4\ Q_w^{0.31}$
8.0	$L_B = 4.1\ Q_w^{0.20}$

Table 2.1 Typical values of jet break–up length for various outlet turbulence levels

Ervine and Falvey (1987) employed a different approach to jet break–up lengths for the case of spreading turbulent jets. The basic premise is based on the ability to predict jet spread due to turbulence, Fig 2.21(b). This is

done by considering the outer edge of the jet to make an angle proportional to v'/ u where v' is the lateral turbulent velocity and u is the jet velocity.

If the outer edge is spreading in a manner indicated, equation (2.52), then the inner core must be reducing in size in a predictable fashion. Referring back to Fig 2.21(b), Ervine and Falvey (1987) extended their jet spread model to estimate when the solid inner core would completely decay. Assuming negligible velocity change over a short distance of high velocity jet, continuity between section 1 and 2 of Fig 2.21(b) gives:

$$U_0 d_0^2 \approx U_0 d_0^2 + (P_1/100)U_0(d_0^2-d^2) + (P_2/100)U_0(de^2-d_0^2) \qquad (2.87)$$

where P_1 is the percentage probability of encountering water in the δ_1 region and P_2 is the percentage probability of encountering water in the δ_2 region. Ignoring second order terms, the ratio of the magnitude of inner core decay to the outer core spread is given by :

$$\delta_1/\delta_2 = P_2/(100-P_1) \qquad (2.88)$$

Equation (2.88) is valid only for the case of a high velocity jet spreading linearly in the atmosphere. An estimate of δ_1/δ_2 was obtained by Ervine and Falvey (1987) from probability measurements made at the edge of typical jets. A probability probe showed that the edge of a jet follows approximately a Gaussain distribution, as shown in Fig 2.25. This is attributed to the turbulent fluctuations within the jet which cause the jet surface disturbances and also follow a Gaussain distribution. However, refering to the observations of Hoyt and Taylor (1977), the probability distribution of encountering water at the edge of the jet may derive more from the helical motion of the flow downstream of the outlet, as shown in Fig 2.23.

Initial estimates of δ_1/δ_2 from probability data Ervine and Falvey

(1987) for high velocity jets with negligable contraction due to gravity revealed a value of approximately 1/5 to 1/7. Thus the angle of jet core decay may be as small as 15% to 20% of the angle of lateral spread, ignoring core contraction due to gravity. For a typical outer spread δ_2/x of 3% to 4%, corresponding to a turbulence intensity u'/ u of 5% to 8%, the inner core decay (δ_1/x) could then be as small as 0.5% to 1%. If the jet begins to break up or to disintegrate when the inner core decays completely, the jet break up length (L_B) is given approximately for rough turbulent jets by:

$$\delta_1/x \approx 0.5\% \text{ to } 1\% - (d_0/2)/L_B \qquad (2.89)$$

or

$$L_B/d_0 \approx 50 \text{ to } 100 \qquad (2.90)$$

This empirical estimate of the break up length of circular jets agree with previous experimental data for rough turbulent jets.

The method proposed above might well be adopted for rectangular turbulent jets such as are found in aerators. This would require a knowledge of jet spread coefficients, and would provide information on the degree of jet break– up at impact with the spillway surface, over a range of discharge values.

There is a further possible form of instability until now not mentioned in aerator literature. This is a form of longitudinal axial swirls generated in the ramp region and transmitted along the jet Gortler (1945). The phenomena is sketched below;

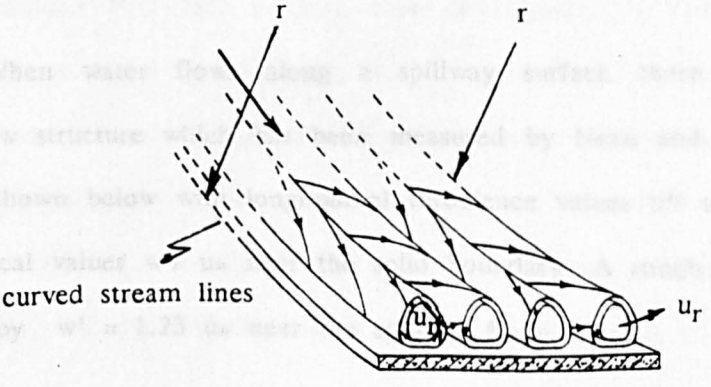

The formation of a ramp on an open channel spillway flow is the equivalent of producing curvature in the streamlines; additional centrifugal pressure on the bed as well as non–uniform shear stress distribution. The latter is likely to set up secondary cells as shown above, the number depending on the aspect ratio of the main channel flow.

Very similar eddy formation were previously shown by G.I.Taylor (1936) to develop in the analogous flow between two concentric cylinders, with the outer cylinder at rest and the inner one is rotating. Gortler's theory shows that instability can develop if

$$\frac{u\,\theta}{\nu} \qquad \text{where} \quad \sqrt{\theta/r} > 0.5 \qquad (2.91)$$

where ;

u = mean flow velocity

r = radius of curvature

θ = bed slope

ν = kinemetic viscosity of liquid

Such secondary currents may well be transmitted along the aerator jet forming an additional instability and certainly forming an additional type of large scale turbulent structure which may influence the air entraining process.

2.4.4 *Transmission of turbulence along an aerator jet.*

When water flows along a spillway surface there is developed a turbulent flow structure which has been measured by Nezu and Rodi (1986). An example is shown below with longitudinal turbulence values u'/u_* about twice as great a vertical values w'/u_* near the solid boundary. A rough approximation of w' is given by $w' \simeq 1.23\,u_*$ near the spillway floor.

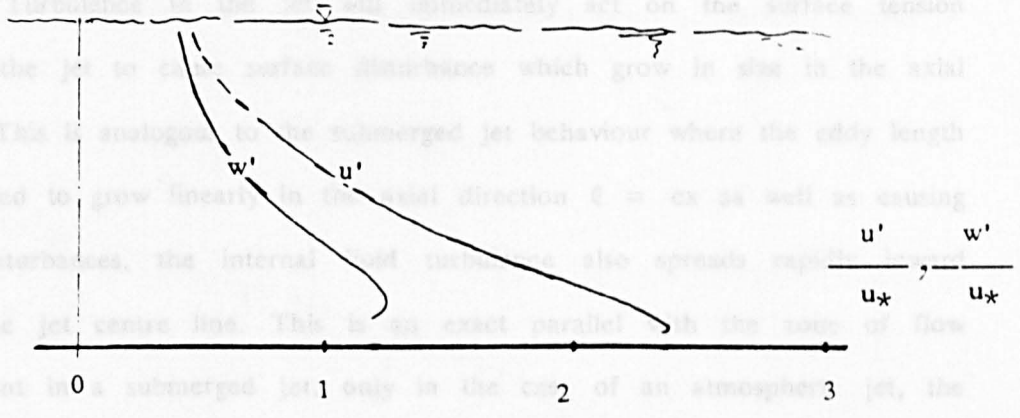

The purpose of a spillway ramp therefore is to lift a jet of water clear of the spillway surface so that aeration may occur into the underside of the spillway jet. The other purpose of the ramp is to generate extra turbulence in the jet so that more air may be entrained. In that sense, ramps act as turbulence generators and one line of research is to vary the ramp angle Φ to maximise turbulence generation.

One of the primary aims of this work is to measure the level of turbulence along the spillway, to measure the increase in turbulence due to a ramp, and also to measure how turbulence gets transmitted along the aerator jet. This should provide insights into the optimum design and maximum air entraining capacity.

As a prelude to these aerator turbulence measurements, the author will present turbulence measurements in circular jets formed by nozzles and orifice to gain insights into turbulence convection, advection and diffusion.

Consider first the idealised case of circular jet issuing from vertical circular nozzle as shown in Fig 2.26. If the nozzle is short, the boundary layer at the edge of the jet will be thin. For very long nozzles the boundary layer may be fully developed. At the point of entry into the atmosphere the jet will contain some turbulence which will be more pronounced at the edges compared with the center. Relative turbulences for short or long nozzles are sketched

in Fig 2.27.

Turbulence in the jet will immediately act on the surface tension "skin" of the jet to cause surface disturbance which grow in size in the axial direction. This is analogous to the submerged jet behaviour where the eddy length is considered to grow linearly in the axial direction $\ell = cx$ as well as causing surface disturbances, the internal fluid turbulence also spreads rapidly inward towards the jet centre line. This is an exact parallel with the zone of flow establishment in a submerged jet, only in the case of an atmospheric jet, the ambient fluid has a density which is only 1/800 of the jet density.

An important aspect of atmospheric jet behaviour is that the equal pressure around the jet periphery will produce a zero pressure gradient across the jet width and hence ultimately a zero velocity gradient (ignoring air resistance) across the jet width. This is shown in Fig 2.28, A zero velocity gradient will in turn mean that no new turbulence is generated as per the relation, $\tau = \rho \ell^2 (\partial u/\partial r)^2$. If there is no turbulence generated along the jet length then existing turbulence after redistribution (advection) will be dissipated in the usual way of energy transfer down the eddy length scales. Davies (1972) also postulates that turbulence is dissipated by the impact of turbulent eddies with the free surface causing bulges or disturbances. A graph showing the growth of surface disturbances in the axial direction is shown from Davies (1972) in Fig 2.9. Davies showed that the disturbances ϵ vary with the distance from the nozzle. It was found that [$\epsilon \propto (\sqrt{x})$] and, similarly with the internal jet turbulent velocity, $u' \propto ([1/x]^{\frac{1}{2}})$.

The important point here is that in atmospheric jets that turbulence will eventually decay downstream because little or no new turbulence is being generated because the shear generated at the air/water interface is not significant compared with shear generated at a solid/water interface. But before turbulence decays, it will first be redistributed according to change in the velocity profile downstream.

One of the main questions asked in this thesis concerns changes in the velocity and turbulence distribution downstream of a ramp as sketched below;

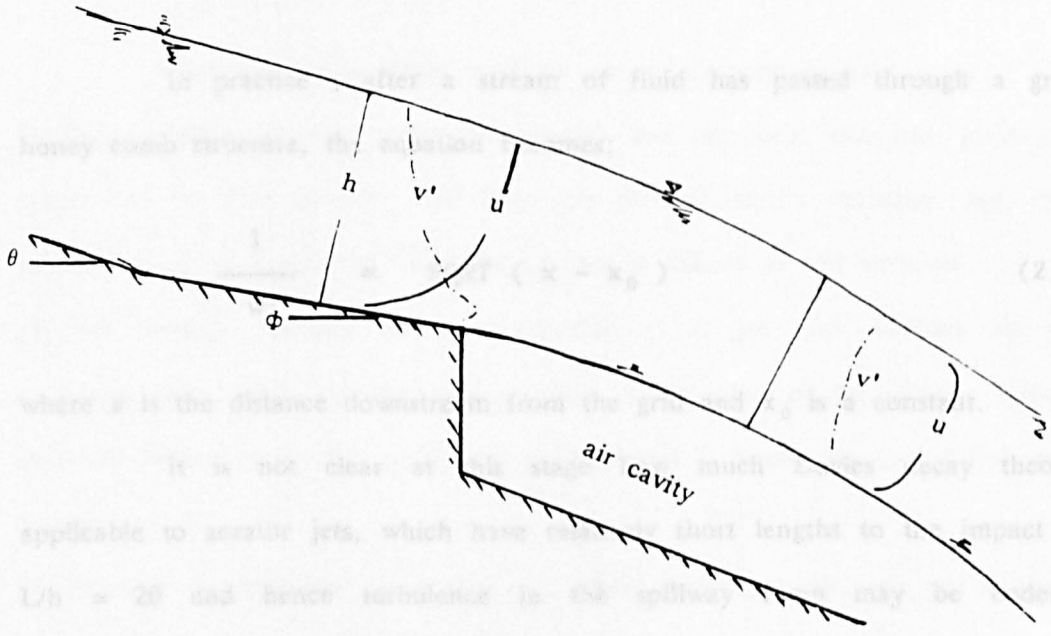

The unknown is the distribution of w' downstream of the ramp, because this parameter may be responsible not only for jet spread but also the rate of aeration into the jet section 2.5.3.

Davies (1972) provided some insights into turbulence decay downstream of a turbulence generator, namely a grid placed in a flow. Dimensional consideration show that the equation must be in the form of power per unit mass of the flow (P_m).

$$P_m = \text{const} \quad \nu / t^2 \qquad (2.92)$$

where ν = kinemetic viscosity of fluid

t = time scale

$$-\frac{3}{2}\frac{d(w')^2}{dt} = \text{const}\ \frac{\nu}{t^2} \qquad (2.93)$$

$$(w')^2 = \text{const}/t + \text{const} \qquad (2.94)$$

In practice , after a stream of fluid has passed through a grid or honey comb structure, the equation becomes;

$$\frac{1}{w'} \propto \text{SQRT}\ (\ x - x_0\ ) \qquad (2.95)$$

where x is the distance downstream from the grid and x_0 is a constant.

It is not clear at this stage how much Davies decay theory is applicable to aerator jets, which have relatively short lengths to the impact point L/h $\simeq$ 20 and hence turbulence in the spillway ramp may be undergoing significant redistribution rather than simply decaying.

Falvey (1988) has discussed this briefly, since a velocity gradient is needed to generate turbulence, turbulence will not be generated within the core of an atmospheric jet. Thus, the scale of the eddies on the interior of a free jet will become increasing smaller in the downstream direction. Although this had not been studied, but it is probably the dispersion of the eddies to both air–water interfaces that is responsible for air entrainment which is observed in the upper of aeration.

2.5 *AIR ENTRAINMENT IN AERATORS AND OPEN CHANNEL FLOWS.*

2.5.1 *Introduction.*

There are three basic types of air entrainment in jets;

(1).Free surface aeration where air bubbles are entrained into the moving jets, across the jet free surface. Whenever this process occurs naturally, say, on the upper surface of a spillway flow, the process is known as self aeration.

(2).Free surface aeration at the underside of a jet. Air bubbles are again entrained across the jet free surface, but in the case of an aerator ramp jet, sketched below, as in this work, the phenomenon is known as forced free surface aeration.

(3).When a jet impinges on a pool (or roller) entraining air, the phenomenon is known as plunge point aeration. This may be occurring to a slight extent at the jet reattachment point sketch below.

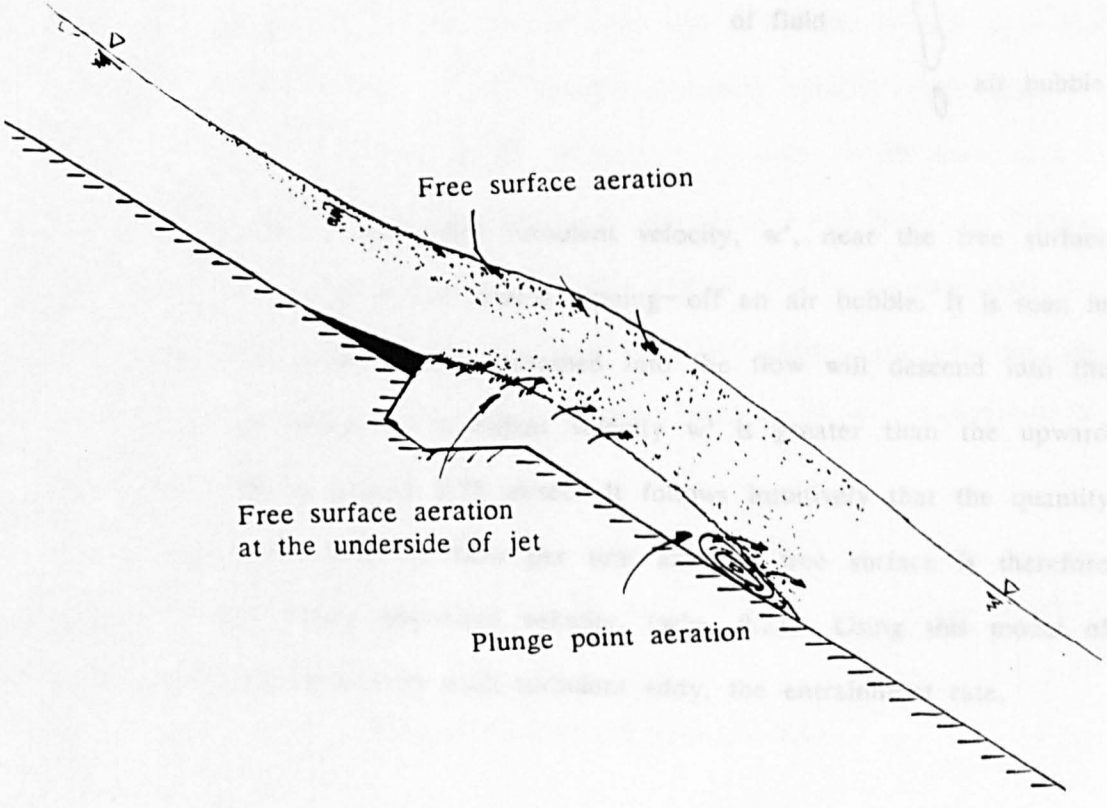

The mechanism of free surface aeration is now reasonabley well understood. On an upper jet surface it is due to falling water droplets, ejected from the flow entraining air on re–entry, sketched below.

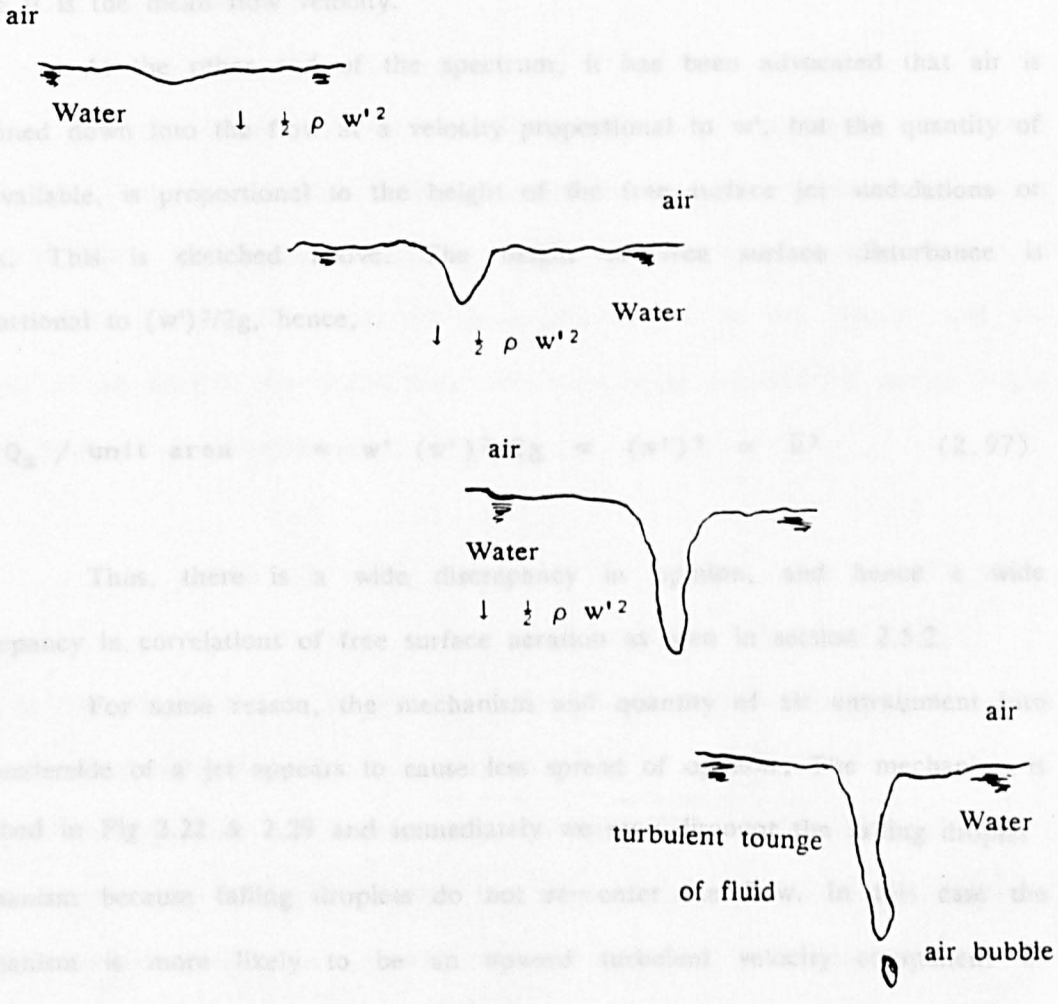

This is combined with a downward turbulent velocity, w', near the free surface causing the free surface to intend inward nipping–off an air bubble. It is seen in sketched above that an air bubble entrained into the flow will descend into the flow only when the downward turbulent velocity w' is greater than the upward bubble buoyant velocity around 0.25 m/sec. It follows intuitively that the quantity of air entrained down into the flow per unit area of free surface is therefore proportional to the excess downward velocity, (w'– 0.25). Using this model of single air bubble entrainment by each turbulent eddy, the entrainment rate,

$$Q_a \text{ / unit area of jet surface} \propto w' \propto \bar{u} \qquad (2.96)$$

where $\bar{u}$ is the mean flow velocity.

At the other end of the spectrum, it has been advocated that air is entrained down into the flow at a velocity proportional to w', but the quantity of air available, is proportional to the height of the free surface jet undulations or waves. This is sketched above. The height of free surface disturbance is proportional to $(w')^2/2g$, hence,

$$Q_a \text{ / unit area} \propto w' \, (w')^2/2g \propto (w')^3 \propto \bar{u}^3 \qquad (2.97)$$

Thus, there is a wide discrepancy in opinion, and hence a wide discrepancy in correlations of free surface aeration as seen in section 2.5.2.

For some reason, the mechanism and quantity of air entrainment into the underside of a jet appears to cause less spread of opinion. The mechanism is sketched in Fig 2.22 & 2.29 and immediately we may discount the falling droplet mechanism because falling droplets do not re-enter the flow. In this case the mechanism is more likely to be an upward turbulent velocity component w' entraining air bubbles in the eddy length range 1 – 10 mm. In this case, once a bubble is entrained its natural buoyancy will transport it up into the flowing water. Falvey and Ervine (1988) argue that this process will occur only once the free surface is "broken", giving a criterion of $w' > 0.3$ m/sec approximately, for this to occur. In this case, most authors assume the rate of air entrainment to be,

$$Q_a \text{ / unit area} \propto w' \propto \bar{u} \qquad (2.98)$$

or alternatively, the rate of entrainment per unit channel width

$$q_a \propto \bar{u}\ L \propto w'\ L \qquad (2.99)$$

where L is the jet length.

Plunge point aeration by jets has well established entrainment mechanisms and air quantities. The mechanism is shown sketched above. Air is entrained when the receiving roller is unable to follow undulations on the jet surface. The quantity of air entrained is proportional to the velocity and the volume of air held in the undulations, the latter being proportional to the height of the free surface disturbances, δ.

$$Q_a \propto \bar{u}\ (w')^2/2g \propto \bar{u}^3 \qquad (2.100)$$

This is the recognised type of correlation for plunge point entrainment where the size of surface disturbance is proportional to $u^2/2g$.

For vertical falling jets the size of surface disturbances may be no longer proportional to jet velocity, but proportional to the distance plunged through the atmosphere. As a general rule $\delta \propto \sqrt{L}$ to L and hence,

$$Q_a \propto \bar{u}\sqrt{L} \quad \text{to} \quad \bar{u}\,L \qquad (2.101)$$

where L is the distance plunged through the atmosphere.

In any case, whatever the type of entrainment, or the mechanism, the intention of an aerator is to introduce air bubbles close to the solid boundaries of a spillway surface. Perterka (1955) has shown that an air concentration around 7 – 9% is sufficient to eliminate cavitation damage on a spillway. At this level of air bubble concentration, the sonic velocity of pressure waves and rebounds is

greatly reduced, producing no damage to solid surfaces.

Consider each form of aeration in more detail.

2.5.2 *Self aeration for the upper free surface.*

An aerator ramp as sketched above usually produces free surface aeration on the upper free surface as well as the lower. A great deal of research has been carried out on upper surface aeration.

The basic terms used for air concentration can be defined in terms of the volumes of air and water

$$c_1 = \frac{v_a}{v_a + v_w} \qquad (2.102)$$

or in terms their flow rates, i.e;

$$c_2 = \frac{Q_a}{Q_a + Q_w} \qquad (2.103)$$

The two definitions are compatible only if the air and water travel at the same velocity (speed and direction). This is a reasonable assumption if the bubbles are small enough for their slip velocity and rise velocity to be small compared with that of the fluid. The choice of definition is usually determined by the experimental technique used to measure the concentration: Eq (2.102) would be appropriate for a device that measure the size and number of bubbles in a given volume whereas Eq (2.103) would be suitable where the total rates of air and water supply are known. The symbol "c" will be used in cases where the concentration is not defined precisely. Results for aerators are sometimes presented in terms of the ratio β as;

$$\beta = \frac{Q_a}{Q_w} \qquad (2.104)$$

At low concentration β and c_2 are nearly equal. (A separate problem of definition occurs where a turbulent water surface causes an instrument to be periodically in and out of the flow; in these conditions it may be difficult to determine what proportion of a measurement is due to air bubbles in water and what is due to air above the free surface).

There is general agreement that air entrainment on a spillway starts when the boundary layer grows sufficiently for its thickness δ to be approximately equal to the depth of flow d. Turbulent clumps of liquid then break through the free surface and fall back again, thereby entraining air. The distance along the channel required for this to occur is called the inception length, L_i. Some authors assume that at the point of inception $d = \delta$, while others assume $d = 1.2\delta$ since turbulent eddies can be projected from below the free surface. Downstream of the point of inception three zones can be defined. In the developing partially–aerated zone, the mechanism of turbulent diffusion causes some of the entrained air to spread downwards as it is carried along by the flow. When air becomes present at the channel bed, the flow enters the developing fully–aerated zone in which the depth of water, the amount of air and its distribution pattern within the flow all continue to vary with distance. Finally, if the channel is long enough and of constant slope, the flow reaches the uniform aerated zone, where there is no further change in depth or in the vertical profile of air concentration. These stages are sketched in Fig 2.30.

A large amount of research has been carried out on self–aeration, and in this review it is appropriate to concentrate mainly on the more recent work. A classic series of experiments on air entrainment in a rough channel was performed by Straub & Anderson (1958), while Anderson (1965) gives

corresponding results for a smooth channel. Test were conducted in a 15.2m long flume with unit discharges up to 0.9 $m^3/s/m$ and longitudinal slopes up to 75 degrees. Measurements were made to determine the mean concentration of the air and its distribution with depth for conditions of uniform aerated flow. Below a certain depth in the flow, d_T, it was found that the flow consisted mainly of air bubbles in water, while above this depth it was predominantly water droplets in air. d_T was identified as the point where rate of change of local air concentration with depth (dc/dy) was maximum. The measured air distributions above and below d_T were able to be fitted to two separate theoretical equations by choosing suitable values of certain coefficients. Based on these and other data, an ASCE Task Committee in 1961 recommended the following formula for predicting the mean air concentration (averaged over depth) in rough channels.

$$\bar{c}_1 = 0.743 \log_{10} (\sin \theta/q_w)^{1/5} + 0.723 \qquad (2.105)$$

where θ is the angle of the channel to the horizontal and q_w is the unit discharge of water in $m^3/s/m$. The corresponding result for flow in a smooth channel was found by Anderson to be

$$\bar{c}_1 = 0.503 (\sin \theta/q_w)^{2/3} \qquad (2.106)$$

Values of the channel Darcy– Weisbach friction factor λ are calculated from the equation:

$$\lambda = (8gd_T \sin \theta)/\bar{u}^2 \qquad (2.107)$$

where d_T is the transition depth, the rate of change of local air concentration with depth (dc/dy) was maximum and $\bar{u}$ is the mean velocity of water.

On this basis, it was found that aeration did not affect the flow

resistance of the rough channel ($\lambda = 0.0315$), but it did reduce the friction factor of the smooth channel from $\lambda = 0.0204$ to $\lambda = 0.0110$.

A series of fairly similar experiments were carried out by Lakshmana Rao et al (1970), Gangadhariah et al (1970) and Lakshmana Rao and Gangadhariah (1971), a summary of which is given by Lakshmana Rao & Kobus (1971). The data on the variation of air concentration with depth were fitted to different theoretical equations from those used by Straub & Anderson (1958), but again it was necessary to choose suitable values for certain coefficients. For the inception of air entrainment, it was suggested that in addition to the boundary layer reaching the surface, it is necessary for the turbulent fluctuations to have sufficient energy to overcome the force of surface tension, Rao et al found the criterion for this to be ;

$$I_0 = \frac{(\rho \, d \, u^2 / \sigma)}{(u_* \, d/\nu)} > 56 \qquad (2.108)$$

where u is the average flow velocity, u_* the shear velocity at the bed, σ the surface tension coefficient and d is the depth of flow. The following equation was obtained for the mean air concentration in uniform aerated flow;

$$1 - \bar{c} = \frac{1}{1 + \Omega \, F_e^{3/2}} \qquad (2.109)$$

Fe = Equivalent Froude Number

where the equivalent Froude Number F_e is defined as;

$$F_e = \frac{\bar{u}}{(g \, d_e \cos \theta)^{\frac{1}{2}}} \qquad (2.110)$$

where $\bar{u}$ = mean velocity of flow

d_e= equivalent water depth ($d_e = \int(1-c) \, dy$)

$\Omega = 1.35n$, for rectangular channels

$\Omega = 2.61n$, for trapeziodal channels

with n being the Manning roughness coefficient of the channel. In the experiments, values of n for aerated flows were determined from an analogue of Eq (2.107) used by Straub and Anderson (1958), i.e;

$$n = (d_T^{2/3} \sin \theta) / \bar{u} \qquad (2.111)$$

where d_T = transition depth

$\bar{u}$ = mean velocity of flow

Application of Eq (2.109) to find $\bar{c}$ in a design situation is not straight forward because values of d_e, $\bar{u}$ and possibly n need to be found first.

Falvey (1979,1980) correlated Straub & Anderson's data with measurements from four prototype structures (three chutes & one spillway) to obtain the following equation for the mean air concentration in uniform aerated flow,

$$\bar{c}_1 = 0.05\, Fr - \frac{(E \sin \theta)^{\frac{1}{2}}}{63} \quad , \; 0 \leqslant \bar{c}_1 \leqslant 0.6 \qquad (2.112)$$

where

Fr = Froude number $u/[gd]^{\frac{1}{2}}$

E = Eotvos number $gd^2\rho/\epsilon$

ϵ = interfacial surface tension

ρ = density of water

g = gravitational force

Air entrainment leads to bulking of the flow, and the depth for design is sometimes assumed to be equal to $d_w/(1-\bar{c})$. However, Falvey (1979) points out that it is not a very useful parameter, because turbulence causes water to rise

well above this level.

Wang (1981) used experimental data on mean air concentrations to compare the predictions of six existing formulae. Using a criterion of minimum standard deviation he found a new equation for mean air concentration in the form,

$$1 - \bar{c} = 0.937 \left[Fr \left[\frac{n^6 g^3}{R_w} \right]^{1/6} \left[\frac{B}{d_w} \right] \right]^{-0.088} \qquad (2.113)$$

where

$$Fr = \frac{u}{(g R_w)^{\frac{1}{2}}} \qquad (2.114)$$

where B = width of the channel

d_w = depth of the flow

R_w = hydraulic radius R_w, assuming non-aerated flow.

Volkart (1982) studied air entrainment in steep partially-filled circular pipes, and obtained both model and prototype data for pipe diameters up to 900mm, and slopes up to 45^0. The resulting equation for the mean air concentration was:

$$1-\bar{c}_2 = \frac{1}{1 + 0.02 (Fr - 6.0)^{1.5}} , \quad 6.0 \leqslant Fr \leqslant 15 \qquad (2.115)$$

where Fr = Froude Number of air/water flow $(v_{aw}/[gh]^{\frac{1}{2}})$ assuming non-aerated flow parameters. The mean velocity v_{aw} of air/water mixture was given by :

$$v_{aw} = (1 - \bar{c}_2^{2.09}) v_w \qquad (2.116)$$

Bruschin (1987) compared Falvey's Eq (2.112) and Volkart's Eq (2.115)

for mean air concentration, and concluded that Eq (2.112) did not give reasonable predictions for prototype conditions, possibly due to the second term on the right hand side not being valid. Wang (1984) used measured data on mean air concentrations to obtain the following best fit equation as:

$$\bar{c} = 0.538 \left[\frac{nu}{R^{2/3}} - 0.02 \right] \qquad (2.117)$$

where n is the Manning roughness of the channel.

An important line of research on air entrainment has stemmed from prototype measurements carried out by Cain & Wood (1981) on Aviemore Dam in New-Zealand. Instruments were developed to determine profile of air concentration and water velocity along the spillway and also the size of the air bubbles. The spillway slope is 45^0 , and data were obtained for unit discharges of up to 3.15 $m^3/s/m$. The channel was not long enough to give conditions of uniform aerated flow. Measurements of the point of inception of air entrainment were found to corresponds reasonably with the emperical equation due to Bauer (1954) for growth of the boundary layer thickness.

$$\frac{\delta}{x} = 0.0254 \left[\frac{x}{k_s} \right]^{-0.135} \qquad (2.118)$$

where k_s is the equivalent sand roughness of the channel. Downstream of the point of inception it was found that the non-dimensional velocity profile did not vary with the amount of entrained air, and had the form,

$$\frac{v}{v_{90}} = \left[\frac{y}{y_{90}} \right]^{0.158} \quad , c > 0 \qquad (2.119)$$

where the subscript $_{90}$ refers to the point above the bed where the air

concentration is 90%. This contradicts the results of other investigators (eg, Straub & Anderson, Lakshmana Rao et al), who found that the velocity did not increase steadily with distance up from the channel bed, but reached a maximum below the surface of the flow. Cain & Wood suggest that the difference arises because they measured the velocity of the water alone, while other investigators measured that of the air–water mixture. If this is the case, it suggests that the two phases travel at significantly different speeds, contrary to what is often assumed. Wood et al (1983), assumed that the formula for the growth of boundary layer was similar in form to Bauer's Eq (2.118), but evaluated the coefficients using Eq (2.119) together with numerical results obtained by Keller & Rastogi (1977) for the point of inception of aerator on standard spillways. This procedure gives,

$$\frac{\delta}{x} = 0.0212 \left[\frac{x}{H_s}\right]^{0.11} \left[\frac{x}{k_s}\right]^{-0.10} \qquad (2.120)$$

where H_s is the vertical distance from the upstream total energy line to the surface of the water in the spillway. The form of the equation allows it to be applied to channels of non–uniform slope. Wood re–analysed Straub and Andersons data, and concluded that uniform aerated flow was not achieved in all the tests. Where equilibrium conditions were reached, Wood found that the mean air concentration and the distribution of the air through the depth of the flow were uniquely determined by the slope of the channel. The variation of $\bar{c}$ with the channel slope is given in Table (2.2). The data in Table (2.2) also indicate that in order to obtain a local air concentration at the bed of about 7%(so as to avoid cavitation damage), the mean air concentration needs to be about 30% and the slope of the channel about 22.5^0. This result applies only after the flow has travelled sufficiently far along the channel for uniform conditions to be attained. Upstream, in the region of developing aerated flow, the air

concentration at the bed will be lower than the final equilibrium value.

Ackers & Priestley (1985) developed a model for predicting air entrainment on spillways which is based on the same information as used by Wood (1985), but with some detailed difference in approach. The point of inception is found numerically by computing the growth of boundary layer until its thickness is equal to the depth of flow.

At this time there appears to be no single relationship for determining free surface aeration, which works for models prototype and with general applicability.

The reason for this concerns the fact that aeration is not a function of Froude Number, whereas most correlations use Froude Number, or a form of it, in their predictions for mean air concentration with depth. Almost all correlations ignore turbulence (w' or u_*) and yet turbulence is responsible for the air being distributed into the flow depth. Most correlations ignore Reynolds Number and yet the Reynolds Number is the most significant term for determining the degree of turbulence which is held is the range of eddy lengths responsible for aeration (1mm to 10mm). The time is now ripe for new research effort in this field.

2.5.3 *Aeration at the lower jet surface.*

A schematic diagram of the underside of a jet aerator is shown below, with jet spread, aeration and air flow patterns shown,

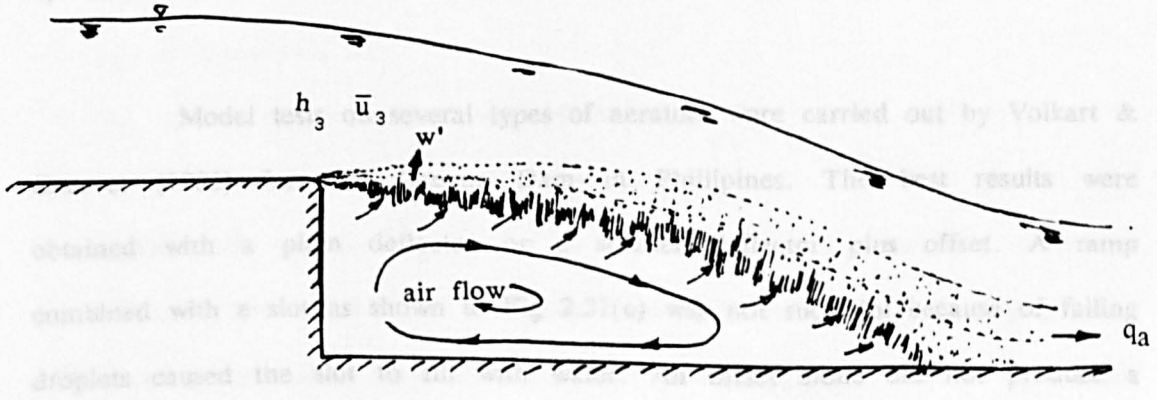

Such devices are now in common use, and all attempt to maximise the air flow q_a, and the air concentration of the spillway bed. This has a dramatic effect on likely cavitation damage. Thus, the use of aerators is appropriate where the standards of surface finish needed to avoid cavitation are too high to be achievable, and there is insufficient entrained air in the flow to prevent erosion by collapsing cavities. Air can be injected by means of pumps, but most aerators work by producing a region of sub–atmospheric pressure which draws air naturally into the flow through side vents. This is achieved by means of a ramp, slot or offset which causes the flow to separate from part of the boundary and form a stable pocket of air.

The air demands depends upon the velocity and depth of water, and upon the geometry of the aerator and the system of ducting which supplies it with air. Model tests are usually carried out to study the behaviour of the flow around an aerator. The phenomenon of air entrainment is subject to significant scale effects, so small models cannot normally provide accurate predictions of air demand. An aerator initially produces a high concentration of air near the boundary, but the distribution becomes more uniform as the bubbles are carried downstream by the flow. The movement of air bubbles is determined by two main effects:

i). Buoyancy forces due to pressure gradient.

ii). Turbulent diffusion away from areas of high concentration.

Model tests on several types of aerators were carried out by Volkart & Chervet (1983) for San Rouque Dam in Phillipines. The best results were obtained with a plain deflector or a smaller deflector plus offset. A ramp combined with a slot as shown in Fig 2.31(c) was not sucessful because of falling droplets caused the slot to fill with water. An offset alone did not produce a

strong enough air demand. Volkart & Rutschmann (1984) mention that although plain deflectors can produce a good length of air cavity, they tend to work satisfactorily for only a limited range of flows. A combined deflector and offset was considered to give the best results.

The length of air cavity produced by an aerator is an important factor affecting its performance especially in predicting the total degree of aeration. Several theoretical methods of predicting this length have been developed by assuming the flow to be irrotational. Schwarz & Nutt (1963) studied the trajectory of falling nappes, but the results can be applied to jets formed by deflectors or offsets. Equations for the horizontal and vertical co-ordinates are given separately, with the time of travel as the common parameter. It is assumed that the initial velocity and angle of projection are known, and that the thickness of the nappe is small so that it behaves effectively as a solid jet of liquid. Account is taken of gravity and any pressure difference between the upper and lower surfaces of the nappe.

The air demand cannot be considered in isolation from the head-loss characteristics of the air supply system, which can be expressed in the general form as;

$$Q_a = c\, A_a \left(\triangle p / \rho_a \right)^{\frac{1}{2}} \qquad (2.121)$$

where

Q_a = the total rate of air flow

ρ_a = density of air

A_a = the cross-sectional area of the duct

c = constant for a particular arrangement.

For a given flow velocity, the rate of air entrainment on the underside of the jet depends upon the length L of the cavity, which in turn is affected by pressure difference $\triangle p$: Increasing $\triangle p$ decreases L, and vice versa. The value of $\triangle p$ adjusts

until the air demand of the jet matches the rate of flow through the air duct. If air is supplied to the cavity from lateral outlets in the side wall, there will be a variation of Δp across the width of the channel; the difference is largest at the outlet and decreases towards the centre of the channel.

Pinto et al (1982) determined values of the parameter q_a/vL for the aerators at Foz do areia dam in Brazil. In this case q_a is the air uptake per unit width, u the velocity of flow at the ramp and L the cavity jet lengths as sketched below,

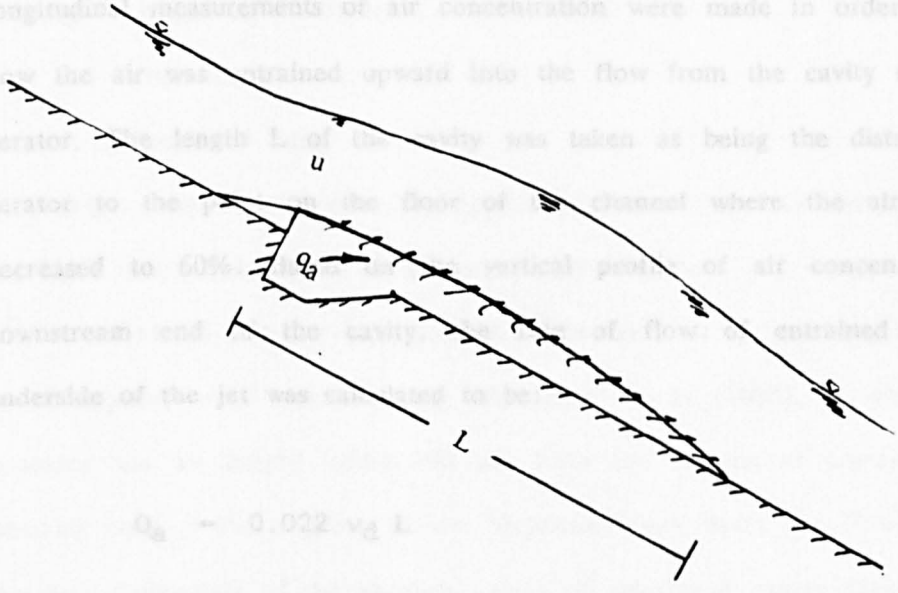

The air demand ratio $\beta = q_a/q_w$ was obtained from prototype measurements, the cavity length L from a 1:50 scale model and the depth flow h determined by continuity. Over a six− fold range of water discharges. Pinto found that the quantity q_a/vL was approximately constant,

$$q_a = k\,u\,L \qquad (2.122)$$

where Pinto suggest that k = 0.033 for symmetric flow of air (air venting from both sides) and k = 0.023 for asymetric flow conditions. However, later model tests which Pinto & Neidert (1983) carried out over wider range of conditions showed that k was not in fact a constant, but varied significantly with Froude

Number Fr = $(u/[gh]^{\frac{1}{2}})$, Euler Number $E_e = (u/[\Delta p/\rho]^{\frac{1}{2}})$ and h_r/d where h_r is the height of ramp and d is depth of flow. Values of Fr and h/d for a particular dam do not alter greatly with the flow conditions, but the significance of Eular number E_e shows that the characteristics of the air supply system have an important effect on the amount of entrainment. Eq (2.122) is not vary suitable for design, as both q_a and L are unknown.

Pan et al (1980) carried out a laboratory study of ramp aerators which lends support to the later work of Pinto et al discribed above. Vertical and longitudinal measurements of air concentration were made in order to determine how the air was entrained upward into the flow from the cavity created by the aerator. The length L of the cavity was taken as being the distance from the aerator to the point on the floor of the channel where the air concentration decreased to 60%. Based on the vertical profile of air concentration at the downstream end of the cavity, the rate of flow of entrained air into the underside of the jet was calculated to be:

$$Q_a = 0.022\ v_d\ L \qquad (2.123)$$

where v_d is the flow velocity at the end of the cavity (not at the ramp). This result agreed well with the model data, and has a similar form to Eq (2.122) which was determined from prototype measurements, although neither equation considered the underpressure Δp in their correlation.

Pan & Shao (1984) also considered an alternative approach to predicting the air demand that would not require prior determination of the cavity length. Analysis of laboratory and prototype data, in terms of the non–dimensional parameter X_u, (Eq 2.125) led to the following empirical equation for air demand produced by a ramp and/or a slot (but no offset) in a channel of constant slope,

$$\beta = \frac{Q_a}{Q_w} = -0.0678 + 0.0982\ X_u - 0.0039\ X_u^2 \quad [X_u > 1.0] \quad (2.124)$$

where X_u = dimensionless parameter defined as,

$$X_u = \frac{v}{(gd)^{\frac{1}{2}}} \quad \frac{(h_1/d)^{\frac{1}{2}}}{\cos\theta\ \cos\Phi} \quad (2.125)$$

where

d = depth of the flow normal to the bed

h_r = height of the ramp

θ = bed slope

Φ = angle of ramp

This result may not be generally applicable because it does not take account of the head loss characteristics of the air supply system.

Model test for four aerators to be used on the spillway of Laiban dam in Philippines were described by Koschitzky et al (1984). It was found that, provided the air supply system did not limit the amount of entrainment, the air demand ratio β for a given aerator depended only upon the Froude Number of the flow (regardless of the absolute values of velocity & water depth). The results also showed that the presence of an aerator upstream tended to increase the amount of air entrained at an aerator downstream.

Useful prototype data on the performance of four aerators tested on chutes 1 and 3 of Guri Dam in Venezuela are reported by Marcano & Castillejo (1984). The values of the entrainment parameter k in equation (2.122) were found to be approximately constant for each aerator, and varied between k = 0.011 for a ramp plus deep grove and offset, and k = 0.073 for a ramp alone. It was found that it was difficult to predict or to reproduce correctly in a model the under pressures that occured at the prototype aerators. As a result, the model tended to over estimate the lengths of the air cavities.

Bruschin (1985) analysed the Foz–do–Areia data togather with results

from a model of Piedra del Aguila Dam in Argentina. Using the overall step height w ($w = h_r + h_{os}$) instead of L as the characteristic length led the following formula for the air demand ratio as;

$$\beta = 0.0334\ Fr\ (w/d)^{\frac{1}{2}} \qquad (2.126)$$

where

Fr = Froude Number $(u/[gd]^{\frac{1}{2}})$

w = $(h_r + h_{os})$ overall step height (ramp+ offset)

d = depth of flow

This result does not take account of the cavity under–pressure, and its validity has been questioned by De Fazio & Wei (1985). Wood (1985) also studied the Foz–do–Areia data and produced the following equation for determining the value of factor k in Eq (2.122)

$$k = 0.0079\ (Fr - F_k) \qquad (2.127)$$

where

Fr = Froude Number $(u/[gd]^{\frac{1}{2}})$

F_k is the Froude Number required to initiate aeration and is given by,

$$F_k = 4.3\ [\ 1 + 4.7\ (\ \Delta p/\rho gd\ )\ (\ h_{os}/d\ )\ ] \qquad (2.128)$$

where

Δp = under nappe pressure

h_{os} = height of offset

d = depth of flow

Model test of an aerator with an offset, but no deflector ($h_{os}=0$) for Clyde Dam New Zealand gave lower values of k then predicted by Eq (2.127).

Low (1986) describes model tests on aerators for the spillway of Clyde Dam carried out at a scale of 1:15. The measured air demands were approximated by an equation of the form:

$$\beta = a_1 (Fr - a_2) - a_3 (\triangle p/\rho gh)^{a_4} \qquad (2.129)$$

where Fr = Froude Number $(u/[gh]^{\frac{1}{2}})$

h = height of flow at ramp

The first term on the right hand side describes the effect of flow velocity and the second term the effect of the sub–atmospheric pressure in the air cavity. The factors a_1, a_2, a_3 and a_4 depended on the geometry of the aerator. Use of a dentated ramp upstream of the slot reduced the tendency for β to decrease as the pressure difference $\triangle p$ was increased (i.e. it had the effect of reducing the value of a_3 in Eq (2.129). Since the test was carried out on a sectional model, it was not possible to determine directly the total air demand for an aerator spanning the full width of the spillway. The problem is complex because the pressure difference $\triangle p$ in the air cavity varies with transverse distance from the duct in the side walls of the spillway. Low describes a theoretical model of air supply system which enables the total air demand to be calculated using the data from the sectional model. Measurements were also made of the vertical distribution of air in the flow downstream of the aerators. These showed that the air concentration close to the bed decreased fairly rapidly downstream of the reattachment point of the flow. In model terms, the concentration at a height of 10 mm above the bed decreased to c = 10% within a distance that varied from about 0.1–1.0m for Froude Numbers between Fr = 7.0 and 13.4.

Bruschin (1987) proposed an alternative type of entrainment function to that given by Eq (2.122). The characteristic length is postulated to be a certain

"roughness" index δ rather than the cavity length L. The value of δ represented a kind of boundary layer thickness. The proposed equation has the form:

$$Q_a = \delta (v - v_k) \qquad (2.130)$$

Use of some prototype data, togather with an assumed threshold velocity of v_k = 1 m/s, gave value of δ = 0.2 – 0.4 m. The factors which may influence δ were not discussed.

Glazov (1985) carried out a study of ramp aerators at San Roque chute spillway. The main parameter of the study was to determine the air–capturing ability of flow. According to Glazov's, the velocity of air entrained by the flow is practically equal to the velocity of water, and therefore the volume flow rate of air being carried away from the under–nappe cavity of width b can be taken proportional to its concentration in water–air layer at the end of the under–nappe space as shown in Fig 2.32. The air entrainment rate is given by,

$$Q_a = b \bar{u} \int_0^{h_a} S\,(h)\, dh \qquad (2.131)$$

where b = width of the channel

$\bar{u}$ = mean velocity

h_a is the thickness of the water–air layer in a cross section normal to the direction of the mean velocity u of this layer and passing through the point of intersection of the lower boundary of the nappe with the bottom of the water conduit behind the ledge: S is the time average local concentration.

P.Rutshmann (1988) also analysed laboratory results for different aerators and obtained the results,

$$\beta = 0.1135\ Fr + 0.3820(w/d)^{1.5} + 15.51 \tan \Phi - 0.9029 \qquad (2.132)$$

where β = air entrainment rate (q_a/q_w)

Fr = Froude Number $u/[gh]^{\frac{1}{2}}$

w = over all step height ($h_r + h_{os}$)

d = depth of flow

This results applies for a channel slope of $\theta = 34.5^0$ and specifically assume that the cavity pressure $\triangle p = 0$. Rutschmann's Eq (2.132) does not give sensible values of β when applied to the types of aerator studied by R.P.May (1987). This appears to be because of the term (15.51 tanΦ) considerably over estimate the effect of ramp angle Φ.

H.Chanson (1988) carried out experimental study on spillway model of Clyde Dam New Zealend. The main aspect of his research was the air concentration downstream of ramp. According to Chanson's that the rise velocity of a spherical air bubble (diameter d_b) subject to such a negative pressure gradient in the cavity, becomes a fall velocity and given by,

$$u_r^2 = \frac{4\ g\ d_b}{3\ C_d} \left[P_n \cos\theta + \frac{\rho_{air}}{\rho_w} \right] \qquad (2.133)$$

where

u_r = bubble rise velocity

d_b = diameter of air bubble

C_d = coefficient of drag

θ = chaneel bed slope

P_n = pressure gradient ($\triangle p/\rho gd$)

d = characteristic depth $d = \int (1-c)dy$

R.P.May and A.P.Deamer (1989) carried out Laboratory experiments at Wallingford. Measurements of air demand were made using four design of aerator

at two channel slopes for a ramp of flow velocities and depth with different head–loss characteristics in the air supply system. The results showed that the values of air demand ratio β (q_a/q_w) is increased by increasing,

a). The Froude Number Fr of the flow

b). The height of the ramp (hr)

c). The slope of the ramp Φ

d). The slope of the channel bed θ

R.P.May agrees with the available formulae suggested by Pan and Sho in Eq (2.124). The advantage of the Eq(2.124) seems to be that it does not require information about the length of air cavity, but still needs to be developed in order to take into account the head–loss characteristics of the air supply system.

The experimental study at McPhee Dam USA and Tarbela Dam Pakistan will be discussed later in section 2.7.

It has become clear in this section that there is a wide range of functional relationship to predict the air uptake at aerator ramps. The most common form is,

$$q_a = K\,u\,L \qquad (2.134)$$

which has the disadvantage of L being unknown, but calculable as a rough estimate from projectile type theory. The value of K turns out not to be constant, but varies over a wide range depending on spillway surface roughness, cavity under pressure $\Delta p/\rho gh$, Froude Number of the flow, Reynolds Number, etc.

One of the main aims of this work therefore is to produce a better functional relationship based on turbulence measurements, which covers both model and prototype situations and also accounts for cavity under pressure.

2.5.4 *Plunge point air entrainment.*

At jet plunging into a receiving pool of water has the ability to entrain substantial quantities of air. The physical mechanisms have been outlined in section 2.5.1. This type of aeration is not important in ramp aerators but it does have some relevance at the jet impact point on the spillway surface, where a reverse roller may form producing a kind of plunge point entrainment.

The general expression for plunge point air entrainment is of the form,

$$q_a \propto \bar{u}\,\delta \qquad (2.135)$$

where δ is the size of jet surface disturbance which may be correlated with the jet velocity $\delta \propto u^2$, or with the distance from the commencement of the jet $\delta \propto L^n$. In either case, the size of the surface disturbances is closely related to the internal turbulence levels in the jet, as well as the degree that the jet has broken–up or disintegrated during its plunge. (Most aerator ramp jets have value of L/h less than 20, and hence are still relatively intact at the impact point on the spillway surface).

McKeogh and Ervine (1981), studied plunge point aeration by circular jets and determined the effect of jet condition on air entrainment rates. It was found that the maximum entrainment rate was reached when the jet had just disintegrated. After this point the jet broke up into discrete droplets, lost momentum to the surroundings and entrained less air. An empirical relationship was determined to predict the rate of air entrainment by considering air being carried along in surface disturbance of the jet and in a boundary layer surrounding the flow as shown in Fig 2.33. The jet surface undulations where found to increase with fall height and turbulence level, until at break up point

they were approximately equivalent in size to the jet radius. The best fit for all results gave the following expression of air water ratio (Q_a/Q_w).

$$Q_a/Q_w = 1.4 \left[(\epsilon/r)^2 + 2(\epsilon/r) - 0.1 \right]^{0.6} \quad (2.136)$$

where ϵ = surface disturbance on jet surface. This relationship is not practical for use, however, as ϵ/r is not known at given point. Bin (1984) has correlated experimental data for circular jet air entrainment from Van de Sande (1974), Cumming (1975), Ervine et al (1980), Henderson et al (1970), Kumagai and Imai (1982) and Van de Donk (1981). For vertical circular jets the air/water flow rate was given by,

$$Q_a/Q_w = 0.04\ Fr_i^{0.56}\ (L/D_0)^{0.4} \quad (2.137)$$

where Fr_i is a Froude Number based on impact velocity u_i and nozzle diameter D_0, and L is the plunge length. ($Fr_i = U_i/ [gD_0]^{\frac{1}{2}}$).

The correlation is shown in Fig 2.34 and the test parameters for each author are given in Table (2.3). Equation (2.137) gives satisfactory agreement provided $L/D_0 \leqslant 100$ and the nozzle length $\geqslant 10$ outlet diameters.

Most of the jets in the data correlation are of relatively small scale, and thus viscous and surface tension forces must influence not only the nature of the surface of the plunging jet but also the inception condition for entrainment. Presumably it can be argued that the parameter (L/D_0) reflects growing jet surface roughness and break up. Initial turbulence intensity is also omitted, but Bin (1984) indicates the sensitivity of the data correlations to the length of the jet nozzle, which in turn reflects the development of turbulent boundary layers with in the jet at the point of entering the atmosphere.

As the velocity and turbulence level of the jet increases, the air entrainment mechanism changes. At low velocity air is supplied from surface

disturbances and an air boundary layer as shown in Fig 2.33. At higher velocity the air entry becomes more continuous from an air layer above the jet surface, and in some cases from within the jet itself. The mechanism for a high velocity wall jet is shown in Fig 2.35. Considering the Froude models tend to underestimate prototype air/water ratios, due to non simulation of turbulence scales and pertinent forces, Ervine (1985), investigated the effect of increasing velocity and geometric parameters to find a more relevant air entrainment expression. With increase in impact velocity (U_i) it had been found from previous experiments, that the functional dependency of the air entrainment rate into the pool altered. Holding fall height and jet dimensions constant, at low velocity the air entrainment rate (Q_a) was found to vary with $(U_i)^n$, (n= 2 to 3), while at higher velocity it was better correlated with $(U_i)^n$, (n = 1 to 2). The effect of jet break up length L_B, was incorporated, from research by McKeogh (1978), to obtain an expression for the air entrainment rate. For vertical circular jets, the air flow entrainment rate is given by,

$$Q_a = K\, d_0\, U_i^n\, (L/L_B)^{0.7 \to 0.8} \qquad (2.138)$$

where U_i = velocity of flow at nozzle

d_0 = diameter of the nozzle

L = jet fall height

L_B = jet break–up length

where n = 2 to 3 at low velocity

n = 1 to 2 at high velocity

From the generality of the above expression it is obvious that a great deal more research into plunging jets, particularly at large scales and velocities, is required to utilize this form of analysis. However, it is clear from the most recent work by Thomas (1978), Sene (1984) and Ervine and Falvey (1987), that

the ratio of air/water ($\beta = Q_a/Q_w$) for a plunging jet varies primarily with plunge length (L) in the form;

$$\beta \propto (L/d_0)^{\frac{1}{2}} \quad f(Tu) \tag{2.139}$$

where d_0 is the nozzle diameter, and Tu is the jet turbulence level. All of these authors above have suggested constants of proportionality to substitute for the turbulence function. For circular jets of high turbulence;

$$\beta \propto 0.3\ (L/d_0)^{\frac{1}{2}} \quad [\ \text{valid for } L/d_0 < 100\ ] \tag{2.140}$$

for circular jets at low turbulence,

$$\beta \propto 0.15\ (L/d_0)^{\frac{1}{2}} \quad [\ \text{valid for } L/d_0 < 400\ ] \tag{2.141}$$

From the range of applicability of the above expression it can be seen that the upper limit of β at the impact point is approximately 3 for circular jets plunging vertically. A practical example of utilising the break up process and air entrainment is shown in work by Mason (1983). Investigation took place into the effectiveness of splitter teeth on dam spillway crest as shown in Fig 2.36. Impact forces on the pool floor are minimised due to this arrangement by splitting the spillway flow and causing the interaction in the atmosphere, at the optimum operating condition. This process helps to break–up the concentration of the falling flow, increases the turbulence level, and entraps a substantial amount of air. The remaining flow falls as disseminated spray onto the pool below. Mason (1983) cites Victoria dam as an example of pressure reduction using this system.

All the examples of plunge point aeration above have been more relevant to steep or vertical jets plunging through the atmosphere. Many authors have investigated more shallow sloping situations such as hydraulic jumps, siphons,

etc, where the jet is often entraining air by the upper surface only, with the bottom surface supported in many cases by the solid boundary. In this case it has been found that the best correlation have been in the form,

$$q_a \propto \bar{u}^3 \quad \text{or} \quad \beta \propto Fr^2 \qquad (2.142)$$

Kobus and Rao (1975), Casteleyn, VanGroen and Volkman (1977), Goldring (1979), Ervine and Ahmed (1984) and Sene (1984) all come to the same conclusion.

The earliest correlation of this type was proposed by Renner (1975) and is the closest physically to the plunge point in a ramp aerator. The experimental set up is shown in Fig 2.37 with a horizontal rectangular jet impinging horizontally on to an inclined wall. Renner changed the wall angle from 45^0 to 90^0 to give air/water ratio β ranging from 0.00172 Fr^2 to 0.00275 Fr^2.

2.6 *DESIGN ASPECTS OF AERATORS.*

2.6.1 *Introduction.*

If the tolerance on the surface finish required to avoid cavitation are too severe to be practicable, and there is not enough self aeration, possible damage to the channel may be prevented by using an aerator to supply air around the perimeter. The air can be pumped under pressure, but nearly all aerators work by creating a suction which is used to draw the air naturally from the atmosphere. Such aerators consist of an offset or deflector which causes the flow to separate from the surface of the channel and form a large air cavity. The water passing over the cavity entrains air strongly, and thereby produces the

necessary sub– atmospheric pressure.

Aerators are often located immediately downstream of gates in high– head tunnels in order to protect the walls and floors from cavitation damage, and these operate in a similar way to aerator in spillways. Ducts may be used to supply air to an offset in the floor or, for example, to the seating of a radial gate with recessed seals. For tunnels flowing partly full, a more common arrangement is to form, just downstream of the gate, a vertical U– shaped slot in the walls and invert so as to allow air from above the water surface to reach the invert.

In terms of the best location for an aerator, it should be considered as a possibility as soon as the cavitation index (section 2.3.1.) drops below 0.25. Falvey (1990) quotes a cavitation index of 0.2 as being tigger point for the inclusion of an aerator, but the final choice is also determined by the tolerance of the surface finish and trying to minimise the number of aerators to be used in series.

2.6.2 *Typical geometries used.*

Aerators can consist of deflectors, offsets, and slot used either singly or in combination. The elements of some typical designs are shown in Fig 2.38. Deflectors tend to produce strong aeration, but may disturb the flow considerably. An offset causes less disturbance but needs to be larger than a deflector in order to provide the same air demand. If an existing structure requires modifications to prevent cavitation damage, it is usually easier to incorporate a deflector than an offset. Means of supplying air to an aerator include ducts discharging air at the base of the side walls or at points across the floor of the channel. Alternatively, deflectors and offsets in side walls can be added so as to allow air to reach aerators located in the channel floors.

Means of air supplying to aerators are shown in Fig 2.38 are:

1). Use of a separation zone formed downstream of a pier or divide wall.

2). Offsets or deflectors at the side walls which allow a flow of air from the surface to the floor of the channel (Self aeration).

3). Ducts discharging air at the base of the side walls.

4). A duct beneath the floor of the channel connecting to a horizontal slot or to the downstream face of a vertical offset.

The design of each aeration system tends to be specific to the particular application, and the data available from some prototype structures.

2.6.3 Ramps and Offsets.

According to practical consideration, aerators should entrain a large quantity of air, so that air concentration is evenly distributed over spillway width and along the length of channel.

The aerator should be simple and economical in design, and it should also prevent any erosion damage to itself. According to the previous study in this area, there are few shapes which are commomly used as aeration devices. These are offset (steps), deflector (ramps), grooves (transverse galleries).

The purpose of ramp is to lift the flow away from the lower boundary of the chute or spillway. By lifting the flow away from the boundary, it forms a free trajectory allowing the underside of the nappe to become aerated. When flow once again rejoins the boundary, it should have entrained enough air to protect the downstream flow surface from cavitation damage. The water trajectory is a function of the following parameters as sketched below:

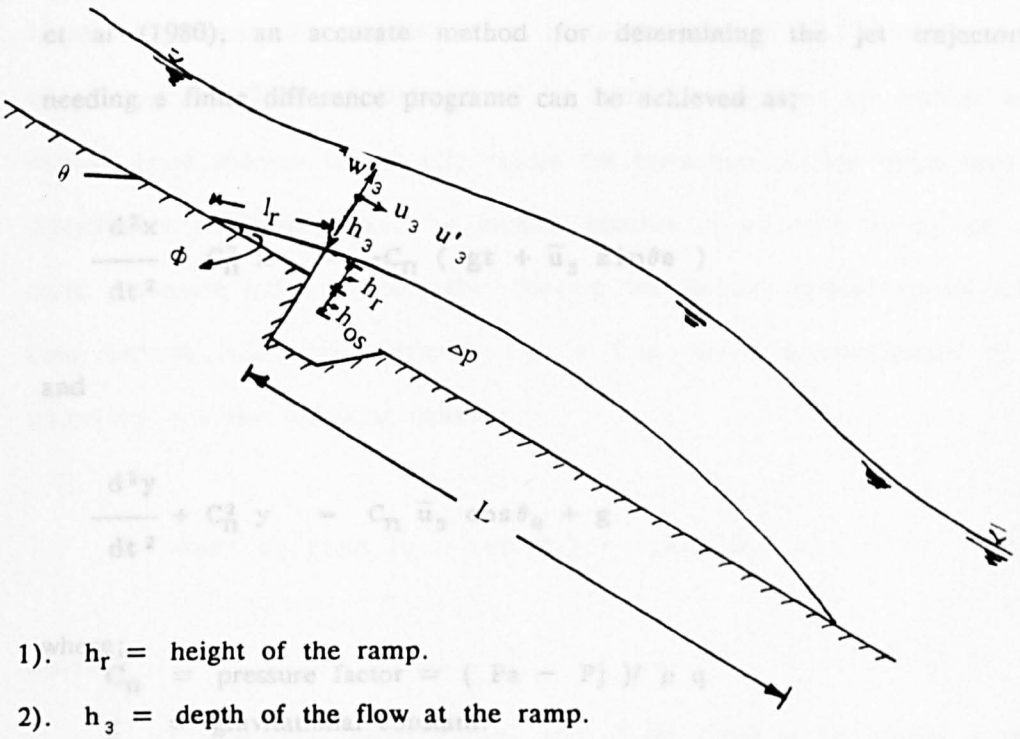

1). h_r = height of the ramp.

2). h_3 = depth of the flow at the ramp.

3). Φ = slope of the ramp.

4). l_r = length of the ramp.

5). Δp = pressure difference underneath the nappe.

6). $\bar{u}_3$ = average velocity of water at the ramp.

7). u'_3= longitudinal turbulent velocity component at the ramp.

8). w'_3= normal to bed turbulent velocity component at the ramp.

The height of the ramp h_r and angle of ramp Φ are the main factors to adjust the nappe length according to the requirement of air uptake by the jet. Several methods are available to determine the jet trajectory. Wei & DeFazio (1982) used a finite element method to solve the Laplace equation for flow over the ramp. This method produces excellent results for both ramps and free overfalls. In addition to solving for the jet trajectory, the pressure distribution around the ramp is determined. Knowledge of the pressure distribution is valuable for design of chute training walls in the vicinity of ramp.

The trajectory angle needs to be corrected when the ramp height is less than one–tenth of the flow depth or when the angle between the ramp and the invert is greater than 2^0. Based upon the studies of Glazov (1985) and Pan

et al (1980), an accurate method for determining the jet trajectory without needing a finite difference programe can be achieved as;

$$\frac{d^2x}{dt^2} + C_n^2 x = -C_n (gt + \bar{u}_3 \sin\theta e) \qquad (2.143)$$

and

$$\frac{d^2y}{dt^2} + C_n^2 y = C_n \bar{u}_3 \cos\theta_e + g \qquad (2.144)$$

where;

C_n = pressure factor = (Pa − Pj)/ ρ q

g = gravitational constant.

Pa = atmospheric pressure.

Pj = Pressure under the jet.

q = unit discharge of water.

$\bar{u}_3$ = mean flow velocity at ramp.

θ_e = angle betweeen the tangent to the nappe at ramp and horizontal.

ρ = density of water.

The angle θ_e, is determined by using the factor "Ar" given in Fig 2.39. This angle, in terms of the invert and ramp angle, is given by;

$$\theta_e = \theta_i(1-Ar) + Ar\theta_0 \qquad (2.145)$$

where

Ar = jet trajectory coefficent from Fig 2.39.

θ_i = angle between invert and horizontal

θ_0 = angle between ramp and horizontal

Through the proper choice of ramp angle and height, it is possible to cause the trajectory to impact the downstream chute at any desired location. Generally, the trajectory should impact downstream of the area that has the smallest value of the cavitation index of the flow. In some cases, this is

impossible because the smallest values occur downstream of the vertical bend of a tunnel spillway. The trajectory should be chosen so it does not impact within the vertical bend because this usually causes the formation of fins which lead to poor downstream flow conditions. An impact location in an area having an extremely small cavitation index is acceptable because the surface downstream of the impact area will be adequately aerated. For a first rough approximation of the jet trajectory, use the following equation:

$$\cos^2 \theta_0 \, (\tan \theta_i - \tan \theta_0) = g X_i / 2\bar{u}_3^2 \qquad (2.146)$$

where ;

X_i = horizontal distance from end of the ramp to jet impact point.

θ_i = angle between downstream chute and horizontal.

Eq (2.146) neglects both the reduced pressure under the nappe and the relative ramp height effect. In circular tunnels, the ramp height must be tapered around the circumference from a maximum value at the invert to zero at or above the point where the free water surface, at maximum discharge, intersect the tunnel wall. Without the taper, the fin size increases as the discharge increases. At large enough flow rates, the fin can fold over and choke the tunnel. With a tapering ramp, the upper portion of the jet is subjected to less contraction than the lower portion of the jet. Because of this, the angle where the jet impinges on the tunnel wall decreases as the flow rate increased.

A further development of the prediction of the jet trajectory is proposed in this thesis and is based on the turbulence measurements to be carried out along the ramp. It involves the outward component of turbulence velocity w' acting normally to the longitudinal velocity of the jet to form a resulting jet spread as sketched below,

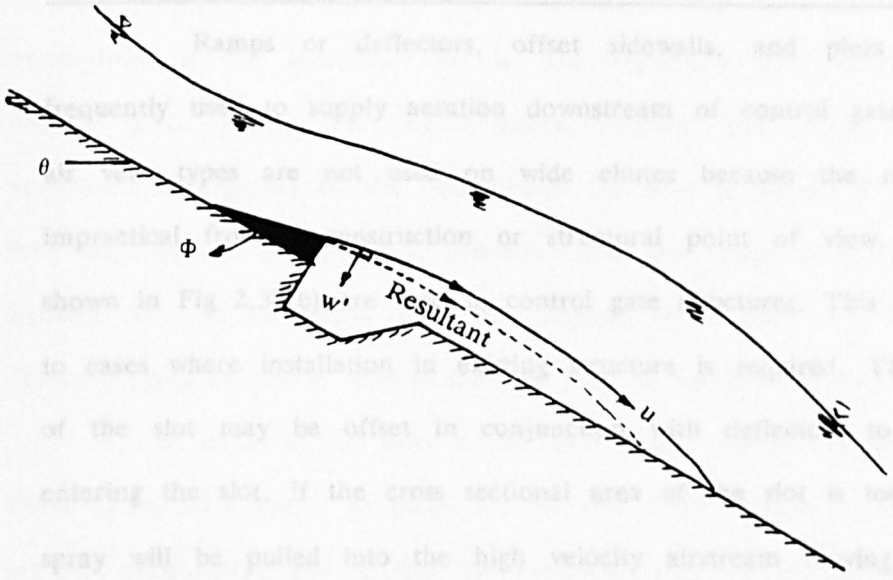

The resultant component of velocity is as sketched above and produces a shorter jet length than computed by normal means. This idea will be discussed further in chapter 7.

As a general rule the slope of the ramp relative to the spillway slope Φ, is less than 10^0, although there are some prototype structures with Φ values upto 15^0. The ramp height is usually quite small and often less than 0.5m prototype. Relevent data are shown in Table (2.4) showing dimensions of both prototype and model studies known to the author.

2.6.4 Air Vent design.

Several methods have been devised to vent air from the atmosphere to the underside of the nappe as shown in Fig 2.39. These includes the following:

1). Ramps or deflector on side walls.

2). Offset sidewalls.

3). Piers in the flow.

4). Slots and ducts in sidewalls.

5). Duct system underneath the ramp.

6). Duct system downstream of ramp.

Ramps or deflectors, offset sidewalls, and piers in the flow are frequently used to supply aeration downstream of control gates. Normally, these air vent types are not used on wide chutes because the required offsets are impractical from a construction or structural point of view. Slots in walls as shown in Fig 2.38(b) are used in control gate structures. This solution lends itself to cases where installation in existing structure is required. The downstream end of the slot may be offset in conjunction with deflectors to keep water from entering the slot. If the cross sectional area of the slot is too small, water and spray will be pulled into the high velocity airstream flowing in the slot. The result will be insufficient air to protect the flow surface on the chute floor. Ducts through the sidewall as shown in Fig 2.38(e) are used on wide chute when the required slot size or sidewall offsets are excessive. A duct is a closed conduit which may have a rectangular or circular cross section. In area where freezing is a problem, ducts are routed through an embankment. This prevent the formation of ice plugs in the duct during times when water may be standing in the chute area.

A duct, under the ramp as shown in Fig 2.38(f), is used on wide chutes or in installations where a hydraulic jump may cover the ramp. In both cases, the system of ducts and vent ensures adequate aeration of the jet undernappe. A duct downstream of the ramp as shown in Fig 2.38(g) used when the ramp height is too small to allow adequate venting. This scheme also simplifies construction. However, a drain for the duct must be provided to keep the duct free of water. Leakage and extremely low flow would tend to fill the duct on flat chutes if drainage is not provided. When operating the chute or spillway, air will enter the aerator not only through the duct but also through the drainage gallery. In circular conduits on steep slopes, filling of the duct is not normally a problem because only a small portion of the duct can contain water. The air duct for circular conduits is commonly called an aeration groove or air slot.

In some cases, an air duct design having a direct connection to the atmosphere is not feasible. This is true especially with tunnel spillways and control gates located in outlet–works tunnels. For these structure types, ventilation is supplied to the duct above the flowing water. If space above the free water surface is too small, pressure under the nappe may begin to fluctuate. Criteria for the air space above the flowing water have not been established. Presently, physical model studies must be used to investigate ventilation adequacy.

In terms of air duct or air vent sizes, typical examples are given in Table (2.5). The aim is to make the air vent large enough so that air velocities are not encountered and so that the pressure under the jet Δp does not fall too far below atmospheric. If Δp is significant than the jet reduces in length and entrains less air into the aerator. Typical values of Δp can be given in the form,

$$\frac{\Delta p}{\rho g h} \cong 0 \rightarrow 0.5 \qquad (2.147)$$

where h is the water depth at the ramp.

The value of Δp can be estimated from Bernoulli's equation and sketched below for typical case. This will be covered in more detail in Chapter 7.

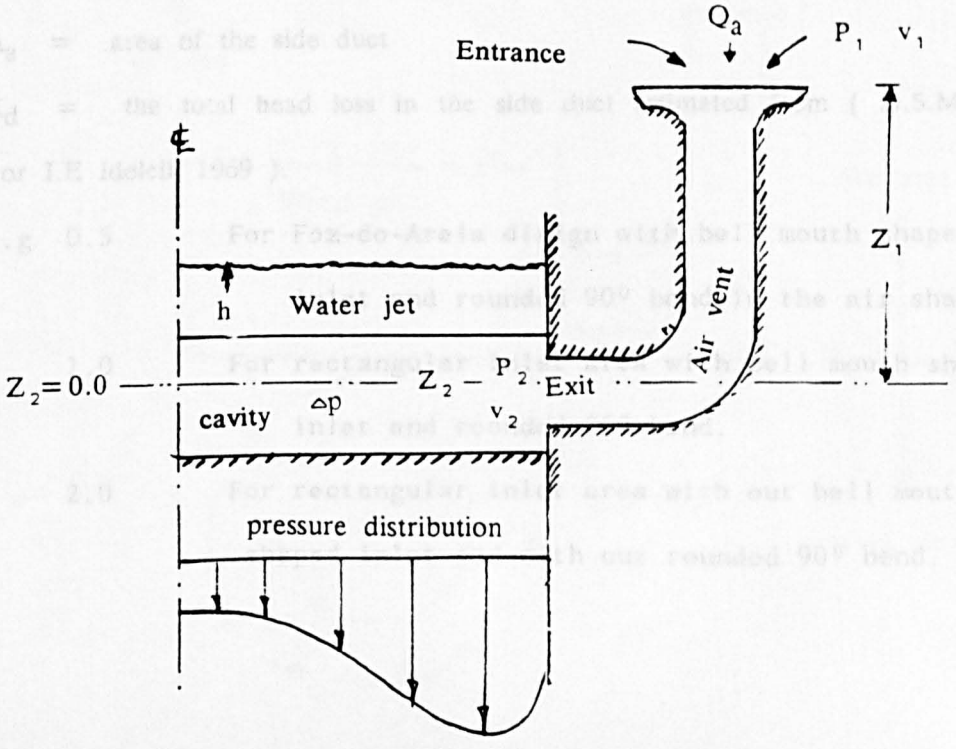

Applying Bernoulli's equation at inlet and exit of air vent

At Entrance = At Exit

$$\frac{P_1}{\rho_a g} + \frac{v_1^2}{2g} + Z_1 = \frac{P_2}{\rho_a g} + \frac{v_2^2}{2g} + Z_2 + h_l \quad (2.148)$$

re-aranging

$$\frac{P_1}{\rho_a g} - \frac{P_2}{\rho_a g} = \frac{v_2^2}{2g} - \frac{v_1^2}{2g} + Z_2 - Z_1 + h_l \quad (2.149)$$

where v_1, Z_2 are zero and $h_l = (k_1+k_2+k_3+k_4)$,

$$\Delta h = \frac{\Delta p}{\rho_a g} = \frac{v_2^2}{\rho_a g} + (k_1 + k_2 + k_3 + k_4)\frac{v_2^2}{2g} \quad (2.150)$$

assuming $v_2 \simeq v_a$
and $K_d = (1 + h_l)$

$$\Delta p = \rho_a \frac{v_a^2}{2} (K_d) \quad (2.151)$$

where,

ρ_a = air density

v_a = velocity of air Q_a / A_a

A_a = area of the side duct

K_d = the total head loss in the side duct estimated from (D.S.Miller, 1978, or I.E Idelcik 1969).

e.g 0.5 For Foz-do-Areia disign with bell mouth shaped inlet and rounded 90° bend in the air shaft.

1.0 For rectangular inlet area with bell mouth shaped inlet and rounded 90° bend.

2.0 For rectangular inlet area with out bell mouth shaped inlet and with out rounded 90° bend.

Typical values of K are given below varying from to 0.5 – 2.0. These includes entry losses to the air vent system, bends losses and friction losses.

There is now considerable discussion as to the best method of modelling the air flow, once it has entered the cavity under the jet. The reason for this discussion is the non– uniform distribution of air flow across the spillway width as sketched above. Most models assume that air has a uniform distribution in the cavity providing uniform entrainment into the underside of the jet.

In an effort to produce more realistic model Rutschmann and Volkart (1988) proposed an analogy for air distribution of a manifold pipe with various offshoots shown in Fig 2.40.

Rutschmann and Volkart's manifold model provided a useful begining point for predicting the distribution of air flow with spillway width. Its basic concept however has been challenged by Frizzell (1988) (private communications), who embarked on a two– dimensional numerical model simulation of air flow patterns in the cavity under the jet.

Considering the plan view only, a schematic representation is given below revealing a large air flow circulation in plan view, which is considerably removed from manifold model discussed above.

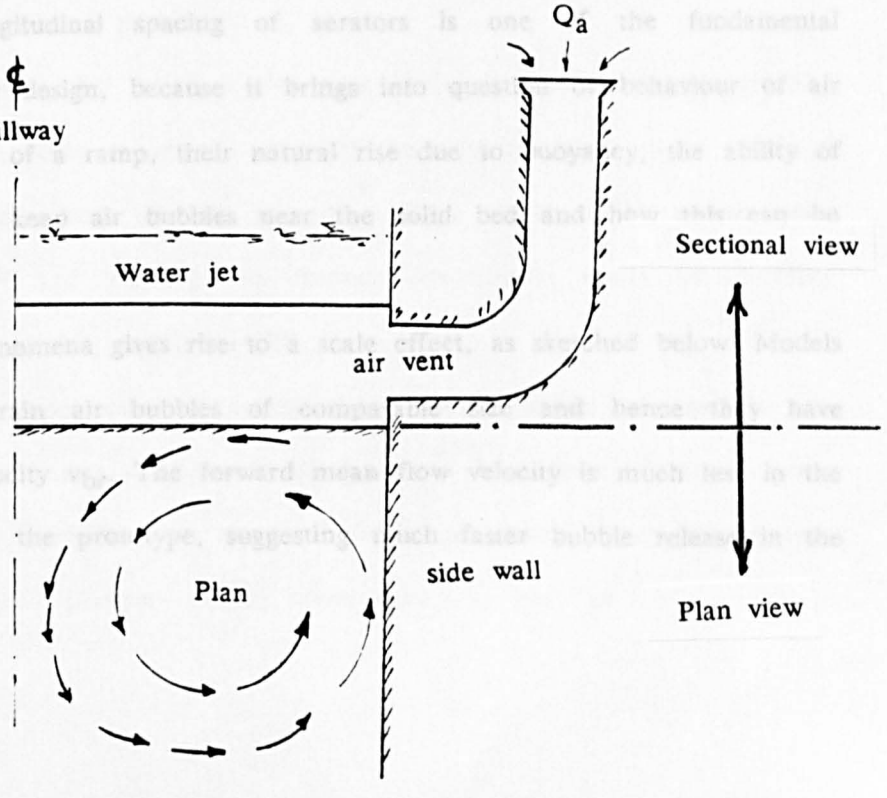

In conclusion, according to Vischer et al (1982) it should be noted that the final air flow occuring in an aerator ramp system depends on the balance between the air pumping capacity of the jet and the supply air vent characteristics. This is sketched below,

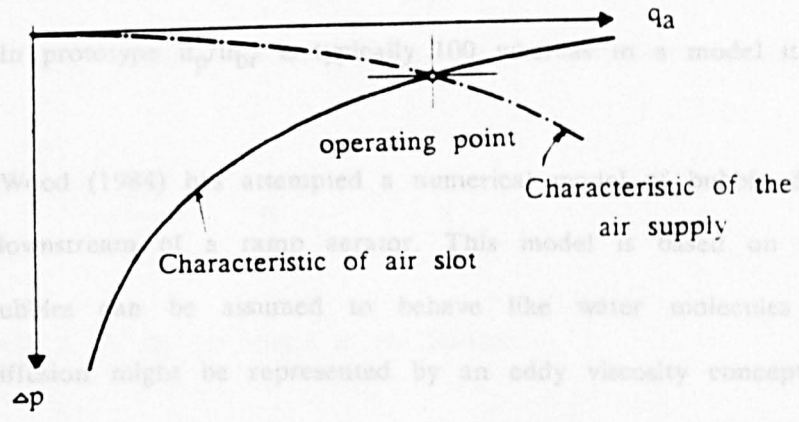

2.6.5 *Longitudinal spacing of aerators.*

The longitudinal spacing of aerators is one of the fundamental questions of aerator design, because it brings into question of behaviour of air bubbles downstream of a ramp, their natural rise due to buoyancy, the ability of turbulent eddies to keep air bubbles near the solid bed and how this can be modelled.

This phenomena gives rise to a scale effect, as sketched below. Models and prototypes entrain air bubbles of comparable size and hence they have comparable rise velocity v_{br}. The forward mean flow velocity is much less in the model compared to the prototype, suggesting much faster bubble release in the model.

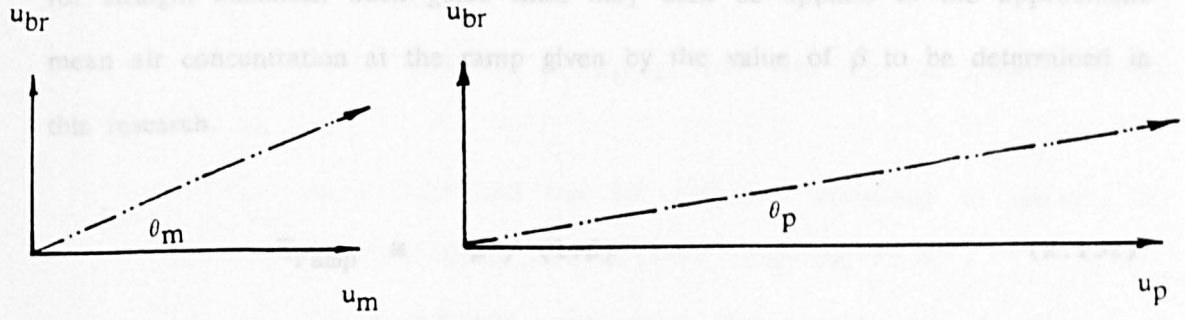

In prototype u_p/u_{br} is typically 100 whereas in a model it is typically 15 – 30.

Wood (1984) has attempted a numerical model of bubble diffusion and advection downstream of a ramp aerator. This model is based on the premise that air bubbles can be assumed to behave like water molecules and hence turbulent diffusion might be represented by an eddy viscosity concept where the velocity is substituted by the air concentration. The turbulent diffussion is outlined in detail in section 2.2.6.

Wood (1984) presented the results for a 45^0 spillway with water velocity of 30m/sec and bubble rise velocity of 0.2 m/sec are shown in Fig 2.41. The Fig 2.41 shows that the velocity distribution in the flow is logarithmic and the diffusivity distribution is parabolic.

This approch by Wood is the most useful in determining longitudinal aerator spacing. It enables air concentration at the solid boundary to be predicted in the downstream direction, starting off with a large source of air concentration at the aerator itself and showing the distance downstream where concentration drop to unacceptable levels, say below 5%.

In the absence of a numerical model, rough guide lines on the loss rates of aeration per meter downstream of the ramp have been observed. Prusza et al (1983) quotes aeration loss rates of 0.2% per meter (straight channels) whereas Semenkov and Lentjaev (1973) quote values as high as 0.8% per meter

for straight channels. Such guide lines may then be applied to the approximate mean air concentration at the ramp given by the value of β to be determined in this research.

$$\bar{c}_{ramp} \cong \beta / (1+\beta) \qquad (2.152)$$

A more sophisticated approach has been advocated by Hamilton (1984) suggesting the mean air concentration at any distance x downstream of the ramp is given by,

$$\frac{\bar{c}_x}{\bar{c}_{ramp}} \cong e^{-0.017(x-x_0)} \qquad (2.153)$$

where x_0 is the jet length at the aerator.

2.6.6 *Design procedures for aerator ramp.*

The purpose of this section is to give a brief outline of cuurent design practice for aerators, and to show what improvement may be made in the light of the research work in this thesis. The following steps are recommended in the design of a structure where cavitation is one of the major aspect.

1). Decide upon a preliminary design configuration of the structure. Include the alignment and profile, the capacity of the structure required to pass the maximum flows, and the location of ancillary structures such as diversion tunnels, plunge pool, energy dissipater etc.

2). Study the cavitation characteristics of the structure.

3). If air slot ramps is decided to install, use the computer programme in Chapter 7, to calculate the gradually varied water surface profile and find out the location of air slot ramps.

4). Select the ramp angle and find out the jet trajectory by using same computer

programme as stated above.

5). Select the optimum ratio of β (q_a/q_w) and find out the quantity of air entrainment required.

6). Adjust the ramp angle and the jet trajectory according to required air entrainment and get an operating point as stated in section 2.6.4.

7). Analyse the bubble dynamics, distribution and concentration downstream of aerator.

8). If air concentration reduces to less then 7% at the bed provide another air slot ramp.

9). Repeat the procedure 3 to 8 until reached at the end of spillway.

2.7 *SCALE EFFECTS IN AERATORS.*

The main scale effects in modelling aerators are viscous and surface tension effects as characterised by Reynolds Number and Weber Number. The viscous effects manifest themseleves in the magnitude of turbulence in the range of eddy length required for air entrainment (1− 10mm). The surface tension effect manifest themselves in the "resistance" of the jet free surface in being broken, to form spray (outwards) and air entrainment (inwards).

For this reason Hunt (1984) first proposed the ratio of disturbing turbulent forces to restraining surface tension forces as a key parameter in determining whether a jet will spread, from spray or cause free surface aeration. Hunt proposed the outward turbulent pressure to be given by $\frac{1}{2}\rho(w')^2$ causing a bulge in the jet free surface which is hemispherical in shape (an idealisation). The surface tension stress in the surface of the bulge is therefore $2\sigma/R$, where R is the bulge radius of curvature

$$\frac{\frac{1}{2}\rho(w')^2}{2\sigma/R} = \frac{\rho R(w')^2}{4\sigma} \qquad (2.154)$$

Therefore the ratio is very significant.

Ervine and Falvey (1987) advanced this argument, showing that $w' \cong 0.4u'$ for a jet and the radius of the bulge is related to the air bubble diameter for an air entrainment (d_b). Subsituting suitable values in Eq (2.154), they showed that the value of u' is the range

$$u' \cong 0.25 \text{ to } 0.3 \text{ m/sec (for aeration to begin)} \qquad (2.155)$$

This can be translated into a mean velocity for aeration to begin, provided the turbulence intensity near the free surface is known. Falvey and Ervine (1988) show the upper free surface of chute to have a turbulence level around 5% longitudinally giving $\bar{u}_{min}$ for free surface aeration around 5 to 6 m/sec (see Fig 2.42).

For the underside of the jet in a ramp aerator, the value of longitudinal turbulence is often in excess of 10% giving mean velocities for aeration to begin around 2 to 3 m/s. Bruschin (1987) suggested the model prototype correlation as,

$$\beta = K \frac{(L)}{d} \left(1 - \frac{V_{min}}{V} \right) \qquad (2.156)$$

where

V = velocity of water
L = length of the jet
d = depth of the flow

$$\beta_* = \frac{\beta_p}{\beta_m} = \frac{V_{min\ p} / V_p}{1 - V_{min\ m} / V_m} \qquad (2.157)$$

$$V_p = \sqrt{\lambda}\, V_m$$

where subscripts p and m stands for prototype and model. λ is the geometric scale function.

Although the criterion u'> 0.25 m/sec is useful as a guide for

inception of aeration, it represent only the threshold over which turbulence needs to go to sustain free surface aeration. It represent the restraining surface tension being overcome, but does not produce a definitive picture of scale effects for any given model study.

Ervine and Falvey (1987) proposed that this is only possible by producing turbulent energy spectra over a wide range of eddy lengths, because the fundamental problem of scaling is that scale models have smaller turbulent energy in the range of eddy lengths required for entrainment. This is sketched below for a small scale model, a large scale model and prototype structure.

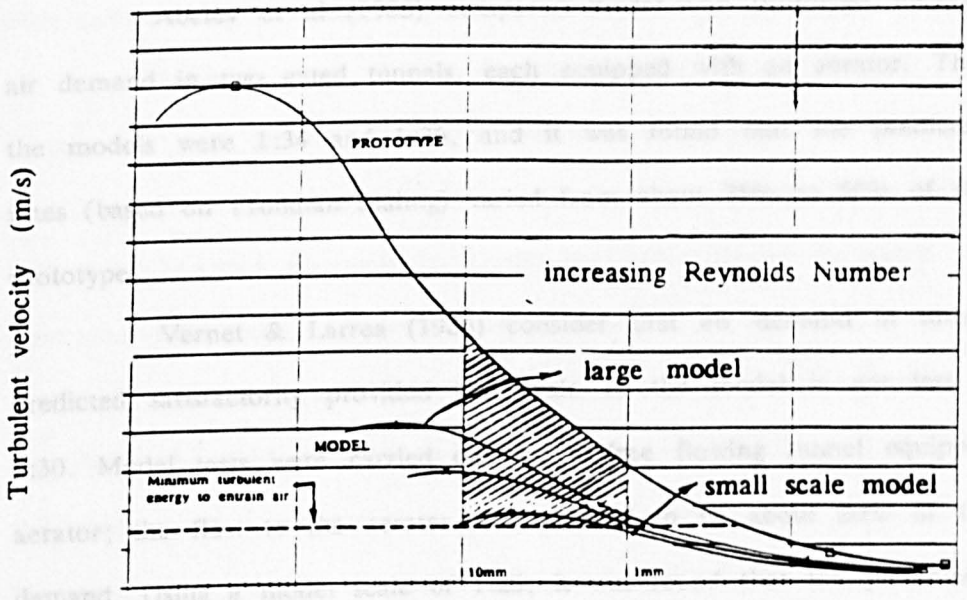

The shaded area under the small model spectrum above is very small compared to either the larger model or prototype, and hence is likely to have substantially less aeration.

Until the process sketched above can be quantified, accurate scale effects assessment will not be possible. Some interesting studies on aeration scale effects were carried out by S.Pan and Y.Shao (1984) at Fengjiashan Project. According to dimensional analysis, Pan suggested that Reynolds and Weber Numbers should also be taken into account when modelling of air entrainment was made on a scale model using Froude law of similitude.

Reynolds Number reflects the turbulence level of the flow. The

characteristic length contained in Reynolds Number should be the cavity length L. Plotting the experimental data of Reynolds Number $Re_L = (v_1 L/\nu)$ against the parameter $\lambda = \beta_p/\beta_m$, Pan obtained a graph which shows that when $Re_L > 3.5 \times 10^6$ in model and the value of λ approaches unity, scale effects can be neglected as shown in Fig 2.43. Furthermore , Pan and Shao ploted V_1 the flow velocity at different model scales verses $\lambda = \beta_p/\beta_m$ shown in Fig 2.44. This clearly shows that when model velocity $V_1 > 6$ to 7 m/sec, the value of λ approaches to unity; otherwise, it will increase rapidly as V_1 decreases as shown in Fig 2.44.

Abelev et al (1983) compared model and prototype measurements of air demand in two gated tunnels, each equipped with an aerator. The scales of the models were 1:34 and 1:36, and it was found that the predicted air flow rates (based on Froudian scaling) varied from about 25% to 50% of those in the prototypes.

Vernet & Larrea (1985) consider that air demand in tunnels can be predicted satisfactorily provided that scale of the model is not less than about 1:30. Model tests were carried out for a free flowing tunnel equipped with an aerator; the flow to the aerator was assessed to be about 20% of the total air demand. Using a model scale of 1:25, it was found that the predicted flow rates of the air were about 90% of those in the prototype. Data from 1:6 and 1:25 scale models of an aerator are presented by Galperin et al (1977). At low discharges, the air demand in the 1:6 model was up to twice that in the 1:25 model, but at higher discharges the two model gave the similar results.

Quintela (1980) describes Russian studies carried out in connection with Nurek Dam USSR. Eight aerators were fitted to a tunnel discharging on to a chute spillway. Tests of a 1:35 scale model predicted air demands that were only about 20– 25% of those subsequently measured in the prototype. Pinto & Neidert (1982) investigated the effect of scale when studying aerators for Foz do Areia Dam Brazil. Sectional models were tested in a 150 mm wide flume at a scales of

1:50, 1:30, 1:15 and 1:8; also a 1:30 general model was used to reproduce one half of the prototype spillway which is 70.6 m wide. The predicted air demands (based on Froudian scaling) in the 1:8 and 1:15 sectional models were found to be in good agreement with measurements made in the prototype. The 1:30 and 1:50 models underestimated the entrainment, but the difference relative to the prototype became smaller as the water discharge increased. However, the results also show that the 1:30 non–sectional but general model gave air demands that were only 40% of those in the 1:30 sectional model. This suggests that the agreement between the two larger scale sectional models and prototype may have been enhanced by increased entrainment at the side walls of the flume.

Zagustin et al (1982) and Zagustin & Castillejo (1983) carried out comparative tests on the ramp–type aerators to be used in chute no 3 of Guri Dam Argentina. Sectional models at scales of 1:50, 1:40, 1:30, 1:25, 1:15 and 1:10 were installed in series in a 300 mm wide flume. Predicted air demands from the 1:10 and 1:15 models were found to be satisfactory agreement with prototype measurements, while the 1:20 model gave values that were about 10% low. Since the width of each model was the same, the effect of the side walls on the amount of entrainment may have increased as the scale become larger. Measured cavity lengths in the 1:50 model were found to be 20–30% greater than those in the prototype; this was due to the fact that the amount of suction at the aerator was too small in the model. Evidence from studies of aerator suggests that they need to be model at larger scale than gated tunnels in order to give reliable estimates of air demand. Aerator entrain air strongly when the water surface above the cavity breaks up into a spray; it is likely that a higher velocity and level of turbulence are required to produce this spray than to draw air along a tunnel flowing partly full.

McPhee Dam (USA) and Tarbela Dam (Pakistan) are the prototype structures which have been studied in this research. McPhee Dam was studied at USBR (Colorado) at a model to prototype scale of 1:36. Measurements were

taken for piezometirc pressure profiles, cavity length under the jet, flow profiles and air demand through the vent. A comparision between model and prototype air demand is shown in Fig 2.45. The model air demand was increased considerably by increasing the turbulence, which reduces the nappe length. However, its prototype air demand was still higher. This may be the case of small scale model which cannot generate proper turbulence for the air uptake in the jet. Air demands for small models (scales less than 1:15) can be brought closer to simulating prototype air demand by including extra turbulence in the model.

Turbulence measurements in both model and prototype are needed to determine the turbulence level in the model that would correctly scale prototype air demand.

Tarbela Dam (Pakistan) was model studied at Colorado State University, at a model to prototype scale of 1:12. Comparision of model to prototype performance of air slot in tunnel 3 and tunnel 4 are shown in Fig 2.46. Observation of tunnel 3 and tunnel 4 indicate that the airslots are functioning very effectively. At Tarbela Dam aspect ratio (B/h) is very small. Hence deep flow over a small ramp produces high turbulance and increases the air uptake ability of the jet.

It is clear that scale effects in aerators are still not properly understood, although it appears that larger sectional model can reproduce prototype aeration. In most cases the sectional models had velocities greater than 8 to 10 m/sec and also enhanced their aeration characteristics by side wall aeration which has relatively greater effect in a sectional model compared with a prototype structure.

It was decided therefore in this thesis to devote some attention to aerator scale effects, based on turbulence measurements carried out in the Glasgow scale model, but also by comparing model and prototype data over a range of situations.

Slope	Air Concentration $\bar{c}$
7.5°	0.137
15°	0.245
22.5°	0.302
30°	0.410
37.5°	0.560
45°	0.618
60°	0.675
75°	0.715

Table 2.2 The Variation of air concentration $\bar{c}$ with channel bed slopes

Author	Nozzel diameter range mm	Jet length range mm	Jet velocity range mm	R_{e_0} range x 10^4	Nozzle geometry L_0/d_0
Henderson	2.54to12.7	10 – 270	10 - 30	max 20	0,1, 10
van de savde	1.95 to 10	100-400	3 - 10	max 5	50
Cunming	4.5 to 9	100-800	1.3-8.7	1 to 8	0,5,10,80
van de donk	10 to 100	260-1070	1.5- 11	13 - 40	2.2 - 22
Ervine	6 to 25	0 - 4700	2 - 6	2 - 10	1 - 4
Kuinagai	2 to 8	20 - 800	1.2 - 37	0.9 -15	50

Notes: (i) All water/air systems

(ii) R_{e_0} = Reynolds number at outlet

(iii) L_0 = length of the cylinderical section of a nozzle.

Table 2.3 Experimental conditions in different authors studies of air entrainment by plunging jets.

DAM	Width of Spillway B (m)	Maximum discharge q_a (m^2/sec)	Spillway slope θ degree	Ramp slope Φ degree	Ramp height h_r h_r (m)	Offset height h_{os} (m)	Groove height h_{gr}(m)	Method of Air supply
Foz-do-Areia	70.6	156	14.5	7.1	0.2	-	1.3	Lateral ducts
Tarbela Dam	4.9	266	0.0	7.125	0.134	-	0.9	Slot in Floor
Emborcacao	58.5	48.3	10.2	7.1	0.3	-	2.8	Slot in Floor
Colbun	50 - 71	54.7	31	11.3	0.39	0.25	2.25	Lateral duct
Amaluza	72.1	18.4	66.8	**	**	-	2.0	Slot in Floor
McPhee Dam	18.3	7.75	16.6	6.4	0.91	-	-	Lateral duct

Table 2.4 Data on Prototype aerators

Friction loss factor fL/D_e	Total loss	Critical pressure ratio P_j/P_i	Pressure drop Kpa	Max Velocity m/sec
0.01	0.51	0.68	6.88	87
0.1	0.6	0.66	6.67	83
1.0	1.5	0.57	5.76	62
10.0	10.5	0.36	3.64	23
100.0	100.5	0.13	1.31	4.6

Table 2.5 Maximum pressure drop and air duct activity (Falvey)

Plate 2.1 Glen Canyon Dam left Spillway tunnel 11m deep hole (Sept 1983)

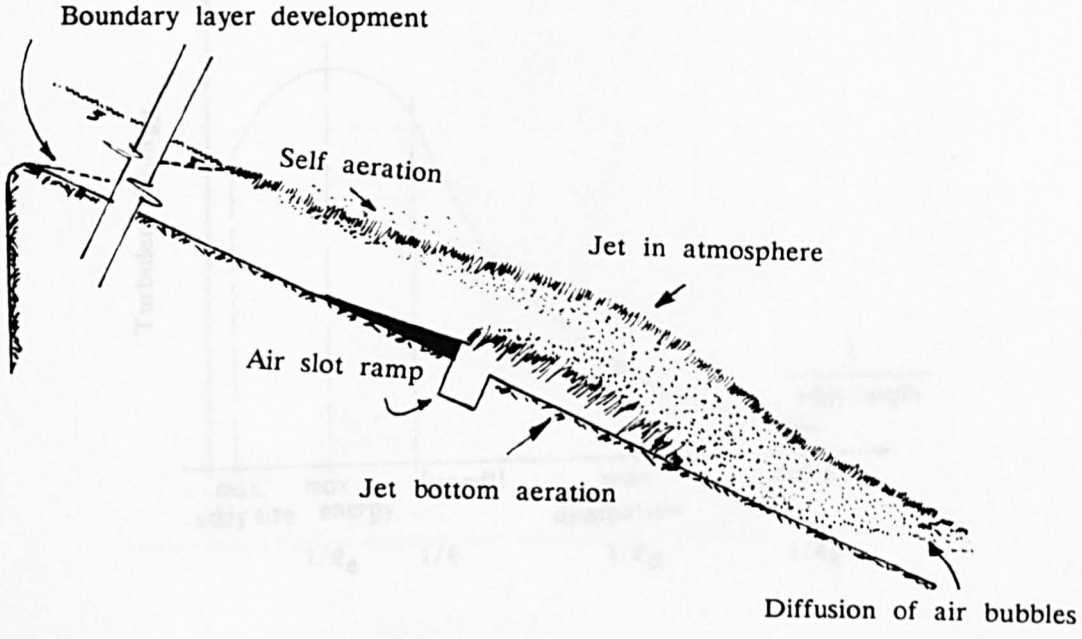

Fig 2.1 Flow phenomena at air slot ramp

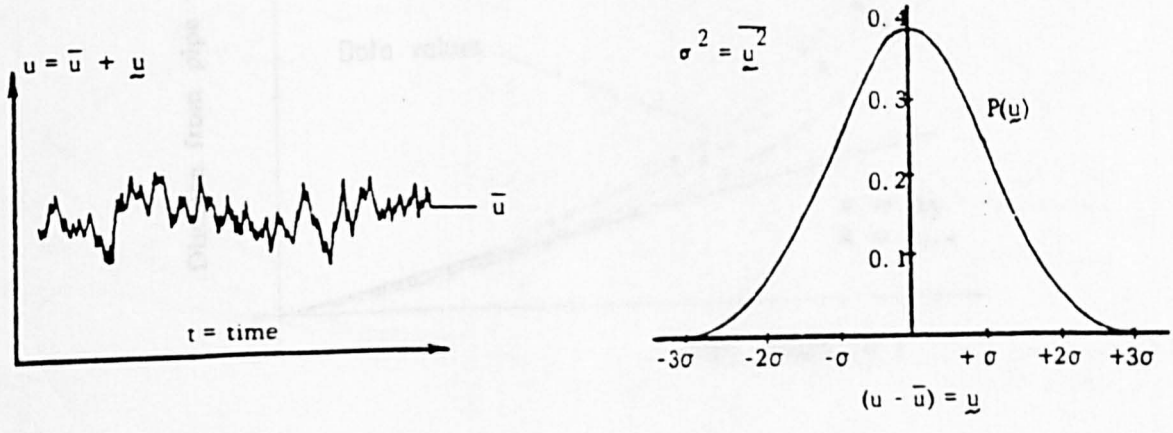

Fig 2.2 Variation & distribution of turbulent velocity

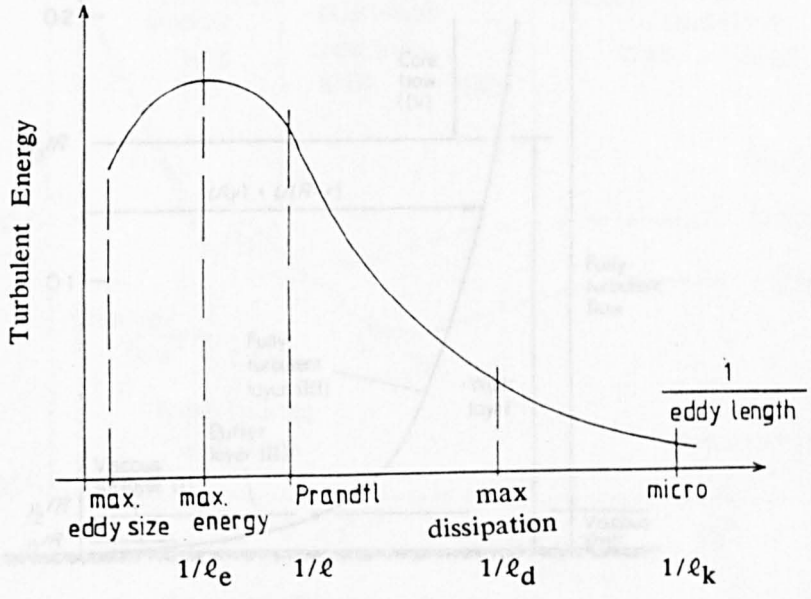

Fig 2.3(a) Turbulent energy spectrum

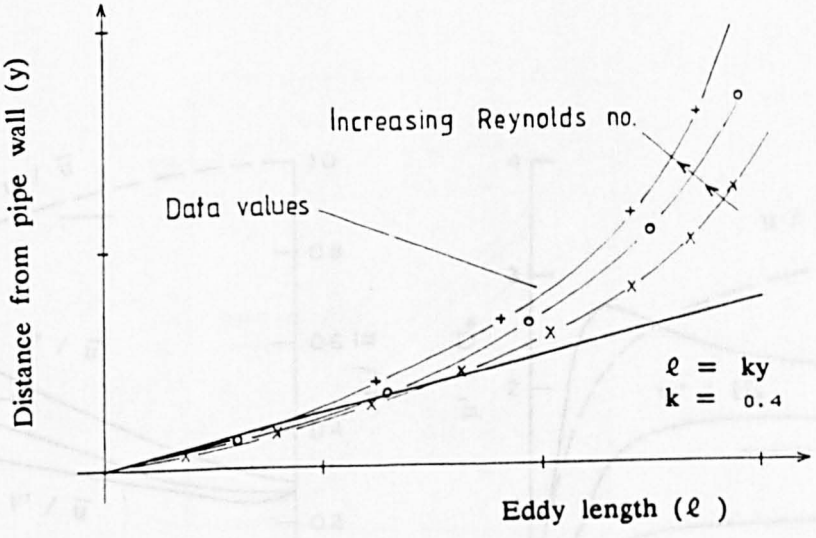

Fig 2.3(b) Eddy length comparison in pipe flow

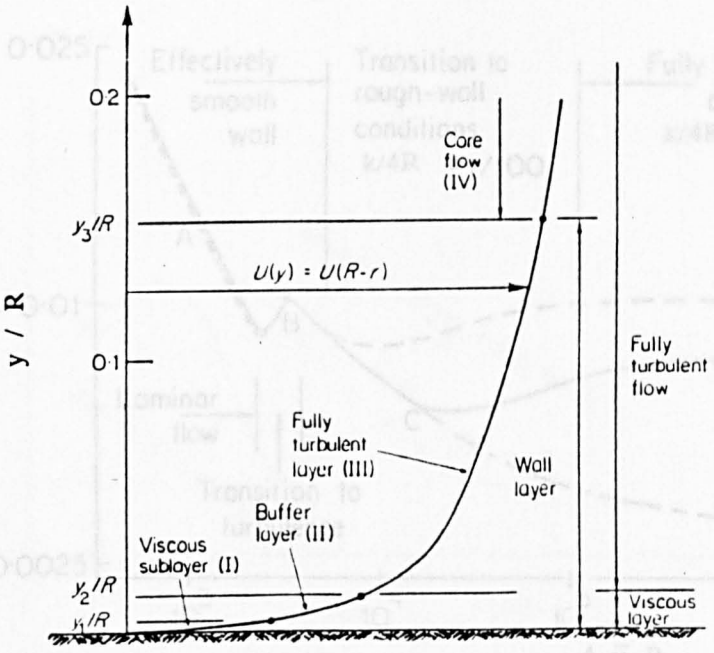

Smooth wall

Fig 2.4 Mean velocity variation near the smooth wall of a pipe radius R

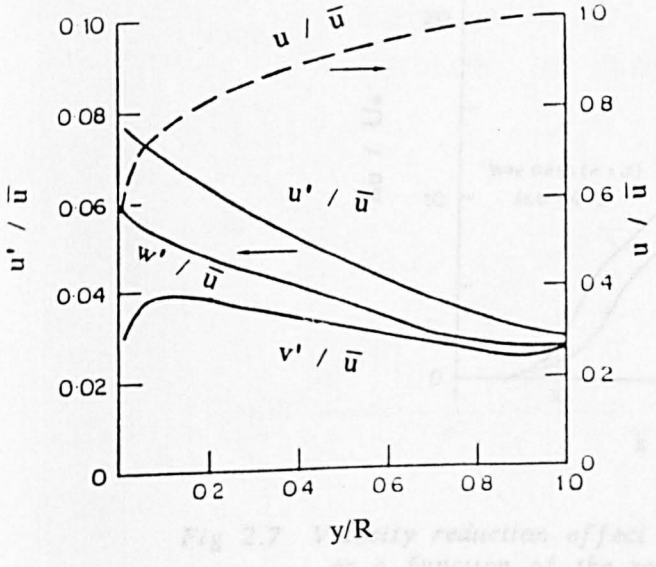

(a) Fully turbulent region

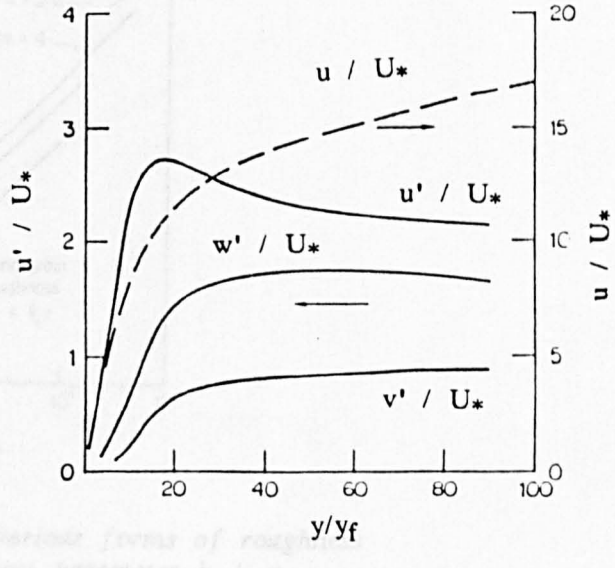

(b) Viscous & wall layers

Fig 2.5 Variation of component intensities and mean velocity in pipe flows, based on measurements of Laufer

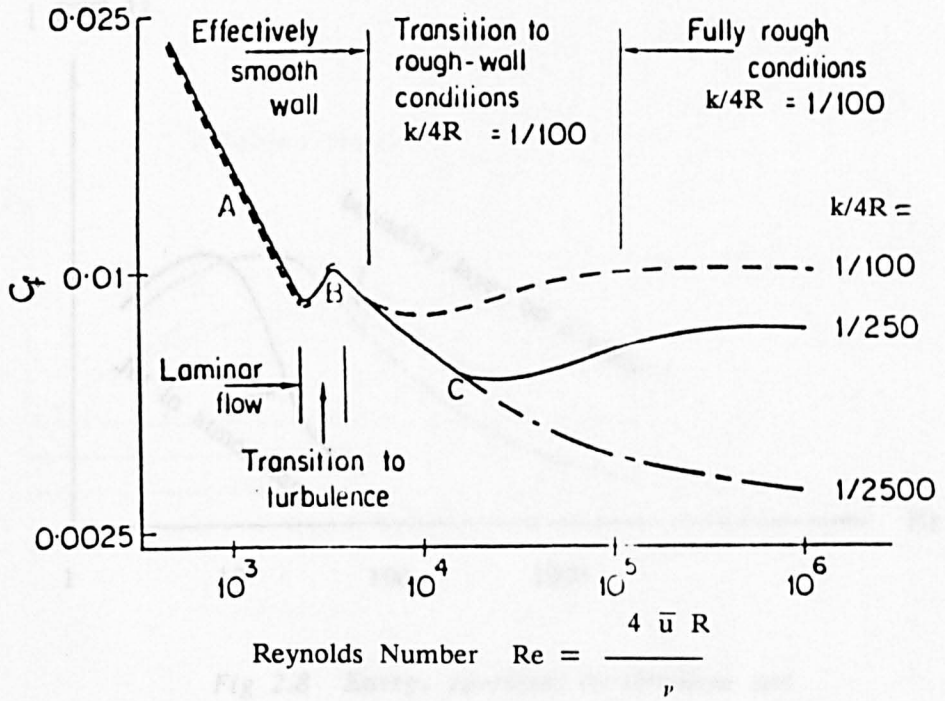

Fig 2.6 Relation between Reynolds Number and Friction factor (Shown by A.J.Reynolds 1974)

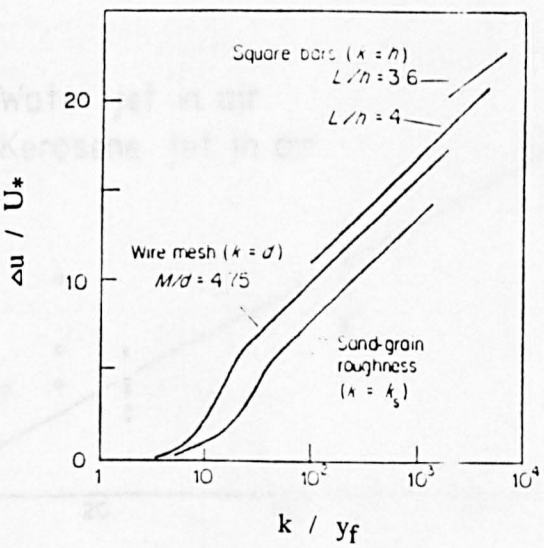

Fig 2.7 Velocity reduction effect by various forms of roughness as a function of the roughness parameter k / y_f

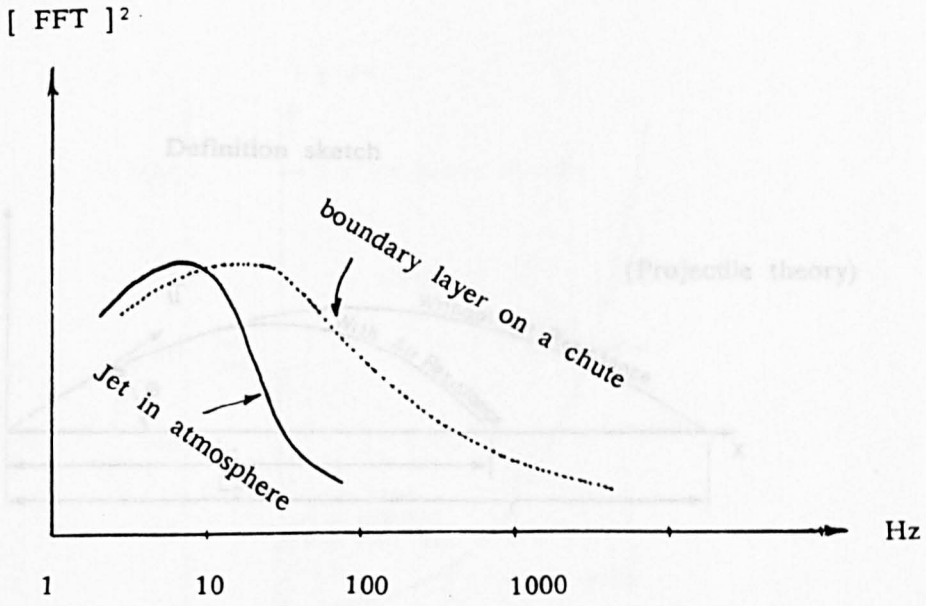

Fig 2.8 Energy spectrum in turbulent jets

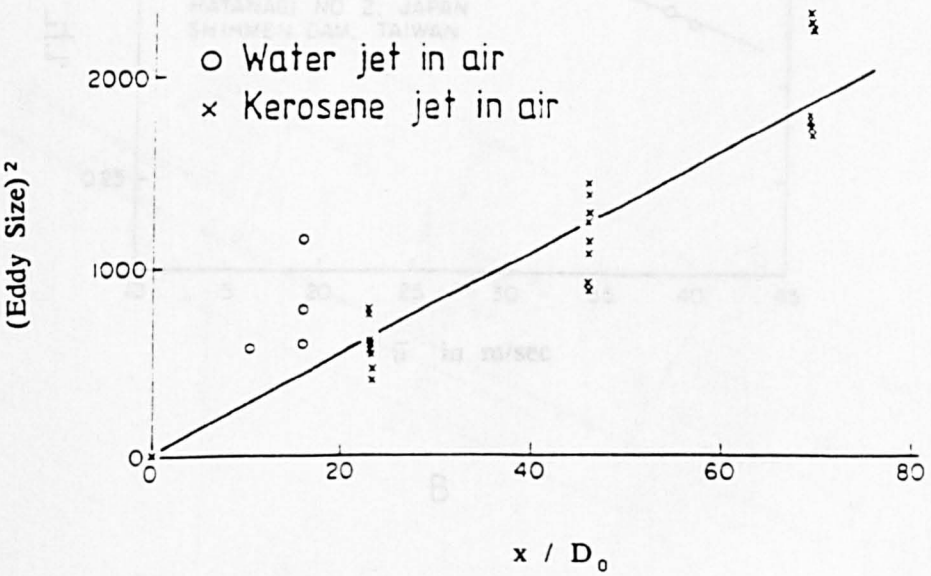

Fig 2.9 Plot of (Eddy size)² with (x / D_0) for restrained turbulent Jets. (Davis)

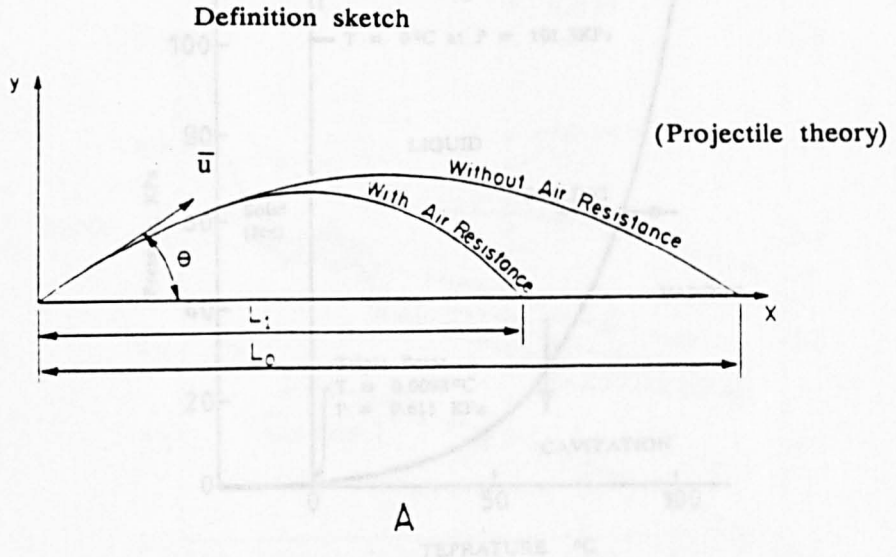

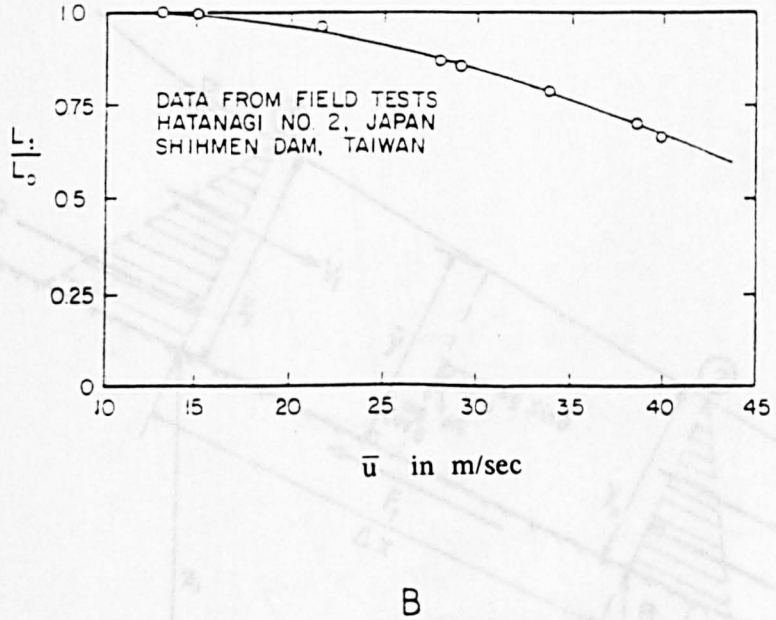

Fig 2.10 Jet trajectory with air resistance (Novak)

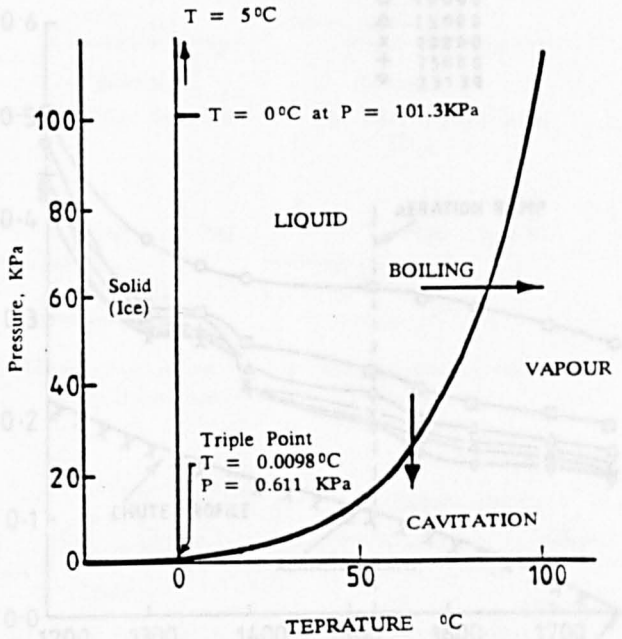

Fig 2.11 Phase diagrame of water

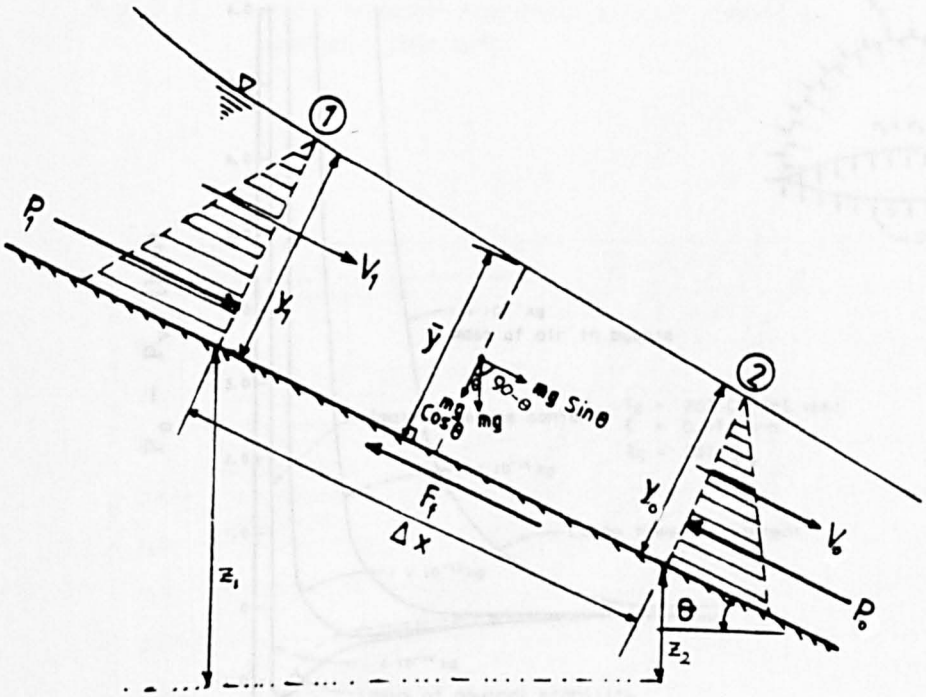

Fig 2.12 Sketch diagram illustrate short channel section Δx apart

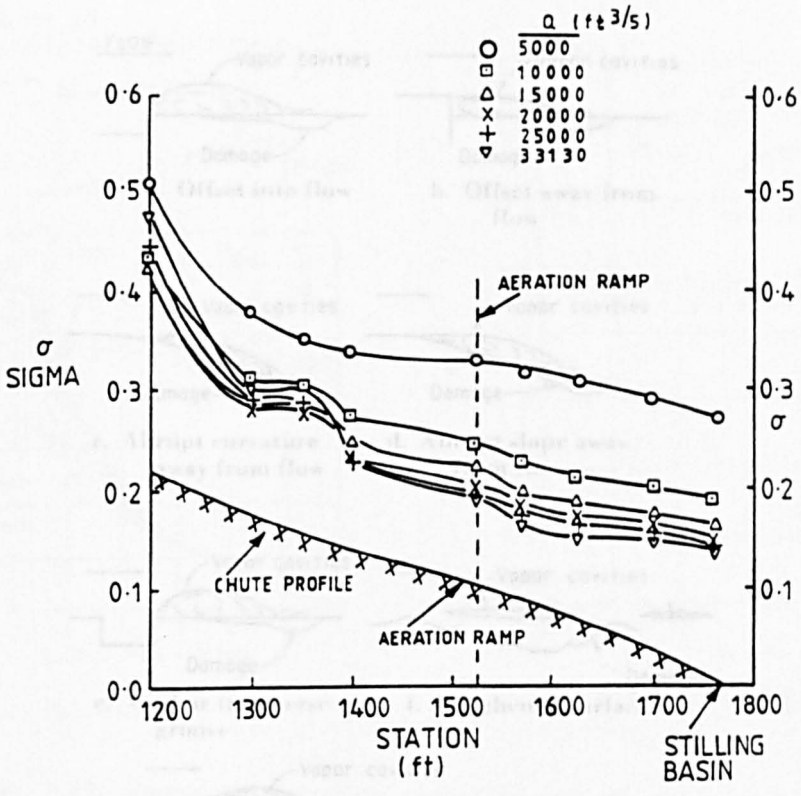

Fig 2.13 Computed cavitation Index for McPhee Dam Spillway (Pugh.C.A)

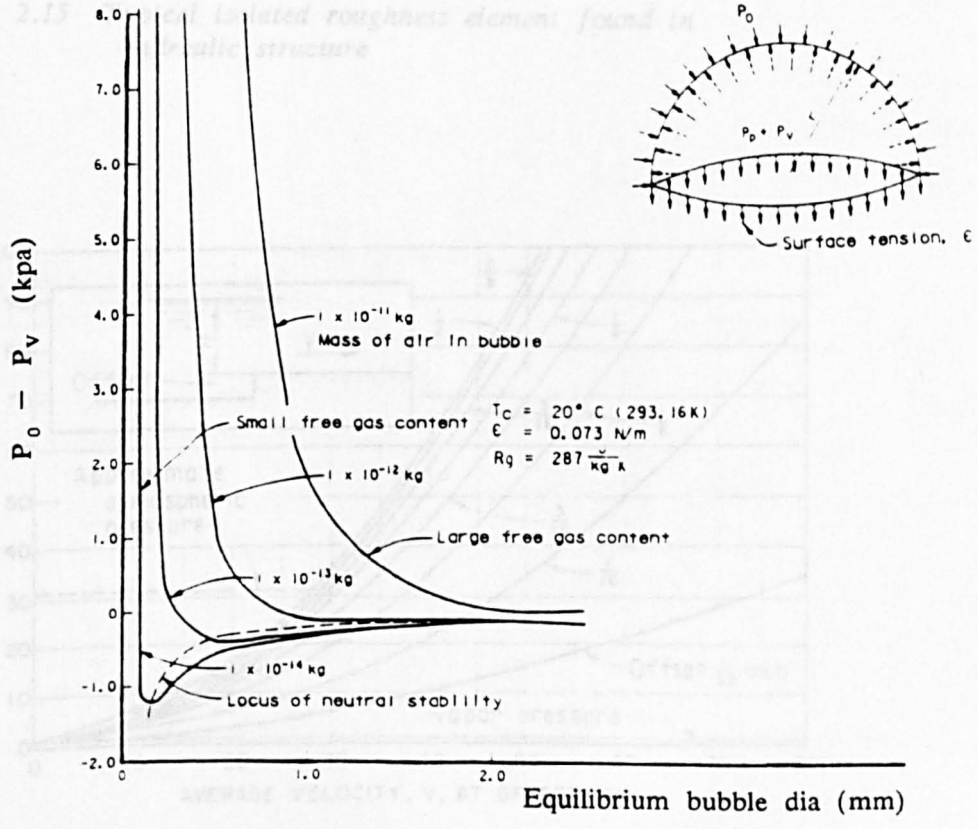

Fig 2.14 Equilibrium conditions for vapor bubble containing air (Falvey)

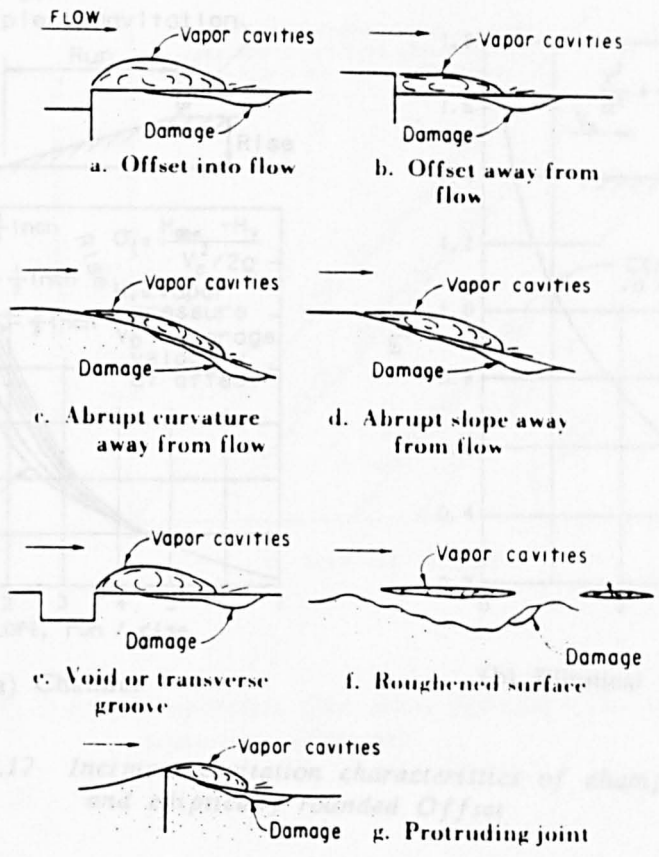

Fig 2.15 Typical isolated roughness element found in hudraulic structure

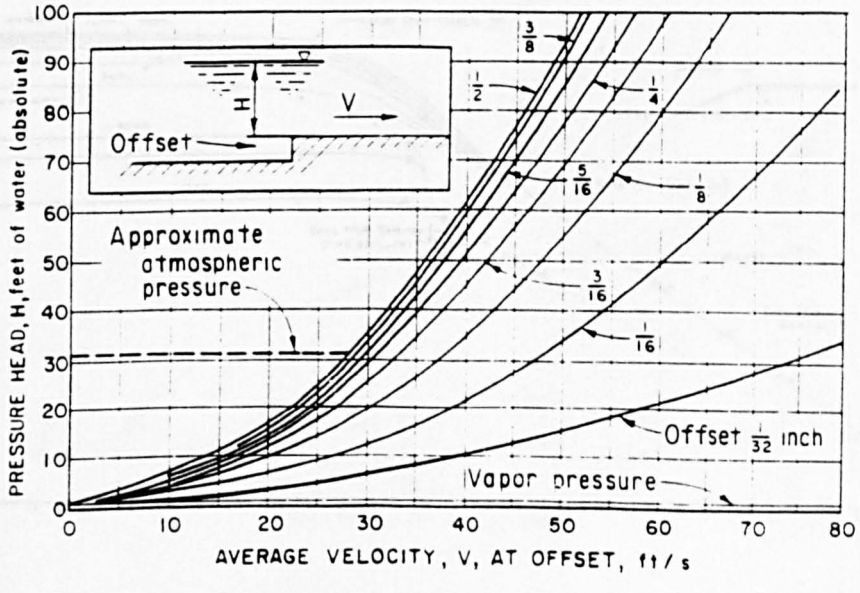

Fig 2.16 Incipient cavitation characteristics of Offsets (Colgate & Elder)

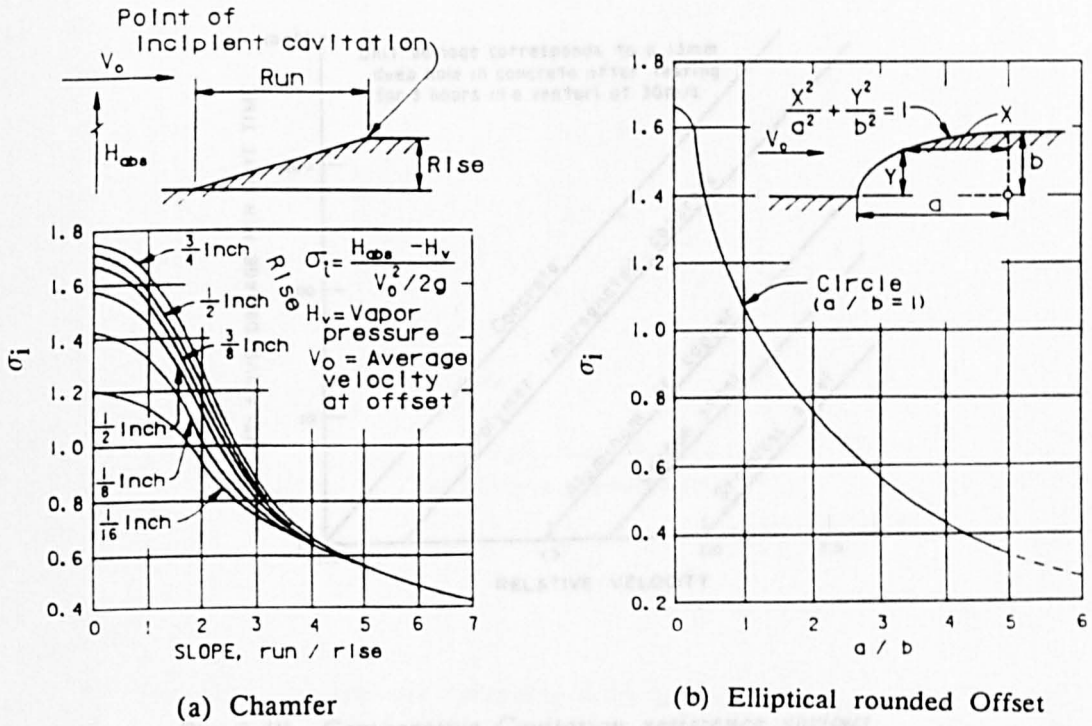

(a) Chamfer

(b) Elliptical rounded Offset

Fig 2.17 Incipient cavitation characteristics of chamfered and elliptically rounded Offset

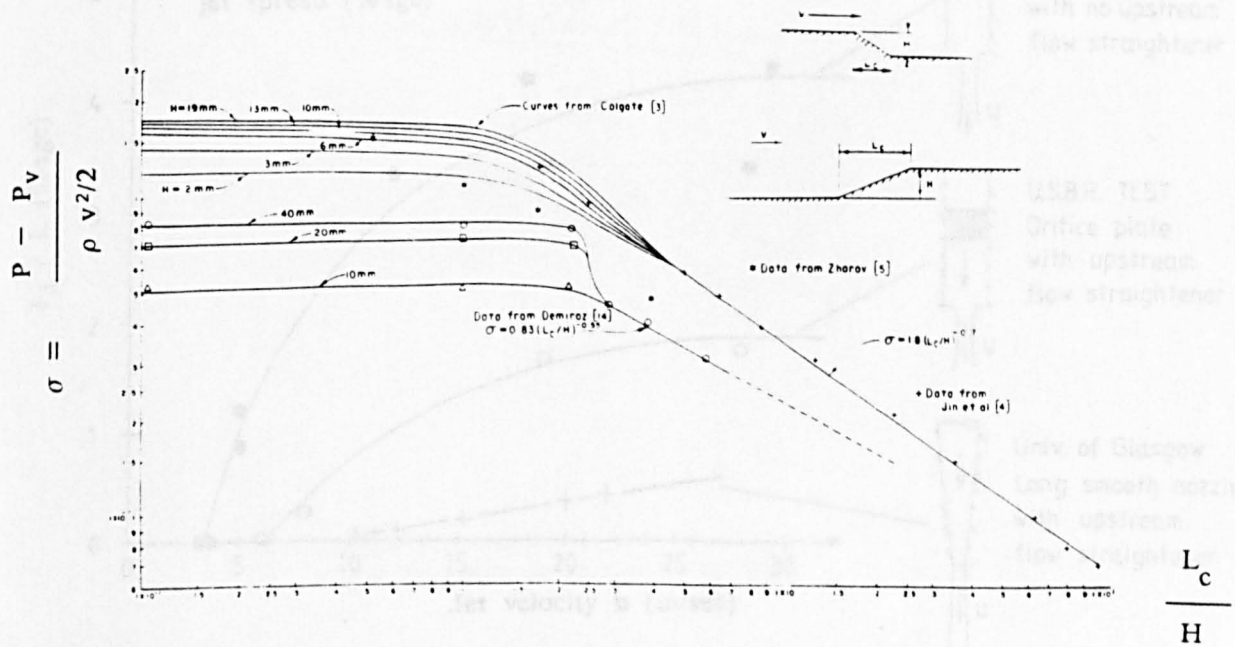

Fig 2.18 Cavitation characteristics of chamfer

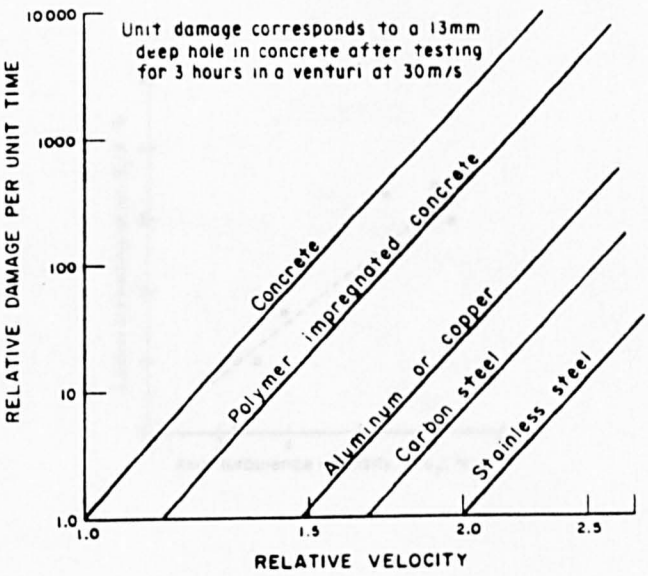

Fig 2.19 Comparative Cavitation resistance various materials (Colgate)

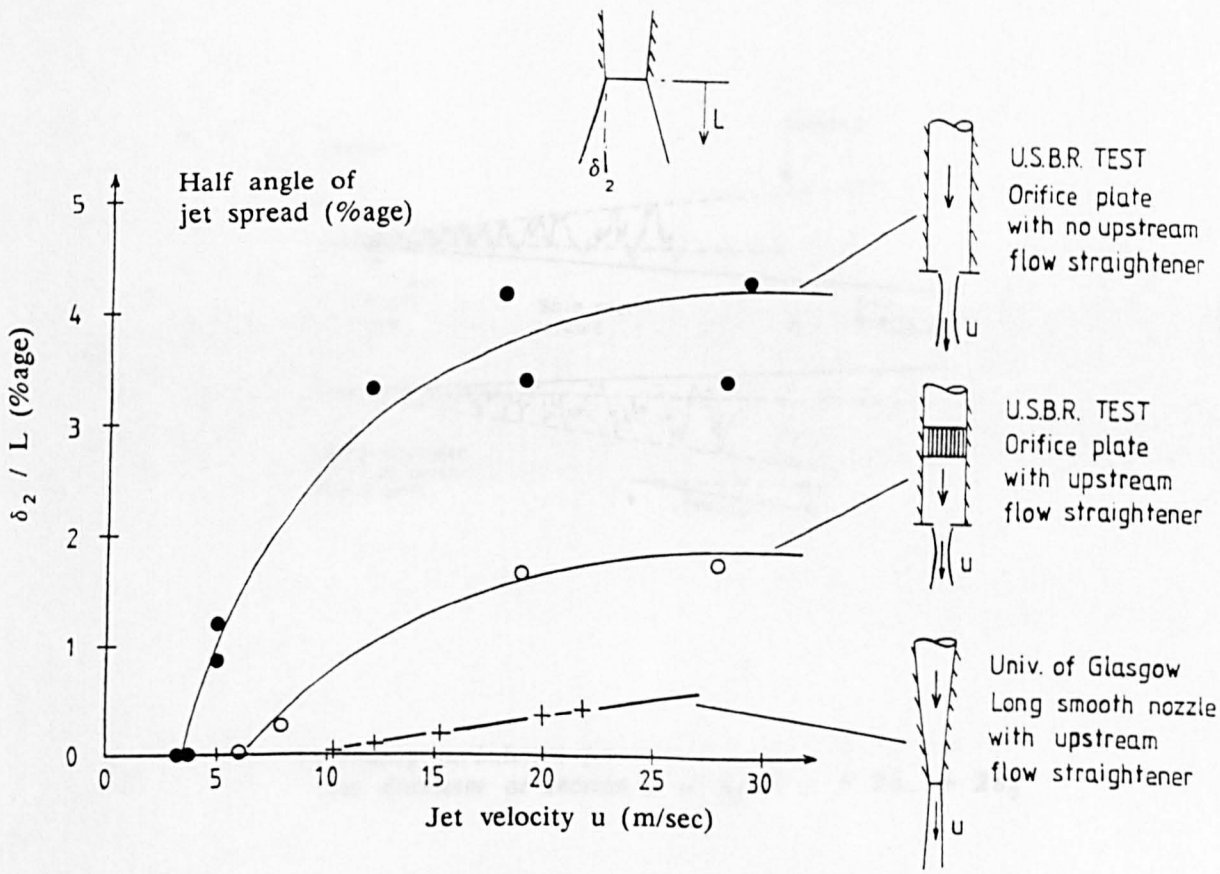

Fig 2.20 Degree of Jet spread in the atmosphere with outlet conditions (Withers)

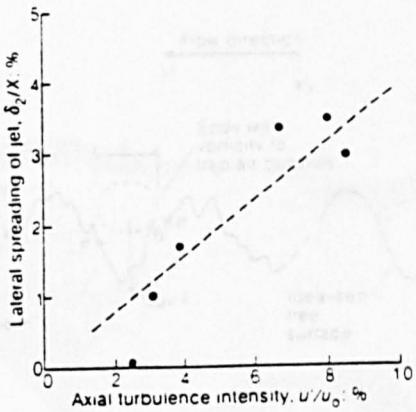

Fig 2.21(a) Lateral Jet spreading with turbulence intensity acting at Orifice Outlet (Ervine & Falvey)

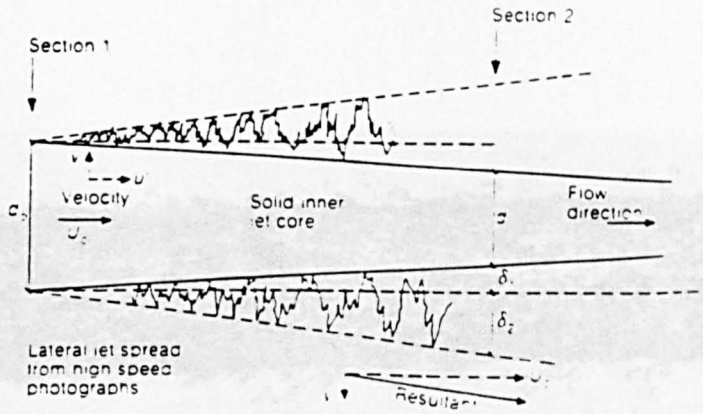

Fig 2.21(b) Spreading turbulence jet
Jet diameter at section 2 is $d_e = d + 2\delta_1 + 2\delta_2$

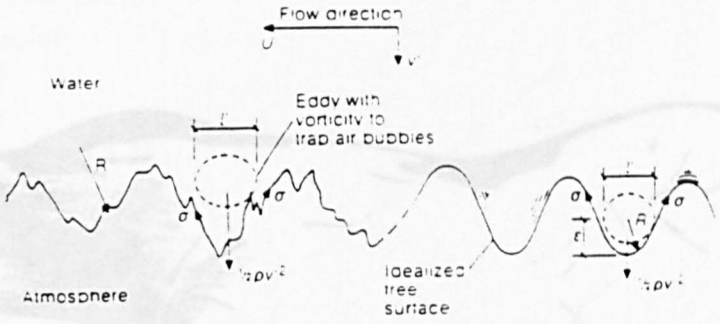

Fig 2.22 Free surfaces disturbance with definition of physical parameters

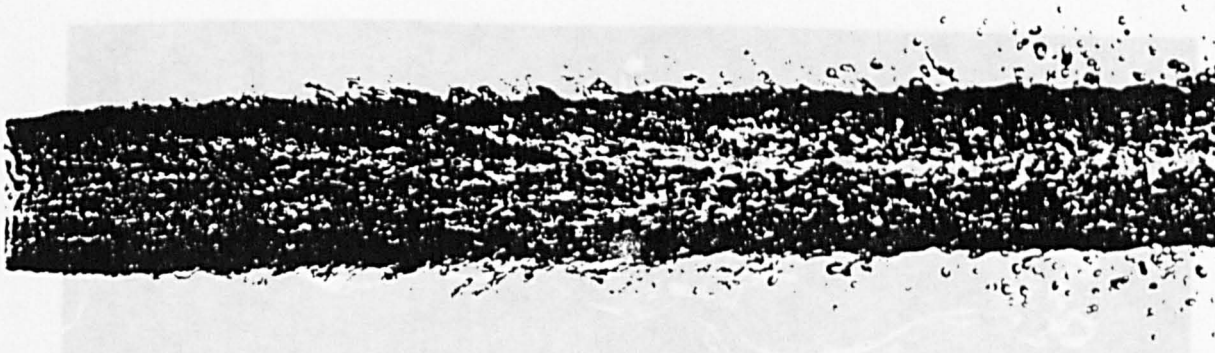

Fig 2.23(a) Water jet emerging into stagnant air (Hoyt & Taylor)

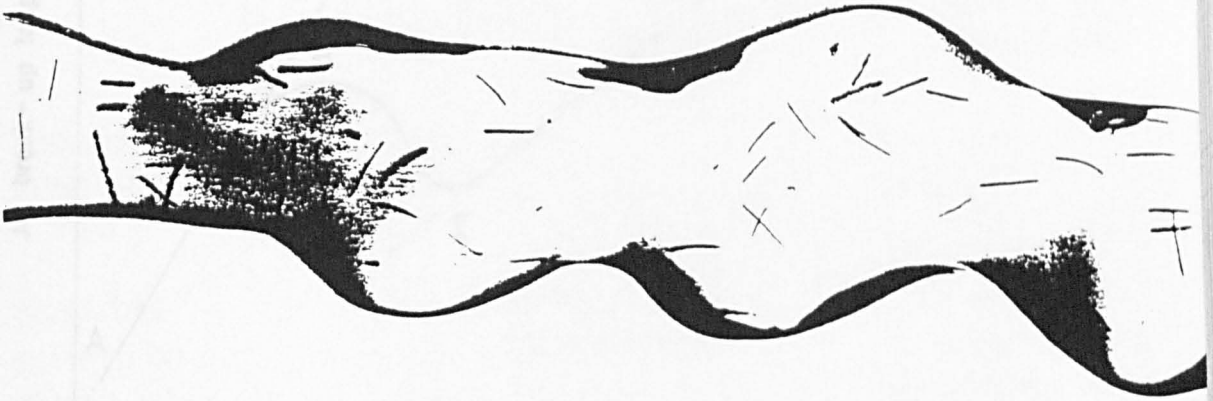

Fig 2.23(b) Water jet about to break–up
(Hoyt & Taylor)

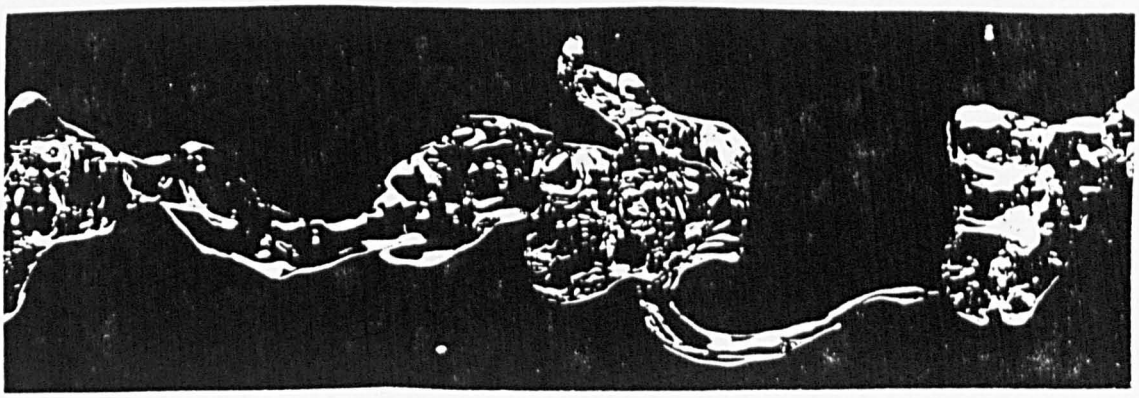

Fig 2.23(c) Water jet in a coaxial air stream
(Hoyt & Taylor)

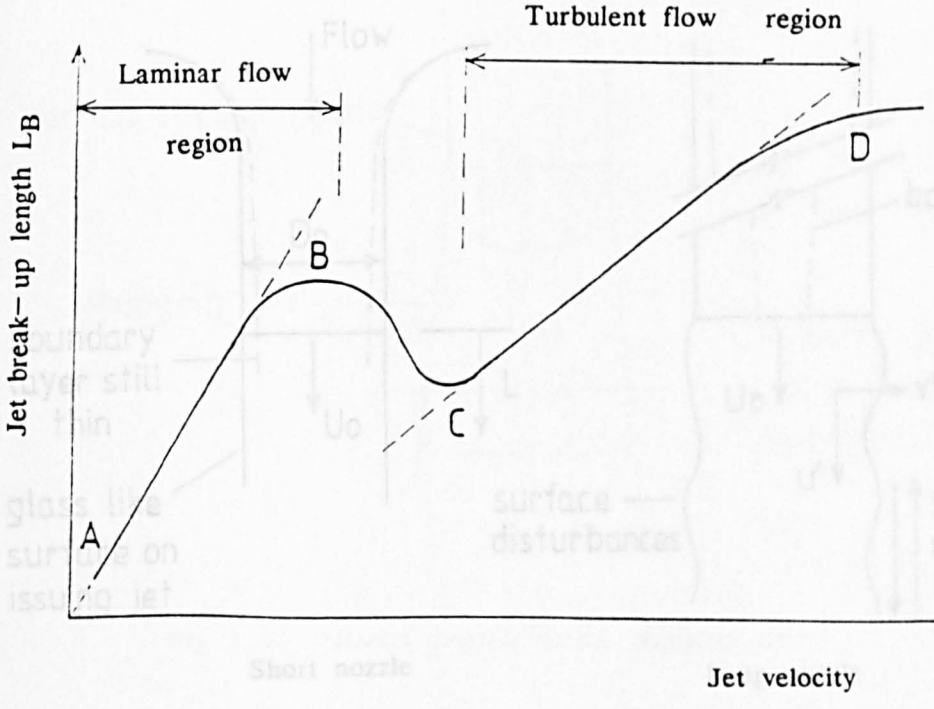

Fig 2.24 Jet stability curve

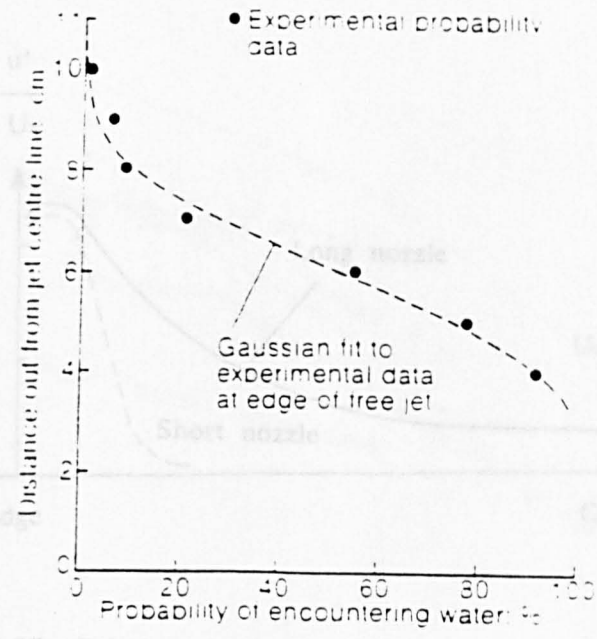

Fig 2.25 Probability of encountering water outside the solid core of a plunging turbulent jet

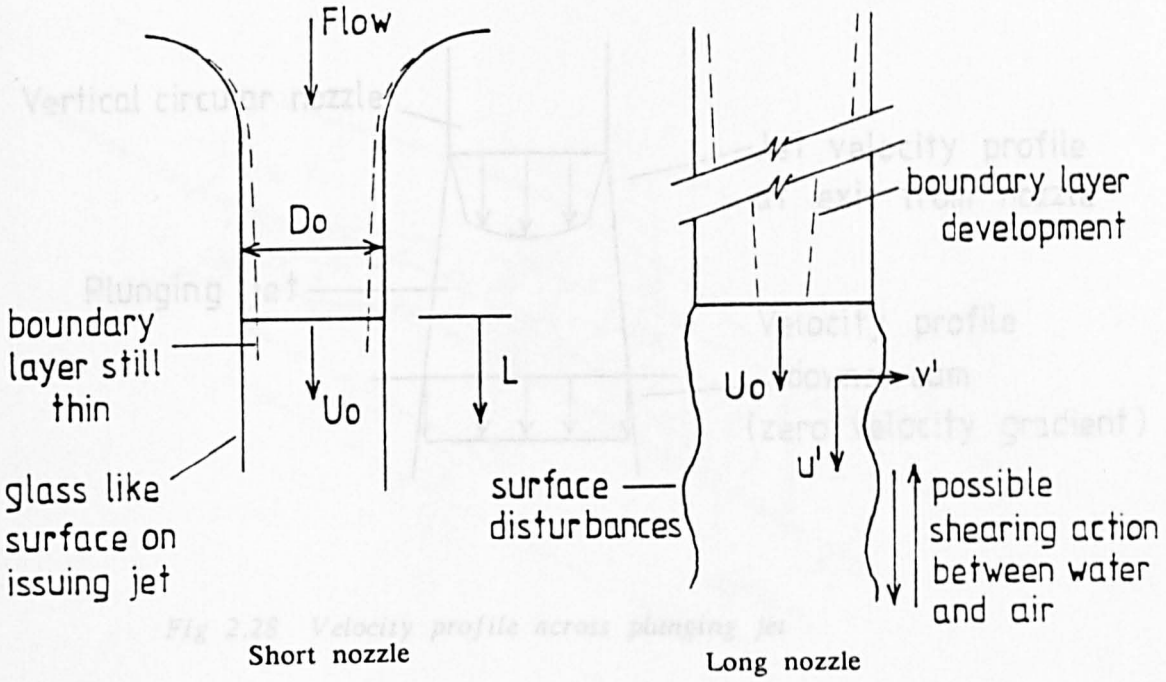

Fig 2.26 Jet issuing from Short / Long nozzle

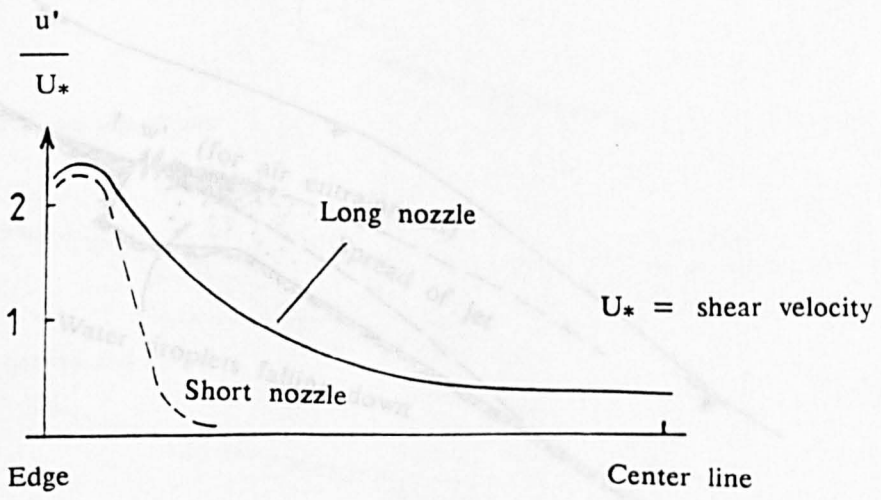

Fig 2.27 Relative turbulence of jet issuing from Short / Long nozzle

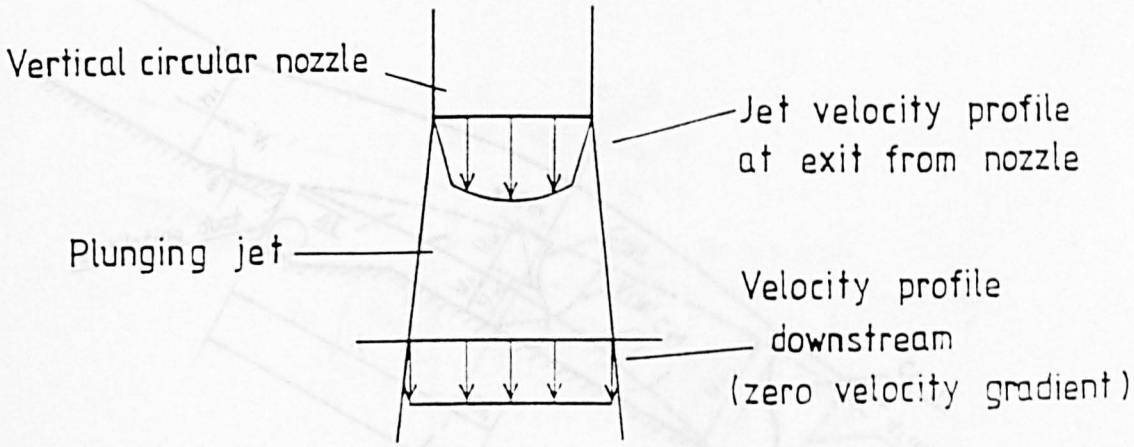

Fig 2.28 Velocity profile across plunging jet

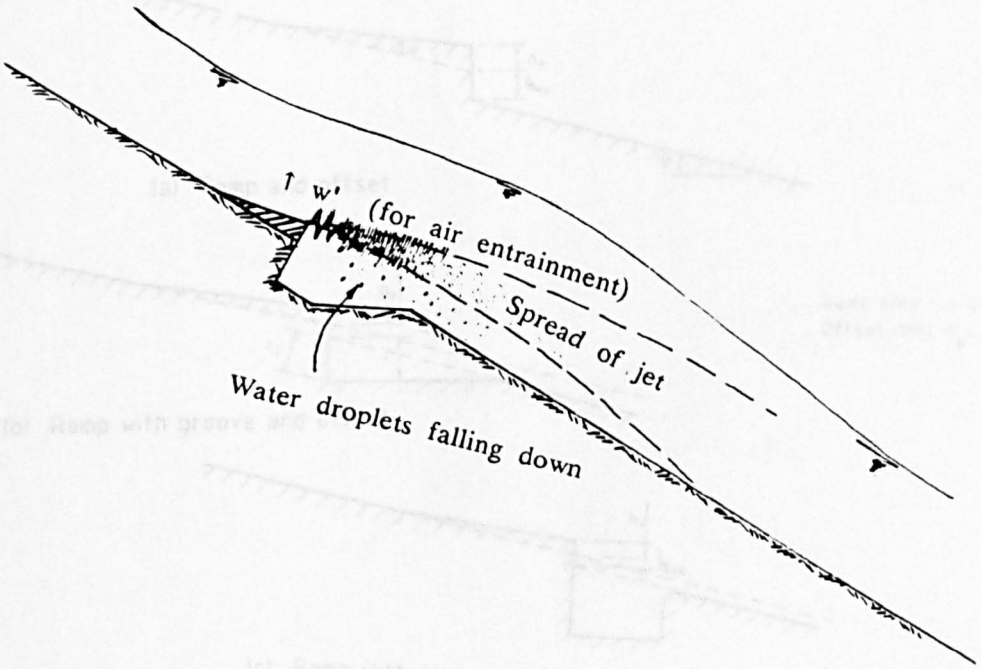

Fig 2.29 Air entrainment at underside of jet

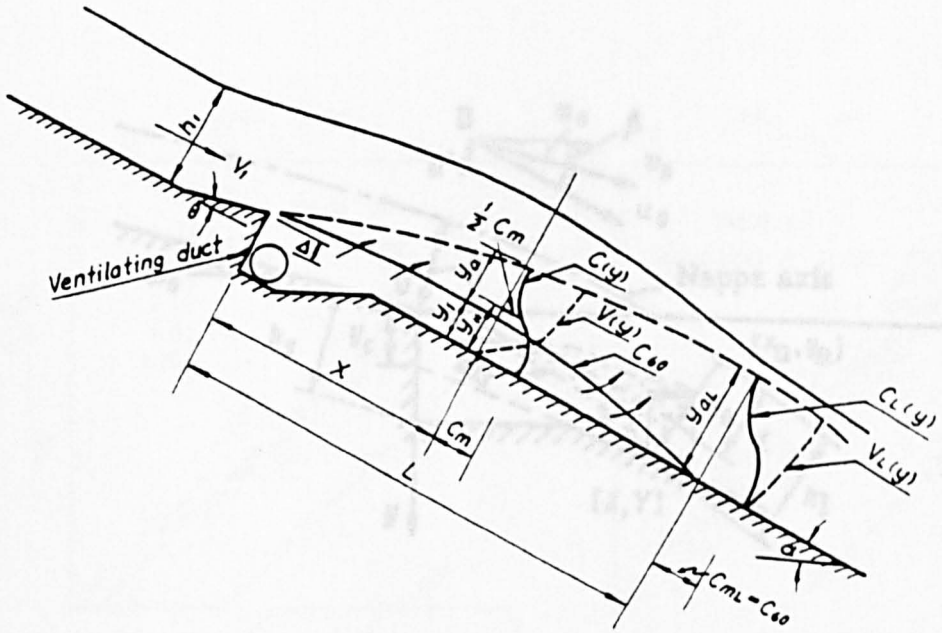

Fig 2.30 Air concentration along the Spillway chute

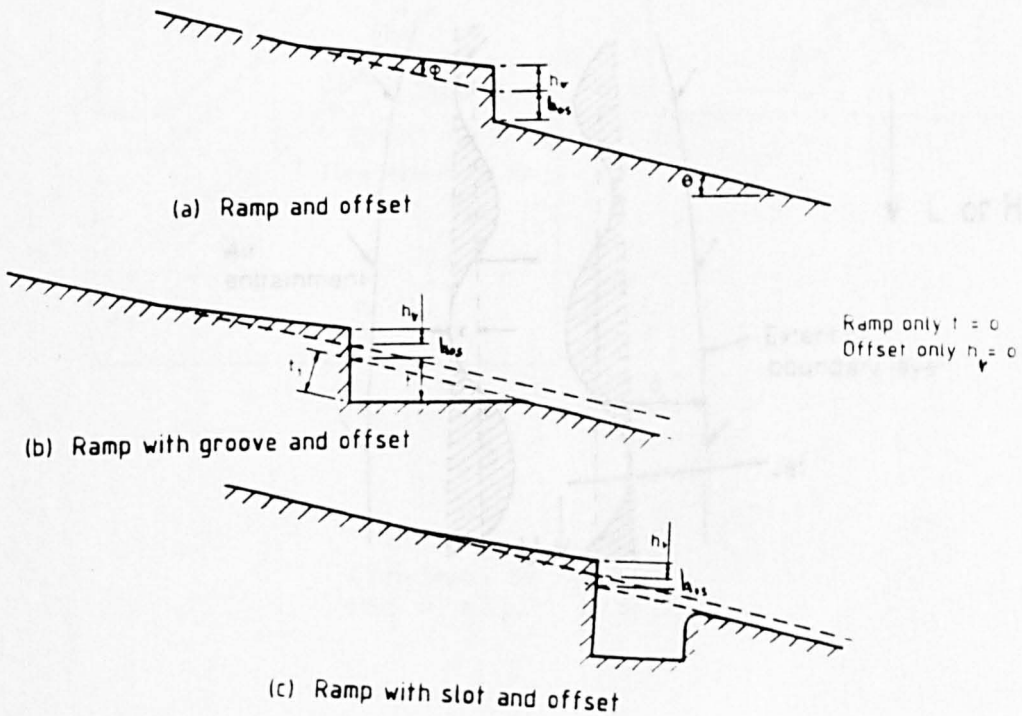

Fig 2.31 Types of aerators

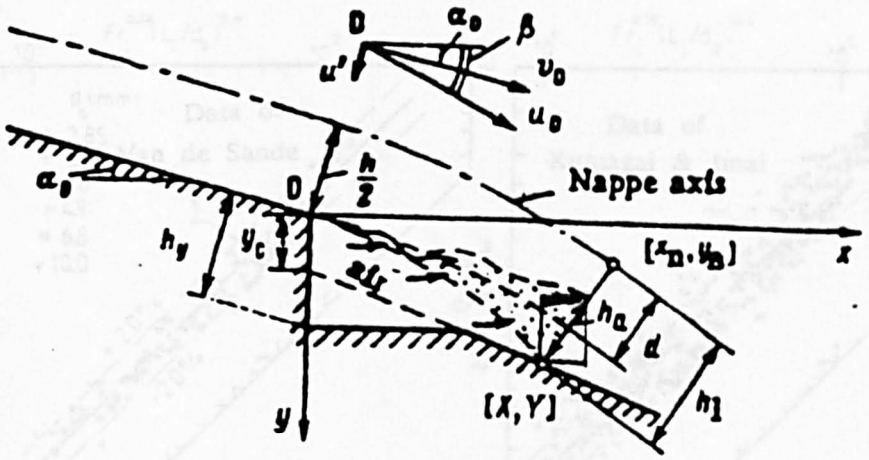

Fig 2.32 Schematic diagram of capture of air by the flow (Glazov)

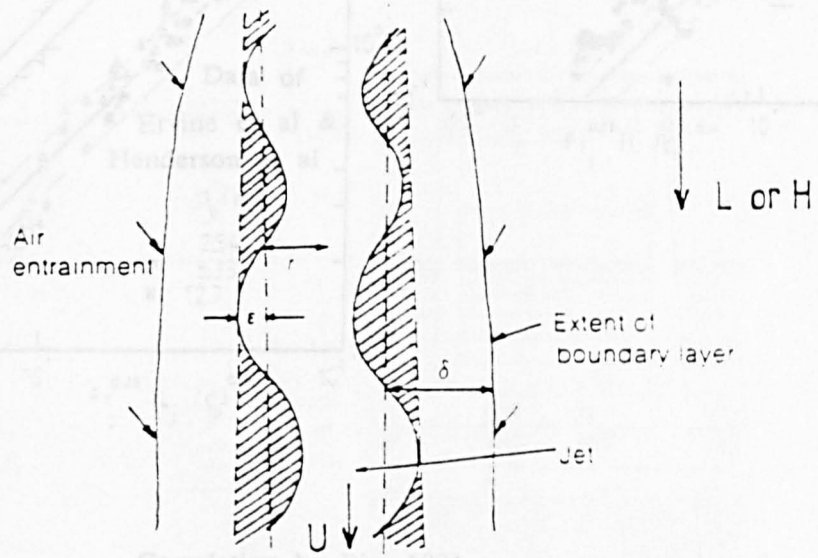

Fig 2.33 Sinous jet waves from showing boundary layer extent & air entrainment with in surface undulations.

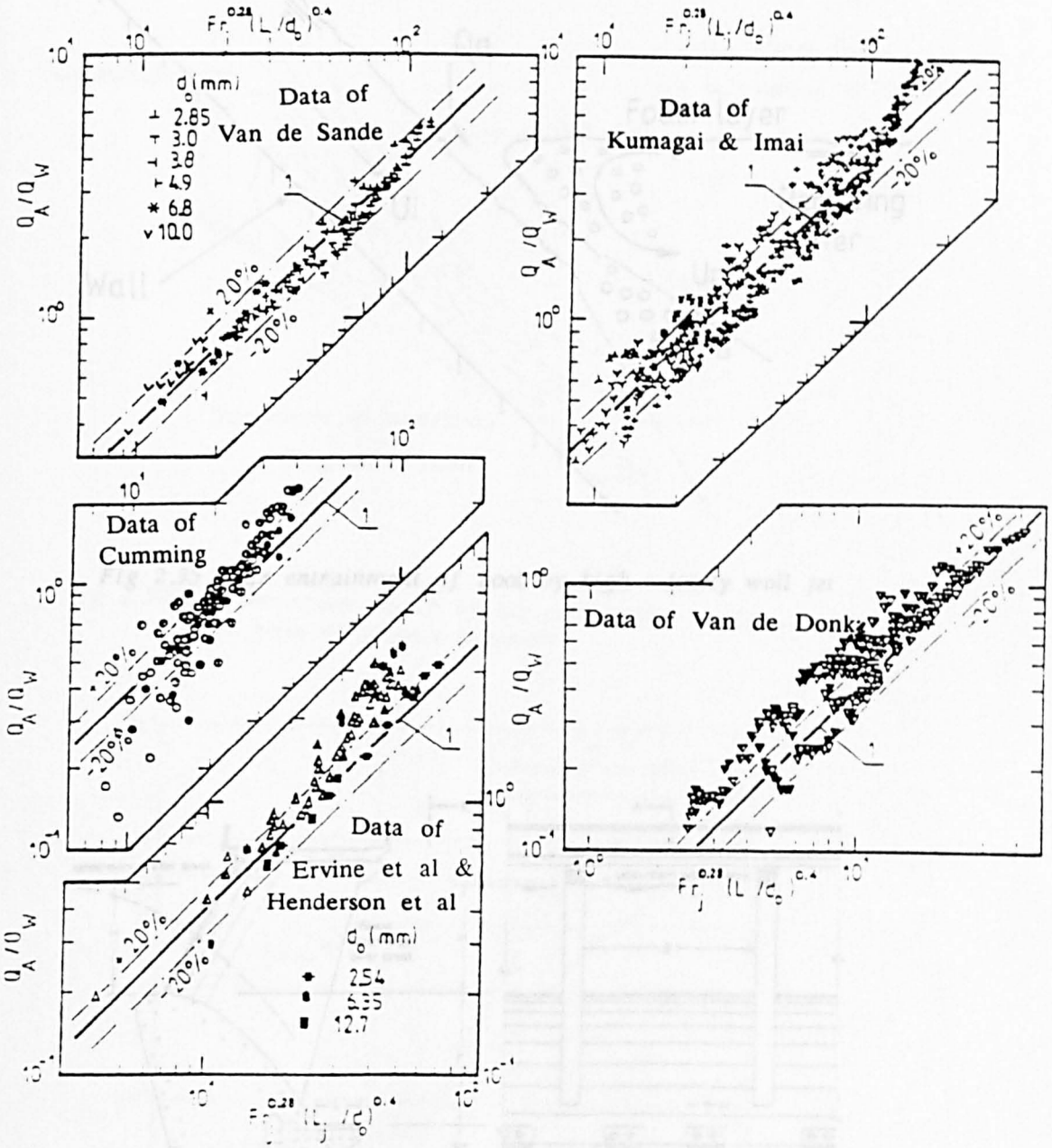

Correlation by Bin 1984
($Fr_j = u^2/gd$ $L_j = L$)

Fig 2.34 Correlation of entrainment ratio (Vertical jets)

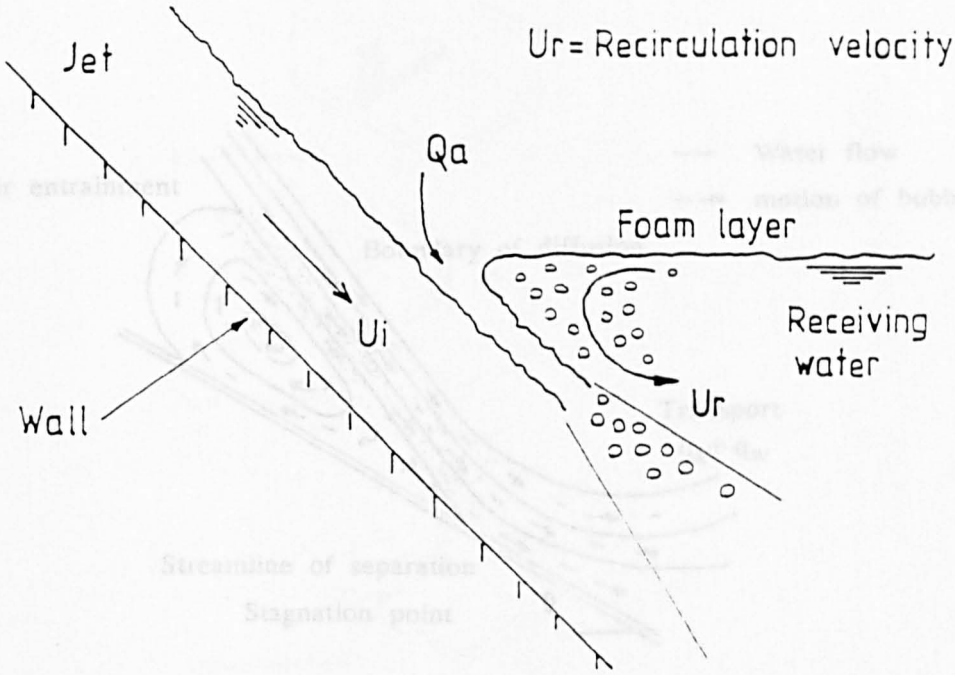

Fig 2.35 Air entrainment of pool by high velocity wall jet

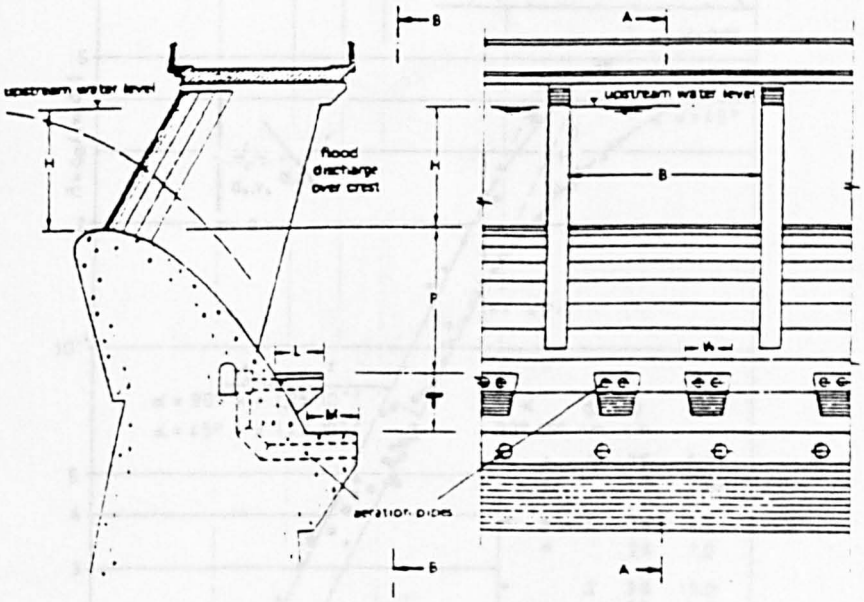

Fig 2.36 Arrangement of crest splitters (Mason)

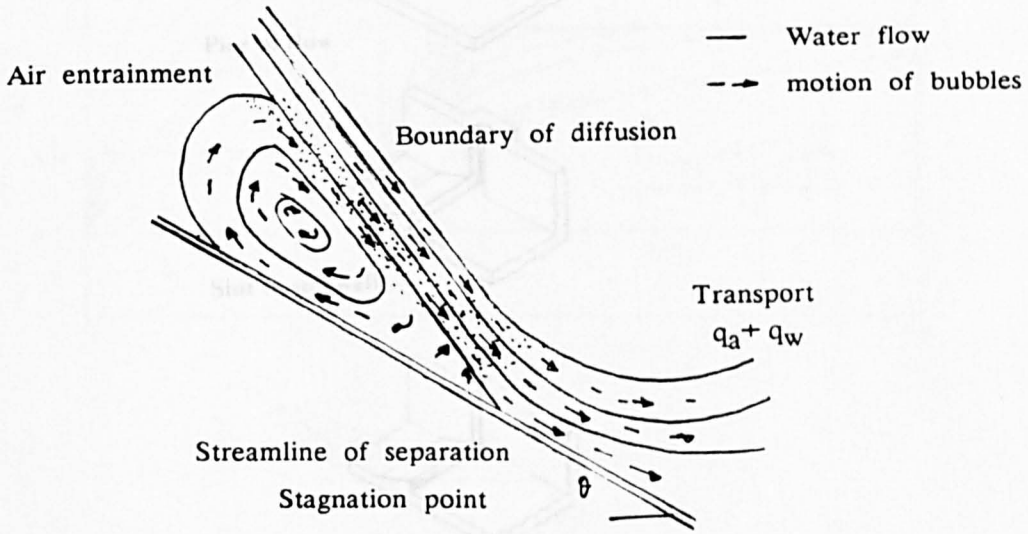

Fig 2.37(a) Illustration sketch of air entrainment model at point of impact (Renner)

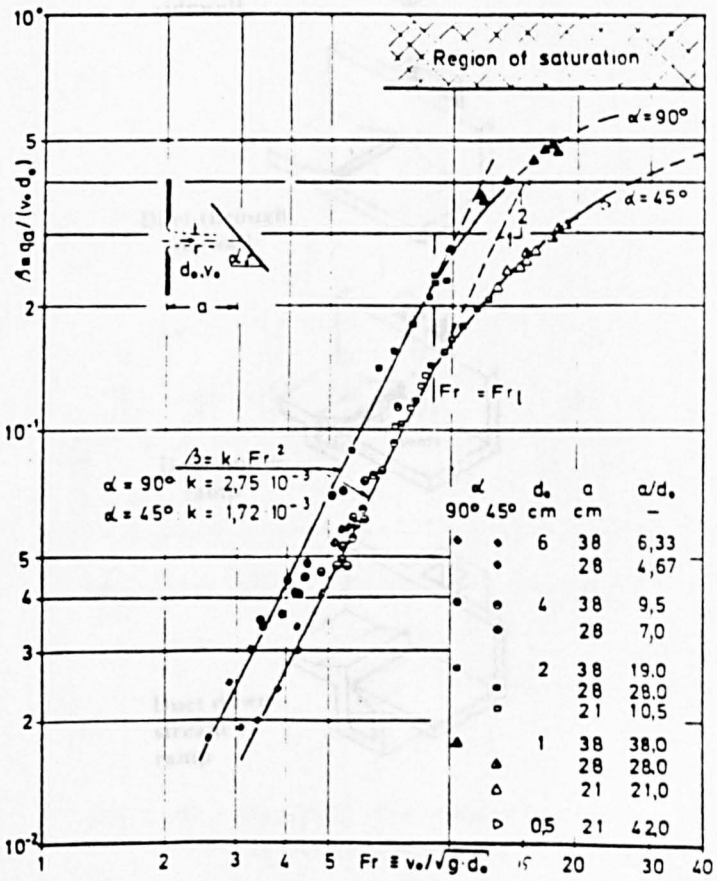

Fig 2.37(b) Relative rate of air entrainment for free a plane Jet as a function of Froude Number (Renner)

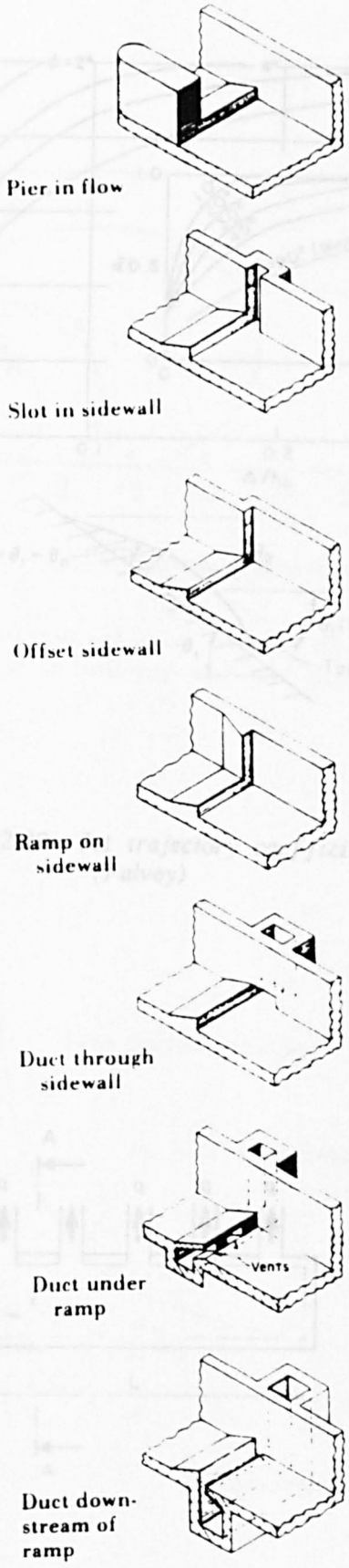

Fig 2.38 Air supply to aerators (Falvey)

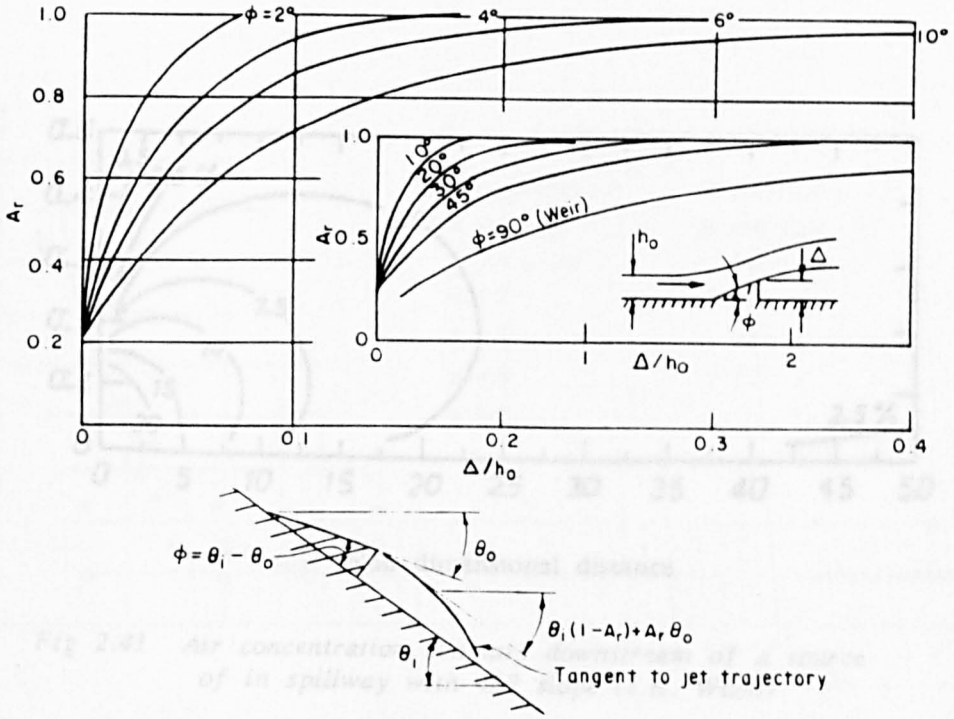

Fig 2.39 Jet trajectory coefficient (Falvey)

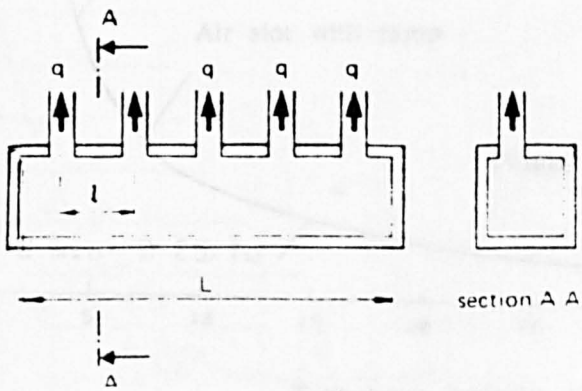

Fig 2.40 Manifold for aerators (P.Rutschmann)

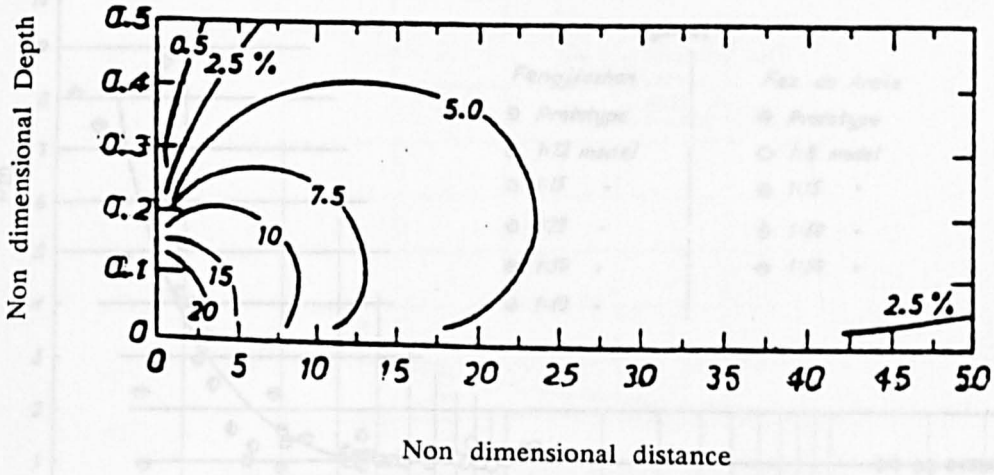

Fig 2.41 Air concentration contours downstream of a source of in spillway with 45° slope (I.R. Wood)

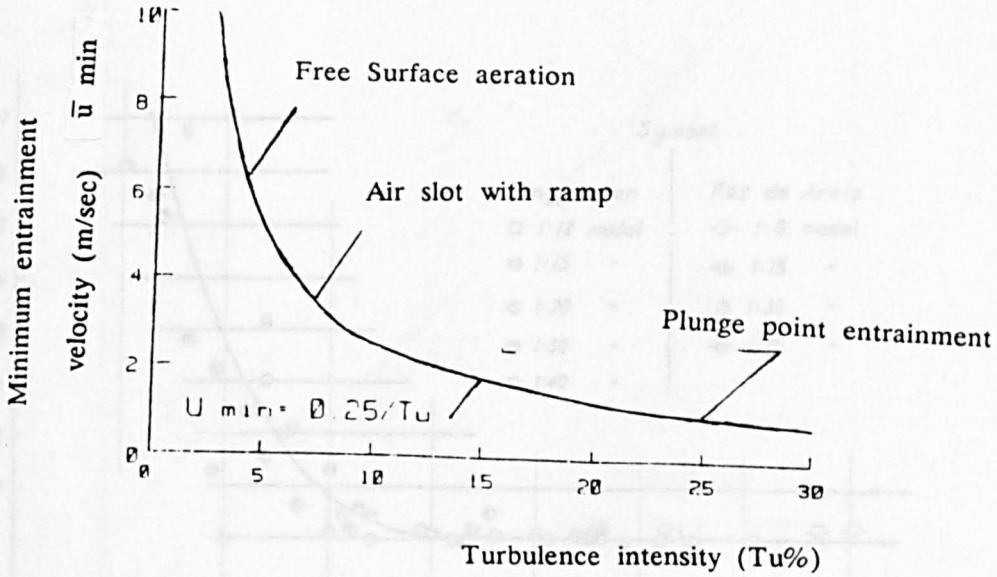

Fig 2.42 Minimum entrainment velocity (Ervine & Falvey 1988)

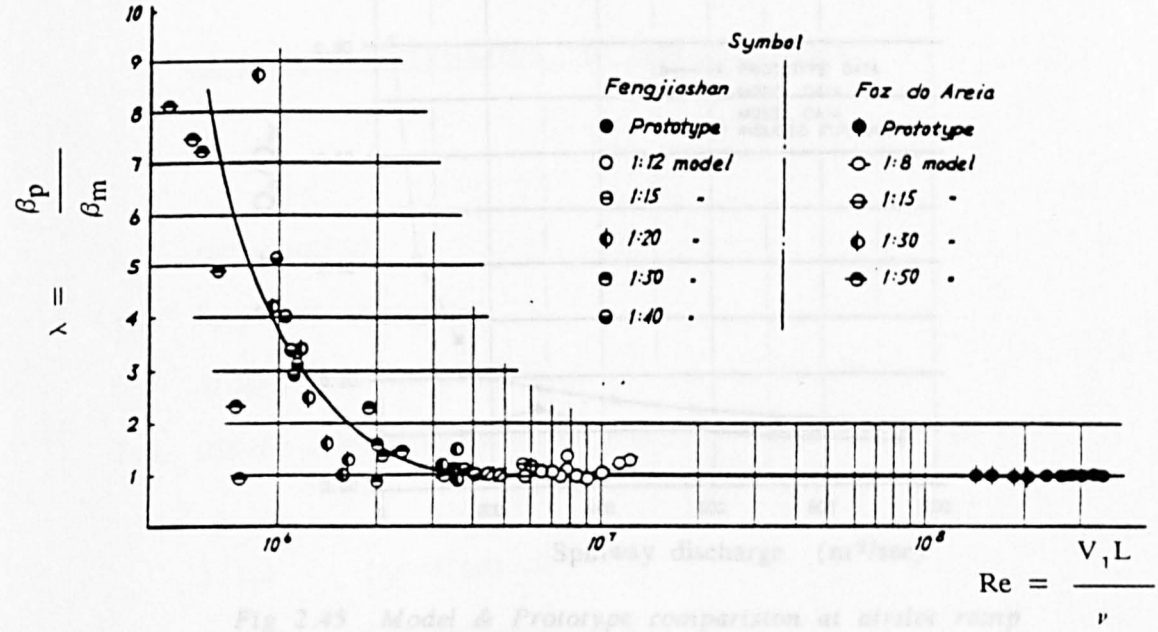

Fig 2.43 Relationship between λ and Re (Pan & Shao)

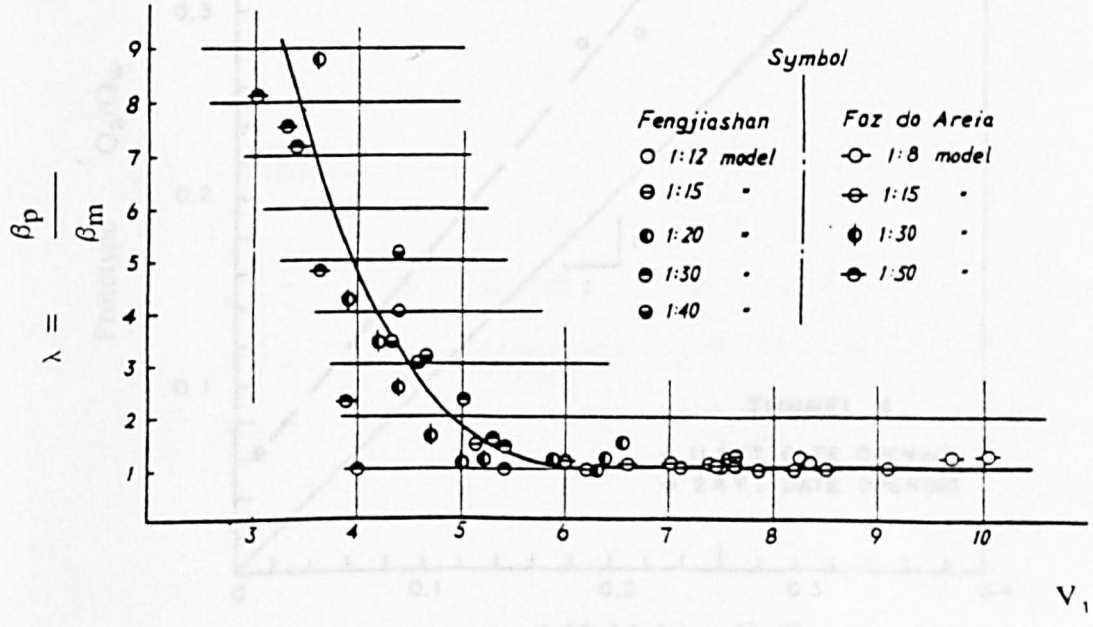

Fig 2.44 Relationship between λ and V_1 (Pan & Shao)

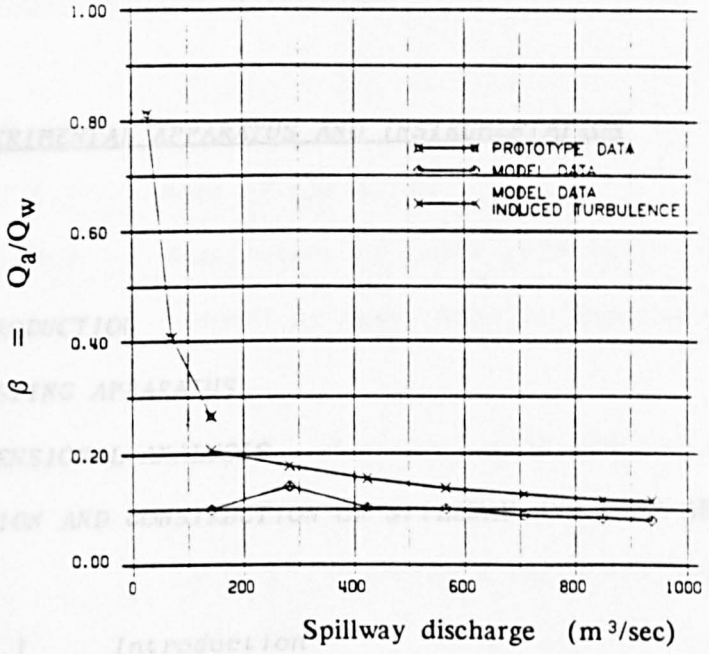

Fig 2.45 Model & Prototype comparision at airslot ramp McPhee Dam U.S.A

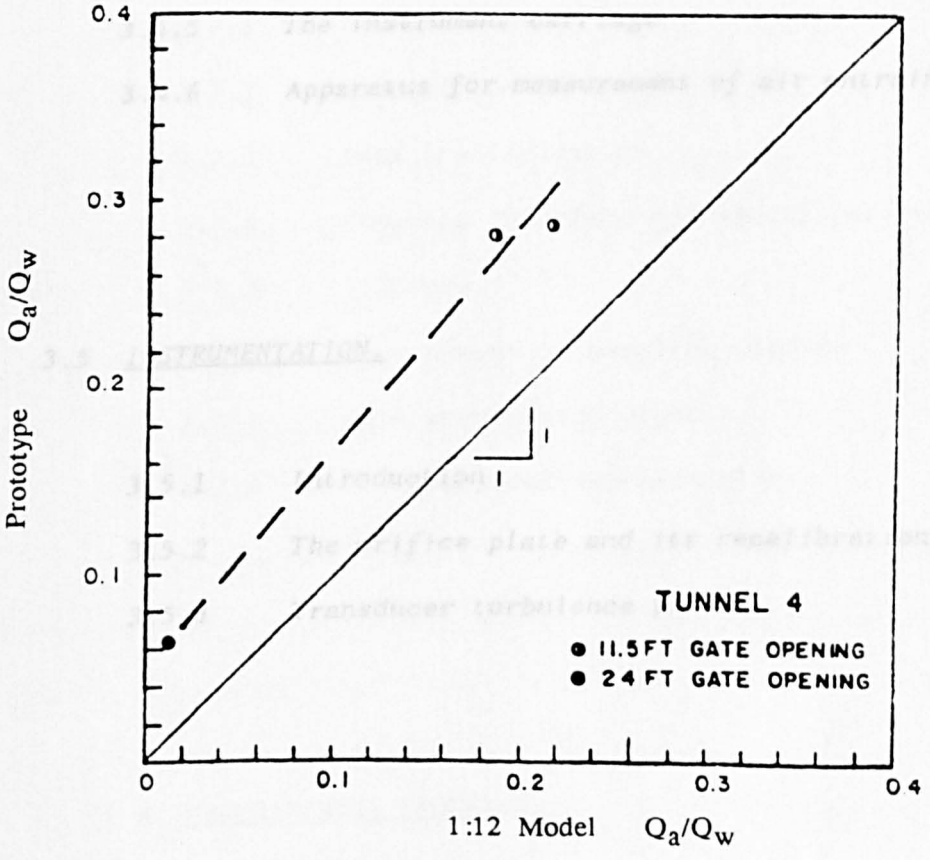

Fig 2.46 Model & Prototype comparision at airslot ramp Tarbela Dam Pakistan

CHAPTER 3.

EXPERIMENTAL APPARATUS AND INSTRUMENTATION

3.1 INTRODUCTION:

The main part of this work is an experimental investigation into the behaviour of ramp aerators. In some ways this is a strange choice of topic in view of the fact that numerous experimental studies had already been conducted at both model and prototype scale (Chapter 2) with apparently little advancement in numerical models which would adequately simulate the physical process occuring in aerators. What use a further model study ?

It should be noted that this research work in fact commenced with a computer model of flow along a spillway and aerator, and which is outlined in Chapter 7. The computer model uses standard techniques in determining the spillway water surface profile, boundary layer development and jet trajectory downstream of the ramp. It became apparent, however, that there were various gaps in our knowledge of the physical process involved, including:—

(i) how a ramp induces extra turbulence in an aerator jet

(ii) the inter-relationship between air entrainment and turbulence in the jet

(iii) the likely decay of turbulence in the jet downstream of the ramp

(iv) the behaviour of entrained air bubbles once the jet has reattached on the spillway slope

(v) scale effects between models and prototypes which were still not convincingly explained in many previous studies

Item (iv) above was not investigated in this work because a full two-dimensional air concentration model would be required, and would constitute almost a full research thesis by itself. The other items (i) (ii) (iii) and (v), have been investigated in some detail, hopefully providing a much sounder basis for computer modelling, at least up to the point of jet reattachment on the spillway

surface.

Other reasons for attempting this study concerned the fact that the author had spent two years at Tarbela Dam, Pakistan, and was aware of the cavitation–aerator situation; plus the fact that Dr. Ervine (Supervisor) had become interested in the McPhee Dam aerators (USA), whose behaviour on air uptake and model–prototype correlation had deviated from previous recognised norms.

3.2 EXISTING APPARATUS :

The University of Glasgow had no existing apparatus for study of ramp aerators, but did have one high–head type rig used by Withers (1987) to investigate pressure fluctuations in a plunge pool due to the impingement of vertical circular jets formed by nozzles and orifices. The existing research apparatus is shown in Fig 3.1. It was decided at an early stage that the two outlet tanks, the high head pump and the existing pipework would be suitable for the inlet and outlet arrangement of the new spillway aerator model, the high head pump therefore being the limiting factor on discharges and heads available. This was a maximum discharge around 60 ℓ/s (0.06 m^3/s) providing velocities in the outlet jets well in excess of 20 m/s. It was decided also in the absence of large underfloor storage tanks to accept the existing recirculating flow system, with special care given to de–aerate the water flow in the two sump tanks.

It was decided also for the initial period of research to use the full apparatus in Fig 3.1 to investigate turbulence in vertical circular jets as a prelude to turbulence study in the aerator jets after the rig had been modified. This initial work of the vertical circular jets was carried out immediately after Withers finished his experimental work and immediately before the rig was modified for spillway and ramp.

The existing rig consisted of a high head pump, already mentioned delivering a source of constant water supply to the jet nozzle. Water to the pump was supplied through the two sump tanks each of size 1.84m long, 1.22m wide and 1.02m high. The inflow turbulence of the flow through pipe was damped by the insertion of tube bundles in the pipe designed in accordance with B.S 1042. This removed axial swirl after the bend. A P.V.C pipe was used to supply the water to the jet, and was supported by scafolding frame work as shown in Fig 3.2. Flow measurement was done by means of an orifice plate with D and D/2 tappings, again designed in accordance to B.S 1042. To minimise head loss in the system the maximum diameter ratio for orifice, d/D = 0.75 was selected.

The jet velocity was varied by controlling the flow through a valve fixed after the pump. Three nozzles 78mm, 52mm, and 25mm diameter formed the outlet jets and were machined from prespex as shown in Fig 3.3. One orifice of 25mm diameter was machined from aluminum, which was designed according to the specification of BS1040 and shown in Fig 3.4.

By testing nozzles and orifices over a wide range of velocities, an early understanding of turbulent behaviour in jets could be obtained. The nozzles represented low turbulence jets with a relatively thin initial boundary layer thickness, whereas jets for the orifice represented much higher turbulence levels that might be found in aerator jets.

Although most work in the thesis involves turbulence measurements by LDA technique, this was not possible for the plunging circular jet because of their very rough jet surface. It was decided to use an existing turbulence probe designed by Withers instead.

It was also decided that the degree of jet turbulence should be quantified by direct measurment at the different locations along the jet, both in the transverse (radial) and longitudinal directions. This was achived by means of the transducer turbulence probe and its associated electronic circuitry.

A description of the design and use of this instrument is given in section (3.5.3).

3.3 DIMENSIONAL ANALYSIS :

Before moving to details of the design of the spillway and aerator ramp system, it was decided to carry out an initial dimensional analysis, to get a feel for the range of parameters involved; which parameters are likely to be significant, which are not; and which are outwith the scope of the experimental equipment.

The geometry of a typical aeration system for a surface spillway is shown diagramatically in Fig 3.5. An aerator is located in the invert of a channel usually consist of a plain ramp, a plain offset or a combination of the two. In well designed aerator, water passing over the ramp forms a stable cavity from which air is entrained and carried downstream by the flow.

Air for an aerator in the invert of a channel can be supplied naturally from the atmosphere by means of a system of ducts having outlets which may be in base of the side walls, in the downstream face of the ramp/offset or in a slot in the bottom of the channel.

The performance of an aeration system may be expected to depend upon the factors given below. The seventeen independent parameters were chosen based on the initial physical understanding of the flow mechanism. Between them, they will determine the magnitude and extent of dependent variables such as air–entrainment, sub nappe pressure and length of the jet. Most of the parameters are sketched in Fig 3.5

Independent Variables.

(i). *The geometry of the Spillway and Spillway entrance.*

θ = spillway bed slope

b = width of the channel

k_s = bed roughness

Yg = gate opening at entrance pressure box Fig 3.6

L_{gr}= length of channel from gate to aerator ramp

(ii). *The geometry and flow conditions at aerator ramp.*

Φ = inclination of ramp (relative to spillway slope)

h_r = height of ramp

h_s = height of the offset

u = velocity of flow (or total discharge Q_w)

h_3 = depth of flow at the end of ramp

(iii). *The characteristics of air supply system.*

A_d = area of air supply duct

K_d = total head loss coefficient in air supply duct

ρ_a = density of air

(iv). *The fluid properties.*

σ = surface tension of water

ρ_w = density of water

g = gravitational constant

ν_w = kinematic viscosity of water

Dependent Variables

q_a = air flow rate per unit width

L = length of the water jet

Δp = pressure underneath the jet (relative to atmosphere)

w' = vertical turbulent velocity along spillway and ramp

Dimensional analysis can be useful in identifying relationships between different factors, but it is important to realise its limitation in complex problems such as the present one. The variables can be grouped in many different ways, and it is usually difficult to establish which combination is most relevant to the problem. In this case the author has chosen flow depth h which is usually known, as the term on the bottom line. This was chosen in preference to L, the jet length which is unknown and a dependent parameter as well.

Consideration of the process of entrainment resulting from flow over an air cavity suggests that the dependent variables such as airflow, underpressure and jet length, will depend primarily upon the following range of parameters.

$$q_a \ , \ \Delta p \ , \ L \ , \ w' = f (\theta \ , \ b \ , \ k_s \ , \ Yg \ , \ L_{gr} \ , \ \Phi \ , \ h_r \ , \ h_s \ , \ u \ , \ h_3, \ A_d, \ k_d \ , \ \rho_a \ , \ \rho_w \ , \ \nu_w, \ \sigma, \ g \ ) \qquad (3.1)$$

The above formulation illustrates range of parameters involved, and the complex inter—relationships which might exist between the dependent parameters q_a , L , Δp and w'. The performance of an aerator is affected by the characteristic of its air supply system. If the head loss in the system is increased, the pressure in the cavity decreases further below atmospheric (i.e Δp increases);

this increases the curvature of the flow over the cavity and shortens its length L; this in turns reduces the rate of air entrainment q_a into the flow, and so on.

When analysing data from tests on aerators, it is simpler to adopt an overall situation of the problem and consider the dependent quantities as separate function of the independent variables.

$$\frac{q_a}{uh}, \frac{L}{h}, \frac{\Delta p}{\rho g h}, \frac{w'}{u} = \left[\frac{u}{\sqrt{gh}}, \frac{uh}{\nu}, \frac{\rho u^2 h}{\sigma}, \theta, \Phi, \frac{b}{h}, \frac{k_s}{h}, \frac{h_r}{h}, \frac{h_s}{h}, \frac{Y_g}{h}, \frac{L_{gr}}{h}, K_d, \frac{\rho_a}{\rho_w}, \frac{b\,h_r}{A_a}\right] \qquad (3.2)$$

Considering each parameter in turn:—

— $u/\sqrt{gh}$ is the Froude Number and is important in determining the jet length L from ramp to reattachment point. In that sense, it will have a significant bearing on the air flow rate even though the air entrainment mechanism is Reynolds and Weber Number dominated. A typical range of of prototype Froude Number is 5 to 15. It is important to reproduce this range in the model.

— uh/ν is the Reynolds Number and is important because of viscous scale effects which lead to aeration scale effects, and also to the inception of aeration problem in model aerators. The magnitude of turbulent fluctuations is also a function of the Reynolds Number. Prototype Reynolds Number can be of the order of 3 or 4 x 10^7 and hence cannot be reproduced in the model. It is important to have the model Reynolds Number as high as possible, at least greater than 10^5. The range of model Reynolds Number in this study was in the range of 3 to 7 x 10^5.

—— $u\sqrt{(\rho L/\sigma)}$ is an alternative form of the Weber Number used by Pinto (1982), and is a measure of the relative influence of surface tension at an air/water interface. It can be considered as a measure of the resistance of the jet surface to causing spray, spreading, air entrainment and jet break–up. In fact the Weber Number is as important in this type of flow situation as the Reynolds Number. A typical aerator prototype Weber Number can be as high as 1000 – 5000, although this is obviously not possible in a model. The model range in this study is around 100 – 300 with model velocities in the 5 – 10 m/s range and jet lengths in the 0.3m to 1.77m range. According to Pinto (1982) surface tension is a factor in aerators for Weber Numbers up to around 150, which would include about half the data in this study.

—— It is not possible to reproduce either prototype Reynolds Number or Weber Number in this experimental test. It was decided, however to make the model as large as possible (velocity and depth) to partially overcome this problem.

In fact it is not even possible to examine Reynolds and Weber Number effects separately from each other without using different fluids. Because only air and water are used, therefore when one is varied then so is the other.

—— θ is the spillway slope, which has some importance in this physical process. A review of prototype aerator spillways showed the value of θ to varies from 0^0 to 70^0 with the median around 30^0. It was decided to adopt 45^0 to best fit in with the existing pipe work arrangement. It was also decided to keep θ constant throughout the work, following work at the USBR Denver which showed θ not to be very significant in terms of the fundamental processes occuring.

—— Φ is the ramp slope relative to the spillway slope and was thought initially to be quite significant in the turbulence generation process in the aerator jet. Of course the value of Φ is very significant in the jet trajectory, although Φ values greater than 10^0 usually force the aerator jet too high off the spillway surface with the attendant potential for jet disruption and break–up. A Φ value of 0^0 was found to produce short jets with low aeration characteristics, so it was decided in this work to pursue the optimum range of 2^0, 5^0 and 10^0 used in prototype aerators. Three values of Φ were chosen based on the principle that any graphs plotted in the later stages of work investigating the influence of Φ would require at least three points to produce a graph or trend.

—— b/h is the aspect ratio of the model spillway and proved to be problematical in choice. There was a desire to faithfully reproduce prototype aspect ratios which are typically of the order of 30. Given the discharge available in the laboratory, this would have meant very thin aerator jets. On the other hand a move towards a sectional model with the flow available concentrated along a narrow model spillway gives better depths of flow, higher Reynolds and Weber Numbers but leaves the study open to criticsm about two elements:–

(i) The small aspect ratio in the sectional model does not reproduce secondary cells due to curvature, explained in section 2.4.2. Such cells are more prominent in wider channels.

(ii) The small aspect ratio gives greater influence to side walls which may be responsible for additional air entrainment and have relatively greater effect compared to prototype wider structure.

In the end, a compromise situation was reached with the spillway channel made 100mm wide throughout giving aspect ratio around unity for the large depths of flow, but up to 10 for shallowest flows around 10mm deep. This was considered preferable to a channel width say of 50mm wide with flow depths up to 200mm, simply because of the two problems mentioned in (i)and(ii) above.

—— k_s/h is the relative roughness of the spillway channel and affects the friction factor λ, the shear velocity u_* ($= \bar{u}\sqrt{\lambda/8}$) and hence the turbulent velocity w' which scales on the value of u_*. w' is a key parameter for aeration and jet behaviour in the atmosphere.

It was decide therefore to test two main k_s values. The first was a smooth prespex surface ($k_s \simeq 0.0$) which is a reasonable representation of a prototype concrete surface. This was done for all three ramp angles Φ. The second was a rough surface with $k_s \simeq 0.35$mm (equivalent roughness [smooth sides + rough base]). This was achieved by a sand paper surface fixed to the perspex underneath. Such a large roughness was used to look at the effects of greater turbulence rather than representing a real prototype spillway surface. The large roughness test was carried out for one ramp angle of 5^0 only.

—— h_r/h is the ramp height to the flow depth ratio. Because the length of the ramp was kept constant and the three angle varied from 2^0 to 5^0 to 10^0, then three ranges of h_r/h were achieved covering the broad range from 0.1 to 0.3 which is compatible with prototype values shown in Table 7.1 to 7.5.

—— h_s/h is the ratio of offset height to flow depth. It was decided not to investigate offset ramps in this work and hence h_s was always zero. This parameter was not considered a fundamental property of the system but sometimes necessary as a design feature.

—— Y_g/h is the ratio of gate opening to flow depth at the ramp. For each ramp geometry tested, it was decided to test three different gate openings namely 60mm, 90mm and 180mm. It should be noted at this point perhaps that a pressure box was required at the upstream end of the spillway to produce the high outlet velocities required in this work. The pressure box will be described in section 3.4.2. The outlet from the pressure box is controlled by a

sliding sluice gate, by which the initial flow depth at the start of the spillway could be varied.

Variation of the gate opening Y_g, varied the aspect ratio of the flow approaching the ramp, as well as the relative effect of the boundary layer thickness (δ/h) developing along the spillway length.

—— L_{gr}/h is the factor representing the length from the sluice gate at the spillway entrence downstream to the ramp. This length was kept constant at 1.9m (at the end of ramp) throughout, although L_{gr}/h of course varied from around 20 to 100. This length is important because it determines how developed the boundary layer is at the point of reaching the ramp, and hence the development of the vertical turbulent velocities w'. It should be noted that the key turbulent velocities in this system are those at or near the bottom of the flow and jet, which remain around the value, $w' \simeq 1.3\ u_*$, extended right to the free surface, Davies (1972).

Thus the parameter may not be as crucial as commonly thought, although early turbulence measurements showed fully developed turbulence at the ramp for most of the flows tested.

In any case, most prototype aerators are installed with in 10 to 200 flow depths downstream of the spillway enterance, corresponding roughly to the range tested in this work.

—— K_d is the head loss coefficient of the air venting system and is determined by the design of the inlet duct including the flared entrance, type of bend, exit conditions and wall friction in the prototype structure.

In the model tests it was decided to simplify this parameter by simply installing a straight pipe for air entry under the jet. The air flow would be controlled by a valve in the inlet pipe thus determining the K_d value for the air duct supply.

A further special set of tests were devised with K_d effectively zero. This was achieved by pumping air into the cavity and controlling the valve so that the sub–nappe cavity pressure was atmospheric rather than sub–atmospheric. This will be discussed in section 3.4.6.

—— ρ_a/ρ_w is the density ratio of air to water and was kept constant at 0.00123.

—— w'/u A special point of interest is the dependent parameter w'/u which is the relative turbulence intensity normal to the spillway base, in the region near the ramp.

This was one of the key parameters measured in this work along with air flow q_a, cavity under pressure Δp and resulting jet length L. Measurements of w'/u as well as u'/u was achieved by Laser Doppler Velocitimeter (Single component) representing the most novel feature of this work.

In summary, all the parameters in Equation (3.2) were varied except spillway slope θ, offset height h_s/h and air water density ratio ρ_a/ρ_w. This represents a significant range of variable tested, but also makes the development of simplified functional empirical relationships more complex.

3.4 DESIGN AND CONSTRUCTION OF SPILLWAY AND RAMP AERATOR.

3.4.1 Introduction.

Following on from the dimensional analysis, it was decided to proceed with the construction of the experimental rig containing the following elements:–

—— the existing MYSON high head pump capable of delivering 60 ℓ/s at a head of 20 m.

—— the existing 6 inch PVC pipe work and gate valve described in section 3.4.4

—— to remove the 90° bend of Withers apparatus and replace with 45° bend leading to a pressure box.

—— to install a pressure box or reservoir being completely water tight to heads of at least 20m. (section 3.4.2)

—— to install a perspex rectangular shaped spillway leading from the pressure box to the sumps tanks. (section 3.4.3)

—— to incorporate and LDA system for turbulence measurements together with instrument carriage capable of moving in all three dimensions. (section 3.4.5)

—— to incorporate a range of equipment for air flow measurement into the air cavity, pressure measurement in the air cavity, jet length of the air cavity, etc. (section 3.4.6)

—— to connect the LDA system to an existing system of data acquisition including transmition panels, A/D converter, computer interface, storage and software (section 3.4.7.)

3.4.2 The pressure box

The pressure box was perhaps the most crucial piece of equipment in the sense that it was required to make the transition from the circular inlet pipe to the rectangular outlet spillway. It was required to make a change of alignment of 90° from pipe to spillway. It was required to take high heads generated by the pump of the order of 20m and still remain water tight. It was required to not generate extra turbulence which might be transmitted into the spillway flow and be mixed up in boundary layer turbulence. It was required to dissipate the

turbulence in the incoming flow from the pipe work and 45° bend. Its position in the rig is shown in Fig 3.7(a). It was required to produce smooth and high velocity flows into the spillway with no obvious disturbances or turbulence.

The design was carried out by structural analysis taking into consideration of space, weight, and high water pressure inside the box during at maximum velocities and minimum gate opening. A 3mm galvanised sheet was required to withstand the water pressure delivered from the pump. A half inch angle iron frame work was designed to hold the joints of the box in order to avoid welding of the galvanised sheet. The top of the box was made with a hole of 6 inch diameter for the insertion of inlet pipe to the box. The front side of the box was fitted with two guided galvanised sheets as shown in Fig 3.6(b), to an opening of 100 mm wide and 180 mm high for outlet into the open channel. The outlet of the box was controlled by a mechanical operating gate of the same size of the opening. The dimension of the pressure box are 500mm long, 300mm wide, and 250mm high as shown in Fig 3.6(a). The guide sheets were essential to ensure transition to the high velocity spillway flow and were designed according to the US Army Corps of Engineers Design Guidelines for elliptical shaped transition pieces.(1964)

The flow was allowed to enter in the pressure box from the top. The box and flow pipe was connected by a 45 degree bend, which was flanged on the top of the box with the help of a aluminum ring. The inside of the box was completely filled with a mesh of chicken wire, in order to reduce the generation of extra turbulence and to dissipate turbulence entering the box. The sides, top and bottom of the pressure box was bolted with nuts and bolts, for reopening if necessary to facilitate changes to the design. The box was sealed with a gasket and white transparent silicon gel from all six sides and rendered completely water tight. The box was aligned at 45 degree with the channel slope by putting extra scafolding to hold it in position as shown in Fig 3.7(a).

In effect the flow is required to turn through an angle of 135° to

reach the spillway. Several test runs were carried out and modifications made to ensure the smoothest flows into the spillway.

3.4.3 *The spillway flume.*

The spillway flume was constructed in perspex 12mm thick, and was made 3.5m long, this being the maximum distance from pressure tank to the free surface of the sump tanks below. This is sketched in Fig 3.7(a).

The spillway was rectangular in cross section being 100mm wide and 200mm deep and shown in Fig 3.8. It was built in three sections, two of which were 1 m long and the middle section 1.5 m long. They were joined together by means of splice plates. Great care was taken with the joints between the 1 m and 1.5 m long spillway sections, including rubber gaskets, and a special flush mounting technique to ensure no disturbance to the flow either on the base or walls.

Once joined, the channel was further supported by 'U' shape aluminum rings for extra support. The channel was joined at the base with two half inch square hallow steel bars, from the pressure tank to the end of the channel. The whole assembly was supported by scafolding as shown in Fig 3.7(a) and Fig 3.7(b). The spillway cross–section is shown in Fig 3.8.

Three diffrent ramp angles were constructed and placed in turn at 1.6 m downstream of the gate. The ramp angle were 2^0, 5^0, and 10^0, and each ramp was 300 mm long, and made of prespex as shown in Fig 3.9(a), (b) and (c). A 90 mm dia of circular hole for air entry was made at the base of the channel just after the ramp. This circular hole was further attached to the air entrainment rig. A measurement tape was glued at the base of the channel for measuring the aerator jet length. The channel was provided with an instrument carriage for the use of Laser and optics along the channel length. The slope of

the channel was selected at 45°, due to the limitation of the space available in the laboratory. Four sections were marked in the channel upstream and down stream of the ramp for Laser measurements (as shown in Fig 3.5), of mean and fluctuating velocity, both in the longitudinal direction and direction normal to the spillway base.

It should be noted here that considerable attention was given to the placing of the ramp downstream of the pressure tank. A distance of 1.6m was chosen, this distance being crucial in terms of boundary layer development of the spillway flow.

Most open channel flow experiments require the flow to be fully developed before the measurement section. This is not the case for this type of spillway flow, simply because prototype aerators are placed where cavitation damage is likely and this is often long before fully developed turbulent flow is achieved. Nevertheless it was decided to investigate the likely boundary layer development in this kind of smooth perspex surface.

The most suitable equation (described in Chapter 7) and used by Falvey (1987) for smooth surface is:–

$$\frac{\delta}{x} = \frac{0.38}{[\,Re_x]^{0.2}} \qquad (3.3)$$

where Re_x is $(v\ x)/\nu$

With x equal 1.9m at the end of ramp and flow depth from 10mm to 80mm approximately, this corresponds to x/h values from 16 to 160 whereas x/δ values from Equation (3.3) vary typically from 50 to 100 showing the most of the shallower flows are fully developed but some of the deeper ones are not. This is typical of prototype spillways.

3.4.5 Water supply system.

A recirculating water flow system was used through out all experiment tests. The water entered the supply system through at 6 inch diameter pipeline from a pump drawing from two sump tanks situated near the pump. The pump and tank is shown in Fig 3.10. With the pump capable of delivering a maximum discharge of 60 ℓ/s (0.06 m^3/s). The flow was controlled by a 6 inch gate valve just after the pump. A 6 inch 90^0 bend section near the laboratory ceiling was followed by a straight section incorporating orifice plate. A calibrated orifice plate was placed in the supply line for water discharge (Q_w) measurements. The piezometric head difference across the orifce plate was determined by means of both mercury and water differential manometers, depending on the flow rate.

After the orifice plate, another 45^0 P.V.C bend section was used to supply water to the pressure tank. The pressure tank was filled by chicken wire rolls to dissipate the extra turbulence generated from the inflowing water. The water received by the pressure tank and guided towards the outlet gate of the tank. Water passed through the sliding gate, (which was set to the required gate opening) into the channel, and from there it flowed as a super–critical gradually varied flow over the spillway and ramp. After forming a jet, the air/water mixture flowed to the one of the sump tanks and became de–aerated before going to the next tank for recirculating again. The schematic representation of the overall system is shown in Fig 3.7(a).

Initial tests showed that entrained air bubbles were able to enter the inlet pipe to the pump, so it was decided to install a length of pipe, shown by the dashed pipe in Fig 3.7(a), which extended right into the centre of the pump sumps. This measurement ensured that no entrained air entered the pump.

3.4.5 The instrument carriage.

All of the velocity and turbulence measurements in this research were carried out using a Laser system. It was crucial to have an instrument carriage for the Laser which could move in three directions with great accuracy. This was the most difficult part of the construction of apparatus.

The principle of a Laser is to keep Laser and receiving optics aligned all the time, while taking readings. Therefore an instrument carriage was required which could move along the length of channel with its 45^0 slope, and also the platform should move up and down for taking measurments at different heights in the flow. As well as this, the Laser had to move horizontally by 100mm to measure at different widths into the flow.

After consuming considerable time designing the traversing carriage, the technicians were able to construct a platform, made of wood and perspex as shown in Fig 3.11. The platform was joined together at the bottom but enabled the spillway to pass– up the middle of the carriage. The end of the carriage was fixed with two wheels at each side, which could easily slide over a rail. The whole system was balanced by a dead load weight system using a pully as shown in Fig 3.7(a). There were slow and fast moving arrangements in the platform for keeping it aligned at different heights. The carriage could easily move between the four sections previously selected for Laser measurements. The perspex platform above the wood was made to keep the platform level (horizontal to the ground). There were two fixing screws at the end of each wheel for keeping it fixed in position while taking measurements. Fig 3.11 shows the final construction of Laser carriage.

Flexible cables were used to enable the Laser to move from section 1 to section 4 with signal sent back continuously to the computer interface.

The four measurement sections are shown in more detail in Fig 3.5 and were chosen section (1), 600mm upstream of the end of the ramp; section

(2), 300mm upstream of the end of the ramp at the start of the ramp; section (3), at the end of the ramp; section (4), and 300mm downstream of the end of the ramp in the middle of the aerator jet.

3.4.6 *Apparatus for measurement of air entrainment*

Although a good deal of time was spent taking velocity and turbulence measurements using the Laser system, a significant proportion of time was also spent taking corresponding measurements of air flow Q_a, jet under pressure in the cavity Δp, and the jet length L.

The principle used for the air flow measurements is sketched below and is based on controlled air flow rates entering the cavity at the underside of the aerator jet.

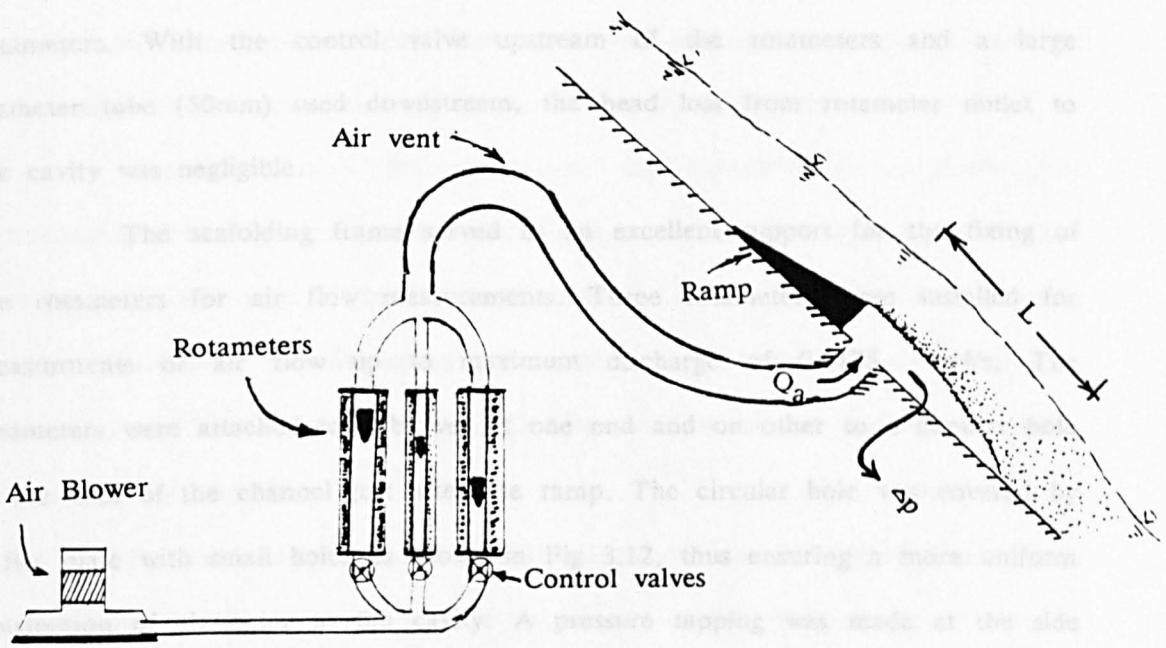

Air flow from an air blower was fed through a control valve through air flow rotameters, and then into a 90mm circular opening under the jet. The valve represented the main control on the air flow system, and ensured that any under-pressure Δp could be organised from zero downwards. Zero represents atmospheric

pressure under the jet and represents zero head loss through the air ducting system.

A sketch of the apparatus for the air flow is also given in Fig 3.7(a). As a general rule, three set of measurements were carried out for each flow

(i) $\triangle h$ = 0.0 (atmospheric) with the largest air flow.

(ii) $\triangle h$ is (maximum) Air flow completely turned off

(iii) $\triangle h$ = ($\triangle h_{max}$ /2) with smaller air flow

(iv) $\triangle h$ either $\triangle h_{max}/4$ or 3 $\triangle h_{max}/4$ with a little less/more air

Using this technique any air flow or any $\triangle h$ could be achieved, although the test runs were carried out over the same range as prototype structures where $\triangle h/h$ ($\triangle p/\rho gh$) $\simeq$ 0.0 to 0.7, where h is the flow depth at the ramp.

Measurements of air flow was achieved using three pre-calibrated rotameters. With the control valve upstream of the rotameters and a large diameter tube (50mm) used downstream, the head loss from rotameter outlet to the cavity was negligible.

The scafolding frame served as an excellent support for the fixing of the rotameters for air flow measurements. Three rotameters were installed for measurments of air flow up to maximum discharge of 0.0175 m^3/s. The rotameters were attached to a blower at one end and on other to a circular hole at the base of the channel just after the ramp. The circular hole was covered by a flat plate with small holes as shown in Fig 3.12, thus ensuring a more uniform distribution of air entry to the cavity. A pressure tapping was made at the side of the channel to measure change in pressure under the nappe, and was used in conjunction with an inclined manometer as shown in Fig 3.13.

The air flow rotameters were designed to be used at 15 degree centigrade to get accurate measurements. This was achieved by allowing cool air to enter the air blower, and also by allowing the air blower itself to cool before

starting a new series of tests. The total capacity of the three rotameters was enough to give zero under–pressure for most of the water flow test through the system. The arrangement of the rotameters is shown in Fig 3.14.

The rotameter consisted of a mild steel channel with welded end plates, through which the connections are secured. The metering tube is held in simple quick release fixing and sealed with internal "O" rings in nitrile rubber. The flow scales are fixed on to vitreous enamelled plates which are pivoted to allow access to metering tube and accessories. The front of the rotameter is protected by a prespex dust cover. The accuracy of the rotameters used was ±2%.

It was decided to use an air blower in order to introduce air at a pressure equal to, or lower than atmospheric pressure at the under side of the nappe. An air blower (Model P180–104–J803) was chosen, which can supply air in excess of 20 litre per second. This value was sufficient for most of the cases causing zero under pressure under the nappe, and was also adequate to cover the entire range of air/water ratios (β) measured in prototype aerator structures.

The outlet from the air blower was connected to a plastic pipe extending to the airflow rotameters where it is connected to a steel pipe with two branches, one for each airflow rotameter with a valve to control the air going through the system, and the other branch with a stop valve for controlling the excess pressure in the system. Fig 3.15 shows the air blower and its connection to the air flow rotameters.

As mentioned before, the proposed air entrainment experiment requires the measurement of change of pressure under the nappe. The change of pressure was so small that an ordinary manometer can hardly identify it, so it was decided to use an inclined manometer with lighter density liquid. The purpose of inclined manometer was to magnify the Δh reading so that any small changes could be easily identified. A magnification of three times column height was selected, giving an angle of 18.43^0 for the manometer. A red coloured methyl alcohol (specific

gravity = 0.8) was used for measurements of pressure difference w.r.t atmosphere. The manometer was attached by a plastic tubing to a pressure tapping at the side of the main channel. Three different values of air supply were used to calculate three different changes of pressure under the nappe. Fig 3.13 shows the connection of the inclined manometer with pressure tapping.

3.5 INSTRUMENTATION

3.5.1 Introduction

The three main components of instrumentation are the orifice plate for discharge measurements, a mechanical turbulence probe for the initial turbulence tests in the vertical circular jet rig (already described in section 3.2), as well as the Laser Doppler System for velocity and turbulence measurement on the spillway aerator.

It should be pointed out that the orifice plate and the turbulence probe both been designed, installed and calibrated by Withers (1987), so that their description in this section is a summary of Withers earlier work. It was decided in the event to recalibrate both devices.

The Laser Doppler system on the other hand had been in the Civil Engineering Department since 1984 but had never been used until the start of this research work. This meant that a good deal of time needed to be spent understanding the Laser system, its mode of operation, and attempting to obtain reliable, repeatable measurements of turbulence from it. This proved to be a time consuming part of the work but proved worthwhile in the sense of using a new technique which did not interfere with the flow, and gave aerator turbulence jet measurements for the first time

3.5.2 *The orifice plate and its re-calibration*

The simplest method of measuring discharge efficiently and cheaply was to use the type of orifice device outlined in BS1042: part 1:1964 and already installed and calibrated by Withers. The orifice had pressure tappings at a distance of D and D/2 upstream and downstream from the orifice plate, where D is the internal diameter of the pipe. It was decided to recalibrate the device.

An orifice plate is a circular disc with a hole of known diameter in the centre. The orifice plate is inserted onto the pipe line acting as a connection to the flow, and producing an energy or head loss as the flow passes through the throat of the orifice plate. This energy loss can be easily measured on the manometer by measuring the pressure difference between two pressure tappings upstream and downstream of the orifice plate.

According to BS1042:Part 1:1964, the discharge is given by

$$Q = 0.01252\ C\ Z\ \epsilon\ E\ d^2 \sqrt{\frac{h}{\rho_w}} \qquad (3.4)$$

where Q is the discharge through the orifice in m^3/s, C is the basic correction factor, Z is the Reynolds number correction factor, ϵ is the expansibility factor which for incompressible flow can be taken as 1.0, E is a velocity of approch factor, h is the difference in pressure , between upstream and downstream pressure tappings at the orifice plate. ρ_w is the density of water and d is the diameter of the orifice throat. The following values for each parameter are given below and were calculated from methods specified in BS1042:Part 1:1964.

$\rho_w = 998\ kg/m^3$

$C = 0.6064$

$Z = 1.02$

$E = 1.206$

$d = 114\ mm$

and $\epsilon = 1.0$

The above design procedure was used for designing 25mm orifice plate for initial turbulence measurements in circular jets as shown in Fig 3.4. The orifice plate used for discharge measurements was designed by Withers and sketched in Fig 3.16.

If the water manometer was used to measure discharges in excess of 30 lit/sec then the expected value of h would be too high, whereas if mercury was used at low discharges the h value would be too low. It was therefore decided to utilize two manometers, one containg water for measurement of low discharges, and the other containing mercury more suitable to measuring high discharges.

An important point of consideration in the design of the orifice plate is the required distance upstream and downstream from the orifice plate to another device such as a pipe bend or a gate valve. The minimum distance required upstream and downstream was more or less satisfied. Recalibration of the orifice plate was carried out by measuring the volume of water passed through the spillway channel through integrated discharge. A section was selected in the spillway chute just after the gate outlet of the pressure box, and 12 different points were selected in a grid for measuring the point velocity using a Pitot tube. The 12 point velocities were integrated to give the total discharge Q_w. The results of a number of such tests are shown in Fig 3.17 and it is clearly seen that for a wide range of discharges the orifice plate prediction of the discharge compares very well with the measured discharge. On the basis of these results the final relationship between head and discharge is:

$$Q_w = 0.1164 \quad (\Delta h_m)^{0.494} \tag{3.5}$$

$$Q_w = 0.0333 \quad (\Delta h_w)^{0.494} \tag{3.6}$$

where Δh_m = head difference of mercury manometer, and Δh_w = head

difference of water manometer

Fig 3.17 shows the experimental calibration compared well with the theoretical head– discharge relationship from B.S 1042. The calibrated orifice was then used to determine the mean velocities in the spillway flume during the experiments.

3.5.3 *Tranducer turbulence probe*

Some initial turbulence data was taken in the existing rig with circular nozzle and orifice outlet. Turbulence was measured using a crude total head probe. The total pressure probe, devised by Arndt and Ippen 1970, is capable of a flat response to total pressure fluctuations in the frequency range (0 – 250Hz) and therefore can be used for approximate turbulence meaurement. It comprises a total head tube connected to a pressure transducer. A schematic representation of the system in question is shown in Fig 3.18. The types of transducer which are suitable for a turbulence gauge consist essentially of a metel diaphragm together with a method of measuring the deflection of the diaphragm under pressure.

The frequency response of the system is given by

$$F(f) = \frac{1}{\{ 1 + (f/f_0)^4 \}^{\frac{1}{2}}} \qquad (3.7)$$

where F(f) = frequency response

f = frequency

f_0 = natural frequency of the system

Since the membrane deflection is directly related to the electrical output of the transducer, it can be stated that frequencies below 75% of f_0 the response will be between 90 and 100% of the static response. In other words, there will be less than 10% distortion in a turbulence signal for frequencies lying below 75% of the natural frequency f_0 Arndt & Ippen (1970). The overall

natural frequency of the instrument, f_0, in terms of natural frequency of the transducer, f_d , can be written in the form:

$$f_0 = 1.11\, f_d^{1.5} \left[\frac{\rho_d}{\rho} \frac{A_1}{L_1} \right]^{\frac{1}{2}} \left[\frac{\rho_d (1-\eta^2)}{E} \right]^{\frac{1}{2}} \qquad (3.8)$$

where: A_1 = Area of chamber 1 as shown in Fig 3.18

L_1 = length of chamber 1 as shown in Fig 3.18

η = poisson's ratio

E = young's modulus

f_d = natural frequency of the transducer

It was required that the probe be suitable for use within the frequency range 0– 250 Hz. Hence, the necessary f_0 to give less than 10% distortion in a turbulence signal within this frequency range was approximately 330 Hz (operational frequency range is 75% of f_0). Fig 3.19 shows the final design and dimensions of the probe as detailed by Withers (1987).

The above designed probe was of 3.2 mm outside diameter and 2.0 mm inside diameter coupled to a pressure transducer of the flush mounting type (4– 327– 0003 Bell and Howell). Because the transducer is designed for flush mounting, an adaptor was used to connect the total head tube and shock chamber. A carrier preamplifier was used to excite the transducer and amplify the output signal. The amplified output from the transducer was fed to both a digital volt meter and to a volt meter for the determination of the root mean square of the signal.

Before using such a turbulence probe as described above, it is imperative to test the natural response frequency of the whole device. This work done by Withers(1987) using a "ballon bursting" technique which provides a shock to the diaphram and the frequency was measured by photographing a trace on the oscilloscope. The particular instrument had a natural frequency around 210 Hz which is relatively low for picking– up fluctuations around the micro– scale, but

fine for picking up broad range of turbulent fluctuation to be found in a vertical circular atmospheric jet.

The probe operates by measuring the total instantaneous pressure at any point in the flow. For an atmospheric jet where the mean pressure is zero (relative to atmosphere) the total instantaneous pressure approxoimates to

$$\underset{\sim}{P_T} \simeq \tfrac{1}{2} \rho [u' + \bar{u}]^2 \qquad (3.9)$$

where $\underset{\sim}{P_T}$ = total instantenous pressure

Which can be resolved to measure the turbulence intensity $u'/\bar{u}$, when the relationship between the time averaged mean velocity is known. This requires a dynamic calibration of the probe which is shown in Fig 3.20(a). This result was found by Withers, but was checked by the author and found to be accurate.

The recalibration of the turbulence probe was carried out by correlating the output voltage from the pressure transducer turbulence probe readings with average velocity measurement from the pitot–static tube. The average velocity readings were taken at the same location and under the same flow conditions that were operating during turbulence probe measurements, but obviously not at the same time period. Fig 3.20(b) shows the relationship between measured velocity by pitot–static tube and calculated velocity by turbulence transducer probe.

The accuracy of this probe was ± 10% at the level of 10% turbulence. It was reasonable for this case because Laser was not suitable on rough jets. The noise was reduced by using short cables, sheilding of cables and by providing extra earthing. The noise was calculated by making a test run without flow conditions. The signal from noise was obtained by plotting voltage against time. This voltage was further deducted from orignal sample signal in order to get signal without noise. Once this relationship is found. it is incorporated inthe computer programme for further test run.

3.6 LASER DOPPLER ANEMOMETRY.

3.6.1 Introduction

Experimental fluid mechanics has, for many years, made use of mechanical measuring probes to obtain information on fluid velocity. Total pressure probes, in conjunction with static–pressure probes, have provided the principal means of measuring mean velocity and hot–wire or hot–film anemometers. The principal means of measuring instantaneous velocity and, therefore, mean velocity, RMS velocities, and velocity correlations. The optical technique considered here allows the measurement of the local, instantaneous velocity of tracer particles suspended in the flow and, hence, does not disturb the flow. Of course, since it is the particle velocity which is measured, the relationship between the particle and fluid velocity must be known if the fluid velocity is to be evaluated. Appropriate particles exist in many liquids and gases and, where they are too few in number, can often readily be supplemented. The availability of a measuring technique which does not distrub the flow is particularly relevent to recirculating flows where mechanical probes cannot be used without disturbing the recirculation pattern and to flows in ducts of small dimensions where mechanical probes cause blockage.

To date, hot–wire and hot–film anemometry has been the principal experimental tool for quantitative investigations of the structure of turbulent flows. Although this technique has provided much quantitative information, its application has been substantially limited to constant property flows of low temperature, low speed and low turbulence intensity, outside regions of recirculation. Laser Doppler anemometry can overcome all of these limitations and, unlike hot–wire anemometry, it is not limited to the controlled flow conditions found in research laboratories.

A Laser anemometer uses a Laser beam for velocity measurement.

When the beam passes through the fluid flow, the light is scattered by particles suspended in the fluid, as shown in Fig 3.21. The scattered light contains information about the velocity which is measured by optoelectronic means, and interpreted using the Doppler principle.

The Doppler effect occurs whenever there is a relative velocity between the sourse of sound or light and an observer. To a stationary observer, the light scattered from a particle moving away from a fixed light source would appear to have a lower frequency than the source frequency, and the light scattered by a particle moving towards a fixed light source would appear to have a higher frequency than the source frequency. The geometry of this situation is shown in Fig 3.21(a). The frequency relationship between a scattered light wave and the light wave it originates from is given according the vector equation and shown in Fig 3.21(b):

$$f_s = f_i - \frac{1}{\lambda} \bar{v} (e_s - e_i) \qquad (3.10)$$

where f_s is the frequency of scattered light, f_i is the frequency of incident light, e_s is the unit vector in scattering direction, e_i is the unit vector in the incident direction, $\bar{v}$ is the velocity vector, λ is the wavelength of incident light. The frequency shift is equal to the Doppler frequency f_D :

$$f_D = f_i - f_s \qquad (3.11)$$

and hence,

$$f_D = \frac{1}{\lambda} \bar{v} (e_s - e_i) \qquad (3.12)$$

It can be seen from Equation (3.12) that the Doppler frequency is directly proportional to the particle velocity.

3.6.2 *Mode of operation*

In order to utilize the measuring principle based on the Doppler effect, a monochromatic light source emitting coherent light waves must be used to produce the incident beam to the flow. The Laser fulfils these requirements of the light source and, with its high beam intensity, is well suited for this purpose. The optical and optoelectronic equipment used the Laser anemometry are, besides the Laser itself, the beam splitter, lenses, apertures, a photodetector and a frequency tracker. These components may be arranged in a number of different modes of operation depending on the type of the flow suituation being investigated. A Differential Doppler mode with forward light scattering was used in this study. The Laser and receiving optics are shown in Fig 3.22.

The Differential Doppler mode using two incident beams of equal intensity is used where the intensity of scattered light is low. In this case, the scattered light can be picked up over a wide angle since the Differential Doppler frequency is independent of direction of detection. A single Laser beam is split by an optical unit as shown in Fig 3.23, and the two resulting beams are focused to the point where they intersect. This point is known as measurement control volume, m.c.v. (i.e the point at which the fluid flow characteristic are measured). The two coherent Laser beams, on intersection, yield a pattern of plane interference fringes as shown in Fig 3.24. According to Bragg's Law the fringe spacing ($\triangle x$) is proportional to the wave length of light (λ) and inversely proportional to the half angle between the two beams ($\theta/2$). As a particle moves through the region of interference fringes, it will scatter light whose intensity will vary according to the light intensity variation inside the bisector of the two beams. These light intensity variation have a certain signal frequency or Doppler frequency f_D . The relationship between particle velocity and signal frequency f_D can be determined as follows:

from the Fig 3.24 we get:

$$f_D = \frac{v}{\Delta x} \tag{3.13}$$

where f_D is the signal frequency, Δx is the fringe spacing, and v is the particle velocity perpendicular to the bisector of the beams.

from Bragg's law,

$$\Delta x = \frac{\lambda}{2 \sin \theta/2} \tag{3.14}$$

where λ is the wavelength of Laser light and θ is the intersection angle. hence,

$$f_D = \frac{2 v \sin \theta/2}{\lambda} \tag{3.15}$$

Hence if the angle between two beams is known and also the wave length λ, then if the Doppler frequency can be measured, so the velocity can be determined. All of this is only possible if the fluid flow contains seeding particles.

Seeding is a fundamental in Laser anemometry. Without the presence of an appropriate concentration of scattering particles the anemometer will not function. In many cases, there is a natural distribution of particles in the flow, such as solid contaminations or bubbles of dissolved media. However, it is often necessary to add particles and these must be of appropriate size and concentration. In general, the particles must be small enough to be able to follow reasonably high frequency turbulent movements with sufficient accuracy but large enough to cause detectable scattering. The diameter of the scattering particles

should be of the order of 1μ to 10μ in liquids. The concentration of particles should be high enough to give an adequate amount of scattered light, but not so high that the whole test area receive diffused light.

3.6.3 *Measurement of point velocities in the channel by Laser Doppler Anemometry.*

The Laser Doppler anemometry was set up in the Differential Doppler mode with forward scattering. The relative positioning of the Laser, optical unit, test rig, and photomultiplier for operation of this mode is shown in Fig 3.25. There are following steps are involved before taking measurement each time:

3.6.3.1 *Positioning of the photomultiplier*

The optical axis of the photomultiplier is aligned so that it intersects the measurement control volume. The photomultiplier is then positioned so that the approximate distance from the m.c.v. to the objective lens corresponds to the focal length of the optical unit lens. The objective lens is used in the photomultiplier to focus the light from the m.c.v., through a pin–hole (for signal optimization purposes) on to the photo–cathode. The image of the beam intersection is than located on a screen in the PM by use of a view finder and the PM moved slightly backwards or forwards until the precise focussing of the beams is achieved. The unshifted and shifted beams forms two crosses with fan–shaped arms. With exact focussing the fan–shaped images are narrowest at the intersection points, as shown in the Fig 3.26. The pin hole position is then adjusted until it is located at the centre of the intersection of the shifted beam.

3.6.3.2 Operation of the frequency tracker

A suitable frequency shift is chosen using Equation 3.15 for the particular measurement application and a matching frequency range is selected on the frequency tracker unit. The matching frequency range has a maximum equal to twice the frequency shift value. This means that zero current will register at mid scale on the Doppler meter. The anode current is set at 50 μA and the Doppler signal from the preamplifier is then viewed on an oscilloscope to ensure that it is of good quality. A poor signal could result from:

a). Poor beam intersection.

b). Incorrect focussing of PM.

c). Particle density too high or too low.

Fig 3.27(a) shows a good quality Doppler signal. The peaks indicates Doppler burst caused by individual particles passing through the measurement control volume. When optimisation of the Doppler signal is completed the tuning of the Frequency Tracker can begin. Upon completion of the preliminary tuning procedures the Doppler frequency f_D can now be found from the scale on the Frequency Tracker and hence the mean flow velocity, U_{mean} can be calculated. The root–mean–square of the instantaneous velocity fluctuations $\sqrt{\underset{\sim}{u}^2}$ can be found by connecting an I.B.M PC computer or by R.M.S volt meter to the output of the frequency tracker. This enables the turbulence intensity u'/u at any point in the flow to be determined. The frequency tracker acts as an amplifier. Therefore it will not only amplify its own power beam, but also the noise on the beam. With Differential mode system the noise source is back ground sky lights, cables, as well as the scattered Laser light itself. To eliminate the Laser plasma noise over a wide range of frequencies an optical method was used. This system was already built–in in the frequency tracker and shown in Fig 3.27(b). In this system the signal from photodectecter is split into two signals of equal amplitude. One of the signal is used in convential way and the other in unmodulated. The

two signals are further combined at differential amplifier. In this way the noise present simultaneously on both channels are eliminated. Therefore the signal obtained at voltage analoge output was without any noise.

3.6.3.3 *Velocity and turbulence measurements.*

For measurement in water the Equation 3.15 can be used to give velocity of water at the point of intersection in terms of Doppler frequency f_D, the wave length of the Laser light λ, and the beam intersection angle θ. The relationship between Doppler frequency and velocity could be written as;

$$u = \frac{f_D}{\left[\frac{2\, n \sin \theta/2}{\lambda}\right]} \qquad (3.16)$$

where u = velocity of particle in water.

f_D = Doppler frequency.

λ = wavelength of Laser light.

θ = Laser beam intersection angle .

n = refrective index.

It should be pointed out that the coefficient :

$$\left[\frac{2\, n \sin \theta/2}{\lambda}\right] \qquad (3.17)$$

is independent of the medium ($f_D = u / \Delta x$). This results from Snell's law and the wave properties of light. Therefore if θ and λ are measured for air ($n=1$), the coefficient can be calculated and used even for water in the experiments.

When making measurement in liquids flow, the location of the measuring point will be different to that in an air. The position of the measuring point can be calculated as:

$$a = b/2 \quad \cot(\theta/2) \tag{3.18}$$

where θ = intersection angle of Laser beams

a,b = as shown in Fig 3.28

The Laser Doppler anemometry method described here was used in the study of the velocity and turbulence distribution over the ramp and in the free jet. Fig 3.22 shows that the working beams of Laser at the time of measurements. Measurements were taken in the spillway flow 600 mm upstream of the end of the ramp; 300 mm upstream of the end of the ramp; at the end of the ramp; and 300 mm downstream of the end of the ramp. The Laser was turned through 90^0 to measure the turbulent velocity w', normal to the spillway bed.

3.7 DATA ACQUISITION , STORAGE & PROCESSING.

3.7.1 Introduction.

The purpose of this section is to describe the link–up between the Laser Doppler system (or turbulence probe) and the computer used in this work. It should be noted that much of the interface infrastructure was in place already, designed by Withers (1987) and used for pressure fluctuation measurements. Some modification were required for the Laser/computer interface.

The system utilised in the present research study consisted of various elements. Fig 3.29 illustrates the method of data collection that was used.

Analog voltage signals from the frequency tracker, representing the flow behaviour at the instrument, were amplified, conditioned, digitised and either stored or processed directly on a micro computer using a program developed from software which had been specifically obtained for the task.

3.7.2 *Acquisition Hard ware*

This section will concentrate on the hardware that was used in the data acquisition process. The hardware consisted of printed circuit boards. Each board performed a specific task which will be detailed below.

Hardware was furnished by the Burr–Brown Corporation (PCI – 20000) and comprised of a termination panel, a analog input module and a carrier card. These elements were accessed with the micro computer via the specialised software. Each of the hardware components and the computer interface are shown in Fig 3.30. The signal termination panel provided convenient screw terminal connections between the internal electronics and the external Laser field readings. Board space was also provided for passive signal conditioning, including extra earthing options.

As all data is represented digitally in the computer, the amplified analog signals from the measurement device had to be converted to digital form for computer manipulation. Therefore, readings from the active channel in the termination panel was passed through a analog input module which performed the analog to digital (A/D) conversion.

3.7.3 *Data quantification.*

The relationship of the digital value produced by the conversion of the

input signal level depends on the resolution, or number of binary digits (bits), of the converter as well as the input voltage range. In this case, for a 12− bit converter with a ± 10 volt input range, there are 4096 (2^{12}) possible values of the digital result and a voltage range of −10 volts to +10 volts, covering a span of 20 volts. This means that the value of each bit of the A/D result is:

1 bit = 20 Volts/4096 = 4.883 mV (approx.)

Therefore, the actual voltage corresponding to any converted value, for a converter with a straight binary code, is:

Voltage = A/D result.(4.883 mV) (approx.)

The resulting relationship between the binary code and the relative voltage is:

Voltage = [A/D result x (20 / 4096)] - 10 (3.19)

3.7.4 *Computer interface and specification.*

The main circuit board in the system is called a carrier, and it inserts into one of the expansion slots in the back of the host micro computer. Interfacing with the internal bus of the micro computer's central processing unit is through the carrier card. It also provides power and a physical mounting for the instrument module. The carrier is functionally programmed by the plug− in instrument module, in this case an analog input device. Communications between the computer and the converter are through the carrier card.

Considering the micro computer itself, certain facilities were required to adequately perform the tasks of data acquisition, processing and storage. An I.B.M. X.T. personal computer had already proved to be a reliable and relatively inexpensive piece of equipment with the capabilities to accomplish the work. The

specifications of the system are:

(i) standard I.B.M. PC–XT system unit with 640 Kb of R.A.M.

(ii) enhanced keyboard

(iii) one floppy disc drive with 360 Kb capacity and one hard disc with 20Mb capacity

(iv) I.B.M. mono display monitor

(v) Hercules compatible graphics card

(vi) 8087 maths co–processor

(vii) disc operating system (version 3.2)

(viii) Epson FX–80 dot matrix printer

A photograph of the system is shown in Fig 3.31.

3.7.5 Software.

As noted before, the computer could read the frequency tracker signal once it had passed through various peripheral units including an analog to digital converter. An A/D board was installed on the carrier card which was connected to the computer. In order to read or sample the output of frequency tracker linked to a channel of A/D, the memory address assigned to the channel had to be accessed by the computer. This was accomplished by creating a computer program or software.

The computer program was fundamental to the collection of data through hardware control, and provided a method to process the readings once they had been acquired. Apart from channel selection, the program was responsible for initiation of (A/D) conversions, synchronisation of events and data pre–processing. Pre–processing involved converting the digitised data (voltage) to physical units of velocity. This step was carried out according to the previously

determined Equation (3.10) which was included in the program.

The computer program had already been written in Asyst (version 1.56); by Withers (1987) and required some modification for use in this equipment. Basically, Asyst is a sophisticated high–level language utilising words or phrases (commands) which perform particular functions. A programme has been generated by sequential combination of these commands.

Together with providing the program structure, the basic functions of the Asyst software are statistical analysis and graphical representation of the data. To interface between the Asyst language program and the system hardware, software support had to be added (PCI–20046S – 4).

By combining the Asyst structured program with hardware control routines, a method was developed which could automatically acquire data from the Laser and then process the resulting array of instantaneous readings.

The instrument sampling routine was therefore defined by the computer program, but, as will be detailed in the following sections, it must satisfy certain requirements to ensure that the resulting measurements are representative of the actual flow phenomenon. A listing of the Asyst language Laser velocity and turbulence detector programme is given in Apendix A.

3.7.6 Requirement of sampling routine.

Digitisation of the continuous signal from the frequency tracker means that it is converted to a digital form by sampling at discrete inervals. The problem is defining the instantaneous points at which the data values are to be observed.

Sampling for digital data processing is usually performed at equally spaced time intervals. The aim is then to determine the appropriate sampling interval which will fully define the signal. On the one hand, sampling at points

which are too close together will yield correlated and highly redundant data, and this unnecessarily increases the labour and cost of calculations. On the other hand, sampling at points which are too far apart will lead to confusion between the low and high frequency components in the original data.

To adequately define the signal with discrete points in time at least two samples per cycle are required. Taking the time period between samples to be 't', the heighest frequencies which can be defined by sampling rate of 1/t samples per second is 1/2t cycles per second. During preliminary testing, the signal was sampled at the highest rate possible supported by software which was around 230 Hz. By inspection it was found that the frequencies were just concentrated well below 50 Hz as shown in Fig 3.32. The minimum sample rate for the experiment was therefore selected 100 Hz in order to ensure that every valuable data had been picked up.

3.7.7 *Data acquisition capacity and quantification.*

The I.B.M PC XT used in this research had a fixed memory of 640KB. This memory was enough to store the software, software support and data from the Laser Doppler Velocimeter. In order to select the time period for sampling routine the stationary method was used. The stationary method is that when basic physical factors will generate the flow phenomena are independent of time. If the flow is constant and the boundary is fixed, it would be reasonable to assume that the resulting velocity data is stationary. Although this argument is correct, but it is slightly over–simplified. Therefore, the stationary of the data must be evaluated by studies of sample time history record. The minimum sample duration may then be determined for which the result may be said to be independent of time. In the above study a time period of 21 seconds was found to sample the routine independent of time, so the total number of data points at

100 Hz would be (100 x 21 = 2100). But this number should be in order of 2^n for calculation in software. Hence 2^{11} = 2048 points which are less than required data points for sampling. The next choice was 2^{12} = 4096 points which satisfy both software and sampling routine. Therefore 4096 data points at 100 Hz will bring a time limit of approximately 41 seconds for each test run.

3.7.8 The graphical representation.

One of the main advantage of the soft−ware was the complicated statistcals procedure could be carried out in very simple steps with individual instructions. The raw data was first called back from disc storage and was plotted directly for visual inspection of the wave form on the computer monitor. Fig 3.32 show typical wave forms from the Laser Doppler measurments. Considering segments of the raw data, the power spectrum was easily obtained and plotted using the software. A listing of the program used to obtained and plot the power spectra and wave forms is given in Appendix (AV).

3.8 EXPERIMENTAL PROCEDURE.

The overall order of the experiment testing programme is as follow :−

(i) Gradually varying flows were measured using a pointer gauge and presented in Chapter 4. This was done for three gate openings, three discharges per gate opening, and for two boundary roughness values (smooth k_s = 0.0 and rough k_s = 0.35 mm equivalent (Sides + bed)).

(ii) The gradually varying flows were analysed to obtain roughness coefficients in the form of Manning 'n', D'arcy Weisbach friction factor λ and surface roughness k_s.

(iii) A ramp of given angle Φ was inserted in the flow.

(iv) A procedure outlined in flow chart below was then carried out including a range of gate openings 60mm, 90mm, and 180mm. A range of discharges was selected for each gate opening, namely 15 ℓ/s to 52 ℓ/s.

(v) The Laser was then used at each of the four cross–section in turn, to measure the mean longitudinal velocity at any point u, the longitudinal RMS component u' and the normal to the bed component, w'. The location of the four cross–section is shown in detail in Fig 3.5.

(vi) Each cross–section required an array or grid of measurement points to properly define the cross–section flow properties. The Laser was then used to measure u, u' and w' at every grid point.

A typical cross–section is shown below indicating five vertical slices across the width and horizontal slices at every 5mm – 10mm intervals. Details of the Laser measurements procedure have been given in section 3.6.

(vii) The water flow depth was measured throughout using a combination of pointer guage and side–wall scale

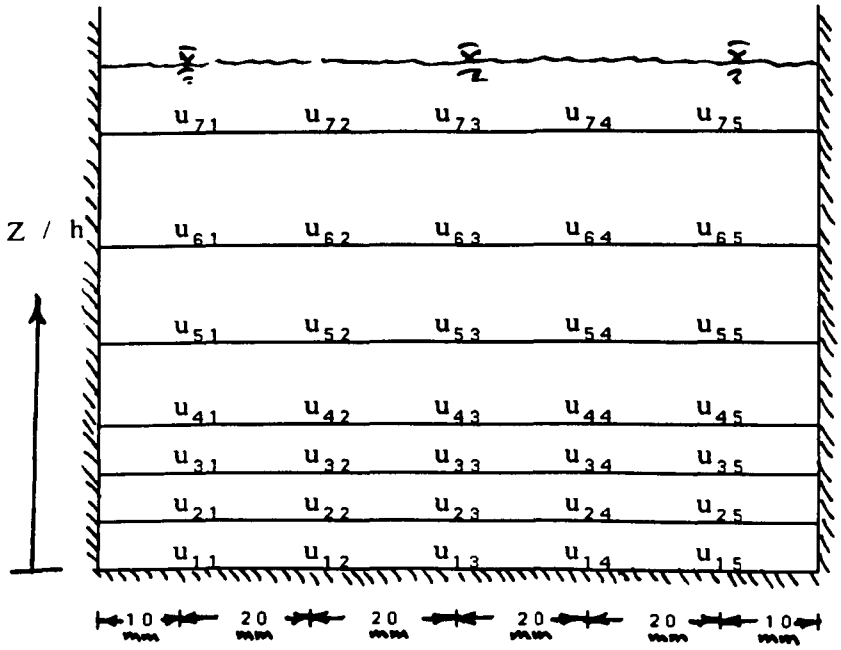

FLOW CHART FOR TURBULENCE MEASUREMENTS

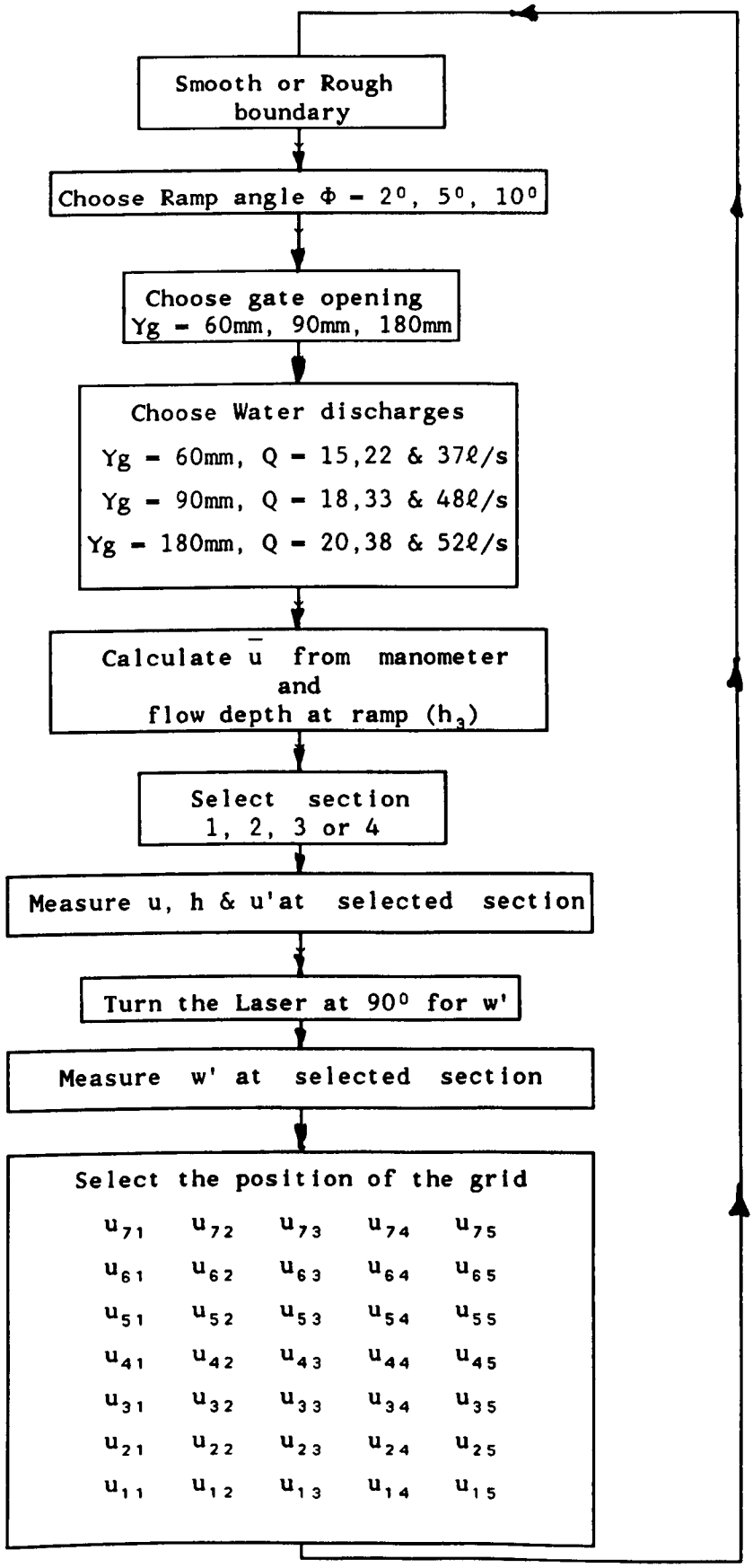

(vii) Having established the turbulence characteristics for the flume, ramp and jet, the whole procedure was repeated, this time with measurements of air flow rate Q_a, aerator jet underpressure Δp, jet length L and ramp flow depth h_3. This procedure is shown below.

(viii) The main choise for each test run is the under–pressure Δp or (Δh). For the first test run, Δp is made zero by blowing air into the cavity as described in section 3.4.6. The air flow rate Q_a, and L and h_3 are measured.

(ix) For the same water discharge, the air supply is turned off, and the maximum under pressure Δh_{max} is measured for zero air flow. The next test run is then carried out at pressure approximately $\Delta h_{max}/2$. again Q_{air}, L and h_3 are measured.

(x) A third under pressure is know chosen somewhere in the range $\Delta h_{max}/4$ to $3\Delta h_{max}/4$ and again Q_a, L and h_3 are measured.

This means that every single test run involves three different underpressure values Δh, and hence 3 different air flow rates, jet lengths and flow depth h. A sketch of this procedure is given below.

(xi) All measurements were carried out over an 18 month period in 1989 and 1990, with a considerable volume of data accumulated which will be presented and discussed in Chapter 4, Chapter 5 and in Chapter 6.

FLOW CHART FOR AIR FLOW MEASUREMENTS

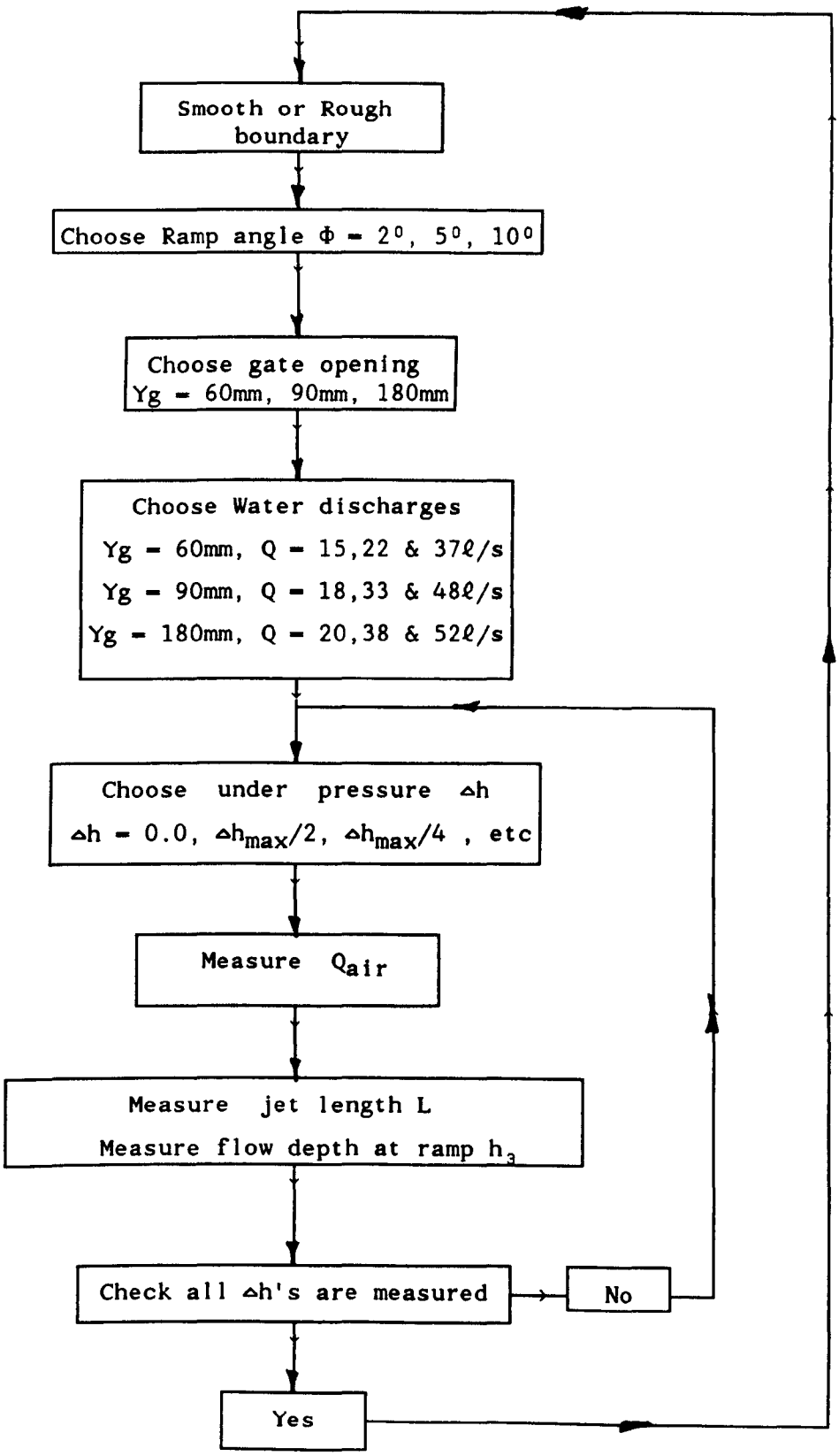

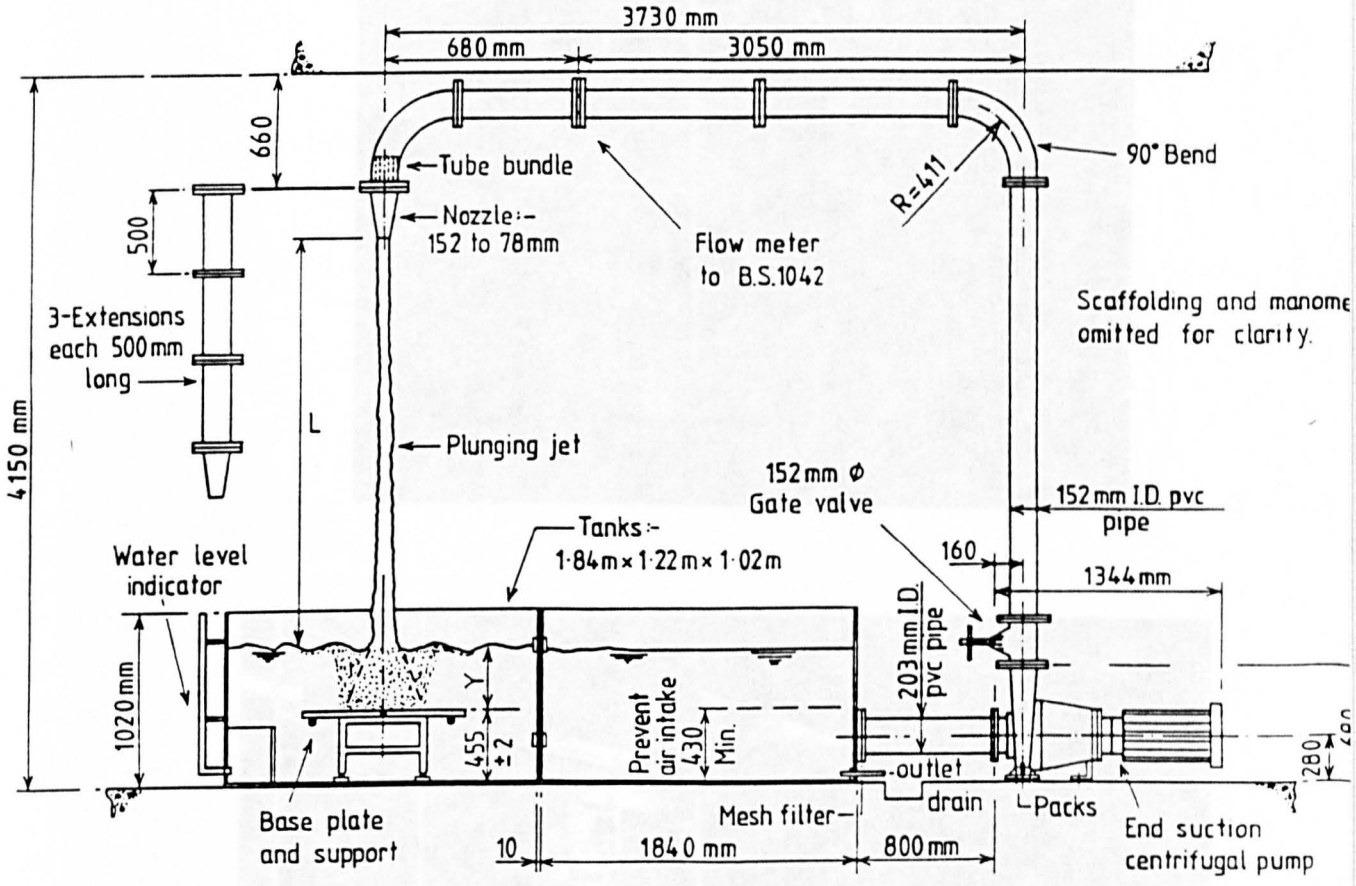

Fig 3.1 Existing research apparatus

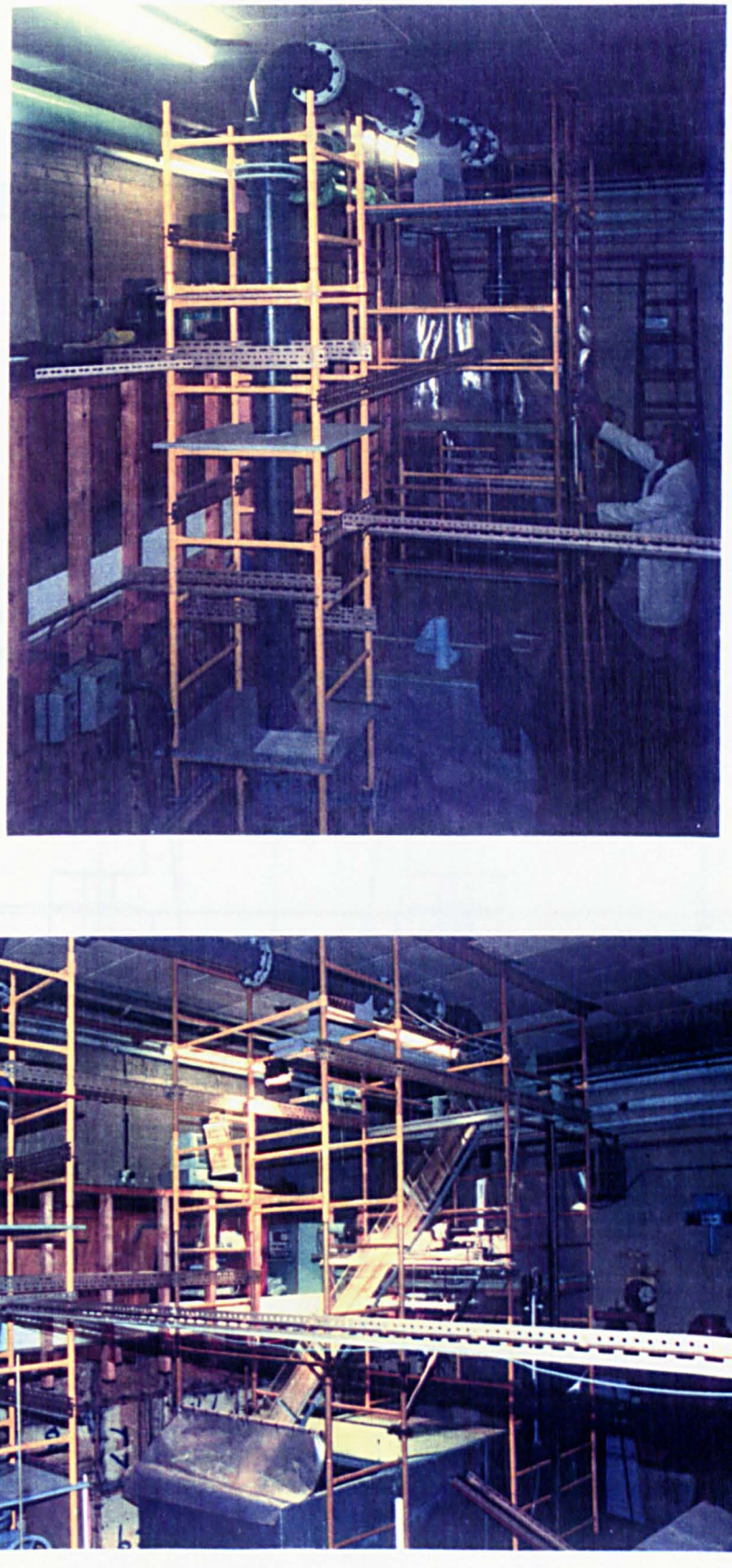

Fig 3.2 Scafolding frame work

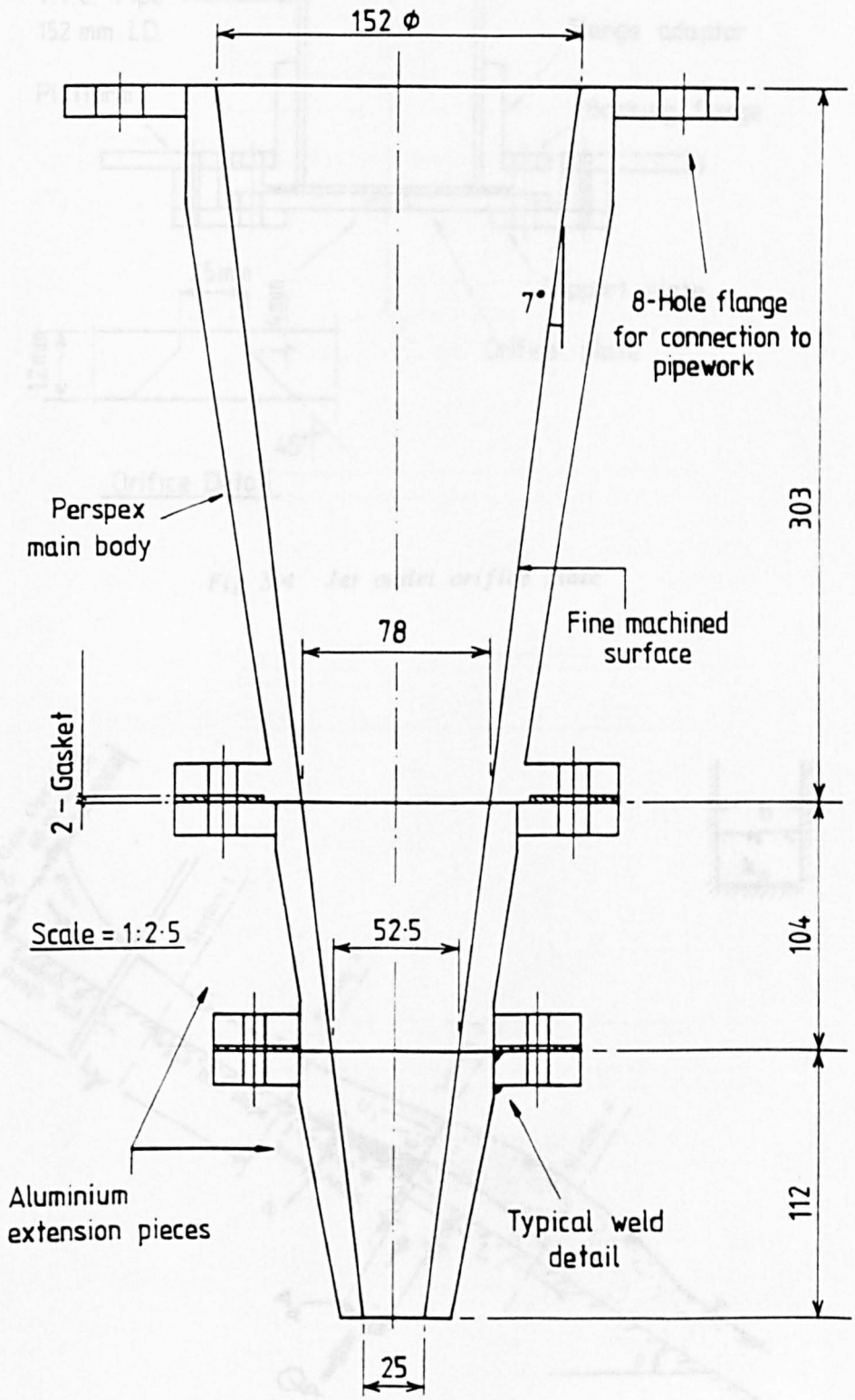

Fig 3.3 Final outlet nozzle arrangement

(All dimensions in mm)

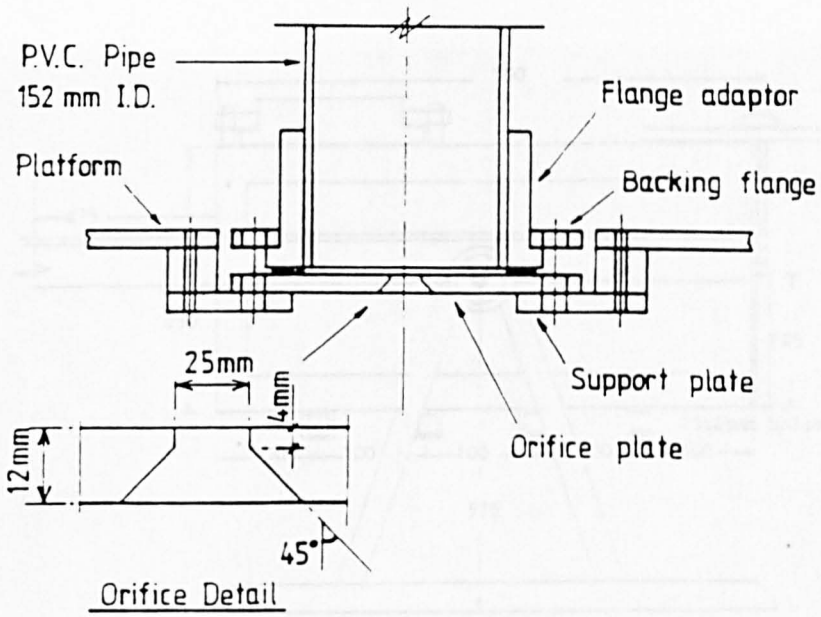

Fig 3.4 Jet outlet orifice plate

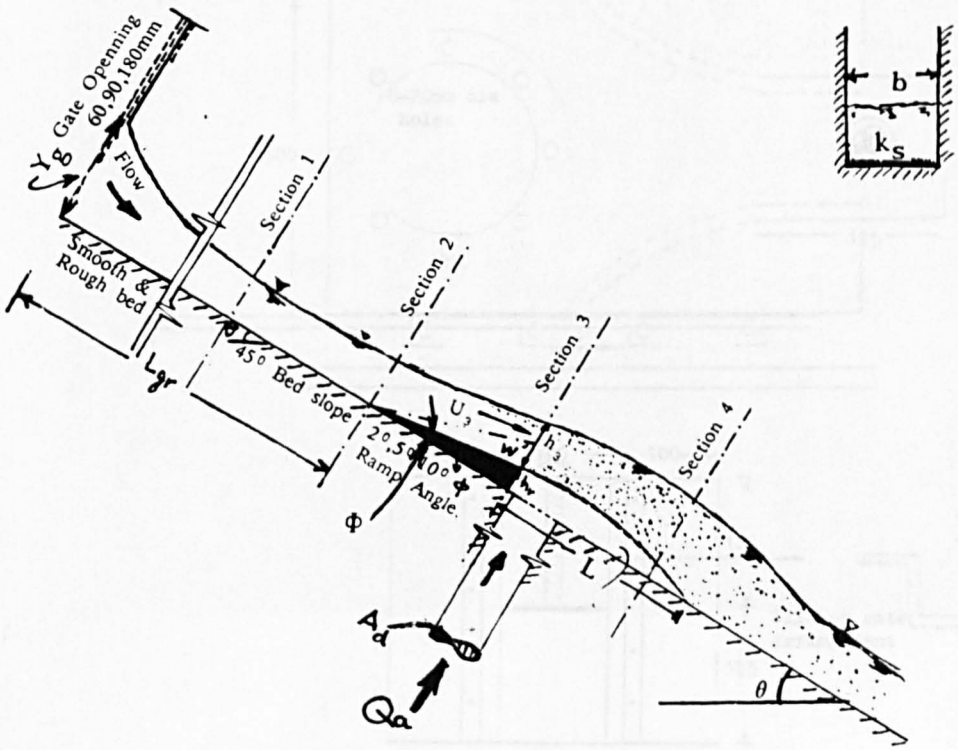

Fig 3.5 Details of parameters involved in dimensional analysis

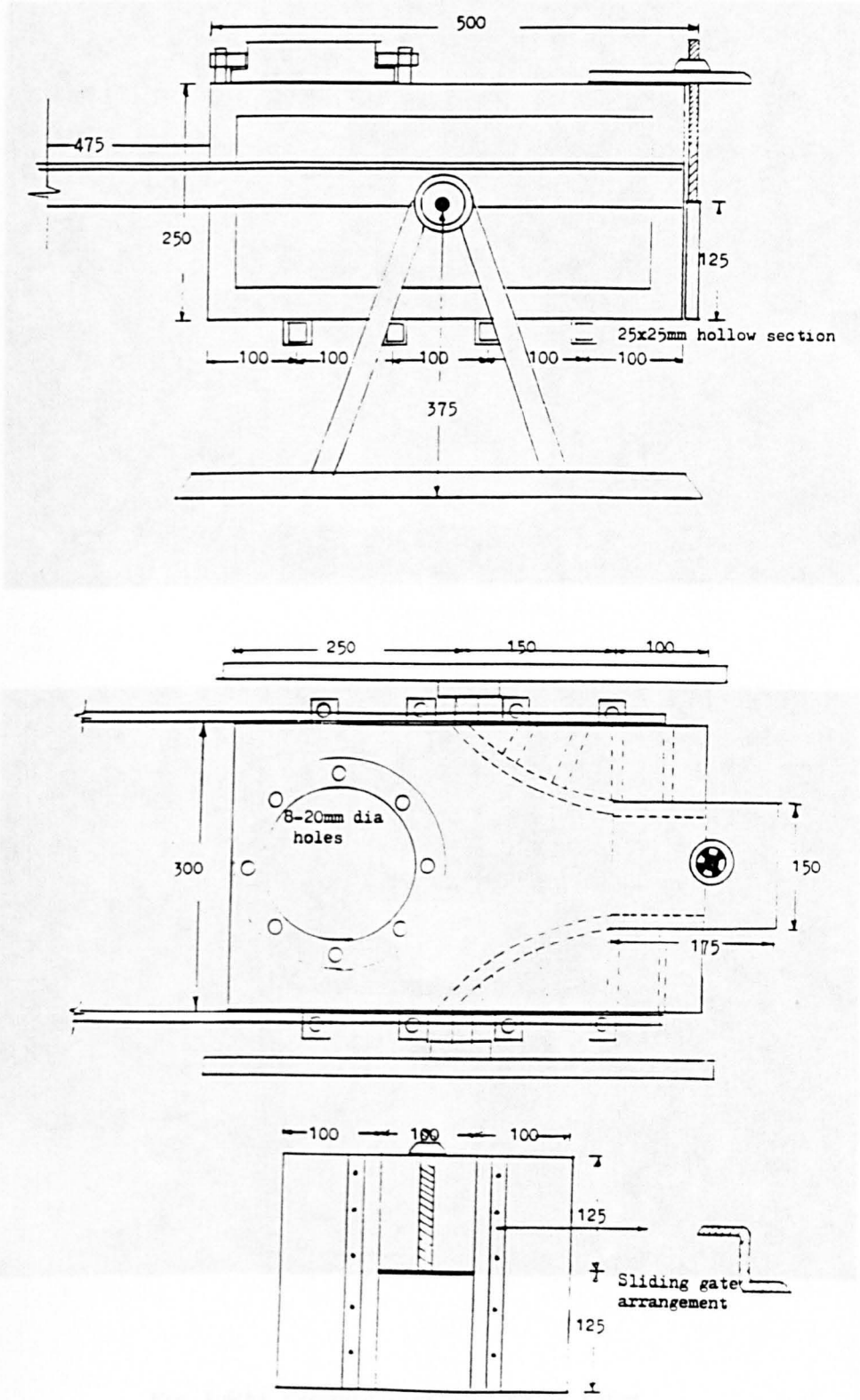

Fig 3.6(a) Design of pressure box

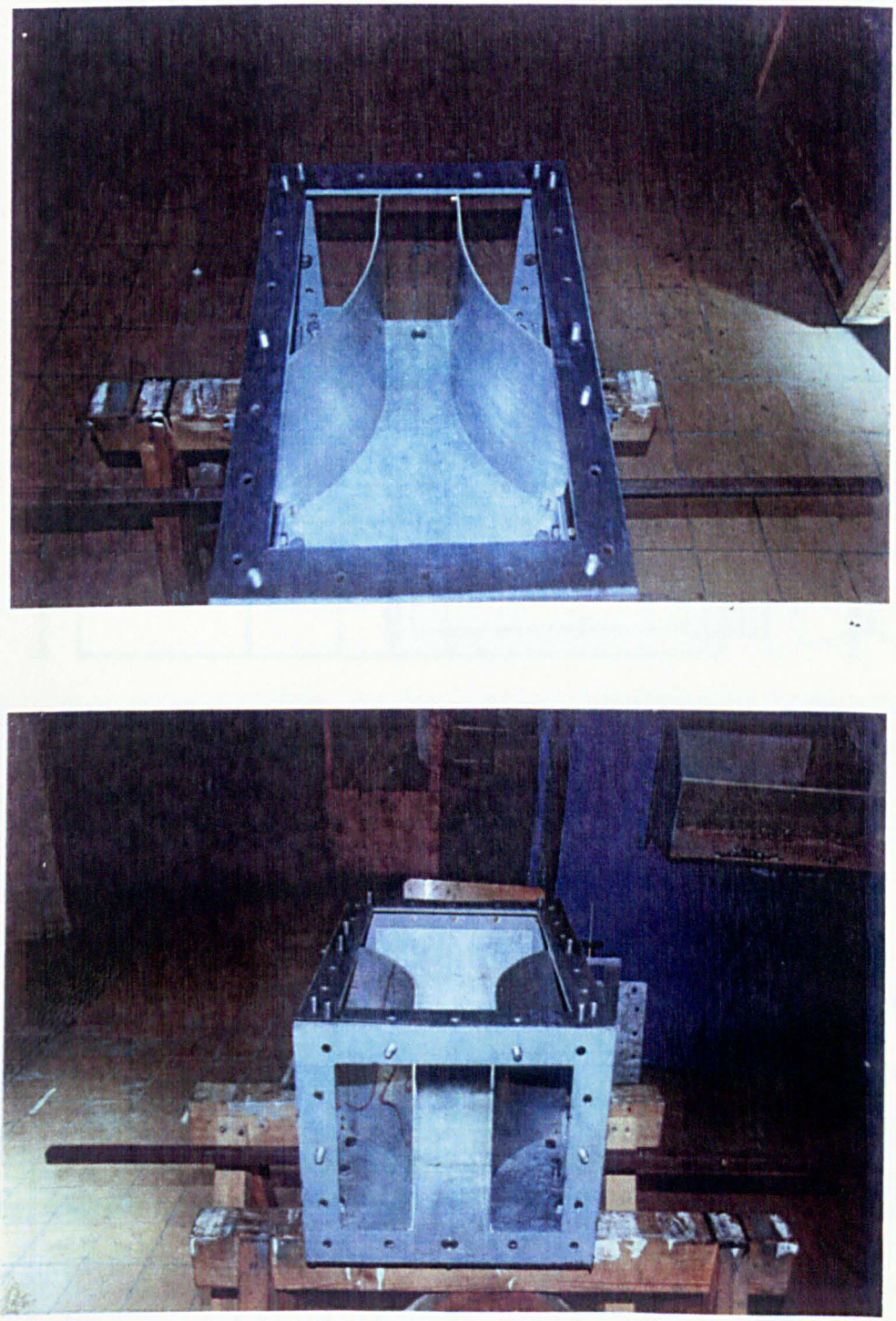

Fig 3.6(b) Pressure tank and guide vanes

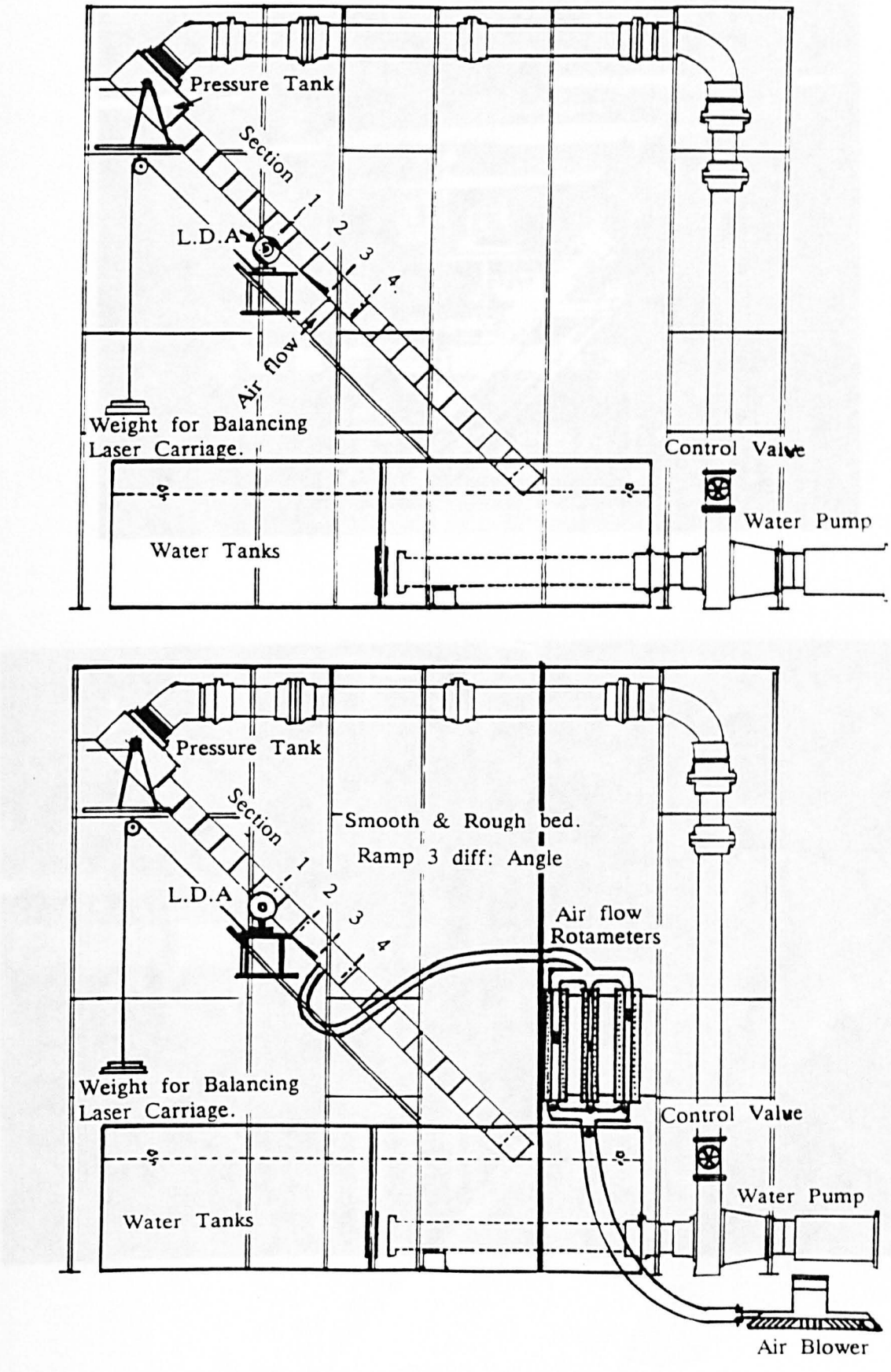

Fig 3.7(a) Turbulence and Airflow measurement Rig

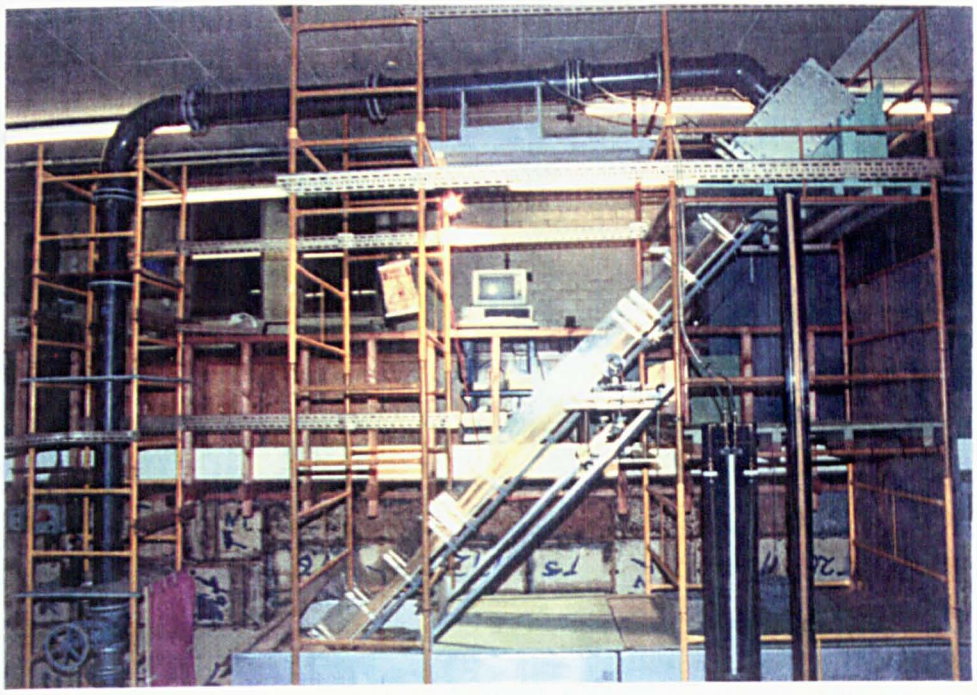

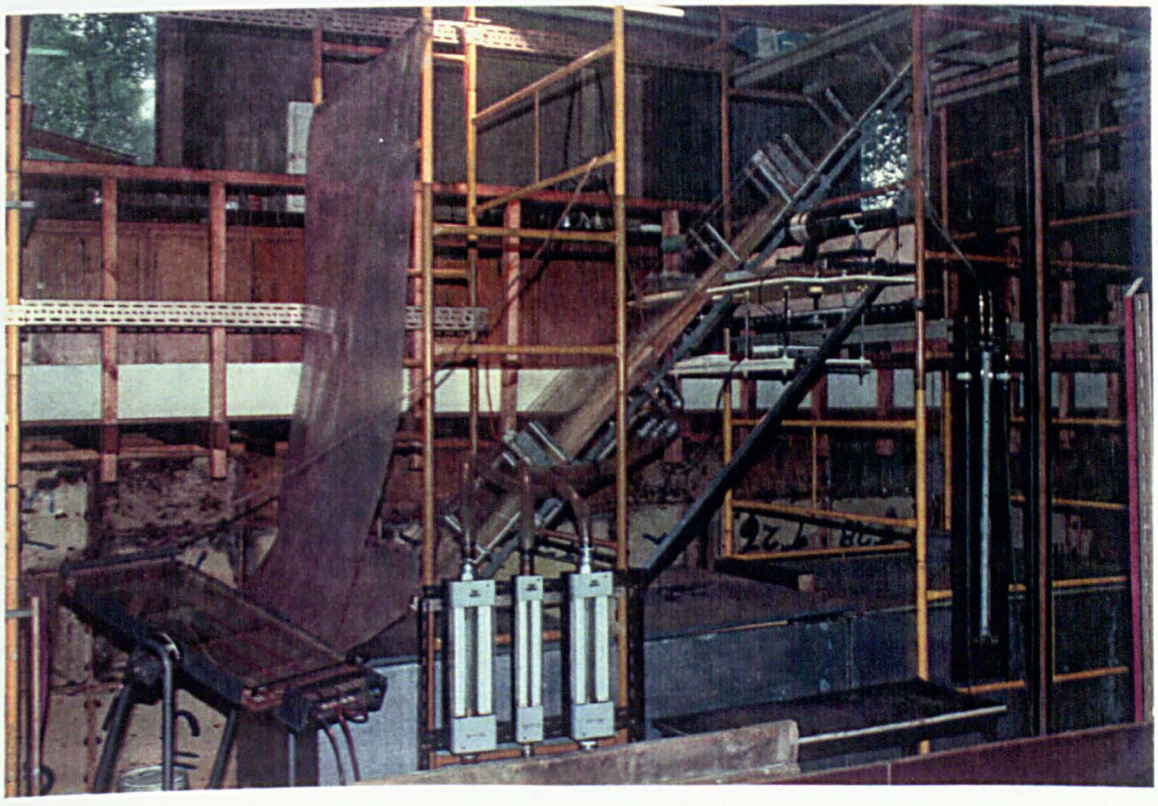

Fig 3.7(b) Turbulence and Airflow measurement Rig

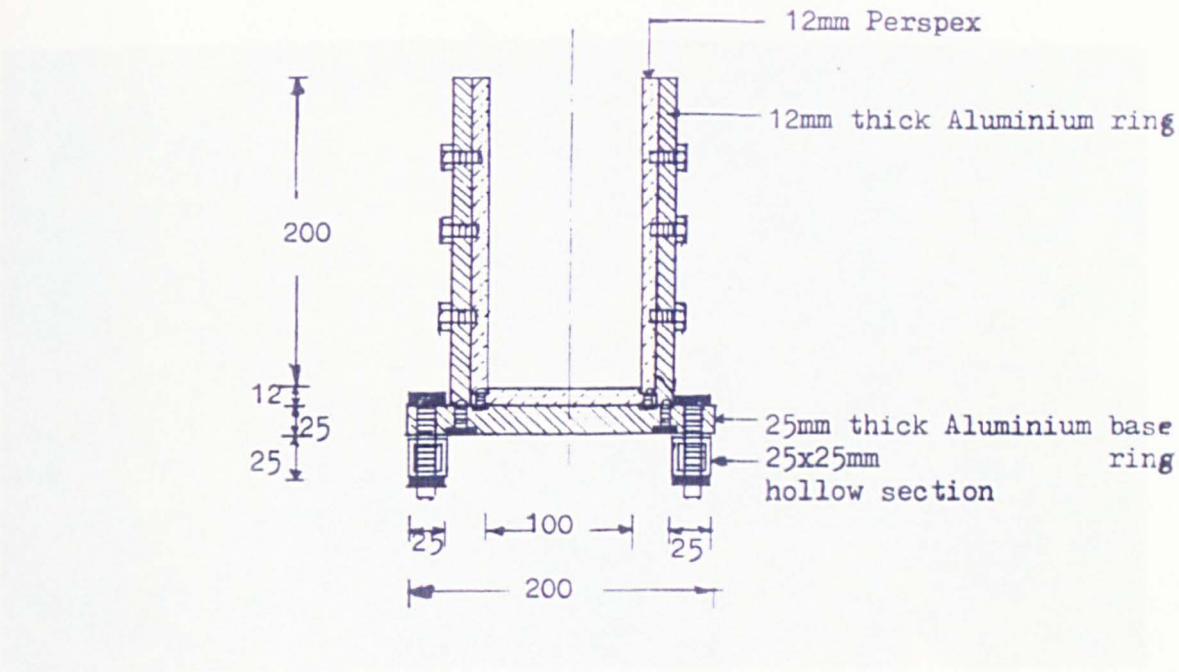

Fig 3.8 Cross-sectional view of spillway channel

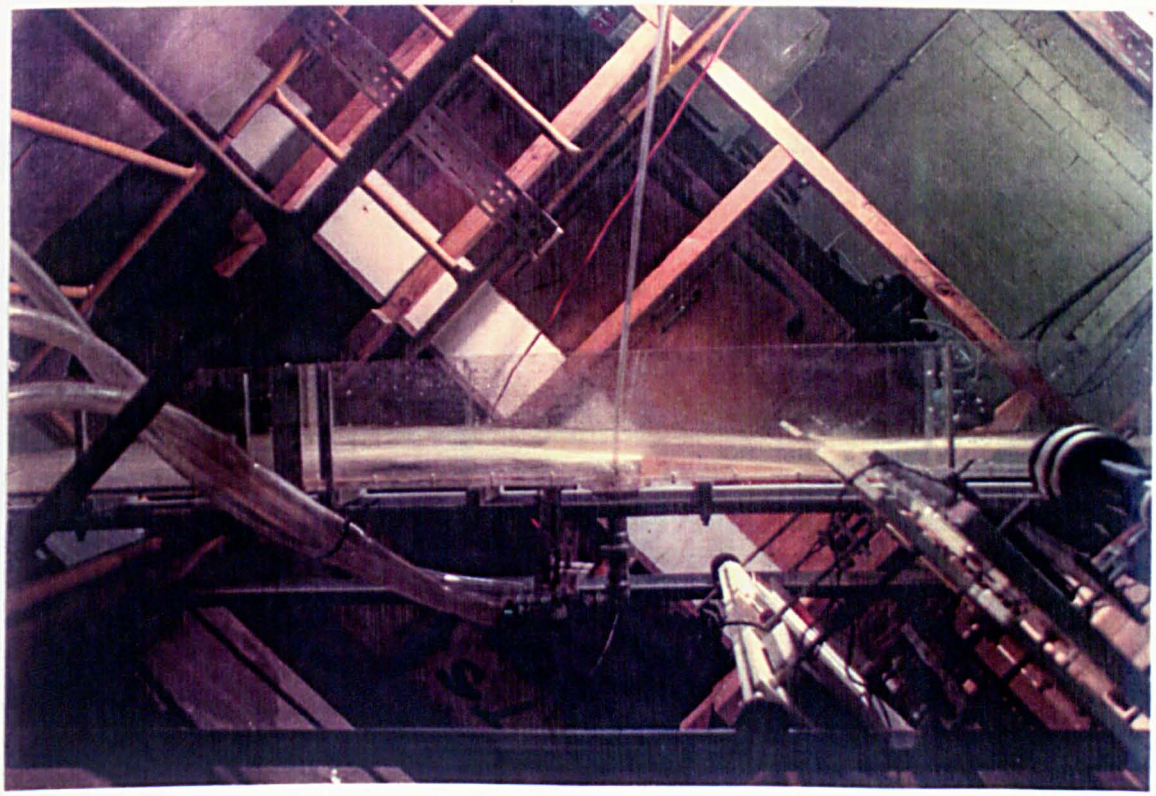

Fig 3.9(a) 2° ramp angle (perspex)

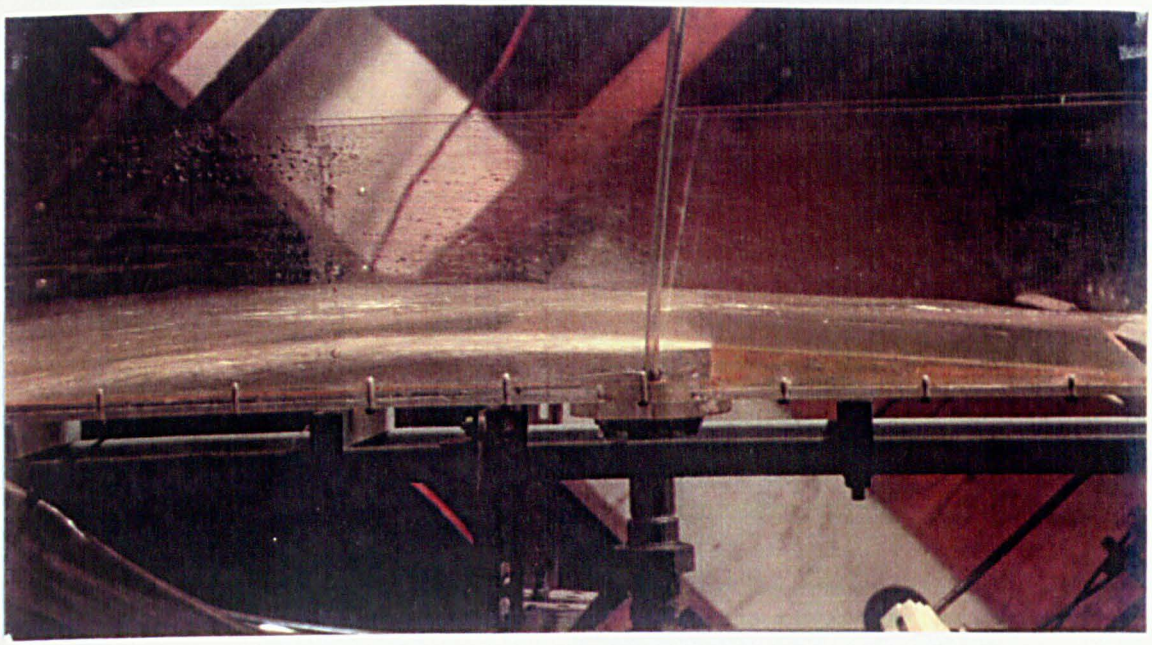

Fig 3.9(b) 5° ramp angle (perspex)

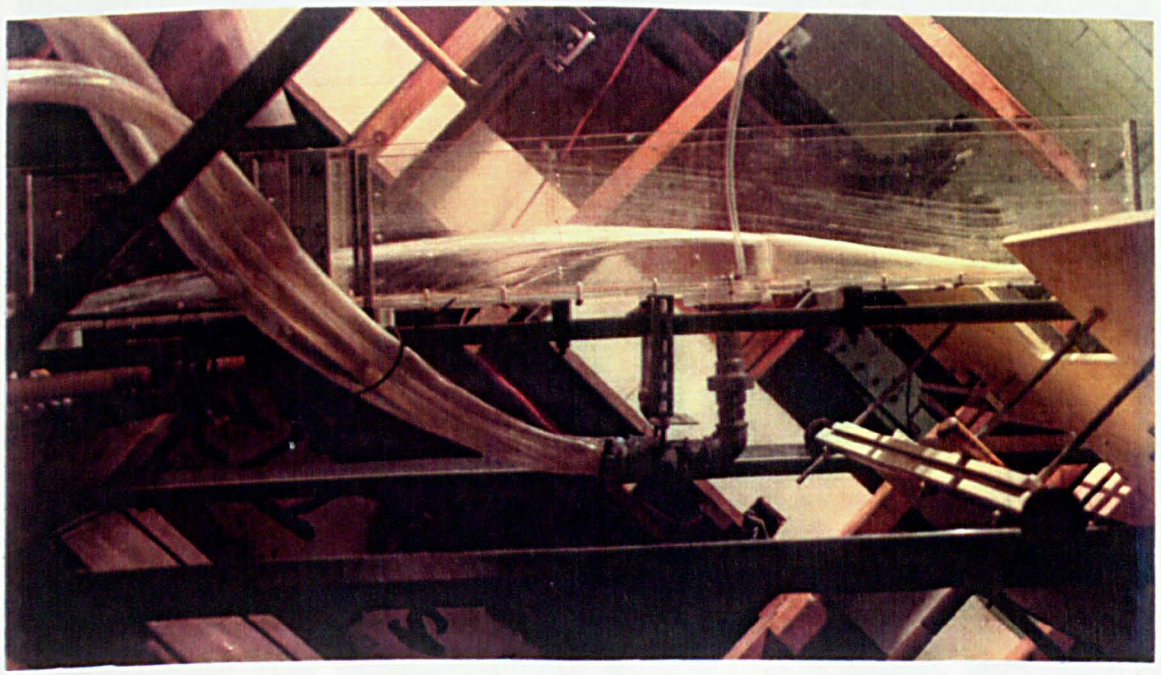

Fig 3.9(c) 10° ramp angle (perspex)

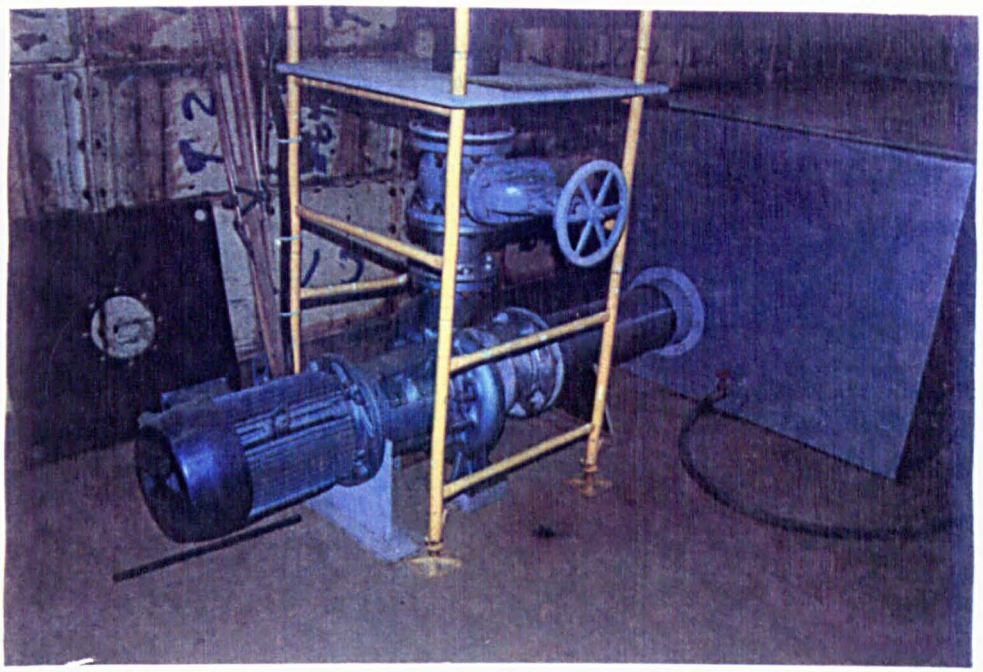

Fig 3.10 Water supply pump & sump tanks

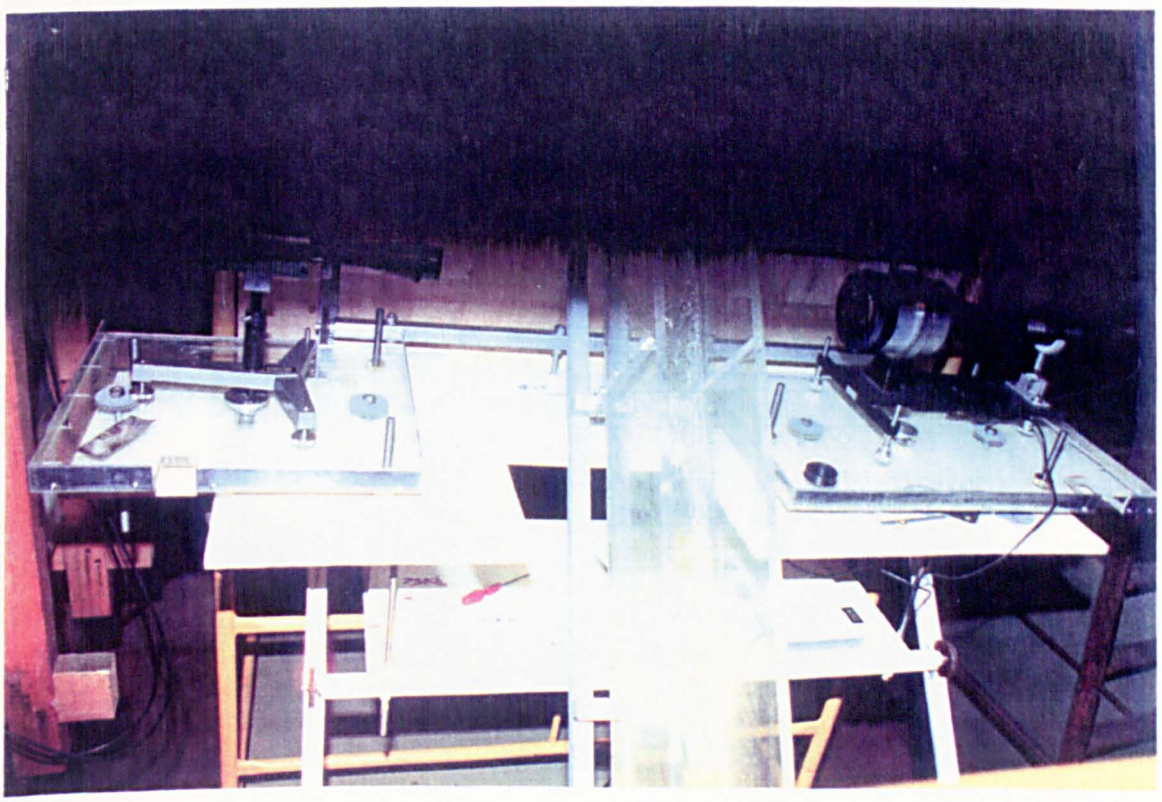

Fig 3.11 Laser carriage

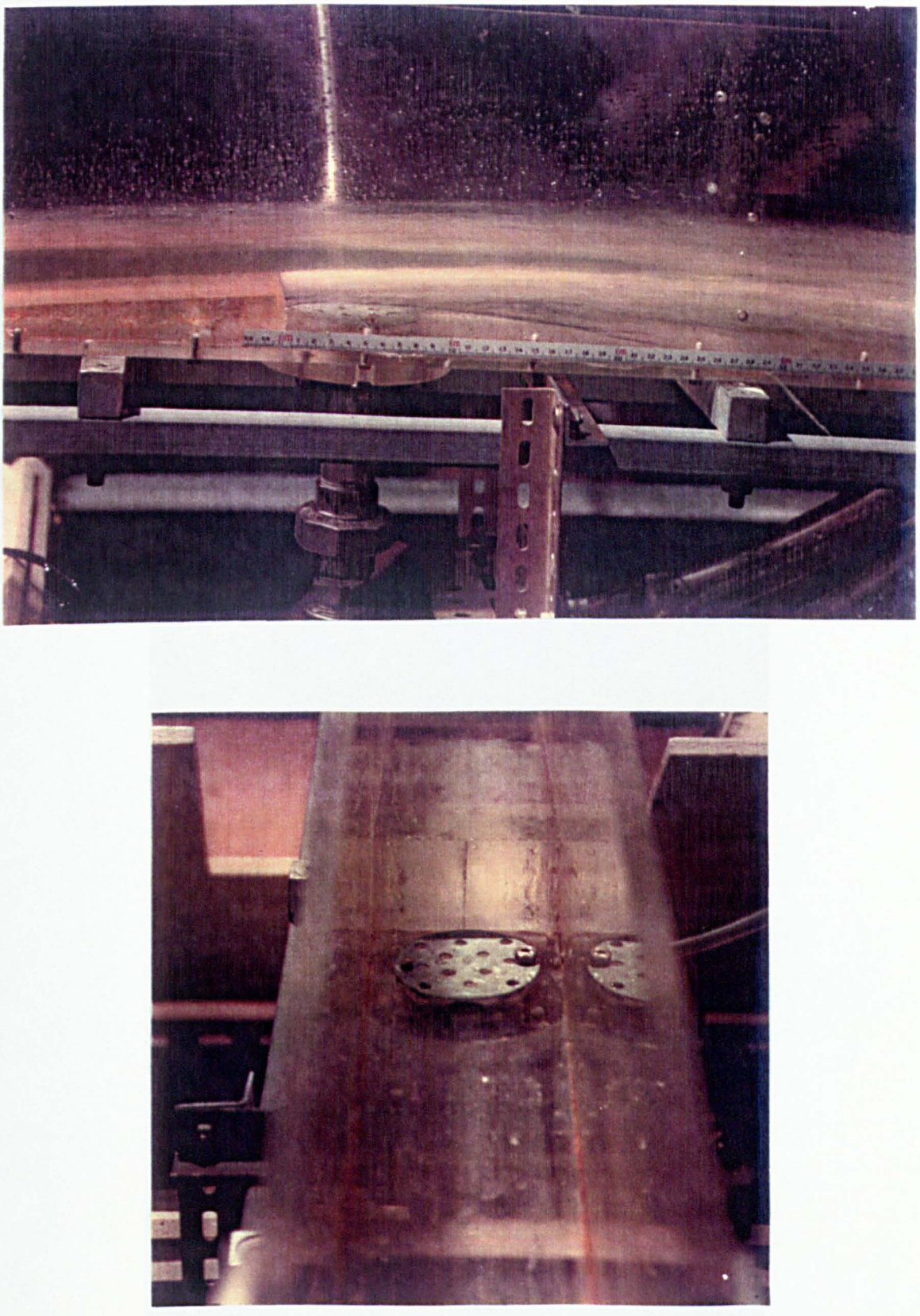

Fig 3.12 Air flow duct and covering plate

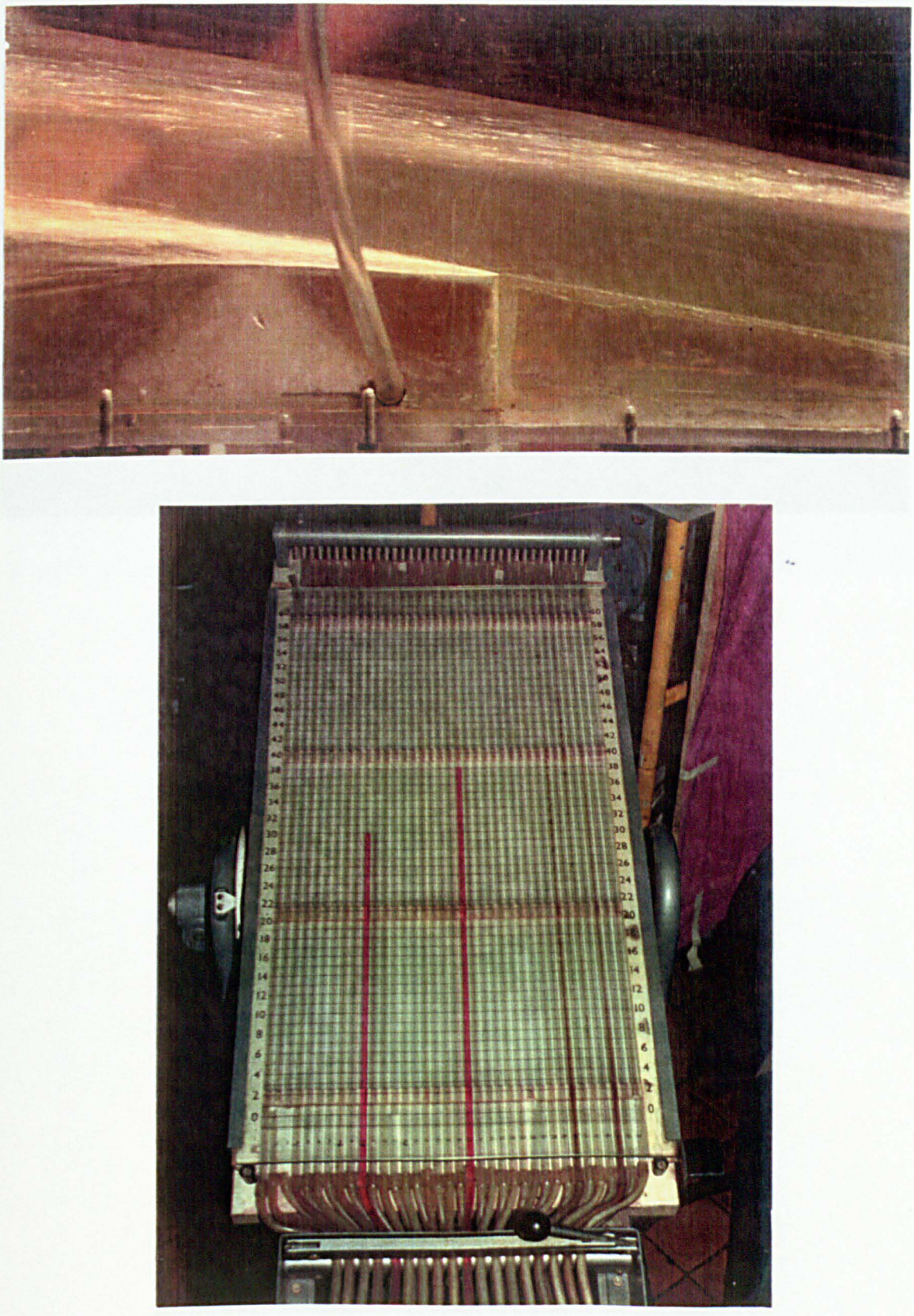

Fig 3.13 Inclined manometer and pressure tapping

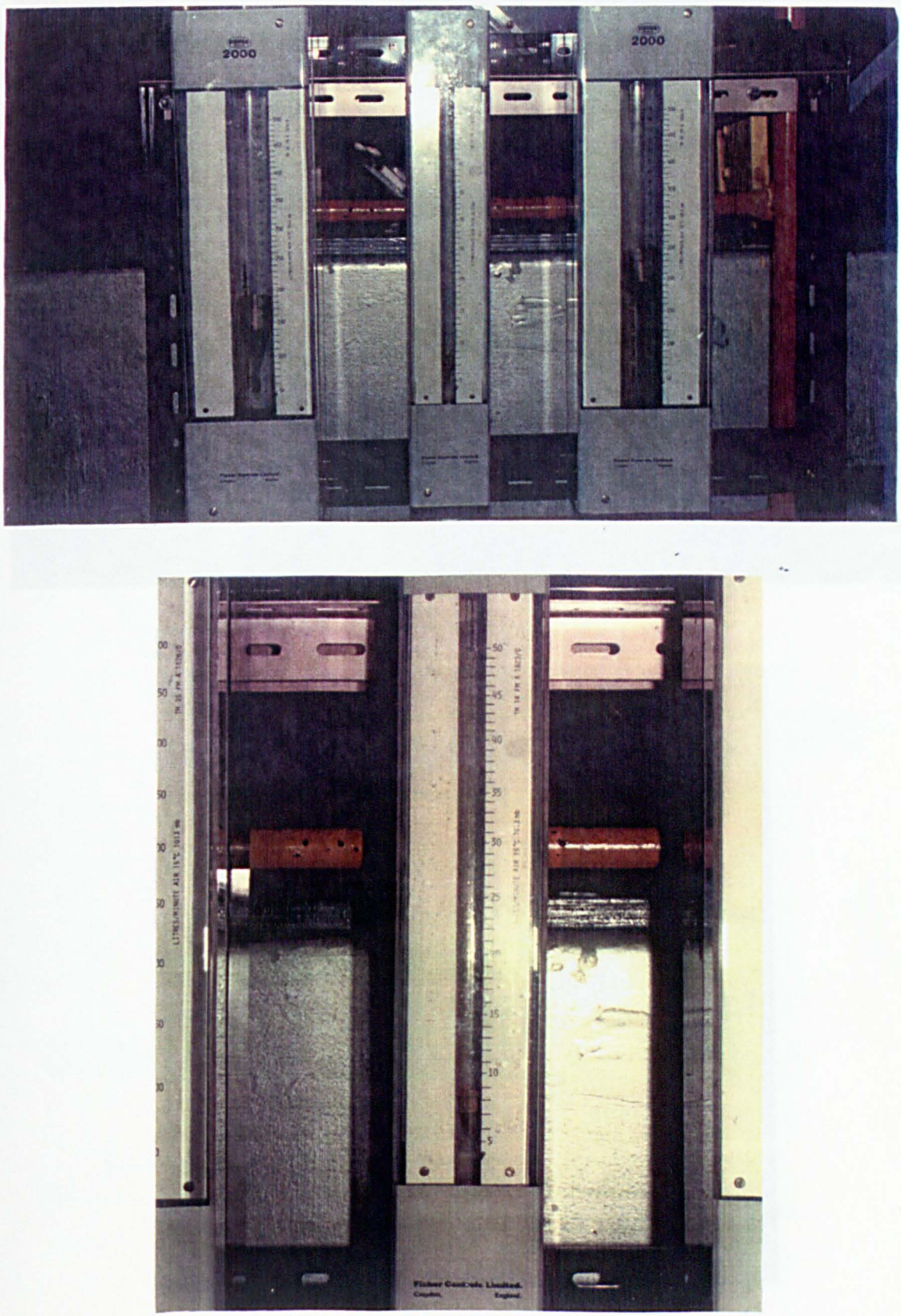

Fig 3.14 Air flow measuring Rotameters

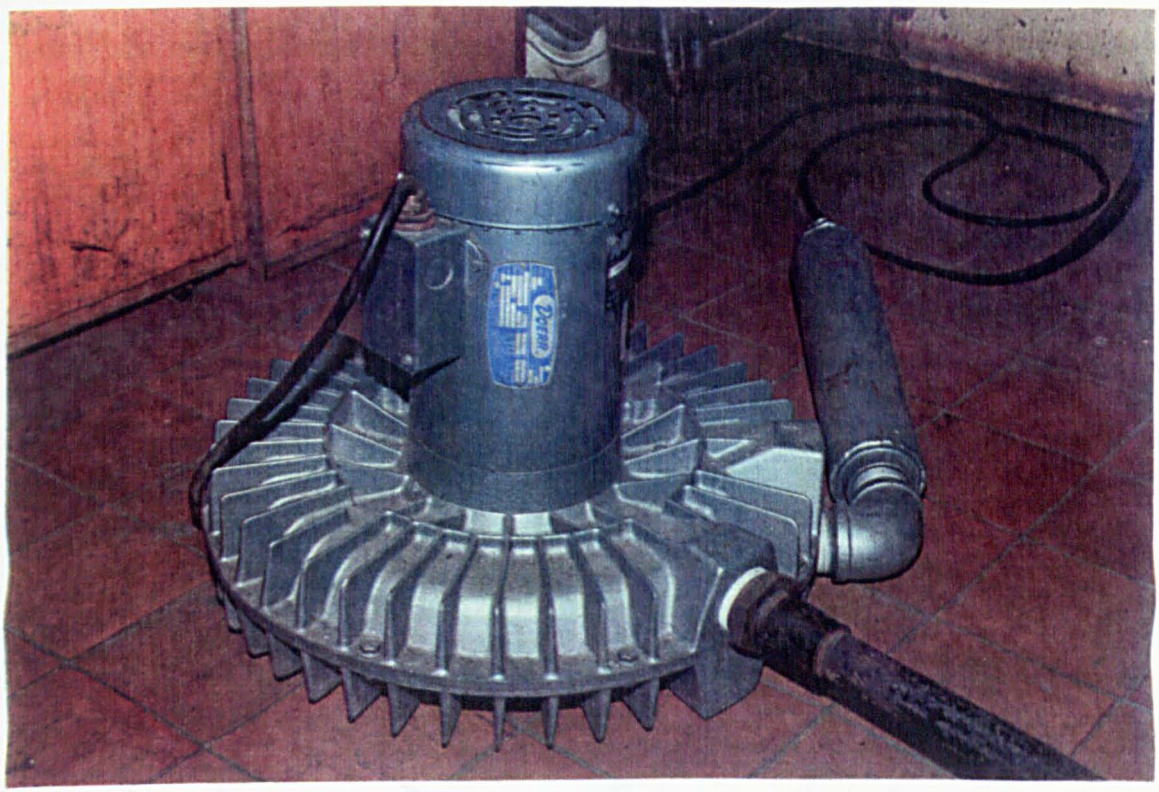

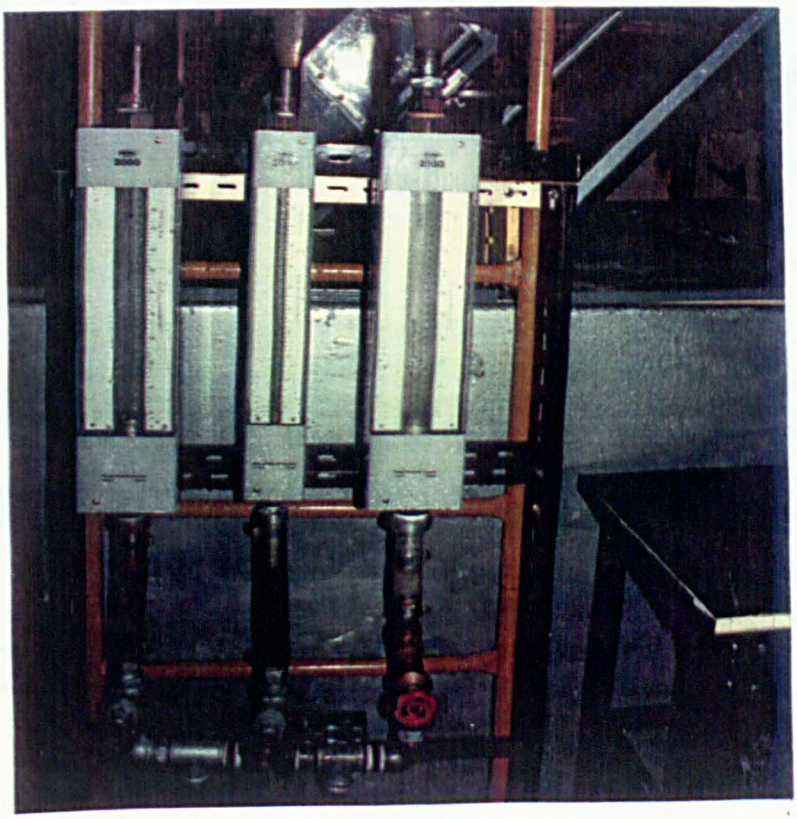

Fig 3.15 Air blower and its connection to Rotameters

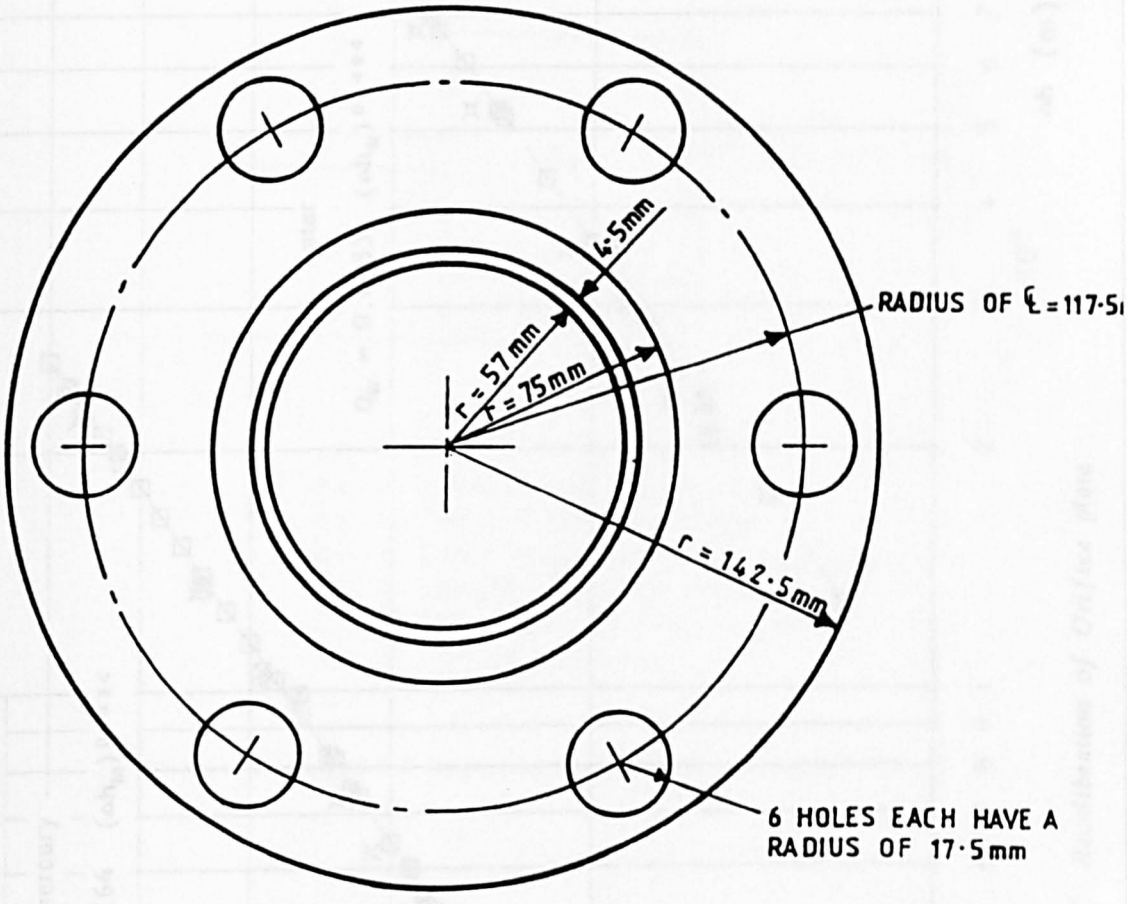

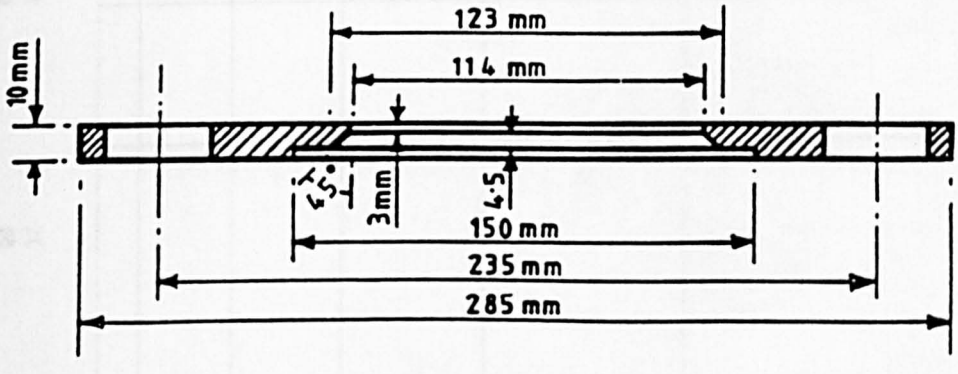

Fig 3.16 Details of Orifice plate (Designed by Withers)

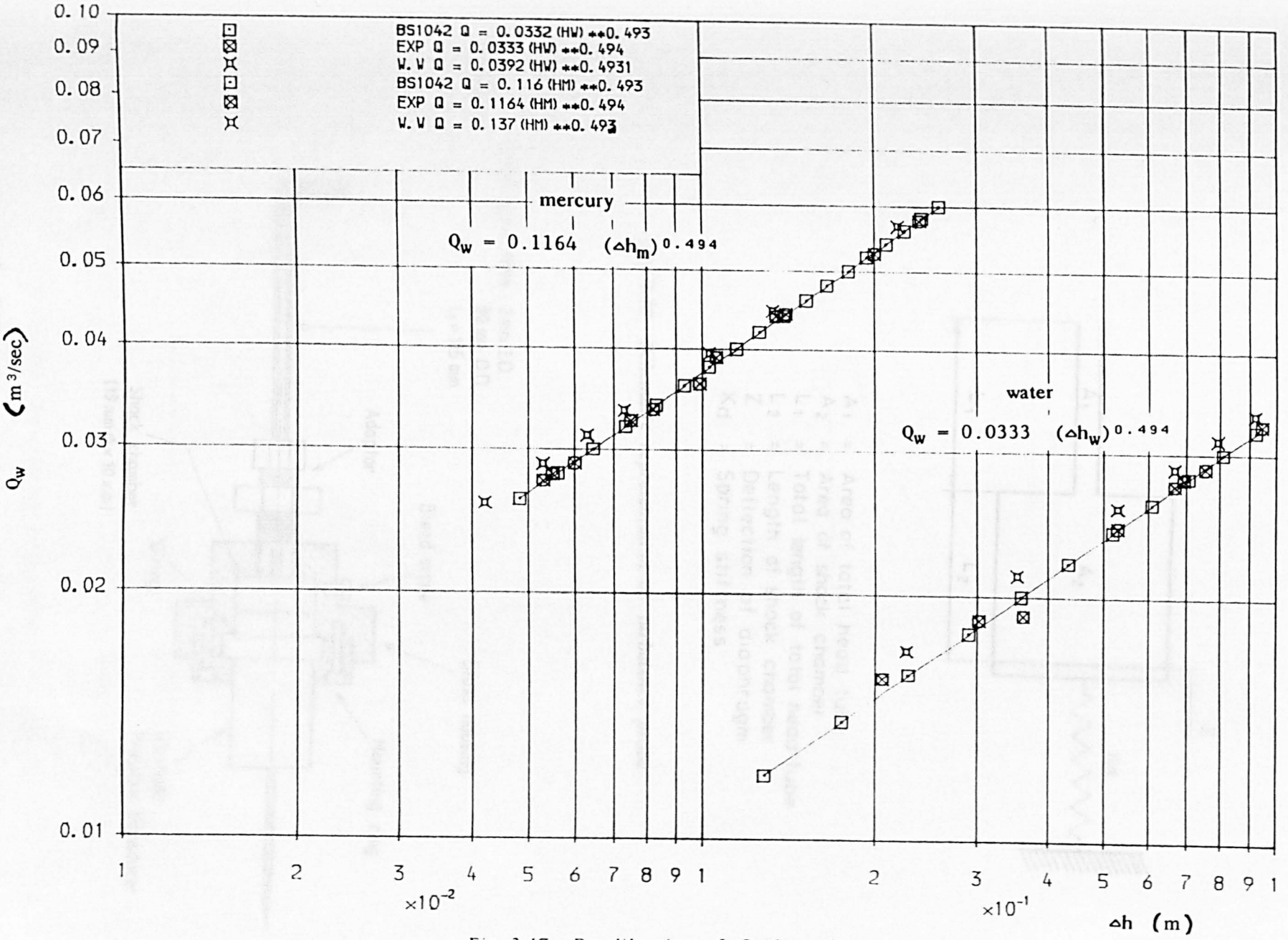

Fig 3.17 Recalibration of Orifice plate

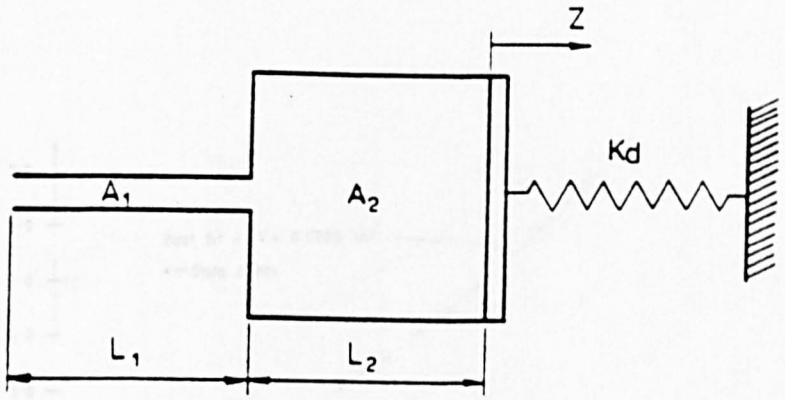

A_1 = Area of total head tube
A_2 = Area of shock chamber
L_1 = Total length of total head tube
L_2 = Length of shock chamber
Z = Deflection of diaphragm
K_d = Spring stiffness

Fig 3.18 Schematic representation of turbulence probe

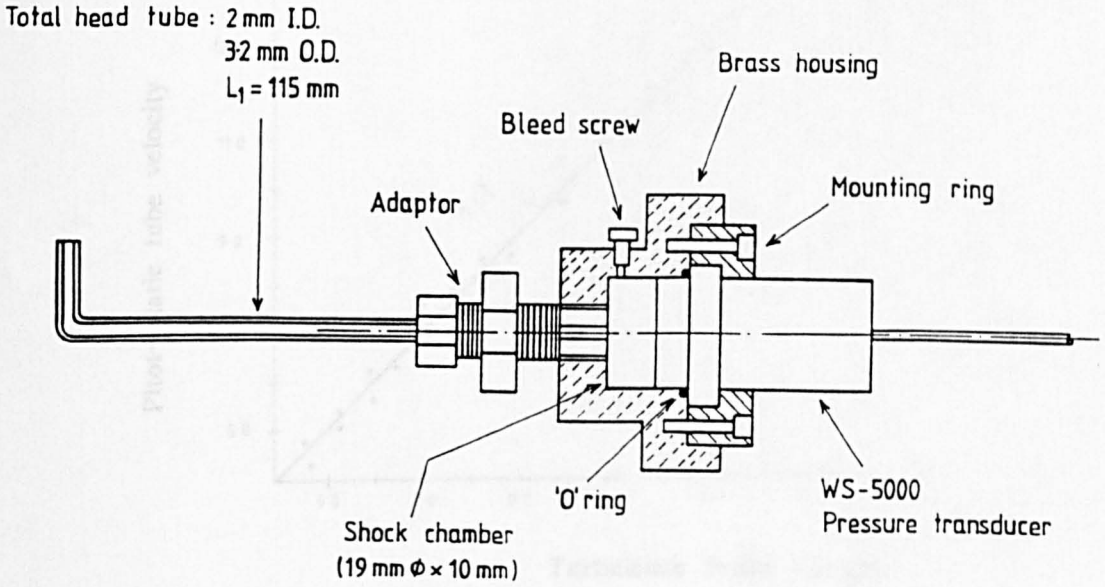

Fig 3.19 Turbulence transducer probe (designed by Withers (1987))

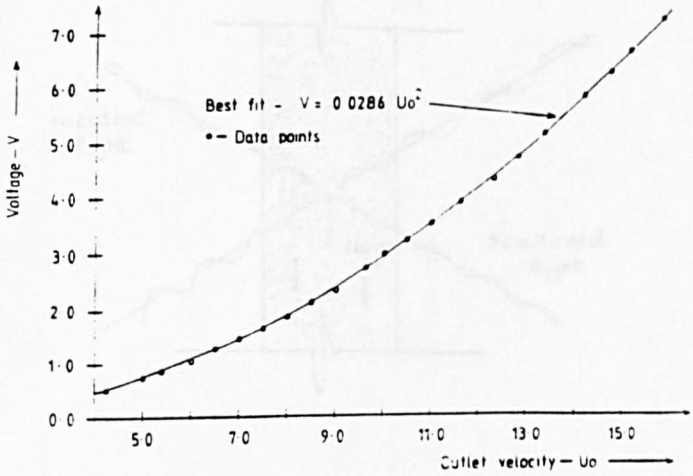

Fig 3.20(a) Dynamic calibration of turbulence probe

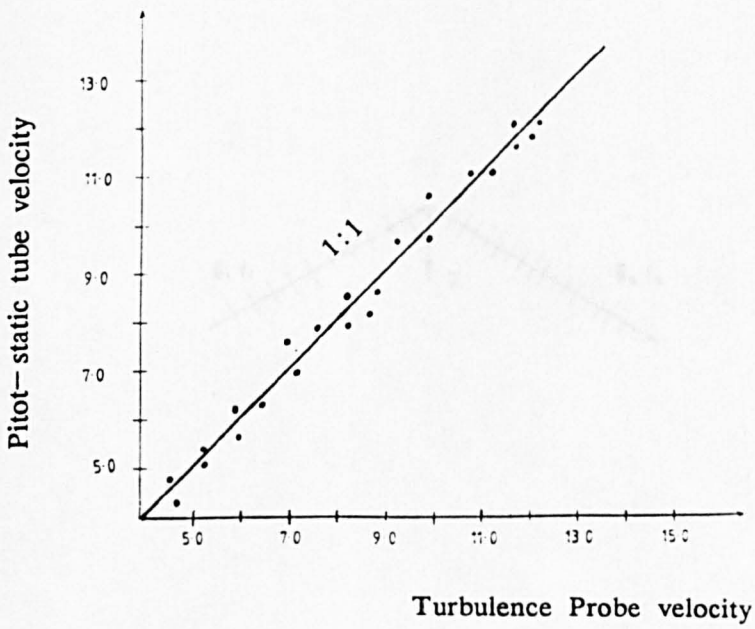

Fig 3.20(b) Relationship between Probe Velocity and Pitot—static tube Velocity.

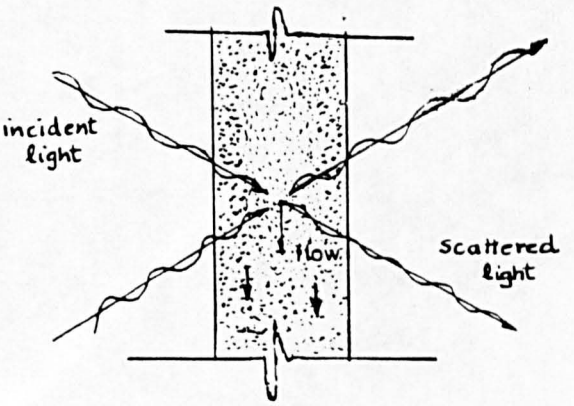

Fig 3.21(a) Scatter of Laser light

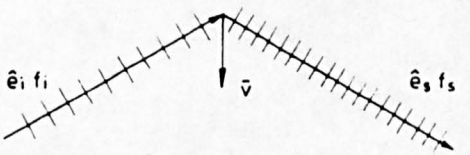

Fig 3.21(b) Vector diagram of Laser frequency shift

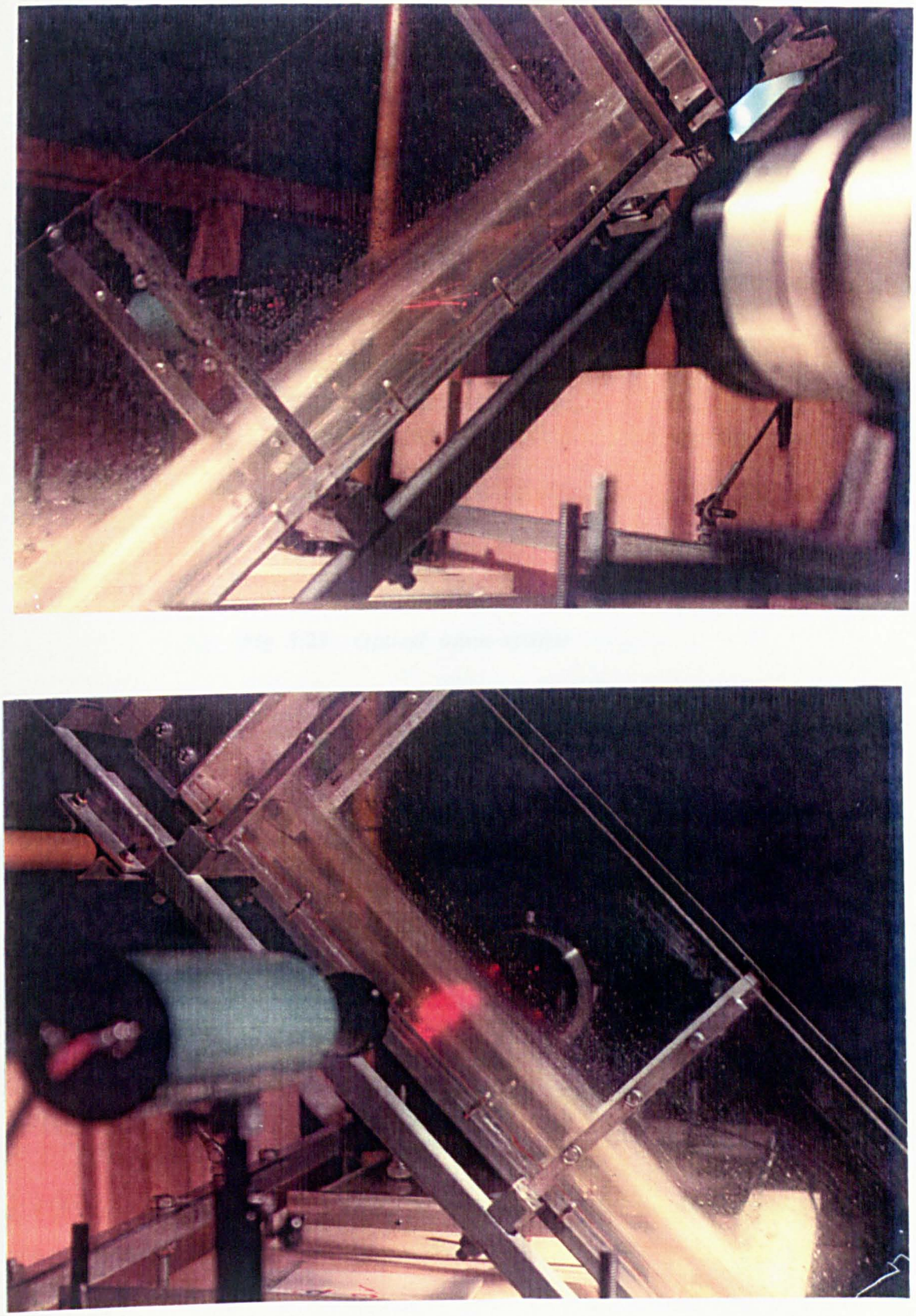

Fig 3.22 Optics receiving Laser beams

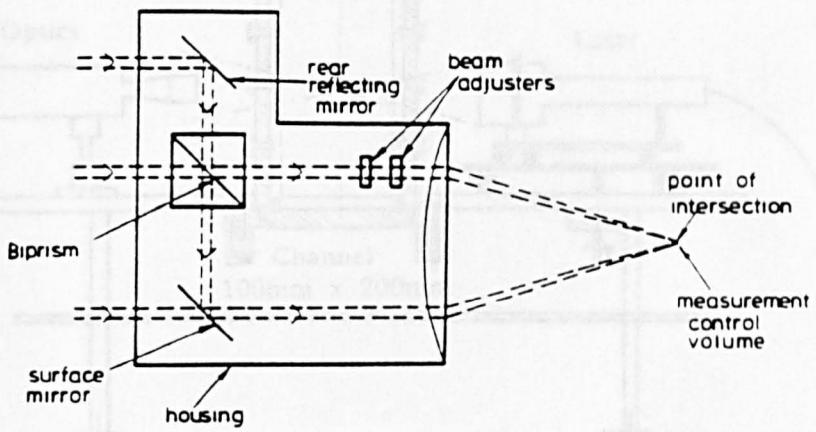

Fig 3.23 Optical beam splitter

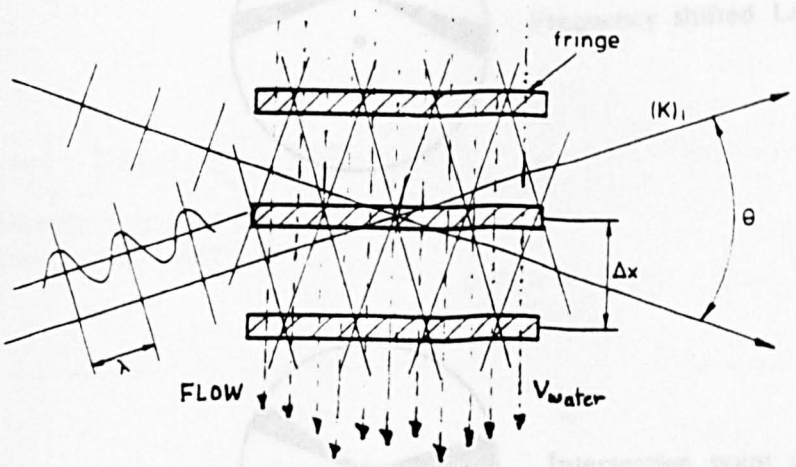

Fig 3.24 Fringe pattern formed at intersection of Laser beams

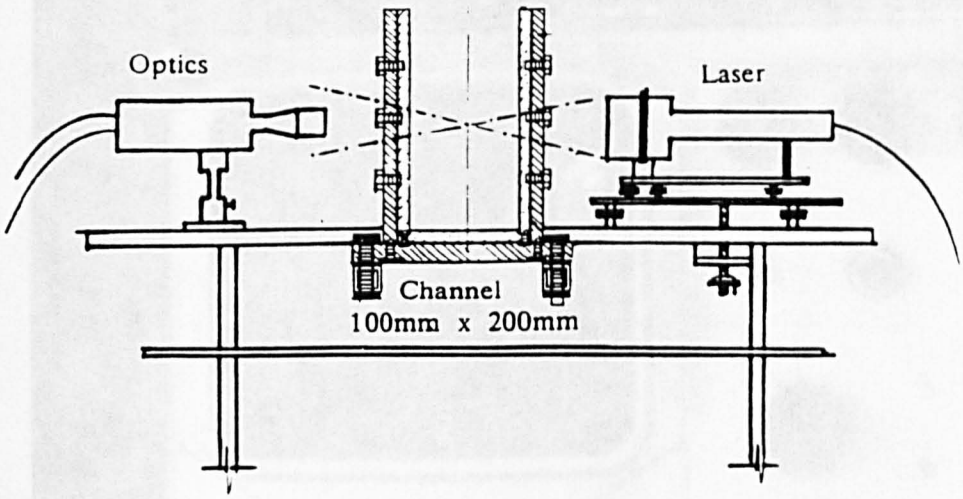

Fig 3.25 Relative position of Laser & optics

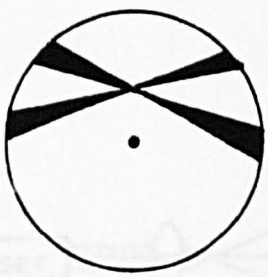

Frequency shifted Laser beam

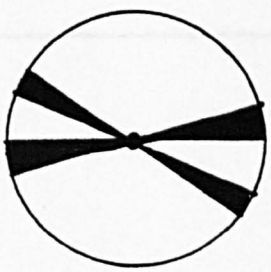

Intersection point of Laser beam

Fig 3.26 View if intersection points of both shifted and unshifted Laser beams

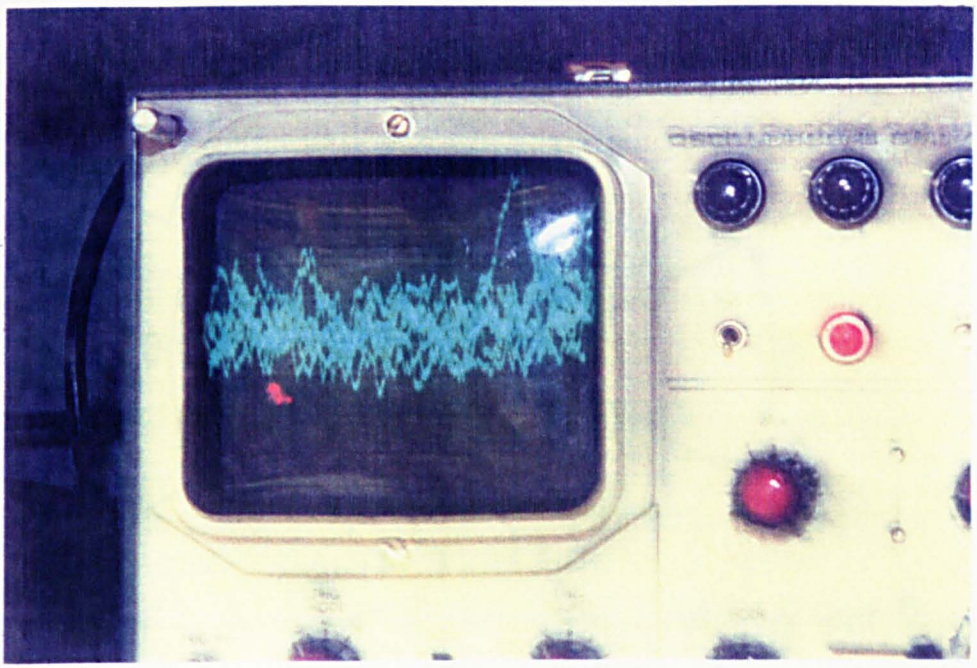

Fig 3.27(a) Doppler Burst on oscilloscope

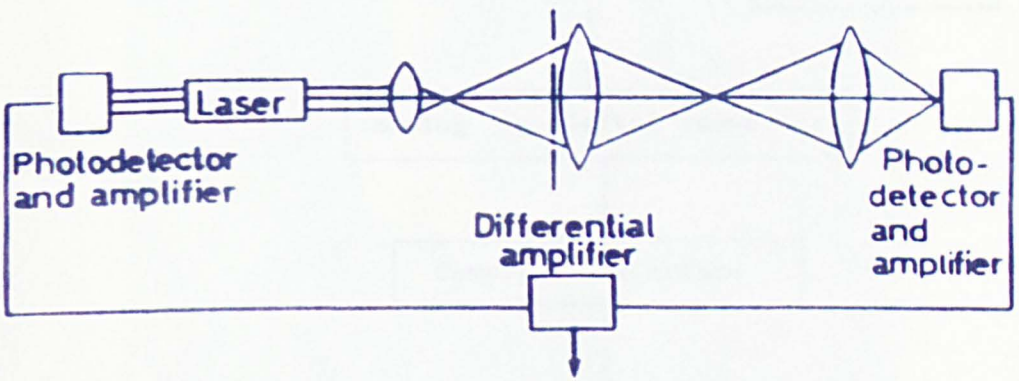

Fig 3.27(b) The optical method for elimination of noise

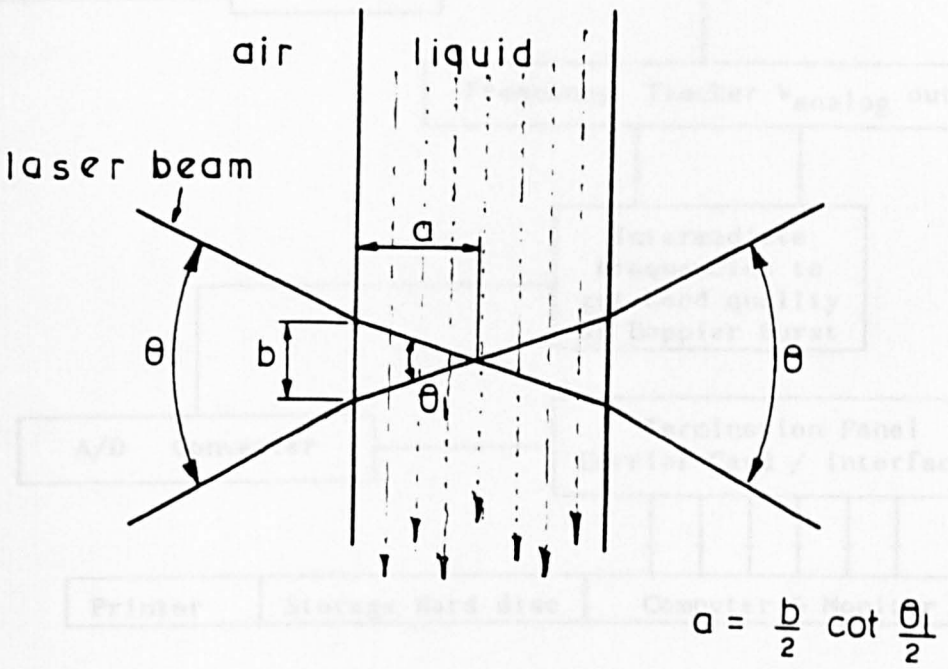

Fig 3.28 Velocity measurements in Water

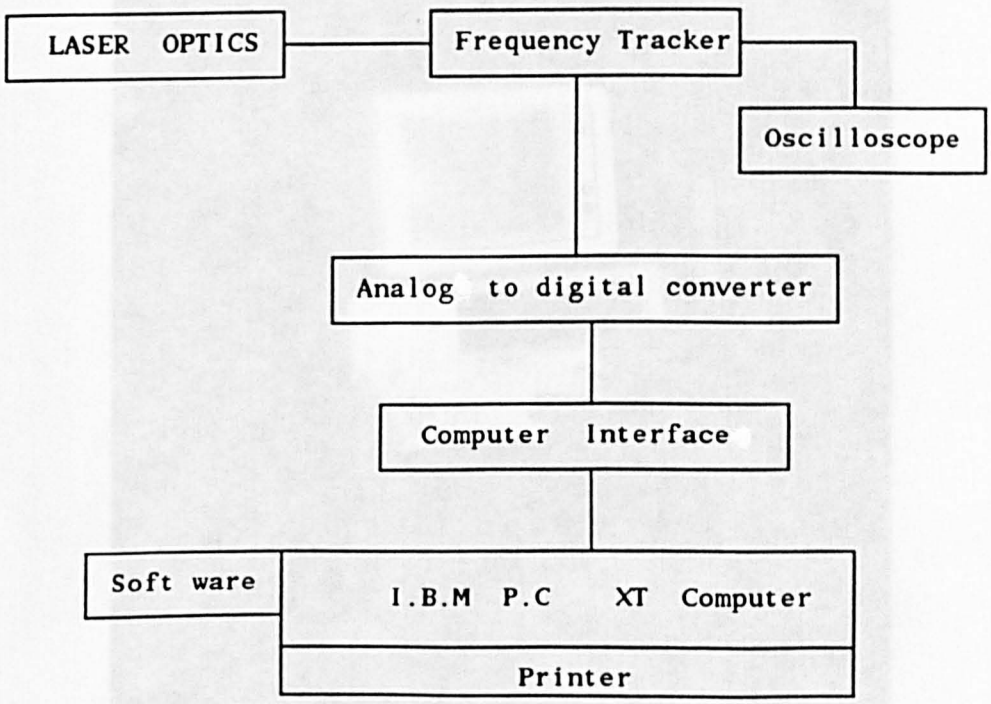

Fig 3.29 Method of data collection

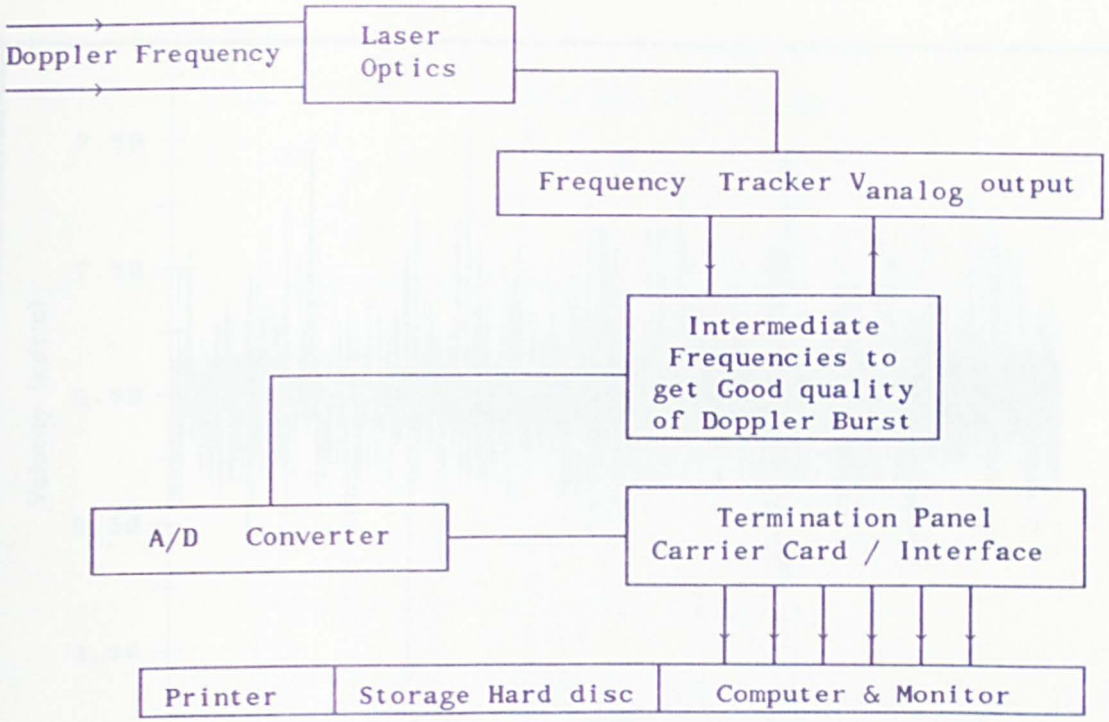

Fig 3.30 Hardware components and computer interface.

Fig 3.31 Photograph of computer

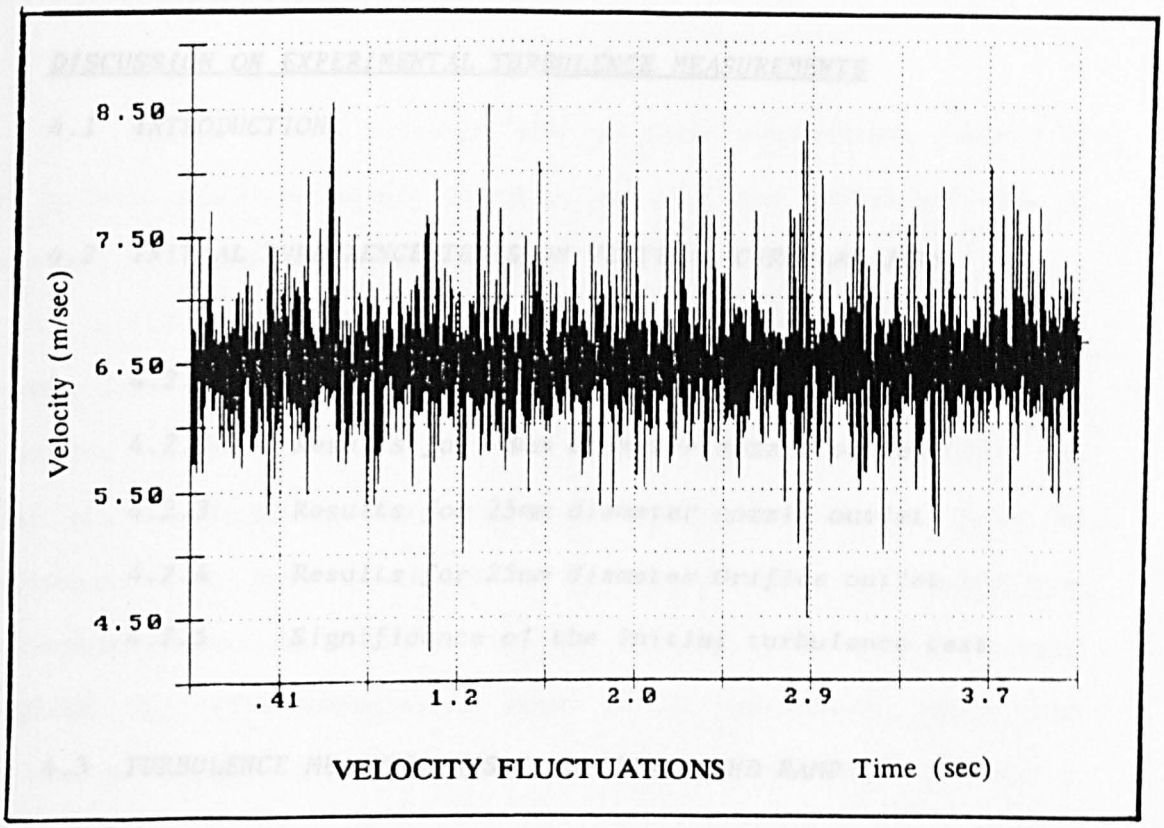

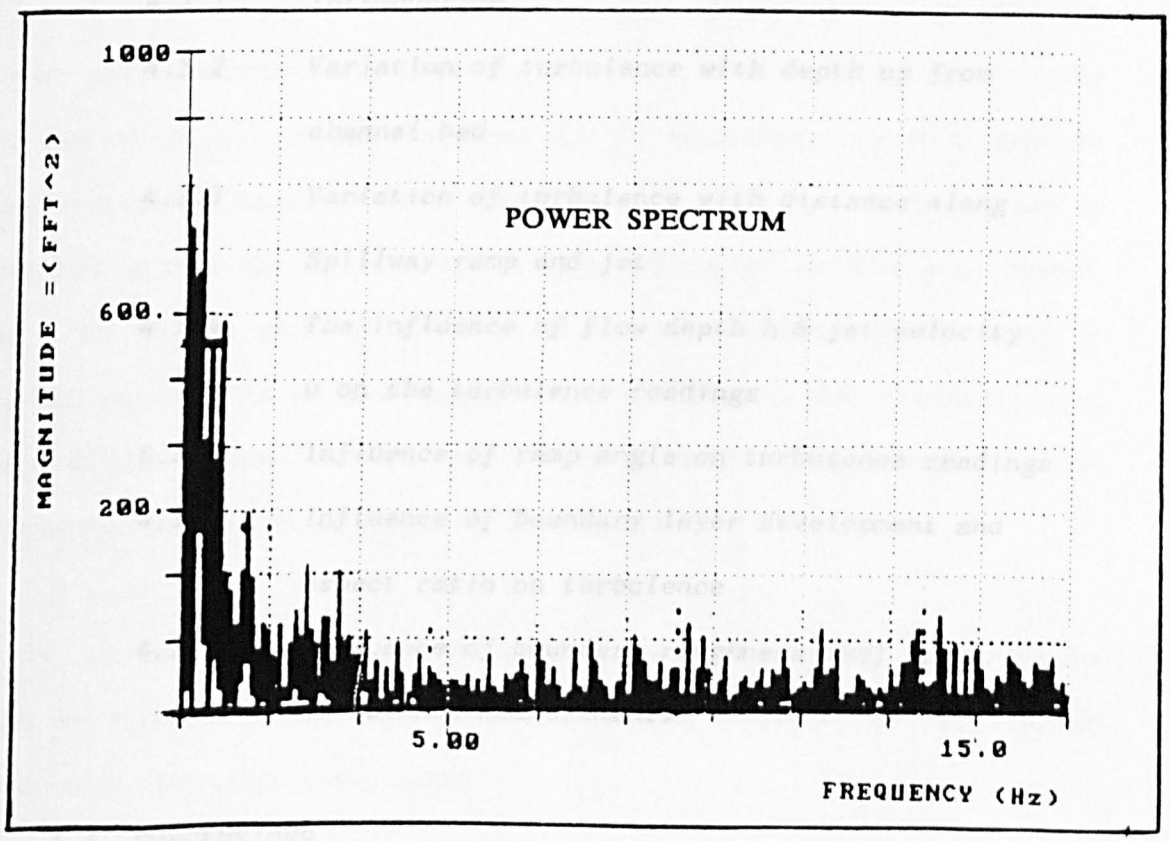

Fig 3.32 Graphical representation of Data

CHAPTER 4

DISCUSSION ON EXPERIMENTAL TURBULENCE MEASUREMENTS

4.1 INTRODUCTION.

4.2 INITIAL TURBULENCE TESTS ON VERTICAL CIRCULAR JETS.

4.2.1 Introduction

4.2.2 Results for 78mm diameter nozzle outlet

4.2.3 Results for 25mm diameter nozzle outlet

4.2.4 Results for 25mm diameter Orifice outlet

4.2.5 Significance of the initial turbulence test

4.3 TURBULENCE MEASUREMENTS IN SPILLWAY AND RAMP

4.3.1 Introduction

4.3.2 Variation of turbulence with depth up from channel bed

4.3.3 Variation of turbulence with distance along Spillway ramp and jet

4.3.4 The influence of flow depth h & jet velocity u on the turbulence readings

4.3.5 Influence of ramp angle on turbulence readings

4.3.6 Influence of boundary layer development and aspect ratio on turbulence

4.3.7 Influence of boundary roughness (ks) on turbulence measurements

4.4 CONCLUSIONS

4.1 INTRODUCTION.

Chapter 4 deals exclusively with turbulence measurements primarily in the spillway, ramp and aerator geometry, but also some preliminary tests of turbulence in vertical plunging circular jets.

The tests on the spillway ramp are presented in section 4.3 and investigate the effect of various parameters on the turbulent flow structure. These parameters include the flow depth, flow velocity, distance along spillway and ramp, effect of Reynolds Number, ramp angle Φ , decay of turbulence in the jet downstream of the ramp, aspect ratio of the channel, degree of boundary layer development before the ramp, as well as the degree of spillway boundary roughness (k_s). (The corresponding values of air entrainment, cavity under pressure, jet length, water surface profiles and friction factors will be presented in Chapter 5.)

The purpose of the detailed turbulence measurements is to provide a better physical understanding of the flow behaviour at an aerator ramp. It is also to look at the link between turbulence and air entrainment rate at a ramp, so that a computer model for air uptake (Chapter 7) might be as soundly based as possible. In particular the role of a ramp in generating turbulence is of interest, as is the possible decay of turbulence in the jet downstream of the ramp. In addition to these the effect of varying Reynolds Number is also of interest in the area of scale effects, but this area will be discussed in more detail in model – prototype comparison in Chapter 6. (Section 6.5)

Initially, however, turbulence measurements in plunging vertical circular jets are presented. These make use of the existing apparatus, and will hopefully complement the ramp measurements.

4.2 *INITIAL TURBULENCE TESTS ON VERTICAL CIRCULAR JETS.*

4.2.1. Introduction

The original existing apparatus consisted of a re–circulating rig generating high velocity jets through nozzles, 78mm diameter and 25mm diameter, as well as an orifice 25mm diameter. This rig has been described in Chapter 3 and was used by Withers (1987) in a study of pressure fluctuations in plunge pools.

Although most of the work in this Chapter concerns turbulence measurements along a spillway, ramp and aerator jet, a few tests were carried out initially in the vertical circular jets, using a turbulence probe also described in Chapter 3. It was not feasible to use the Laser system because of very uneven disturbances on the jet surface.

The main reasons for carrying out the circular jet test were as follows:–

– to investigate how turbulence varies over the jet diameter from edge to centre– line.

– to investigate how turbulence varies in the longitudinal direction along the jet length.

– to investigate the effect of increasing jet velocity on turbulence levels. It was known that velocities of the order of 15 to 20 m/s could be achieved, approaching the prototype range.

– to investigate the effect of jet dimension on the turbulence levels. Tests were carried out at 25mm diameter and 78mm diameter.

– to investigate the effect of initial jet turbulence condition on the turbulence levels. The nozzle tests produced glass– like jets and represented very low turbulence jets ($<1\%$).

The orifice jet contained higher turbulence readings ($\simeq$ 5%) and approached more the character of aerator ramp jets whose turbulence was thought to vary from 4% near the free surface to around 10% near the spillway base.

It was hoped that these results would in some way complement the turbulence measurements on the spillway ramp and provide some insights into the effect of Reynolds Number, turbulence redistribution in jets, and so on.

A sketch of the arrangement is shown in Fig 4.1 with the major parameters defined. The turbulence probe was inserted in the flow and used to measure only the longitudinal RMS turbulence component u'/u as described in Chapter 3.

The results are presented in the following way. For each outlet (nozzle and orifice), the radial distribution of the longitudinal turbulence intensity u'/u_0 is plotted first with the values normalised relative to the outlet conditions, i.e. u_0 and R_0 (where u_0 and R_0 are the outlet velocity and radius respectively). Subsequent radial distributions are plotted with the R.M.S. component of velocity u' and the radial distance to the measurement point from the jet centre lines r_j, made dimensionless with the local parameters u and Rj. The local parameters being the mean velocity and the jet radius at the measurement point respectively. Each figure applies at a specific distance downstream from the outlet and covers a range of tested outlet velocities. Following this, the longitudinal variation of the turbulence values is presented for each radial position but varying in the downstream direction. Similar to above, the first version is made dimensionless with the outlet conditions and the second relative to the local conditions.

Certain restrictions applied to the radial and longitudinal extent of the measurement positions within the plunging jet. Radial measurements were kept away from the jet edge to ensure that intermittency at the jet outer surface and air bubbles would not effect the results. Measurements along the jet length were limited to the initial portion of the jet length to prevent aeration influencing the results. A brief discussion of the turbulence results will be included in the

following sections.

4.2.2 *Result for 78mm diameter nozzle outlet.*

Figs 4.3 and 4.4 shows the variation of the longitudinal jet turbulence in the radial direction for various distances from the outlet. The range of initial velocities covered is 7 to 13 m/s. There is not much difference between the two figures as the condition of the plunging jet from the 78mm diameter nozzle had not changed much over such a small distance from the outlet. Considering Figures 4.3 and 4.4 it can be seen that:

(i) The values of turbulence intensity are under 1% which represents a low turbulence intensity jet. This was made possible by the combined use of a tube bundle upstream of the nozzle and a smooth tapered nozzle.

(ii) Values of turbulence intensity increase with jet velocity. This is due to the increase of Reynolds Number which almost doubles, from $5x10^5$ to $1x10^6$

(iii) Values of turbulence intensity increase with radial distance out towards the jet edge. This is due to a thin boundary layer forming along the nozzle, which occupies only a small thickness (relative to the jet diameter) at the outlet. This is sketched in Fig 4.2.

(iv) The thickness of the turbulent boundary layer increases with distance along the jet L/Do. This is seen when comparing graphs (a), (b) and (c) which reveal the high turbulence levels at the jet edge moving towards the jet centre line as we move downstream.

(v) The preceding point is also noticeable when considering the longitudinal variation of the jet turbulence in the downstream direction at given radial positions, as shown in Figs 4.5 and 4.6. The centre line (rj/Ro= 0) and intermediate radial positions show fairly constant values, however, near the jet edge, Fig 4.5(c), the turbulence intensity is seen to increase as the distance from

the outlet is increased. This is attributed to the development of the turbulent boundary layer into the body of the plunging jet by a process of redistribution or advection.

4.2.3 Results for 25mm diameter nozzle outlet.

From Figs 4.7 and 4.8 it can again be seen that the level of turbulence is very small. In fact, the results for the 25mm nozzle are even less than the core values for the 78mm diameter nozzle outlet. This is to be expected as the Reynolds Number in the 25mm nozzle is in the range of $2x10^5$ to $4x10^5$, which is only 40% of the 78mm nozzle value. It can be noted that for L/Do = 17.2, Fig. 4.7(c), the turbulent boundary layer is much thicker. At this distance relative to the outlet diameter, the turbulence has redistributed further towards the jet centre line so that it is now occupying almost half of the jet radius. Figs. 4.9 and 4.10 also show the increase in turbulence near to the jet edge with distance from the outlet, due to boundary layer ingress towards the jet centre line.

4.2.4 Results for 25mm diameter orifice outlet.

It was thought that the more turbulent condition of the plunging jet issuing from the 25mm orifice outlet would manifest itself in the magnitude of the jet turbulence readings. This is shown to be the case in Figs. 4.11 to 4.14. Due to the more irregular nature of these jets several runs were taken to obtain consistent RMS results, and also the plunge length was investigated at several more downstream positions than the corresponding smooth turbulent nozzle jets. Hence, with the larger volume of results, both Figs 4.11(a) and 4.11(b) represent

the radial variation of turbulence at given positions along the jet length relative to the outlet condition, while Figs. 4.12(a) and 4.12(b) represent the results relative to the local velocity and jet radius.

From the turbulence readings at the contraction, produced just downstream of the orifice (Figs 4.11(a) and 4.12 (a)), the glassy nature of the flow is indicated by the small magnitude of the longitudinal jet turbulence values. Increases in jet fall length beyond the contraction produce a turbulence level which is greatly increased, especially at higher outlet velocities. Thus at L/Do= 17, the jet turbulence reaches 6% – 7%. The increase in jet turbulence beyond the contraction was noticeable in the visual inspection of the jet condition.

The results are much more irregular than those previously considered, however, it can be seen that at the larger fall lengths and velocities, the maximum turbulence values are displaced from the jet edges into the central portion of the flow. This is particularly true for L/Do= 17, Figs 4.11 (e) and 4.12 (e) where it is seen that the variation with velocity (or Reynolds Number) is also much more significant.

The final diagrams in this section, Figs. 4.13 and 4.14, show the longitudinal variation of the turbulence results for a given jet radius. It can be seen in these figures the difference in the turbulence structure for the jet issuing from the orifice compared with the nozzle outlets. The centre line (rj/Ro= 0) (Graph (a)) turbulence intensity increases for greater jet fall lengths and at higher velocity, indicating migration of the boundary layer into the central portion of the jet. Near the jet edge, Graph (c), the turbulence reaches a maximum before reduction with further distance from the outlet. The maximum occurs at L/Do≈15 as shown on Graph 4.13(c).

4.2.5. Significance on the initial turbulence tests.

It is clear from Figs 4.3 to 4.14 that internal jet fluid turbulence is greater at the jet edges than at the jet core. This is because turbulence is generated at the solid boundary in the nozzle (or orifice). Turbulence which stems from the edge eventually propogates towards the centre of the jet.

This is shown for clarity in Fig 4.15 both for nozzles and orifice jet, showing the gradual transfer of turbulence towards the jet centre line. It is not clear how this result will translate to the ramp jet because many of the spillway jets contain fully developed turbulence over their depth, even before leaving the end of the ramp.

One important observation concerns the effect of jet length on the degree of turbulence. Fig 4.14 for the orifice jet for instance, shows that turbulence gradually increases along the jet length, reaches a peak around L/D_o of 12–14 and decreases there after. The decrease in turbulence may be associated with the fact that the jet eventually has a zero velocity gradient which means that it generates no new turbulence $\tau = \rho \ell^2 (du/dr)^2$, and hence the existing turbulence must eventually decay. Any initial increases in turbulence are more likely to be redistribution rather than generation. The same phenomenon is not clear in the nozzle jets, which are still re–distributing turbulence at the longest length of $L/D \simeq 20$.

The implications for the spillway aerator jets is enormous, as they also must eventually decay in turbulence at some distance after leaving the ramp, and that distance is likely to be much shorter than low turbulence, non–developed, circular jets. If the turbulence decays in the aerator jet, then so also does the rate of air entrainment to the underside of the jet.

Another important observation from the initial turbulence measurement is that jet turbulence increases with velocity and jet diameter and jet Reynolds Number. This is shown for the case of the smooth nozzle tests and plotted in

Fig 4.16 (a) and (b).

Fig 4.16(a) contains the jet centre–line turbulence plotted with increasing velocity, showing a steady increase in turbulence with velocity up to 11–13 m/s, and leveling–off there after. The 78mm nozzle has significantly higher turbulence than the 25mm nozzle.

Fig 4.16(b) shows approximately linear increase in turbulence with Reynolds Number for both nozzles. This may have significant implications for scaling and scale effects in aerators, where the prototype Reynolds Number may be in exess of 10^8 (uh/ν) whereas the model may be only 10^6 . The degree of turbulence alters the air entrainment rate and jet spread significantly.

4.3. *TURBULENCE MEASUREMENTS IN SPILLWAY AND RAMP*

4.3.1. Introduction

The purpose of the turbulence measurements along the spillway, ramp and aerator jet can be summarised as follows:–

(i) to obtain a deeper physical understanding of the flow behaviour so that a better computer model may be evolved.

(ii) to look at the role of an aerator ramp in generating extra turbulence and hence extra air entrainment.

(iii) to look at the interaction between turbulence intensity and jet phenomena, such as jet spreading, degree of air entrainment, and jet length.

(iv) to investigate the decay in turbulence in an aerator jet once it leaves the spillway surface.

(v) to investigate scale effects by varying the Reynolds Number.

The categories above are broad and will be addressed gradually

between this Chapter and the end of this thesis. In this Chapter the intention is to take a detailed look at the turbulence measurements taken, with a more in–depth analysis of the results to be presented in Chapter 6.

The turbulence results are presented from Figs 4.17 to 4.47 with Figs 4.17 to 4.25 representing the ramp angle Φ of 2^0 and a smooth boundary; Figs 4.26 to 4.34 representing the 5^0 ramp angle with smooth boundary; Figs 4.35 to 4.40 representing the 10^0 ramp angle with smooth boundary; and Figs 4.41 to 4.47 representing the 5^0 ramp angle with roughened boundary.

In each case the results are presented for the three gate openings namely 180mm, 90mm and 60mm, this being the depth of sluice gate opening in the upstream pressure box.

Each gate opening is tested over a range of three discharges usually lying within the range of 15 l/s to 52 l/s (0.015 m^3/s to 0.052 m^3/s). This represents the effect of the changing the depth and velocity of the supercritical flow. The results are presented in the form of both the longitudinal turbulence intensity u'/u and the component normal to the channel bed w'/u. In this case u' and w' are the RMS value of the fluctuations determined from the Laser measurements using the Asyst software package. The value of u is the local mean velocity at the point where the Laser is taking the measurement. This is different from the mean velocity of the flow $\bar{u}$, which is averaged over the whole cross–section.

Each graph shows the variation in turbulence intensity u'/u or w'/u with flow depth z/h. It also shows the variation of turbulence intensity with distance along the spillway, ramp and jet, at the four cross–sections shown in Fig 3.5. These cross sections are 300mm apart, with section 1 being 600mm upstream of the downstream end of the ramp, section 2 at the start of the ramp 300mm upstream of section 3, section 3 at the end of the ramp, and section 4 in the jet, 300mm downstream of the end of the ramp. All the results shown are averaged across the channel width.

The intention in this Chapter is to investigate the turbulence results in the light of the various parameters varied, and using this information to present a more detailed analysis both in this Chapter 4 and in Chapter 6. The sub– divisions of interest include the following.

– Variation of turbulence with depth up from channel bed.

– The variation of turbulence with distance along the spillway, ramp and jet.

– The influence of different gate openings.

– The influence of velocity on turbulence readings. Both gate opening and velocity will determine the Froude Number, Reynolds Number and Weber Number of the flow.

– The influence of the ramp angle Φ on turbulence.

– The influence on the degree of boundary layer development on the turbulence readings. This might be measured by L_{gr}/h, where L_{gr} is the length from gate to the ramp (1.9m) and h the flow depth. Alternatively it might be measured by the aspect ratio b/h, this being important in determining the influence of the side walls and the development of secondary cells.

– The influence of the degree of boundary roughness, k_s.

In all cases the emphasis is placed on the value of turbulence velocity normal to the channel bed w', as this is thought to be the key indicator in determining air uptake in the aerator.

4.3.2. Variation of turbulence with depth up from channel bed.

It should be noted at the start of this section that the author is not aware of any turbulence measurements in highly supercritical, steep (45^0), open channel flows done by previous authors. This makes any meaningful comparison difficult, as most previous research on turbulence in open channel flows has been for sub– critical near horizontal flows.

Over the past twenty years, extensive experimental research has been performed on the mean flow and turbulence structure of open–channel flow with the aid of hot–film anemometers and various visualization methods such as hydrogen–bubble technique. It was thereby established that, like boundary layers and closed duct flows, open channel flows also consist of two regions: a near wall region (inner region) and a outer region near the free surface. The near–wall region is controlled by the inner variables, namely the kinematic viscosity, ν, and the friction or shear velocity, u_*, and its features are virtually the same as those observed in boundary layers and closed channel flow [e.g Coles (1978)]. On the other hand, the outer region is controlled by the flow depth, h, and the maximum velocity u_{max}. The free surface exercises an influence only on this outer region. One noticeable influence is the damping of the vertical fluctuations (w') by the free surface, which was examined in detail by Celik,I (1984), Komori,S (1982), Nakagawa,H (1975) and Smuket,R (1969). Associated with this, is a reduction in eddy viscosity near the surface as compared with the centre region in closed channel flow.

The experimental data gathered in this work not only give a qualitative picture of the turbulence over a ramp in an open channel flow, but also gives a reasonable quantitative description. However, this data will not yet have reached the standard of closed channel air measurements [e.g Laufer(1954), Clark (1968)]. The reason is that turbulence measurements in water with hot–film probes are much more difficult and, thus, inherently less accurate than hot–wire measurements in air flows. With the advent of Laser Doppler Anemometers (LDA) a powerful measurement technique became available which is especially suited for velocity and turbulence measurements in water. This technique does not require any calibration. A Differential Doppler mode with forward light scattering (LDA) was used for measuring longitudinal and vertical velocity and turbulence with great accuracy.

Good examples of LDA measurements in sub–critical open channel

flows include those of Nezu and Rodi (1986) and Rashidi et al (1987). Nezu and Rodi showed that the variation of longitudinal turbulence with flow depth could be approximated by

$$u'/u_* = 2.26\ e^{-0.88\ z/h} \qquad (4.1)$$

Whereas Rashidi et al present a relationship in the form

$$u'/u_* = 1.95 - 2.85(z/h)^2 + 2.1\ (z/h)^3 \qquad (4.2)$$

In both cases h is the total flow depth, z is the height above channel bed and u_* the shear velocity for a wide channel given by $\sqrt{gRS_f}$

Similar results have been presented for turbulent components normal to the channel bed w', and are shown in graphical form in Fig 4.48. It is clear comparing this graph and Equations (4.1) and (4.2) above, that the value of u' is approximately 1.6 to 1.8 times greater than w' especially near the wall region.

It is also clear from Fig 4.48 that the turbulence values decay substantially with depth so that the value near the surface is typically around two– thirds of that near the wall. i.e. $w'/u_* = 0.75$ to 0.8 near the surface and 1.2 near the wall. In contrast values of u'/u_* are approximately half at the free surface compared with the wall value.

The reason for presenting this information is to provide the reader with a frame work for interpreting the graphs showing turbulence variation with depth in Figs 4.17 to 4.47. These graphs are presented, as measured, normalised by the local mean velocity u. The nearest we can come to Equation (4.1) and Equation (4.2) above and Fig 4.48 is to translate from shear velocity u_* into mean cross sectioned velocity $\bar{u}$. The two are related by

$$u_* = \bar{u}\ \sqrt{\lambda/8} \qquad (4.3)$$

The value of λ for both rough and smooth boundaries are shown in Chapter 5 (section 5.2.3.) and indicated λ to be around 0.0155 to 0.0188 for the smooth surface and 0.0275 approximately for the rough surface. If we examine the smooth surface only, and assume $\lambda = 0.01715$ then $u_* = 0.0463\ \bar{u}$ typically. This means that the graphs shown in Fig 4.48 translate into $w'/\bar{u} = 0.0565$ (5.65%) near the wall, and reduce down to $w'/\bar{u} = 0.0291$ (2.91%) near the free surface. This is a typical range of vertical turbulence velocities (w') in a sub critical open channel flow.

The results in Figs 4.17 to 4.47 are for a steep supercritical flow over a ramp, and a glance at the values of w'/u do indicate a range higher than that which might be predicted from subcritical open channel flows w'/u mentioned above. The value of w'/u are tabulated below for clarity giving the range (min. to max.) over the flow depth for various angles and gate openings, and also at all three measurement section 1, 2 and 3 along both spillway and ramp.

TABLE:(4A) Typical range of Turbulence intensities w'/u for Sections 1,2 and 3.

Gate openning Yg = mm	RAMP ANGLE Φ = degree			
	2° smooth	5° smooth	10° smooth	5° Rough
	surface → wall	surface → wall	surface → wall	surface→ wall
180	3.75% → 7.25%	4.0% → 8.0%	5.1% → 7.6%	5.4% → 8.25%
90	4.5% → 8.1%	4.75% → 8.3%	4.5% → 7.25%	4.8% → 8.5%
60	4.0% → 8.25%	4.0% → 8.4%	4.2% → 7.3%	4.8% → 10.1%

It is clear from this Table 4A that the measurements of free surface turbulence are all around 4% to 5% which is greater than previous measurements on sub critical open channel flows. It should be noted that data of Laufer (1954)

for air in a circular pipes shows w'/ $\bar{u}$ approximately 4% to 5% to the central pipe region, which is the equivalent of near the free surface in this work.

One difference between this data Table (4A) and previous sub– critical flow measurements, concerns w'/u values nearer to the wall. In this ramp measurement the values range from 7% to around 10% which is considerably greater than estimates from open channel flow. However, it should be noted that the "wall" values in Table (4A) refer in almost every case to section 3 at the end of the ramp and hence reflect the influence of the ramp in generating turbulence rather than simply open channel turbulence.

It would be more correct to compare with wall values for section 1 or 2 upstream of the ramp and clear of any influence of ramp generating turbulence. A look through Figs 4.17 to 4.40 reveals values of w'/u near the wall around 5% to 7.5% for section 1 and a comparison of section 1 values with previous sub– critical flows values is given below. This graph shows the turbulence values to be larger and to give a flatter distribution with depth, compared with previous sub– critical flow measurements.

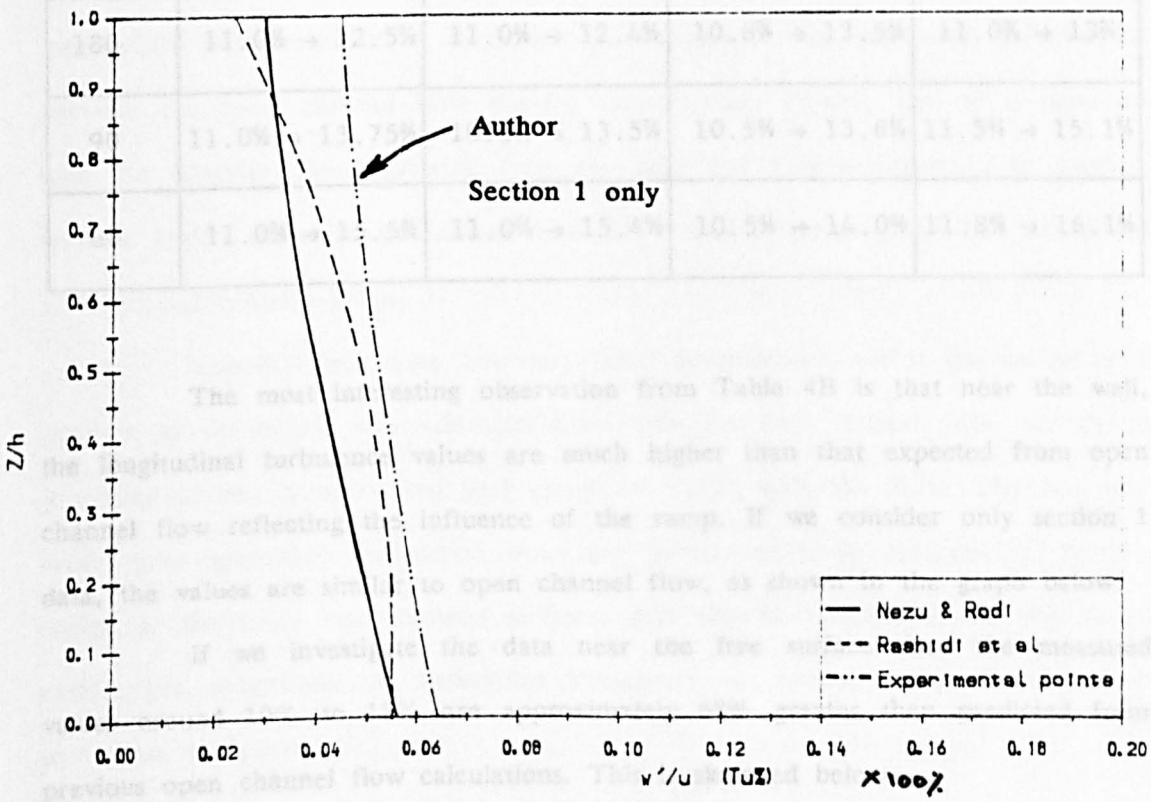

Variation of w'/u along the channel depth at section 1

Variation of longitudinal turbulence components u'/u with depth is also of interest. Previous open channel flow values are given by Equations (4.1) and (4.2) ranging from u'/u_* around 2 to 2.3 at the bed to values of u'/u* around 1.1 to 1.2 nearer the free surface.

If we use the same model for the smooth boundary in this $u_* = \bar{u}\sqrt{\lambda/8}$ and $\lambda = 0.01715$ then u'/ $\bar{u}$ should be of the order of 10.4% near the wall, reducing to values of u'/ $\bar{u}$ around 4.34% near the free surface.

The measured LDA data in this case is shown in Table below, again for all three sections 1, 2 and 3 including both spillway and ramp.

TABLE (4B): Typical range of Turbulence intensities u'/u for Sections 1,2 and 3.

Gate openning Yg - mm	RAMP ANGLE Φ - degree			
	2° smooth	5° smooth	10° smooth	5° Rough
	surface → wall	surface → wall	surface → wall	surface→ wall
180	11.0% → 12.5%	11.0% → 12.4%	10.8% → 13.5%	11.0% → 13%
90	11.0% → 13.75%	10.5% → 13.5%	10.5% → 13.6%	11.5% → 15.1%
60	11.0% → 15.5%	11.0% → 15.4%	10.5% → 14.0%	11.8% → 16.1%

The most interesting observation from Table 4B is that near the wall, the longitudinal turbulence values are much higher than that expected from open channel flow reflecting the influence of the ramp. If we consider only section 1 data, the values are similar to open channel flow, as shown in the graph below.

If we investigate the data near the free surface then the measured values around 10% to 11% are approximately 68% greater than predicted from previous open channel flow calculations. This is sketched below

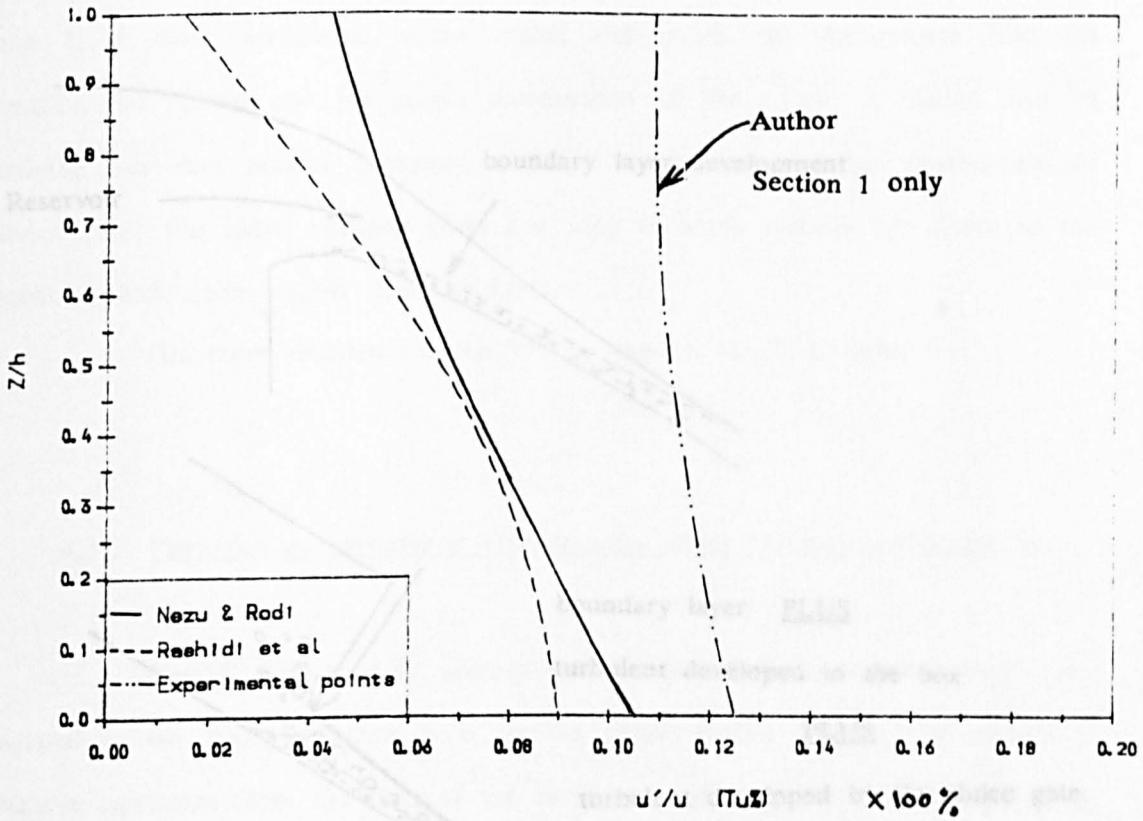

Variation of u'/u along the channel depth at section 1

Both w' and u' measurements in this work are higher than conventional estimates especially near the free surface and especially for the longitudinal measurements u'. In order to understand this, one must differentiate between an open channel flow derived from simply flowing out of a reservoir with the boundary layer growing from the bed; and a flow derived from passing from a highly turbulent pressurised box and under a sluice gate. The difference are sketched below(overleaf)

The first is a pure boundary layer development, whilst the second is a mixture of boundary layer development from the bed, mixed with turbulence generated in the pressure box and convected along with the flow. The box and sluice gate generated turbulence may not have completely disappeared by the region of the ramp measurement sections, and may be responsible for the flatter and larger magnitude of turbulence compared to normal open channel flow turbulence measurements.

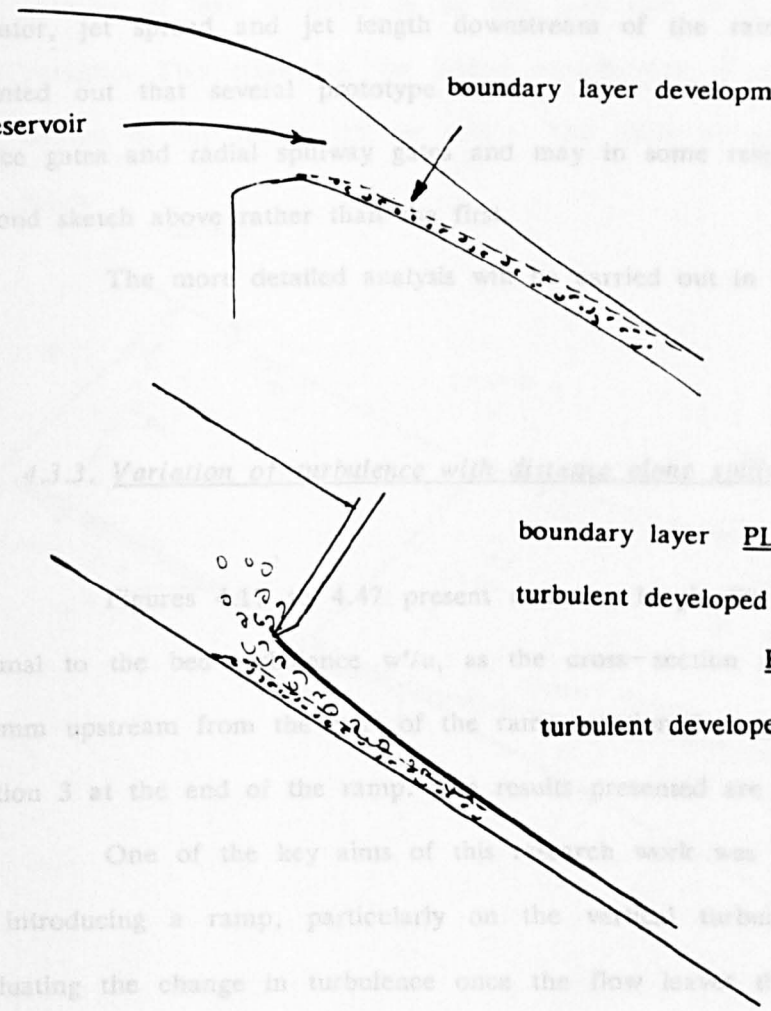

Of course, previous data sets have all been for subcritical open channel flows, and the introduction of steep supercritical flows may change the turbulent flow structure appreciably, especially in the region of the free surface. Hence at this stage it is not absolutely clear as to why $u'/\bar{u}$ values (and w'/u values) deviate from previous norms.

In any case, the flatness of the turbulence structure with depth may not be a crucial factor. Values of $w'/\bar{u}$ near the bed are approximately the same in these measurements compared to previous open channel data sets. This is particularly true of the section 1 measurements for upstream of the ramp. The

turbulence measurements near the bed in fact are very similar to previous data, and it is these turbulence values which determines air entrainment into the aerator, jet spread and jet length downstream of the ramp. It should also be pointed out that several prototype aerators have been installed downstream of sluice gates and radial spillway gates and may in some respects be closer to the second sketch above rather than the first.

The more detailed analysis will be carried out in Chapter 6.

4.3.3. *Variation of turbulence with distance along spillway ramp and jet.*

Figures 4.17 to 4.47 present data for longitudinal turbulence u'/u and normal to the bed turbulence w'/u, as the cross–section moves from section 1, 300mm upstream from the start of the ramp, section 2 at the start of the ramp, section 3 at the end of the ramp. The results presented are width–averaged.

One of the key aims of this research work was to evaluate the effect of introducing a ramp, particularly on the vertical turbulence w', as well as evaluating the change in turbulence once the flow leaves the spillway to form a jet.

One of the flow characteristics of a ramp and jet is shown sketched below. It concerns the variation in internal fluid pressure and the subsequent fluid acceleration over the ramp.

Section 1 is essentially straight spillway flow with a hydrostatic pressure distribution and logarithmic velocity distribution. On moving to section 2 the ramp effectively produces streamline curvature, and extra centrifugal pressure on the spillway base. The curvature is also likely to produce additional momentum transfer and the formation of secondary cells, or longitudinal helical swirls as noted in Chapter 2. By the stage of section 3 the internal fluid pressure is almost zero or at least is likely to be less than one third of the normal

noted in Chapter 2. By the stage of section 3 the internal fluid pressure is almost zero or at least is likely to be less than one third of the normal hydrostatic pressure. This stage has the added complication of a negative pressure at the bottom of the jet in the air cavity. The likely pressure distribution is sketched below

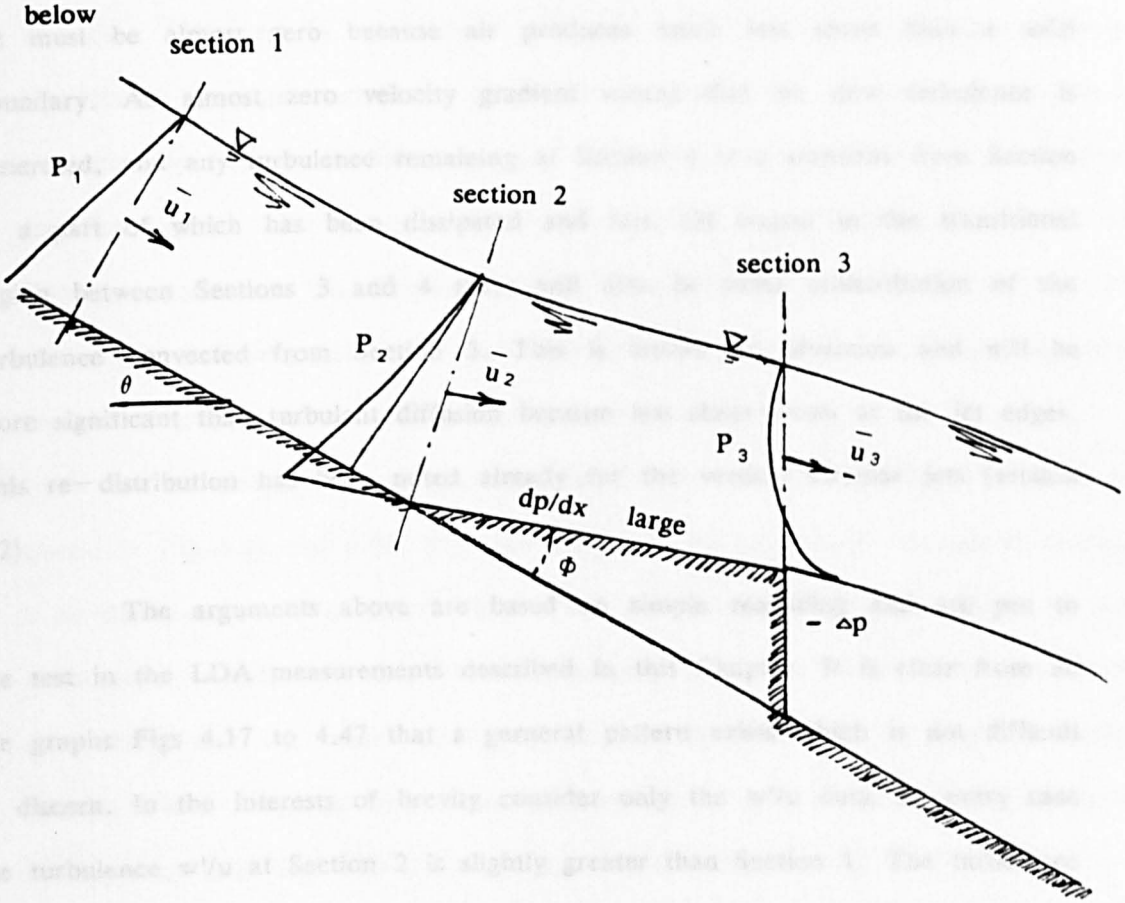

Applying Bernoullis equation between section 2 and 3 will show an increase in velocity between u_2 and u_3 because of the large reduction in pressure. Therefore flow over the ramp accelerates. The pressure along the base of the ramp has a large gradient moving from a large positive pressure at section 2 to a negative pressure at section 3. dp/dx will have a large negative value especially near the spillway base giving rise to a large positive velocity gradient du/dx near the base. Remember the jet downstream eventually has a uniform velocity distribution and hence a significant change from a logarithmic distribution on the spillway.

The result of these observations is that velocity increases near the

base must be accompanied by transfers of momentum from the upper layers towards the base and hence a likely increase in turbulence in the flow along the ramp.

Moving from Section 3 to Section 4 in the jet downstream may produce even more significant changes. The velocity gradient downstream in the jet must be almost zero because air produces much less shear than a solid boundary. An almost zero velocity gradient means that no new turbulence is generated, and any turbulence remaining at Section 4 is a remnant from Section 3, a part of which has been dissipated and lost. Of course in the transitional region between Sections 3 and 4 there will also be some redistribution of the turbulence convected from Section 3. This is known as advection and will be more significant than turbulent diffusion because less shear exists at the jet edges. This re–distribution has been noted already for the vertical circular jets (section 4.2).

The arguments above are based on simple reasoning and are put to the test in the LDA measurements described in this Chapter. It is clear from all the graphs Figs 4.17 to 4.47 that a gerneral pattern exists which is not difficult to discern. In the interests of brevity consider only the w'/u data. In every case the turbulence w'/u at Section 2 is slightly greater than Section 1. The turbulence w'/u is significantly greater at section 3 compared to either Section 1 or 2. Finally, the turbulence at Section 4 is significantly less than at Section 3 revealing turbulence decay in the aerator jet.

A review of Figs 4.17 to 4.47 reveals than in every case the turbulence measurements at Section 2 lie between those of Section 1 and Section 3 in numerical value. This suggests a steady increase in turbulence from the spillway to the start of the ramp.

Closer inspection of the results show that in most cases the increase in w'/u between Section 1 and 2 is significantly less than the increase from Section 2 to 3 Relative increase in w'/u from section 1 to 2 vary from 0% to almost 10% but

average less than 5%, meaning that most af the turbulence generation occurs along the ramp itself from Section 2 to 3.

Turning our attention to increases in w'/u from Section 1 to Section 3, there is clear evidence of significant increase. In some cases the increase is less than 10% and in other cases is greater than 30%, revealing that a ramp significantly increases turbulence in a spillway flow. This has never been shown quantitatively before. Furthermore, until this stage it has not been known how turbulence varies with key parameters such as ramp angle Φ, velocity u, depth of flow h, aspect ratio b/h, Froude Number, Reynolds Number or Weber number or the degree of boundary layer development. The answer to this qestion may become clearer as we investigate each parameter in turn.

A clearer idea of the increase in turbulence from Section 1 to 3 is shown in Fig 4.49 and 4.50. Fig 4.49 shows all the turbulence readings at section 1 in the form of w'/u_* rather than w'/u. The problem with normalising by the local mean velocity u is that it keeps changing from test to test. The benefit of normalising with the shear velocity u_*, is that the turbulence is meant to scale with the shear velocity and hence it becomes a good parameter to compare various tests with. Fig 4.50 is all the data taken at Section 3.

It is clear from these two figures that there is a significant difference in the values of w' at both sections and can be attributed to the effect of the ramp. At Section 1, the median turbulence values reach approximately $w'/u_* = 1.35$ near the bed which compares very favourably with $w'/u_* = 1.23$ by Nezu and Rodi (1986).

At Section 3 on the other hand at the end of the ramp—, this median turbulence value has increased to around $w'/u_* = 1.75$ near the bed showing very clearly that the ramp acts as a turbulence generator.

Figs 4.17 to 4.47 also reveal a further phenomenon in the jet downstream of the end of the ramp. It concerns the turbulence measurement in the core of the jet at a point 300mm downstream of the end of the ramp at

section 4. This data is represented by dashed lines in the Figures, often giving measurements only around the jet centre line. The reason for this is sketched below and concerns the fact that air bubbles can become entrained both on the lower and upper regions of the jet. Hence LDA measurements are only possible within the core of the jet where air concentration are not significant.

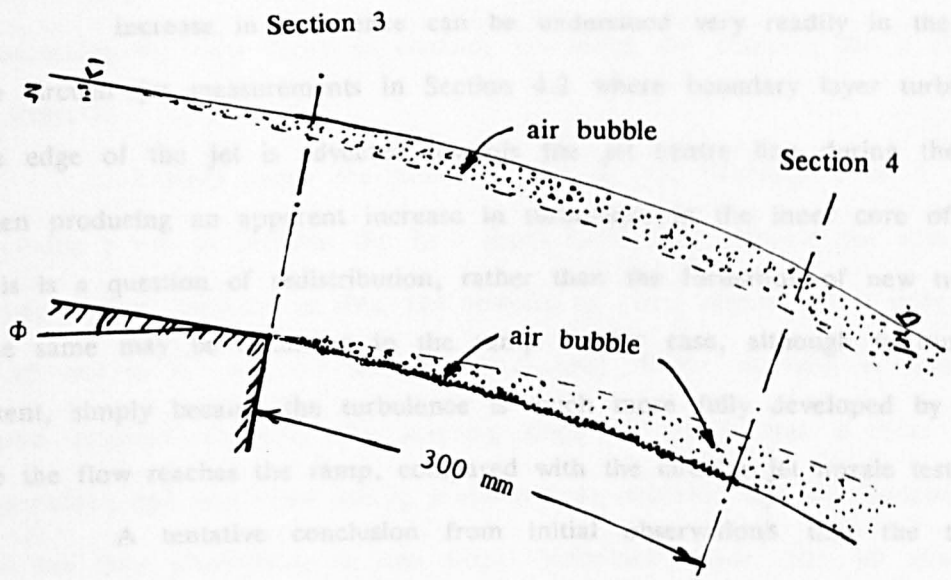

Returning to Figures 4.17 to 4.47 it is clear in many cases that w'/u values at Section 4 are significantly less than those at Section 3, indicating turbulence decay. In some cases the decay is so large that the values of w'/u at Section 4 are less than those that Section 1,2 and 3, indicating that ramp generated turbulence quickly decays in the aerator jet downstream.

One point worth noting here is that Section 4 measurements were carried out at a fixed distance of 300mm downstream of the end of the ramp, thus varying the ratio x/h considarably from around 4 to 12 depending on the flow depth h.

An analysis of the results revealed that the greatest decays in turbulence occured at the largest non−dimensional distances from the end of the ramp x/h_3. Values of x/h_3 greater than 8 or 10 produced significant decays. The

5° smooth ramp also produced slightly greater decay than the other two angles but not significantly so. This will be discussed further in Chapter 6 section 6.2.2.

Comparing the value of w'/u between Section 3 and 4, but only along the jet centre–line (depth h/2) shows a mean decay of turbulence averaged over all the results of around 10%. The value however disguises the fact that some turbulence values showed much higher dicreases, and some in fact showed increases in turbulence, albeit slight.

Increase in turbulence can be understood very readily in the light of the circular jet measurements in Section 4.2 where boundary layer turbulence at the edge of the jet is advected towards the jet centre line during the plunge, often producing an apparent increase in turbulence in the inner core of the jet. This is a question of redistribution, rather than the formation of new turbulence. The same may be occurring in the ramp aerator case, although to much lesser extent, simply because the turbulence is much more fully developed by the time the the flow reaches the ramp, compared with the circular jet nozzle tests.

A tentative conclusion from initial observations that the turbulence velocity w' does not remain constant along the length of the aerator jet L. This means that the quantity of air entrainment may also decrease along the jet length, particularly at values of x/h greater than 10. This will be explored in more detail in Chapter 6 section 6.2.2.

4.3.4. The influence of the flow depth h and jet velocity u, on the turbulence readings

The experimental procedure consisted of varying the gate opening at outlet of the pressure box from 180mm to 90mm to 60mm openings. For each gate opening the discharge was varried though the gate, broadly in the range 0.015 m^3/s to 0.052m^3/s. Flow under the gate entered the 45° spillway channel

forming a gradually varied flow profile. The range of profiles are presented in Chapter 5 together with the friction factors determined for a gradually varied flow analysis.

Inspection of the smooth gradually varied flow profiles in Fig 5.3 to Fig 5.6 show that because of the steep slope and distance along the channel to the ramp, the effect of varying gate opening was not all that significant in terms of changing the flow depth at the ramp region . This can be seen by in Fig 5.3 comparing the flow depth at distance 1m along the channel, for a discharge of $0.038m^3/s$, for instance.

Further more the effect of varying the discharge (at a given gate opening) was to increase the flow depth more than increase the velocity at the ramp region. Because of this, the velocity at ramp region varied only the range 6.25 m/s to 7.7 m/s for the smooth channel. Wider variation in velocity would have required changing the spillway slope θ, which was a time consuming operation, and was ruled out in preference to obtaining a more fundamental grasp of the flow phenomena at one slope. Velocities higher than 10 m/s could be achieved (especially a smaller gate openings and larger discharge) but tended to produce jets at the ramp which did not re—attach on the spillway before entry into the sump tanks below.

In this section therefore an attempt is made to look at the effect of velocity and flow depth h on the turbulence readings. Remarks will be concentrate initially on section 1 so that effect of the ramp is removed. Remarks will also concentrate on the normal to the bed turbulence components w'/u, as these are more significant for subsequent air uptake and jet spread.

The first point of note is that w'/u values generally increases with increasing flow depth. This is seen very clearly in the first three graphs Fig 4.17(b), Fig 4.18(b) and Fig 4.19(b). If we consider only the highest value of w'/u experienced at section 1, then it is approximately 4.6% with h = 0.0315m, 6.25% with h = 0.06m and 6.5% with h = 0.08m. A very similar pattern is

experienced at other gate openings as can be seen for instance by comparing Figs 4.23(b) to 4.25(b). Turbulence intensity increases with flow depth h.

The observation is not surprising in the light of turbulence measurements carried out in section 4.2. Inspection of Fig 4.16(a) and Fig 4.16(b) reveals that the jet centre line turbulence in the plunging circular jets increases with jet diameter (as well as velocity).

In fact the circular jet measurements have shown that the jet turbulence measurements increases with Reynolds Number in an almost linear fashion as shown in Fig 4.16(b). It was also thought that the turbulence level in this work would also vary with the Reynolds Number simply because higher Reynolds Number produce higher turbulent energy in the smaller eddy length ranges.

As a first crude attempt, the maximum values of w'/u at section 1 are plotted against a kind of Reynolds Number, namely q (= uh). This was chosen in the first instance for convenience. Reynolds Number of the flow Re = $4uR/\nu$ which for a wide channel approximates to $4uh/\nu$, and because ν is constant at constant temperature, than the product of u.h can be used as a representative Reynolds Number type value. This result is shown in Fig 4.51, showing that w'/u increases with Reynolds Number. Fig 4.51 highlights the problem with scale effects in aerators, because prototype values of q can often reach values of 30 to 50 m^2/s (or Reynolds Number around $4uh/\nu = 1$ to 2×10^8.)

The graph of w'/u against the actual Reynolds Number ($4uR/\nu$) is shown in Fig 4.52 giving very similar results. Extrapolation of model turbulence data to the prototype scale is very difficult in this case because of the large difference in Reynolds Numbers of the two cases. One thing is certain is the prototype will have higher w'/u values than the model and hence entrain more air. There are no other previous sets of turbulence measurements to compare with.

The maximum w'/u values at section 3 at the end of the ramp are

shown in Fig 4.53 and reveal a very similar pattern.

Fig 4.54 is a plot of maximum w'/u_* value at section 1 plotted against Reynolds Number. It is clear from this graph which is normalised by the shear velocity rather than the local mean velocity u, that the pattern with increasing Reynolds Number is similar to the above.

The next point of interest concern the separation of the influences of velocity u and flow depth h on the turbulence values. Fig 4.51 or Fig 4.52 contain a mixture of increase in u and h together. Refering to Fig 4.51 for instance, it is clear that the mean velocity range for this graph is very narrow, varying only from 6.25 m/s to 7.7 m/s, with all the higher points on the graph representing velocities in excess of 7 m/s. This means that the graph can be re-interpreted, as shown in Fig 4.55 corresponding to the velocities ranges indicated.

This Figure now reveals a high dependence on the mean velocity of the flow u and a similar dependence on the flow depth h. This graph is very significant, showing that the turbulence in the flow increases significantly with velocity. It also rises the question about extrapolation to prototype velocities around 30 m/s.

This question will be addressed in Chapter 6, but mean-time some clues may be seen in the turbulence measurements from the circular nozzles and orifice described in section 4.2.

It is clear from Fig 4.16(a) for the smooth nozzle jet centre-line that internal turbulence does not increase significantly for jet velocities greater than 11-13 m/s, and up to that point turbulence varies almost linearly with jet velocity. A very similar pattern is found for the orifice jets, implying that velocity increases do not continue to produce increases in turbulence but that turbulence increases are more likely to level off at velocities in excess of approximately 10 m/s. Scale effects are liable to be relatively small beyond this velocity range provided the flow depth is reasonable.

4.3.5 Influence of ramp angle on turbulence readings.

The purpose of a ramp is to cause that jet trajectory to spring clear of the spillway surface and to produce a jet length (L) where the underside of the jet is in contact with the atmosphere.

Ramp angles Φ are traditionally not made much larger than 10^0 because the resultant jet would rise too high, touching the tunnel soffitt, or alternatively rising above the side walls of an open channel chute spillway. For this reason, the range of angles chosen is usually less than 10^0 relative to the spillway slope θ. The range chosen in this work is 2^0, 5^0 and 10^0.

Section 4.3.3 has already revealed that the ramp acts as a turbulence generator with values of $w' \simeq 1.35\ u_*$ upstream of the ramp, and $1.75\ u_*$ at the end of the ramp at section 3. It was felt intuitively that larger ramp angles would produce greater turbulence generation and hence more air entrainment at the aerator jet. This was argued in the sense that larger ramp angles produce a larger shock to the supercritical flow, greater streamline curvature, greater pressure gradient and possibly greater turbulence.

In order to test this thesis, maximum values of w'/u at the end of the ramp section 3 are plotted against ramp angle Φ. This is done for constant values of discharge along spillway, q and shown in Fig 4.56(a), (b) and (c).

Referring to Fig 4.56(a),(b) and (c) it is clear that the changing ramp angle makes no significant difference to the turbulence generated at the end of the ramp. This result is surprising, in the sense that a 2^0 ramp with its small deviation from the spillway slope should generate just as much extra turbulence as a 10^0 ramp with its much greater deviation from the spillway slope. Whatever physical process is involved in additional turbulence generation it is not much affected by ramp slope.

4.3.6 *Influence of boundary layer development and aspect ratio on turbulence.*

It is apparent that the degree of boundary layer development will influence the magnitude of turbulence felt at the region of the ramp. As a first estimate, the boundary layer thickness δ on a smooth boundary can be given as

$$\delta = \frac{0.38\ x}{[\ Re_x]^{0.2}} \qquad (4.4)$$

where x is the distance from the start of the spillway and $Re_x = ux/\nu$, where u is the flow velocity.

It follows therefore that the velocity at the ramp is around 7 m/s and the distance x is 1.9 m, therefore the boundary layer thickness δ, in the region of ramp is;

$$\delta \simeq 0.028m \qquad (4.5)$$

An inspection of the data in Figs 4.17 to 4.40 for smooth boundaries only, reveals that the flow depth in the ramp region varies approximately 0.023 m to 0.08 m for the turbulence measurements. This means that the shallowest flow depths in fact represent fully developed flow as $\delta/h \simeq 1.0$. The deepest flows represent $\delta/h \simeq 0.3$ and therefore have turbulence developed only in the lower third of the flow. This in fact is not the case, as already discussed in section 4.3.2. The deepest flows (and the lowest δ/h values) in almost all cases that have greatest values of turbulence intensity over the flow depth h, either because they have much higher Reynolds Numbers of flow, or there is more turbulence transmitted from the upstream pressure box and sluice gate.

It follows therefore that no meaningful analysis can be carried out on boundary layer development in this work. This is because greater boundary layer development δ/h is achieved by lowering the flow depth h, which in turn lowers

the Reynolds Number of the flow and in turn lowers the turbulence. One effect is counter– balancing the other.

A similar argument applies to the aspect ratio of the channel. It is thought that the curvature of the streamlines passing over the ramp will cause longitudinal vortices to form (secondary cells) as shown below and described by Goertler (1945).

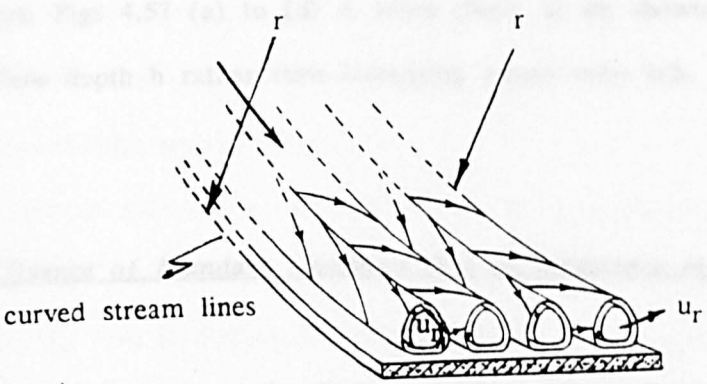

Such helical cells increase the turbulence felt in the flow and are likely to be a maximum when the aspect ratio of the channel is 2,4,6, etc.

On the other hand varying the aspect ratio b/h, is likely to produce a varying influence from the side walls so that if a boundary layer of 0.028 m thickness has formed on the channel bed, then it is likely to have comparable magnitude in width for each of the side walls. Thus a channel of 0.1 m wide as in the case, will have boundary layers from the side walls, each 0.028m wide and occupying approximately half the channel width (total).

Combining these two ideas for the fixed channel width in this work 0.1 m, the maximum turbulence is likely for an aspect ratio around 4 (or depth $\simeq$ 0.025 m).

The results of maximum turbulence intensity $(w')_{max} / \bar{u}$ at the end of the ramp (at section 3) are plotted against aspect ratio and shown in Figs 4.57 (a),(b),(c) and (d), for the 5^0, 2^0, and 10^0 smooth cases, as well as 5^0

rough case.

It appears from all four graphs, at every ramp angle, the maximum turbulence decreases with aspect ratio. Again, it must be stated that this may be a very misleading picture. This is because the aspect ratio b/h, has a fixed value of b , and was increased by decreasing the value of flow depth h. By decreasing h, the Reynolds Number is greatly reduced and hence the turbulence values resulting.

Hence Figs 4.57 (a) to (d) is more likely to be showing the influence of decreasing flow depth h rather than increasing aspect ratio b/h.

4.3.7 *Influence of boundary roughness (k_s) on turbulence measurements.*

One of the key tests for both turbulence measurement and air uptake measurement concerned the variation of the upstream spillway boundary roughness. In the case of this work, boundary roughening was achieved by means of adhesive sand paper from the pressure box to the end of the ramp. Details of this have been described in section 3.3 and friction factors for the roughened bed are given in Chapter 5, section 5.2.3. A typical friction factor for the smooth case is around 0.018 whereas for the roughened case it is more of the order of 0.027, a 50% increase.

The purpose of introducing boundary roughness was to induce extra turbulence at the ramp and jet. This is based on the premise that w'/u_* is approximately the same for rough and smooth boundaries. That is, at any given depth up from bed, $w'/u_* \simeq K$, whether rough or smooth.

It follows therefore that because

$$u_* = \bar{u}\sqrt{\lambda/8} \quad \text{then,} \tag{4.6}$$

$$w'/u_* = \sqrt{\lambda/8}\ K \qquad (4.7)$$

and hence turbulence intensity $w'/\bar{u}$ can be increased by simply increasing the friction factor λ via the boundary roughness.

The values of w'/u at section 1 along the spillway, are shown in Fig 4.58 for both smooth and rough boundaries. Based on Equation (4.6) above we would expect an increase of $w'/\bar{u}$ of the order of $(0.027/0.018)^{\frac{1}{2}} \simeq 20\%$. It can be seen from Fig 4.58 that the values of w'/u_* are similar for both rough and smooth cases, whereas the value of w'/u is approximately 15% to 20% greater in rough case compared with smooth case.

This implies that if air entrainment rate is dependent on the turbulent velocity w', then it is preferable to scale w' on the shear velocity u_* rather than the mean velocity u. This is discussed further in Chapter 5 and Chapter 6.

4.4 *Main conclusions from turbulence measurements.*

Initial turbulence measurements on the vertical plunging circular jets reveal :—

(i) For the low turbulence circular nozzle jets, the centre line turbulence increases with jet plunge length. This is due to a redistribution of turbulence from the edge of the jet towards the centre.

(ii) For the higher turbulence circular orifice jet, the jet centre line turbulence increases initially with jet length, reaching a maximum and decaying thereafter. Atmospheric jet turbulence must eventually decay because velocity gradients decay to almost zero.

(iii) Turbulence values generally increases with velocity, jet diameter and hence Reynolds Number.

Turbulence measurements along the spillway, ramp and jet reveal :–

(i) Variation of turbulence with depth up from the channel bed is flatter and of greater magnitude than previous subcritical open channel flow measurements. This is connected with the fact that turbulence is transmitted from the upstream pressure box as well as boundary layer turbulence, and also because of the supercritical nature of the flow.

(ii) Values of turbulence are also higher than previous subcritical measurements, particularly in the case of u'/u more than w'/u.

(iii) The ramp acts as a turbulence generator with values of $w' \simeq 1.35\ u_*$ near the wall upstream of the ramp, increasing to $w' \simeq 1.75\ u_*$ near the wall at the end of the ramp.

(iv) Downstream of the ramp, turbulence decays in the jet the decay becoming significant at jet lengths (x/h_3) greater than 10.

(v) Turbulence measurements along the spillway increases with jet velocity, flow depth and Reynolds Number. (observation from circular jet measurements shows that turbulence does not increase significantly for jet velocities greater than 10 – 13 m/s).

(vi) The effect of varying the ramp slope Φ from 2^0 to 5^0 and to 10^0 produces negligible change in the turbulence values generated at the end of ramp, section 4..

(vii) Variation of aspect ratio (b/h) of the flow, shows an apparent decrease in turbulence as b/h increases from 1 to 5. This, for the most part, might simply reflect the reduction in h to produce increase in b/h. A reducing flow depth h, reduces Reynolds Number and turbulence values.

(viii) Introducing a rougher boundary increases the values of relative turbulence intensity w'/u by around 15% to 20%.

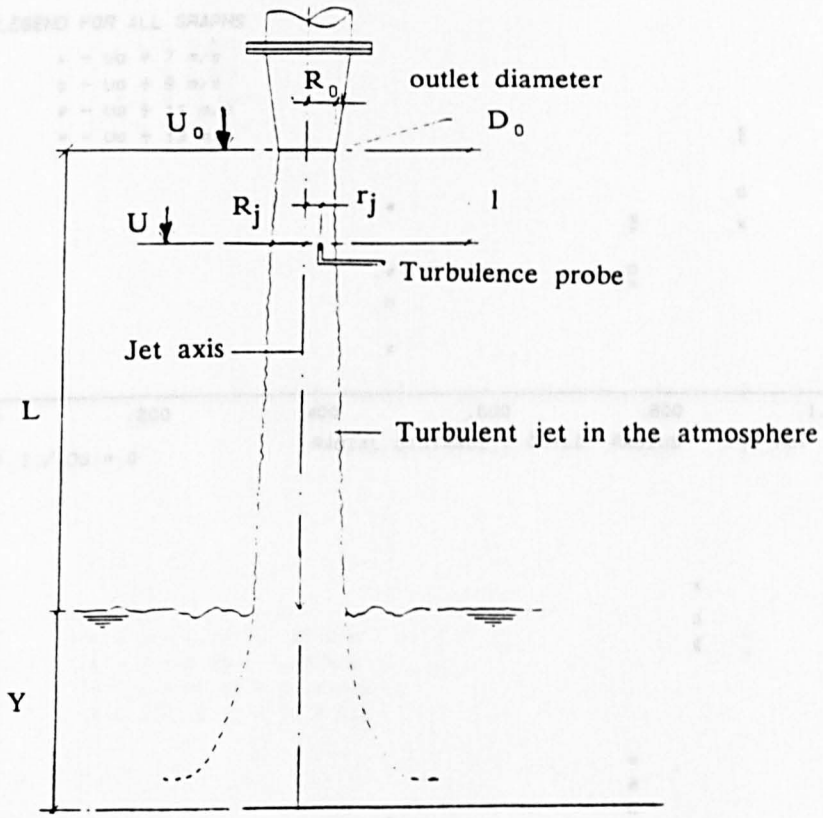

Fig 4.1 Sketch of initial testing programme

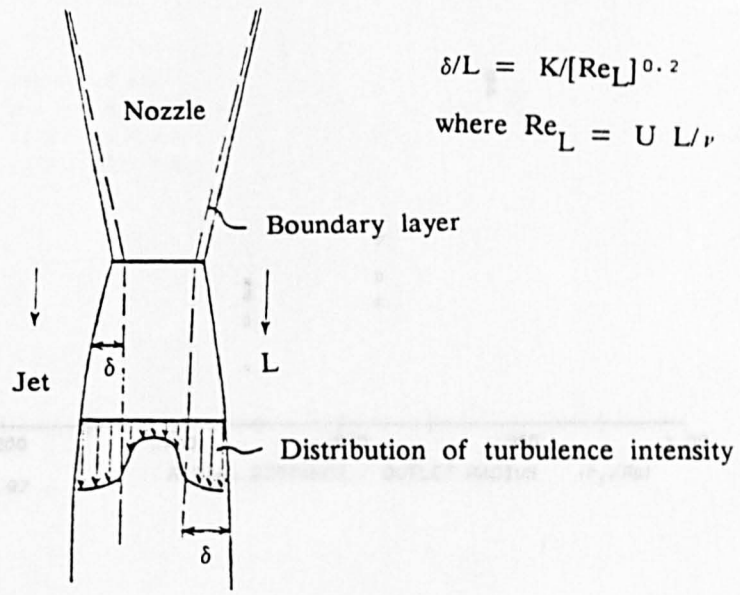

Fig 4.2 Boundary layer development along nozzle

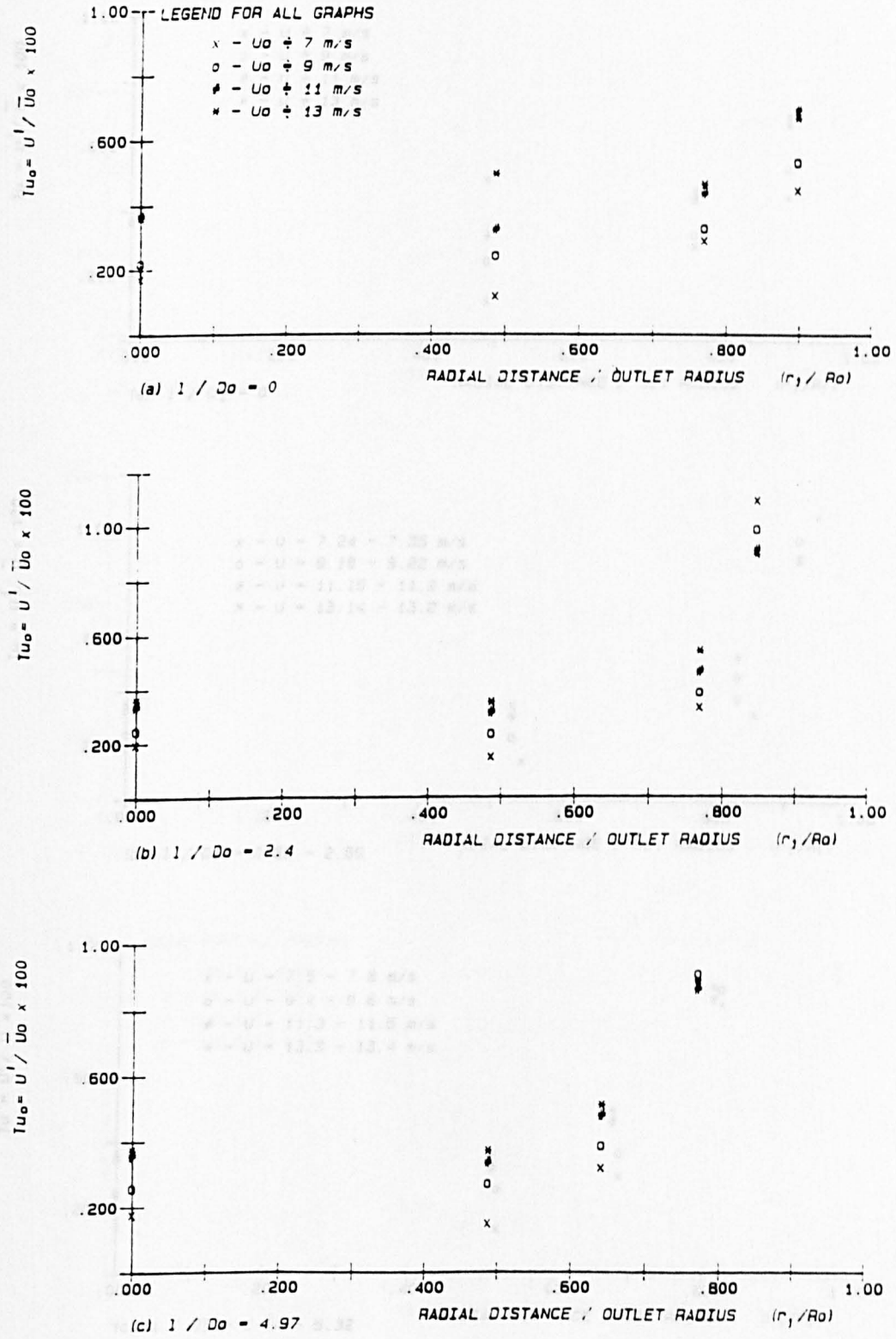

Fig 4.3 Variation of Turbulence intensity (Tu%) in Radial direction (r_j / R_j).[Nozzle: D_0=78mm]

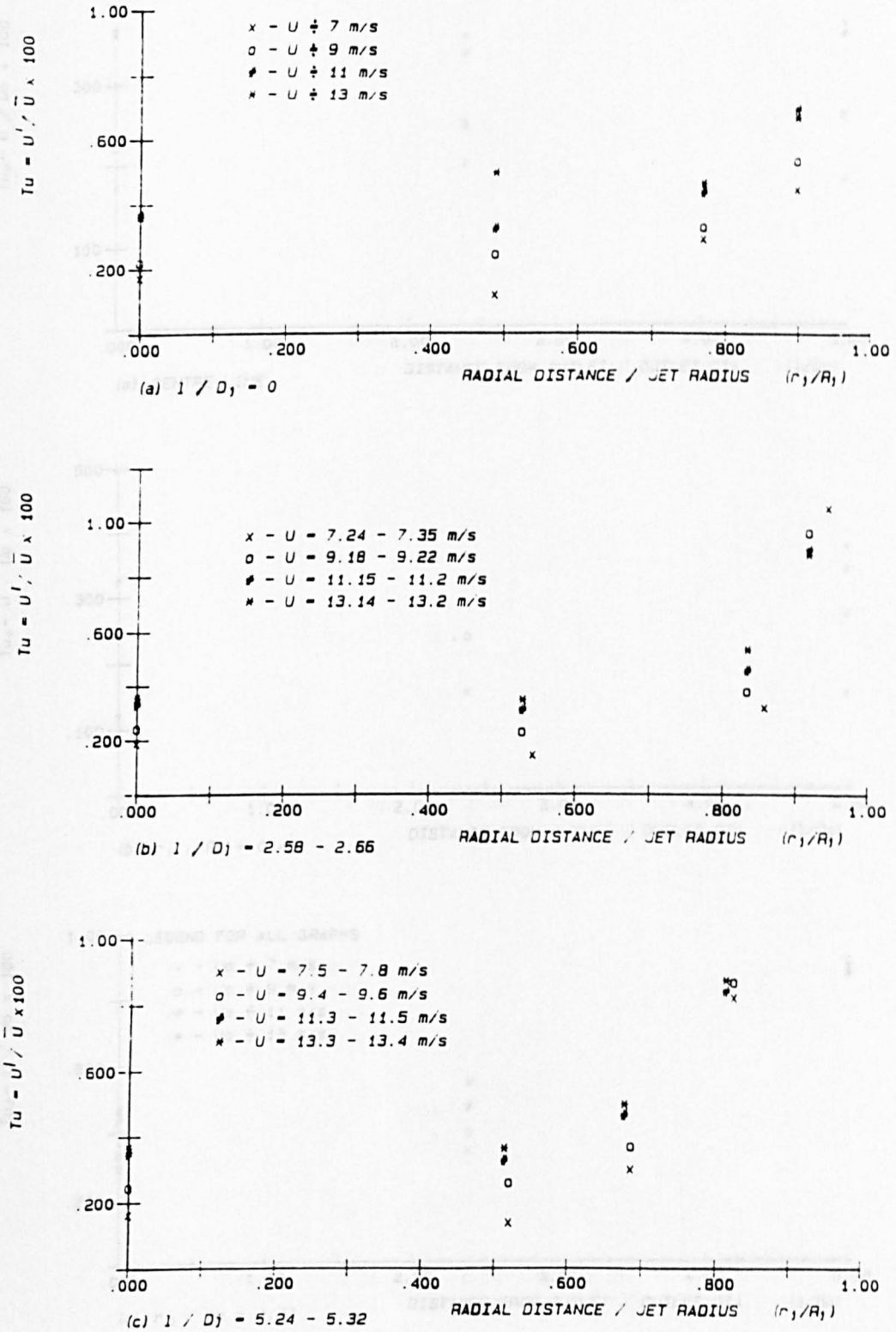

Fig 4.4 Variation of Turbulence intensity (Tu%) in Radial direction (r_j / R_j).[Nozzle: D_0=78mm]

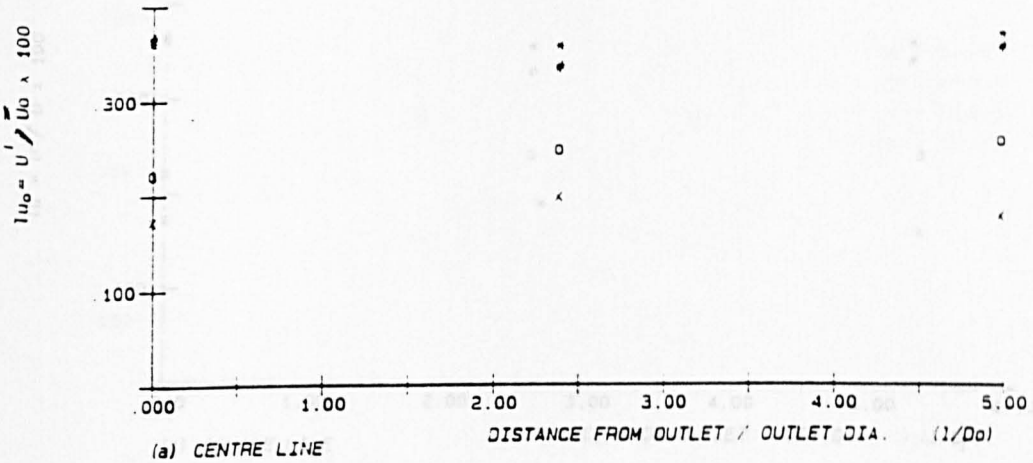

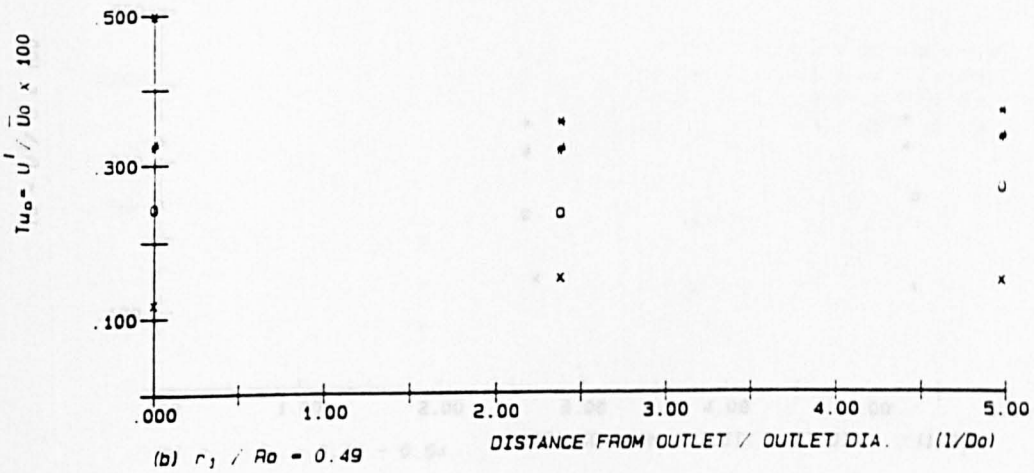

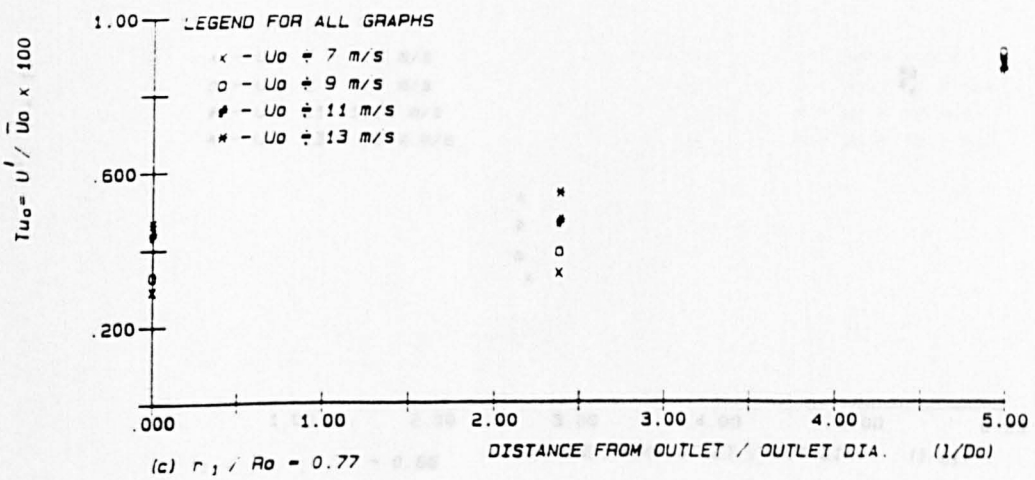

Fig 4.5 Variation of Turbulence intensity (Tu%) in Longitudinal direction (L / D_0).[Nozzle: D_0=78mm]

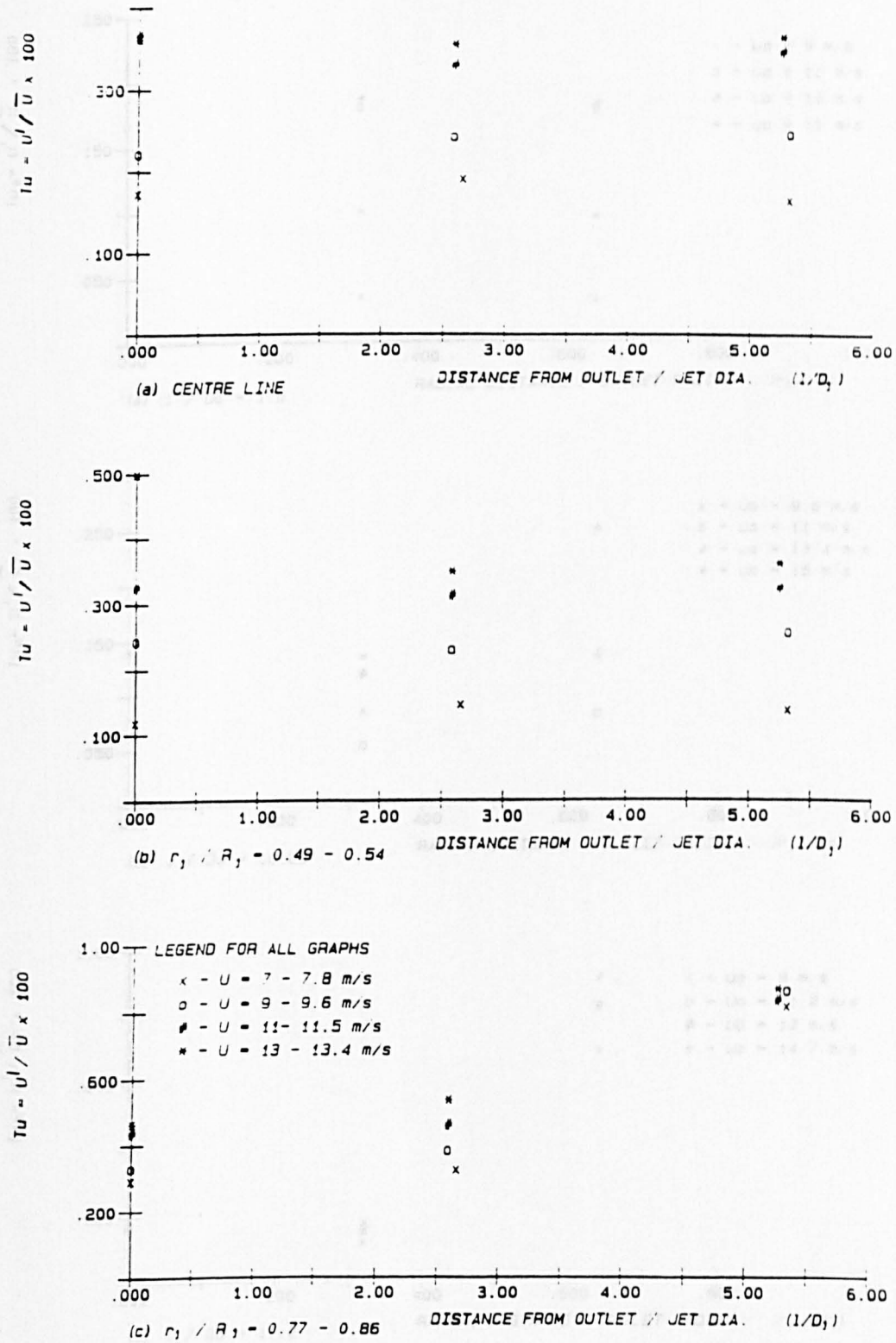

Fig 4.6 Variation of Turbulence intensity (Tu%) in Longitudinal direction (L / D_0).[Nozzle: D_0=78mm]

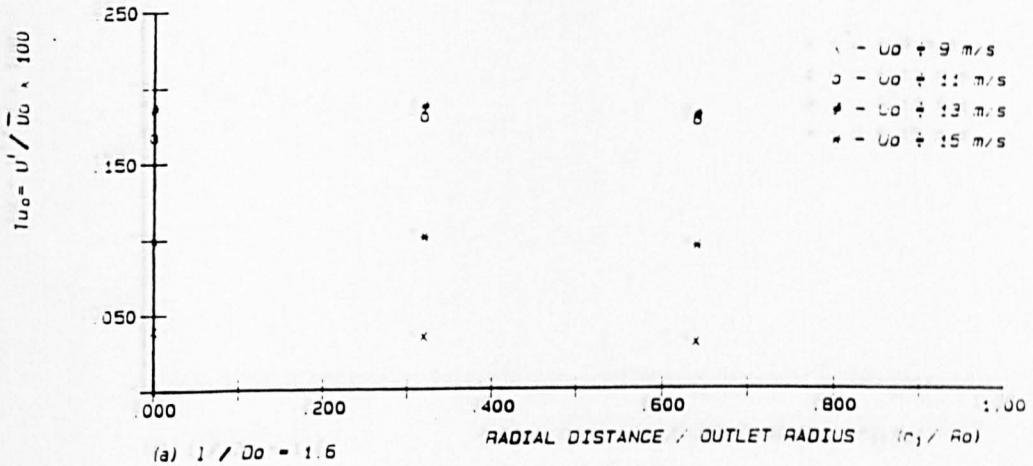

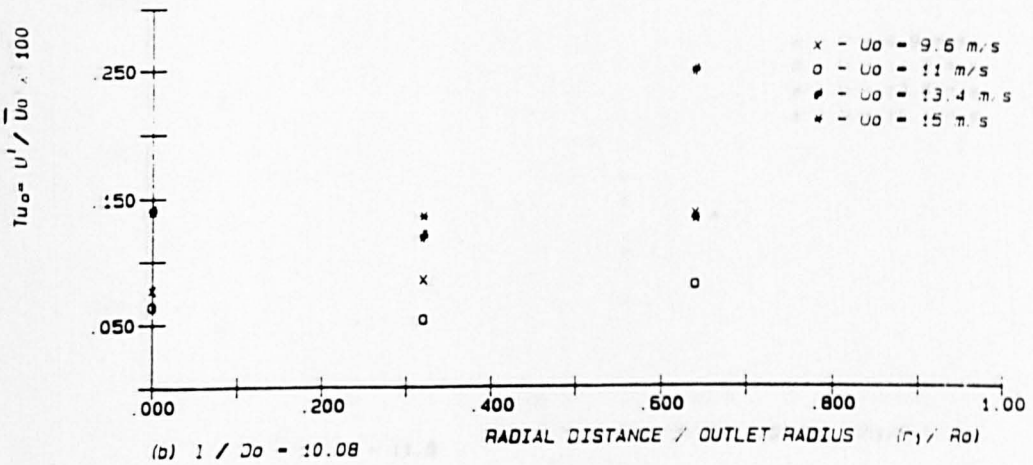

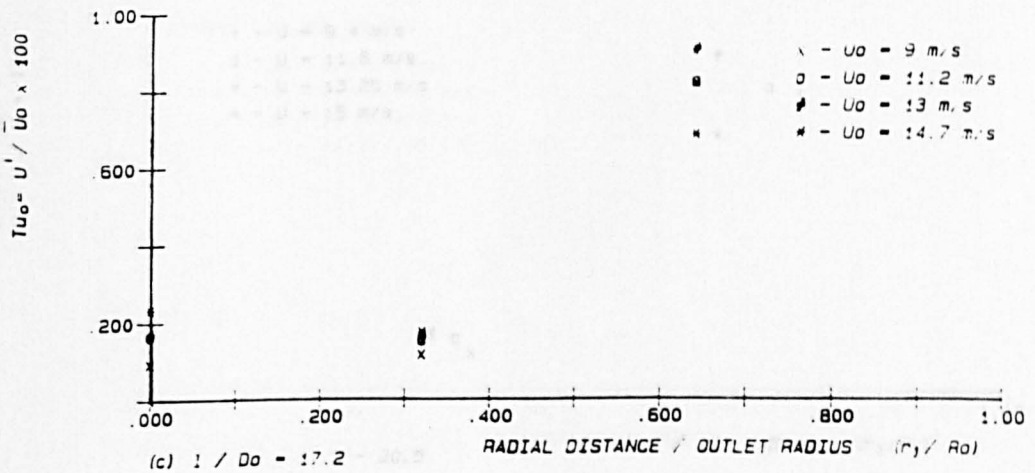

Fig 4.7 Variation of Turbulence intensity (Tu%) in Radial direction (r_j / R_j).[Nozzle: D_0=25mm]

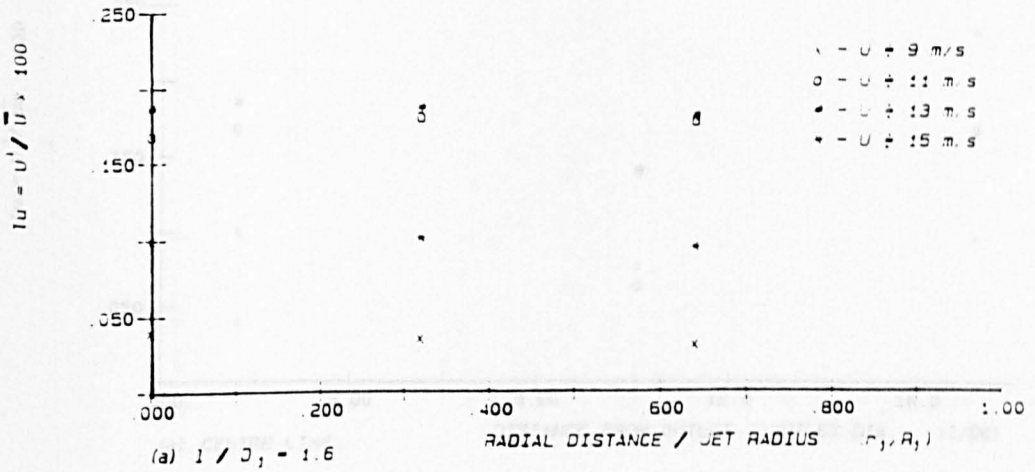

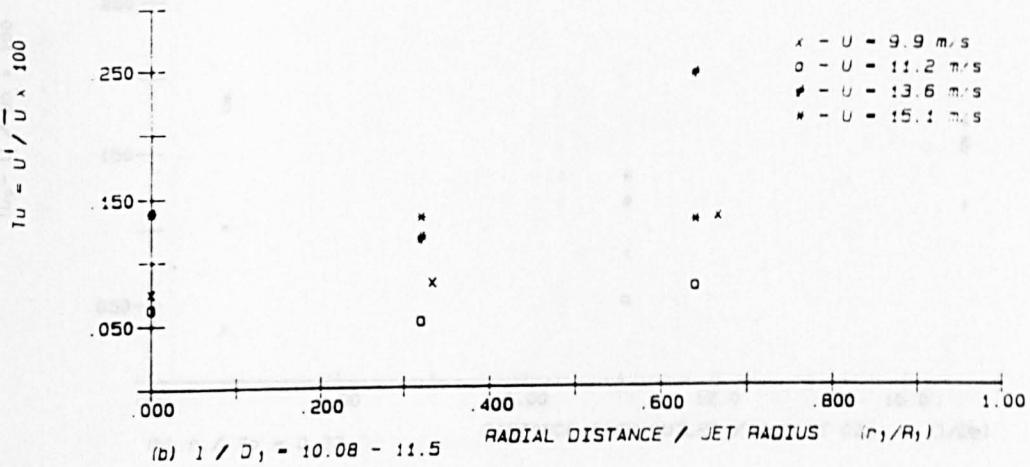

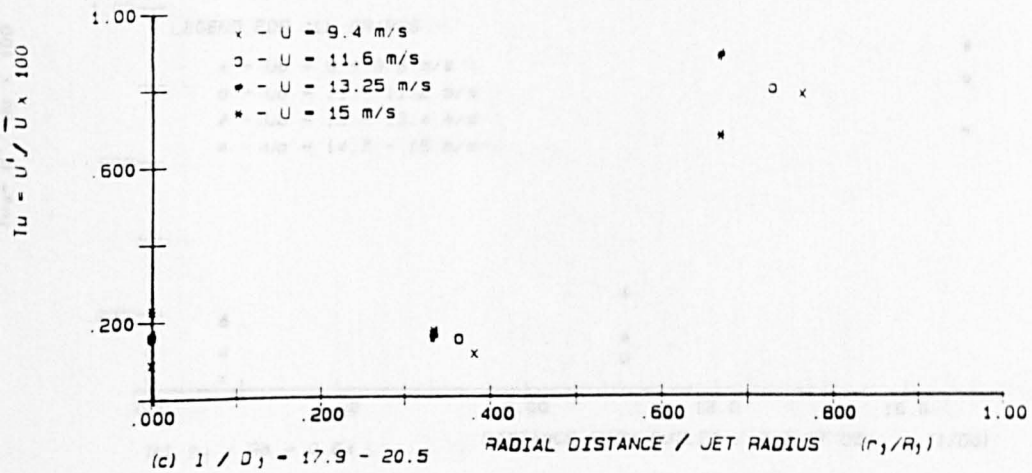

Fig 4.8 Variation of Turbulence intensity (Tu%) in Radial direction (r_j / R_j).[Nozzle: D_0=25mm]

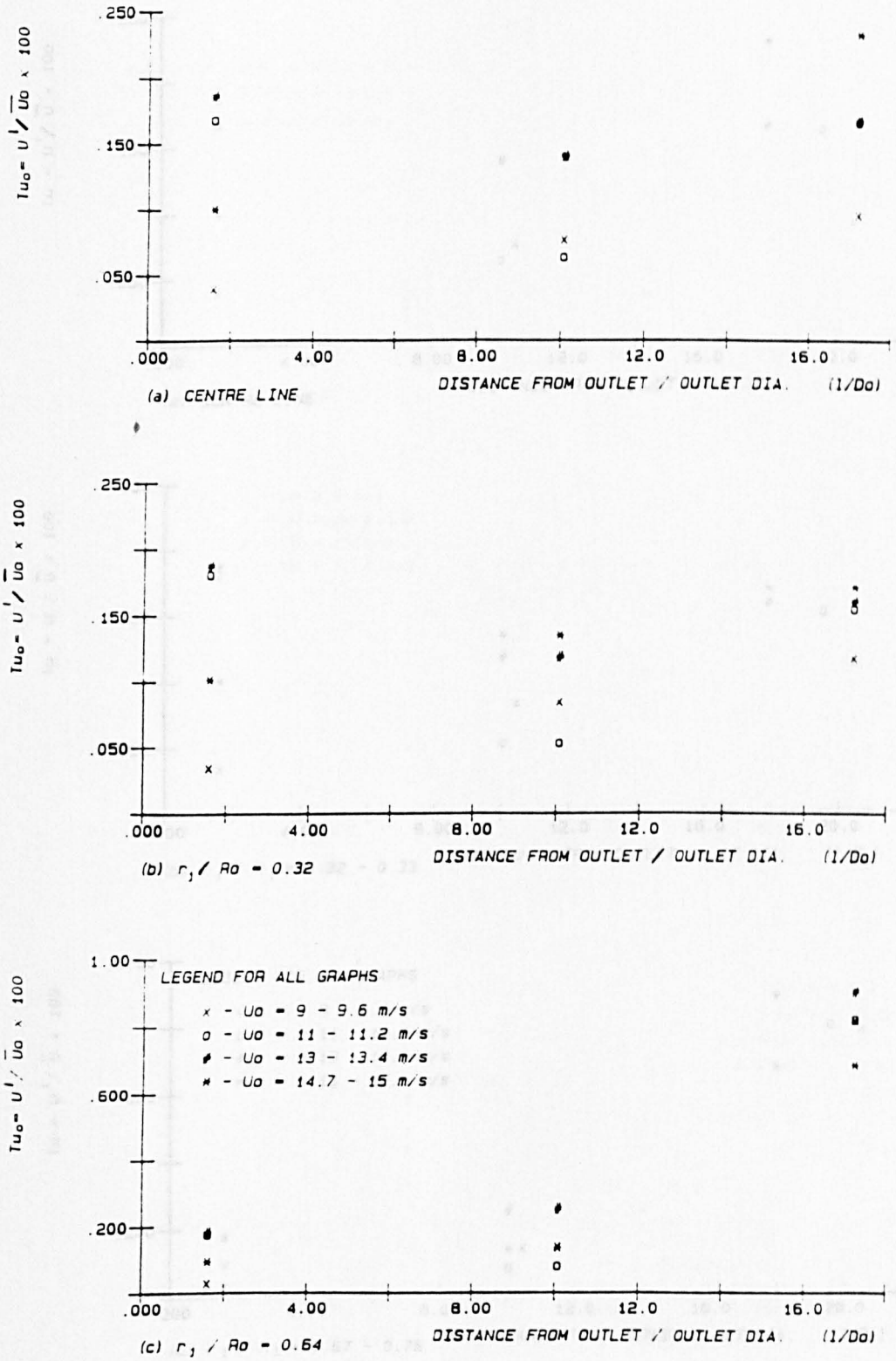

Fig 4.9 Variation of Turbulence intensity (Tu%) in Longitudinal direction (L / D_0).[Nozzle: D_0=25mm]

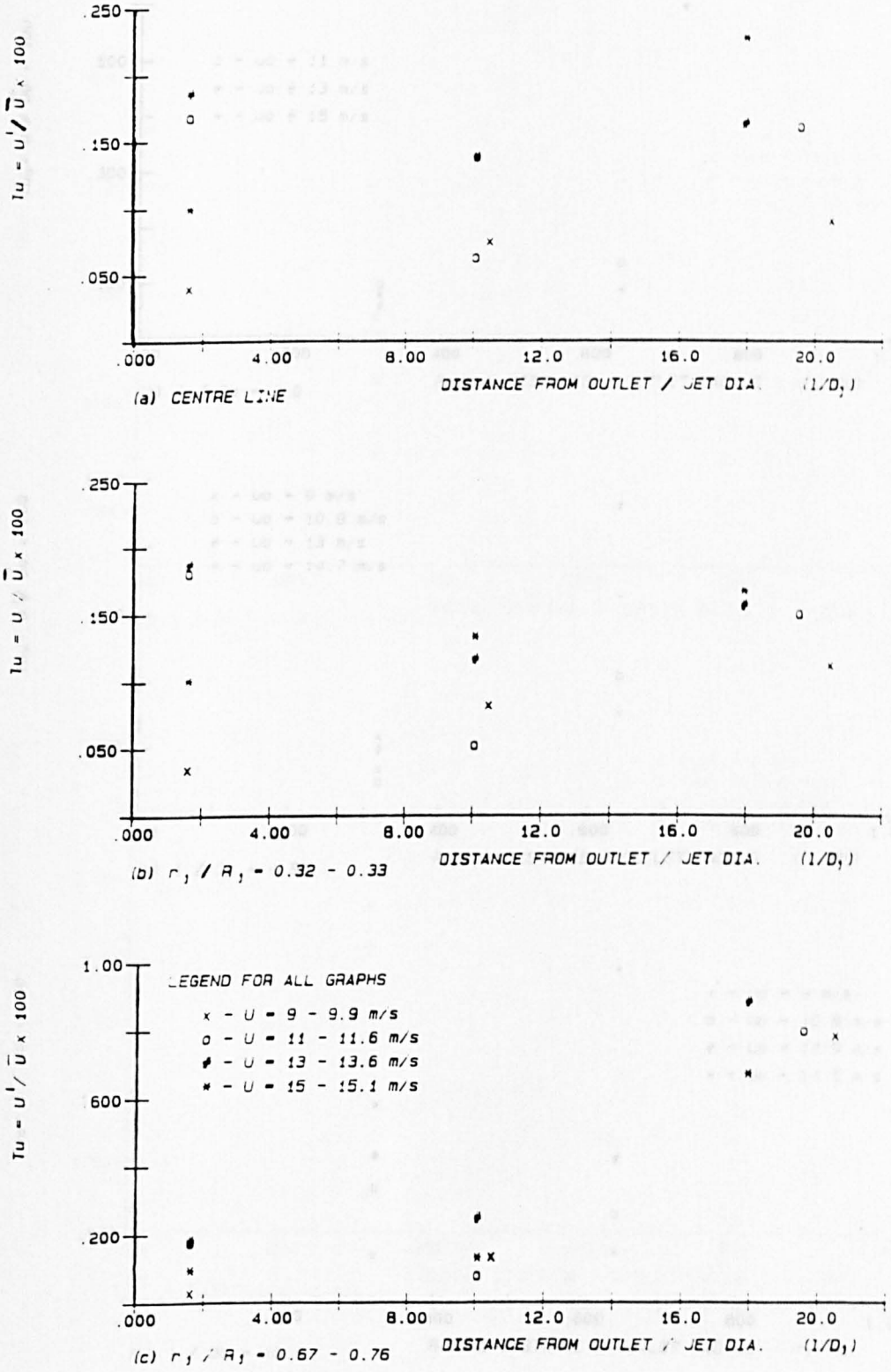

Fig 4.10 Variation of Turbulence intensity (Tu%) in Longitudinal direction (L / D_0).[Nozzle: D_0=25mm]

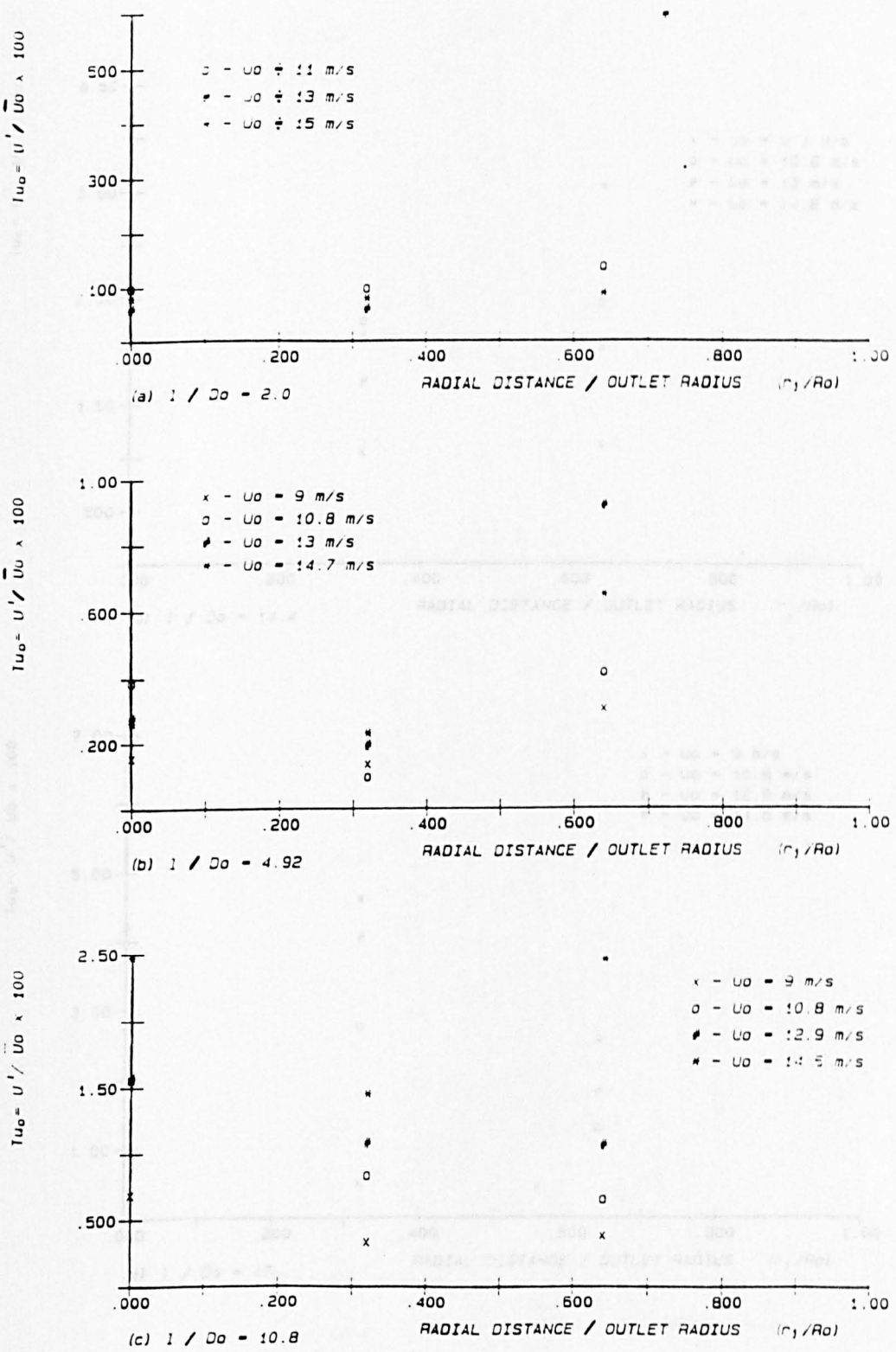

Fig 4.11(a) Variation of Turbulence intensity (Tu%) in Radial direction (r_j / R_j).[Orifice: D_0=25mm]

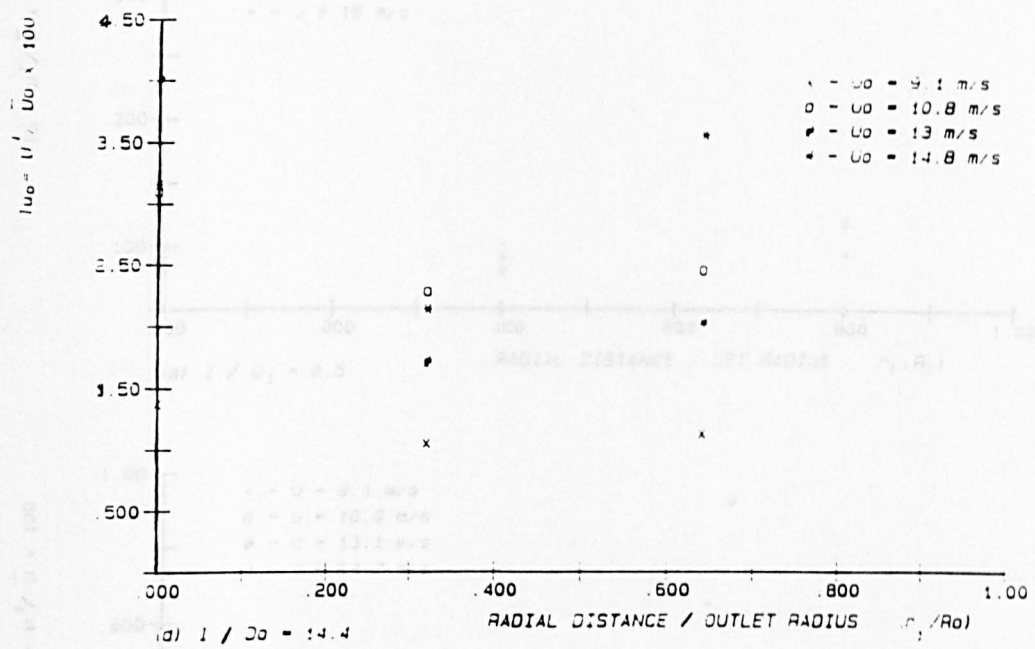

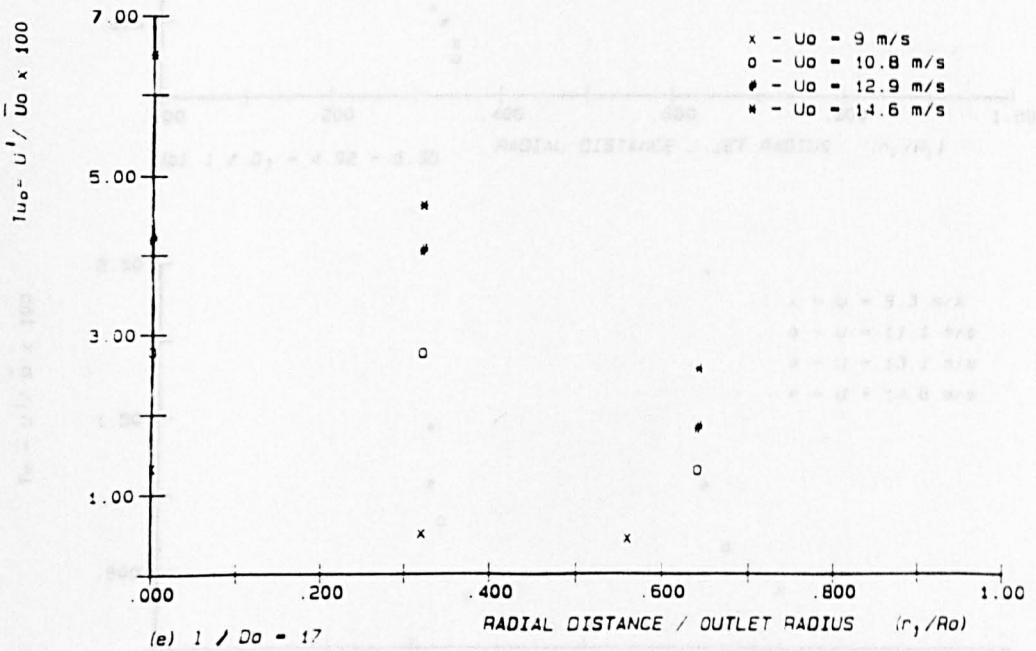

Fig 4.11(b) Variation of Turbulence intensity (Tu%) in Radial direction (r_j / R_j).[Orifice: D_0=25mm]

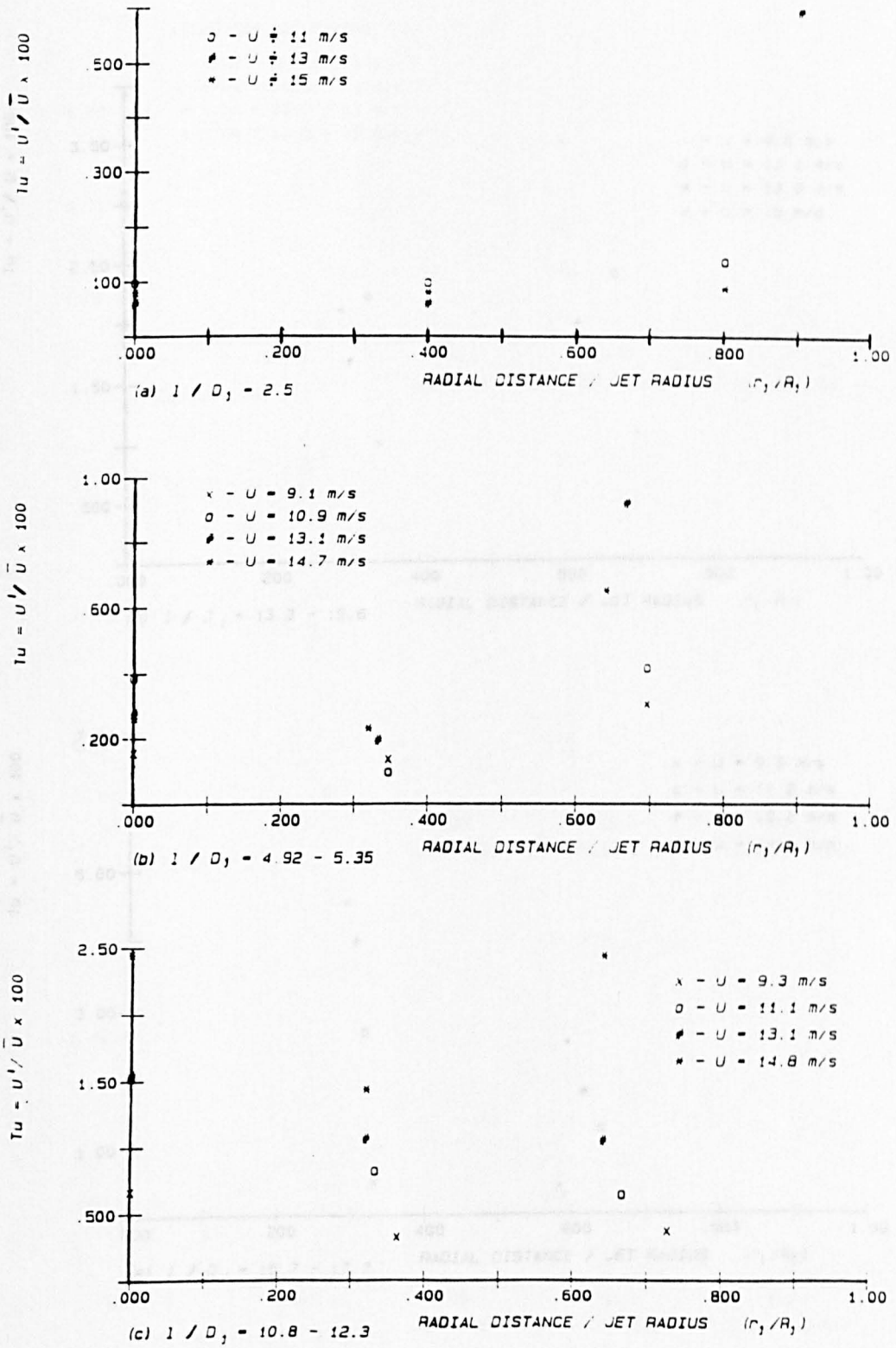

Fig 4.12(a) Variation of Turbulence intensity (Tu%) in Radial direction (r_j / R_j).[Orifice: D_0=25mm]

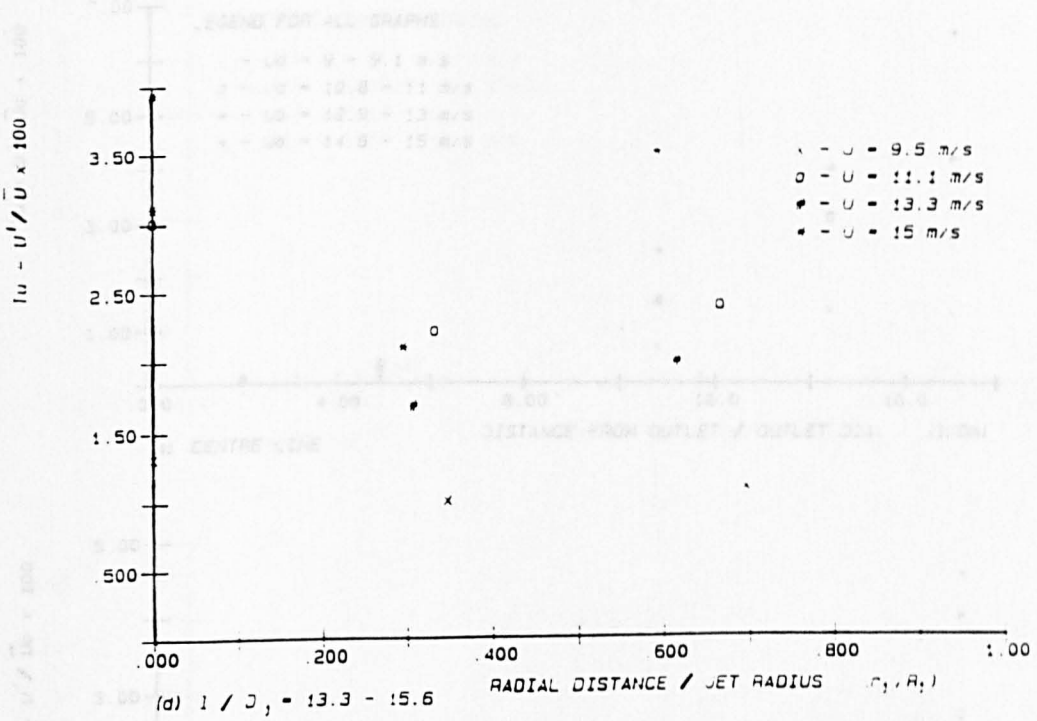

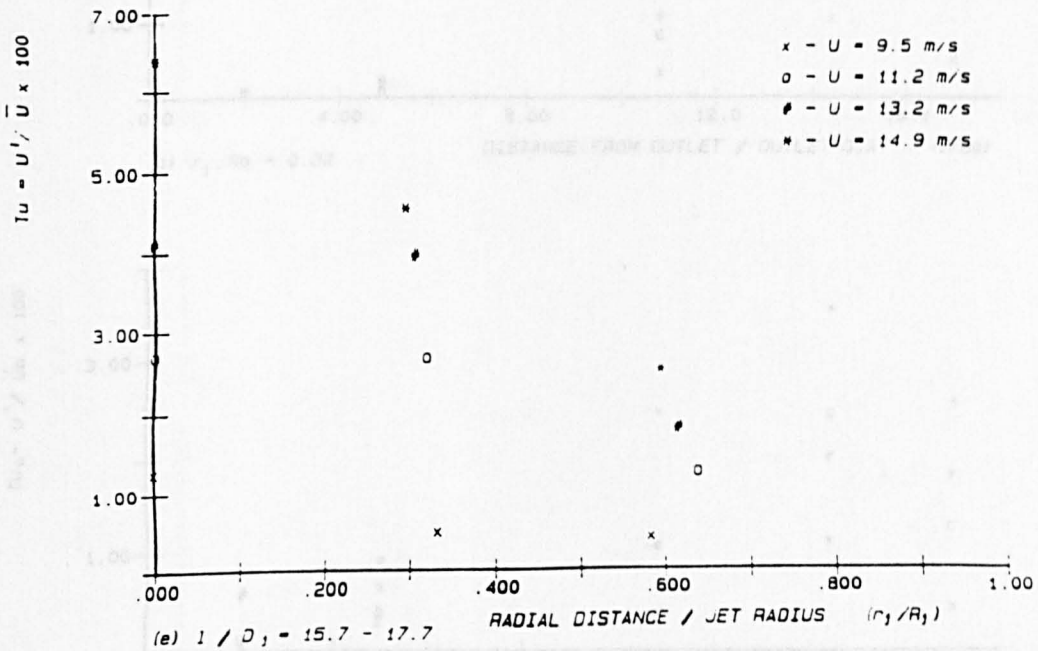

Fig 4.12(b) Variation of Turbulence intensity (Tu%) in Radial direction (r_j / R_j).[Orifice: D_0=25mm]

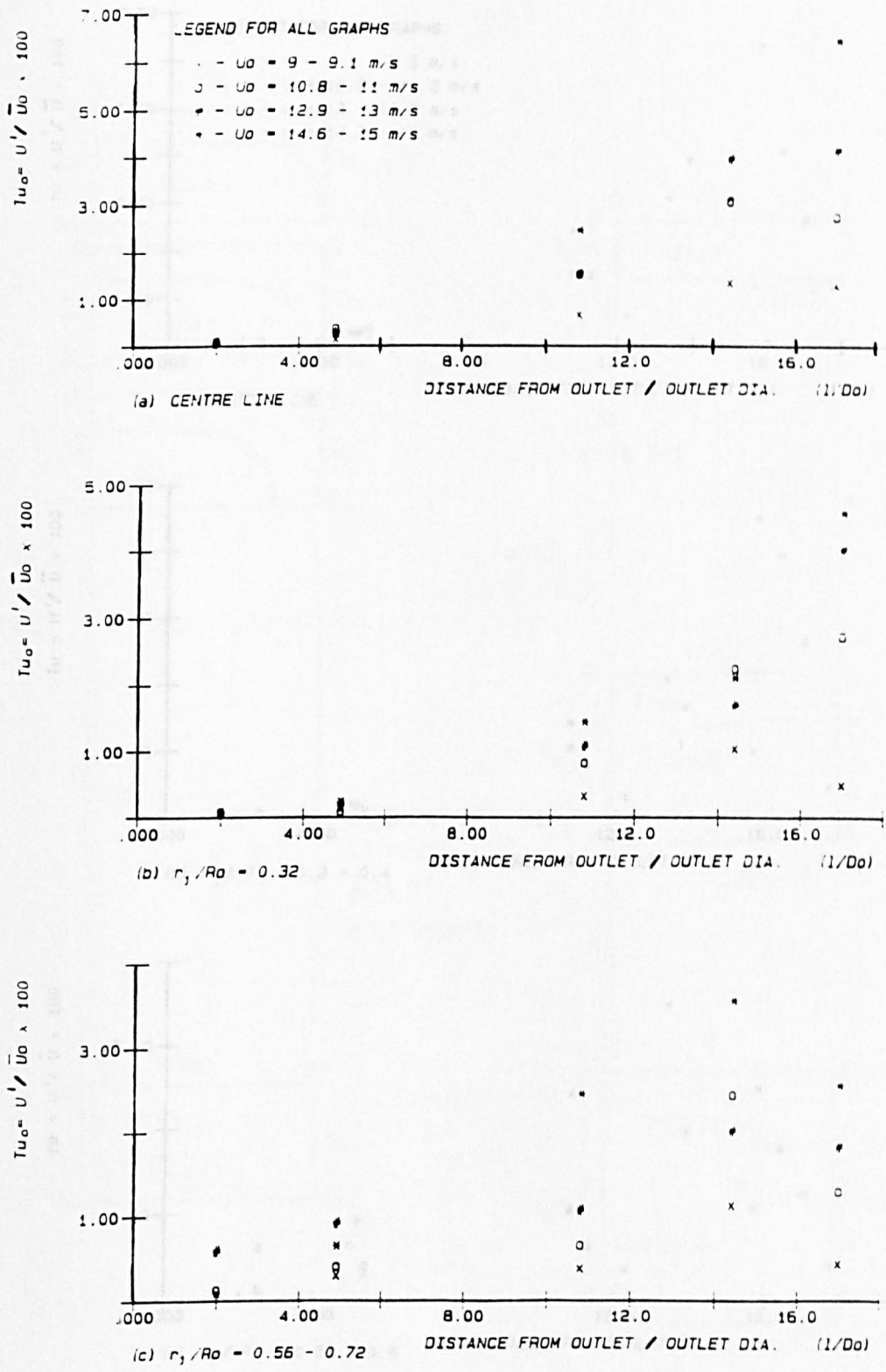

Fig 4.13 Variation of Turbulence intensity (Tu%) in Longitudinal direction (L / D_0).[Orifice: D_0=25mm]

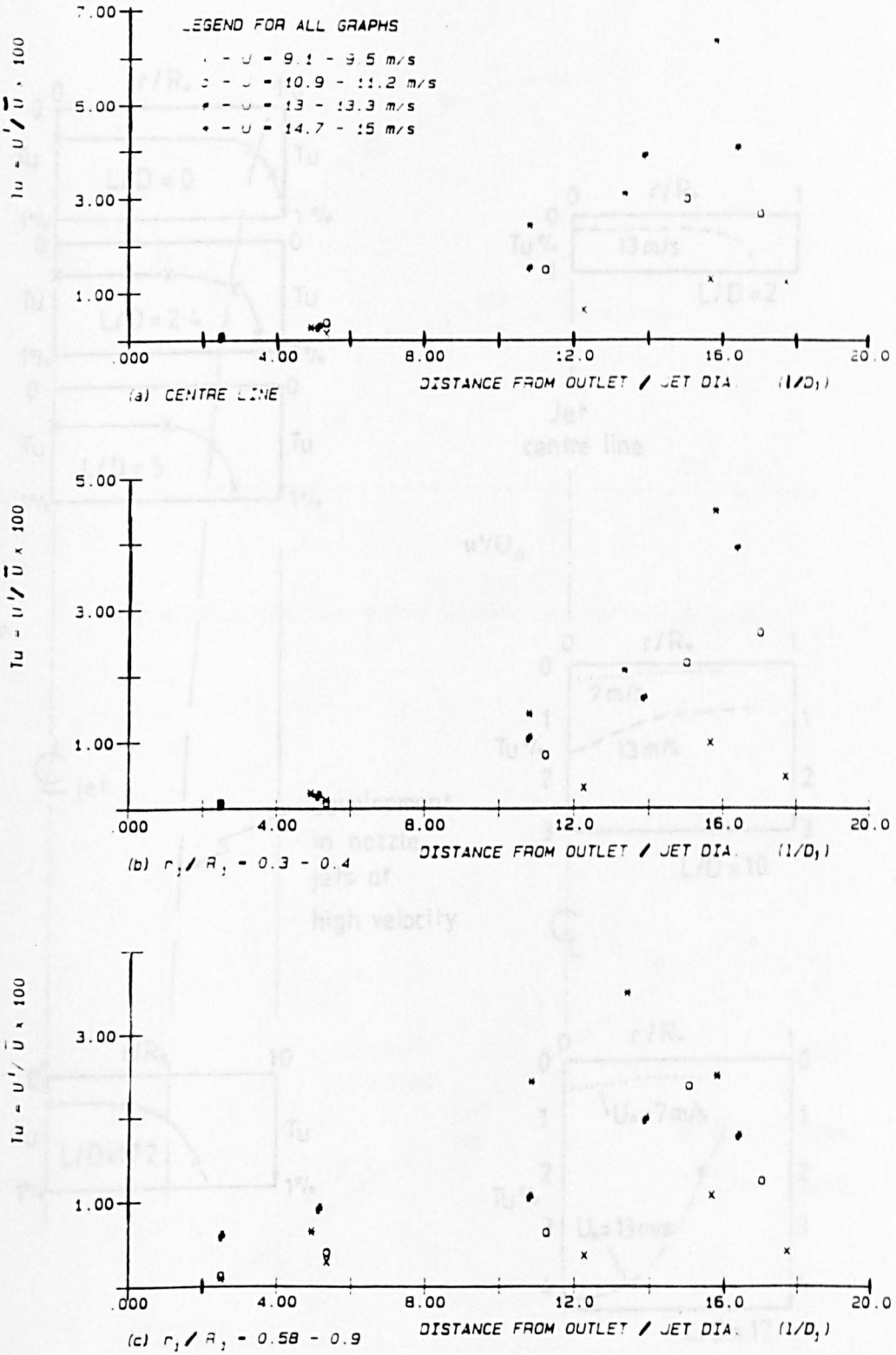

Fig 4.14 Variation of Turbulence intensity (Tu%) in Longitudinal direction (L / D_0).[Orifice: D_0=25mm]

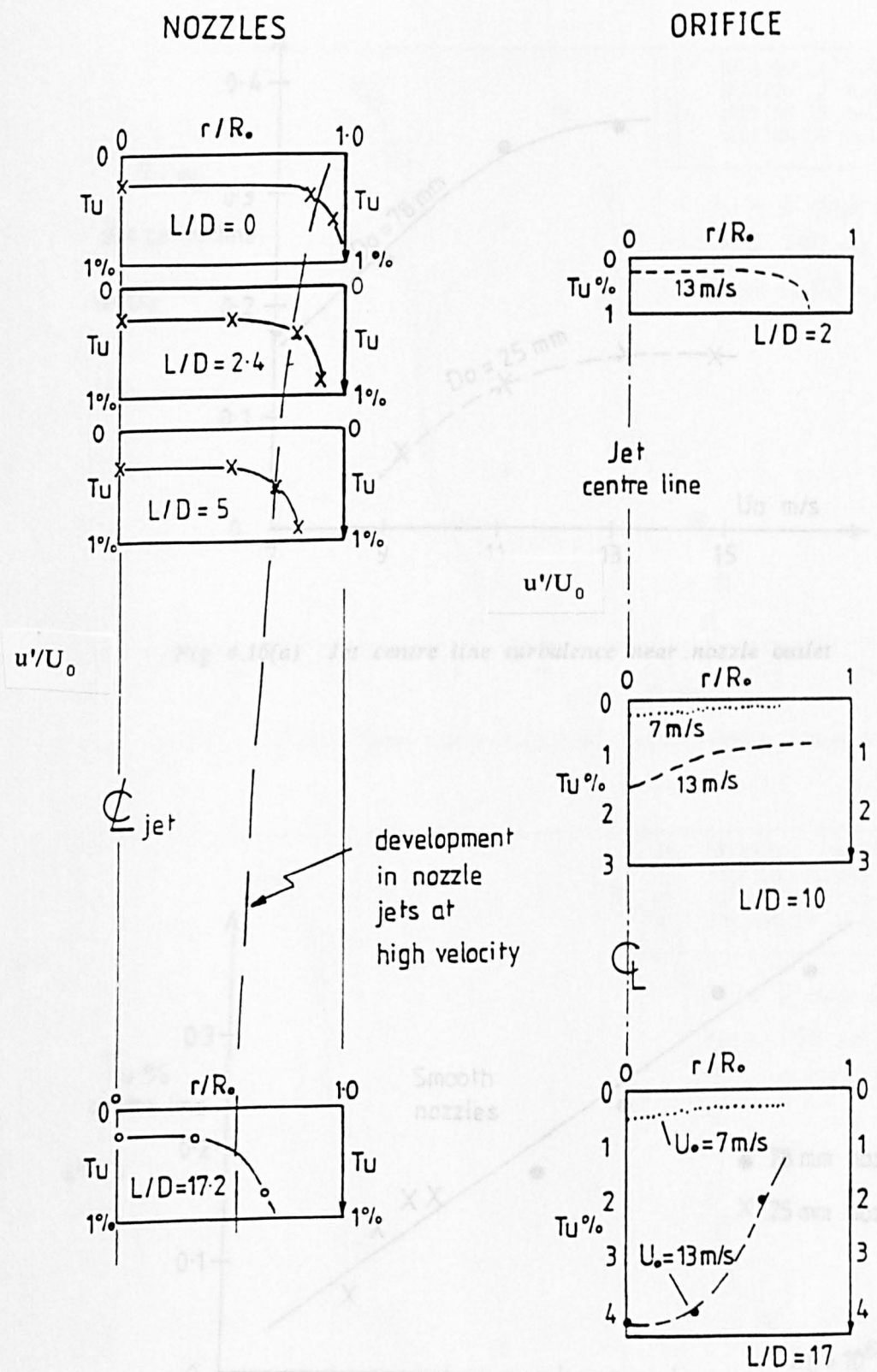

Fig 4.15 Gradual transfer of turbulence towards the jet centre line

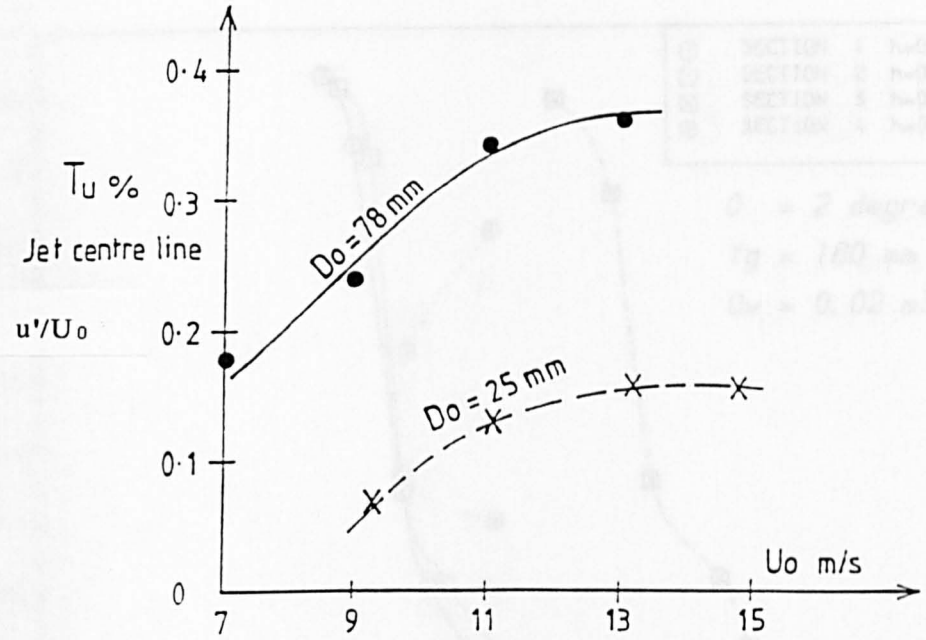

Fig 4.16(a) Jet centre line turbulence near nozzle outlet

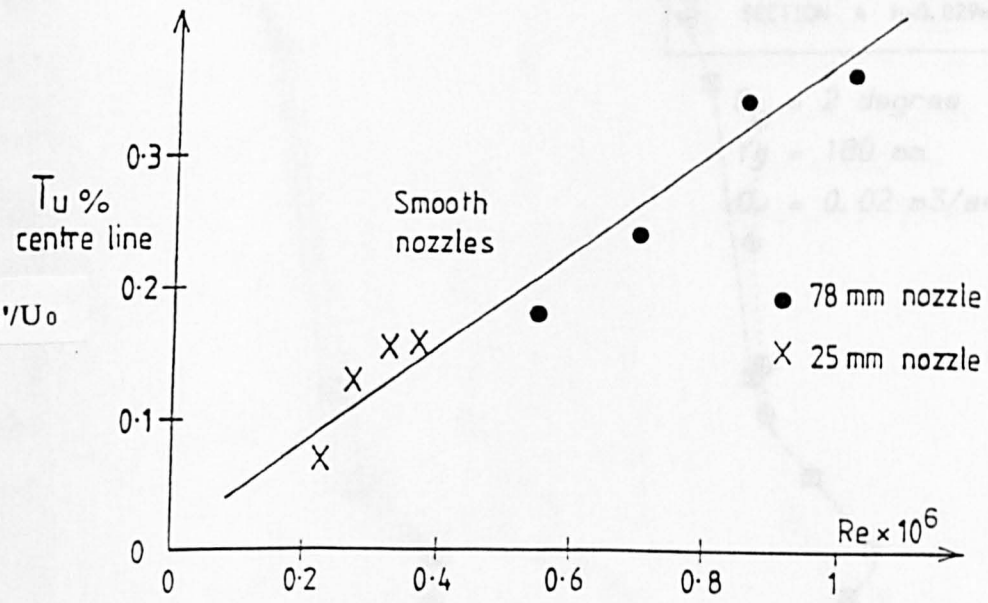

Fig 4.16(b) Jet centre line turbulence near nozzle outlet

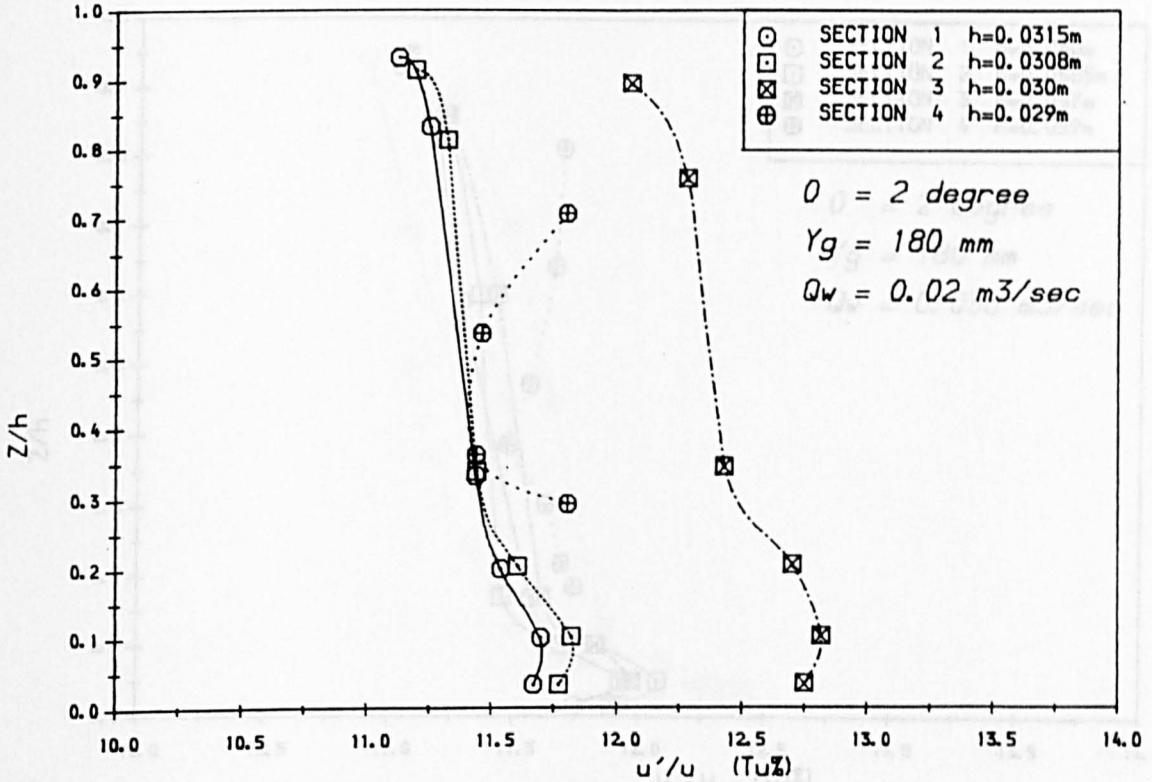

Fig 4.17(a) Mean Longitudinal Turbulence Intensities

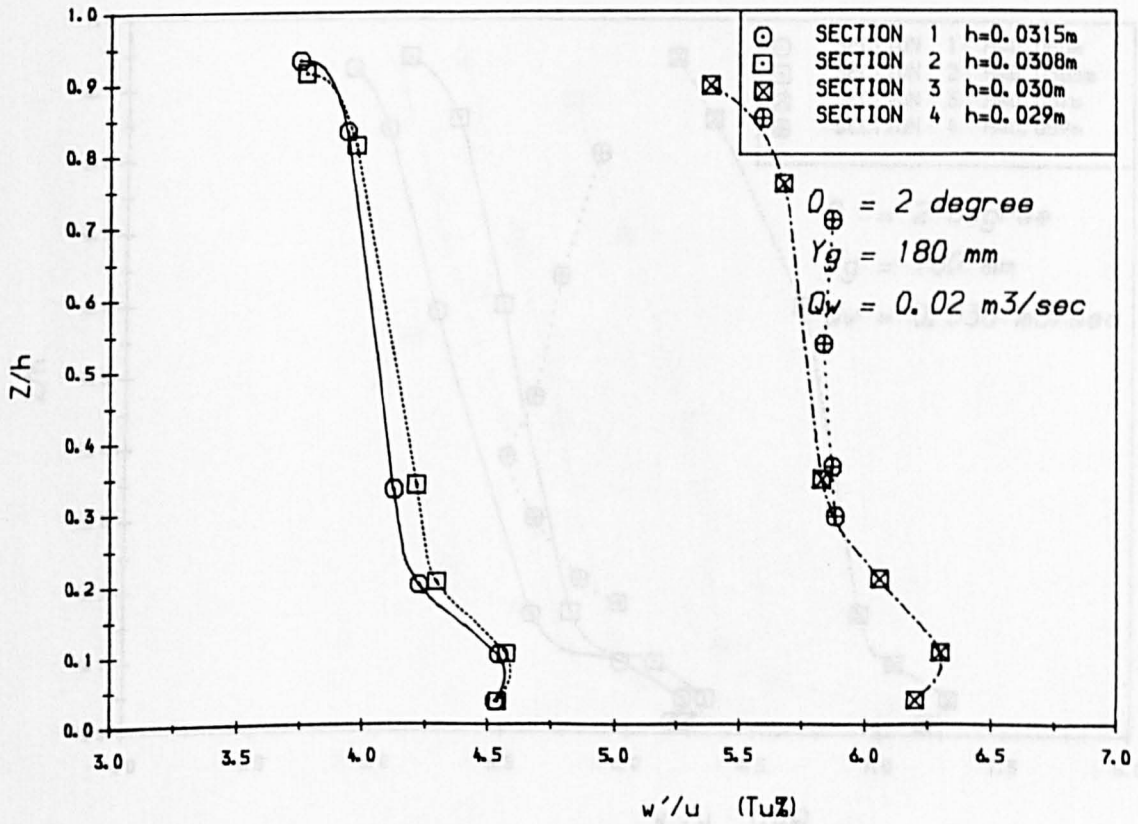

Fig 4.17(b) Mean Vertical Turbulence Intensities

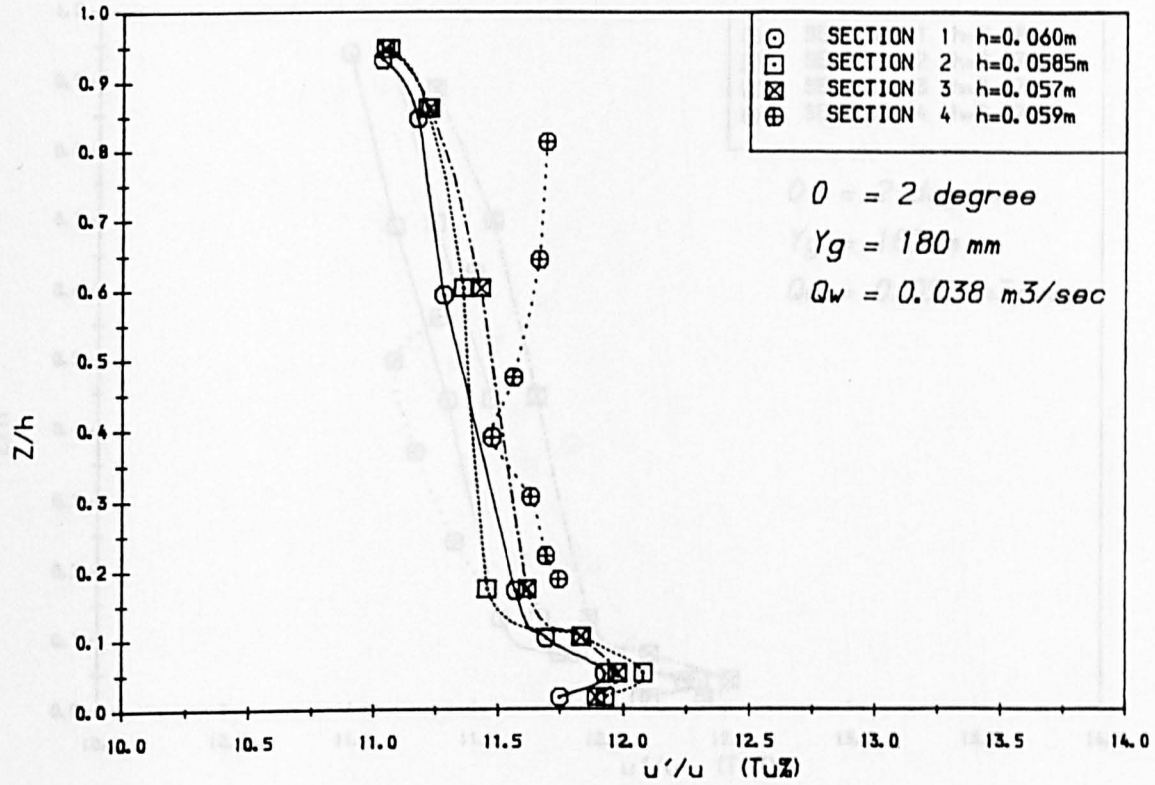

Fig 4.18(a) Mean Longitudinal Turbulence Intensities

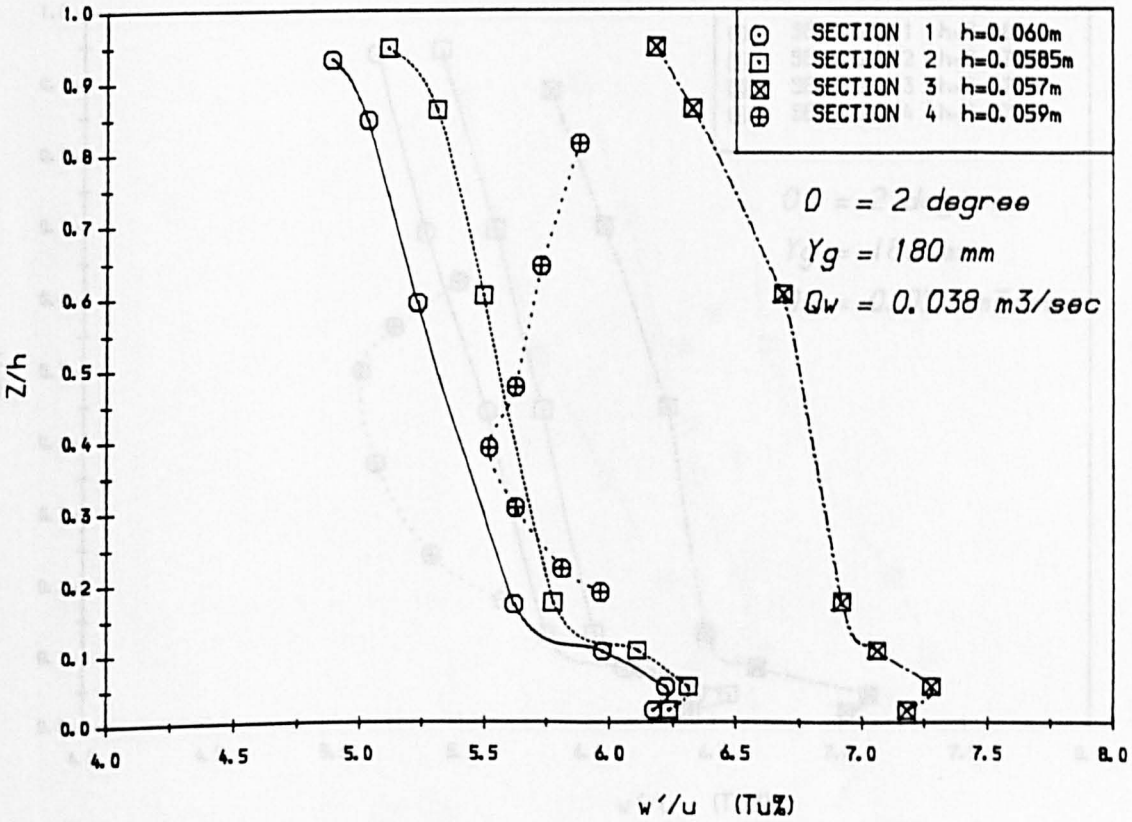

Fig 4.18(b) Mean Vertical Turbulence Intensities

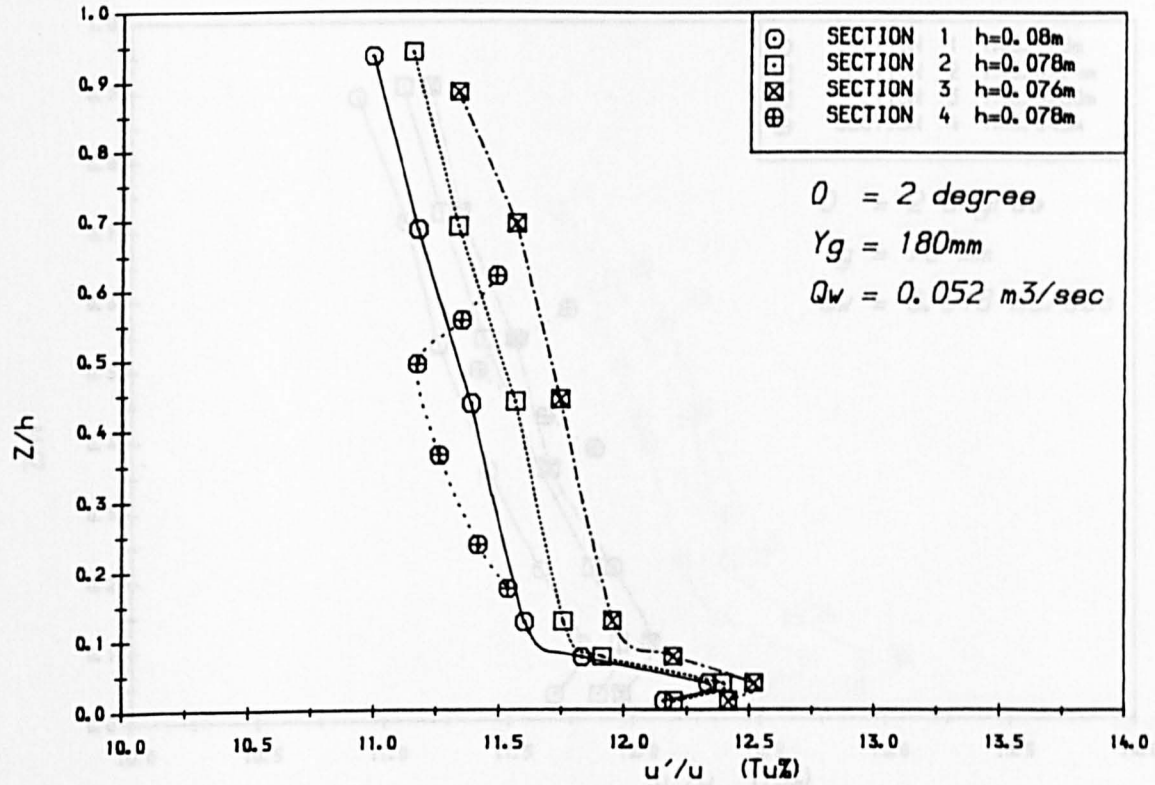

Fig 4.19(a) Mean Longitudinal Turbulence Intensities

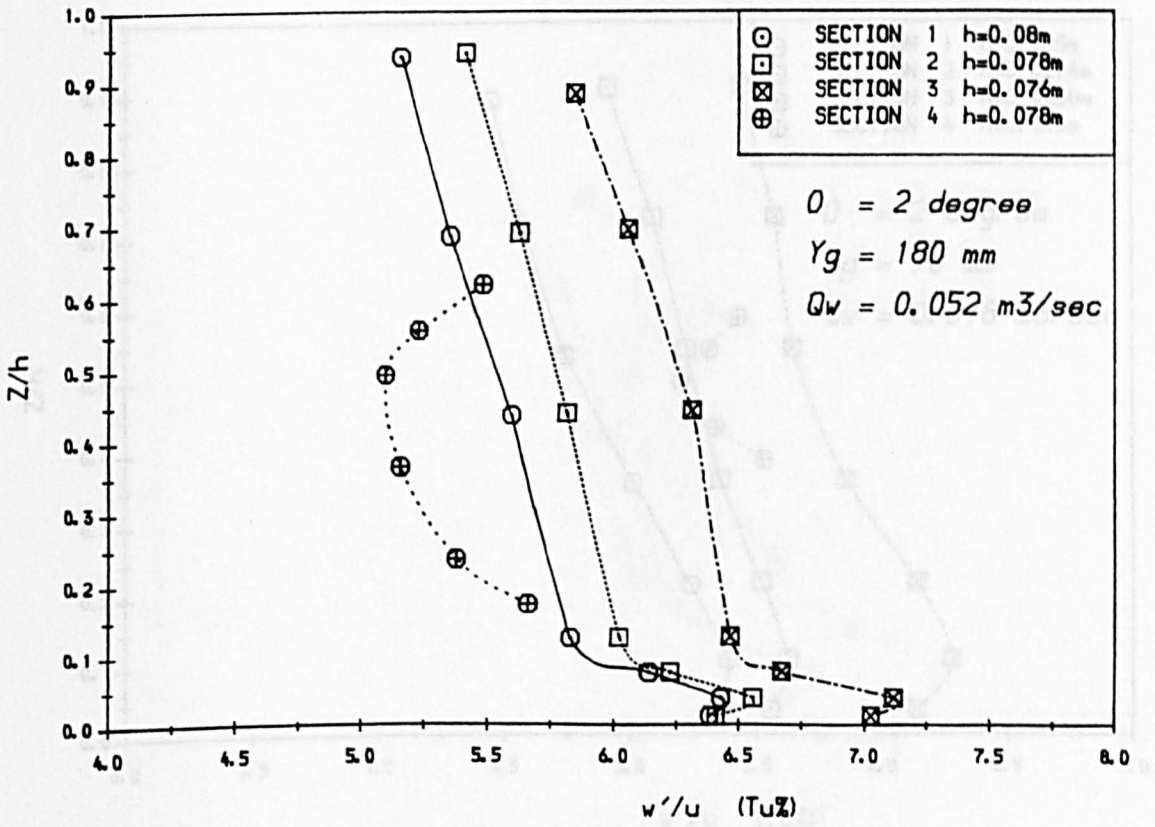

Fig 4.19(b) Mean Vertical Turbulence Intensities

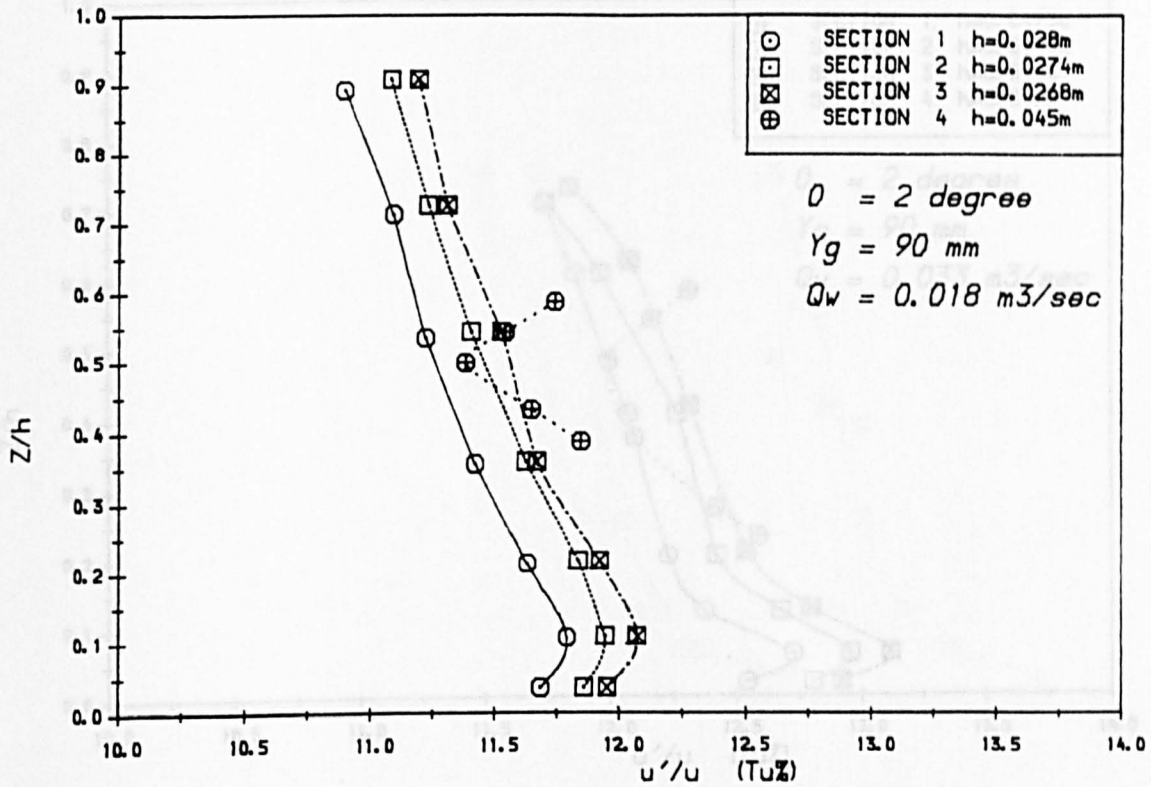

Fig 4.20(a) Mean Longitudinal Turbulence Intensities

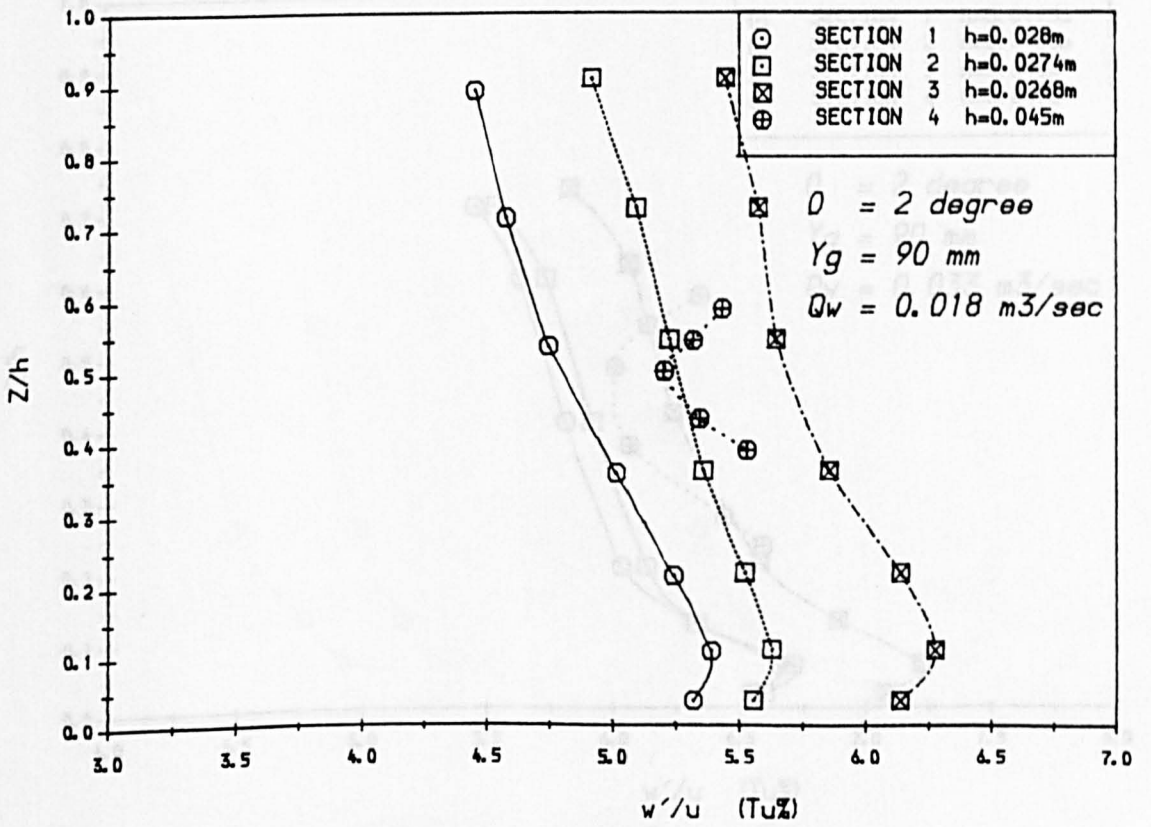

Fig 4.20(b) Mean Vertical Turbulence Intensities

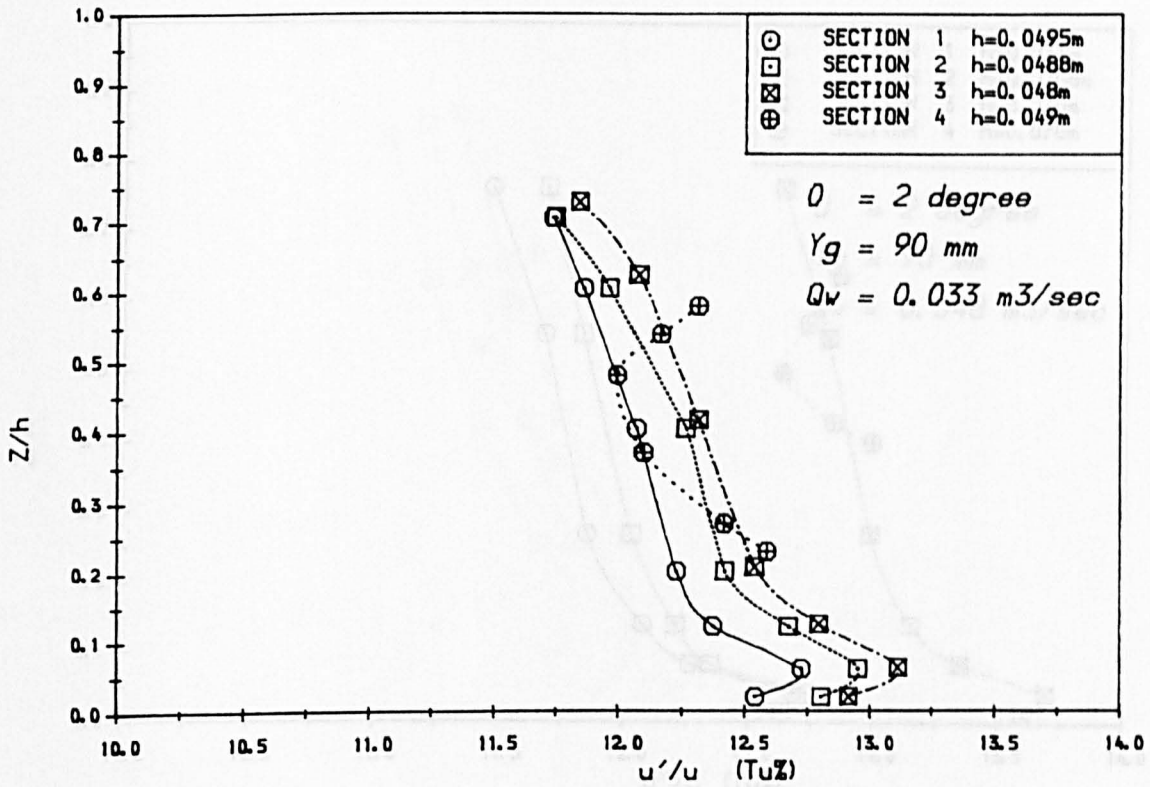

Fig 4.21 (a) Mean Longitudinal Turbulence Intensities

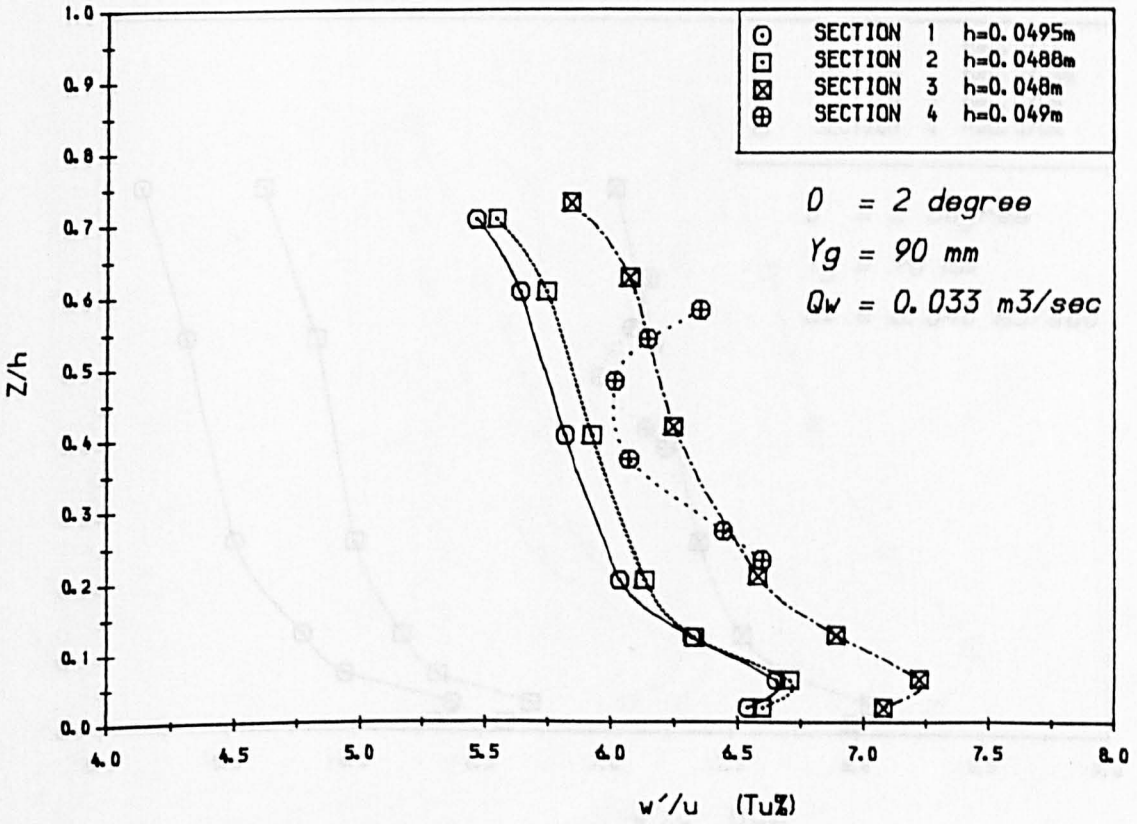

Fig 4.21 (b) Mean Vertical Turbulence Intensities

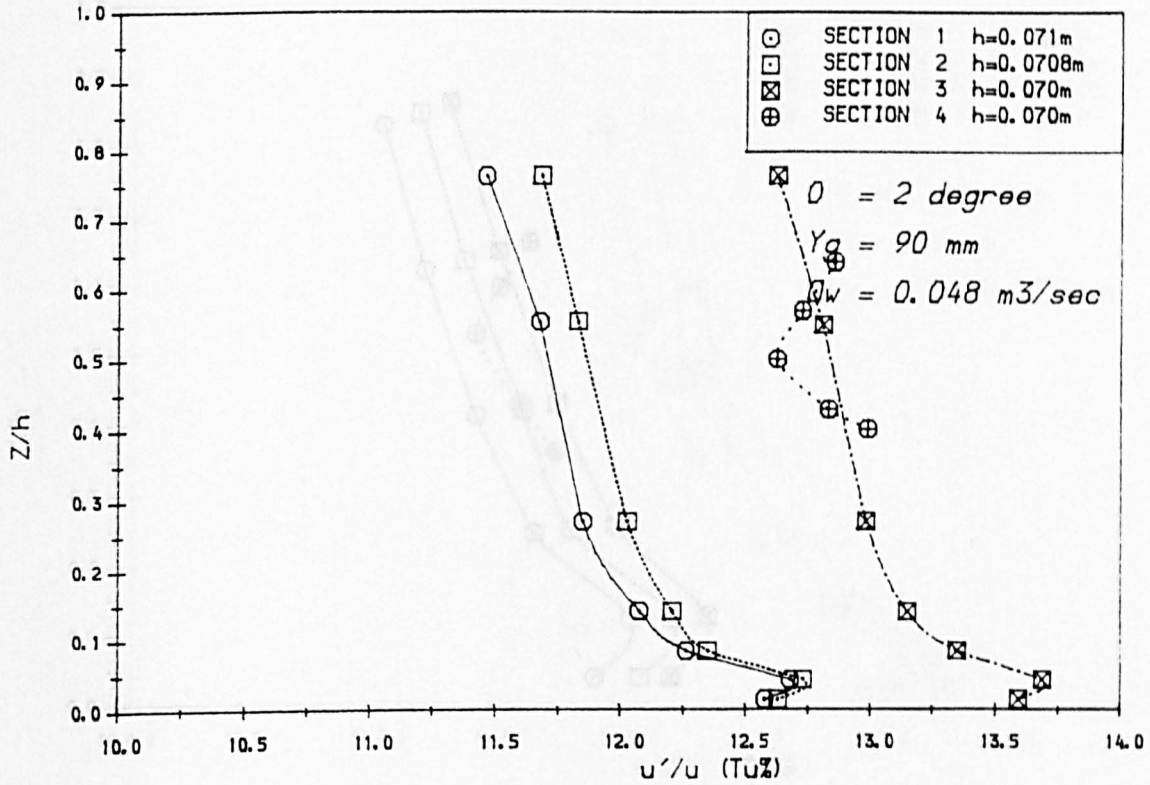

Fig 4.22(a) Mean Longitudinal Turbulence Intensities

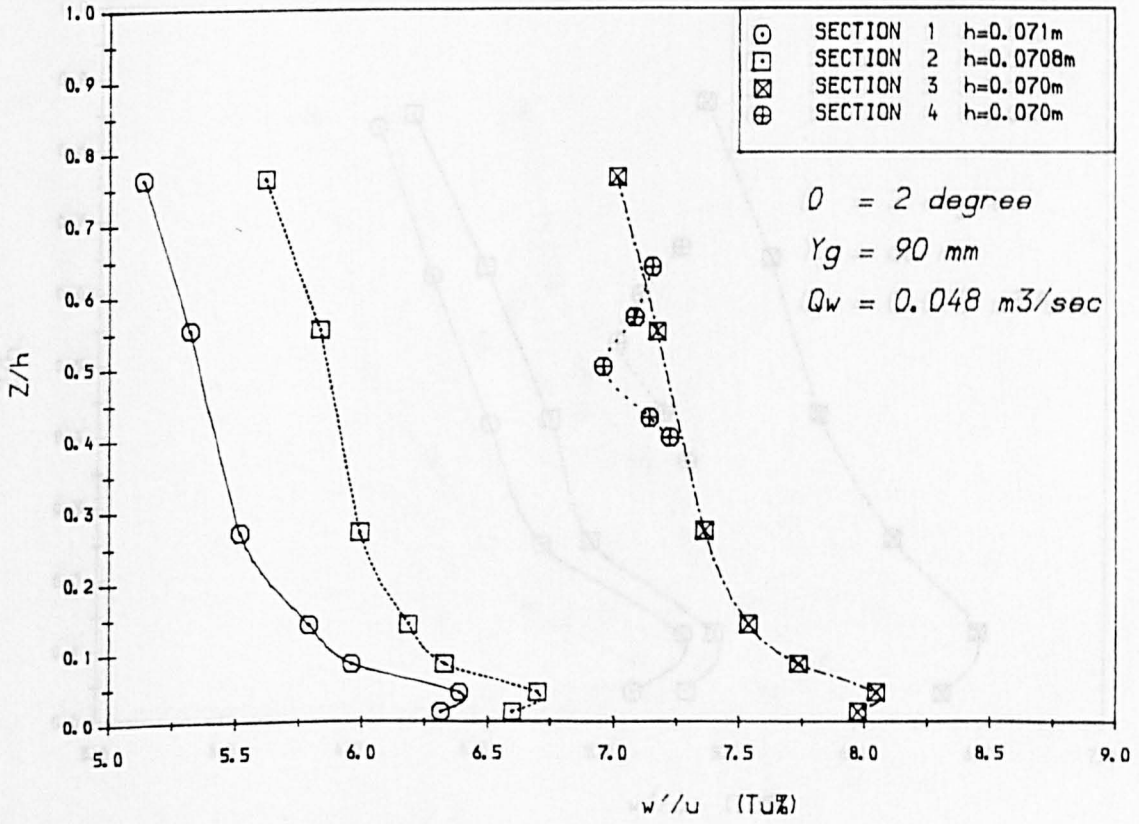

Fig 4.22(b) Mean Vertical Turbulence Intensities

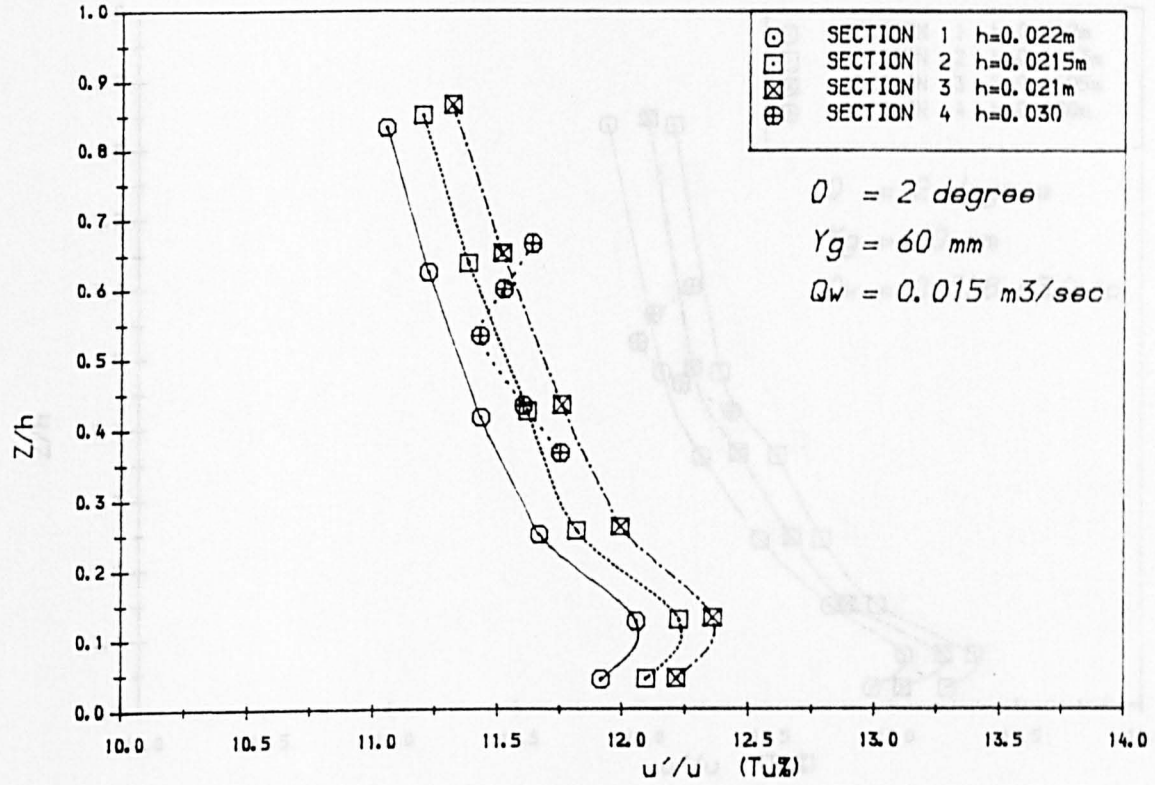

Fig 4.23(a) Mean Longitudinal Turbulence Intensities

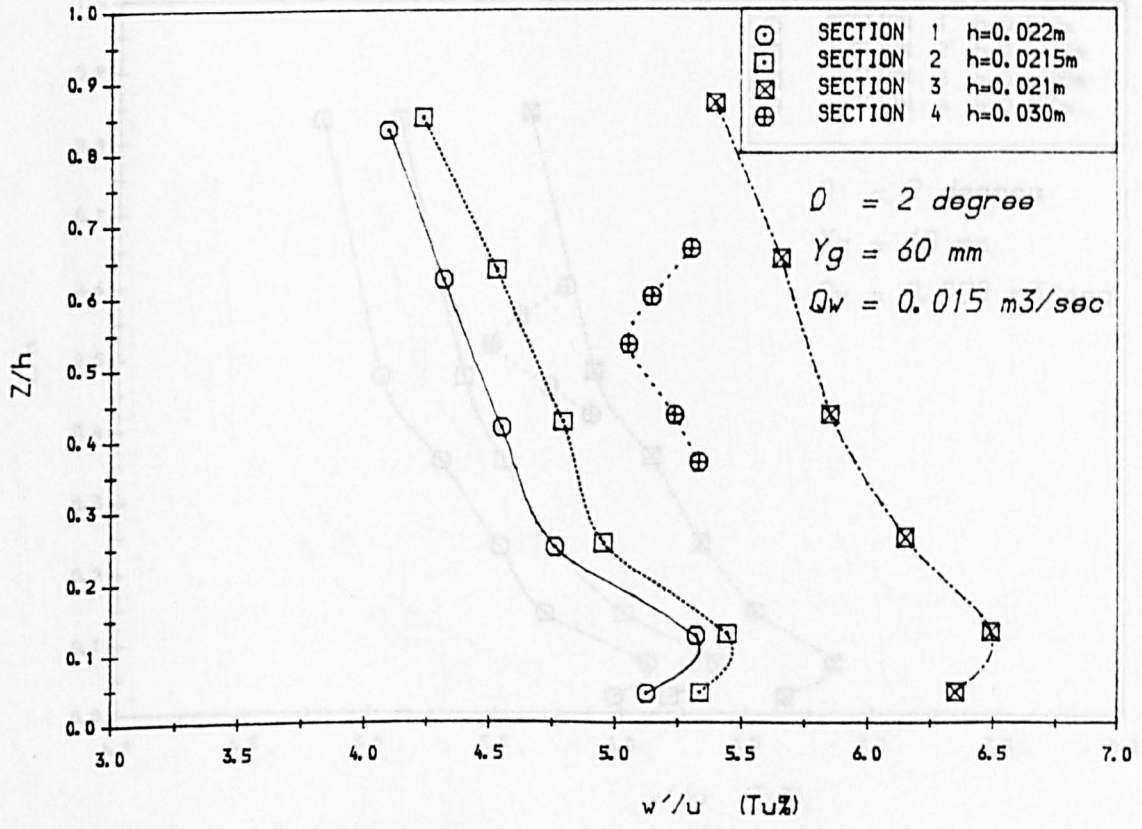

Fig 4.23(b) Mean Vertical Turbulence Intensities

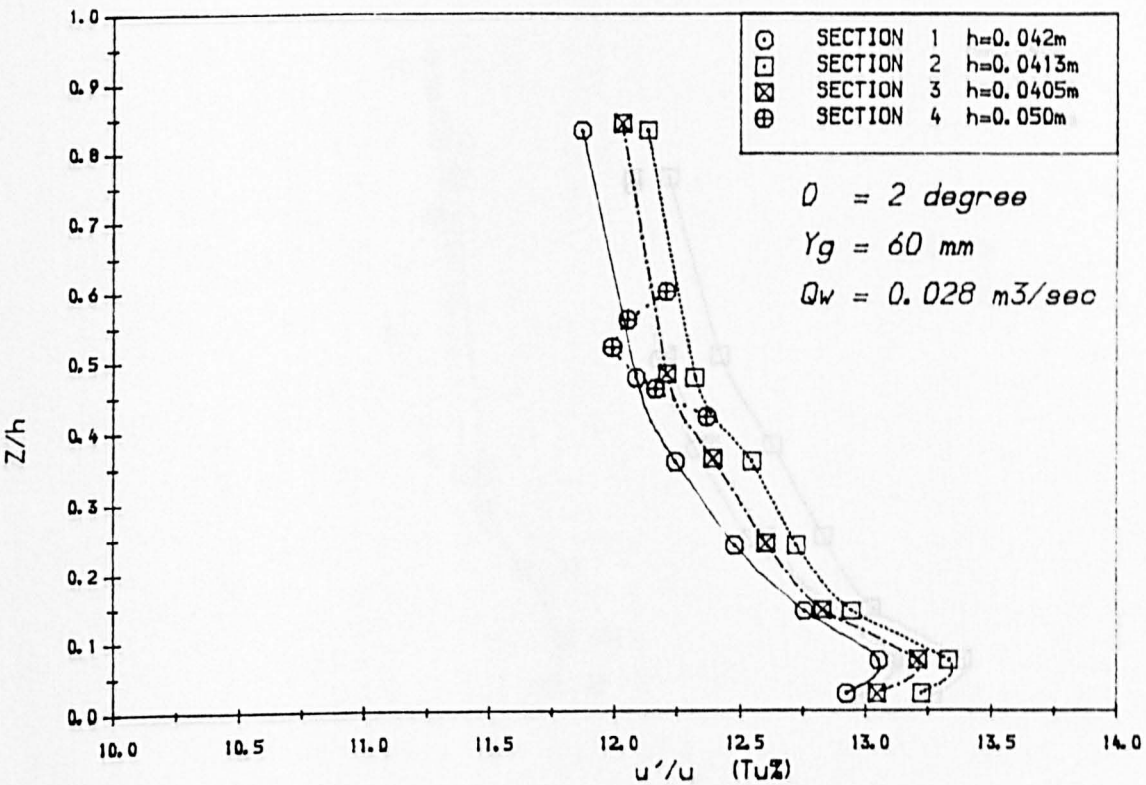

Fig 4.24 (a) Mean Longitudinal Turbulence Intensities

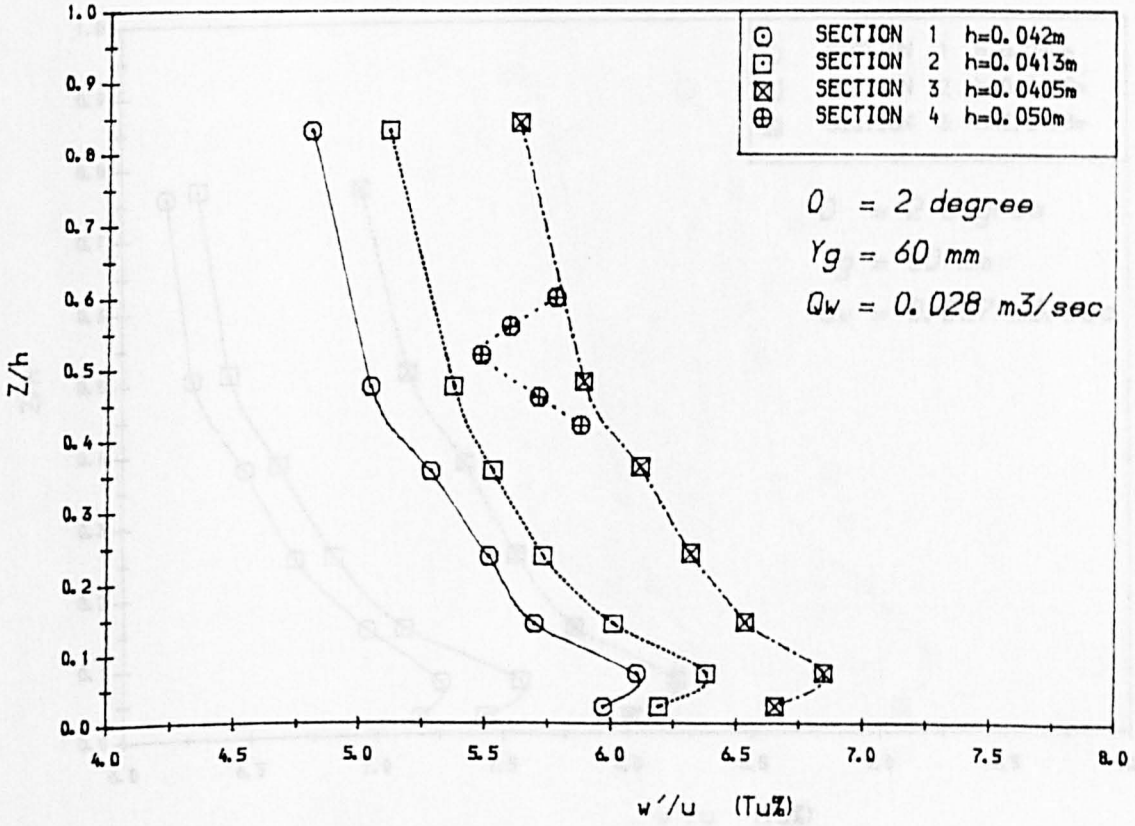

Fig 4.24 (b) Mean Vertical Turbulence Intensities

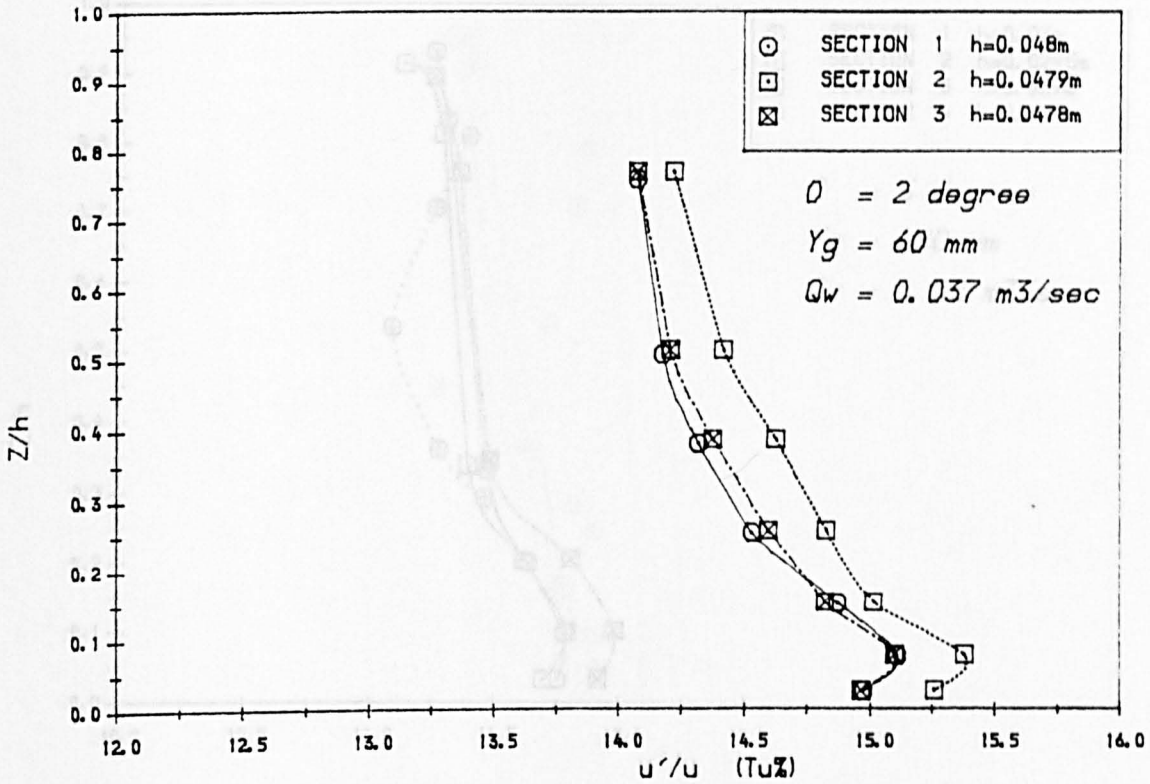

Fig 4.25(a) Mean Longitudinal Turbulence Intensities

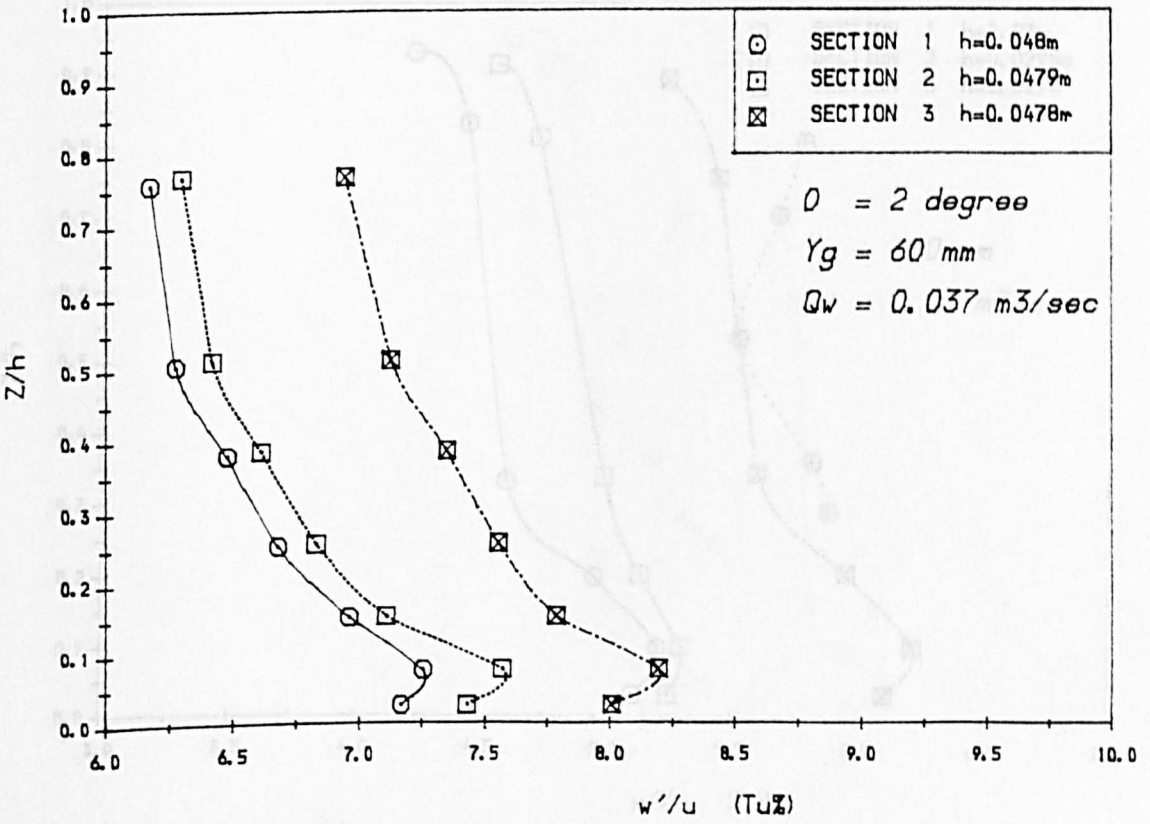

Fig 4.25(b) Mean Vertical Turbulence Intensities

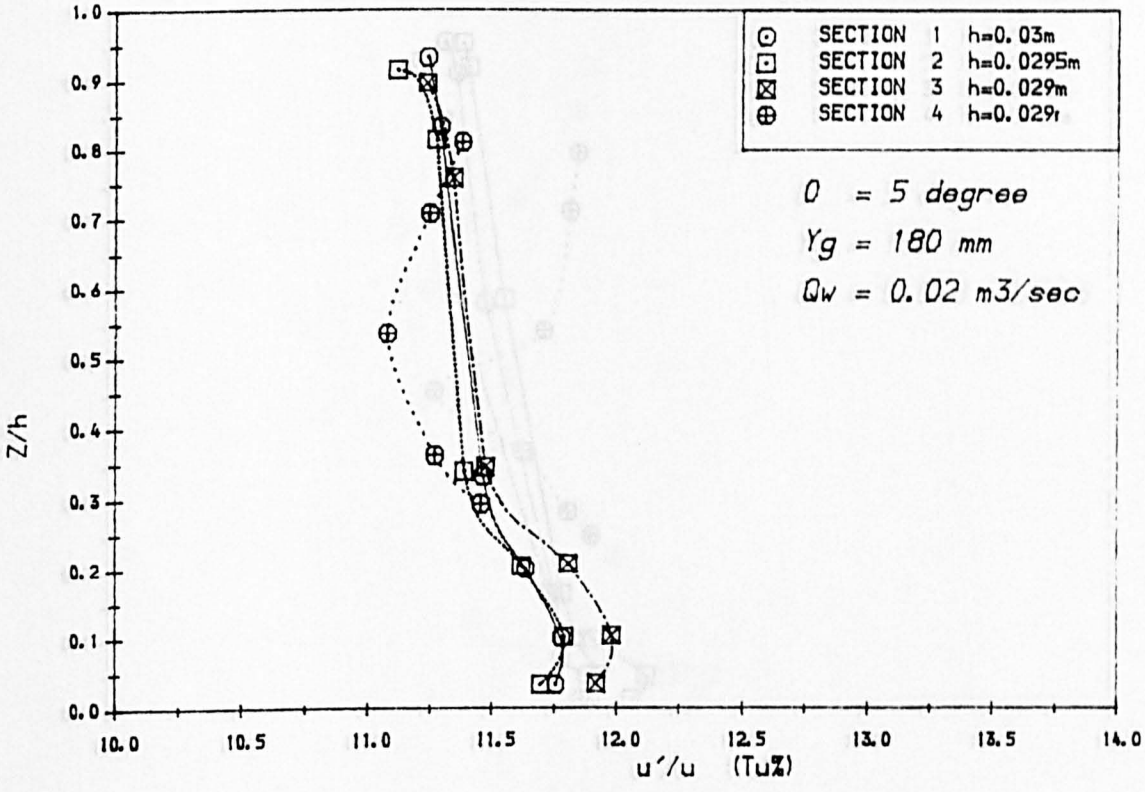

Fig 4.26(a) Mean Longitudinal Turbulence Intensities

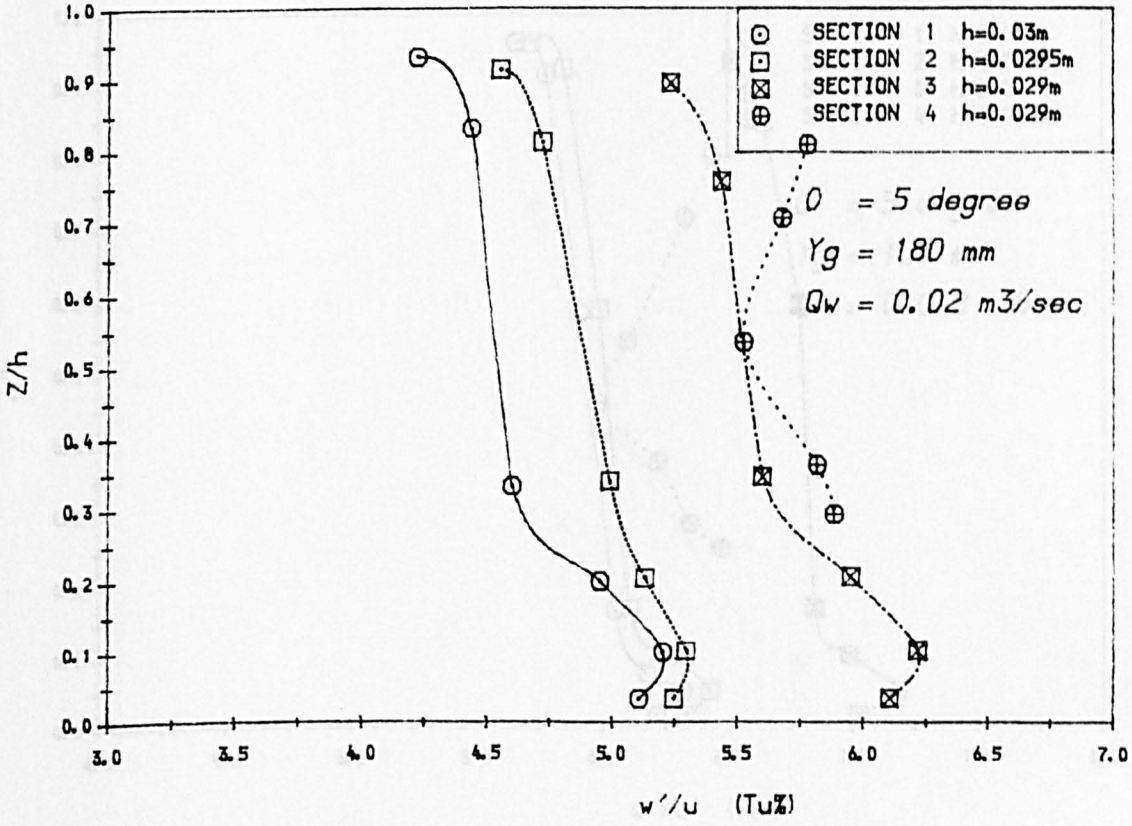

Fig 4.26(b) Mean Vertical Turbulence Intensities

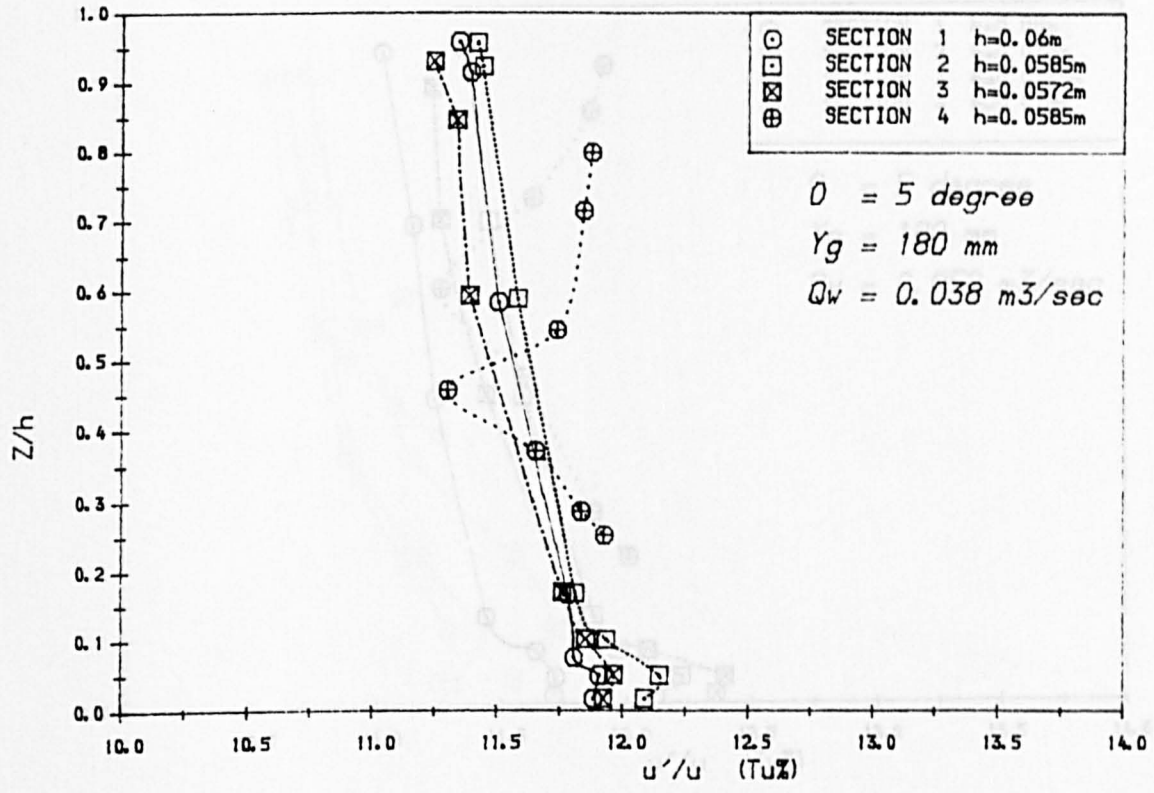

Fig 4.27(a) Mean Longitudinal Turbulence Intensities

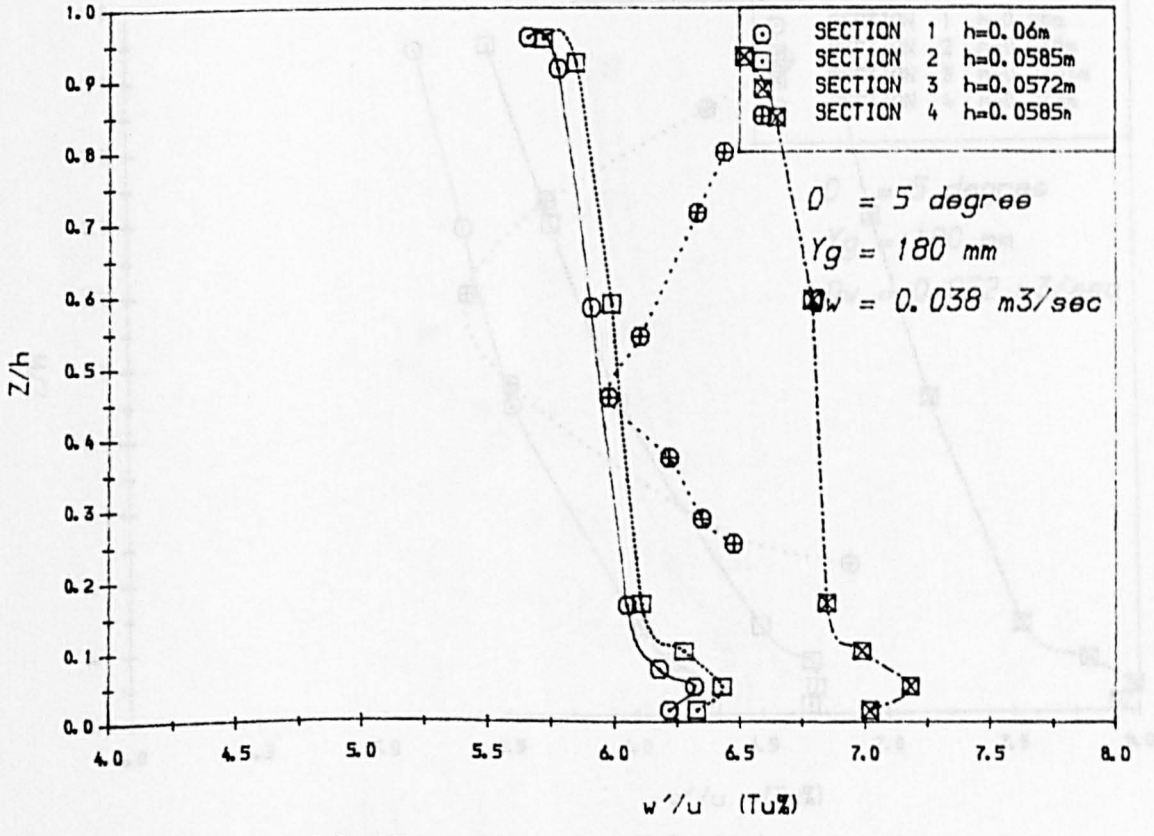

Fig 4.27(b) Mean Vertical Turbulence Intensities

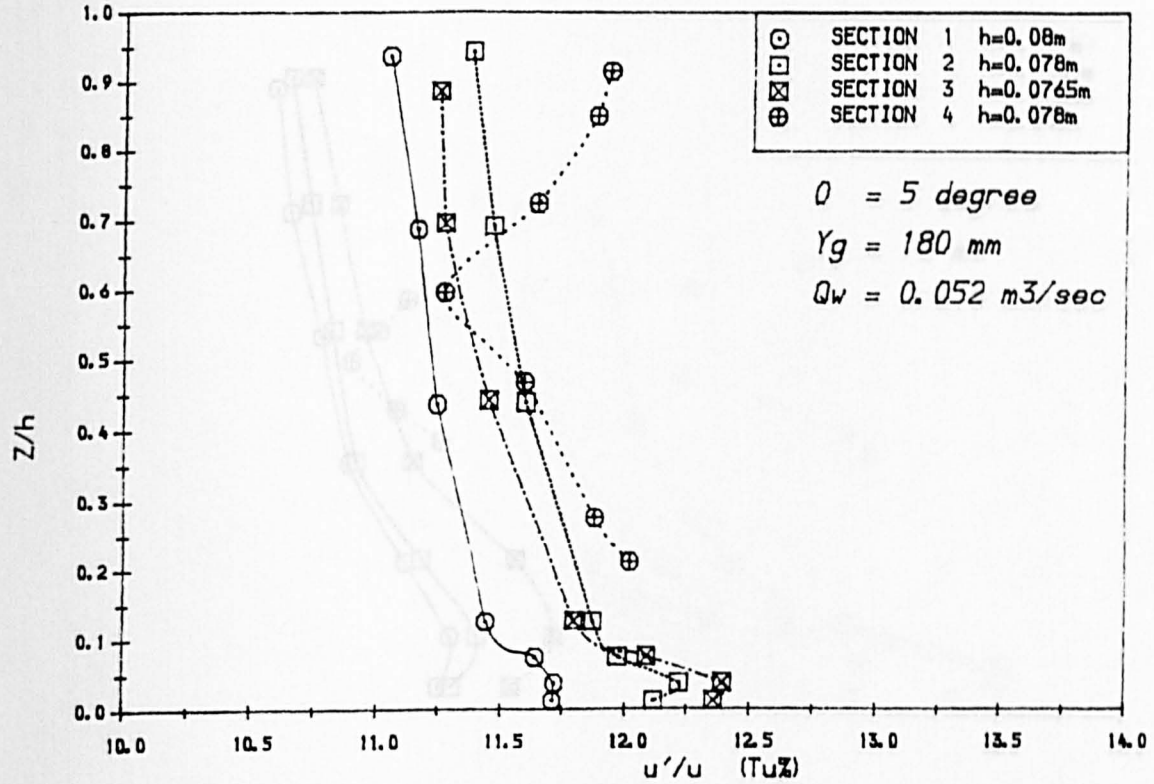

Fig 4.28(a) Mean Longitudinal Turbulence Intensities

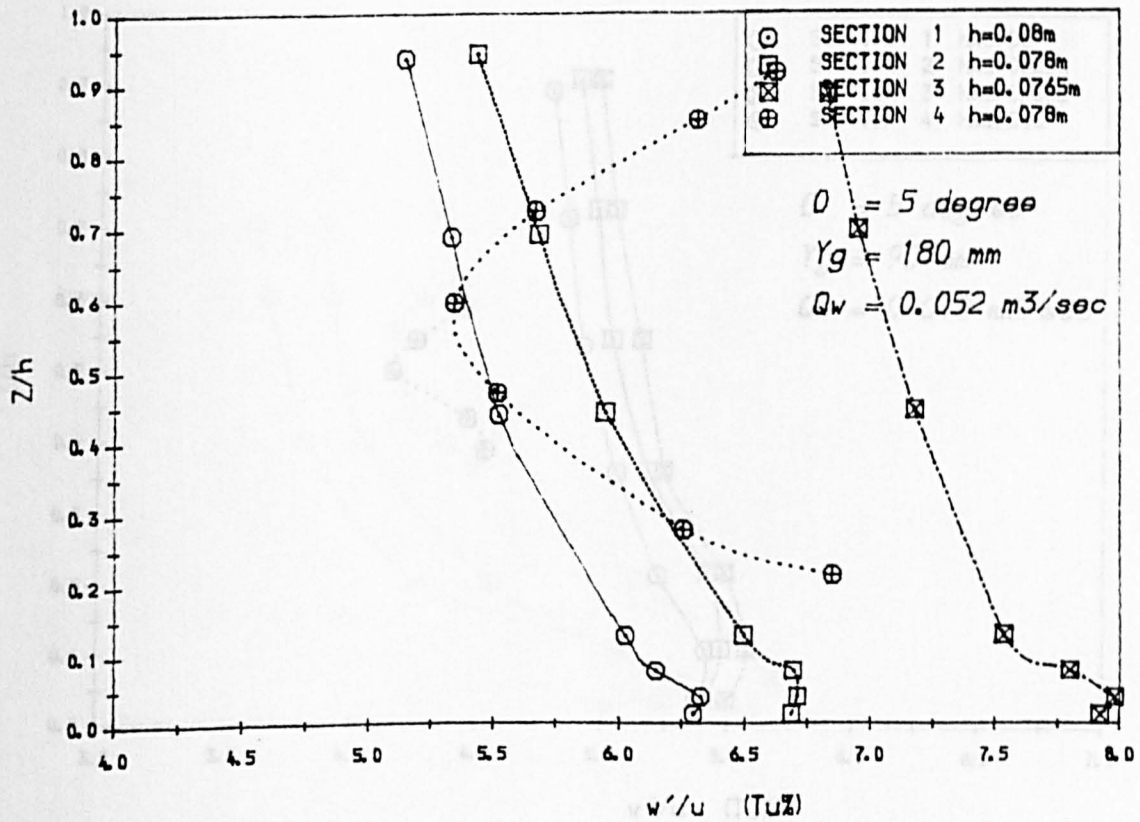

Fig 4.28(b) Mean Vertical Turbulence Intensities

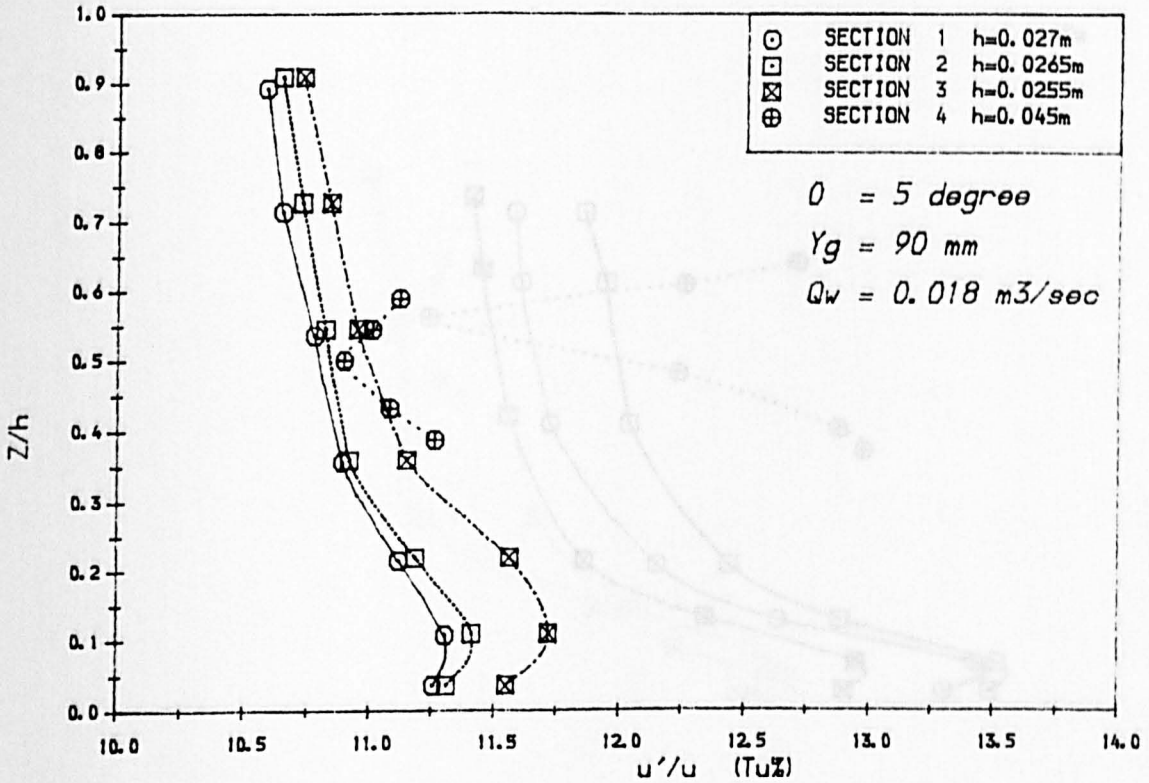

Fig 4.29(a) Mean Longitudinal Turbulence Intensities

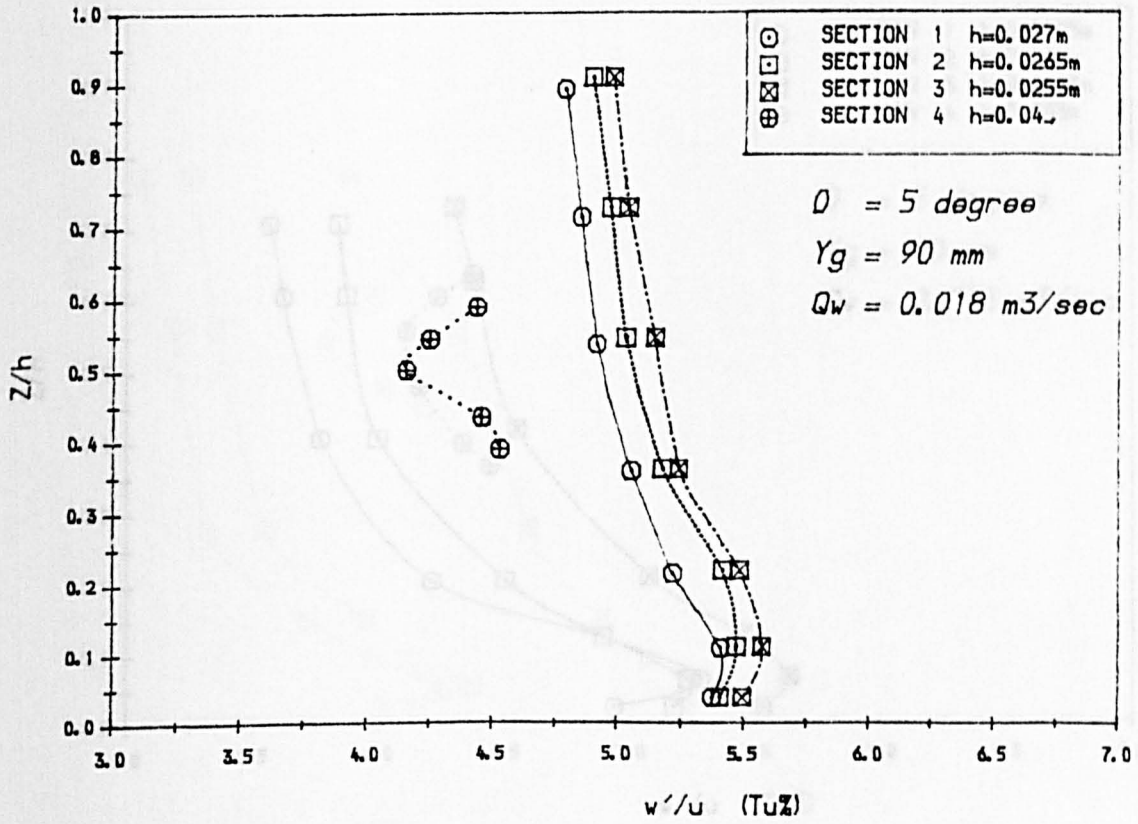

Fig 4.29(b) Mean Vertical Turbulence Intensities

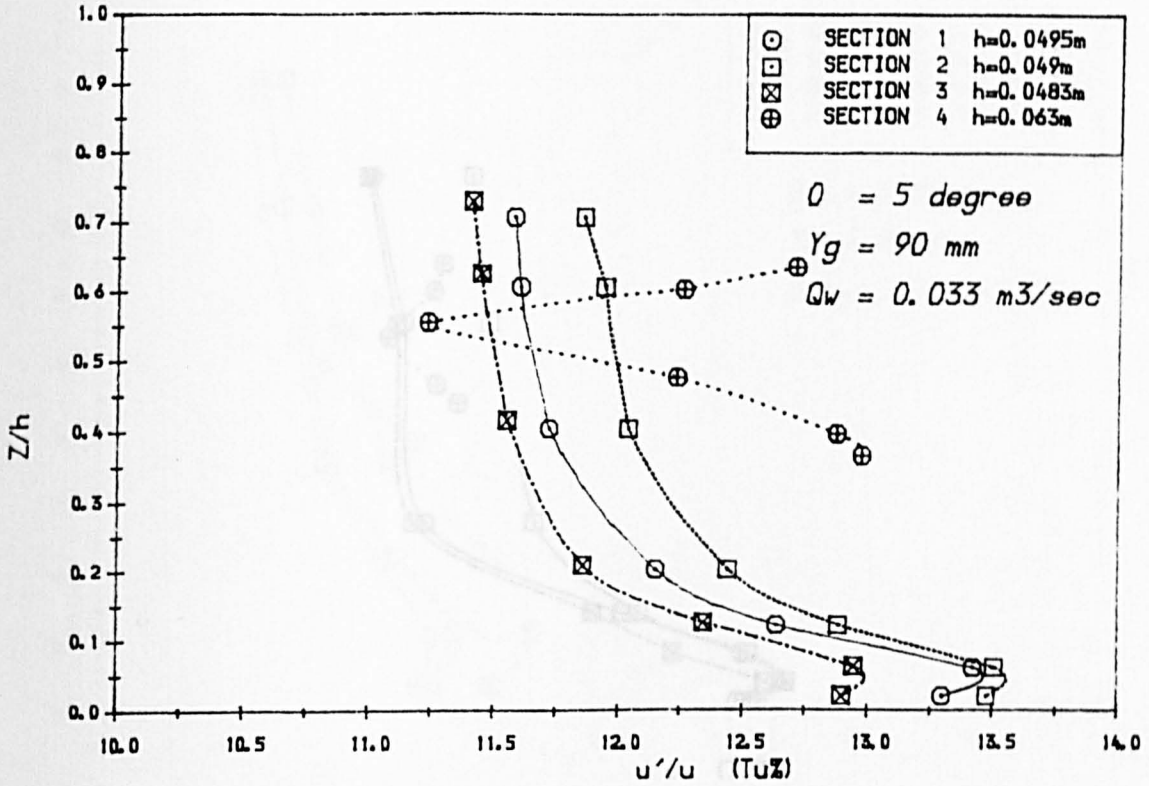

Fig 4.30(a) Mean Longitudinal Turbulence Intensities

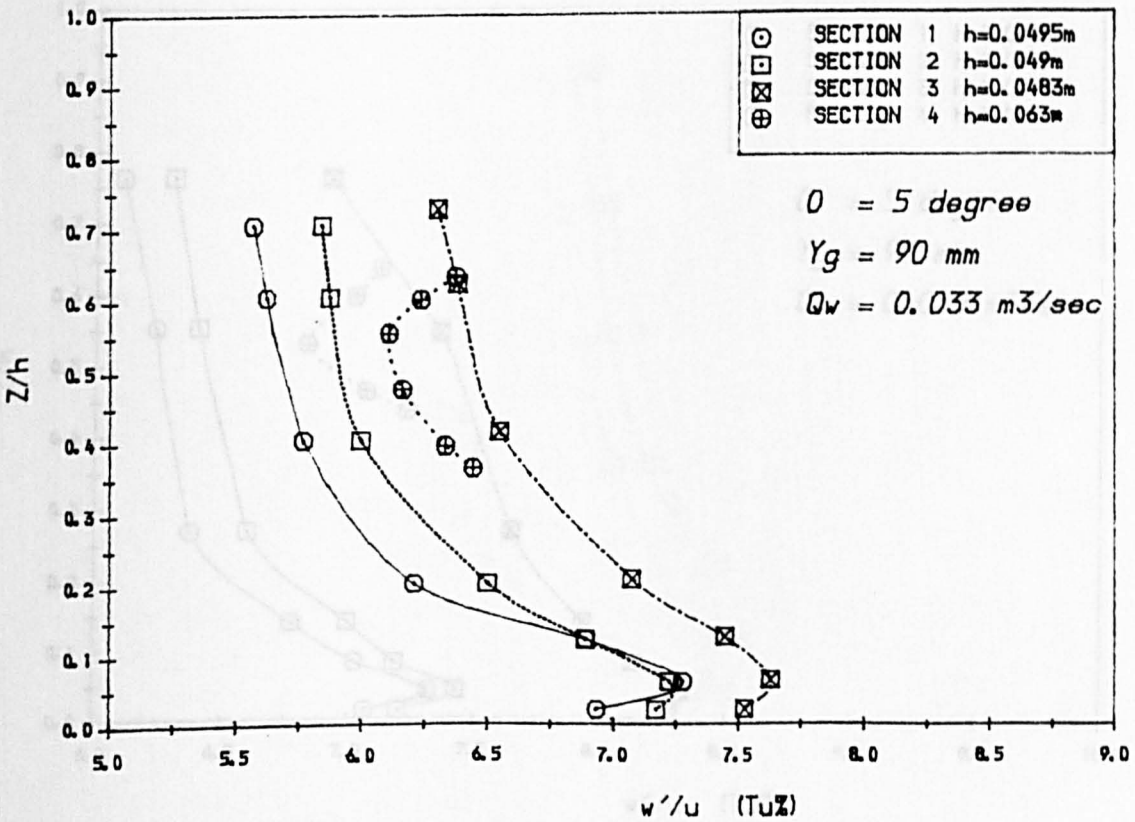

Fig 4.30(b) Mean Vertical Turbulence Intensities

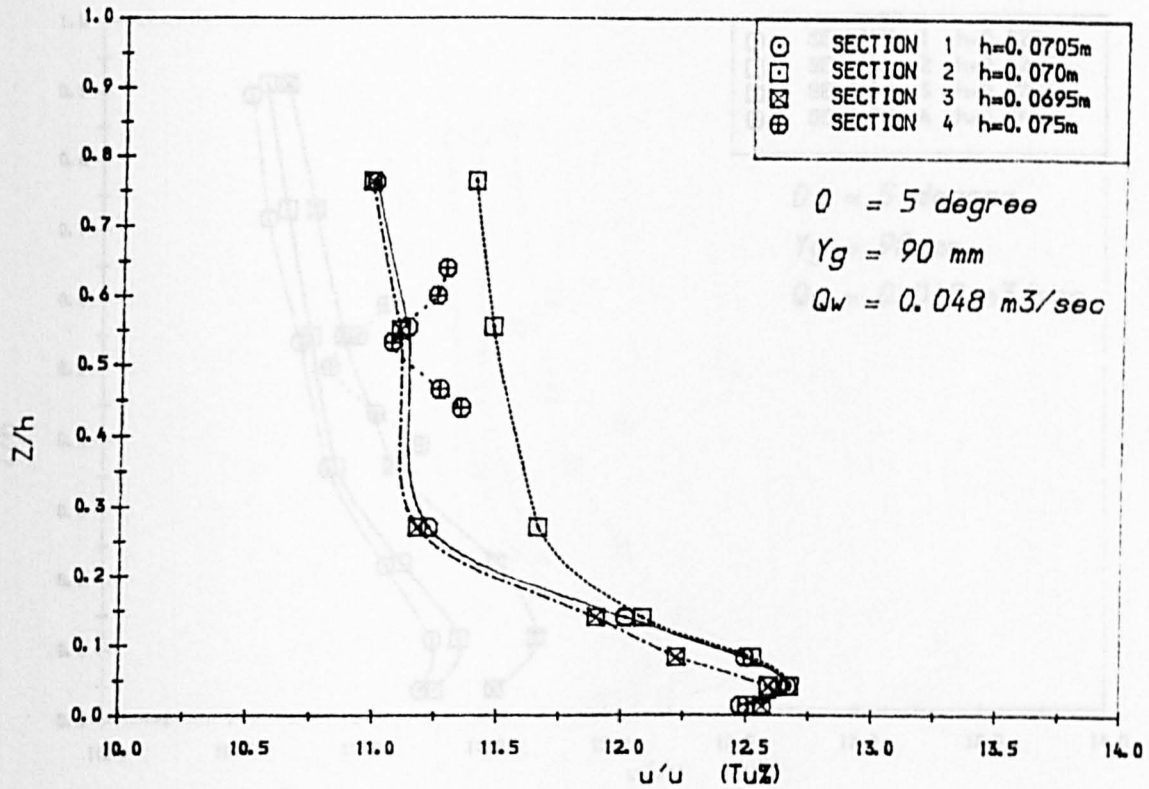

Fig 4.31 (a) Mean Longitudinal Turbulence Intensities

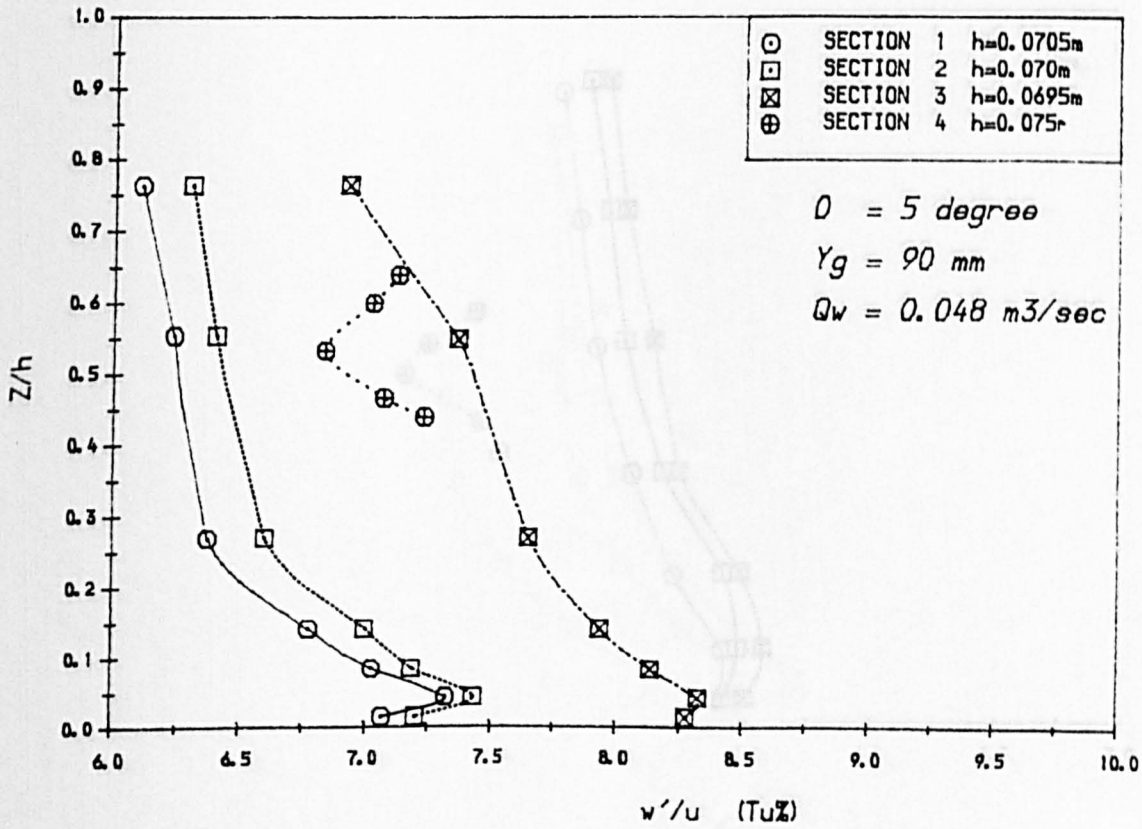

Fig 4.31 (b) Mean Vertical Turbulence Intensities

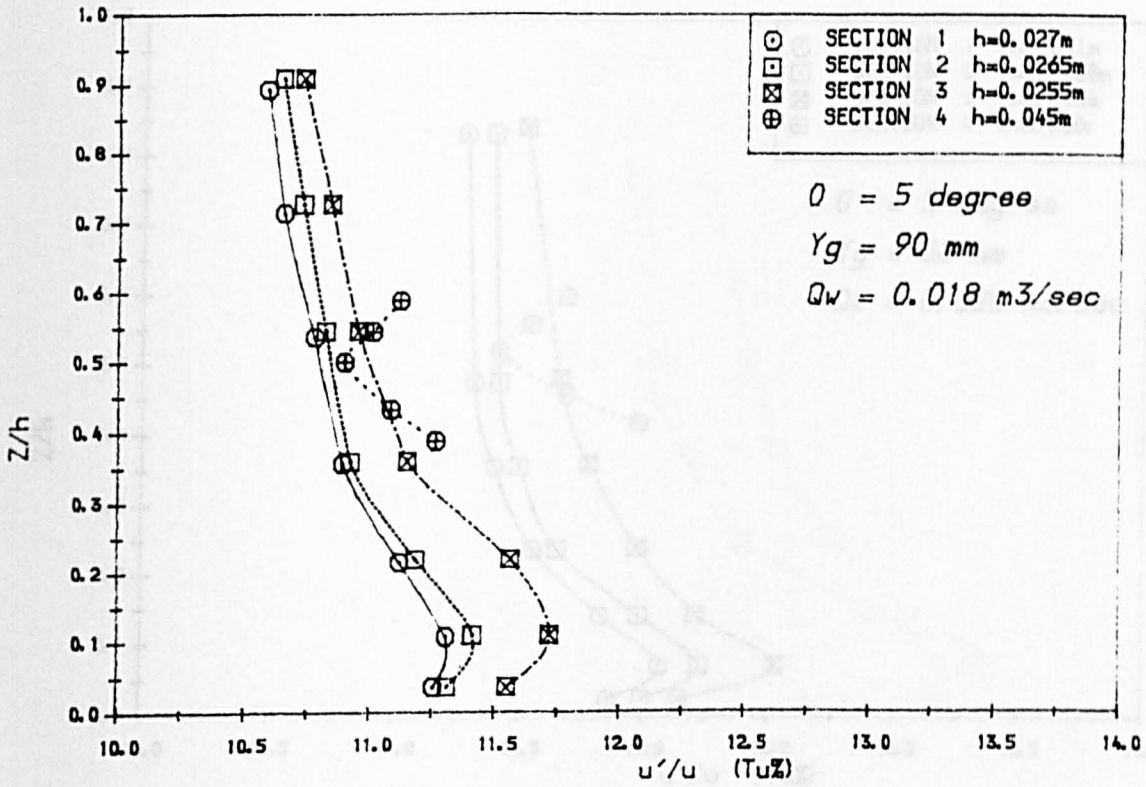

Fig 4.29 (a) Mean Longitudinal Turbulence Intensities

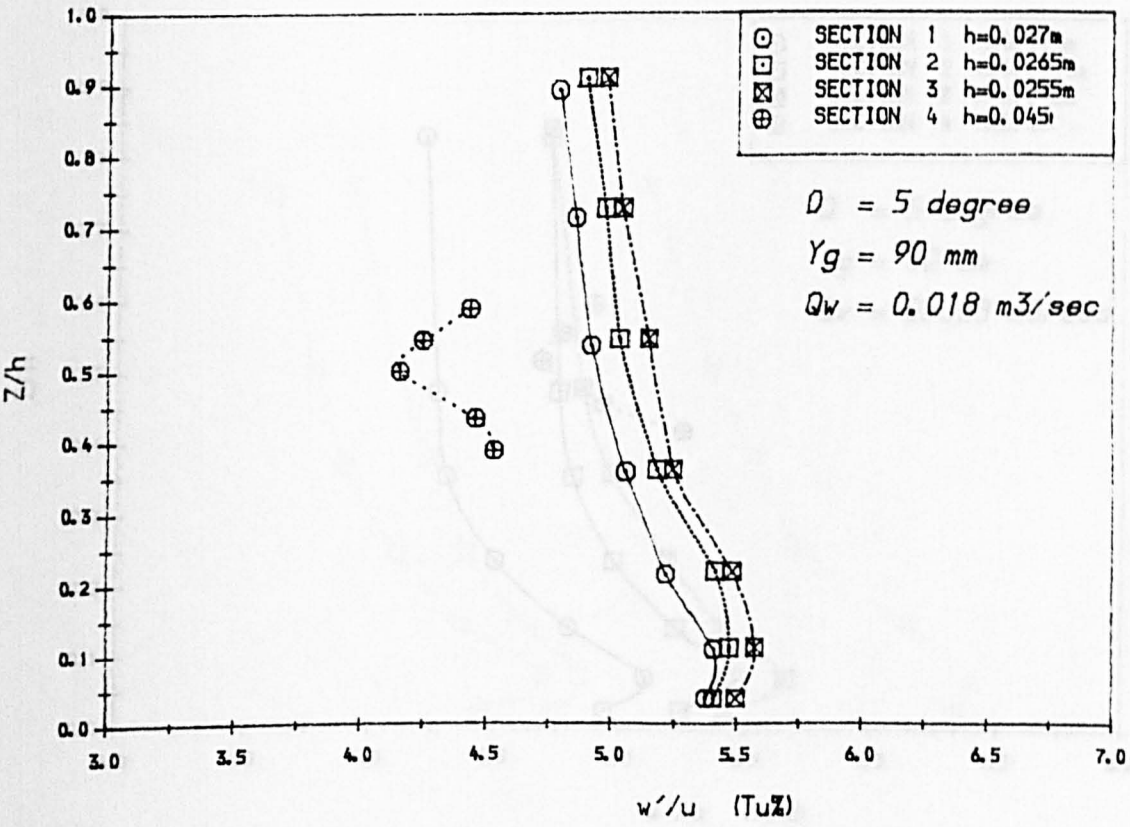

Fig 4.29 (b) Mean Vertical Turbulence Intensities

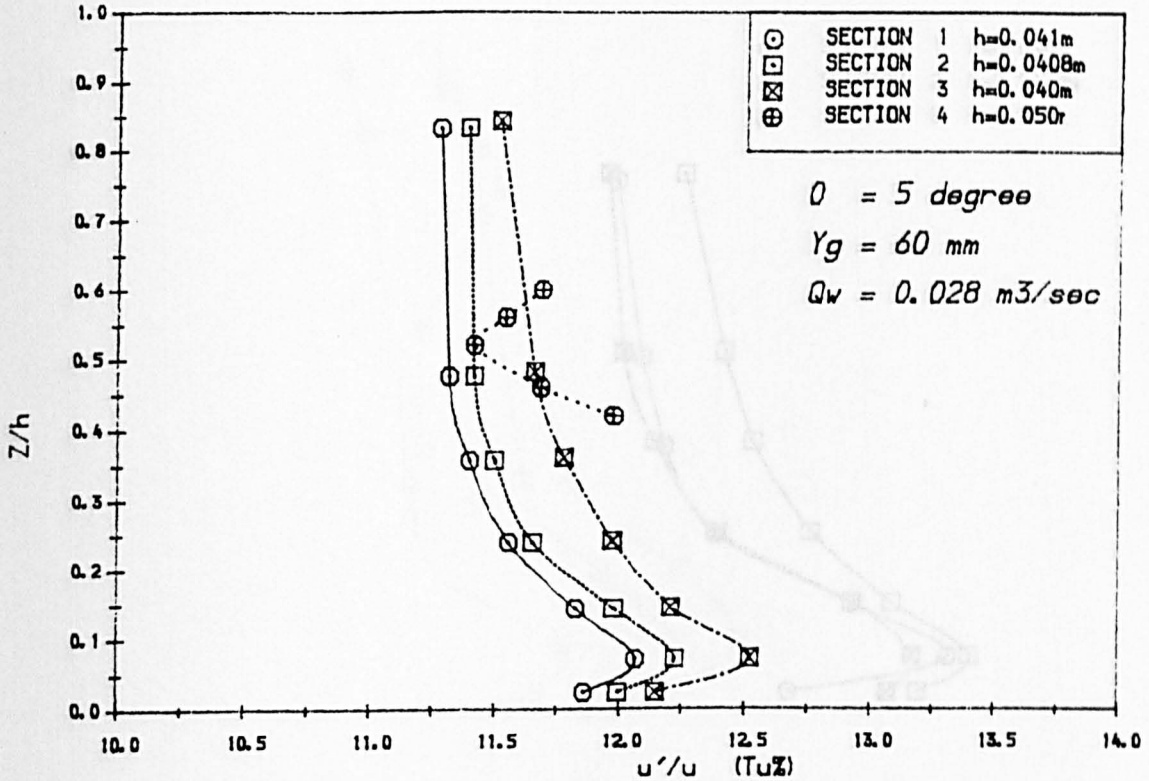

Fig 4.33(a) Mean Longitudinal Turbulence Intensities

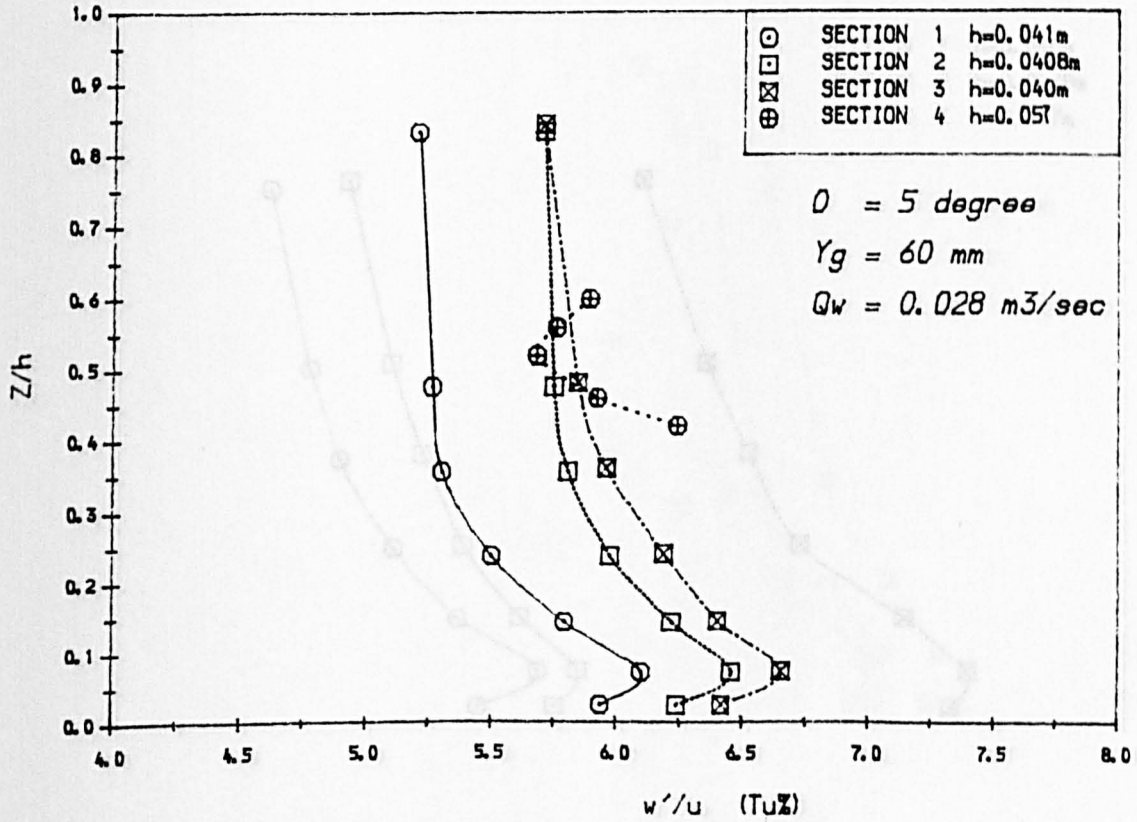

Fig 4.33(b) Mean Vertical Turbulence Intensities

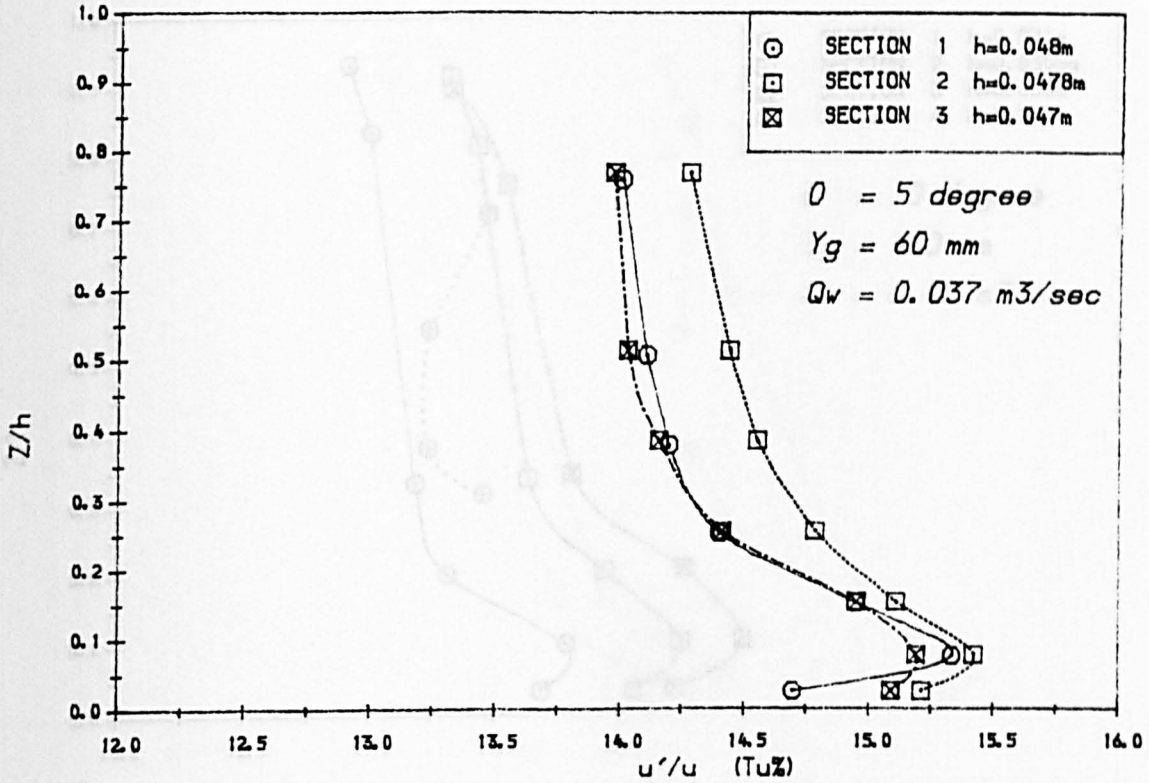

Fig 4.34(a) Mean Longitudinal Turbulence Intensities

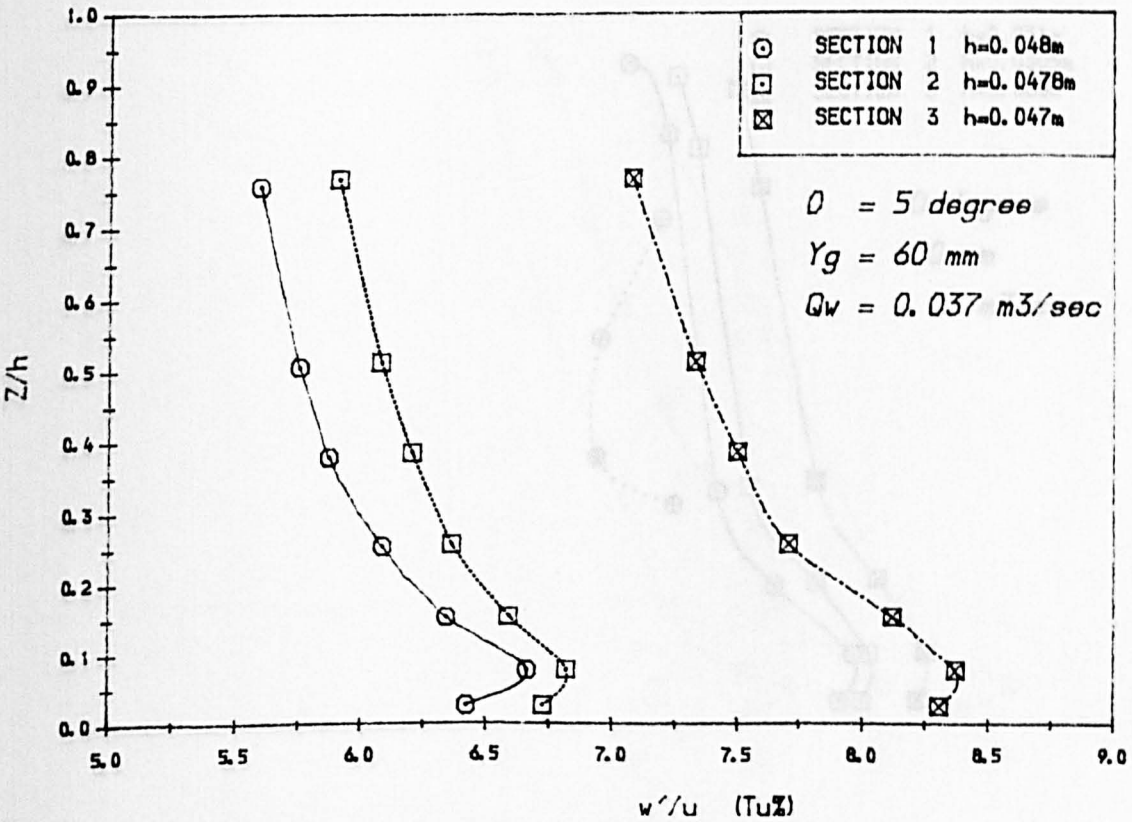

Fig 4.34(b) Mean Vertical Turbulence Intensities

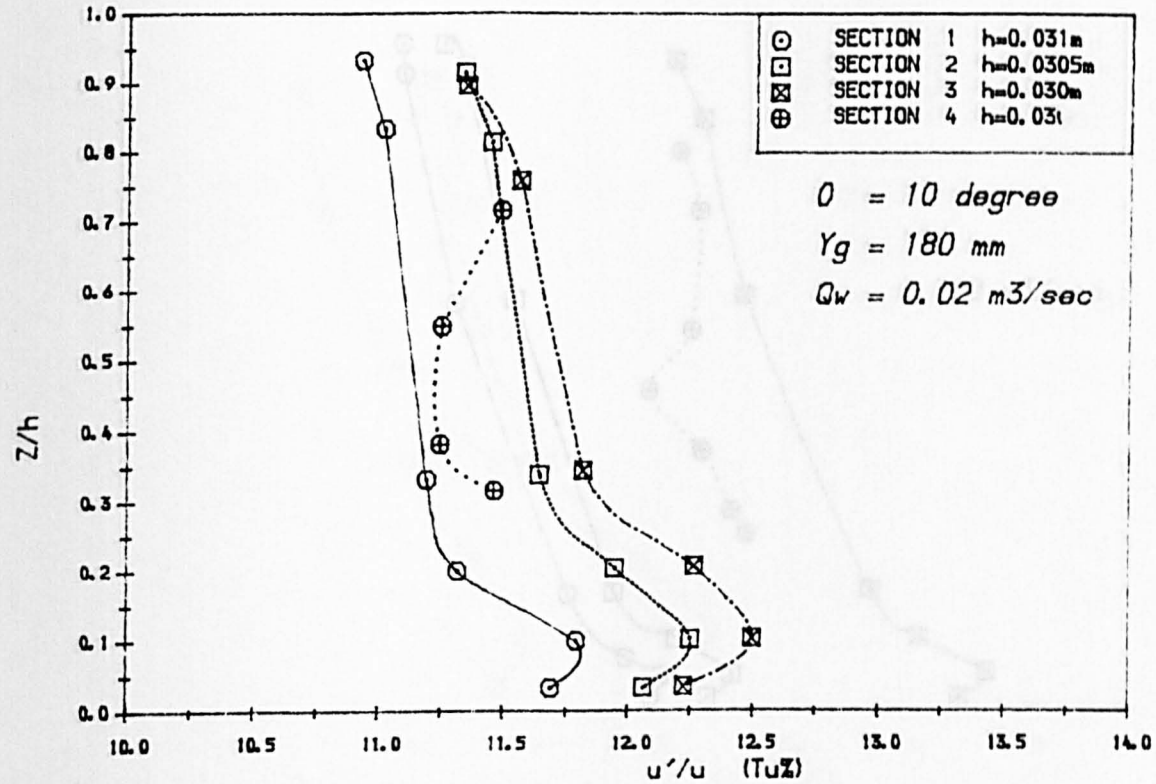

Fig 4.35(a) Mean Longitudinal Turbulence Intensities

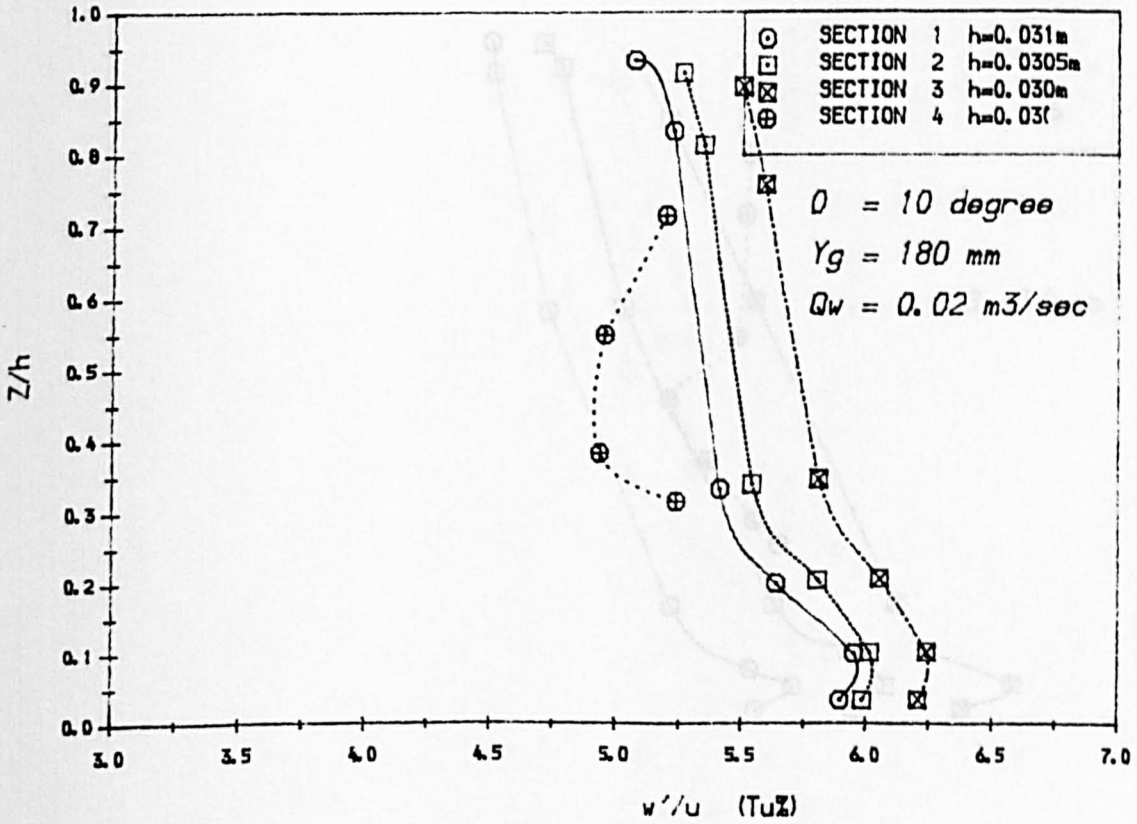

Fig 4.35(b) Mean Vertical Turbulence Intensities

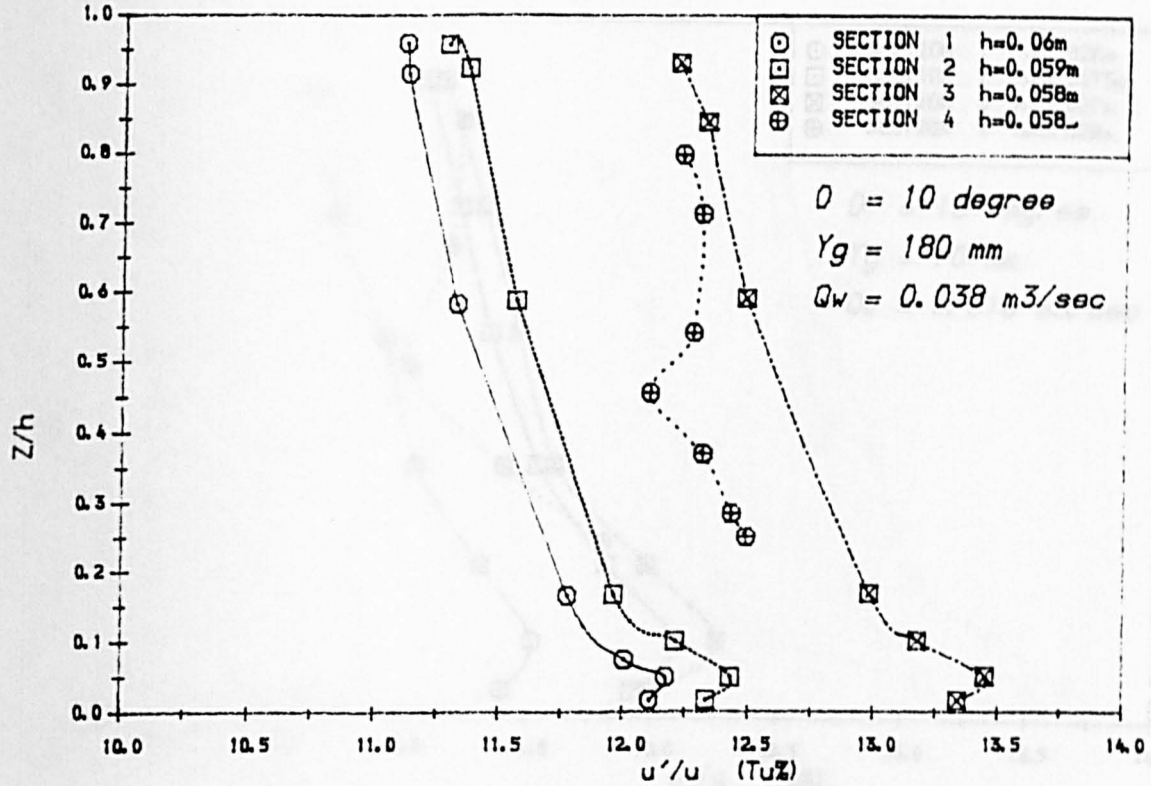

Fig 4.36(a) Mean Longitudinal Turbulence Intensities

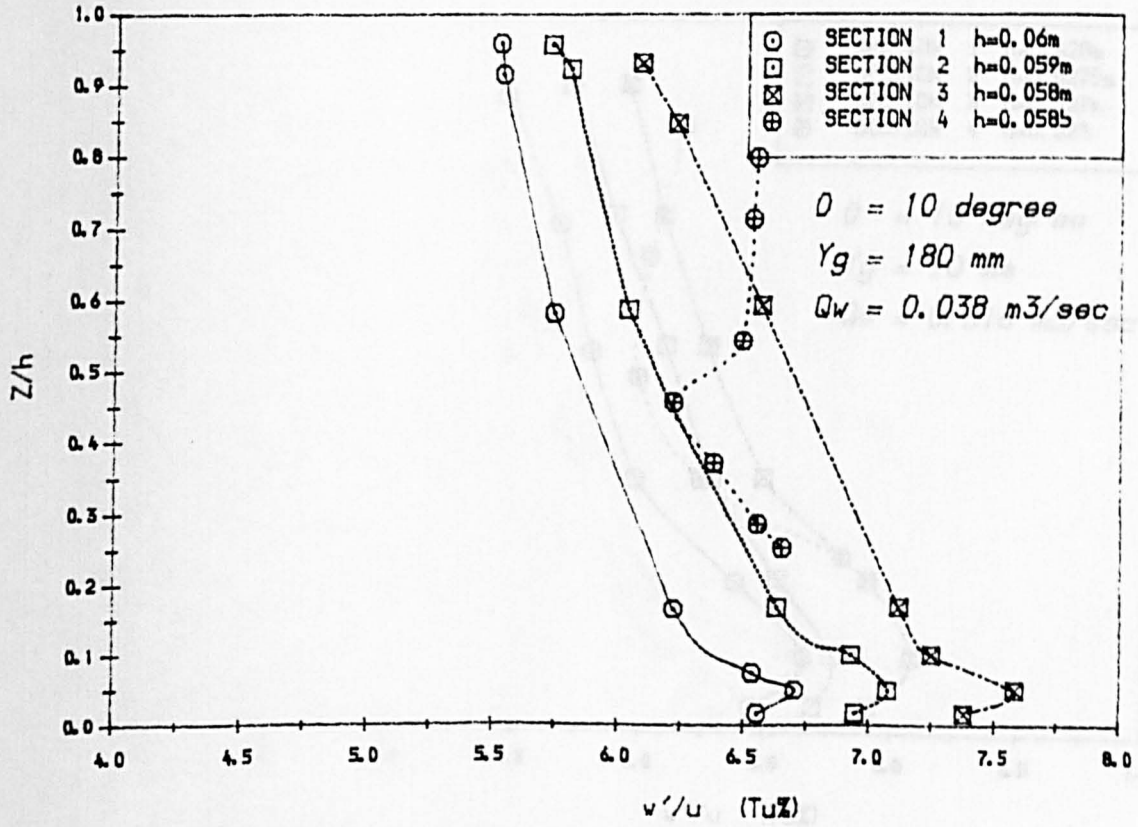

Fig 4.36(b) Mean Vertical Turbulence Intensities

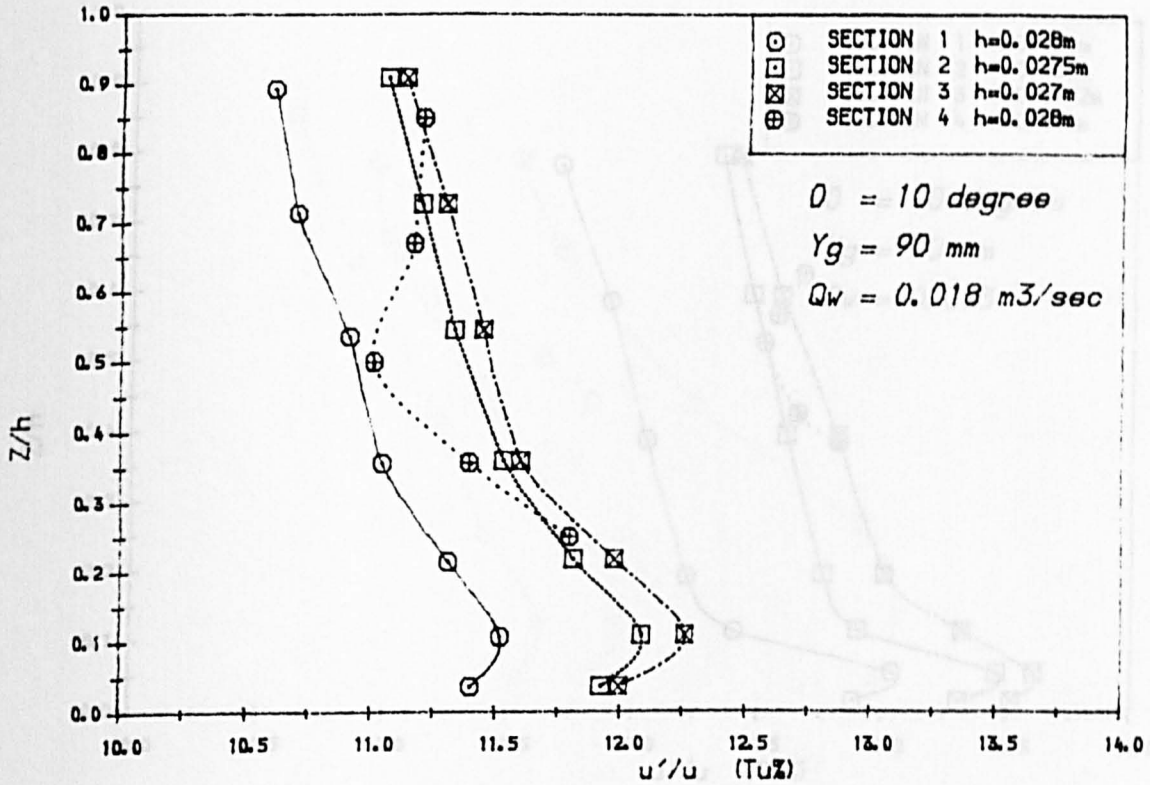

Fig 4.37(a) Mean Longitudinal Turbulence Intensities

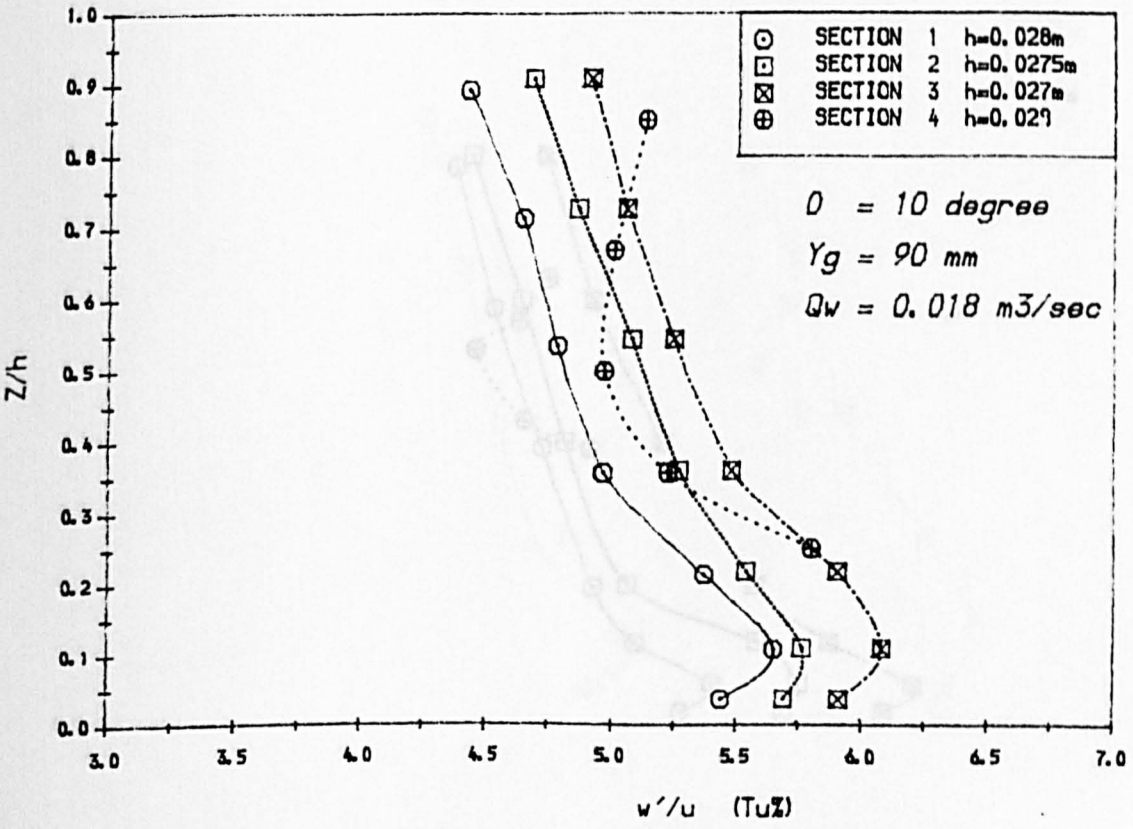

Fig 4.37(b) Mean Vertical Turbulence Intensities

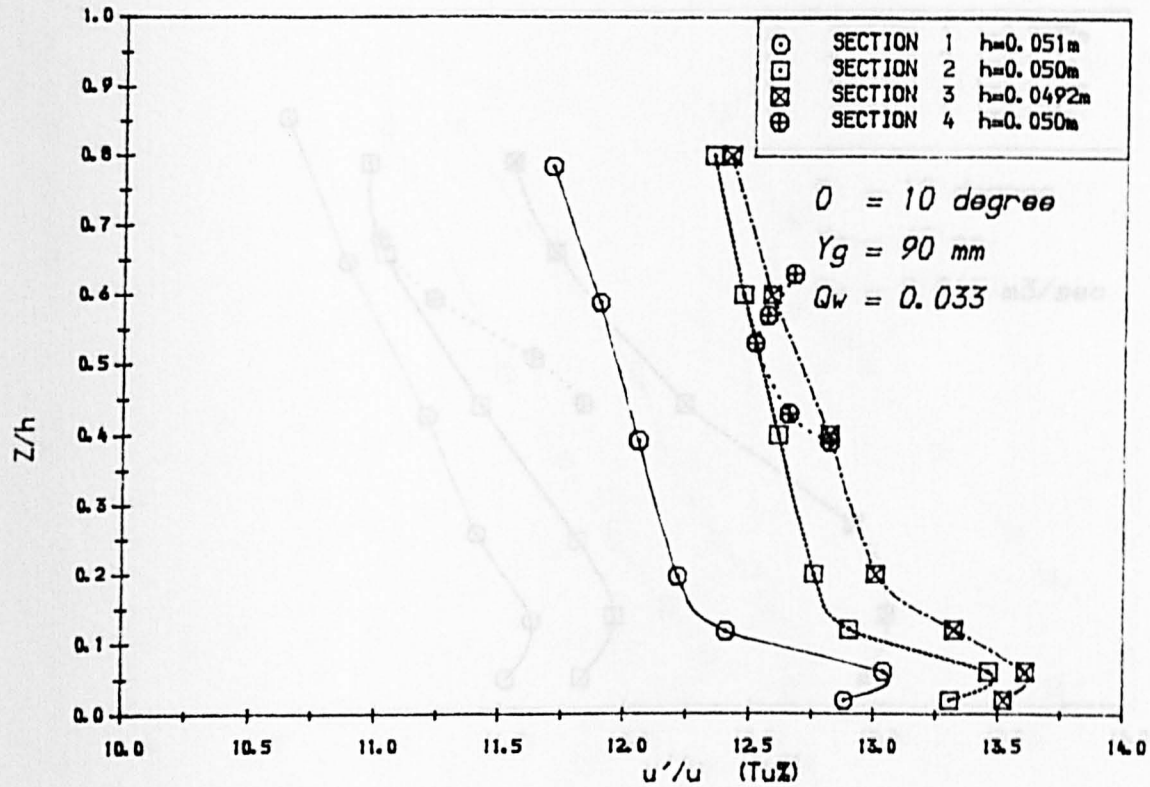

Fig 4.38(a) Mean Longitudinal Turbulence Intensities

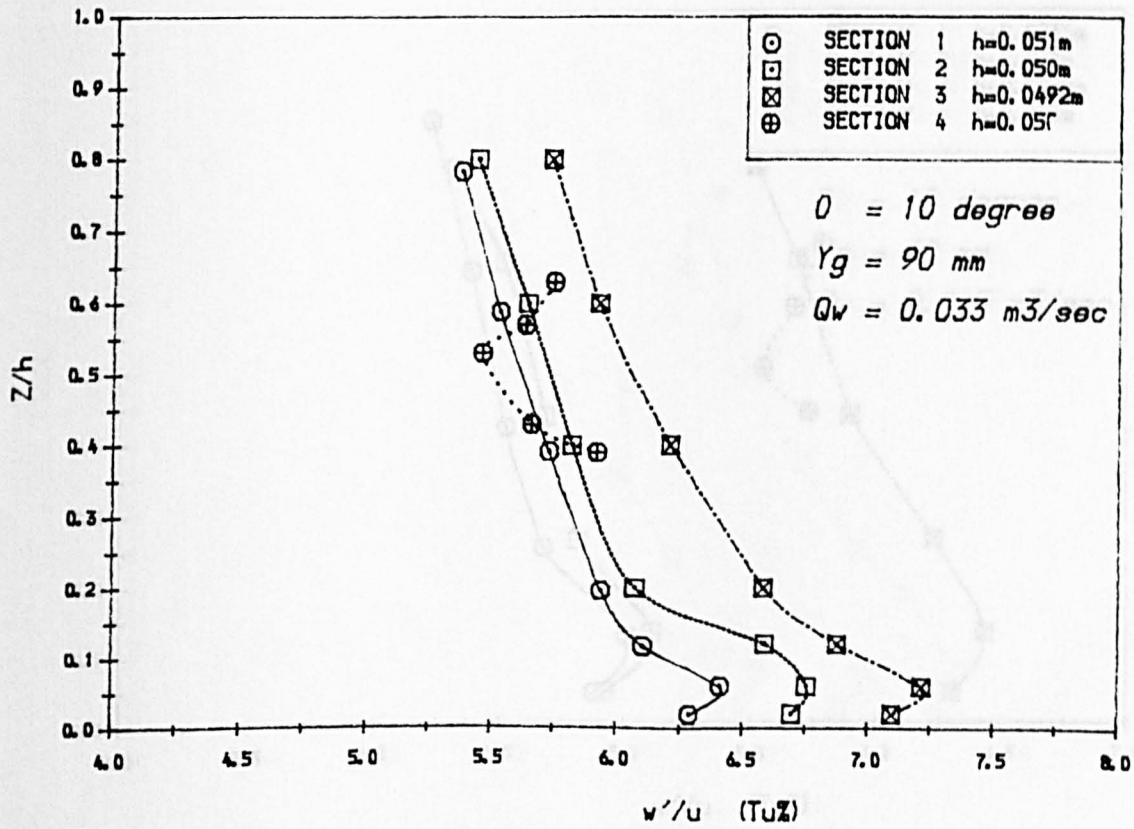

Fig 4.38(b) Mean Vertical Turbulence Intensities

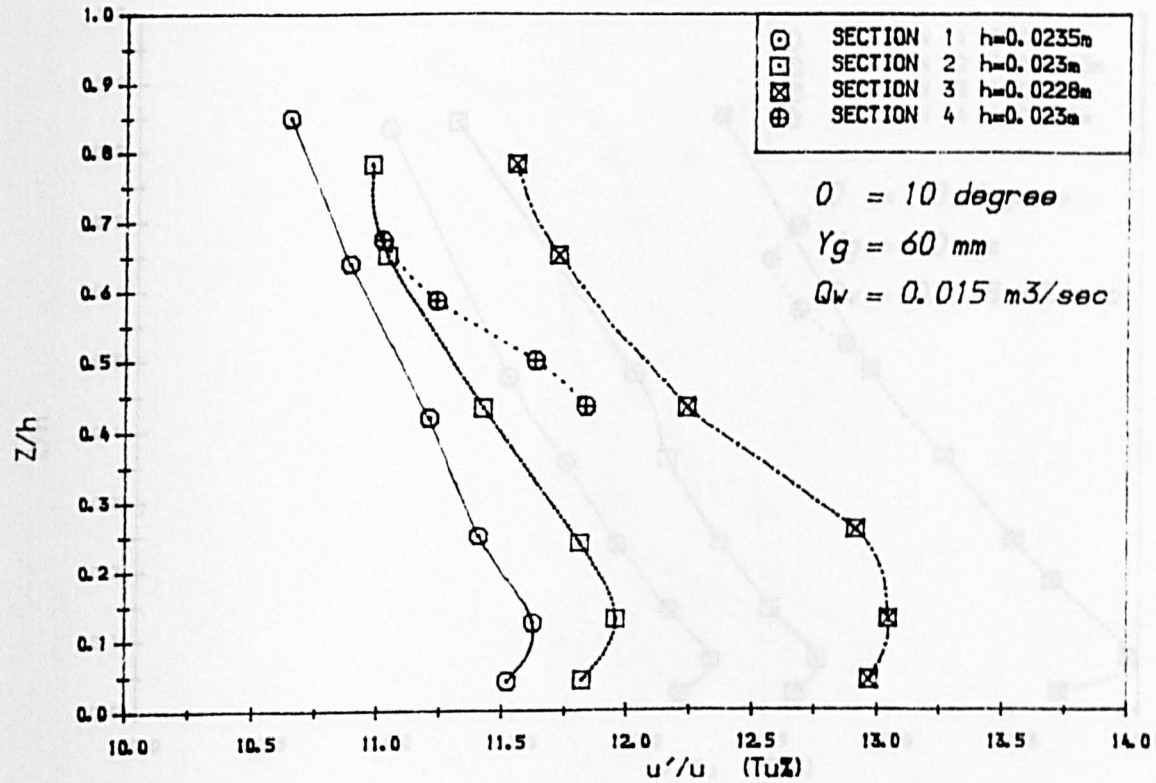

Fig 4.39(a) Mean Longitudinal Turbulence Intensities

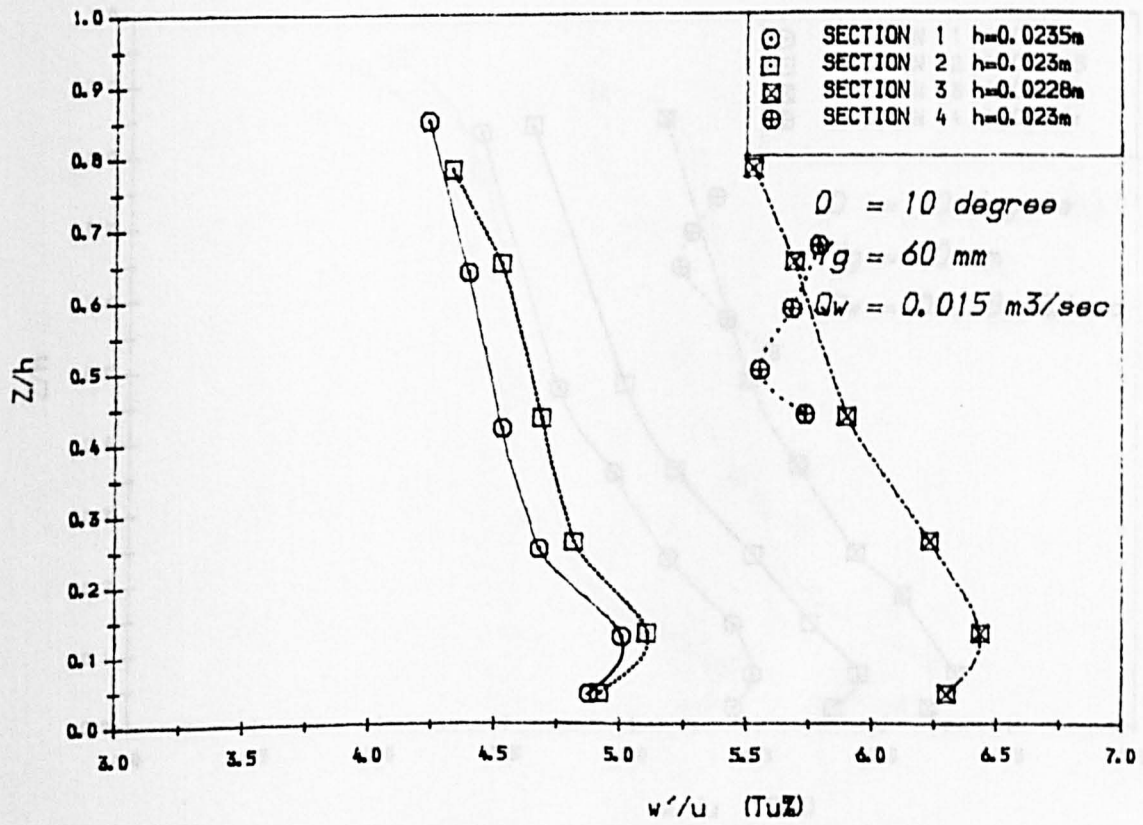

Fig 4.39(b) Mean Vertical Turbulence Intensities

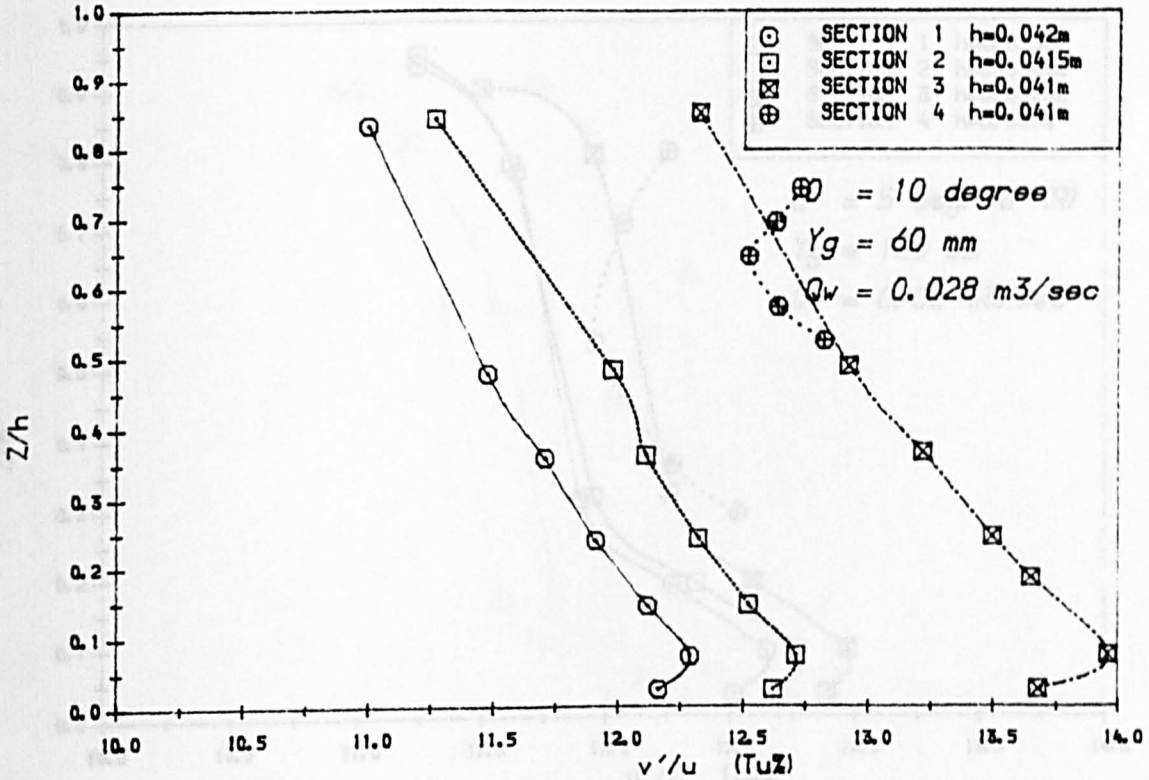

Fig 4.40(a) Mean Longitudinal Turbulence Intensities

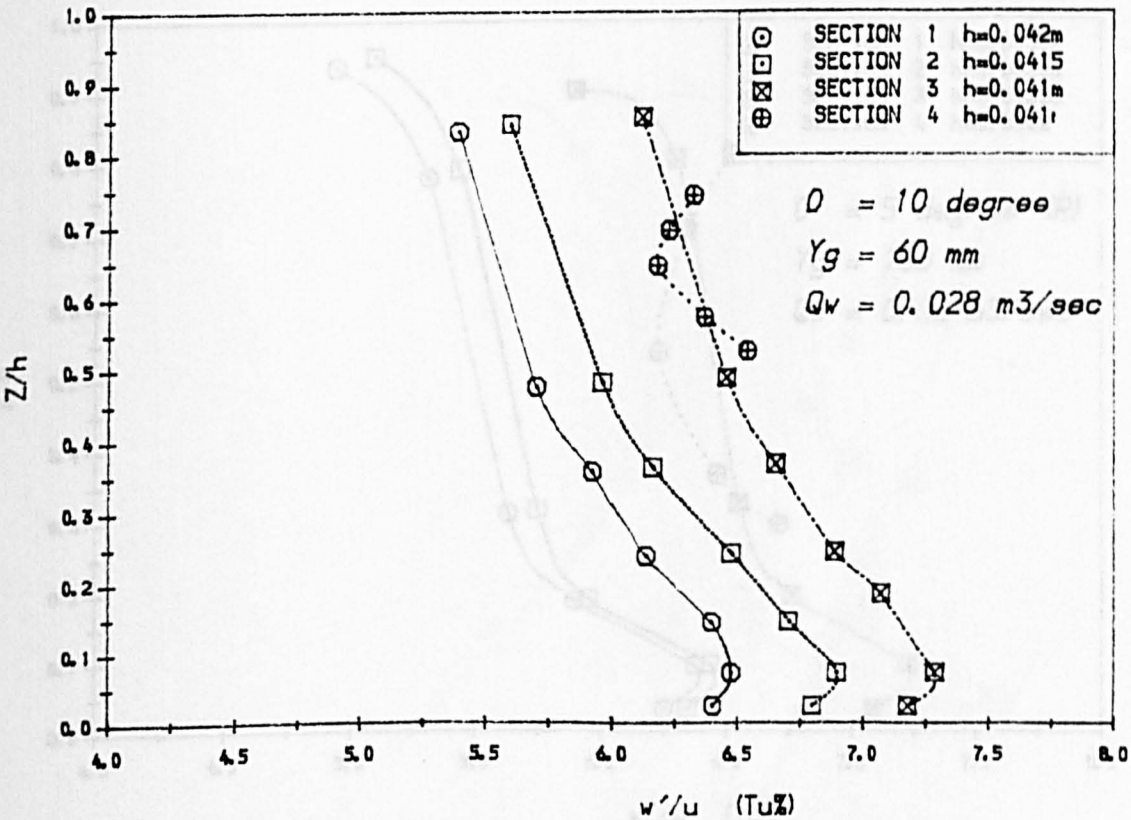

Fig 4.40(b) Mean Vertical Turbulence Intensities

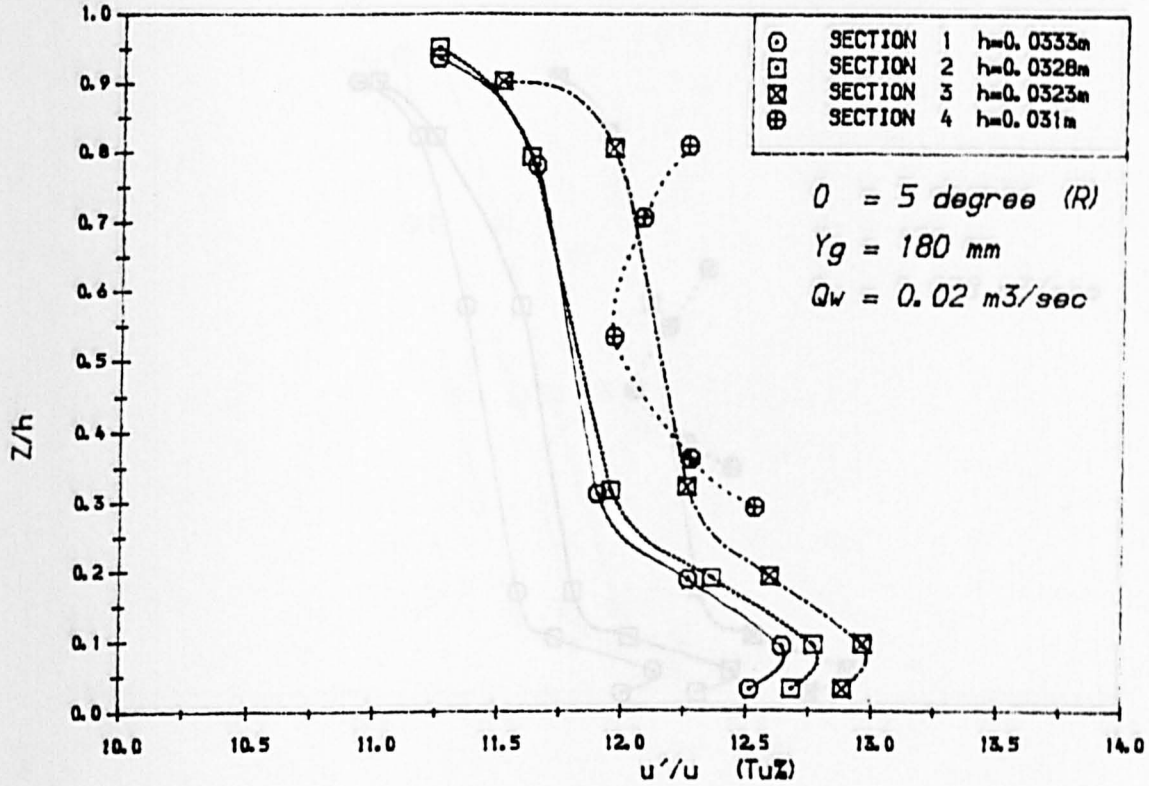

Fig 4.41 (a) Mean Longitudinal Turbulence Intensities

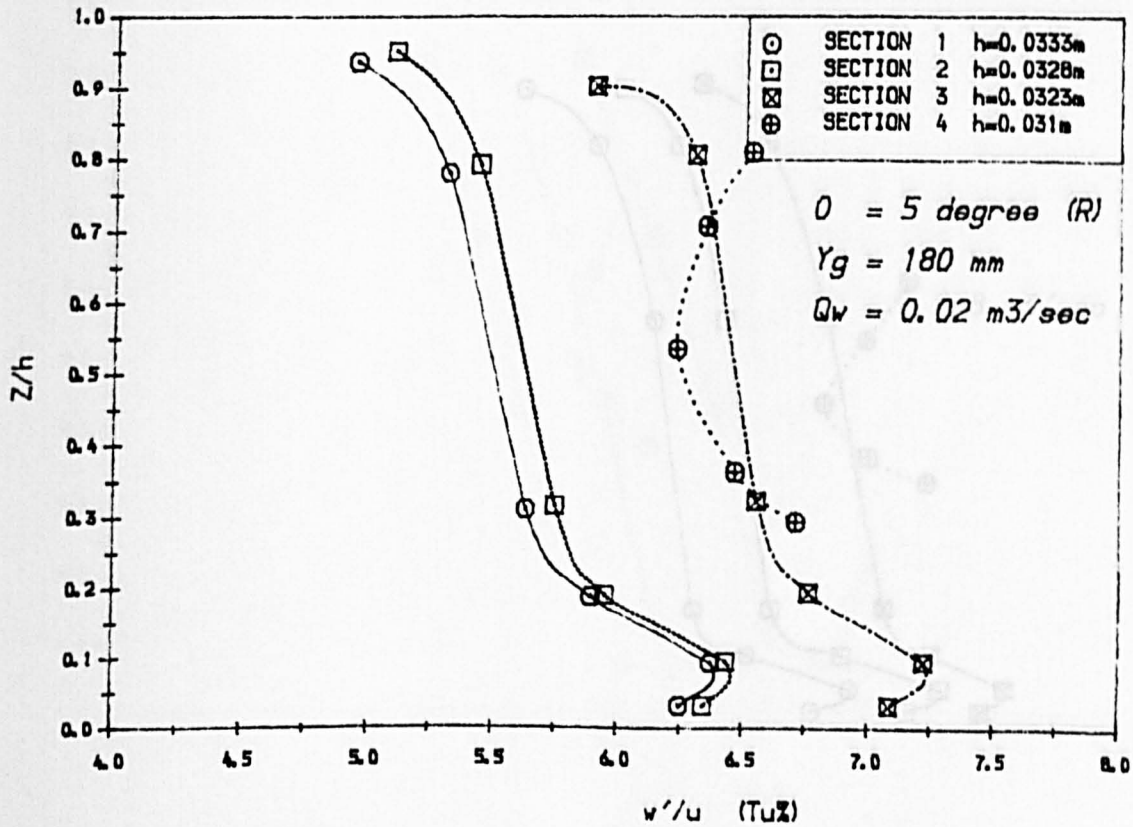

Fig 4.41 (b) Mean Vertical Turbulence Intensities

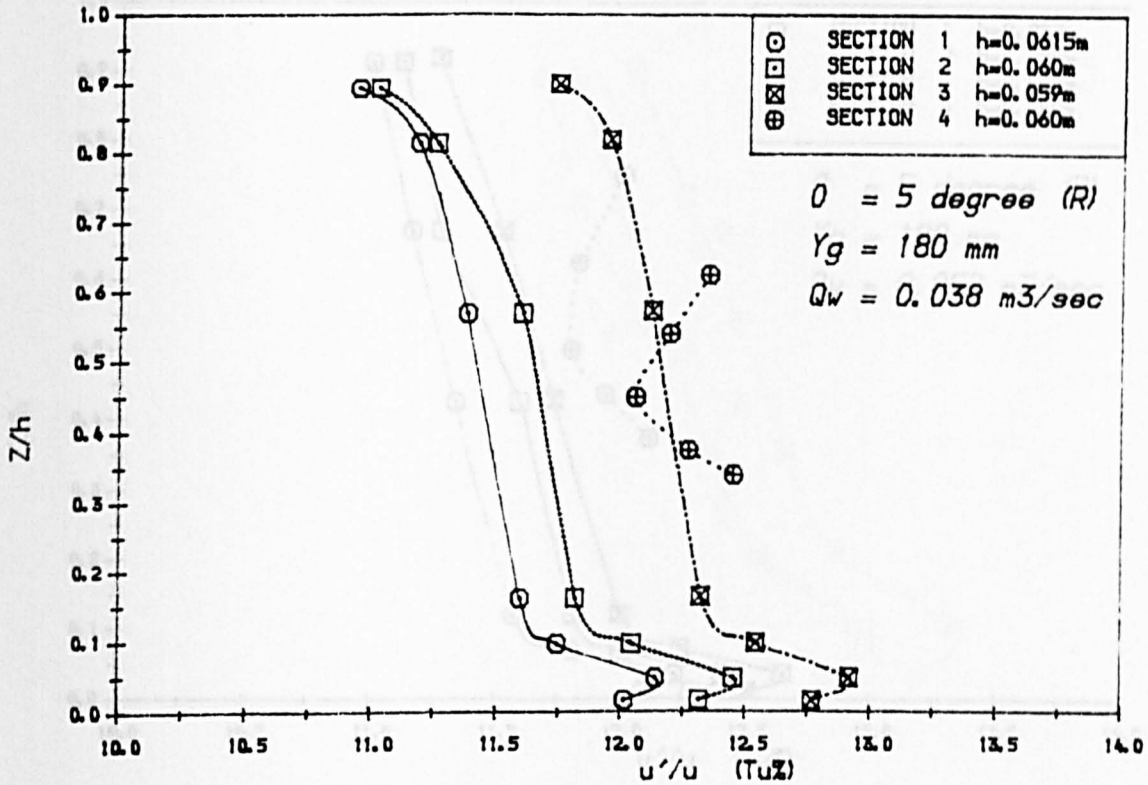

Fig 4.42(a) Mean Longitudinal Turbulence Intensities

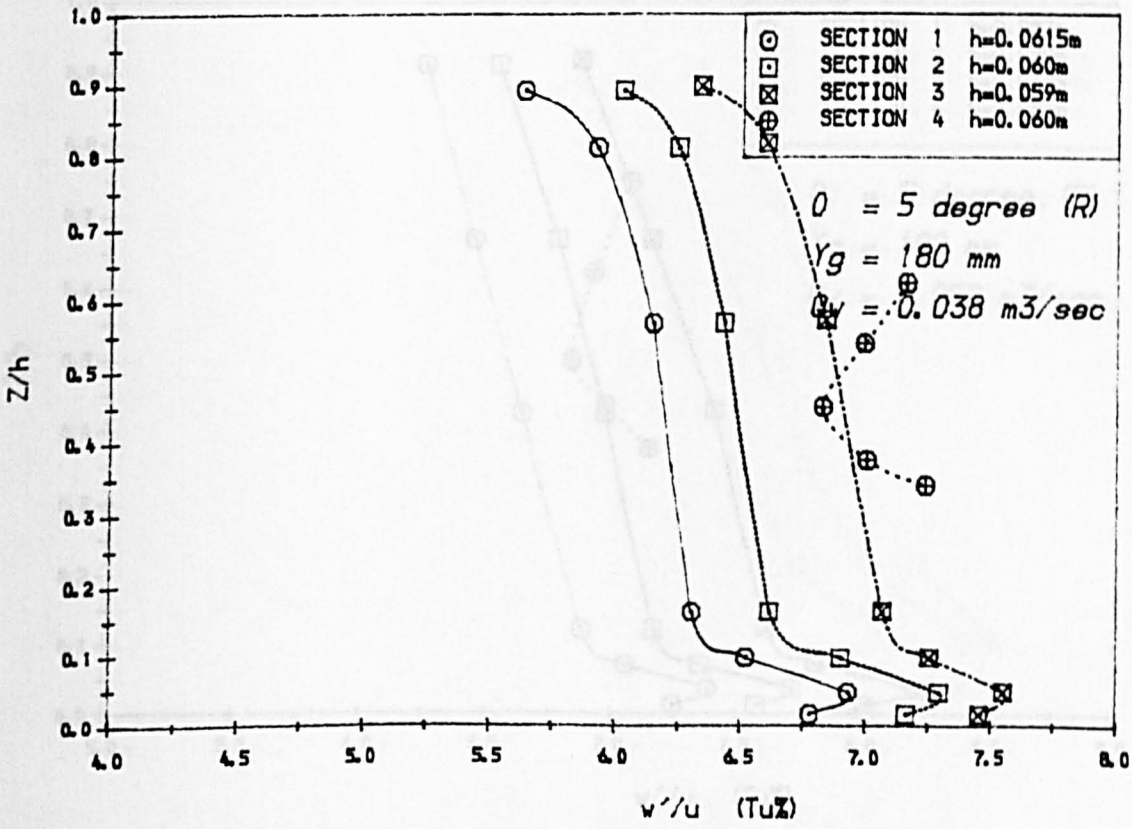

Fig 4.42(b) Mean Vertical Turbulence Intensities

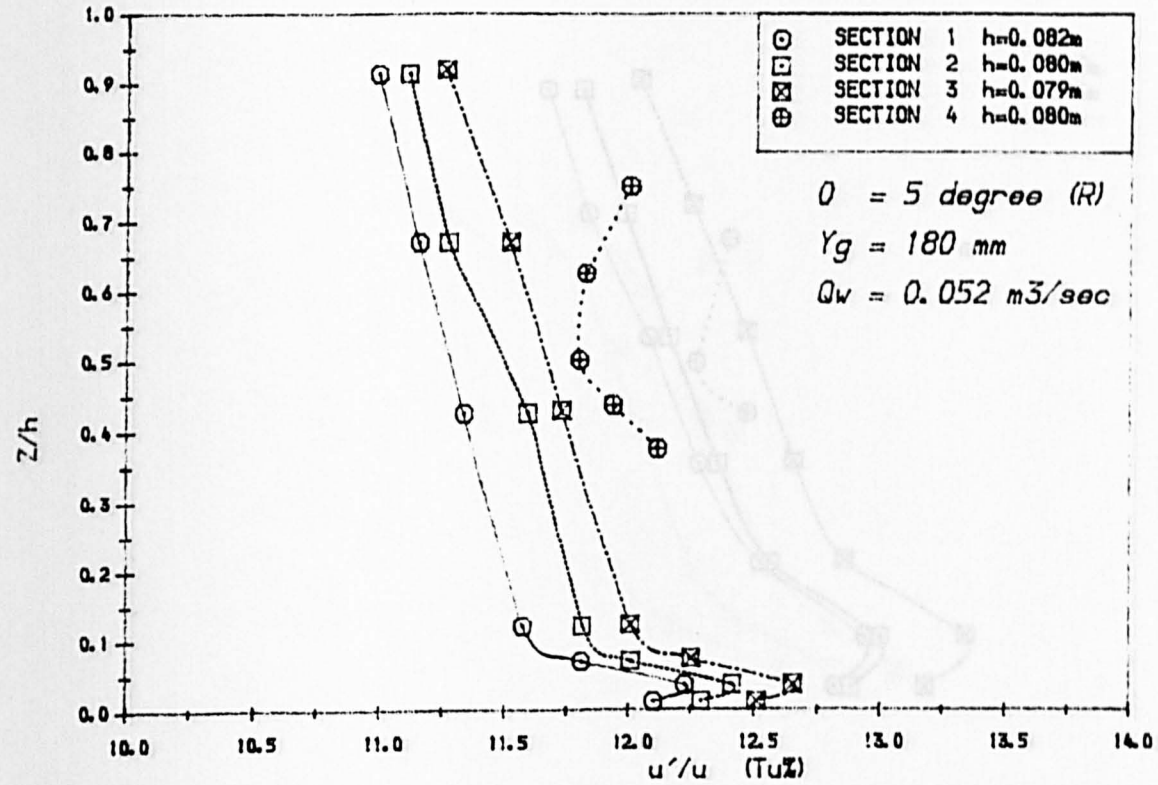

Fig 4.43(a) Mean Longitudinal Turbulence Intensities

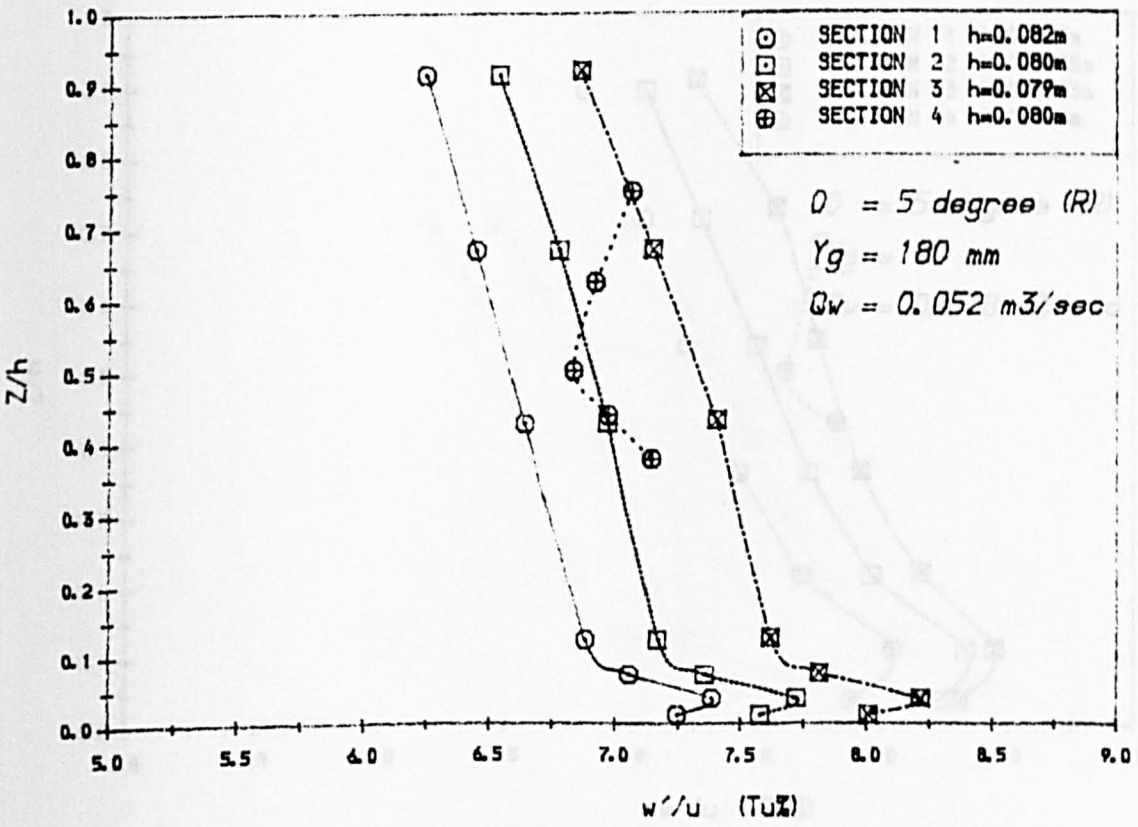

Fig 4.43(b) Mean Vertical Turbulence Intensities

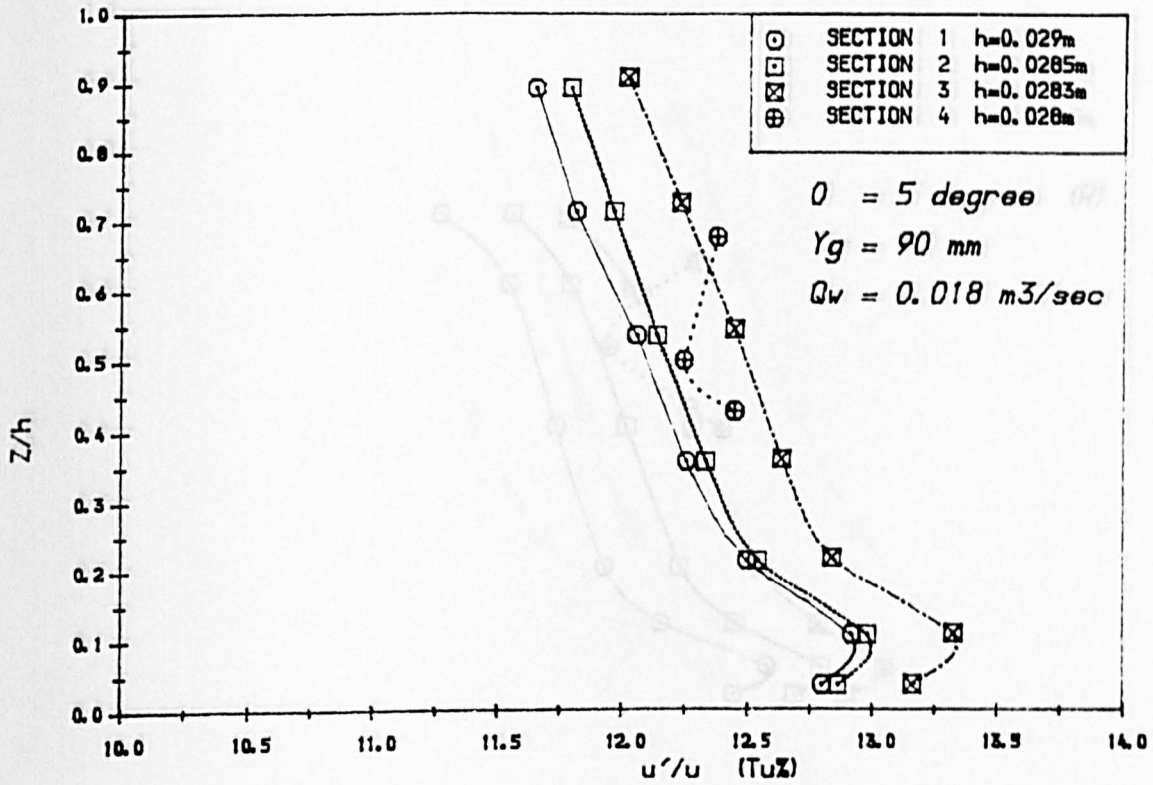

Fig 4.44 (a) Mean Longitudinal Turbulence Intensities

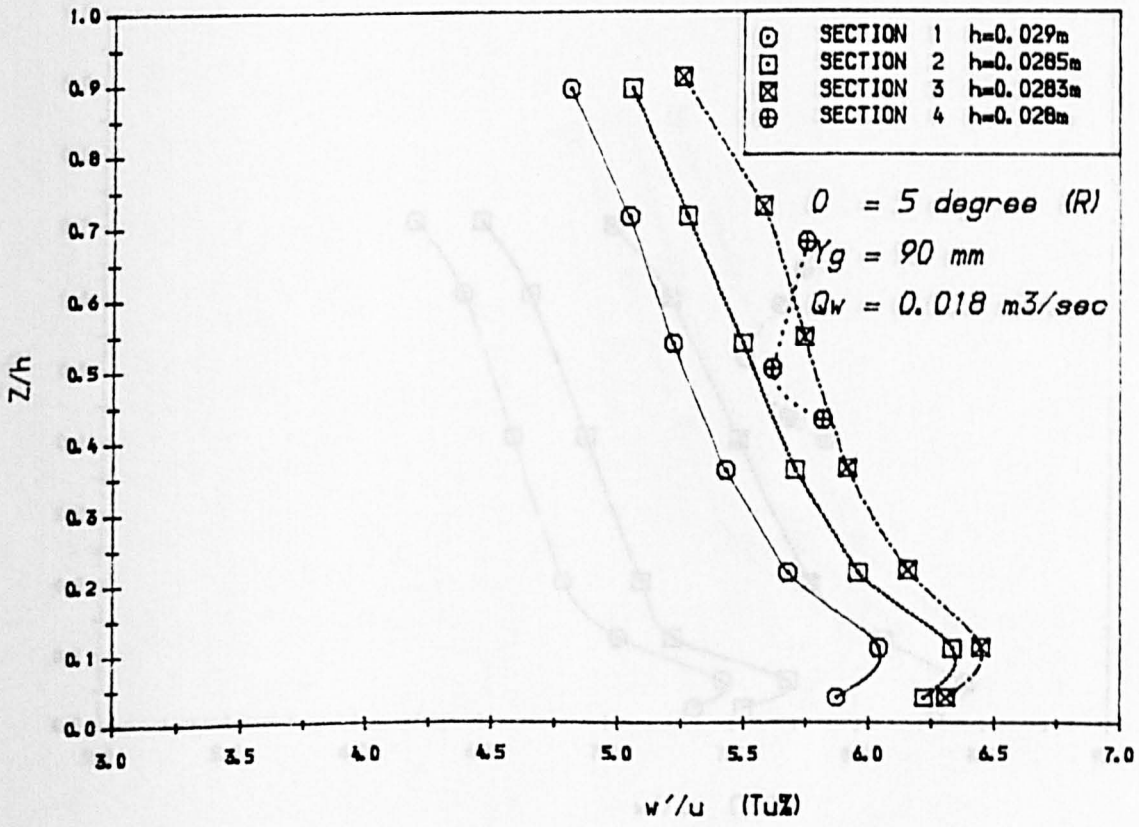

Fig 4.44 (b) Mean Vertical Turbulence Intensities

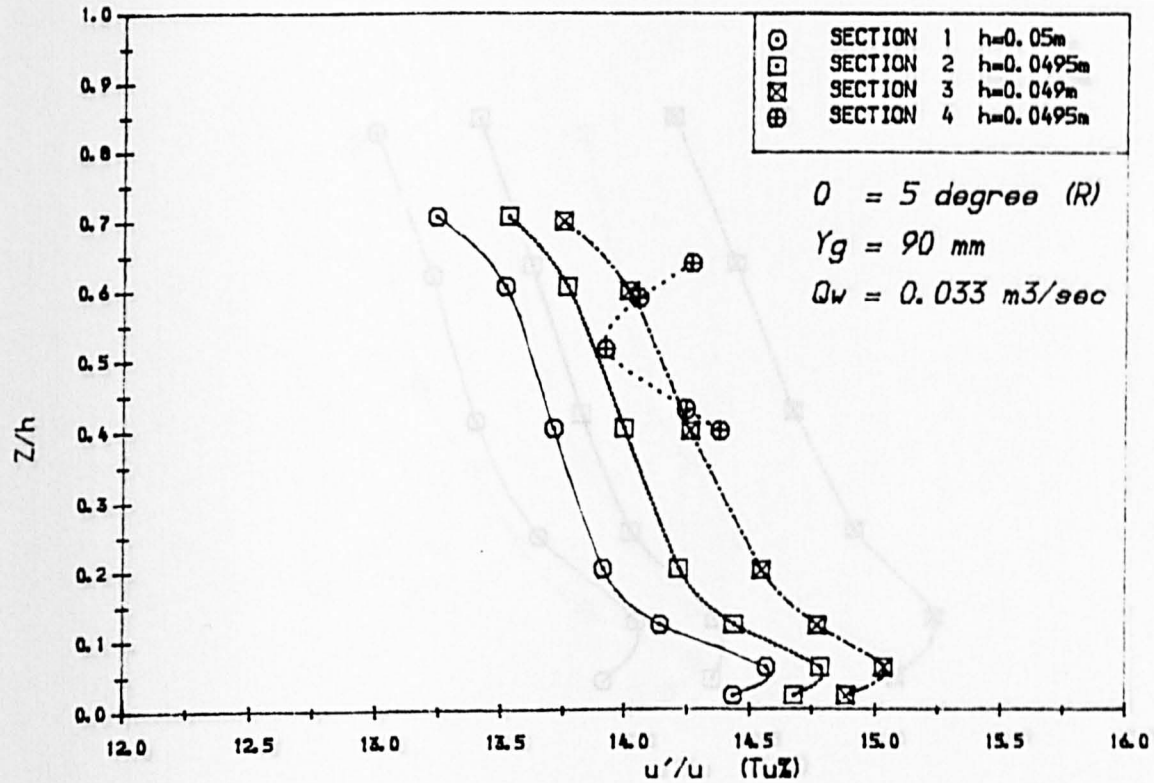

Fig 4.45(a) Mean Longitudinal Turbulence Intensities

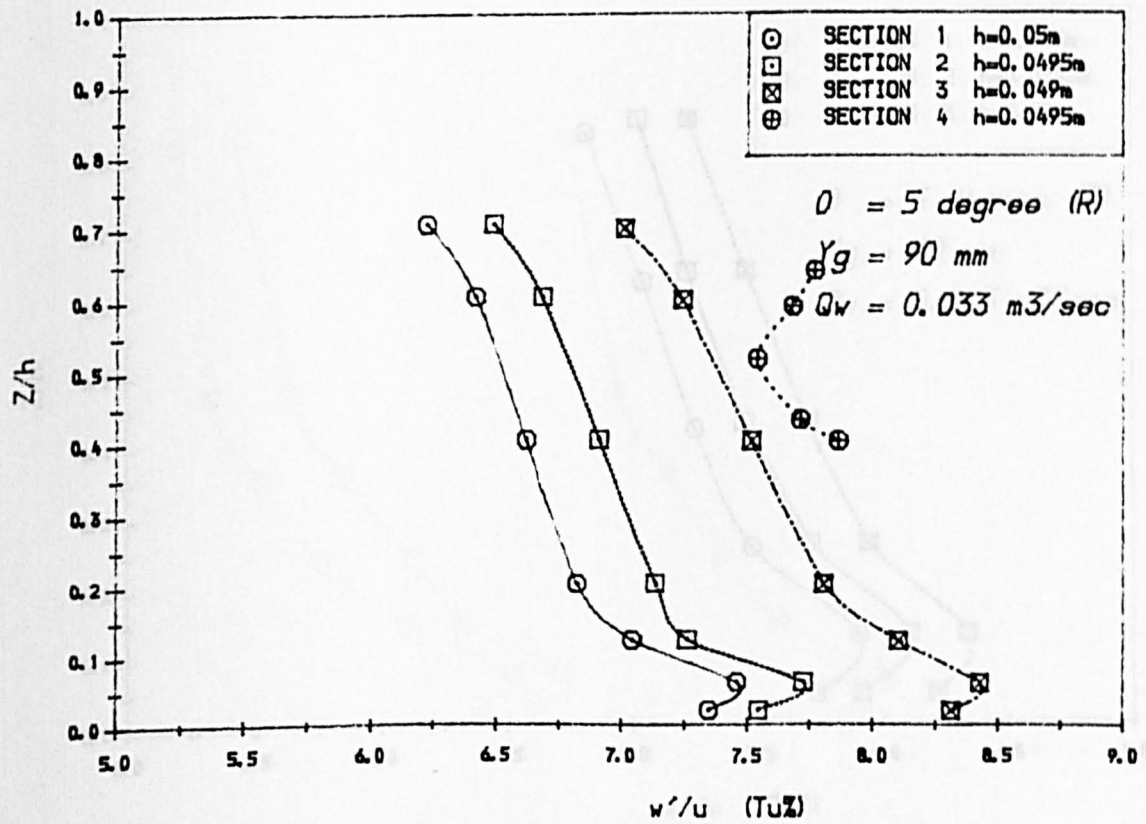

Fig 4.45(b) Mean Vertical Turbulence Intensities

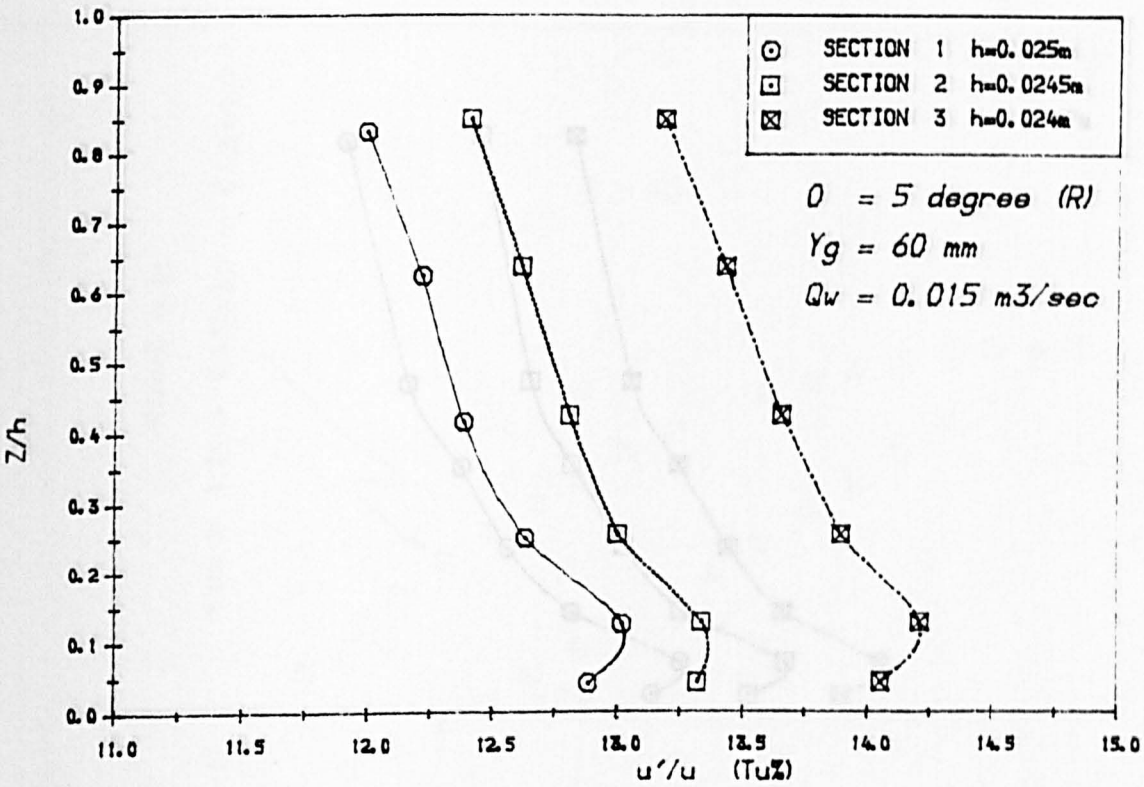

Fig 4.46(a) Mean Longitudinal Turbulence Intensities

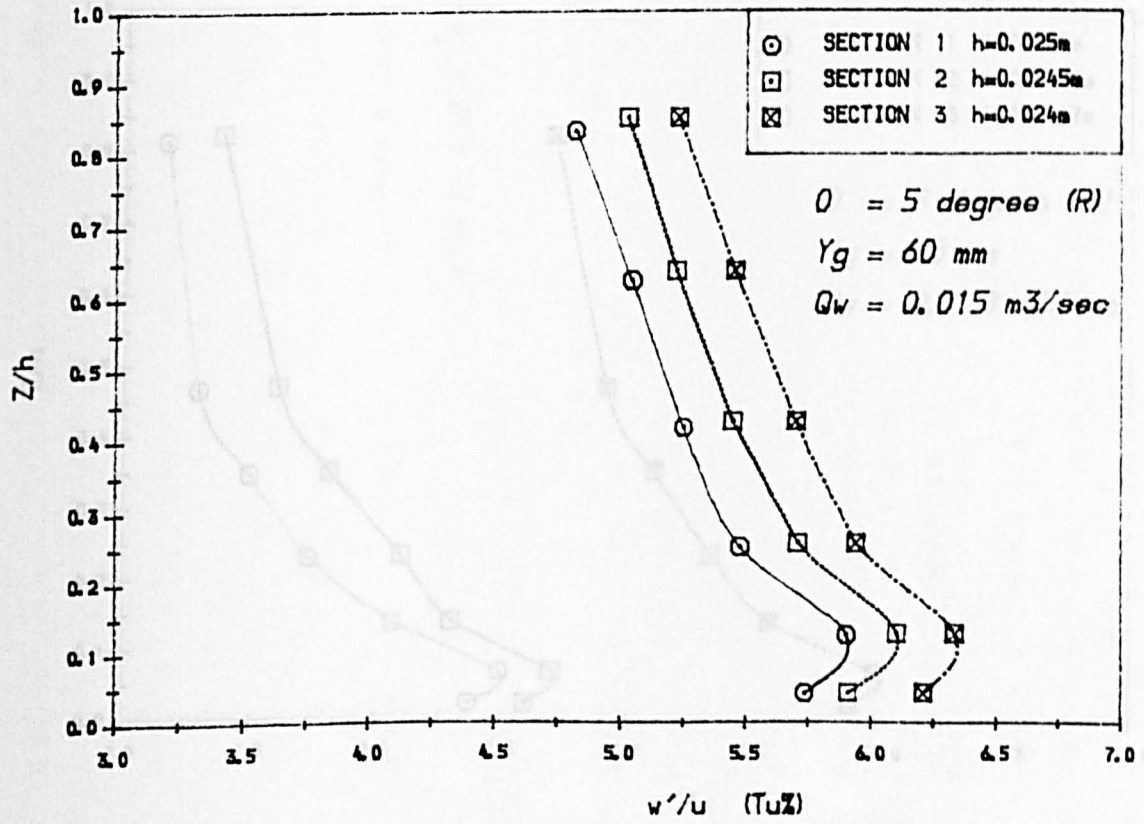

Fig 4.46(b) Mean Vertical Turbulence Intensities

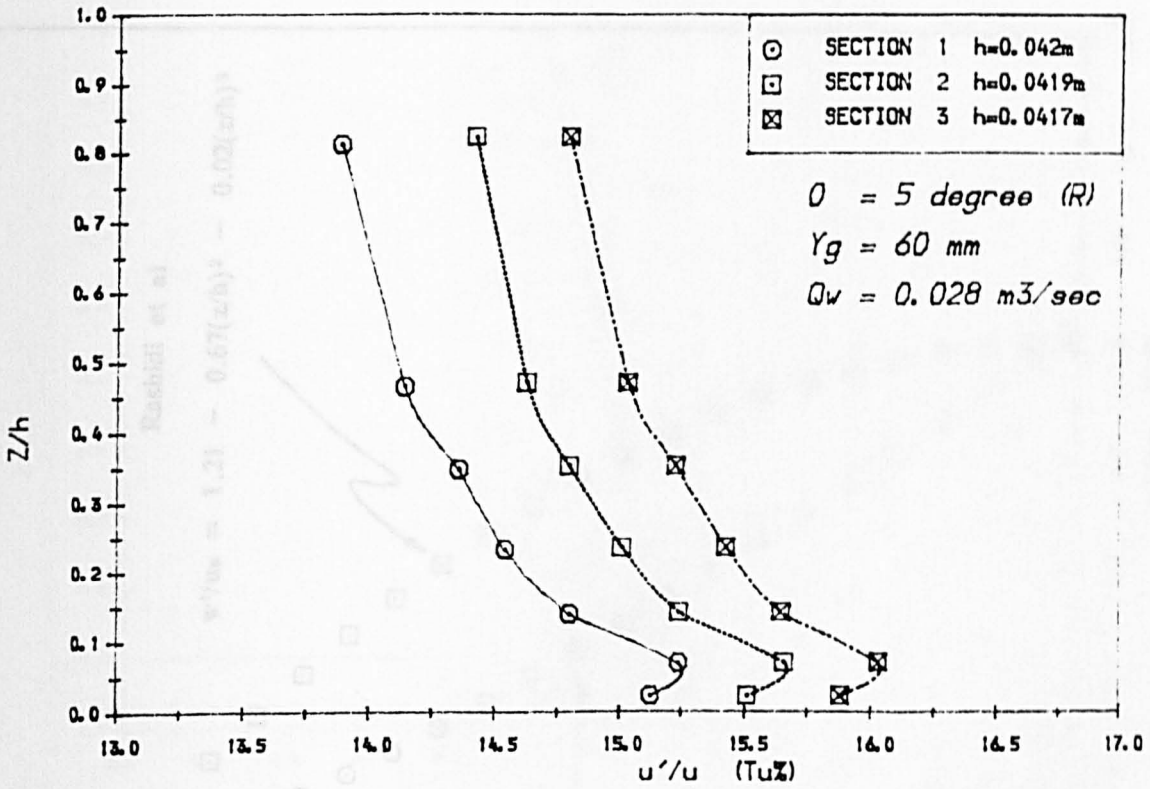

Fig 4.47(a) Mean Longitudinal Turbulence Intensities

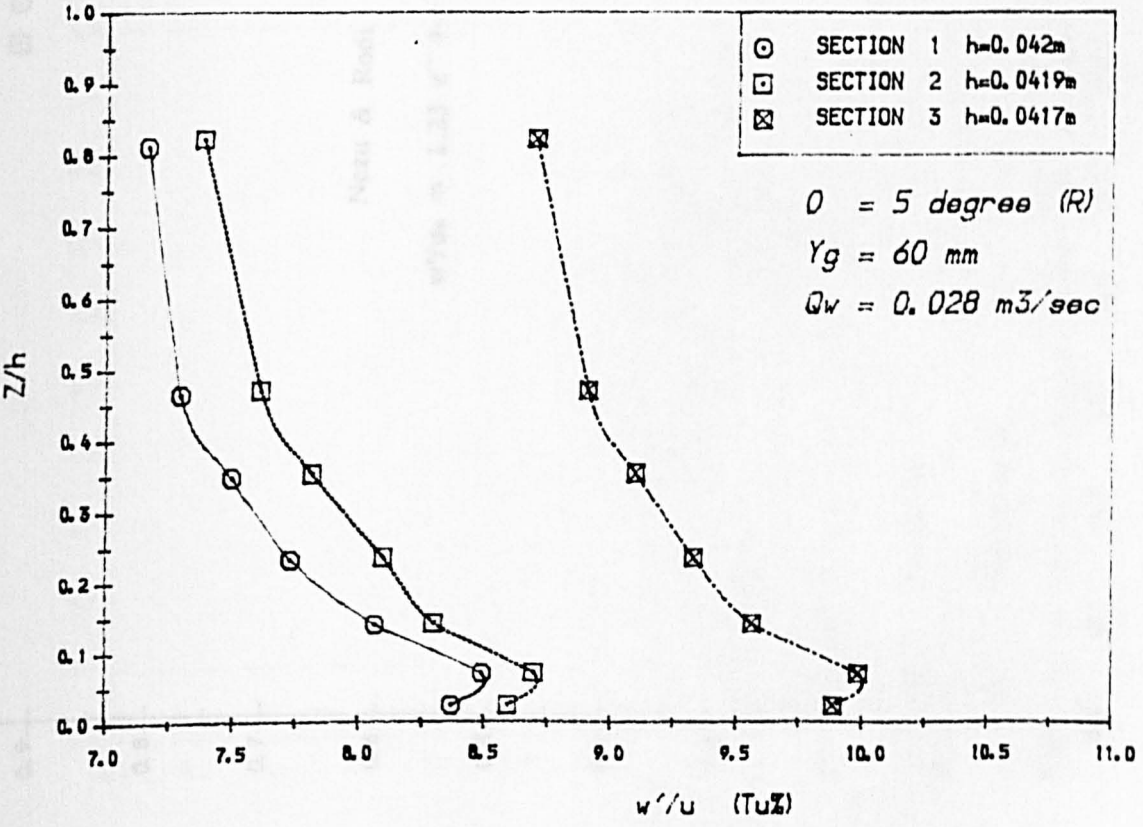

Fig 4.47(b) Mean Vertical Turbulence Intensities

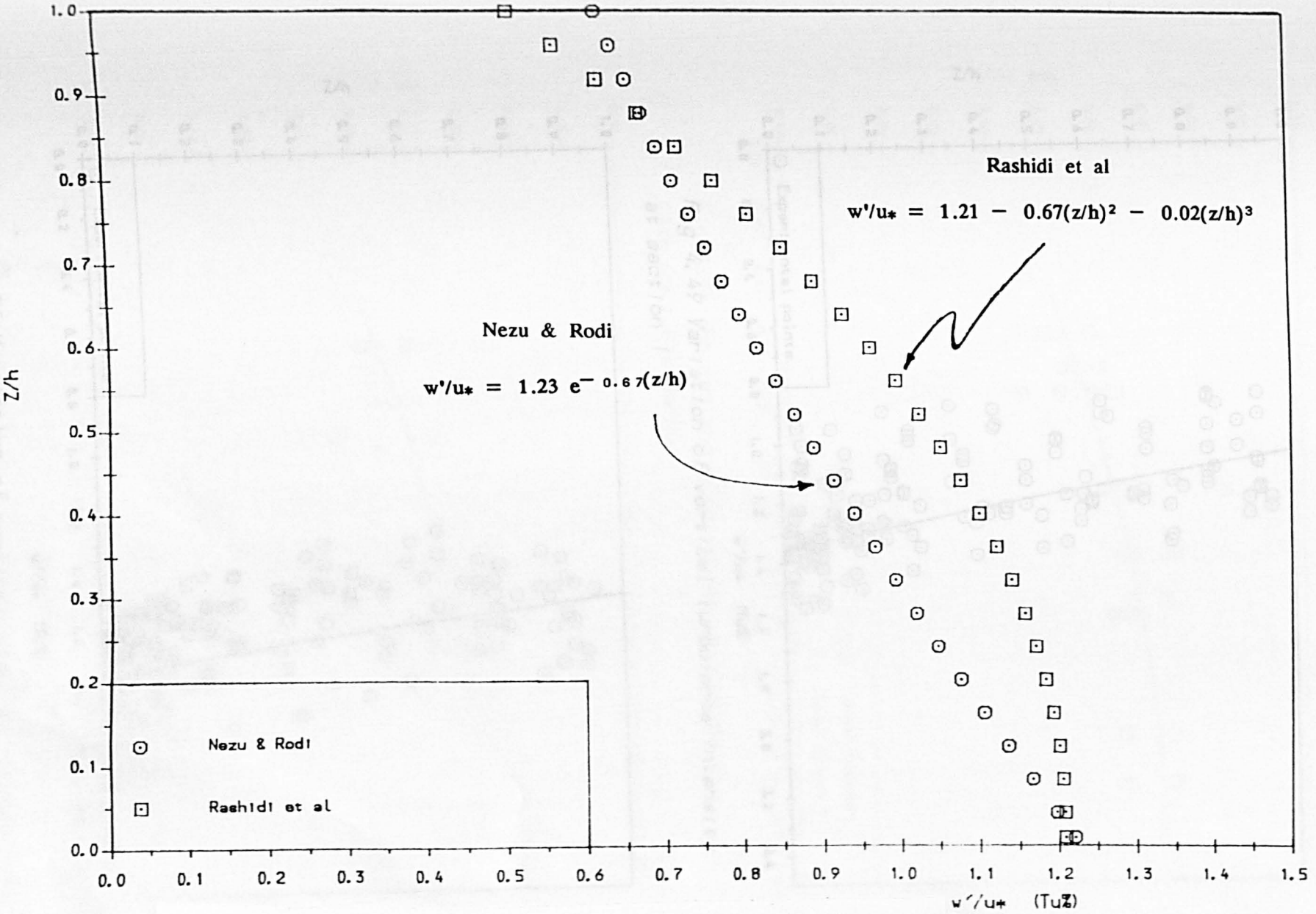

Fig 4.48 Vertical turbulence intensities with height above the channel bed

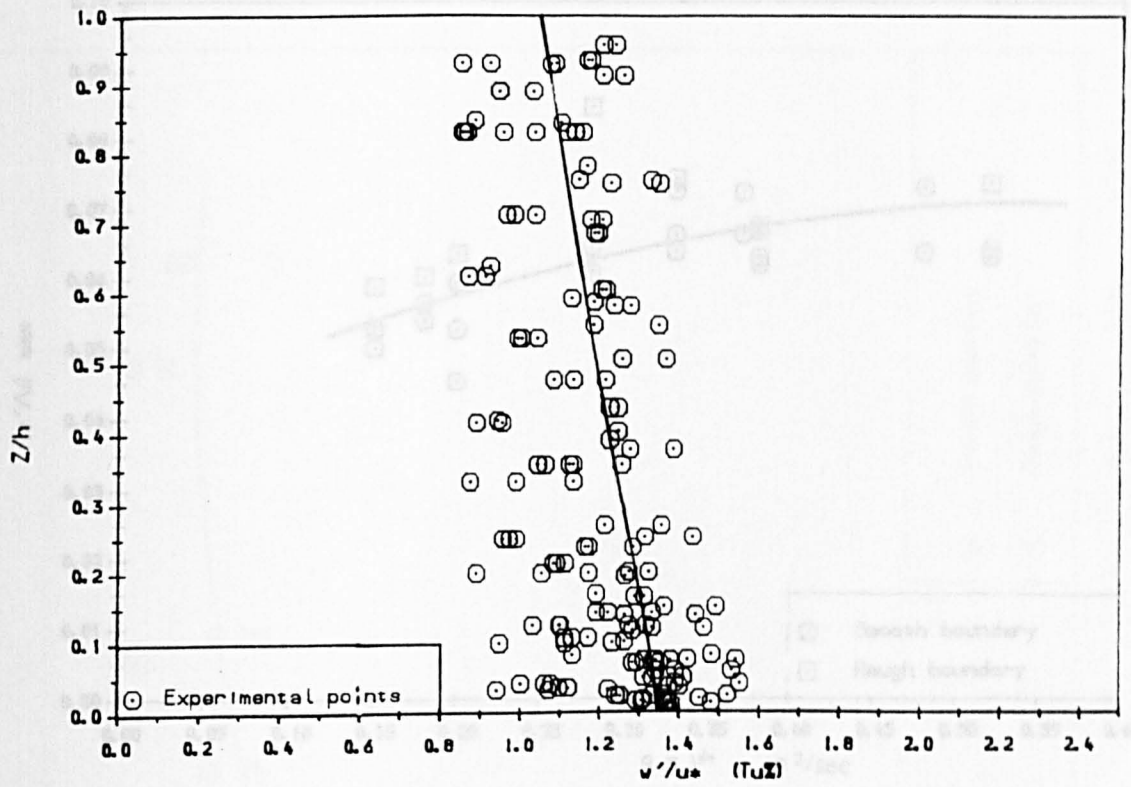

Fig 4.49 Variation of vertical turbulence intensity at section 1

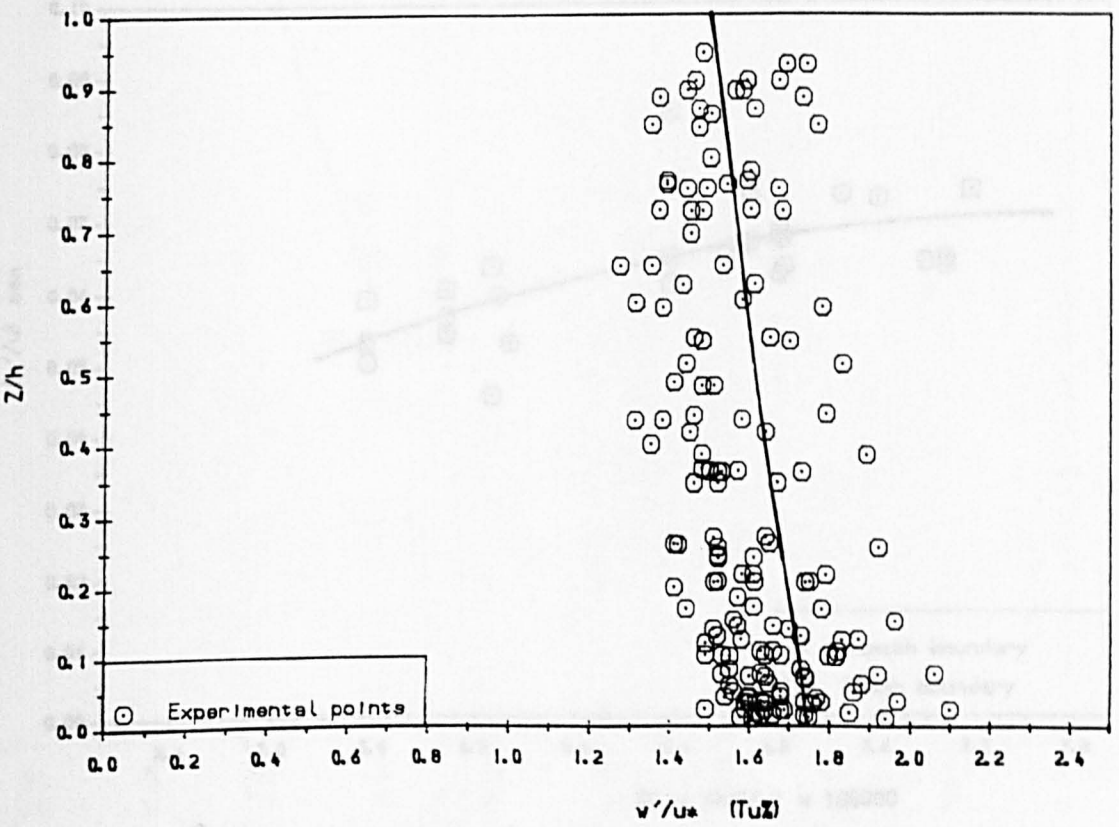

Fig 4.50 Variation of vertical turbulence intensities at section 3

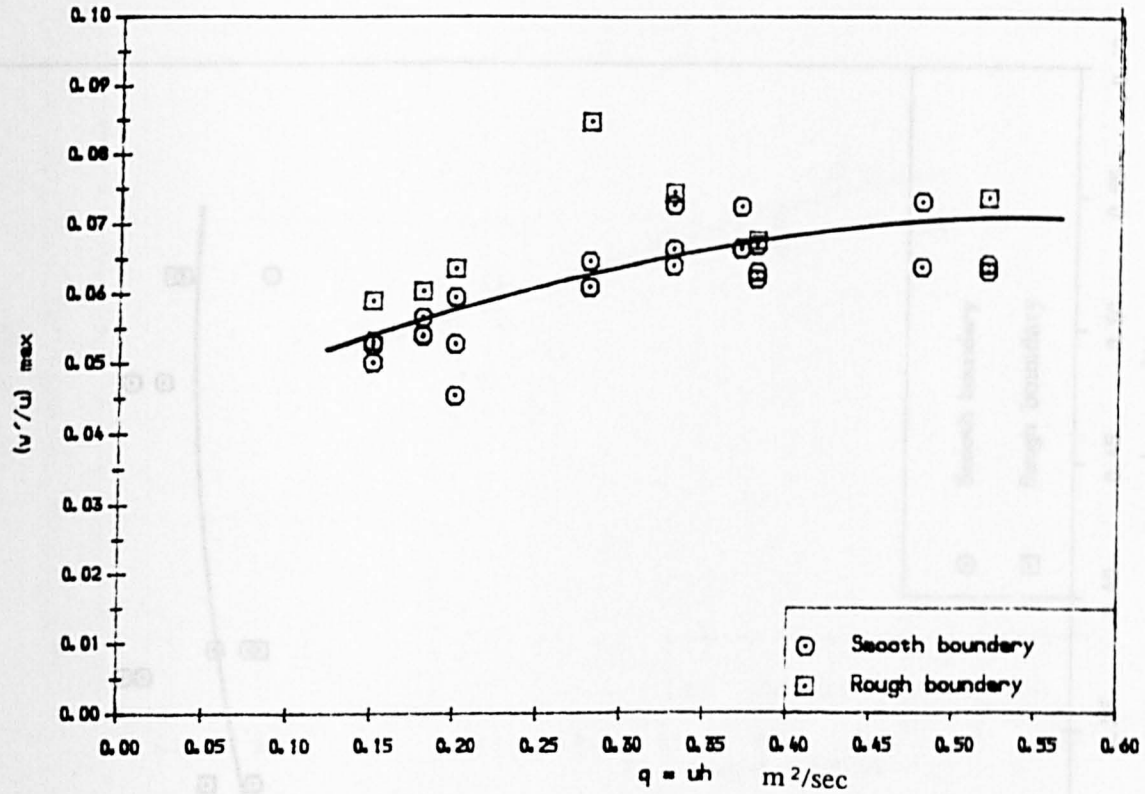

Fig 4.51 The Maximum v'/u values at section 1 with unit discharge

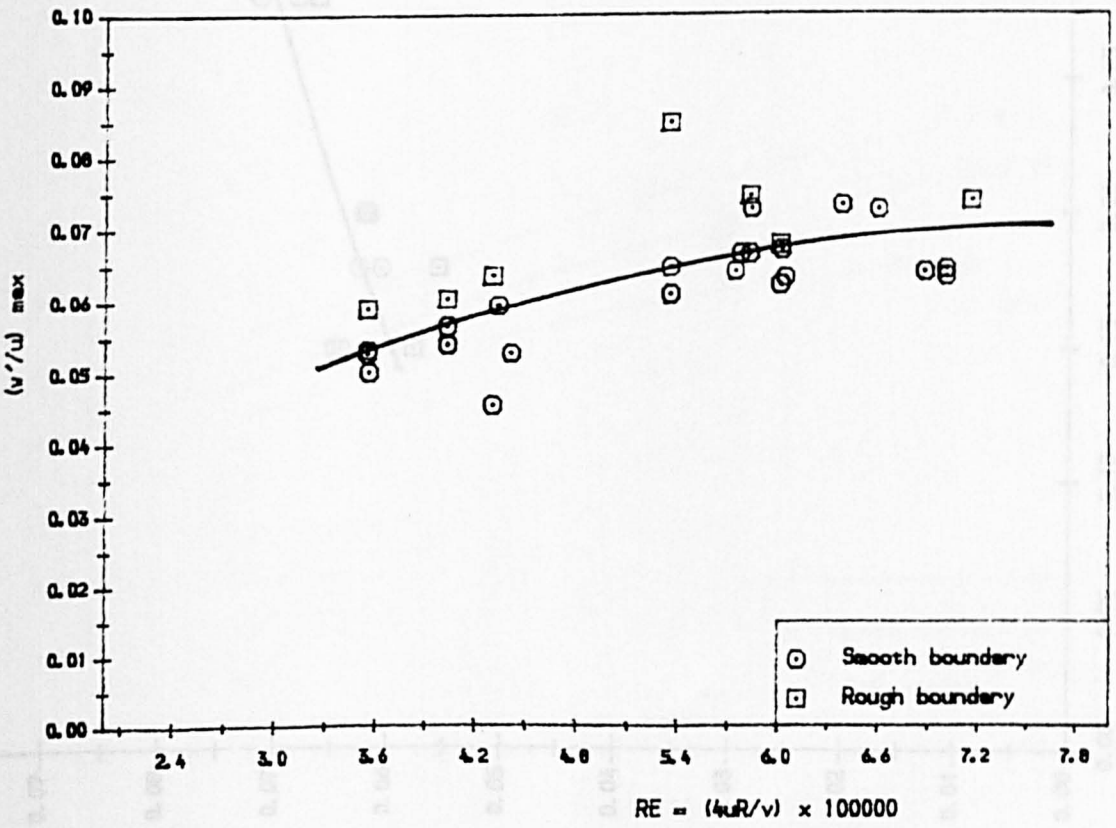

Fig 4.52 The Maximum v'/u values at section 1 with Reynolds number

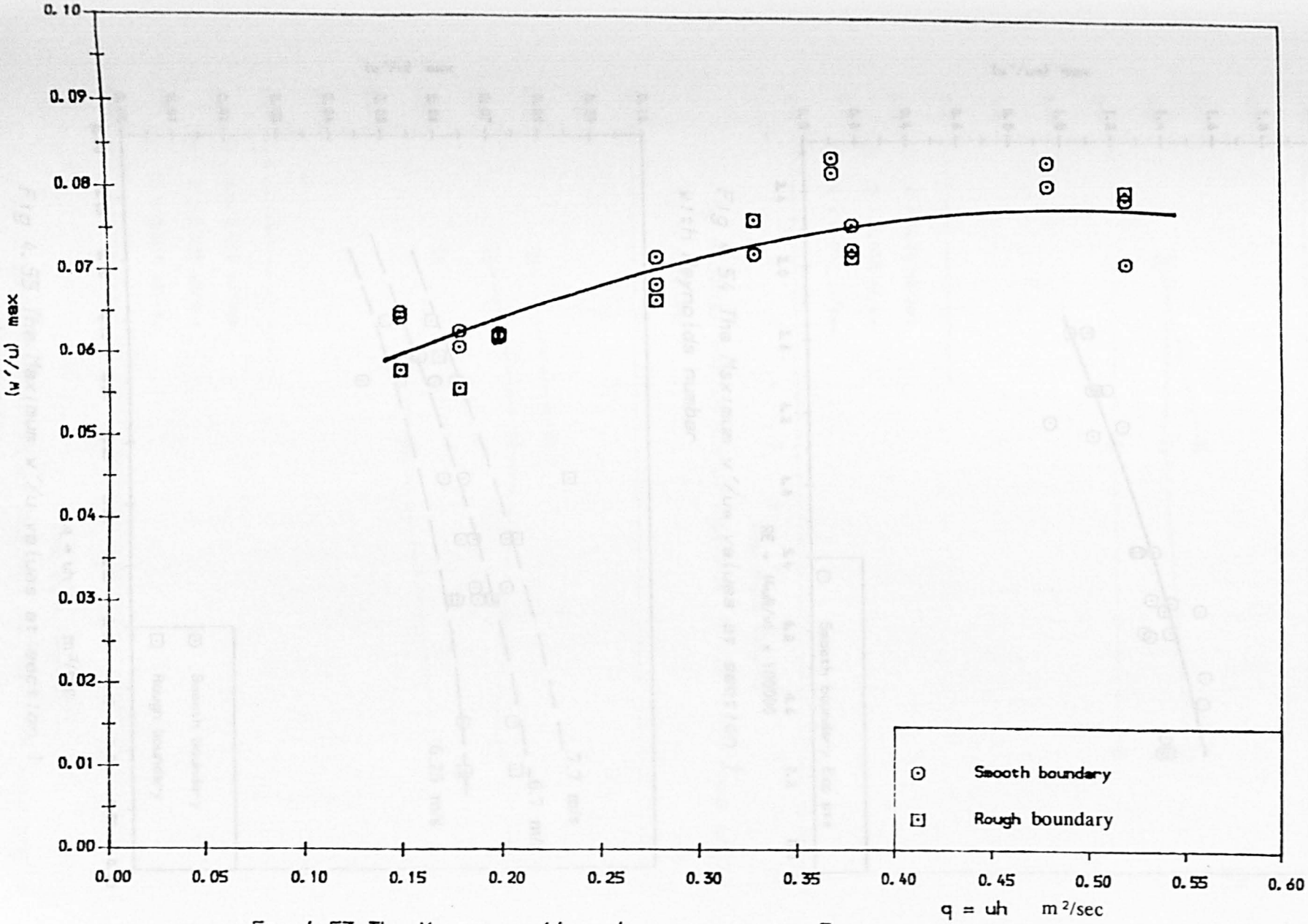

Fig 4.53 The Maximum w'/u values at section 3 with unit discharge

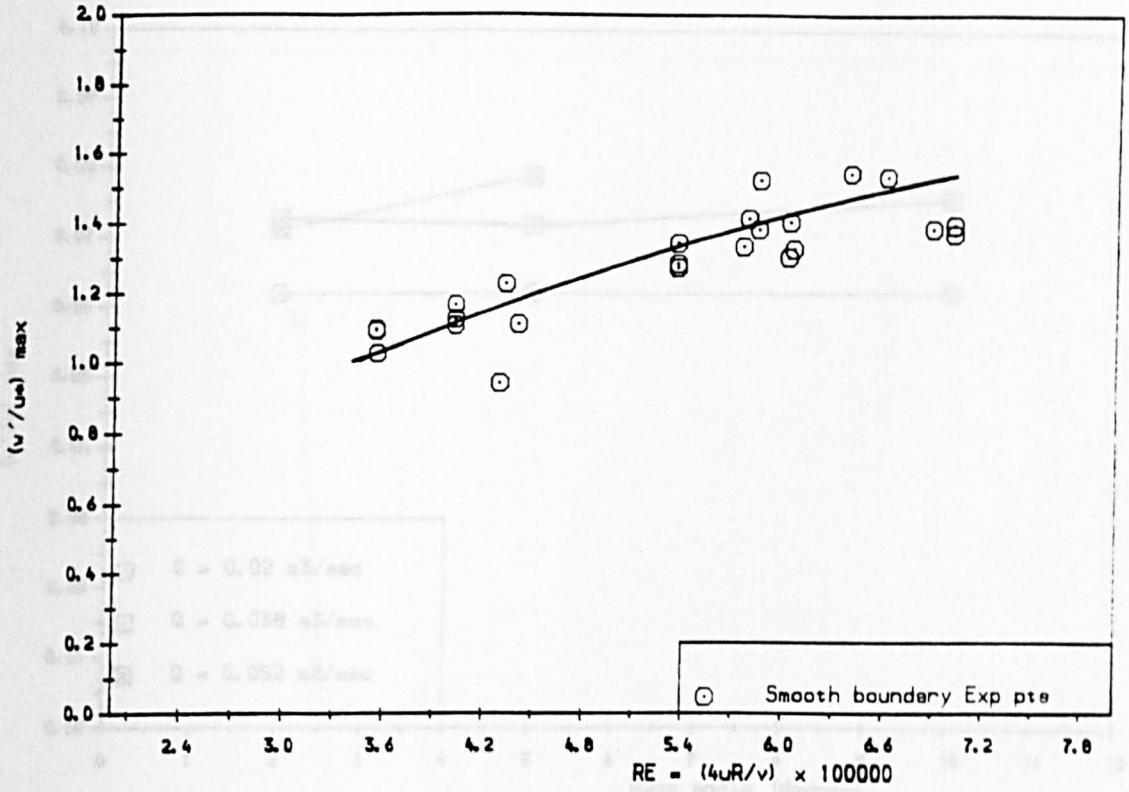

Fig 4.54 The Maximum w'/u values at section 1 with Reynolds number*

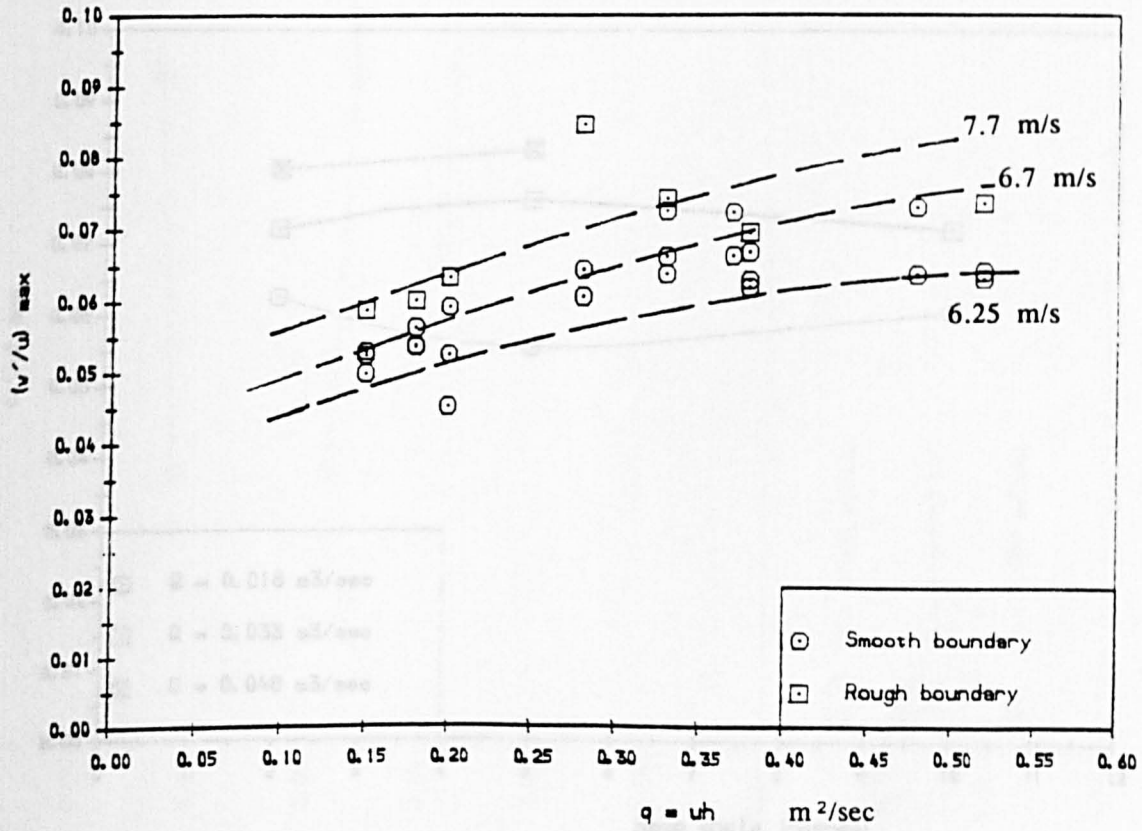

Fig 4.55 The Maximum w'/u values at section 1 with unit discharge

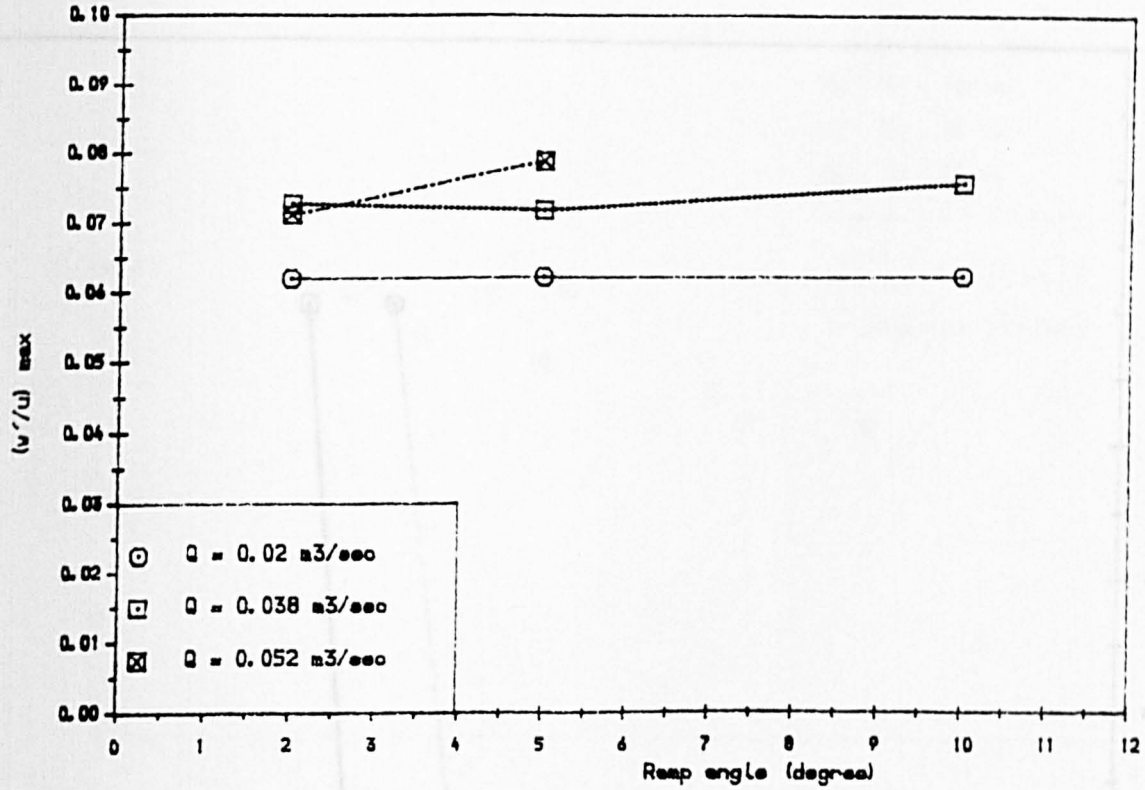

Fig 4.56(a) Variation of Maximum (w'/u) with ramp angle Yg = 180 mm

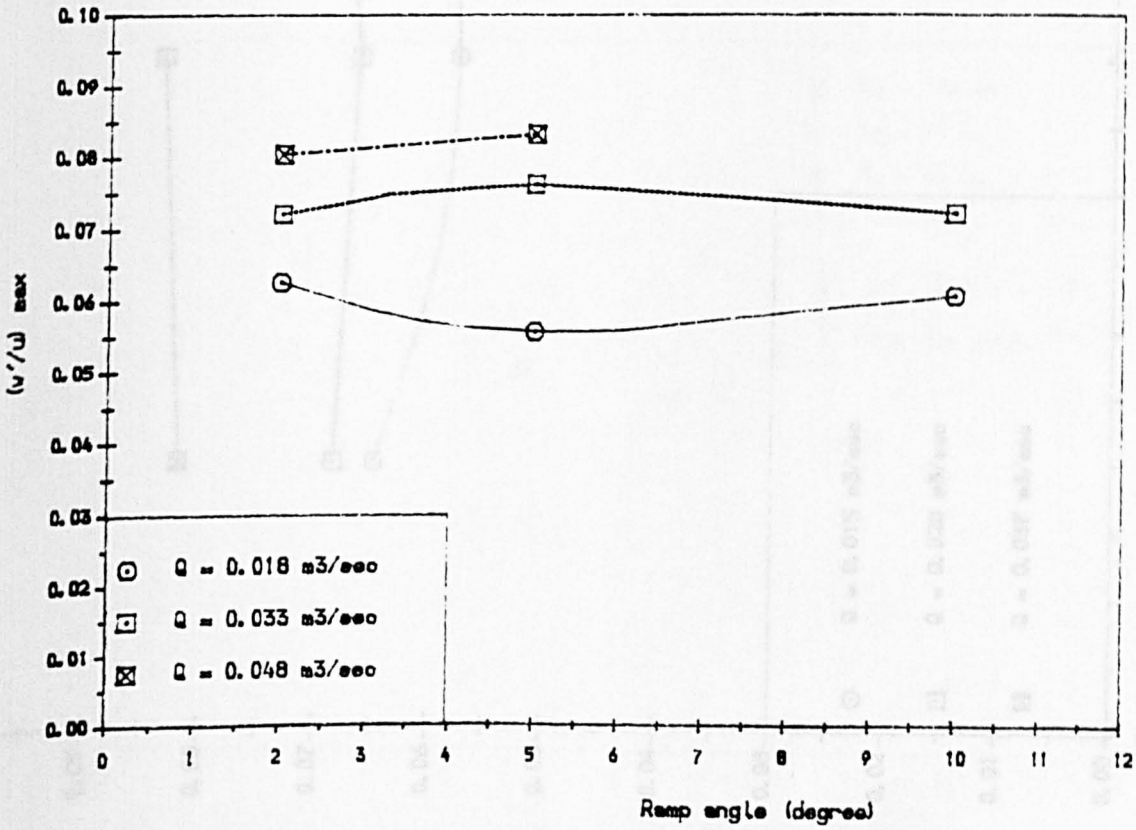

Fig 4.56(b) Variation of Maximum (w'/u) with ramp angle Yg = 90 mm

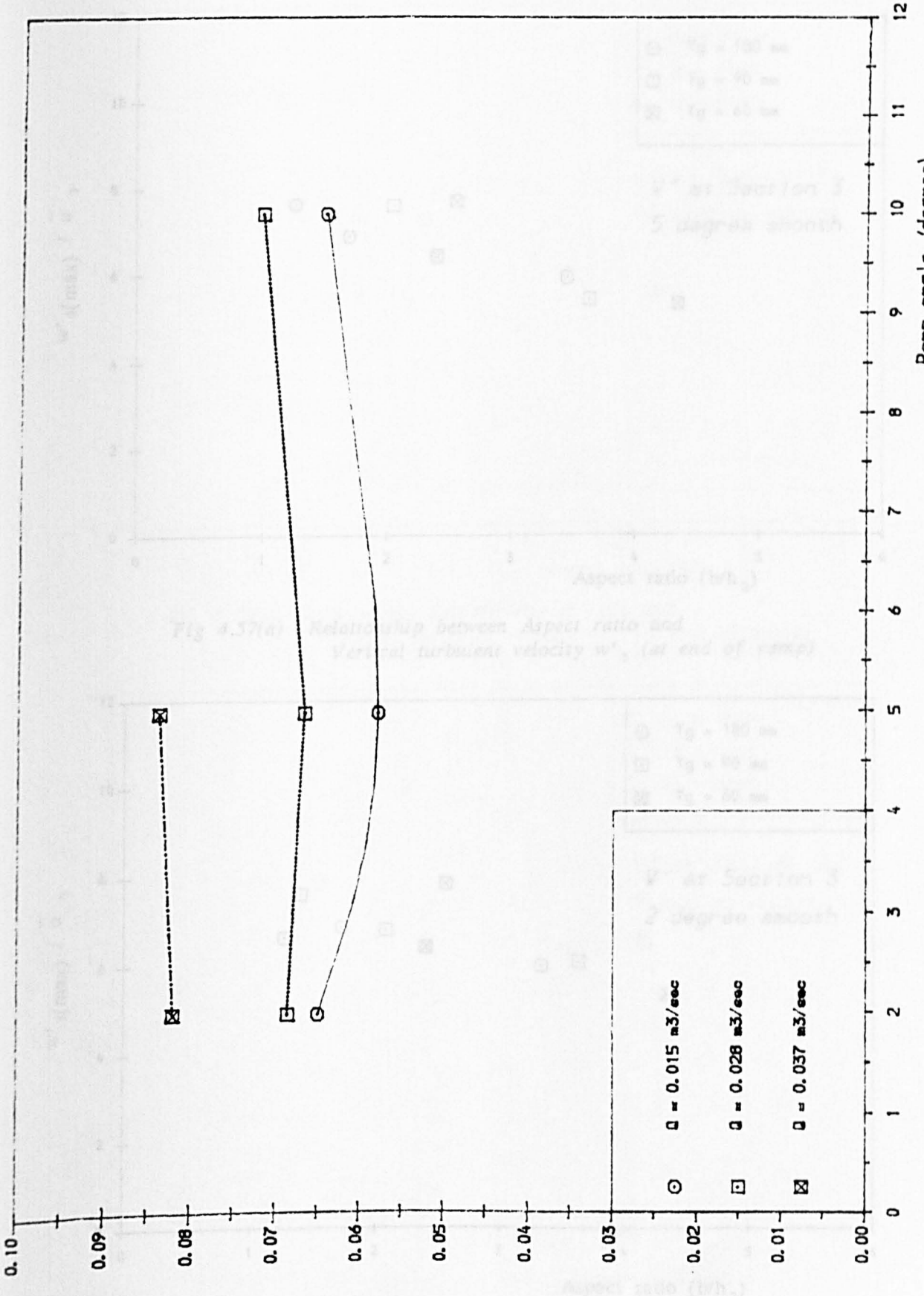

Fig 4.56(c) Variation of Maximum (w'/u) with ramp angle Yg = 60 mm

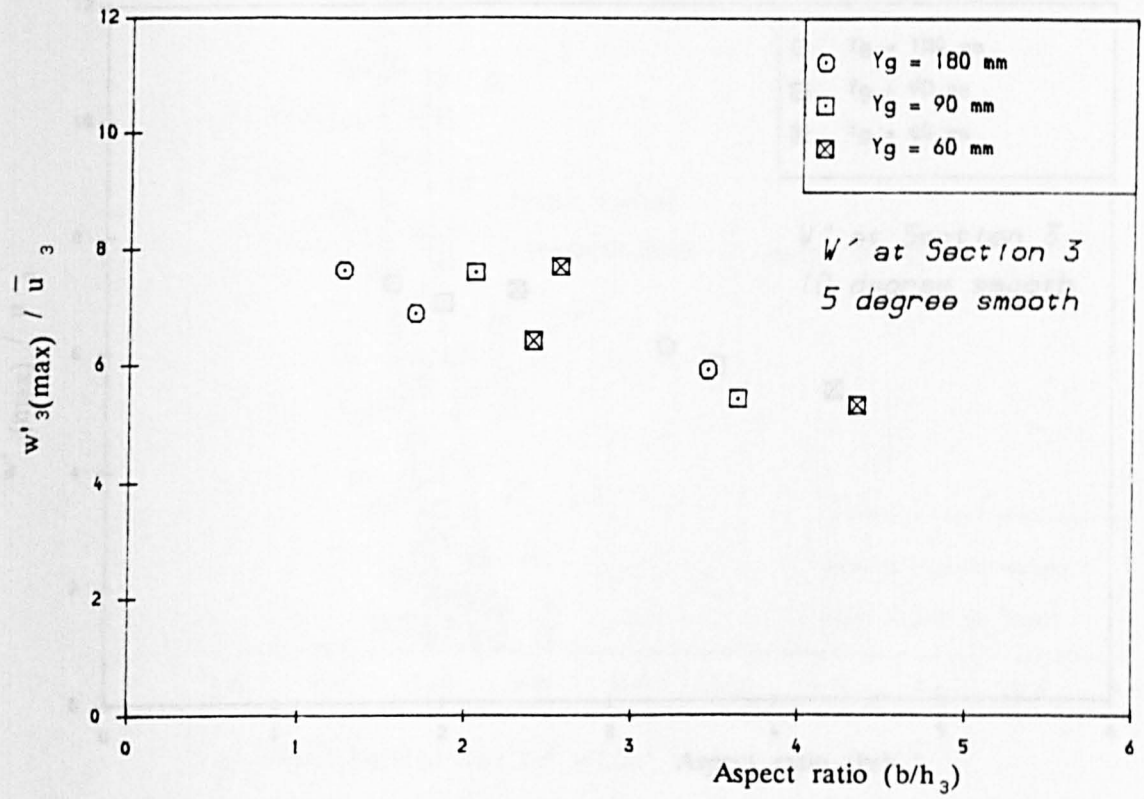

Fig 4.57(a) Relationship between Aspect ratio and Vertical turbulent velocity w'_3 (at end of ramp)

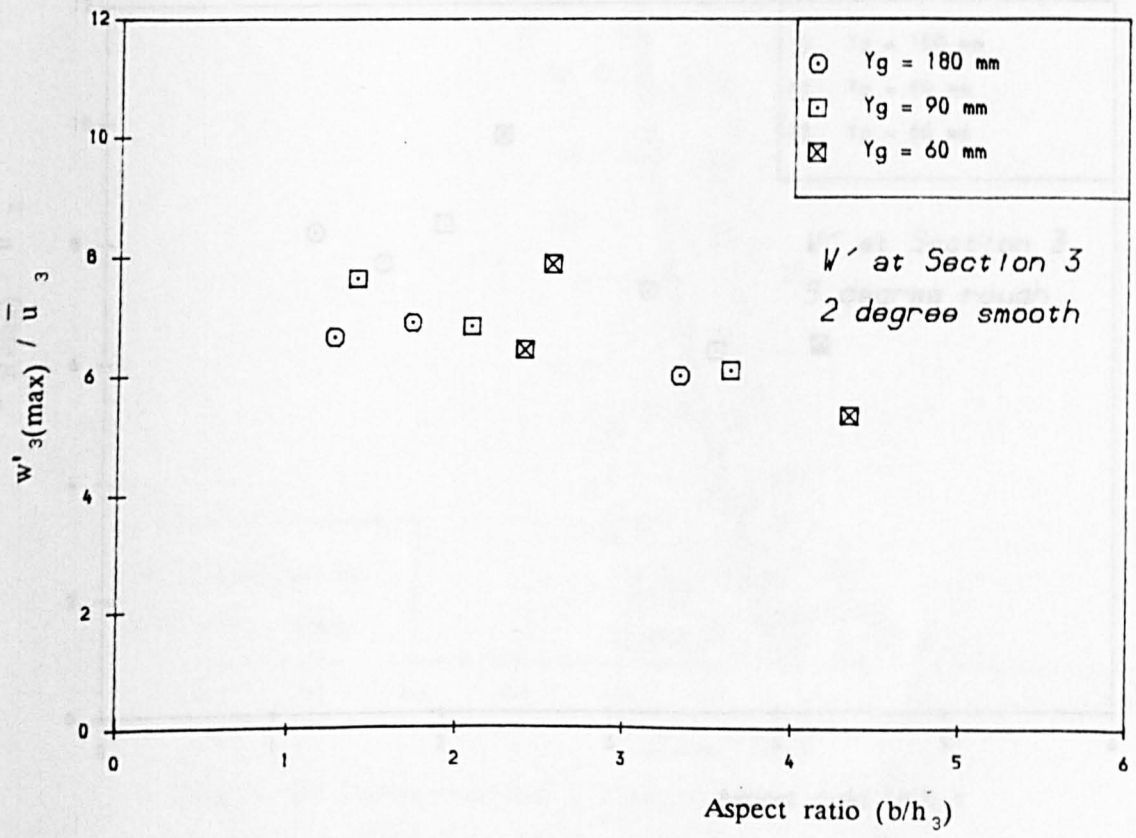

Fig 4.57(b) Relationship between Aspect ratio and Vertical turbulent velocity w'_3 (at end of ramp)

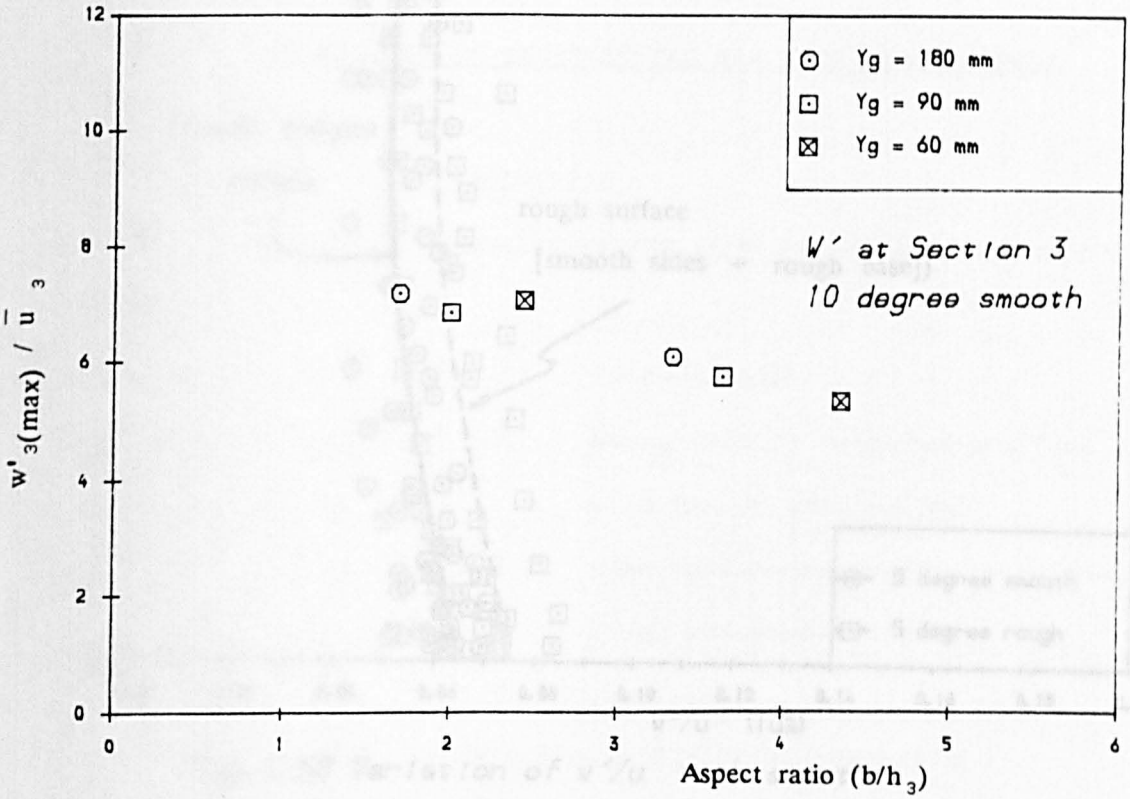

Fig 4.57(c) Relationship between Aspect ratio and Vertical turbulent velocity w'_3 (at end of ramp)

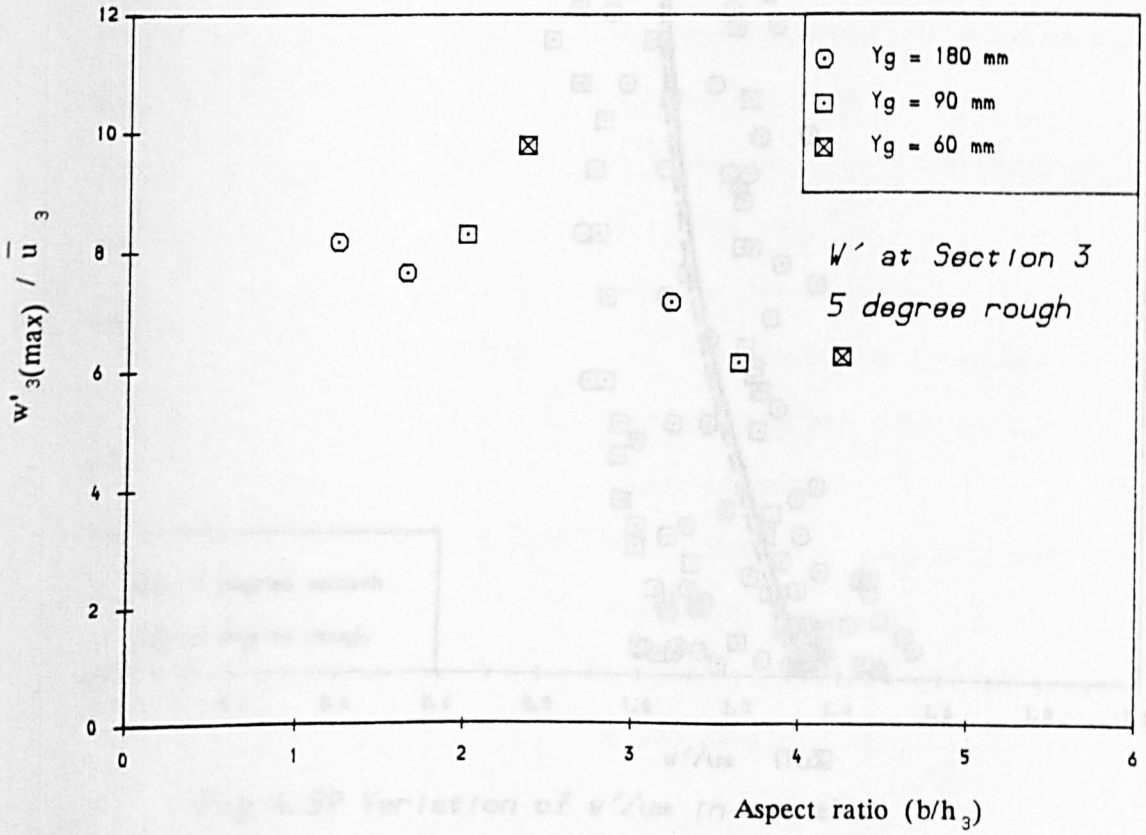

Fig 4.57(d) Relationship between Aspect ratio and Vertical turbulent velocity w'_3 (at end of ramp)

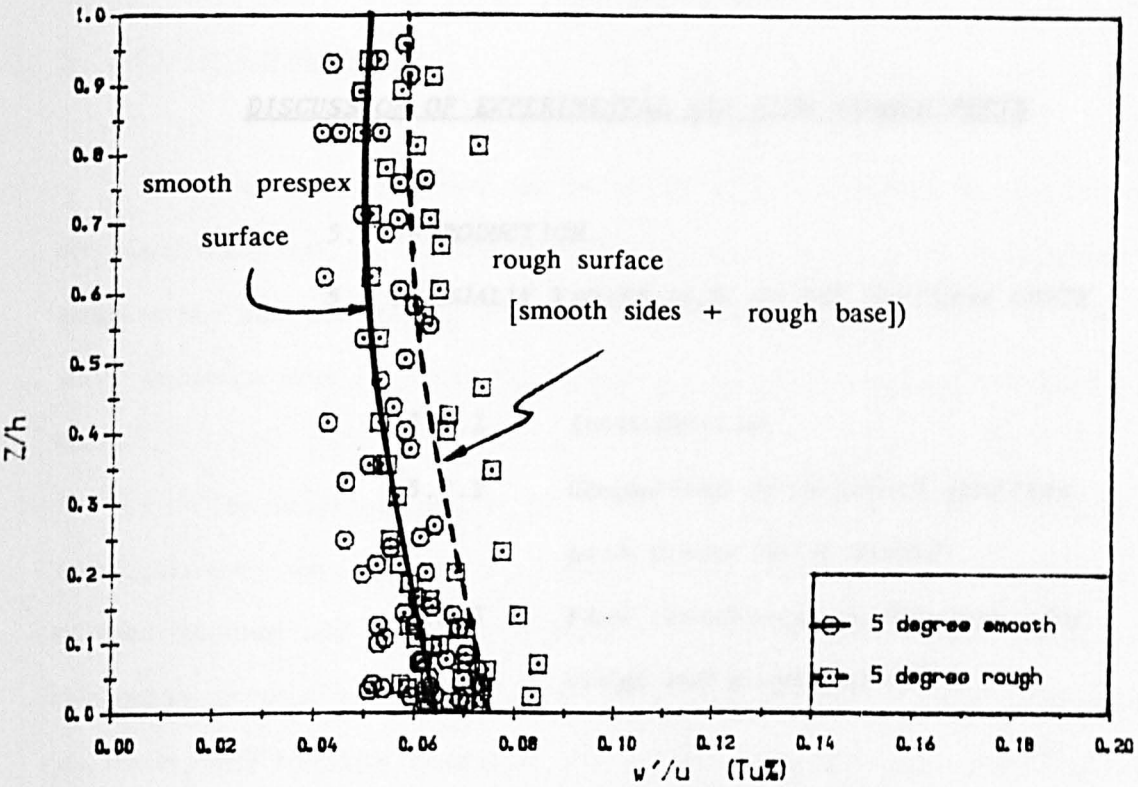

Fig 4.58 Variation of w'/u with smooth and rough boundary at section 1

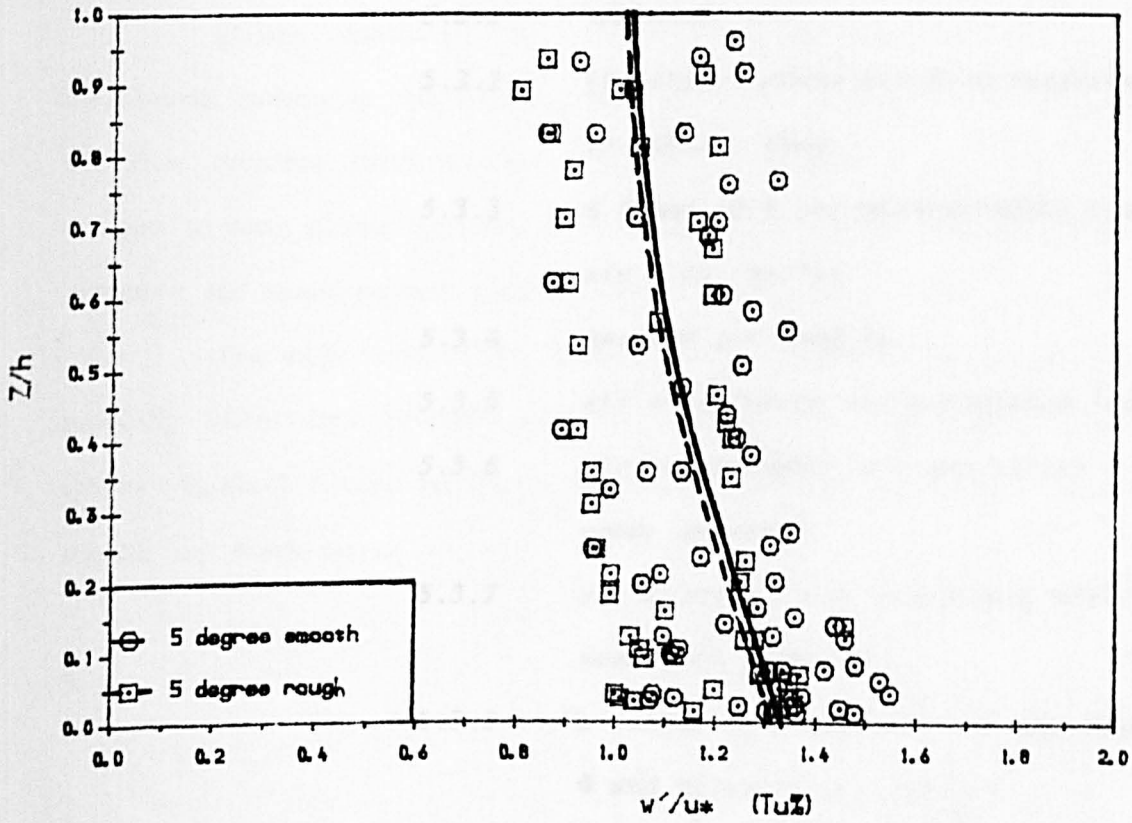

Fig 4.59 Variation of w'/u in smooth and rough boundary at section 1*

CHAPTER 5.

DISCUSSION OF EXPERIMENTAL AIR FLOW MEASUREMENTS.

5.1 INTRODUCTION

The results presented in this Chapter concentrate on the air flow or air entrainment rate, in the aerator. This is done for a range of ramp angles Φ, pressure box gate opening Y_g, for two boundary roughness values, for a range of water discharge rates Q_w, and for a controlled range of underpressure under the jet, Δh.

The main purpose of this Chapter is to investigate the influence of each parameter on the air entrainment rate. This includes the relationship between aeration and turbulence generated at the ramp, and also includes the relationship between aeration and cavity under pressure, flow velocity, ramp angle, jet length, and boundary roughness. This procedure is some what complicated by the fact that many parameters depends upon each other, as well as determining the air entrainment rate.

Having established the influence of each parameter on the air entrainment process in this Chapter, then the role of Chapter 6 is to combine the flow turbulent structure from Chapter 4 with the air flow data in this Chapter to form a new approach to aerators, which hopefully can be applied to prototype and model aerators alike, and to a range of design types.

The early part of the Chapter, however, establishes the nature of the gradually varied flow profiles along the spillway chute and offers values of D'arcy– Weisbach friction factors 'λ' as well as Mannings 'n' values for both the smooth and rough cases.

5.2 *GRADUALLY VARIED FLOW IN THE SPILLWAY CHUTE.*

5.2.1. Introduction

Before discussing the air flow measurements proper in section 5.3, it is important to establish the gradually varied flow profiles along the spillway chute for the range of discharges and gate openings involved.

This investigation was done by measuring the gradually varied flow profiles and then comparing with gradually varied flow analysis using the Direct Step method. By adjusting the friction factor in the Direct Step method, the best fit between the two is achieved and hence estimates of the D'arcy– Weisbach friction factor and Mannings 'n' value are possible both for the rough and smooth boundaries.

There are two possible approaches to Direct Step method for calculating the gradually varied flow profile along a spillway chute, namely the energy method and the momentum method.

(a) *The Energy method.*

From hydraulics theory the total energy in any streamline passing through a channel section may be expressed as total head in meters of water, which is equal to the sum of the elevation above a datum, the pressure head, and the velocity head as shown on Fig 5.1. Equating the total heads at the two end sections 1 and 2, we can write the following equation,

$$\Delta x \sin\theta + h_1 \cos\theta + v_1^2/2g = \Delta x \bar{S}_f + h_2 \cos\theta + v_2^2/2g \qquad (5.1)$$

where

h_1 = depth of water at section 1 normal to channel bed.

h_2 = depth of water flow at section 2 normal to the channel bed.

$\triangle x \sin\theta$ is the distance between the bottom of channel at section 1 and the datum. "θ" is the inclination of the channel to the horizontal. $v_1^2/2g$ is the velocity head at section 1 and $v_2^2/2g$ is the velocity head at section 2, assuming α to be 1.

h_f = energy head loss $\simeq \bar{S}_f \triangle x$, where

$\bar{S}_f$ = average of friction slope.

Reorganising equation (5.1),

$$\triangle x \sin\theta - \triangle x \bar{S}_f = (h_2 - h_1)\cos\theta + [\, v_2^2/2g - v_1^2/2g \,] \quad (5.2a)$$

$$\triangle x (\sin\theta - \bar{S}_f) = (h_2 - h_1)\cos\theta + [\, v_2^2/2g - v_1^2/2g \,] \quad (5.2b)$$

Therefore,

$$\triangle x = \frac{(h_2 - h_1)\cos\theta + [\, v_2^2/2g - v_1^2/2g \,]}{\sin\theta - \bar{S}_f} \quad (5.2c)$$

For the case when the angle is 45^0 (i.e experimental setup)

$$\triangle x = \frac{(0.7071\, h_2 + v_2^2/2g) - (0.7071\, h_1 + v_1^2/2g)}{\sin\theta - \bar{S}_f} \quad (5.2d)$$

or

$$\triangle x = \frac{\triangle E}{\sin\theta - \bar{S}_f} \quad (5.3)$$

where $\triangle E$ is the change in specific energy between the two sections. Equation (5.3) is reasonably accurate for small increments of $\triangle x$, but not in the region of a control section.

In considering parameters for the calculation of the energy line slope, either Manning's or D'arcy– Weisbach equation could be used. The Darcy– Weisbach equation derives from the pipe head loss equation,

$$h_f = \lambda \frac{L}{D} \frac{v^2}{2g} \qquad (5.4)$$

where h_f/L is the slope of the energy line ($\bar{S}_f$), and when applied to open channels, the pipe diameter is substituted by 4R (where R is the hydraulic radius). Thus equation 5.4 becomes;

$$\bar{S}_f = \frac{\lambda}{8gR} v^2 \qquad (5.5)$$

where λ is D'arcy– Weisbach friction factor, which in turn may be determined from the Colebrook– White Equation provided the Reynolds Number and equivalent sand grain roughness size k_s, are known. Some Engineers resort to use of the Manning's Equation, where friction factor (n) remains almost constant. The Manning's equation could be rewritten as:

$$v = \frac{1}{n} R^{2/3} S^{\frac{1}{2}} \qquad (5.6)$$

or

$$\bar{S}_f = \frac{n^2 v^2}{R^{4/3}} \qquad (5.7)$$

(b) *The Momentum method.*

Considering Fig 5.2 and according to Newton's second Law of motion, the change of momentum per unit of time in a body of water in a flowing channel is equal to the resultant of all the external forces that act on a body. Applying this principle to the sectional elevation shown in Fig 5.1 the result is;

$$P_1 - P_2 + Mg \sin\theta - F_f = \rho \beta Q_w (v_2 - v_1) \qquad (5.8)$$

where:

P_1 = resultant pressure at section 1

h_1 = depth of flow at section 1

v_1 = mean velocity of flow at section 1

P_2 = resultant pressure at section 2

h_2 = depth of flow at section 2

v_2 = mean velocity of flow at section 2

F_f = frictional force

β = momentum correction factor

$\bar{h}$ = average depth of the flow

M = mass of the water

θ = inclination of the bottom of the channel to the horizontal

$\triangle x$ = distance between section 1 and section 2

Assuming the width of the rectangular channel is b,

β = momentum correction factor = 1.0

ρ = density of water

g = gravitational constant

Q_w = discharge of water

hence, pressure, mass and frictional force can be written as;

$$P_1 = \tfrac{1}{2} \rho g b h_1^2 \cos\theta$$

$$P_2 = \tfrac{1}{2} \rho g b h_2^2 \cos\theta$$

$$M = \rho b \bar{h} \triangle x \text{ , where } \bar{h} = (h_1 + h_2) / 2$$

$$F_f = (\rho g \bar{h} b \triangle x n^2 v^2) / R^{4/3}$$

The value of frictional force (F_f) above and shown in Fig 5.2 is derived from uniform flow considerations, as it can be shown for open channel flow that the weight component along the plane of the channel is exactly balanced by friction, as;

$$\tau_f \, p \, \Delta x = \rho \, g \, A \, \Delta x \, \sin\theta \qquad (5.9)$$

Now, from Manning's equation (5.7),

$$\tau_f = \rho \, g \, \frac{n^2 \, v^2}{R^{1/3}} \qquad (5.10)$$

and hance the total friction force ($\tau_f \, p \, \Delta x$) is given by,

$$F_f = \rho \, g \, p \, \Delta x \, \frac{n^2 \, v^2}{R^{1/3}} = \rho \, g \, \frac{h \, b}{R} \, \Delta x \, \frac{n^2 \, v^2}{R^{1/3}} \qquad (5.11)$$

subsitutiting the values of P_1, P_2, M and F_f in equation (5.11) and dividing by ($\rho \, g \, b \, \bar{h}$) the equation 5.11 becomes as;

$$(h_2 - h_1) \cos\theta + \Delta x \sin\theta - \Delta x \, \frac{n^2 \, v^2}{R^{4/3}} = \frac{q_w}{g \, \bar{h}} \, (v_2 - v_1) \qquad (5.12)$$

where q_w is the water discharge per unit width but,

$$\frac{q_w}{\bar{h}} = \frac{(v_2 + v_1)}{2} \text{ , and from Manning's equation } \bar{S}_f = \frac{n^2 \, v^2}{R^{4/3}}$$

Therefore,

$$(h_2 - h_1) \cos\theta + \Delta x \, (\sin\theta - \frac{n^2 \, v^2}{R^{4/3}}) = \frac{1}{2g} \, (v_2 - v_1)(v_2 + v_1) \qquad (5.13)$$

Arranging equation 5.13 ,

$$\Delta x\ (\sin\theta - \bar{S}_f) = \frac{1}{2g}(v_2^2 - v_1^2) + (h_2 + h_1)\cos\theta \qquad (5.14)$$

finally,

$$\Delta x = \frac{(h_2 - h_1)\cos\theta + [\, v_2^2/2g - v_1^2/2g \,]}{\sin\theta - \bar{S}_f} \qquad (5.15)$$

which is same as the energy method, when $\alpha = \beta = 1.0$

5.2.2 *Comparison of measured profiles with direct step method.*

The gradually varied flow water surface profiles were measured for a range of gate openings, and for each gate opening, a range of discharges up to 0.052 m^3/s. This was done for both the smooth and rough boundaries.

A pointer gauge was used for the measurements of the water flow depth although this procedure is difficult for high velocity steep flows. The experimental results using a pointer gauge were complemented by estimates of flow depth from the known total discharge Qw, combined with a knowledge of the mean velocity u from the array of pitot–tube measurements over the cross–section.

The results are shown in Fig 5.3 to Fig 5.6 covering the 180mm, 90mm and 60mm gate openings for the smooth boundary, as well as the 180mm gate opening for the rough boundary. The theoretical water surface profile was plotted by trial and error method, by obtaining the best fit friction factor once the rough estimate of friction factor was obtained by using Equation (5.5). The

comparison between experimental data and theoretical water surface profile using Direct step method is shown in Fig 5.3 to Fig 5.6 revealing a good correlation.

5.2.3 *Flow resistance coefficient for the rough and smooth channel.*

The three main relationships for discharge in an open channel are Chezy, Manning and D'arcy– Weisbach equations.

(i) Chezy's equation is given by:

$$Q = C A \sqrt{R S} \qquad (5.16)$$

where C is Chezy's coefficient for frictional resistance.

(ii) Manning's equation is given by:

$$Q = \frac{1}{n} R^{2/3} S^{\frac{1}{2}} A \qquad (5.17)$$

where;

Q = Discharge of flow

R = Hydraulic radius

A = Cross sectional area

S = Longitudinal slope of the channel

n = Manning's coefficient

Manning's equation is often chosen to give a quick and reasonably accurate prediction of the water surface profiles. The main draw back of equation 5.17 is assumption of a constant " n " value for all flow depths.

The third relationship is the D'arcy– Weisbach equation:

$$Q = A \sqrt{\frac{8\ g\ R\ S}{\lambda}} \qquad (5.18)$$

where;

λ = D'arcy– Weisbach coefficient.

The three equations are related by:

$$C = \sqrt{\frac{8\ g}{\lambda}} = \frac{R^{1/6}}{n} \qquad (5.19)$$

The D'arcy– Weisbach equation is now the most widely accepted in this field because of the non– dimensional term of λ. The value of friction factor λ is most commonly evaluated from Colebrook– White equation for pipes.

$$\frac{1}{\sqrt{\lambda}} = -2.0\ \mathrm{Log}_{10}\left[\frac{k_s}{14.81\ R} + \frac{2.51}{Re\sqrt{\lambda}}\right] \qquad (5.20)$$

where;

λ = Friction factor

Re = Reynolds number

R = Hydraulic radius

k_s = Equivalent sand grain roughness size

The above equation (5.20) for pipe flow contains both smooth and rough part together. When the value of k_s is zero, the smooth part of equation (5.20) can be written as in the form,

$$\frac{1}{\sqrt{\lambda}} = A\ \mathrm{Log}_{10}\left[Re\sqrt{\lambda}\right] - B \qquad (5.21)$$

The values of A & B for the water surface profiles in steep slopes were calculated by using Direct Step method. This was achieved by knowing S_f experimentally, and then using Equation (5.5) to obtain the friction factor λ. The λ value was then plotted against Reynolds Number, and by regression analysis the best curve fit (Fig 5.7) reveal the following mean values.

For Yg = 60mm, 90mm and 180mm A = 2.0 B = 1.99

The general equation becomes;

$$\frac{1}{\sqrt{\lambda}} = 2.0 \, \mathrm{Log}_{10} \left[\mathrm{Re} \sqrt{\lambda} \right] - 1.99 \qquad (5.22)$$

The comparison between the experimental data and Eq (5.22) is given in Fig 5.7 revealing a good correlation.

Having establised the friction factor λ for the smooth channel, it was decided to use this value of λ to calculate the equivalent Mannings "n" value for each flow. This is achieved using the relationship,

$$\sqrt{\frac{8\,g}{\lambda}} = \frac{R^{1/6}}{n} \qquad (5.23)$$

The theoretical curve of Mannings "n" based on Equation (5.22) above is now compared with the experimental values of Mannings "n" as shown in Fig 5.8. The experimental values of Mannings "n" is determined from Direct Step method using the Eqution (5.7) or directly from Equation (5.23) above.

Finally the same procedure was carried out for the roughened boundary. The roughness was achieved by using a water proof, self–adhesive strip of emery paper along the length of the spillway from the pressure box to the end of the ramp. The roughened paper had a texture of sand paper and was placed on the bed only, but not the side walls. The aim of this was to produce

extra turbulence near the channel bed in order to entrain more air into the aerator jet.

The experimental friction factors were determined as before ($\lambda = 8gRS_f/u^2$) and plotted with the Reynolds Number as shown in Fig 5.9.

These experimental values are now correlated by the full Colebrook White equation to determine the best-fit value of k_s. The full equation including the modified smooth part from Equation (5.22) is given by;

$$\frac{1}{\sqrt{\lambda}} = -2.0 \, \mathrm{Log}_{10} \left[\frac{k_s}{14.81 \, R} + \frac{9.89}{Re \sqrt{\lambda}} \right] \qquad (5.24)$$

It can be seen from Fig 5.9 that the best fit for k_s is 0.35mm. It is clear from Fig 5.9 that λ had increased by a substantial amount, going from approximately 0.018 in the smooth case to 0.027 in the rough case.

The equivalent values of Mannings "n" for the roughened channel are shown in Fig 5.10. Fig 5.10 shows that Mannings 'n' increases very sharply at lower depths because of greater roughness at the bed.

5.3 *EXPERIMENTAL AIR FLOW MEASUREMENTS*

5.3.1 *Introduction*

In this section the experimental results of air entrainment rate are presented in relation to turbulence measurements (Chapter 4), cavity under pressure, flow velocity, jet length, ramp angle and surface roughness.

Each parameter will be investigated within one particular frame work of understanding, namely, that air flow is proportional to turbulent velocity w' and the jet length L, for any given geometry.

$$q_a \propto w' L \tag{5.25}$$

Because the value of w' scales on the shear velocity u_*, as we have discovered in Chapter 4, and the value of u_* also scales on the mean velocity, $u_* = \bar{u} \sqrt{\lambda/8}$ then for a given velocity we might write tentatively,

$$q_a \propto \bar{u} L \tag{5.26}$$

or in non-dimensional terms, the air/water ratio may be expressed as,

$$\frac{q_a}{\bar{u} h_3} = \frac{q_a}{q_w} = \beta \propto \frac{L}{h_3} \tag{5.27}$$

In an aerator design, q_a (above) is unknown, but so is the jet length L. For this reason many authors have opted for a simpler solution by recognising that the jet length L/h is dependent primarily on the Froude Number of the flow at the end of the ramp, then

$$\beta \propto Fr_3 \tag{5.28}$$

The Froude Number can be calculated by gradually varied flow analysis so that at the ramp, ($Fr_3 = u_3 / \sqrt{g h_3}$). This means that β may be determined directly.

Many authors including Wood (1984), Kobus (1984), Bruschin (1987) and P. Rutschmann (1986) have shown Froude Number correlations. The problem with each correlation is that the equation $\beta = K\ Fr$, requires a knowledge of K, which apparently varies with every geometry tested showing no consistent pattern, and also varies between model and prototype results. This is unacceptable, because it means that a new aerator cannot be designed without further model

studies. The fact that K keeps varying inconsistently shows the Froude Number correlation to be suspect.

The main thrust for this work therefore was not to provide new correlation between air/water ratio and Froude Number, but instead to use a more fundamental approach to the physical flow behaviour involved, in order to produce more reasoned method of calculating the aeration rate.

This would mean an understanding of the role of a ramp in generating turbulence, the subsequent decay in turbulence in aerator jet, the link between turbulence and aeration rate, as well as a fundamental view of scale effects. As a first step the intention is to investigate how aeration varies with geometrical and flow parameters. These include the turbulence generated at the end of the ramp, the cavity underpressure, the velocity of the flow, the ramp angle, the jet length and the spillway surface roughness.

5.3.2. The experimental air flow measurements in tabular form

The main experimental parameters for the air flow tests are shown in Fig 5.11. The range of variation of each parameter has been discussed already in Chapter 3. The ramp angle Φ was varied from 5^0 to 2^0 to 10^0 each with a smooth boundary, and back to 5^0 with a rough boundary. Each ramp angle was tested over a range of three gate openings, namely 180mm, 90mm and 60mm for smooth and rough boundary. The three ramp angles, two roughnesses and three gate openings gave rise therefore to 12 main test situations. The experimental results from these are listed in Tables (C.1) to (C.12) in Appendix C.

A review of the experimental data in Tables (C.1) to (C.12) is given in this Chapter. The first column in each table gives the water discharge measured from the orifice plate and as seen, varies in the range approximately 15 ℓ/s to 52 ℓ/s. The depth of flow at the end the ramp, h_3 is given, this with

most of the depth measurements varying in the range 20mm to 80mm. The mean velocity at the ramp section $\bar{u}_3$, is now determined from water discharge and flow depth h_3.

It is seen from Tables (C.1) to (C.12) that three values of $\triangle h$ are measured with corresponding jet lengths L and air flow rate Q_a. The values of $\triangle h$ were arrived at as follows:–

—— the first result always read zero $\triangle h$, this being the test where air is blown into the cavity, with the cavity pressure reading at atmospheric. This is adjusted by valves upstream of the cavity.

—— the valves are then closed completely allowing no air along the duct pipe. The underpressure $\triangle h_{max}$ is measured. The second measure of $\triangle h$ has been made approximately equal to $\triangle h_{max}/2$ and again adjusted by valves in the air line.

—— the final reading is then usually somewhere between $\triangle h = 0$ and $\triangle h = \triangle h_{max}/2$, although occasionally it is greater than $\triangle h_{max}/2$ depending on the limits of inclined monometer, used for $\triangle h$ measurements.

The subsequent value of jet length is measured for each value of $\triangle h$ underpressure as is the air flow rate Q_{air}. The air flow rate did not required to be adjusted to atmospheric pressure because of the small head loss from the measurement point to the cavity.

5.3.3 *A frame work for understanding the air flow results*

It is useful in discussing the air flow data, to build–up a picture of the physical flow behaviour, even in simple terms, to allow an in–depth analysis to proceed in Chapter 6. The physical frame work used in this work is sketched below.

It is argued that the air entrainment per unit channel width q_a, is dependent mainly on the turbulent velocity w' (which varies along the jet length) and also the jet length itself.

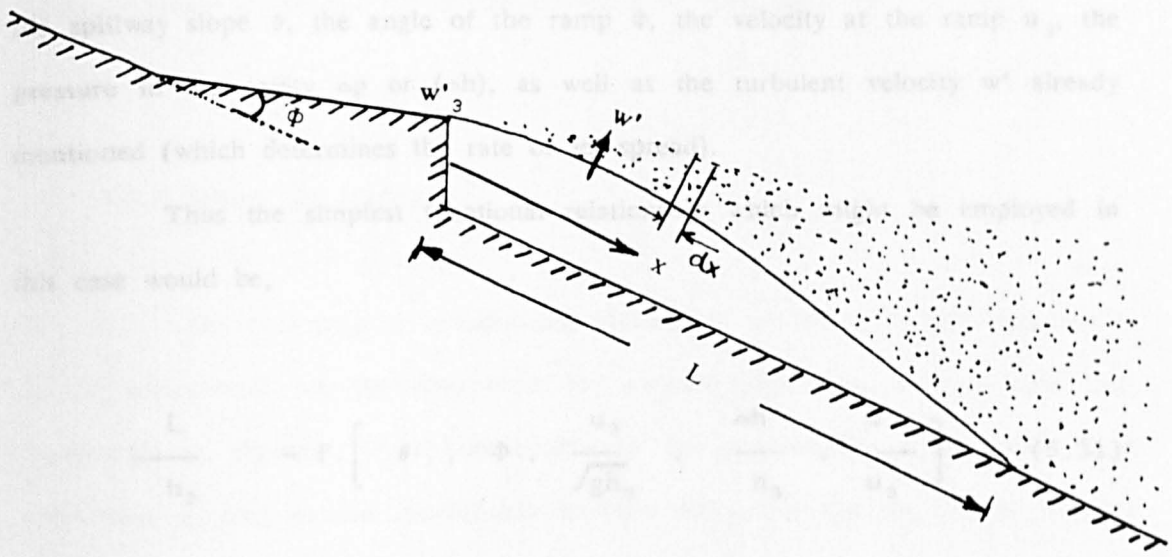

The simplest possible relationship can be given by;

$$q_a = \int_0^L w'(dx) \cong w'(L) \qquad (5.29)$$

Such a relationship seems deceptively simple, but hides a range of complex interactions.

For instance, the value of w' along the jet length has been discussed in Chapter 4. It is clear that the value of w' along the jet is dependent on the turbulent value at the end of the ramp (w'_3), which in turn is heavily influenced by the flow Reynolds Number. The value of w' also decays in the x direction, showing little decay for x/h_3 values less than 10, but considerable decay after that value. This means that even the simplest functional relationship for w' along the jet downstream of the ramp might be of the form

$$\frac{w'}{u_*} = f\left[\frac{w'_3}{u_*}, \frac{x}{h}, Re\right] \qquad (5.30)$$

Exactly the same argument is valid for the jet length L in Equation (5.29). The values of jet length L must be a complex function of the angle of the spillway slope θ, the angle of the ramp Φ, the velocity at the ramp u_3, the pressure in the cavity $\triangle p$ or $(\triangle h)$, as well as the turbulent velocity w' already mentioned (which determines the rate of jet spread).

Thus the simplest functional relationship which might be employed in this case would be,

$$\frac{L}{h_3} = f\left[\theta, \Phi, \frac{u_3}{\sqrt{gh_3}}, \frac{\triangle h}{h_3}, \frac{w'}{u_3}\right] \qquad (5.31)$$

In this research work 'θ' is constant and hence is ignored in the ensuing discussion. The ramp angle Φ may be important as may be Froude Number at the end of the ramp. It is a matter of interest that many correlations include Froude Number in describing the air entrainment rate in aerators, but ignore all three terms in Equation (5.30). The term $\triangle h/h_3$ is also significant and w'/u_3 is already included in Equation (5.31). It is of interest to note that $u_3 = \sqrt{8/\lambda}\, u_*$, and hence includes the frictional resistance coefficient of the spillway.

Thus combining Equation (5.30) and Equation (5.31) we conclude that the air flow rate (w'L) in its non–dimensional form is a complex function,

$$\beta = \frac{q_a}{q_w} = f\left[\theta, Fr_3, \frac{\triangle h}{h_3}, \frac{w'_3}{u_*}, \frac{x}{h_3}, Re, \frac{k_s}{h_3}\right] \qquad (5.32)$$

Even though this relationship is complex, it assumes that air is entrained freely over the free surface and that surface tension effects are negligible. This may not be the case in such model studies as this, and hence Weber Number should also be included.

The important thing now, is to work through these parameters one by one, to obtain a clearer idea of the influence of each one.

5.3.4 *Aerator jet lengths.*

The first step in investigating the nature of the $q_a \propto w'L$ relationship is to concentrate on the expression for aerator jet length L and how each parameter in Equation (5.31) contributes to the jet length. In particular it is important to look at the relationship between L/h_3 and the jet Froude Number (Fr_3) as this is the most common substitution in determining the air/water ratio of aerators. i.e rather than use $\beta \propto L/h$, it is common to have $\beta \propto Fr$.

It was decided therefore to plot graphs of the experimental values of non–dimensional jet length L/h_3 against the Froude Number of the flow at the end of the ramp ($Fr_3 = \bar{u}_3 / \sqrt{gh_3}$). This has been done for each ramp angle Φ from 2^0, 5^0 and 10^0, for both boundary roughness values, and for discrete bands of measured cavity under pressure $\Delta h/h$. The result is shown in Fig 5.12(a) for zero underpressure ($\Delta h/h = 0$),and in Figs 5.12(b),(c),(d) and (e) for under pressure bands $\Delta h/h = 0.1$ to 0.2; 0.2 to 0.3; 0.3 to 0.4; and 0.5 and above, respectively.

The most striking feature of Figs 5.12(a) to (e) is the apparent linearity between measured jet length L/h_3 and jet Froude Number explaining why many previous correlations for air entrainment rate have proved popular, namely that Fr can be substituted for L/h.

The second feature is that once linearity is assumed, then lines extrapolated to the x axis cut at a certain Froude Number, (around 2.5 to 4 in the case) which appears to be the minimum Froude Number to cause L/h to be greater than zero. This patently has little physical meaning, but can be used as a device meantime to explore the w'L relationship.

Each graph in Figs 5.12(a) to (e) therefore takes up a form

$$L/h_3 = K_1 (Fr_3 - K_2) \qquad (5.33)$$

where K_2 has a value around 2.5 to 3 for the 2^0 and 5^0 ramp, rising to $K_2 = 4.0$ for the 10^0 ramp. The value of K_1, therefore depends on the ramp angle, the degree of underpressure $\Delta h/h$ and the degree of boundary roughness, as predicted in Equation (5.32). For instance, if we plot the value of K_1 (slope of each line) for Figs 5.12(a) and (b) only, then the variation of K_1 for each ramp angle for the smooth boundaries only, is shown in Fig 5.13 revealing a non-linear variation of jet length with ramp angle Φ. It should be noted immediately that this relationship is valid only for a 45^0 spillway slope, zero offset, smooth boundary and for a range of Reynolds Number tested. It is not valid for any other geometry and highlights very clearly the problem with Froude correlations, requiring unique values of K_1 and K_2 for each geometry tested.

The effect of increasing $\Delta h/h$ at a given Froude Number for the 2^0, 5^0 and 10^0 ramps, covering the full range of underpressures is shown in Fig 5.14. This graph shows that as the $\Delta h/h$ value increases from zero to 0.5, then the L/h_3 value decreases substantially. This graph is for one Froude Number range, namely Fr = 10.

The variation of jet length with boundary roughness is also indicted in Figs 5.12(a) to (e) by comparing the jet length for 5^0 smooth with 5^0 rough. For Fig 5.12(a) for $\Delta h/h = 0.0$, the 5^0 rough boundary produces slightly lower jet lengths than the 5^0 smooth boundary. This was to be expected because the

values of turbulent velocity w' are greater in the rough case and hence the bottom edge of the jet spreads more rapidly, hence producing a shorter jet length effectively. A similar picture is obtained from Figs 5.12(c),(d) and (e).

At this point we note the most likely explanation for previous correlation of air/water ratio in aerators. If we take a typical example, such as the one produced by P.Rutschmann (1986) and Kobus (1988) of the form

$$\beta = K_1 (Fr - K_2) \qquad (5.34)$$

then it appears that previous authors were simply using formulation of the jet length (L/h) to describe the air/water ratio (β). This approach cannot be valid because:–

(a) It takes no account of reduction in w' along the jet length and hence assumes no variation in entrainment rate along the total jet length.

(b) The empirical constants are relevant only to one geometry and scale and cannot have general applicability.

5.3.5 *Air entrainment and turbulence level.*

At this point we return to the simple formulation $q_a \propto w'L$. It has become apparent in section 5.3.4 that the jet length L/h is a complex function of Froude Number, ramp angle Φ, cavity underpressure $\Delta h/h$, the boundary roughness k_s, as well as other parameters not varied such as spillway slope θ and offset height h_s.

However, if the measured value of jet length is used then the parameter q_a/L is the rate of air entrainment per unit surface jet area exposed in the cavity region. This is because $q_a/L = Q_a/bL$, where b is the spillway width. Therefore q_a/L becomes a measure of the efficiency of the jet in

entraining air for each range of conditions.

If the measured value of q_a/L is plotted against the jet turbulent velocity w', then it can be seen if there is any validity in the $q_a \propto w'L$ concept. The problem in this plot is that w' keeps reducing along the jet length and also it has not measured continously along the jet length. To overcome this problem it was decided to plot q_a/L against w'_3, the turbulent velocity at the end of the ramp. This is a measure of w' along the jet. Hence, any spread of results in the q_a/L against w'_3 graph will reflect the variation in w' along the jet length.

The result is shown in Fig 5.15 for all results with zero cavity underpressure $\Delta h/h = 0$. The result is extremely interesting because the data shows linearity between q_a/L and w'_3 when the lines are drawn through $w'_3 \simeq 0.3$m/s on the x − axis. By coincidence, this is the value of minimum turbulent velocity to entrain air predicted by Ervine and Falvey (1986). Inspection of the results shows that lines fan−out from this point at a slope depending on the jet length L/h. Short jets $L/h < 10$ produce the steepest slopes, whilst very long jets $L/h > 50$ produce shallow slopes.

The general form becomes,

$$q_a/L = C_1 (w'_3 - 0.3) \qquad (5.35)$$

where C_1 becomes the slope of each line and hence is a function of L/h. Hence $w'_3 = 0.3$ m/s is confirmed as a good approximation for the onset of air measurement.

The same graph is repeated in Figs 5.16(a),(b),(c) and (d) with the data points sub−divided in each geometry tested, namely 5^0, 2^0 and 10^0 smooth together with the 5^0 rough. Again this refers only to zero underpressure $\Delta h/h = 0$. For each of the four graphs, a minimum turbulent velocity to entrain air of 0.3m/s was assumed, and the value of C_1 in Equation (5.35) above was

determined, from the upper and lower range of slopes. The result showing how C_1 varies with jet length is given in Fig 5.17.

Fig 5.17 is very significant in the sense that it indicates that short jets L/h < 10 are most efficient in entraining air giving air entrainment rates of the order

$$q_a/L = 1.3\ (w'_3 - 0.3) \qquad \text{for } L/h < 10 \qquad (5.36)$$

whereas very long jets L/h > 50 reveals an approximate relationship of the order

$$q_a/L = 0.3\ (w'_3 - 0.3) \qquad \text{for } L/h > 50 \qquad (5.37)$$

5.3.6 *Air entrainment rate and cavity underpressure.*

Even a cursory glance at the experimental data in Tables (C.1) to (C.12) in Appendix C, reveals a strong inter–relationship between air entrainment Q_a and underpressure value $\Delta h/h$ (sometimes written as $\Delta p/\rho gh$).

It was decided to investigate the effect of $\Delta h/h$ because of its importance in the design of the air venting system. An under sized air vent will result in a large underpressure $\Delta h/h$ and hence less air intake. Values of $\Delta h/h$ in this work were adjusted by values in the air inlet system and covered approximately the same range as prototype structures namely $\Delta h/h \simeq 0.0$ to 0.7.

The simplest possible presentation of the effect of cavity underpressure is a plot of air flow (Q_a) against water flow (Q_w) for each of the four geometries tested, and for each band of cavity underpressure ($\Delta h/h$) an increment of $\Delta h/h$ of 0.1. The result is shown in Figs 5.18(a),(b),(c) and (d) representing the 5^0, 2^0 and 10^0 smooth, plus the 5^0 rough geometry. Figs 5.18(a), (b), (c)

and (d) clearly shows the bands of $\triangle h/h$. As the values of $\triangle h/h$ increases the quantity of airflow decreases, which is true of course for all geometries i.e 2^0, 5^0 and 10^0 smooth boundary and as well as 5^0 roughened boundary.

The next method of presenting the effect of cavity underpressure concerns the result of dimensional analysis given in Equation (5.32). In this case it is advantageous to plot the air/water ratio β against the Froude Number $(u_3/\sqrt{gh_3})$ for each of the four geometries (Φ and k_s) but also for each band of cavity underpressure $\triangle h/h$. This is shown in Figs 5.19(a) to (d) corresponding to the 5^0, 2^0 and 10^0 smooth, together with the 5^0 rough case. Figs 5.19(a), (b), (c) and (d) also shows clear bands of $\triangle h/h$.

5.3.7 *Variation of air entrainment rate with mean flow velocity.*

The reason for investigating this area is that many early correlations of aeration used the mean flow velocity in the form

$$q_a = K \bar{u} L \qquad (5.38)$$

which never proved satisfactory because of large variation in K. The reason the formulation above is unsatisfactory is now easily seen in the light of earlier discussion in Chapter 4 and Chapter 5. For example,

(i) Aeration in ramps occurs only when a certain minimum velocity is exceeded of the order $u_{min} \simeq 3$m/s. This is easily seen from section 5.3.5 which reveals that aeration commences around $w'_3 \simeq 0.3$m/s. At the end of the ramp the turbulence $w'_3/\bar{u}$ is typically 10%, giving a minimum mean velocity to cause aeration around 3m/s. This is reflected in Equation (5.38).

(ii) Equation (5.38) takes no account of the effect of jet length L/h. We have seen already that long jets are not efficient at entraining air and hence the K value is likely to decrease for L/h > 10, but remain reasonably constant for L/h < 10.

(iii) Equation (5.38) takes no account of cavity underpressure and hence must represent only the upper limit situation where $\Delta h/h = 0.0$.

(iv) Equation (5.38) takes no account of Reynolds Number or turbulence in the flow. That is, the value of K would be different comparing model and prototype, mainly because the value of w'_3 is greater in prototype compared with model.

One drawback with this experimental research project is the small range of ramp velocities mainly in the range of 6 m/s to 7.7 m/s. The reason for this was the constant spillway slope used $\theta = 45^0$. The narrow range of velocity makes an analysis of Equation (5.38) above more difficult although additional model and prototype data from other sources will be used in Chapter 6.

The first step was a plot q_a/L against the mean flow velocity at the end of the ramp section 3. This is shown in Figs 5.20(a) to (d) covering 5^0, 2^0 and 10^0 smooth, as well as 5^0 rough case respectively.

In order to provide a frame work for this data, it is important to guess the minimum flow velocity to cause any aeration. Using section 5.3.5 as a clue, it was generally recognised that the minimum turbulent velocity to entrain air is around

$$w'_3 = 0.3 \text{ m/s}$$

From section 4.3.3 we know that at the end of the ramp

$$w'_3 \simeq 1.75\, u_* \simeq 1.75\, \bar{u} \sqrt{\lambda/8} \qquad (5.39)$$

Therefore at the onset of aeration

$$0.3 \simeq 1.75\, \bar{u} \sqrt{\lambda/8}$$

or $$u_{min} \simeq 0.5 / \sqrt{\lambda} \qquad (5.40)$$

For smooth boundaries $\lambda \simeq 0.018$ and for rough $\lambda \simeq 0.027$, giving $u_{min} = 3.7$m/s smooth, and $u_{min} = 3$ m/s for rough.

Assuming these minimum values and assuming linearity between q_a and $\bar{u}$ we obtain a series of slopes in Figs 5.20(a) to (d) for each geometry. These graphs refer to zero cavity subpressure only. Figs 5.20(a) to (d) shows very narrow range of variation which is due to the limitation of flow velocity $\bar{u}$. Consider Fig 5.20(a) which shows that $\bar{u}$ is proportional to jet length ratio L/h. The values of K in Equation 5.38 above was determined from experimental data and plotted against the jet length ratio L/h as shown in Fig 5.21. The result of Fig 5.21 is similar as Fig 5.17, with K heavily dependent on jet length, and varying between 0.01 and 0.032.

5.3.8 *Variation of aeration with ramp angle Φ and aerator jet length L.*

The purpose of a ramp is to cause the aerator jet to have a higher trajectory, a longer jet length and hence more aeration, as $q_a \propto$ jet length, from Equation (5.25). Little appears to be known about efficiency of various ramp angles in generating turbulence.

It was decided to test this efficiency by plotting the air uptake per unit jet surface area q_a/L against the turbulence generated by each ramp w'_{3max} for the three ramp angles. The beauty of this method is that the ability of greater ramp angles in producing longer jets (and hence more air), is hidden in this plot in Fig 5.15 because L is included in the q_a/L term. The result shows the air entraining efficiency irrespective of the jet length and is plotted in Fig 5.15 for the case of $\Delta h/h = 0.0$, only.

It is clear from the plot that small jet length produces steep slopes while longer L/h produces shallow slopes. Fig 5.16 shows very clearly the efficiency of ramp. The 2^0 smooth ramp showed the maximum efficiency during this study while the 5^0 smooth ramp showed better results than 10^0 smooth ramp. The roughened boundary case also showed an increase in the air uptake efficiency of an aerator jet.

At this point it is useful to explore the inter–relationship between ramp angle Φ, and jet underpressure $\Delta h/h$, with jet length.

It is generally recognised that the jet length is proportional to mean velocity and hence the non–dimensional jet length can be described by the Froude Number of the flow. Higher Froude Numbers produces longer jet length. Figs 5.12(a) to (e) shows a plot of non–dimensional jet length L/h_3 against the Froude Number $\bar{u}_3/\sqrt{gh_3}$ for the three different ramp angle.

Fig 5.12(a) shows this relationship for zero underpressure $\Delta h/h = 0.0$, whereas Figs 5.12(b), (c) and (d) shows the inter–relationship for $\Delta h/h = 0.1$, 0.2 and 0.3 respectively.

It is clear from Figs 5.12(a) to (d) that higher ramp angle shows steep slopes while small ramp angle i.e 2^0 ramp shows the shallow slopes. This means that lower ramp angle are subjected to much greater variation of $\Delta h/h$ which increases jet air uptake per unit length.

If there is general validity in the correlation for air entrainment at ramps in the form $q_a \propto uL$ or $q_a \propto w'L$ then there is implied in this a linear

relationship between air flow and jet length.

To test this assumption as simply as possible, it was decided to plot q_a / w'_{3max} against measured jet length, for each ramp angle Φ, and for the case of zero underpressure ($\triangle h/h = 0.0$). The result is shown in Fig 5.22 representing the three ramp angles and also the rough case. Fig 5.22 shows very clear slopes of each ramp angle. The 5^0 ramp with roughened boundary showed the steepest slope and following by 2^0, 5^0 and 10^0 ramp angle with smooth bed. Fig 5.22 confirmed that the shorter the jet length the more efficient is the aerator.

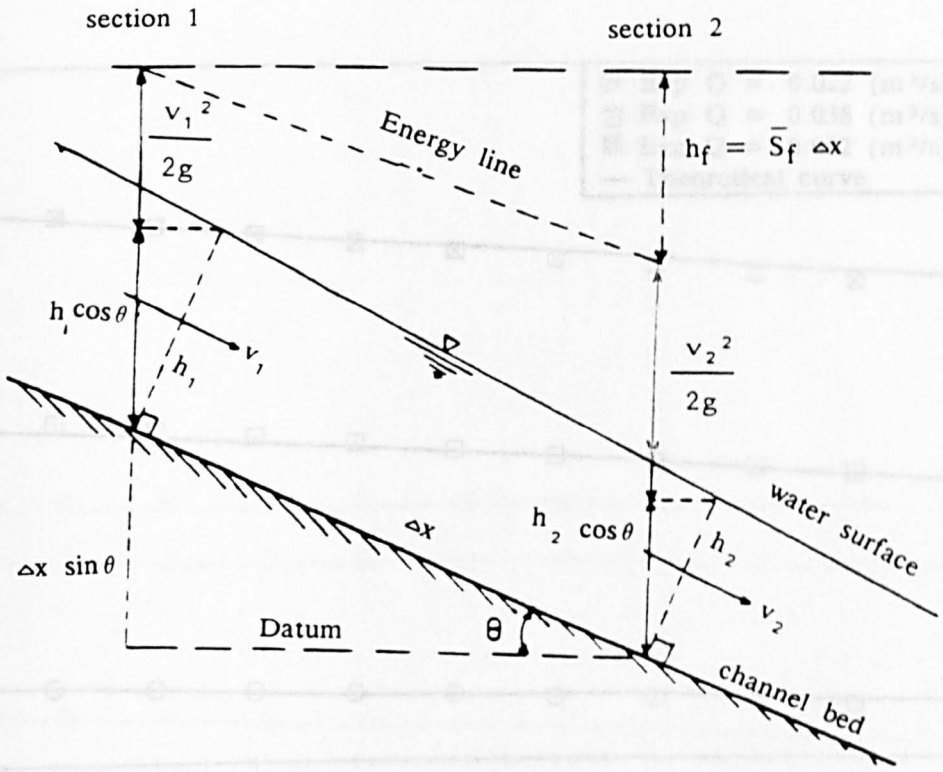

Fig 5.1 Sketch diagrame illustrate a short channel reach length Δx (Energy method)

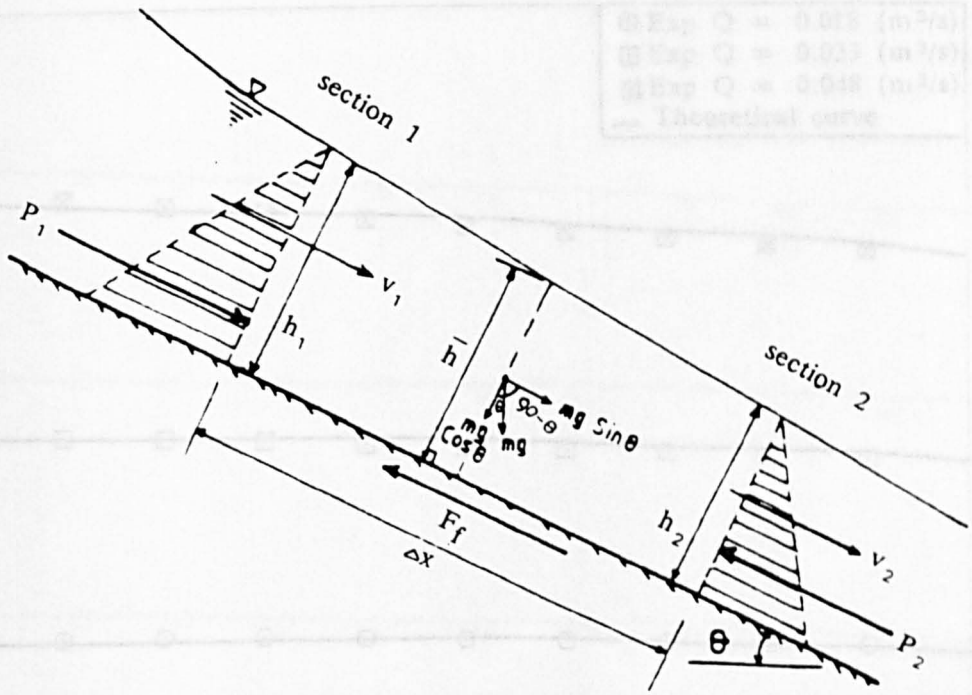

Fig 5.2 Sketch diagrame illustrate a short channel reach length Δx (Momentum method)

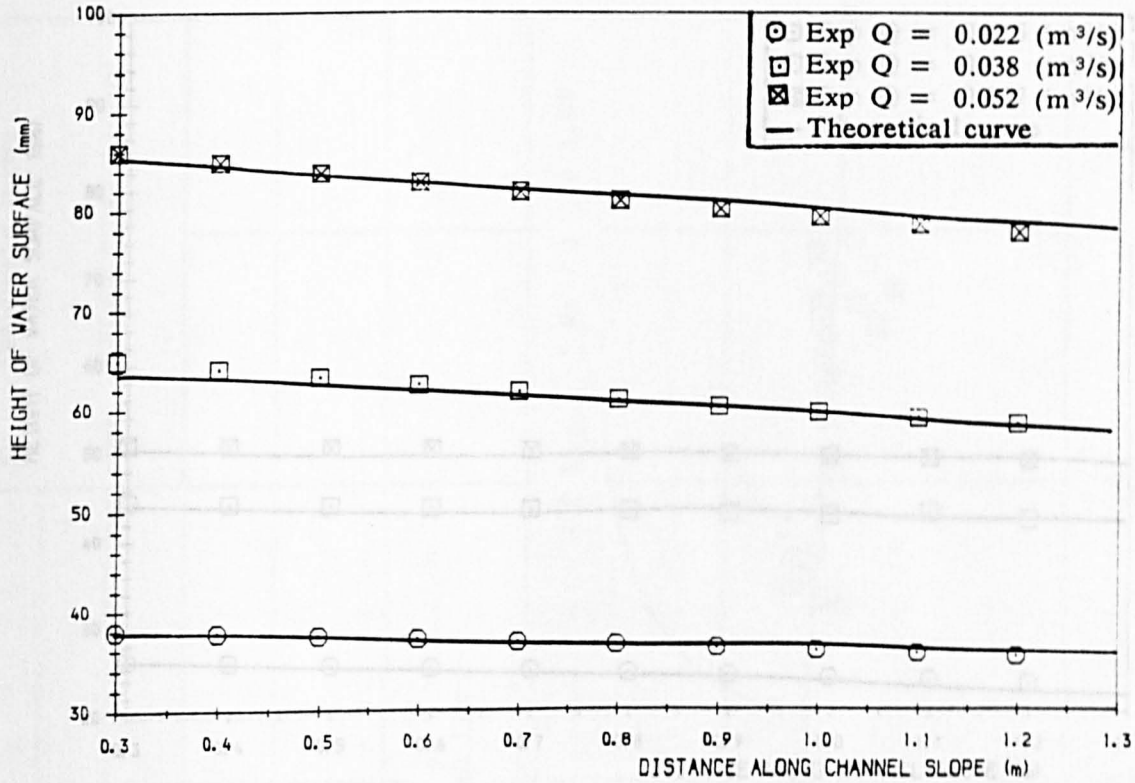

Fig 5.3 Water Surface Profile at section 1 and 1m upstream
Yg = 180 mm ϕ = 5 degree (smooth)

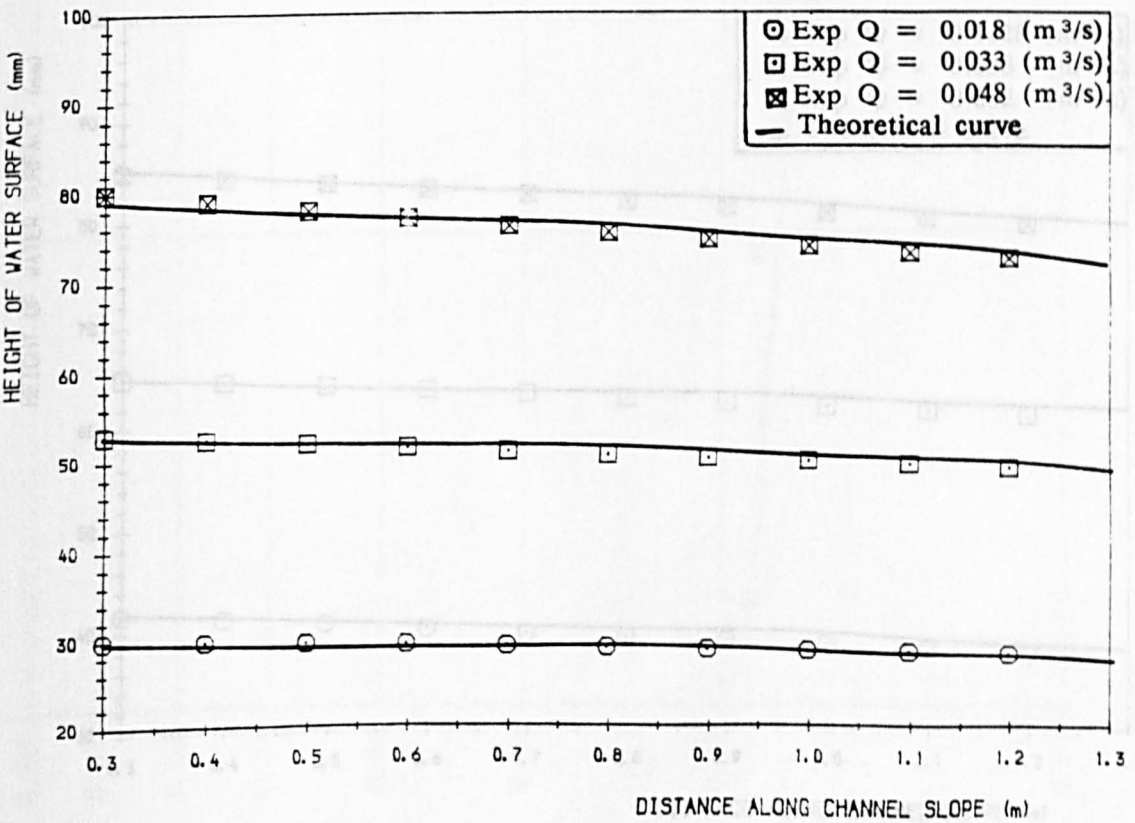

Fig 5.4 Water Surface Profile at section 1 and 1m upstream
Yg = 90 mm ϕ = 5 degree (smooth)

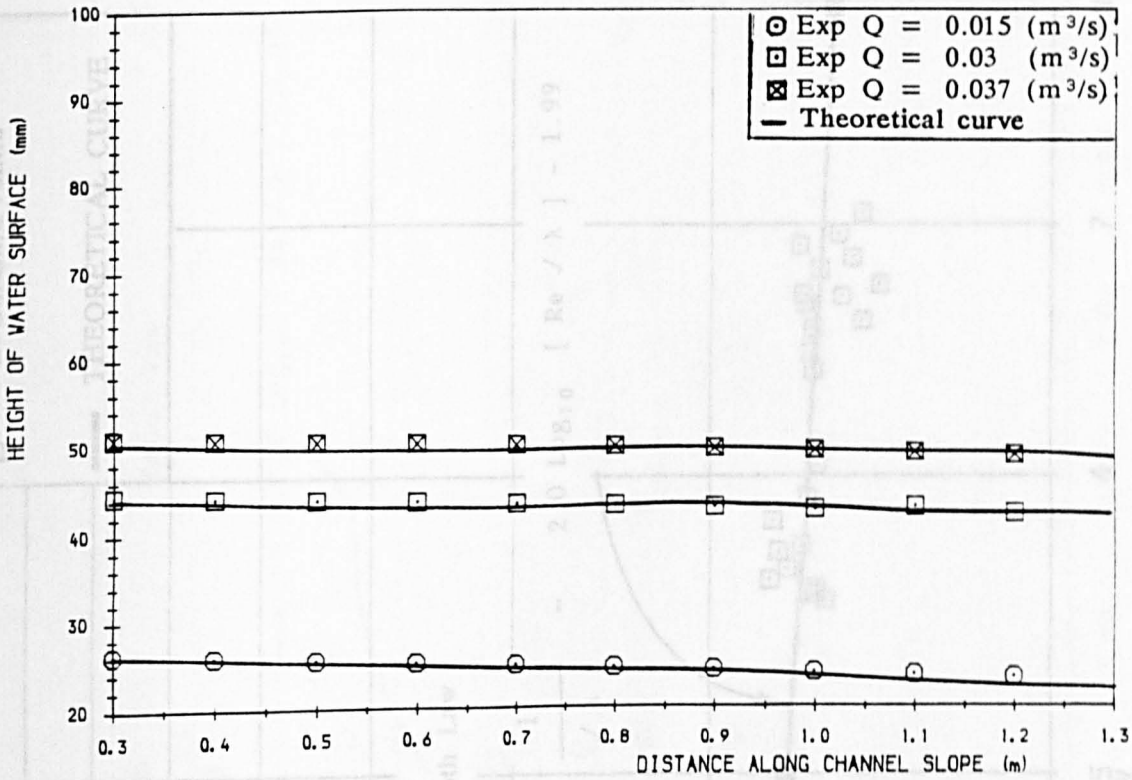

Fig 5.5 Water Surface Profile at section 1 and 1m upstream
Yg = 60 mm ϕ = 5 degree (smooth)

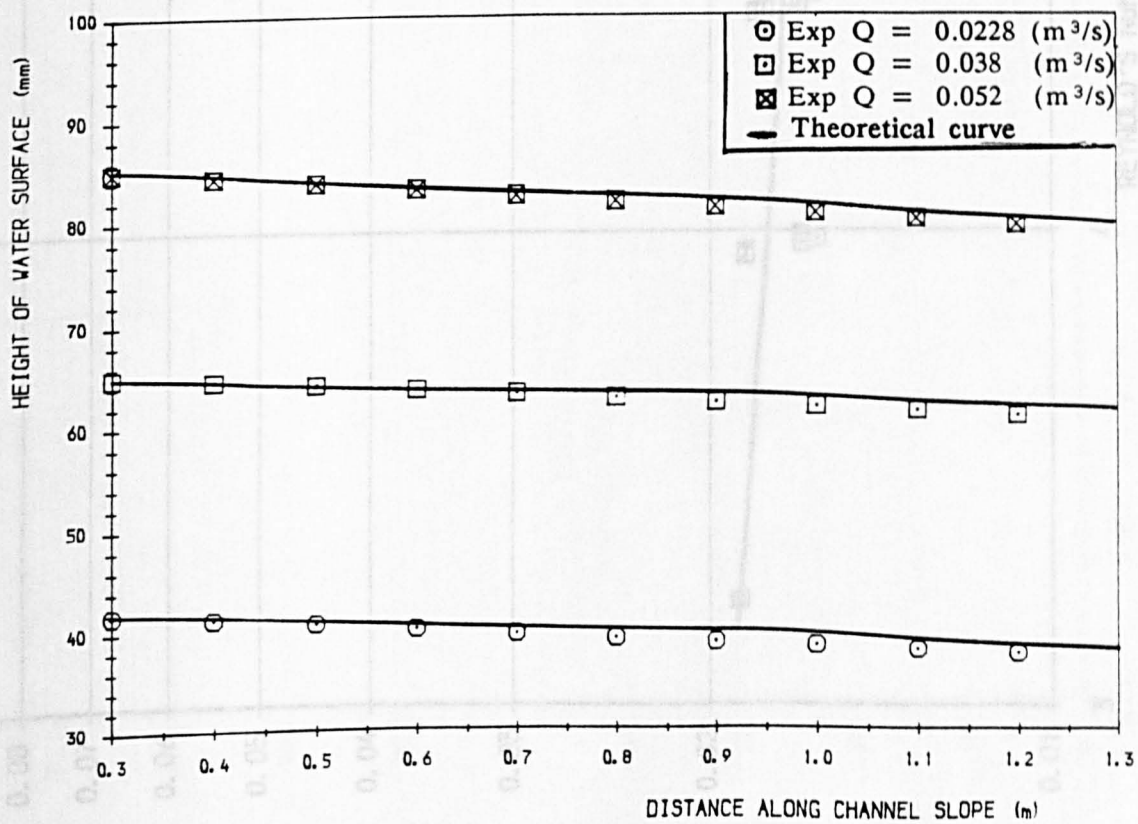

Fig 5.6 Water Surface Profile at section 1 and 1m upstream
Yg = 180 mm ϕ = 5 degree (rough)

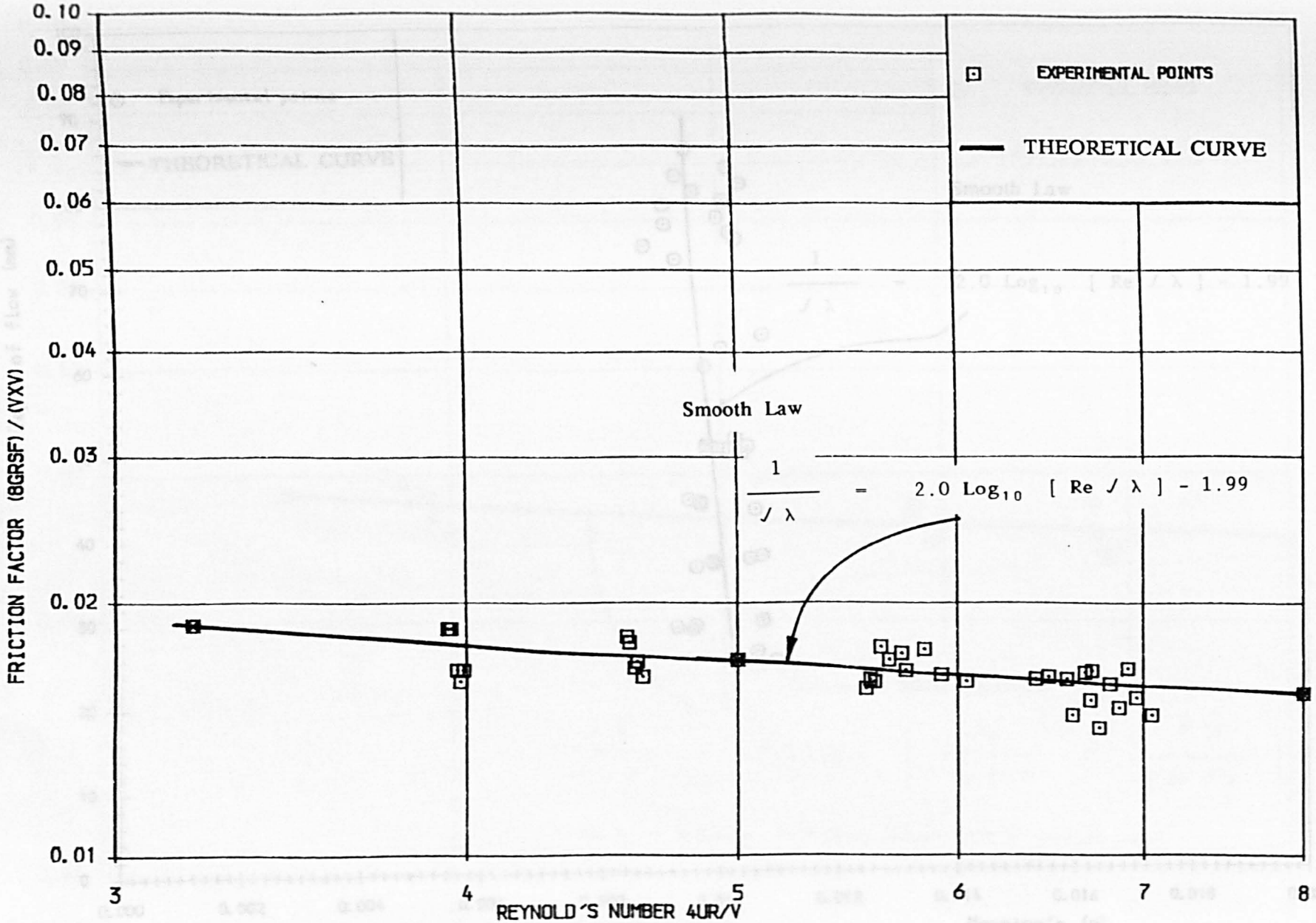

FIG 5.7 RELATIONSHIP BETWEEN
FRICTION FACTOR FOR THE CHANNEL MATERIAL & REYNOLD'S NUMBER

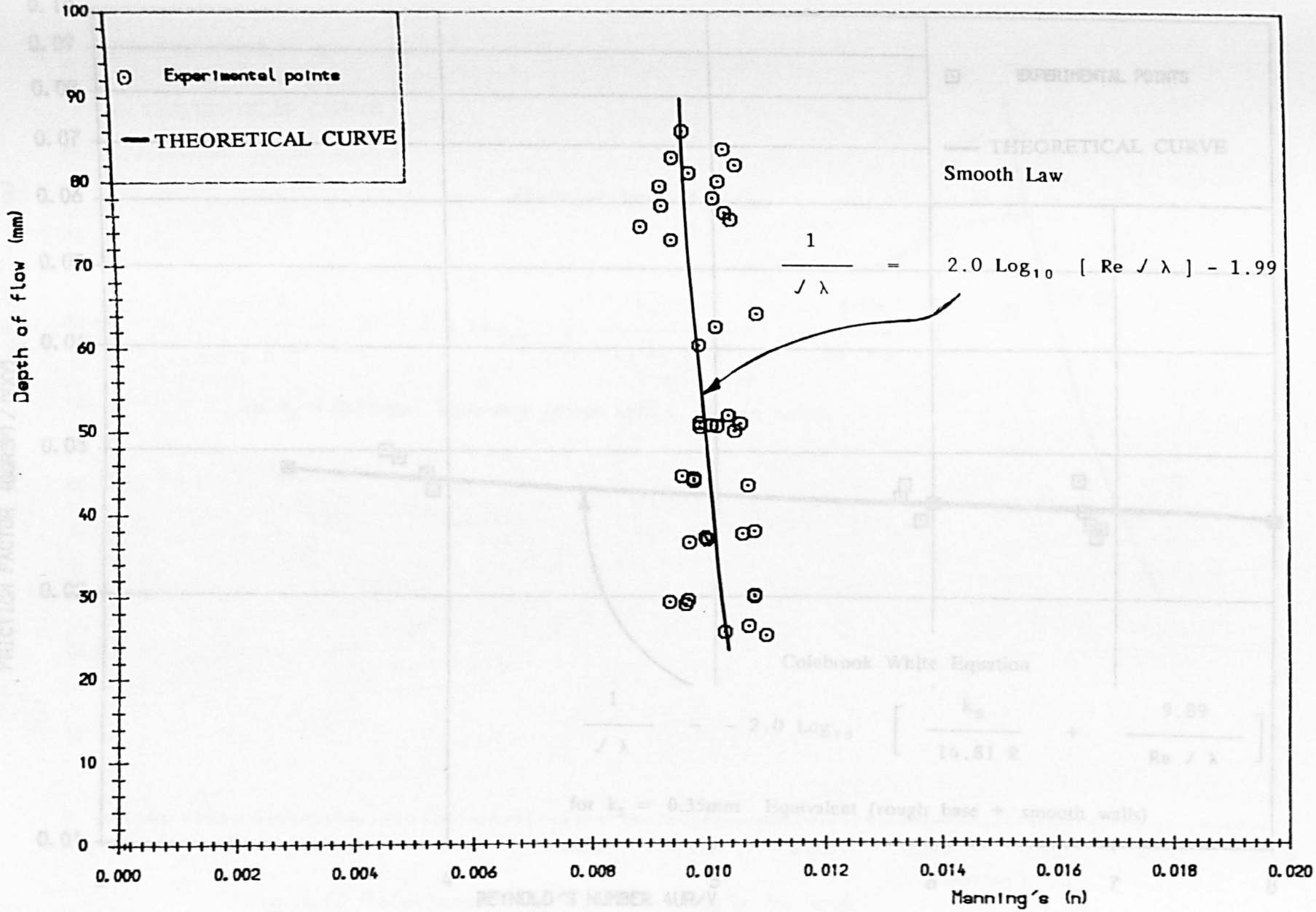

Fig 5.8 Relationship between Manning's (n) and depth of flow for material used in open channel

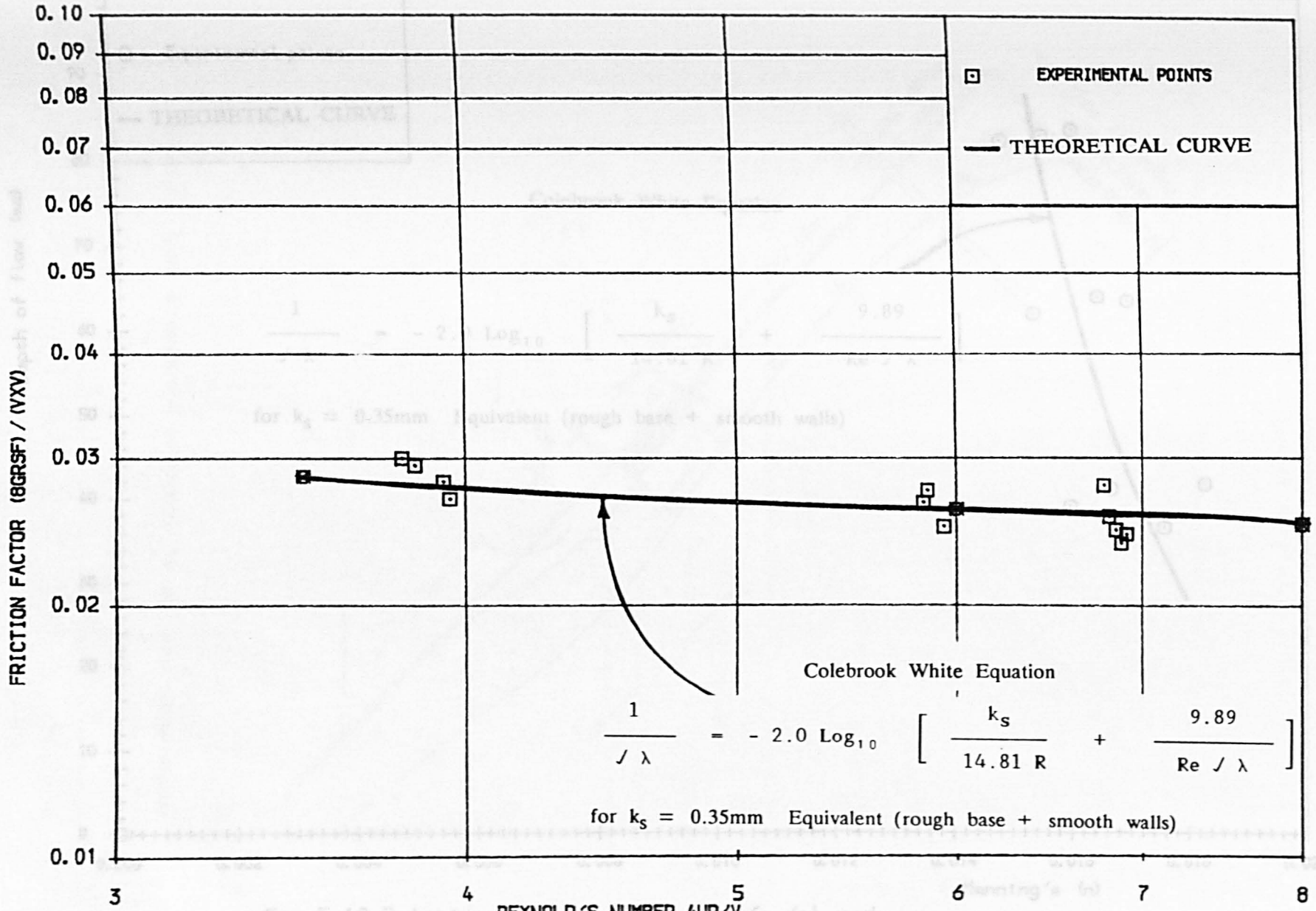

FIG 5.9 RELATIONSHIP BETWEEN
FRICTION FACTOR FOR THE CHANNEL MATERIAL & REYNOLD'S NUMBER

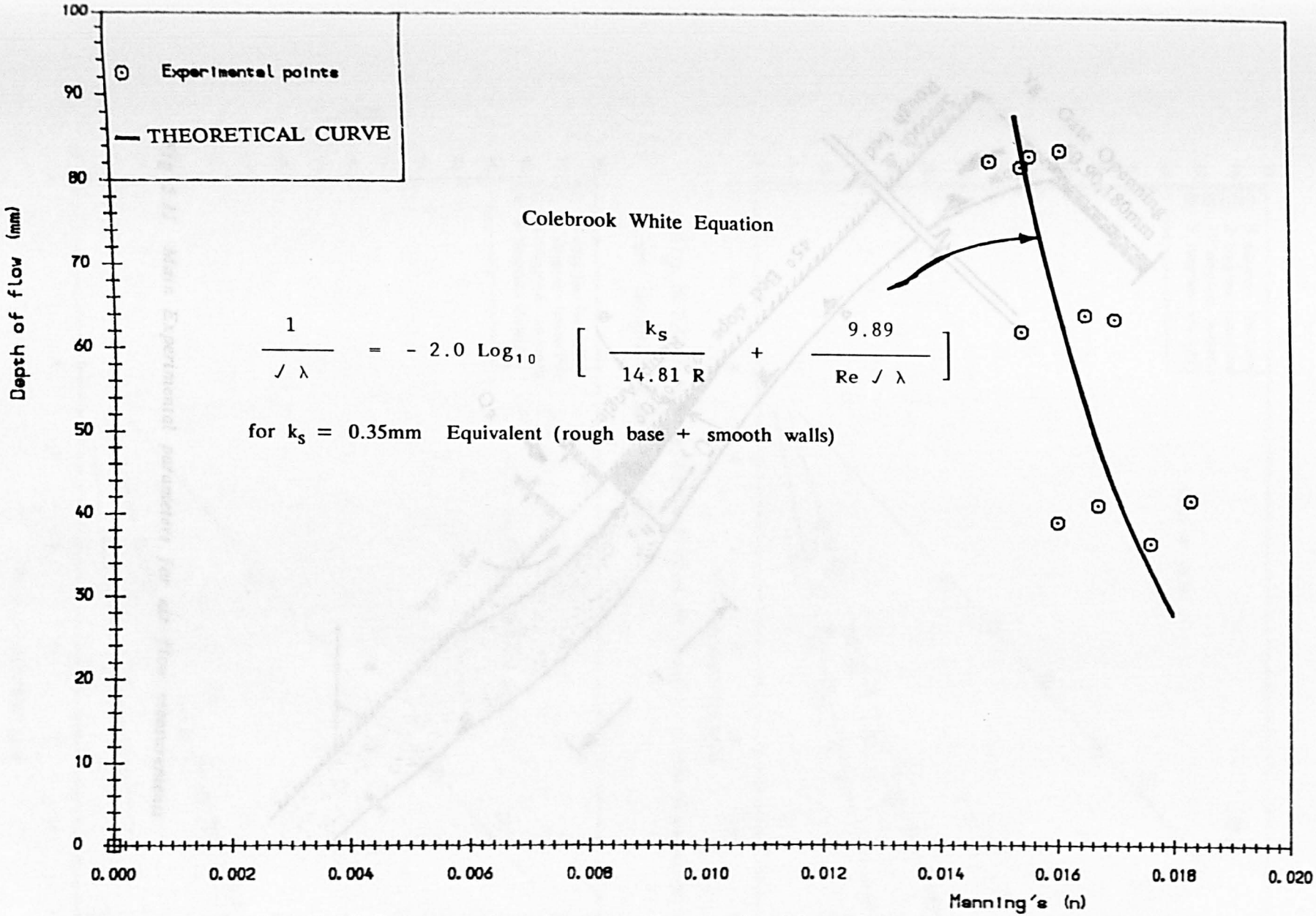

Fig 5.10 Relationship between Manning's (n) and depth of flow for material used in open channel

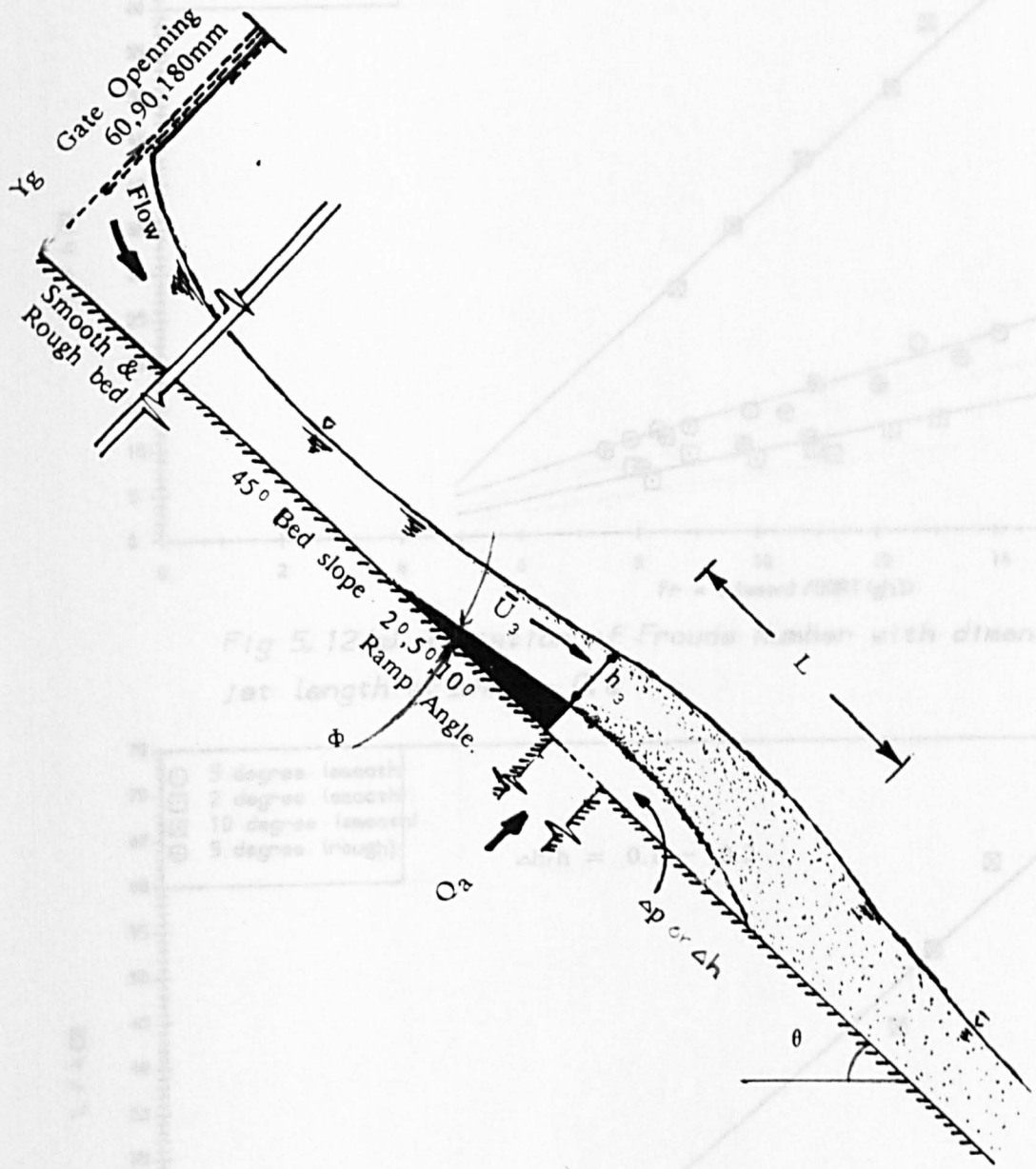

Fig 5.11 Main Experimental parameters for air flow measurements

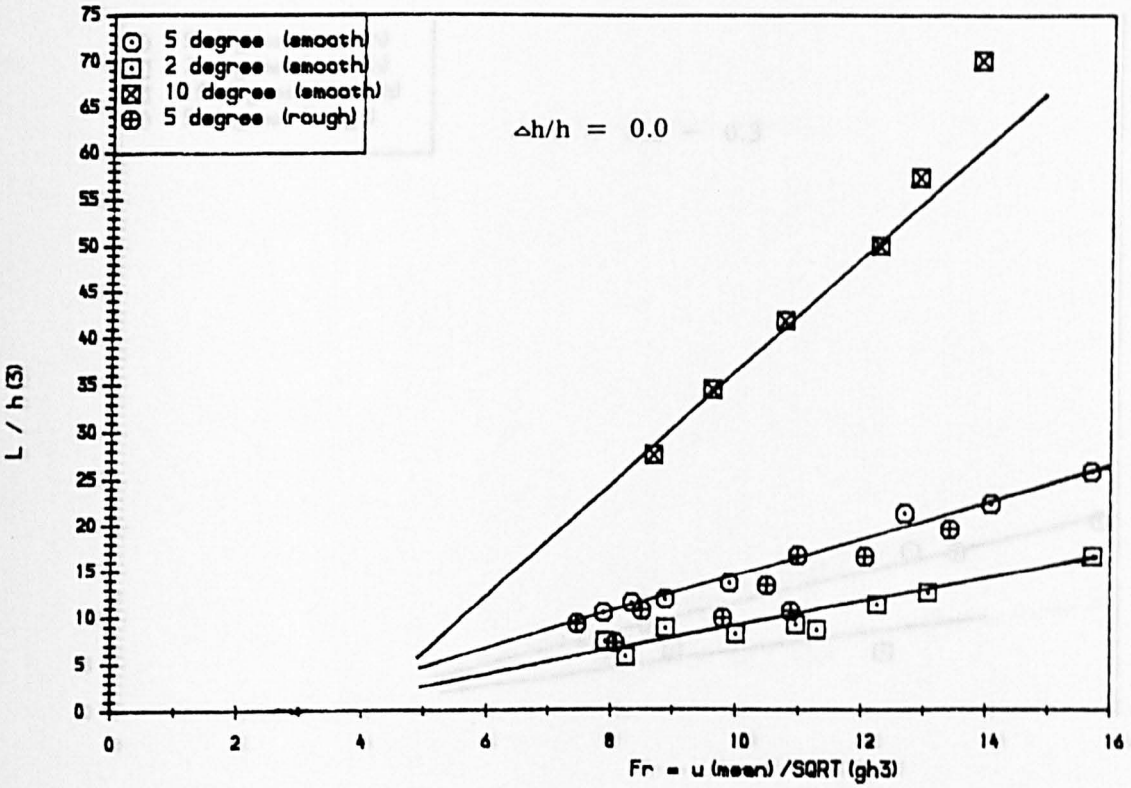

Fig 5.12(a) Variation of Froude Number with dimensionless jet length at Δh/h = 0.0

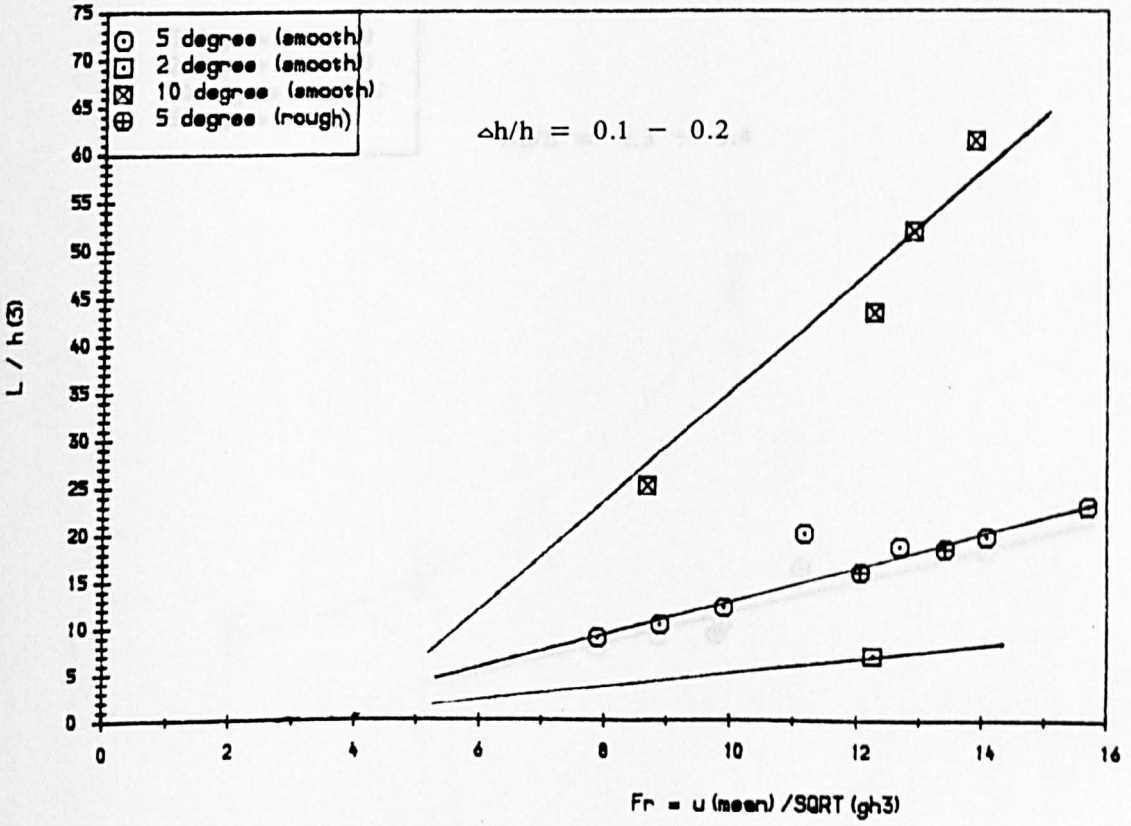

Fig 5.12(b) Variation of of Froude Number with dimensionless jet length at Δh/h = 0.1 - 0.2

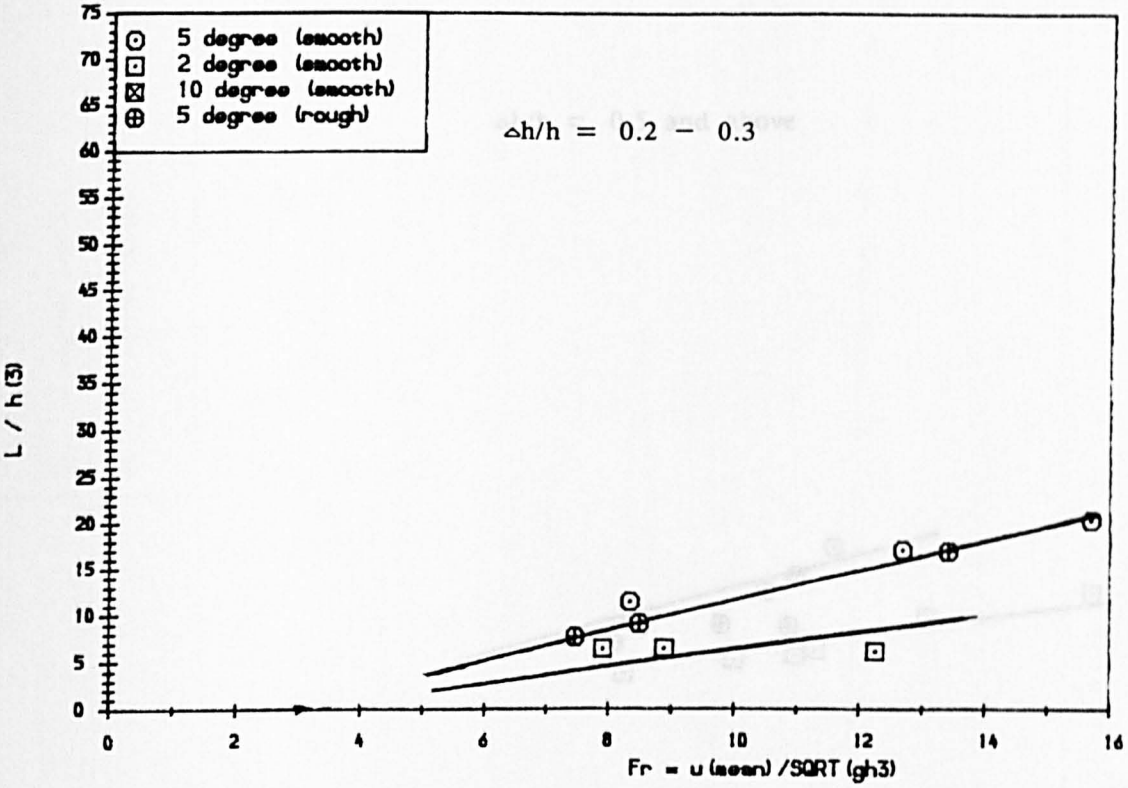

Fig 5.12(c) Variation of Froude Number with dimensionless jet length at Δh/h = 0.2 - 0.3

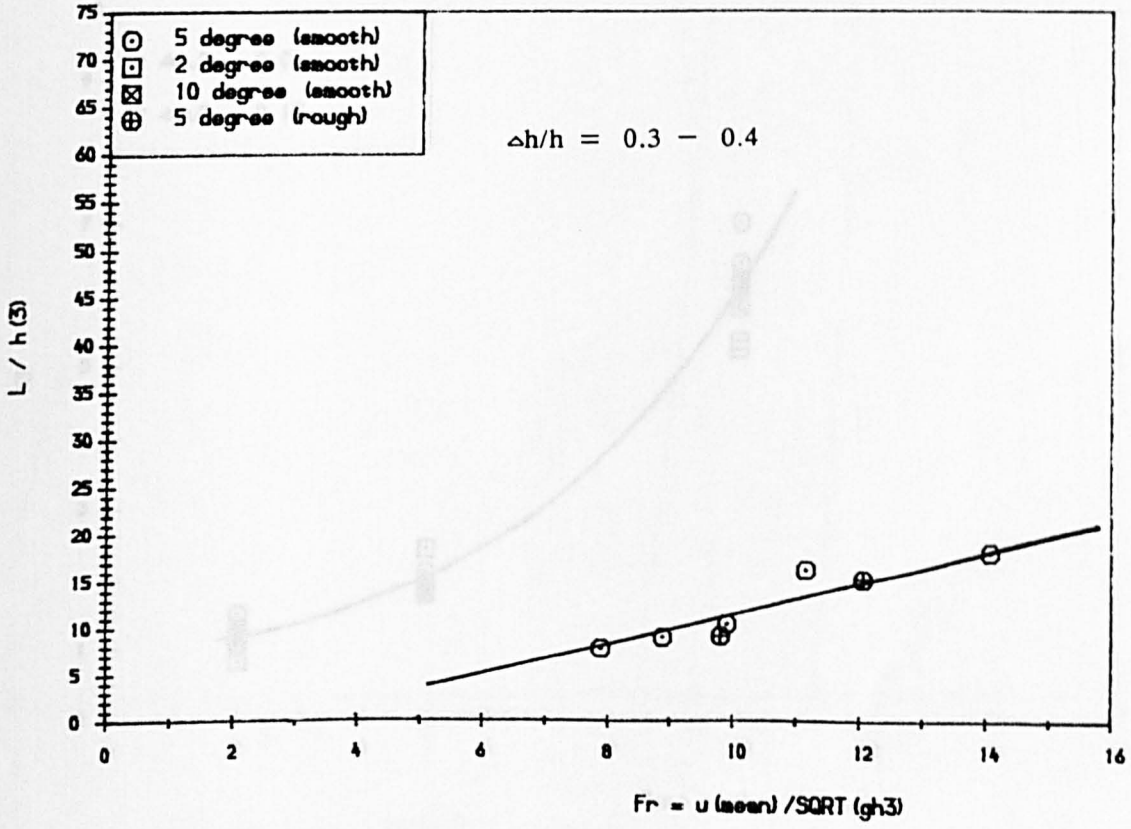

Fig 5.12(d) Variation of Froude Number with dimensionless jet length at Δh/h = 0.3 - 0.4

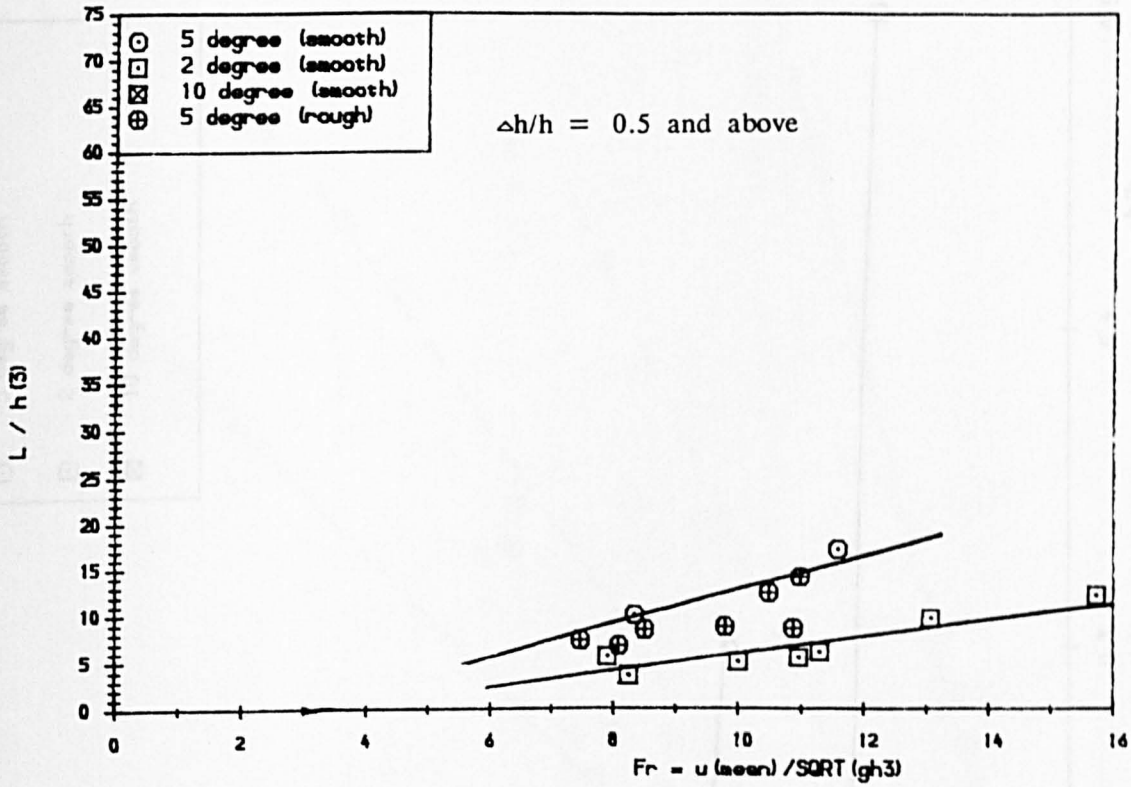

Fig 5.12(a) Variation of Froude Number with dimensionless jet length at Δh/h = 0.5 and above

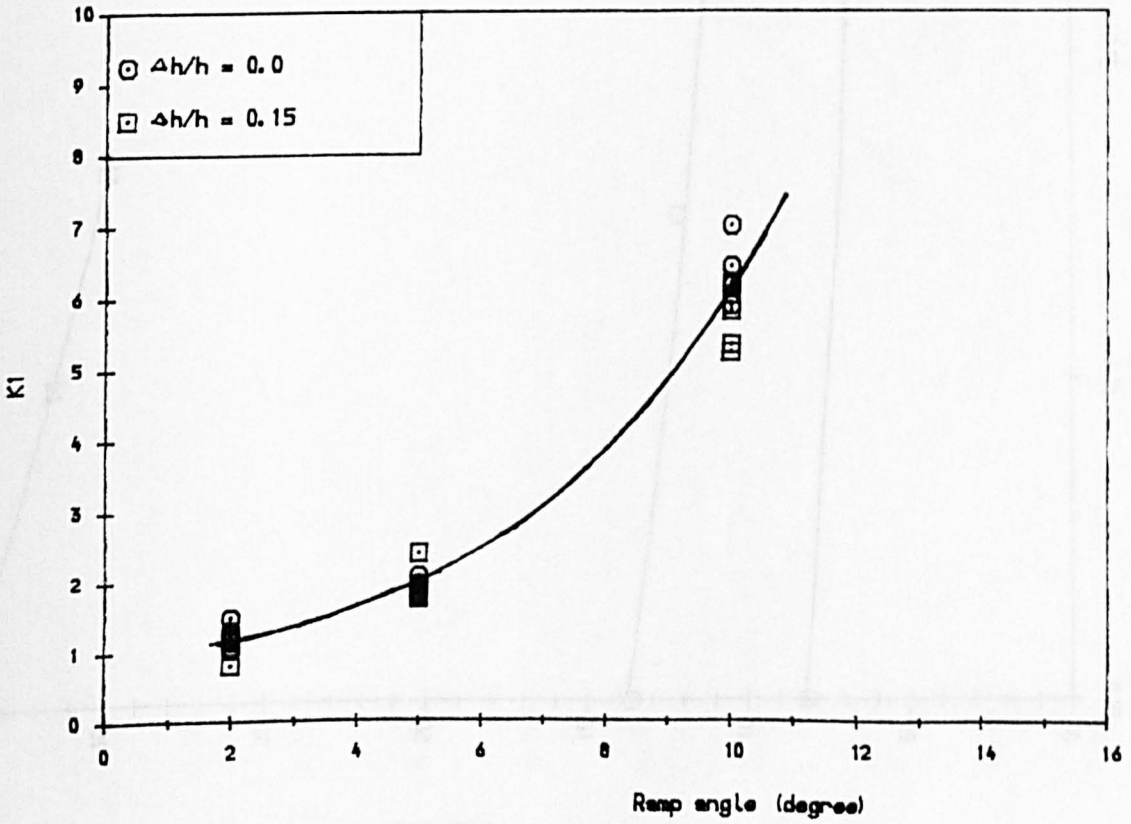

Fig 5.13 Variation of K1 with ramp angle

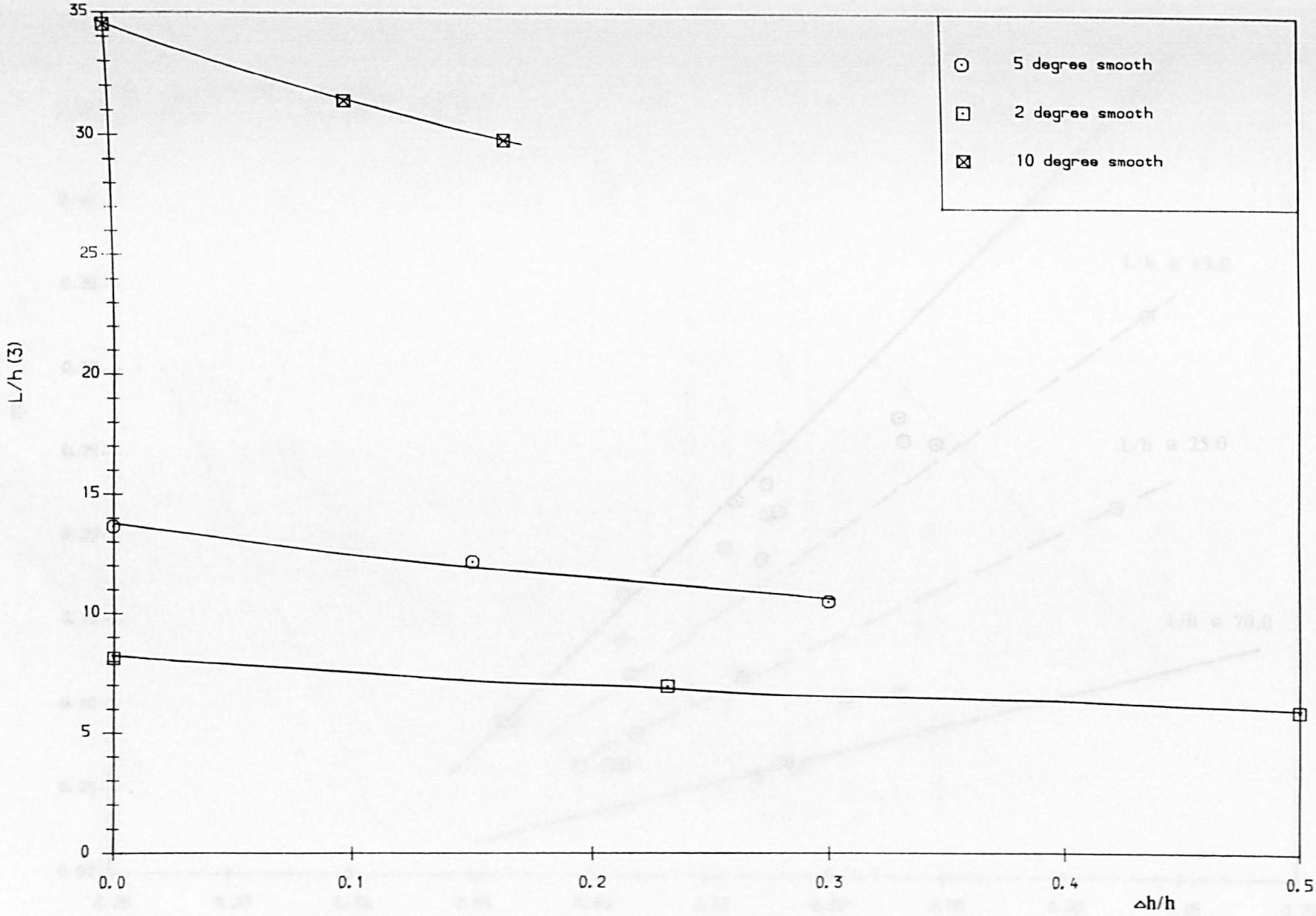

Fig 5.14 Variation of jet length with underpressure at Froude Number of 10.0

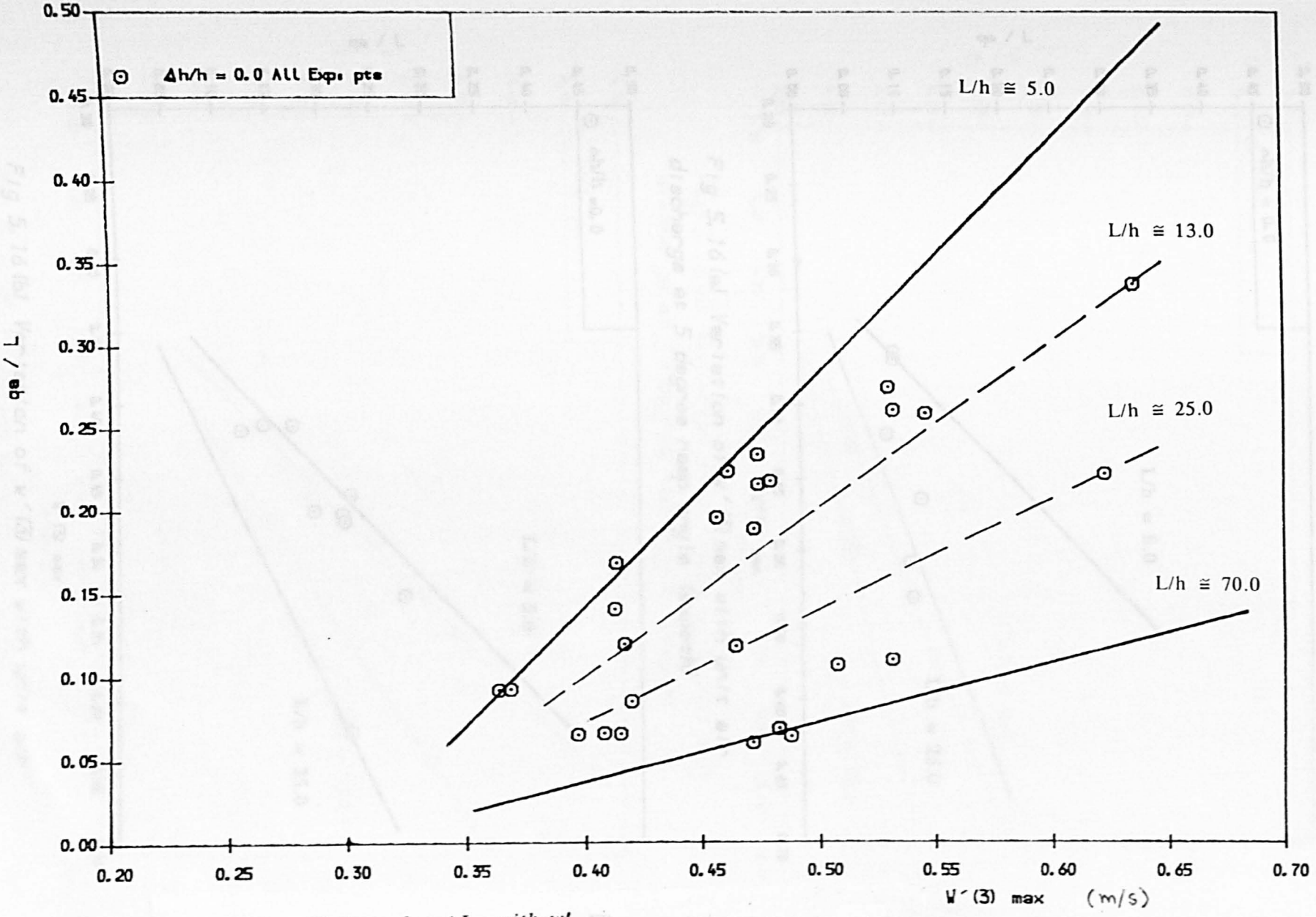

Fig 5.15 Variation of q_a / L with w'_3

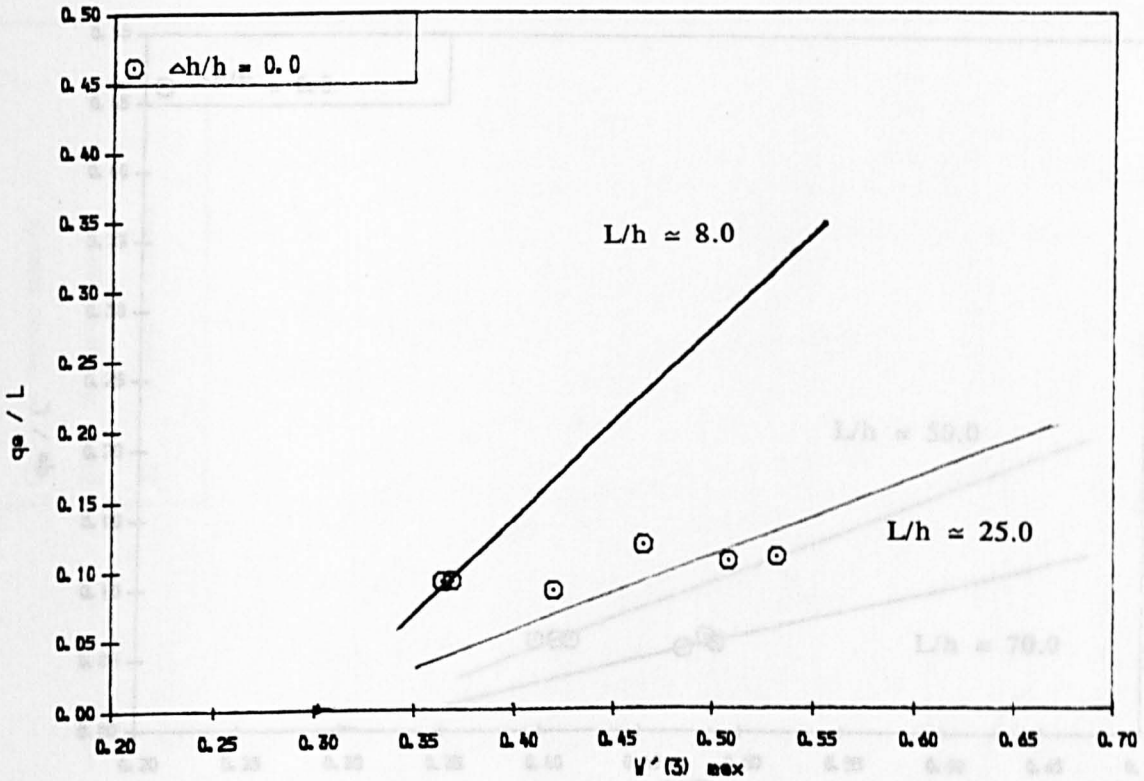

Fig 5.16(a) Variation of w'(3)max with unit air discharge at 5 degree ramp angle (smooth)

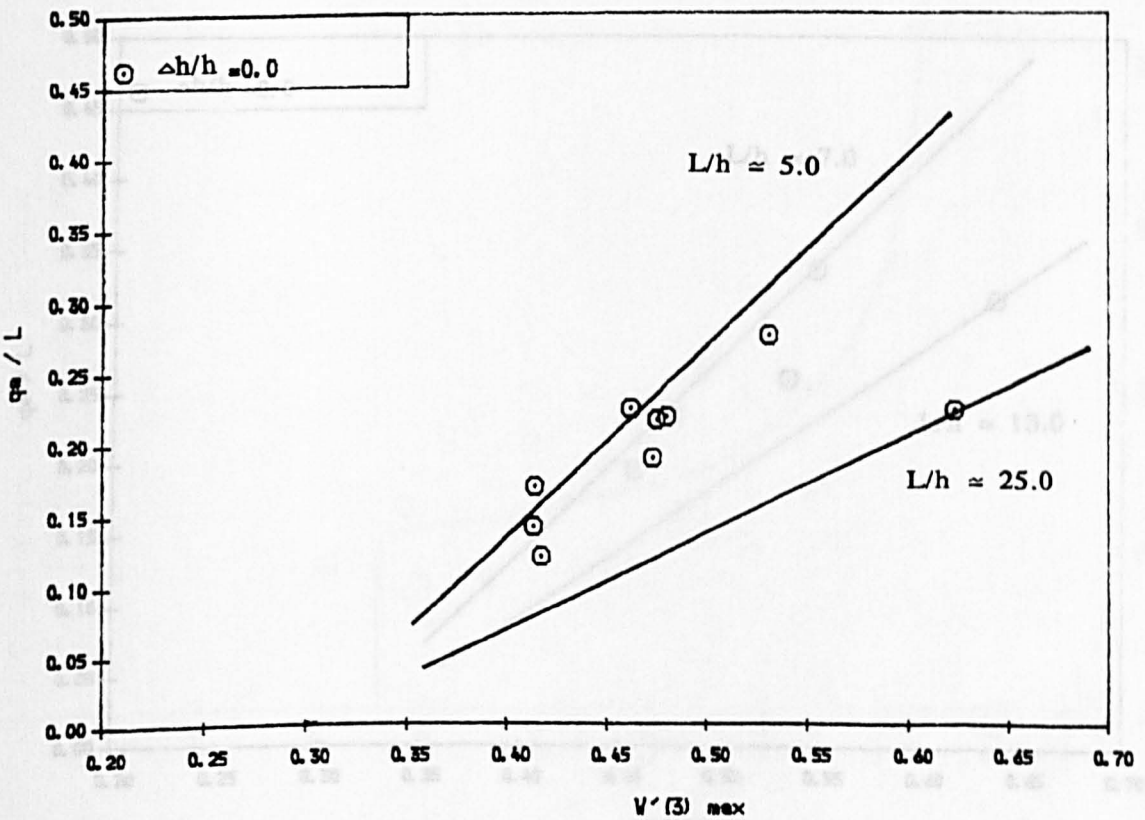

Fig 5.16(b) Variation of w'(3)max with unit air discharge at 2 degree ramp angle (smooth)

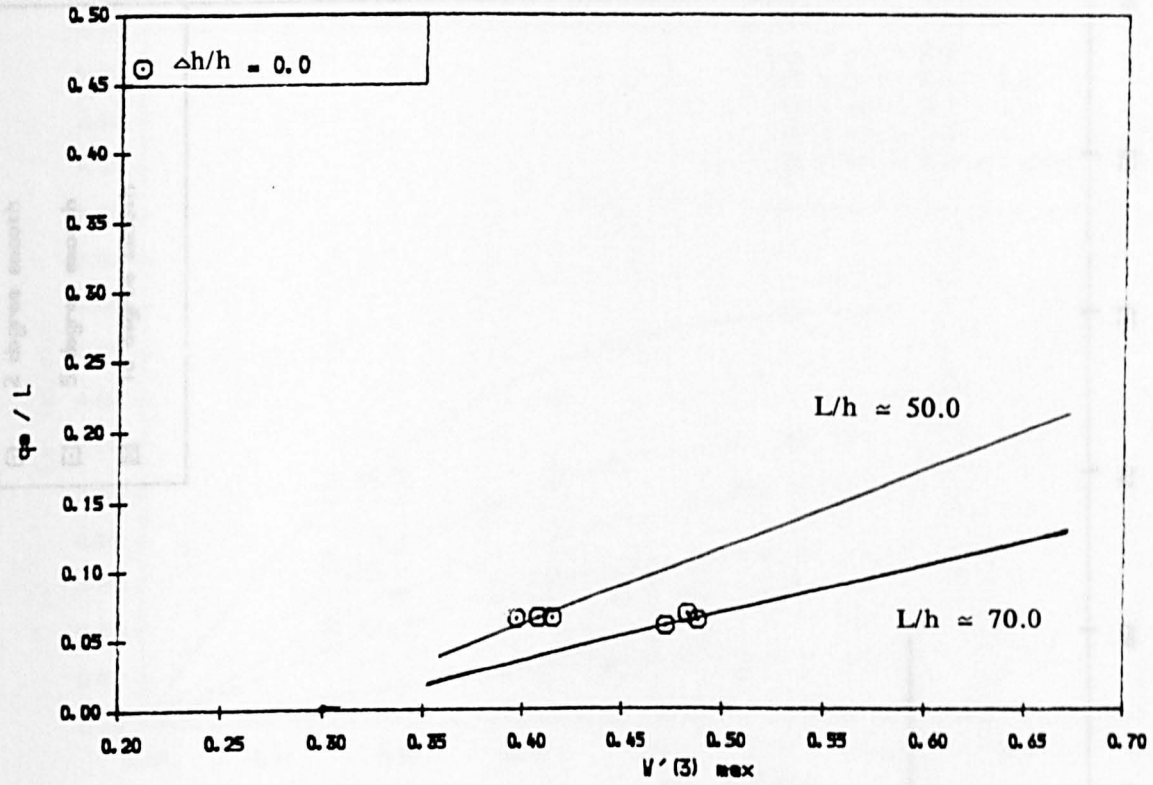

Fig 5.16(c) Variation of w'(3)max with unit air discharge at 10 degree ramp angle (smooth)

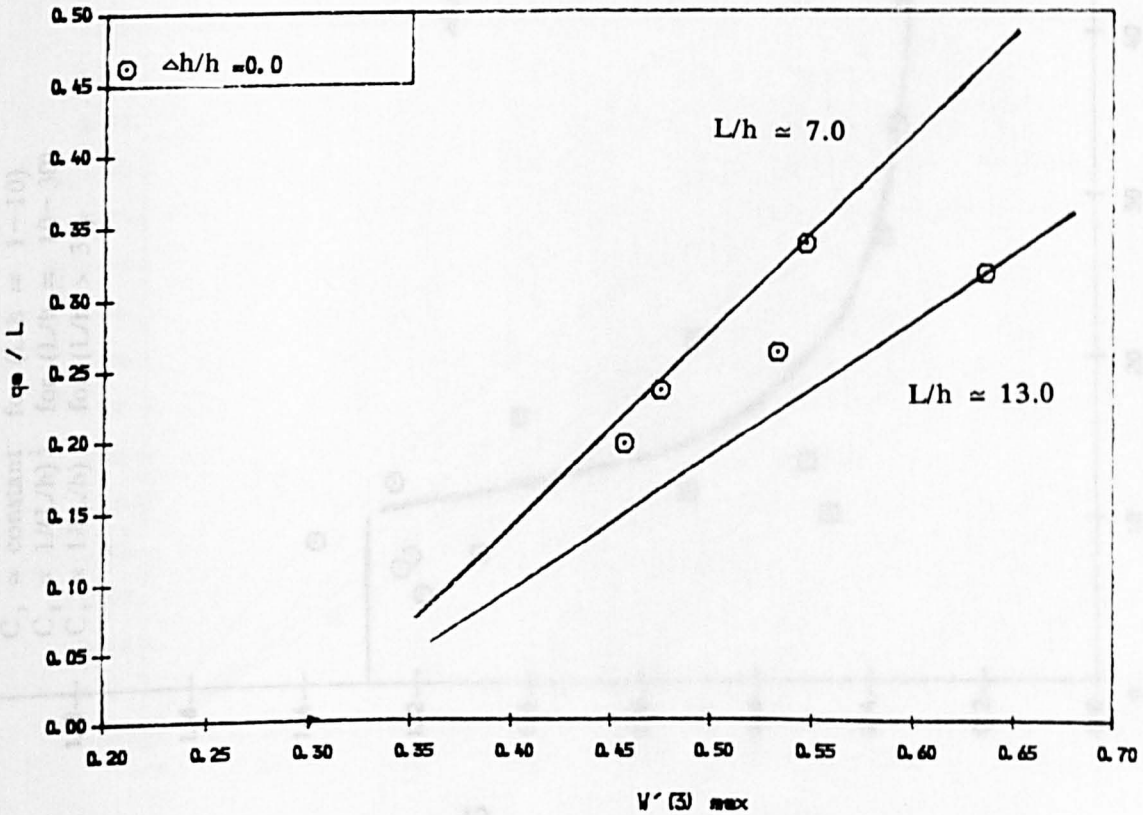

Fig 5.16(d) Variation of w'(3)max with unit air discharge at 5 degree ramp angle (rough)

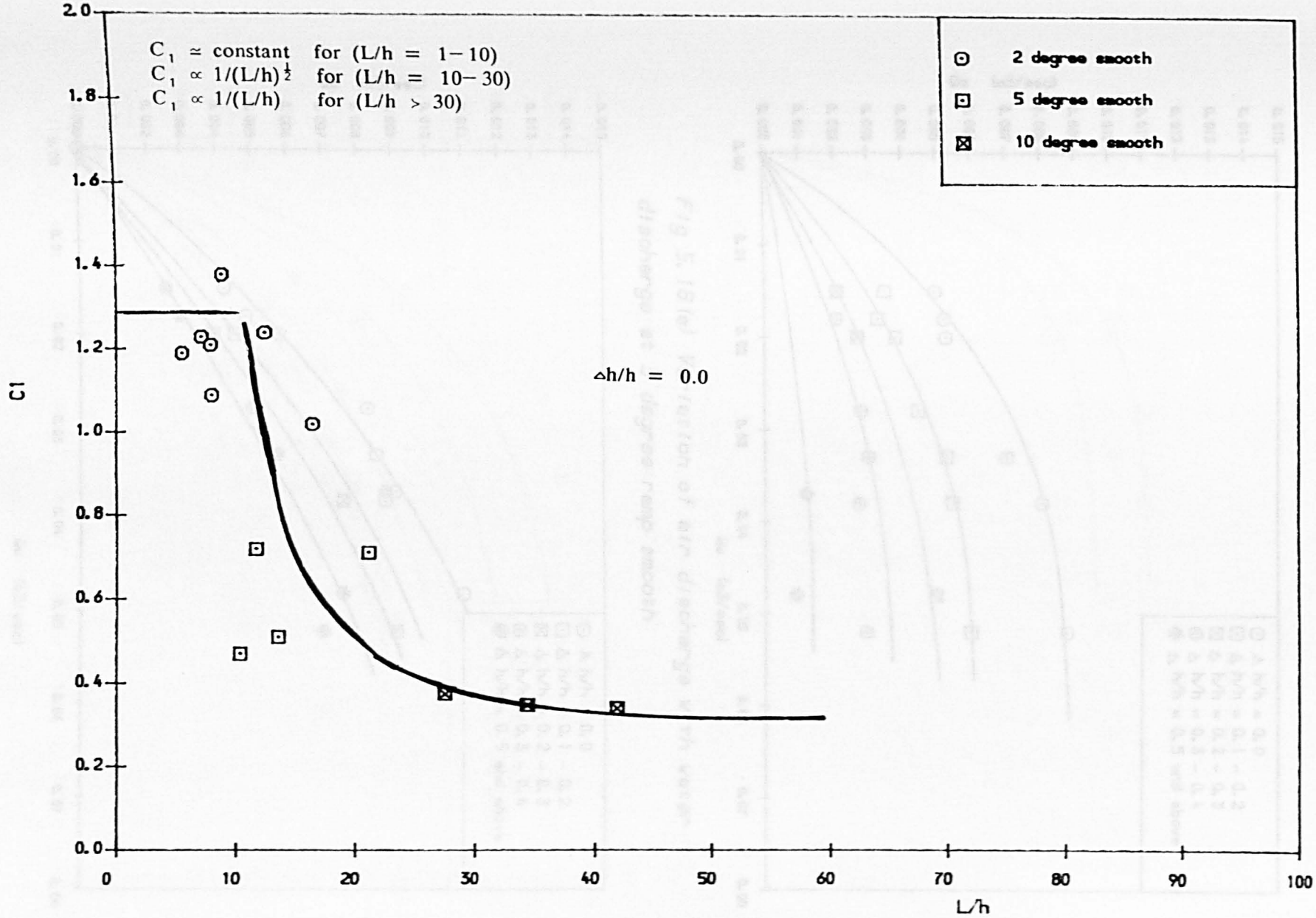

Fig 5.17 Variation in C1 with increasing jet length
Δh/h = 0.0

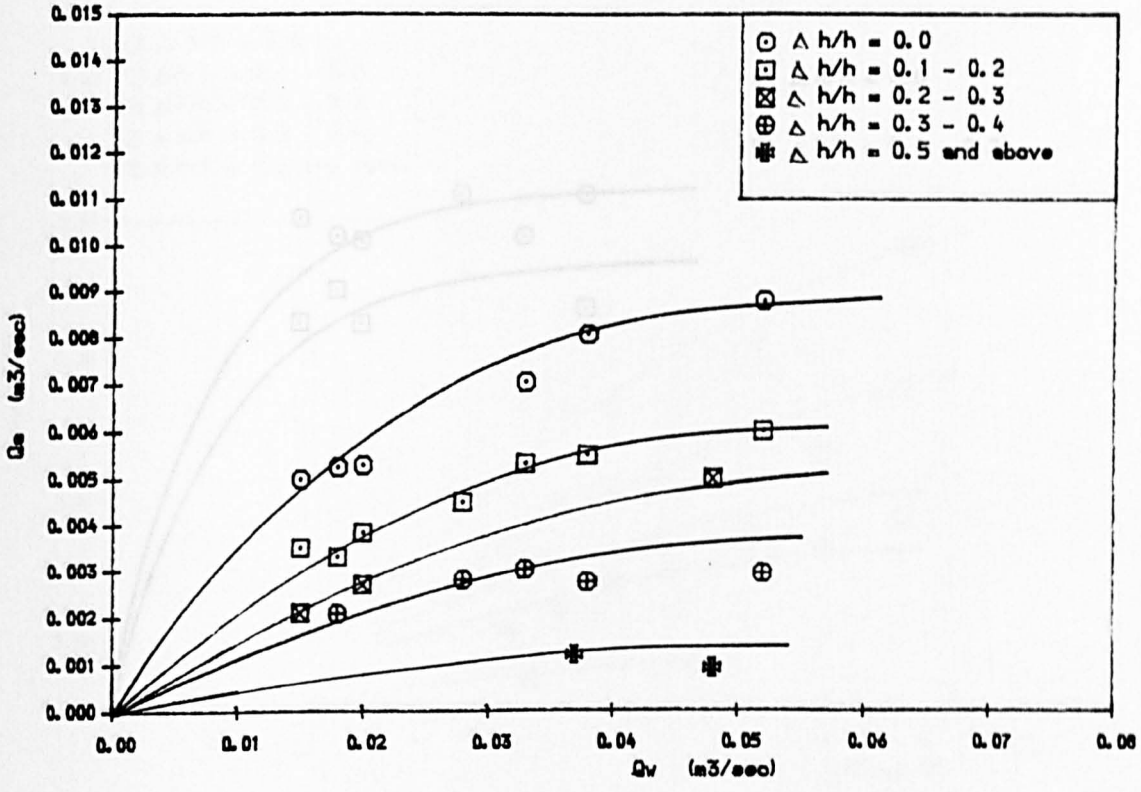

Fig 5.18(a) Variation of air discharge with water discharge at 5 degree ramp smooth

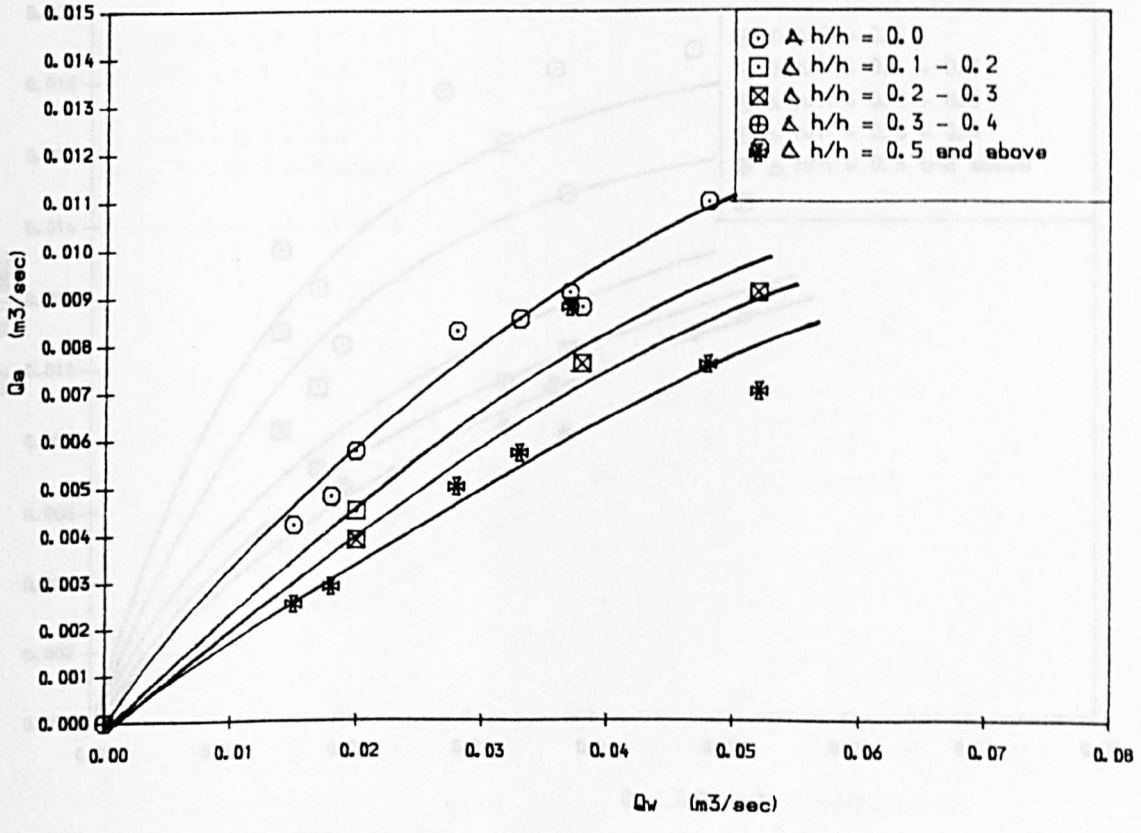

Fig 5.18(b) Variation of air discharge with water discharge at 2 degree ramp smooth

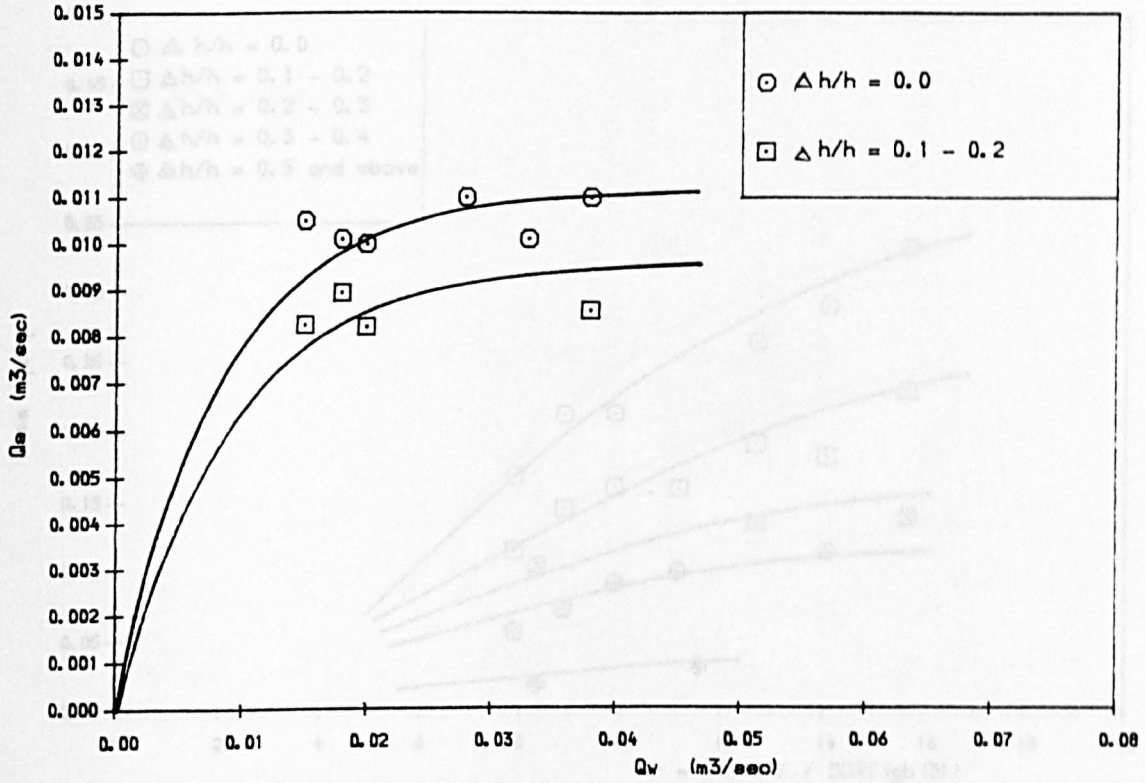

Fig 5.18(c) Variation of air discharge with water discharge at 10 degree ramp smooth

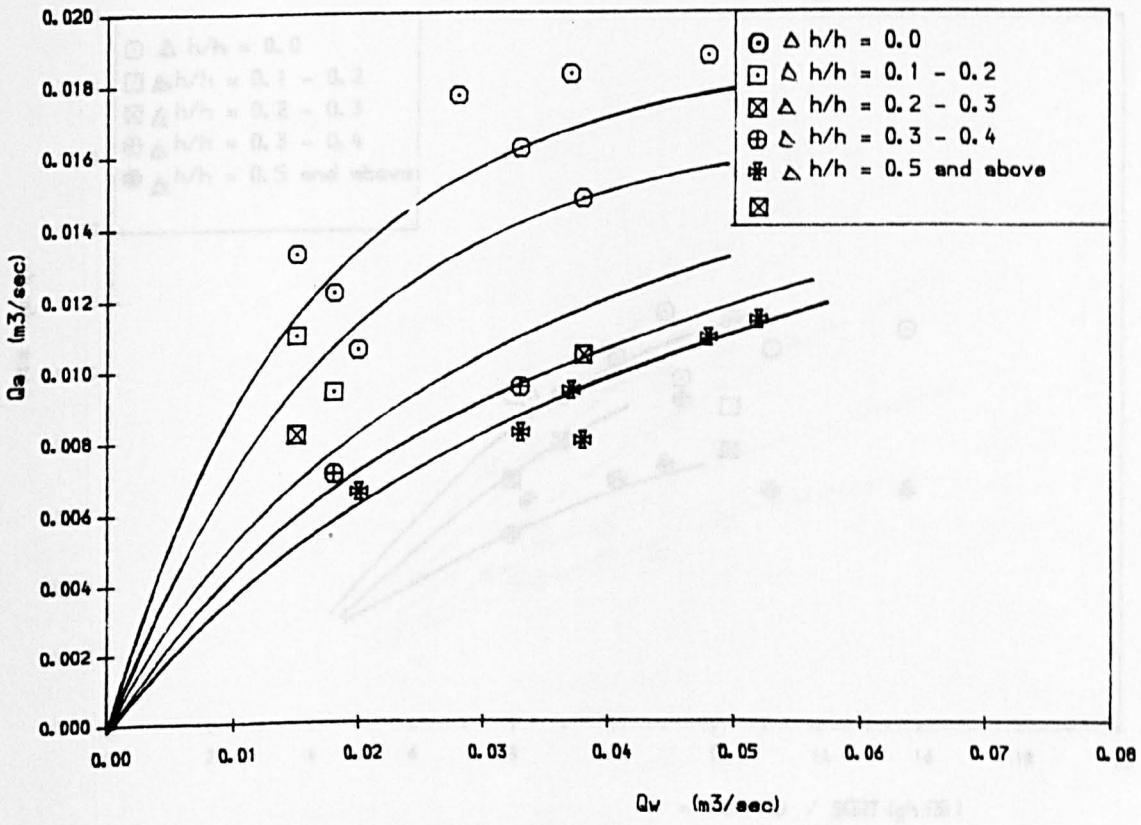

Fig 5.18(d) Variation of air discharge with water discharge at 5 degree ramp rough

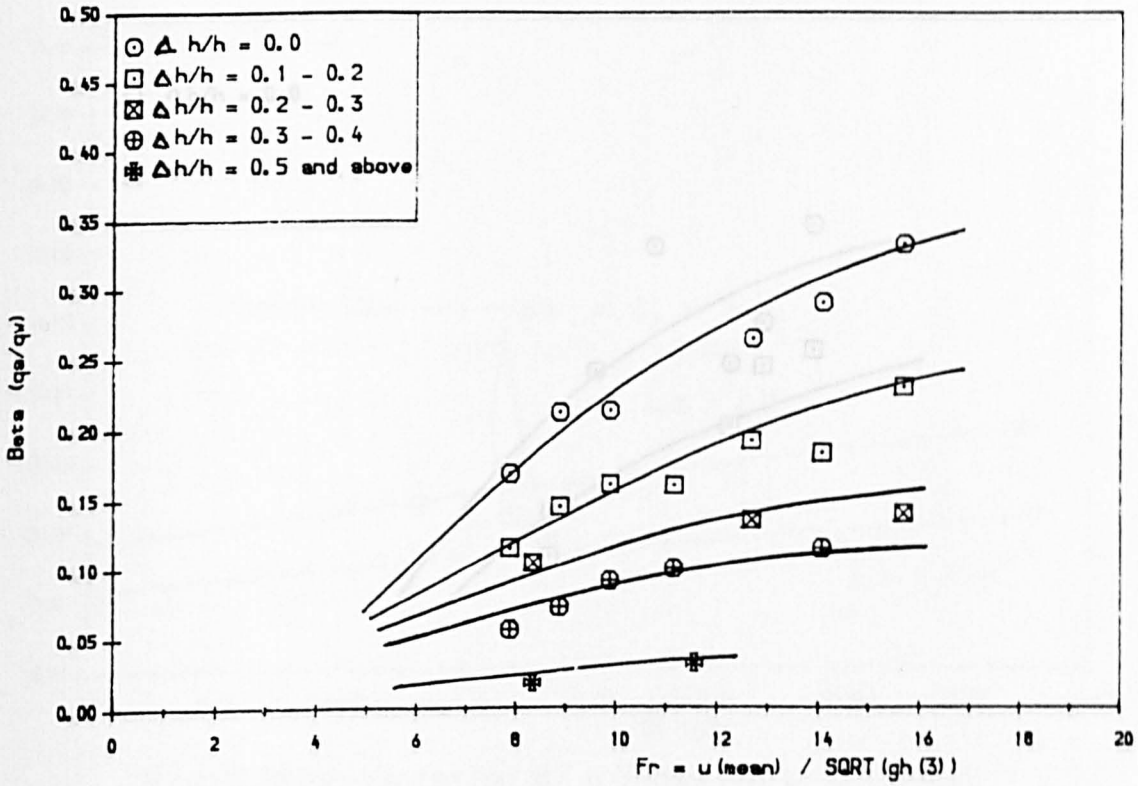

Fig 5.19(a) Variation of Froude Number with Beta (qa/qw) at 5 degree ramp angle (smooth)

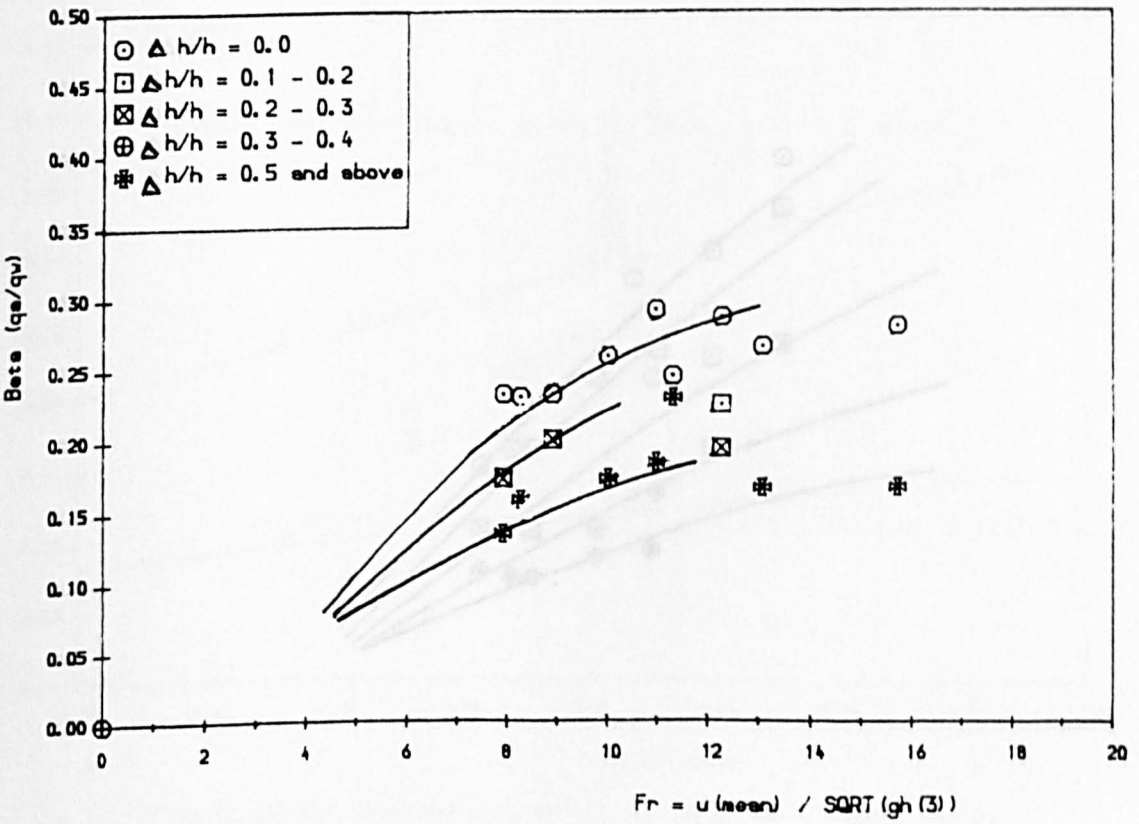

Fig 5.19(b) Variation of Froude Number with Beta (qa/qw) at 2 degree ramp angle (smooth)

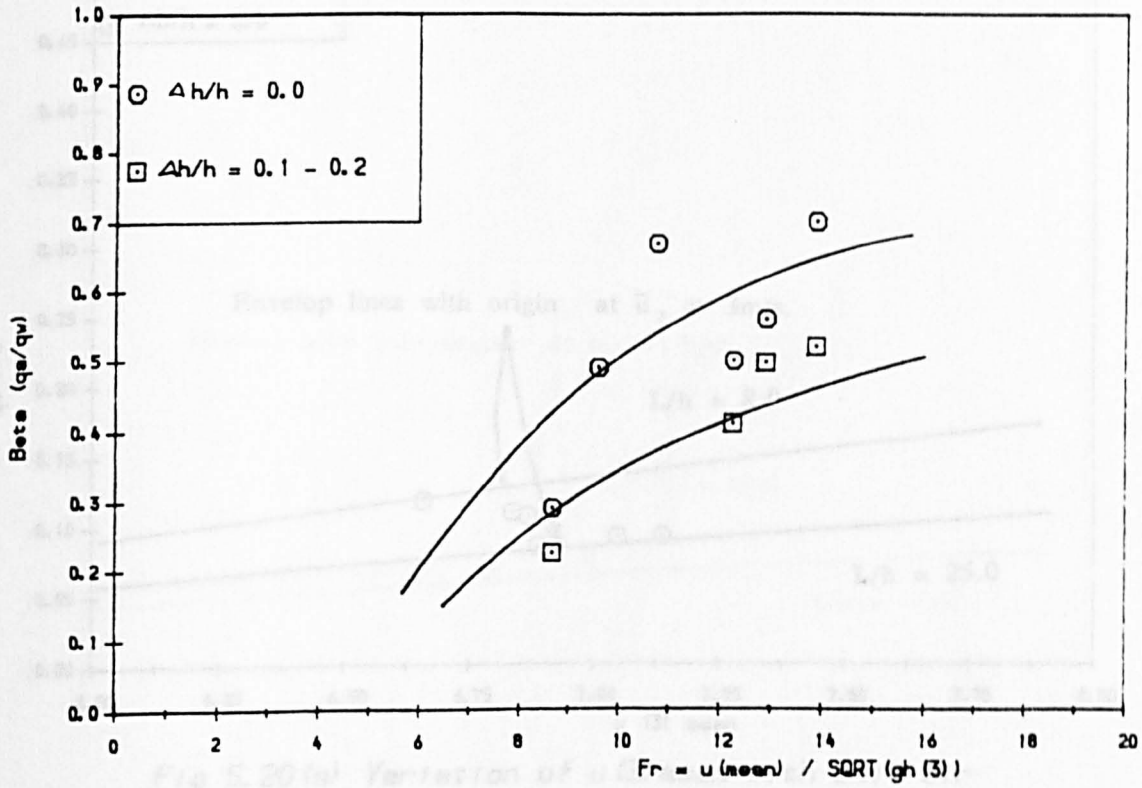

Fig 5.19(c) Variation of Froude Number with Beta (qa/qw) at 10 degree ramp angle (smooth)

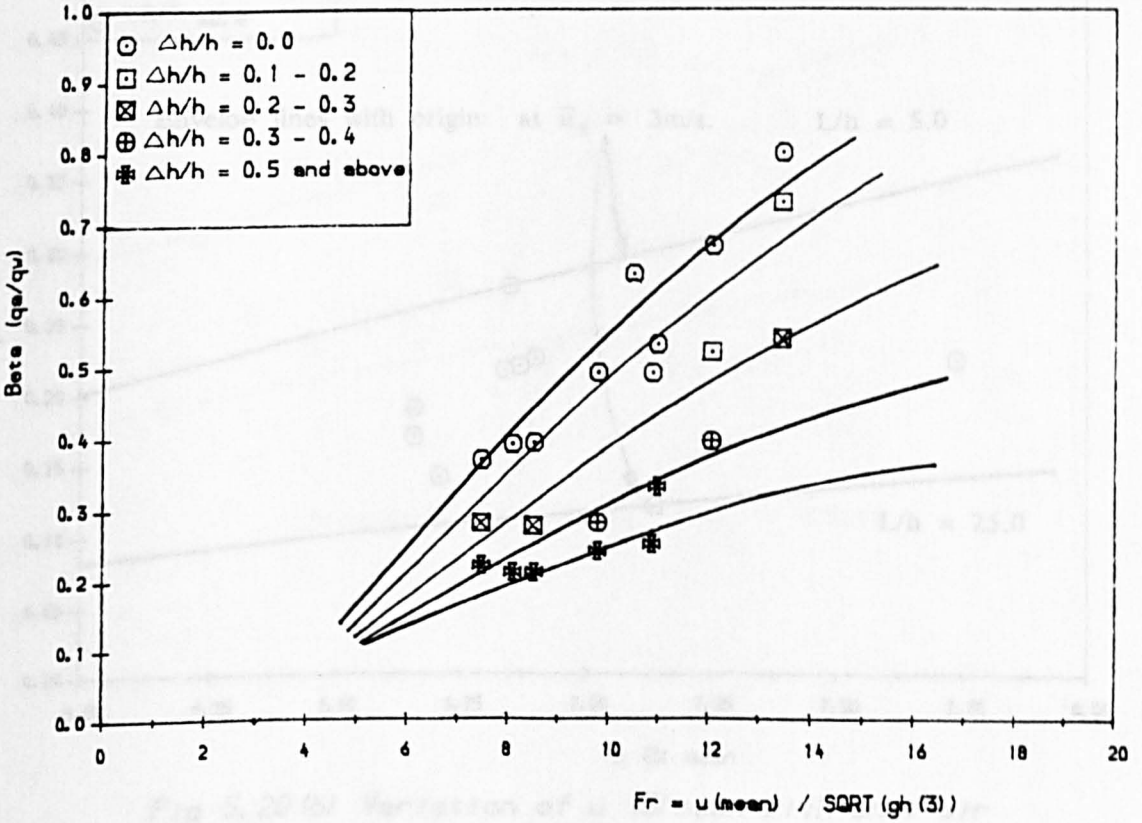

Fig 5.19(d) Variation of Froude Number with Beta (qa/qw) at 5 degree ramp angle (rough)

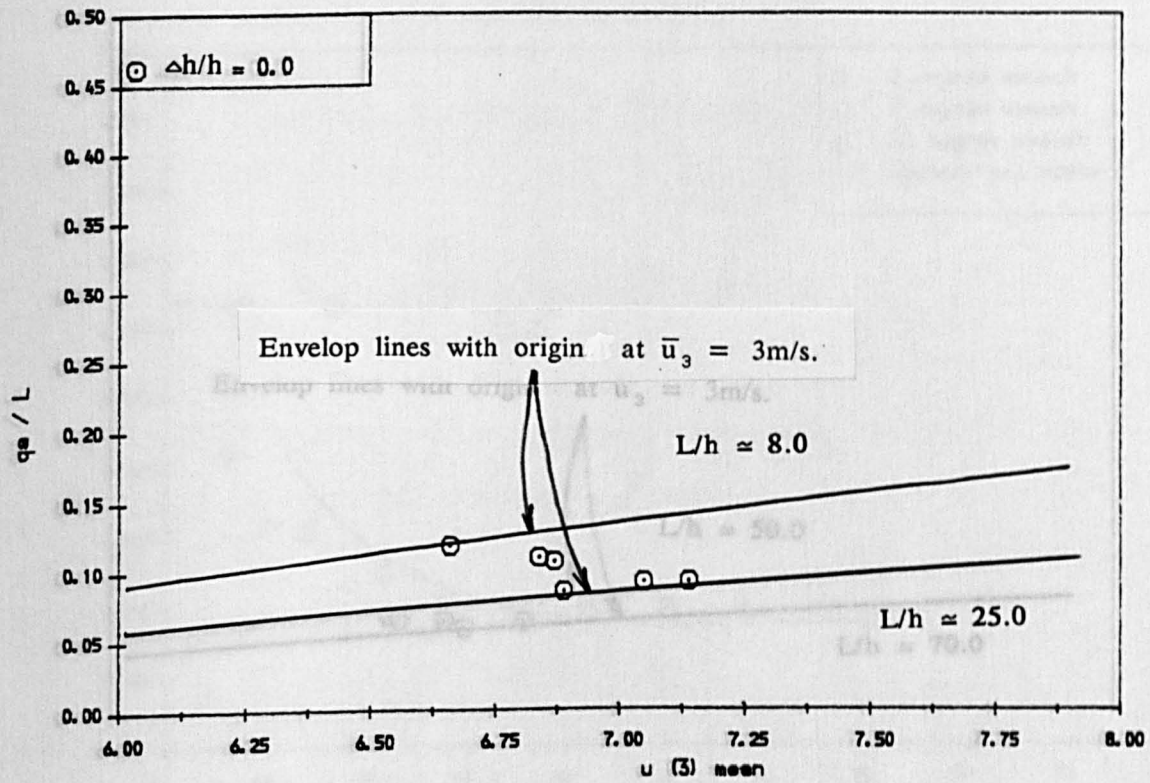

Fig 5.20(a) Variation of u(3) mean with unit air discharge at 5 degree ramp angle (smooth)

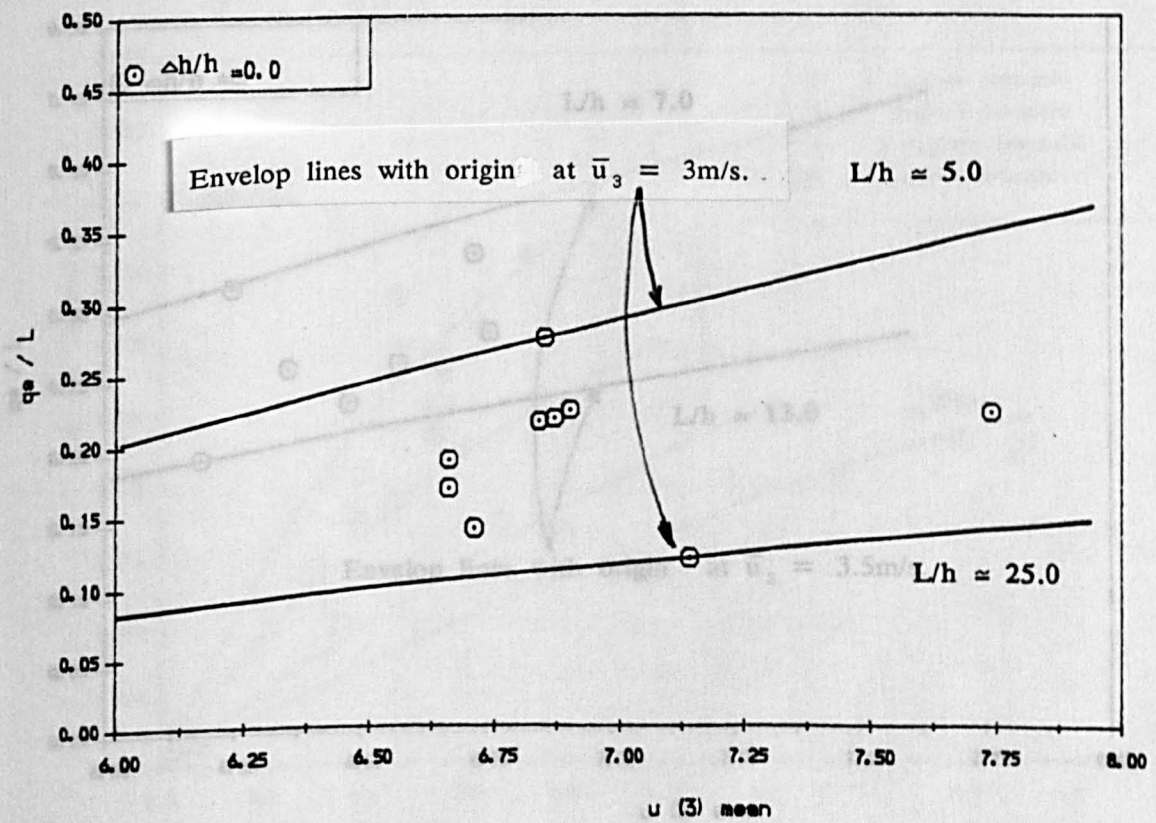

Fig 5.20(b) Variation of u (3) mean with unit air discharge at 2 degree ramp angle (smooth)

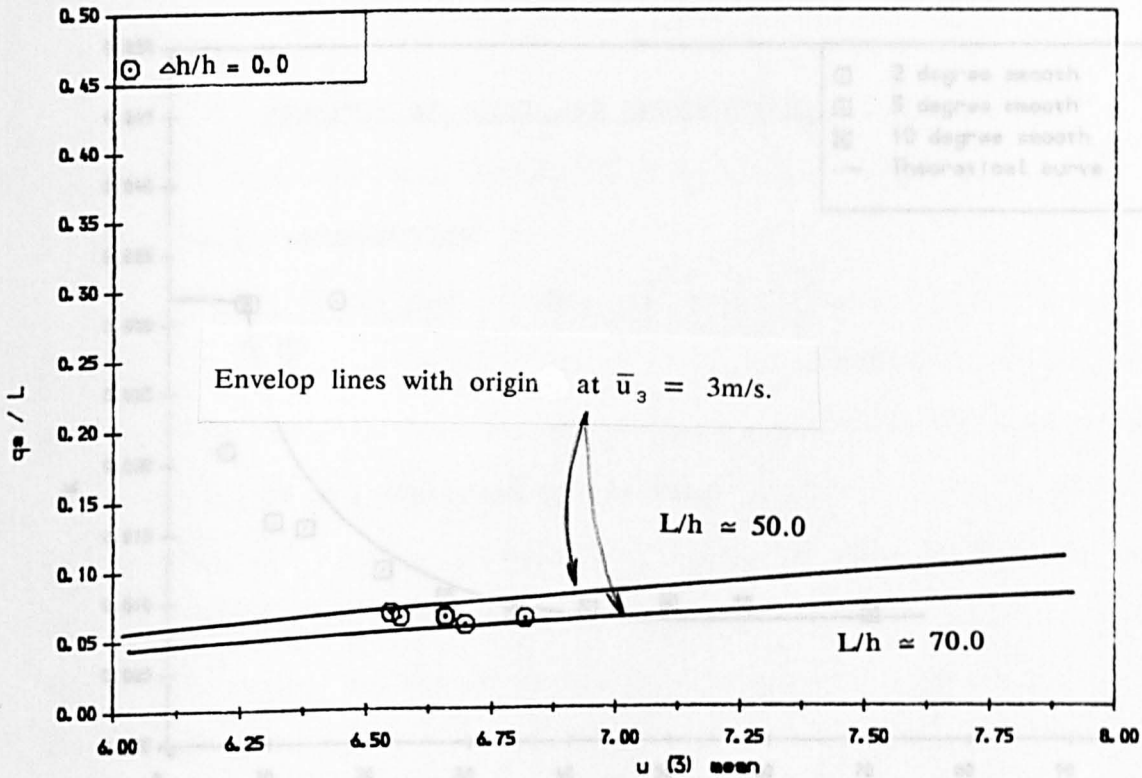

Fig 5.20(c) Variation of u (3) mean with unit air discharge at 10 degree ramp angle (smooth)

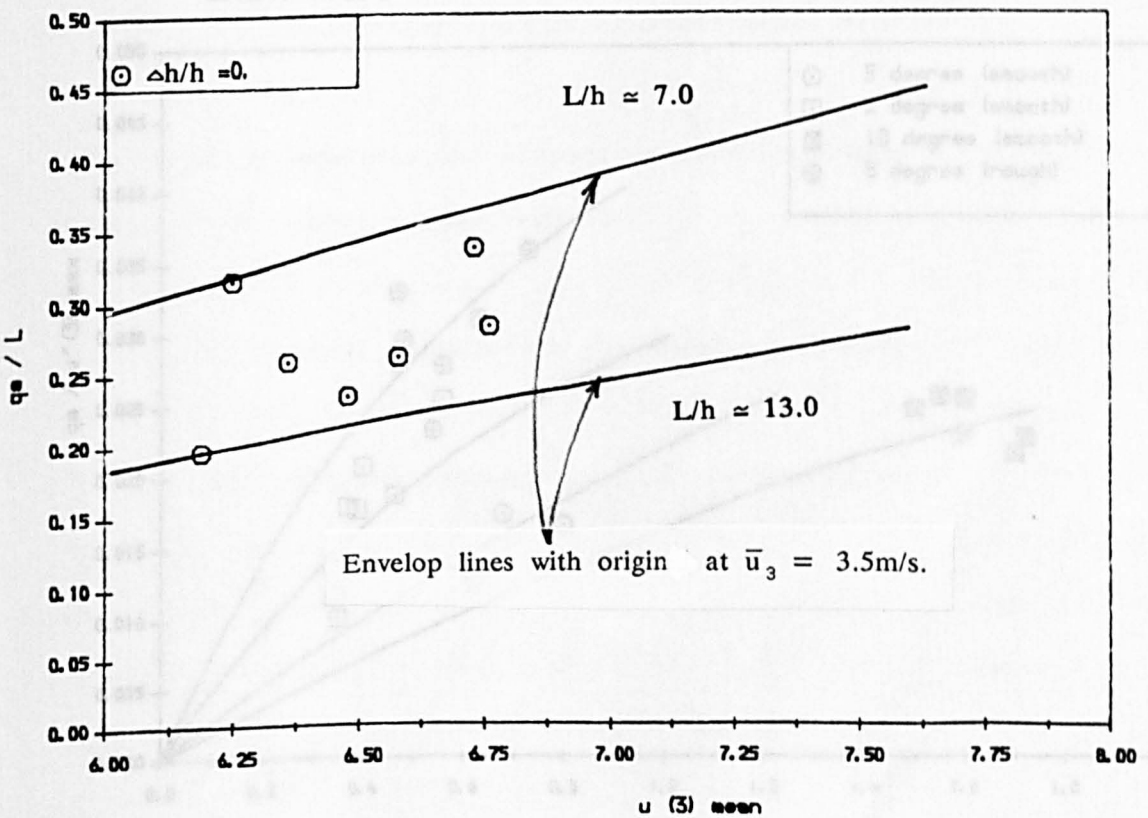

Fig 5.20(d) Variation of u (3) mean with unit air discharge at 5 degree ramp angle (rough)

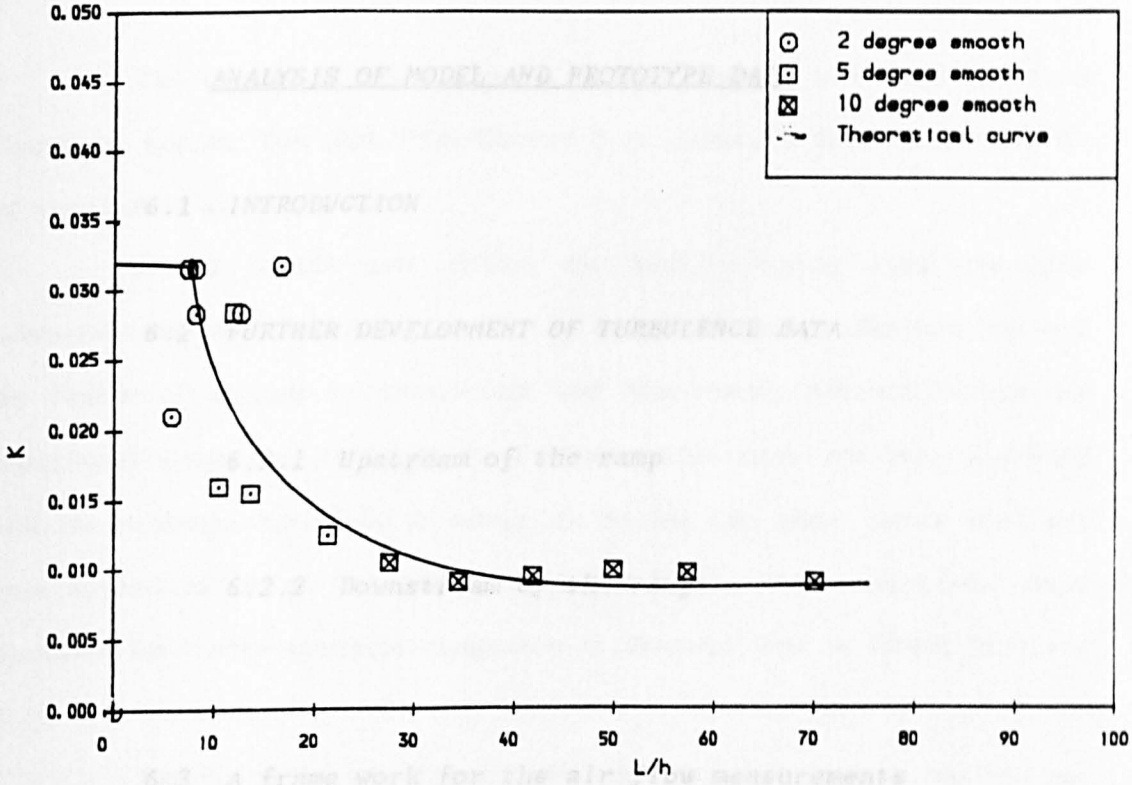

Fig 5.21 Variation in K with increasing jet length
$\Delta h/h$ = 0.0

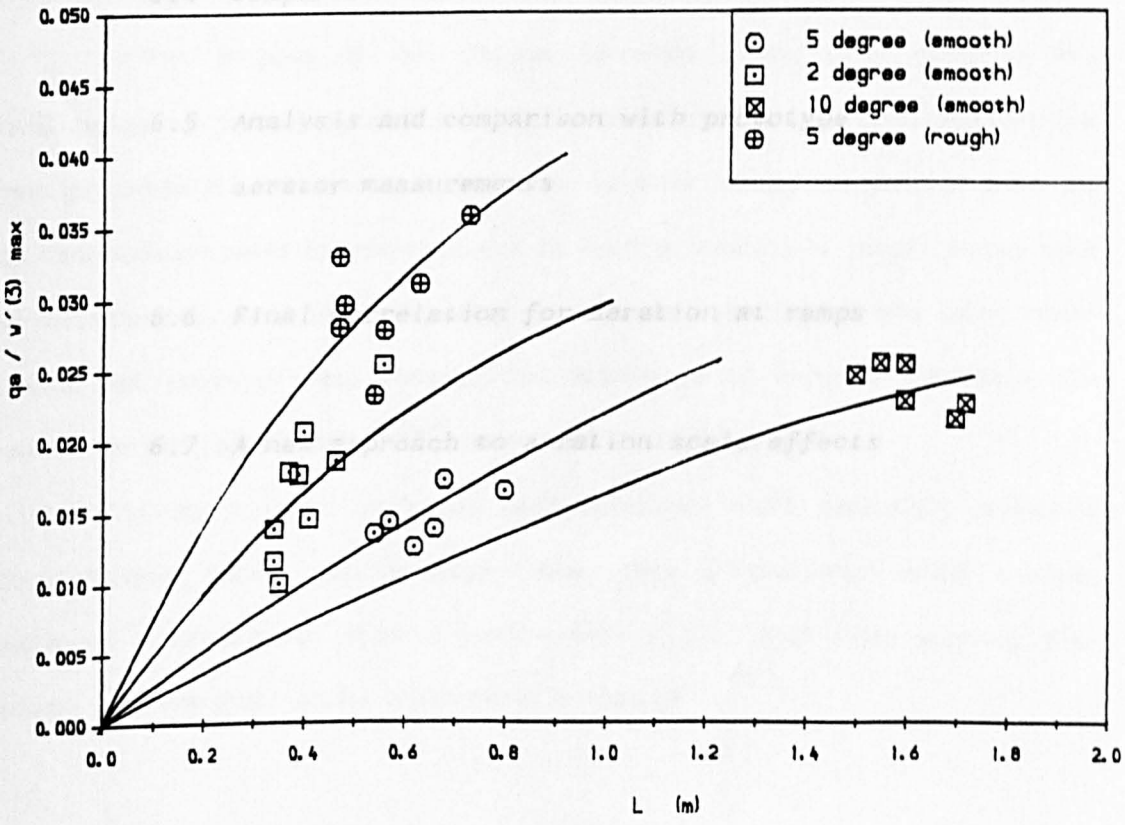

Fig 5.22 Variation of Jet length L with qa/w'(3)max
at$\Delta h/h$ = 0.0

CHAPTER 6

ANALYSIS OF MODEL AND PROTOTYPE DATA

6.1 *INTRODUCTION.*

The purpose of this Chapter is to draw together turbulence data from Chapter 4, and air flow data from Chapter 5 to produce a final frame work for air entrainment at ramp aerators.

For a decade now, debate has been on–going about the most satisfactory method of predicting aeration at ramps. Previous studies have not had the benefit of detailed turbulence data and have usually assumed uniform air entrainment along the jet length L. Previous studies have not been concerned with the minimum conditions to entrain air in the first place, which from this work appears to be of the order of $w_3' \simeq 0.3$ m/s. This concept may prove significant for model–prototype comparison as discussed later in section (6.5) and (6.6).

Despite all the advantages of this research effort, there is in–built one disadvantage, namely, the use of only one spillway slope ($\theta = 45^0$) and hence a narrow range of velocities were used at the ramp.

The purpose of this Chapter therefore is to partly overcome this disadvantage by comparing with other scale model studies and field measurements from prototype structures around the world. In other words, the detailed laser and air flow measurements in this work can be used to establish a proper frame work for describing air entrainment in ramp aerators, and comparison with other model studies and prototype tests covering the full range of expected conditions can confirm or otherwise, whether the framework is satisfactory or not.

Once a frame work has been developed which reasonably represents most previous model and prototype data, then a computer model can be developed simulating the physical process with a good deal more accuracy than before. The computer model is discussed in Chapter 7.

6.2 *FURTHER DEVELOPMENT OF TURBULENCE DATA*

6.2.1 *Upstream of the ramp*

Details and analysis of the turbulent flow structure upstream of the ramp have been presented in Chapter 4 (section 4.3). Turbulence values along the spillway and ramp are seen to increase with velocity, depth, Reynolds Number, boundary roughness and to vary with ramp angle, aspect ratio of the flow, and with depth– up from the channel bed.

Perhaps the key findings from turbulence measurements upstream of the end of the ramp can be summarised as:–

(i) At section 1, 600mm upstream of section 3, and in the straight spillway region, turbulence readings are similar to previous measurements of open channel flows.

(ii) The ramp itself acts as a turbulence generator, as evidenced by the increase in turbulence values from section 1 to section 3.

(iii) At the end of the ramp (section 3) the maximum turbulence readings $(w_3')_{max}$ are still related to the flow shear velocity u_*, hence can be used in any air flow predictive frame work. A sketch of the location of each measurement section is given in Fig 6.1.

Consider each concept in turn it was decided to plot maximum turbulence value of w' at section 1, near the channel base, for each of the four geometries tested, (Φ = 2°, 5°, and 10° smooth, as well as 5° rough) as well as each gate opening tested. The result is shown in Fig 6.2 with $(w'_1)_{max}$ plotted against the shear velocity u_* at section 1.

The result is substantially linear relationship giving;

$$w'_1 \approx 1.35\ u_* \qquad (6.1)$$

near the channel bed of a steep supercritical flow. The result is important because it reveals the close inter–relationship between turbulent and shear velocities. More importantly it shows a similar relationship to subcritical open channel flows which have revealed $(w'_1)_{max} \simeq 1.23\ u_*$ (Nezu and Rodi) which is within 10% of the result in this work. This is a good result despite the fact that the turbulence transmitted from the pressure box upstream seems to be convected along with the flow. It appears to have made little difference to turbulence near the channel bed. The result also reveals that supercritical flows are not unlike subcritical flows.

Considering the proposition that the ramp behaves like a turbulence generator, it was decided to plot maximum values of w_3' (at section 3, end of ramp, near the channel base) against the shear velocity u_* at section 3.

The procedure was carried out as before, for all four geometries and for each gate opening. The result is shown in Fig 6.3 revealing at the end of a ramp that,

$$w_3' \approx 1.75\ u_* \qquad (6.2)$$

irrespective of the ramp angle Φ, the boundary roughness k_s or the gate opening.

This result is also important because it shows that the ramp generates extra turbulence at least nearer the channel bed, with an increase of almost 30% over the section 1 value. It should be noted that the value of u_* in Equation (6.2) is that obtained at the end of the ramp and can be determined using the computer programme outlined in Appendix A VI.

More importantly, Fig 6.3 reveals that in any new relationship for

aeration at ramps, and where the rate of air entrainment is thought to be dependent on the turbulence velocity w', then Equation (6.2) above can be substituted for the turbulent velocity.

Finally the relationship between $(w_3')_{max}$ at section 3, and $(w'_1)_{max}$ at section 1 is given in Fig 6.4. This graph gives the approximate relationship

$$w_3' \simeq 1.29\ w'_1 \qquad (6.3)$$

showing that no particular ramp angle from 2^0 to 10^0 is more efficient than any other at generating extra turbulence. This is interesting in view of the fact that a 2^0 ramp would produce less streamline deviation than a 10^0 ramp.

6.2.2 *Downstream of the ramp*

Turbulence measurements in the aerator jet downstream of the ramp have been presented in section 4.3. Measurements were carried out at section 4 only, a fixed distance of 300mm downstream of the end of the ramp. Varying the flow depth h enabled the non-dimensional distance x/h_3 downstream of the ramp to be varied.

Measurements downstream of the ramp proved difficult because of air bubble entrainment on the upper and lower surface of the jet, sketched below. Proper comparison of turbulence at section 4 compared to section 3 is thus only possible either by comparing comparable points such as jet centre line at both sections, or alternatively by depth averaging turbulence values over the depth AB as shown below.

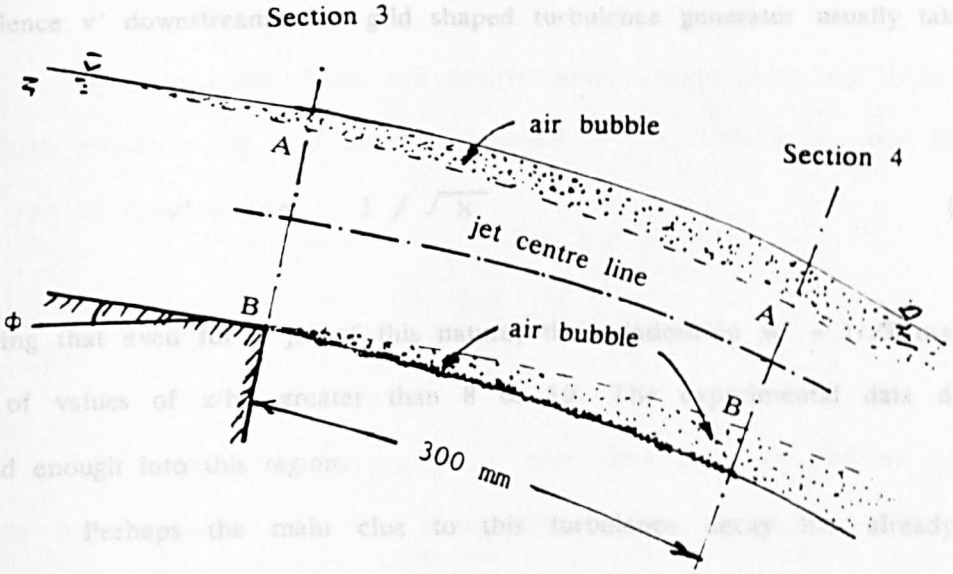

The first observation comparing turbulence at section 4 and section 3 is the decay in w'. This is shown approximately by depth averaging w' at section 4 (w_4') and comparing with depth average w_3'. This result is shown in Fig 6.5 for all four geometries and each gate opening showing that as a rough approximation

$$w_4' \approx 0.9\, w_3' \quad \text{for } x = 300\text{mm} \qquad (6.4)$$

This observation hides the variation in decay for each values of non–dimensional distance downstream x/h_3 which is varied by changing values of h_3.

Values of $w_4'/\bar{u}$ are plotted against x/h_3 in Fig 6.6, the values of w_4' being the depth–average values. At $x/h_3 = 0.0$, the turbulence values are those pertaining to section 3. It is apparent form Fig 6.6 that turbulence values internally in the jet remain more or less constant for values of x/h_3 up to 8 approximately and decay for $x/h_3 > 8$. Unfortunately the range of measurements

was not sufficiently large to obtain the nature of the decay beyond $x/h_3 > 12$.

It should be noted that Davies (1972) comments that the decay of turbulence v' downstream of a grid shaped turbulence generator usually takes the form

$$v' \quad \propto \quad 1 / \sqrt{x} \qquad (6.5)$$

meaning that even for a jet of this nature, the relationship $w' \propto 1/\sqrt{x}$ may hold true of values of x/h_3 greater than 8 or 10. The experimental data did not extend enough into this region.

Perhaps the main clue to this turbulence decay has already been discussed in Chapter 5 (section 5.3.5) where the air entrainment rate is plotted as a function of jet length L/h. The coefficient of air entrainment rate C_1 is shown in Fig 5.17 revealing that $C_1 \simeq$ constant for L/h upto 10, $C_1 \propto 1/\sqrt{(L/h)}$ for L/h between 10 and 30 and for $L/h > 30$, $C_1 \propto 1/(L/h)$. Thus it appears that if air entrainment rate $q_a \propto w'$ and air entrainment rate coefficient decays rapidly for $L/h > 10$, then it follows that this decay is due to decay in w'.

The decay rate along the jet centre–line is shown in Fig 6.7 revealing a similar decay as the depth–averaged version, and also showing that the decay rate is similar for each ramp angle and roughness tested.

6.3 *A frame work for the air flow measurements*

A frame work for aeration at ramps has already been developed in Chapter 5.

Ignoring scale effects, and for atmospheric pressure in the cavity $\Delta h/h = 0.0$ and for a given non–dimensional jet length L/h, the value of aeration per unit width is given by

$$q_a = C_1 (w_3' - 0.3) L \qquad (6.6)$$

Ignoring scale effects and underpressure effects $\Delta h/h$, the value of C_1 has been shown in Fig 5.17 to be a function of L/h. This means that Equation (6.6) can be rewritten as

$$q_a = f_1(L/h) (w_3' - 0.3) L \qquad (6.7)$$

We may make this expression non–dimensional by dividing q_a by a velocity times a length term. The chosen velocity term is $(w_3' - 0.3)$ and the length term is flow depth h. This is preferable to jet length L which is unknown, whereas h is known.

Thus

$$\frac{q_a}{(w_3' - 0.3)h_3} = f_1\left[\frac{L}{h}\right] \frac{L}{h_3} \qquad (6.8)$$

$$= f_2\left[\frac{L}{h}\right]$$

We may now introduce turbulence information from Chapter 4 to substitute for w_3'. This is based on the approximate relationship between w_3' and the shear velocity at the ramp.

$$w_3' \approx 1.75\, u_{*3} \qquad (6.9)$$

and hence after substituting Eq 6.8 becomes, (note for convenience the subscript has been omitted and h used to donate the depth at the end of the ramp)

$$\frac{q_a}{1.75(u_* - 0.18)h} = f_2\left[\frac{L}{h}\right] \qquad (6.10)$$

This means that a plot of $q_a / (u_* - 0.18)h$ against jet length L/h should reveal the nature of f_2. This is done in the first instance for the Glasgow data only and for zero underpressure, $\Delta h/h = 0.0$. The result is given in Fig 6.8 for all four geometries. It is clear from the Fig 6.8 that air entrainment rate remains linear for L/h up to 10 – 12. As the value of L/h increases further the air entrainment rate shows non–linear behaviour.

The next step in the analysis concerns the influence of the cavity underpressure $\Delta h/h$. A more generalised expression for Equation (6.10) which relates only to the case $\Delta h/h = 0.0$, might be expressed in the form

$$\frac{q_a}{(u_* - 0.18)h} = 1.7\ f_2\left[\frac{L}{h}\right] f_3\left[\frac{\Delta h}{h}\right] \qquad (6.11)$$

The experimental data from this research is plotted in Fig 6.9 for the full range of $\Delta h/h$ values again in the form of $q_a / (u_* - 0.18)h$ against L/h for each increment of $\Delta h/h$. Fig 6.9 shows the clear bands of $\Delta h/h$ from 0.1 to 0.4, which is linear up to $L/h \simeq 10$ and then again follows non–linear behaviour.

6.4 *Comparison with other scale model studies*

In this section it is intended to re–analyse scale model studies by other authors in the light of the air flow frame work above. The reason for carrying out this exercise is obvious especially in view of the fact that the spillway slope θ, and the mean velocities in this work covered only a small range, and hence need comparison with other model studies at other slopes,

velocities, Reynolds Numbers, etc.

Although none of the previous model studies measured the turbulence structure at ramp aerators, many model studies have measured the aeration rate for a range of other parameters. In order to compare with the frame work outlined in section 6.3., the model studies require to have measured air flow,(Q_a), water flow Q_w, mean velocity $\bar{u}$, flow depth h, aerator jet length L and the cavity sub–pressure Δh, to allow a comparison. One benefit of model studies is the ability to measure jet length L with reasonable accuracy, which is often not possible with prototype structures.

It was decided therefore to compare with different set of model studies, namely Foz–do–Areia model studies, Clyde dam model studies and Wallingford model studies. Brief details of the range of each set of model studies is given below. Data sets were chosen because each contained a full set of accurate data, as well as representing the major centre for research in this area:–

(i) *Foz – do – Areia model studies*

Model studies for the aerated chute spillway of 160m high Foz–do–Areia dam was carried out at University of Parana, Brazil. Model scales ranging from 1:50 to 1:8 of one of the Foz–do–Areia aeration groove were tested in a glass walled flume. The data of the 1:30 general model is used in this research for comparison. The bed slope $\theta = 14.5^0$ and ramp angle $\Phi = 7.125^0$. Typical model velocities were in the range of 3.6 m/s to 6 m/s.

(ii) *Wallingford (UK) model studies*

General Laboratory experiments were carried out at 1:10 and 1:20 scale to investigate the amount of air entrained by water flowing over ramp

aerator at River Engineering Department of Hydraulics Research, Wallingford. The flume was 4 m long and varyied in width up to 0.3 m. The flume can be set at an angle between horizontal and 45°. Typical bed slope θ used for comparison was 15° and 45°. Typical flow velocities were in the range of 6 m/s to 15 m/s.

(iii) *Clyde model studies*

Model studies for the aerator chute spillway of Clyde Dam was carried out at the University of Canterbury, Christchurch, New Zealand. Model scale of 1:15 was selected for the spillway chute. Typical velocites were in the range of 5m/s to 11 m/s. The bed slope θ = 51.34° and channel width of 0.25m was used for Clyde dam model study.

The data from the all model studies above are plotted in Fig 6.10 and sub– divided into bands of $\Delta h/h$. Fig 6.10 shows that the above frame work shows a reasonable correlation with other model studies carried out in this area.

6.5 *Analysis and comparison with Prototype aerator measurements*

As a rule, the field of hydraulic research is characterised by a lack of field or prototype measurements. One exception to this rule is the field of ramp/slot aerators which have a reasonable number of spillways, which have been monitored in the prototype case usually for at least the air flow rate in the air ducts Q_a, the water discharge rate along the spillway Q_w, the gate opening or overflow depth at the top of the spillway and the sub atmospheric pressure under the jet Δh. In some cases the depth of flow at the ramp h is also measured. For cases where h has not been measured it can be determined from gradually varied flow analysis along the spillway or alternatively extrapolated from model studies of

the prototype structure at the corresponding water discharge rate. The most suspect of the prototype measurements is usually the air flow which is often measured within the air ducts often using air flow velocity meters which measure a few air flow point velocities which then require to be integrated over the full duct area to obtain the total air flow rate. This process is often carried out in a field of very high air velocities in the duct V_a > (100m/s − 200m/s) and the results require adjustment for temperature and pressure. The value of jet length L is also suspect as it is difficult to measure in a prototype but may be scaled up from model tests or computed from jet trajectory theory. A list of prototype structures and some of their characteristics has been given in Table 6.1 to 6.5.

In this section, aerators of prototype structures will be analysed. These were chosen because access was available to the prototype data either through personal contacts or from literature. The friction factor for prototype structure is calculated by using Colebrook White equation for wide open channel flow.

$$\frac{1}{\sqrt{\lambda}} = -2.0\ \mathrm{Log}_{10}\left[\frac{k_s}{12.3\ R} + \frac{1.51\nu}{R\sqrt{(32gRSin\theta)}}\right] \qquad (6.12)$$

where;

λ = Friction factor

ν = kinematic viscosity of water

R = Hydraulic radius

k_s = Equivalent sand grain roughness size

g = gravitational constant = 9.81

θ = bed slope

Brief details of each prototype structure are given below.

(i) *Foz – do – Areia*

Foz– do– Areia Dam is a 160m high concrete face rockfill dam with an embankment volume of about 14 million cubic meter. Its chute spillway is a 400m long and 70.6m wide. Three aeration steps are provided along the chute to prevent cavitation. The bed slope of the chute spillway is 14.5^0. The jet length L was measured in field and published by Pinto(1982). The details of aerator is given in Table 6.1 below and shown in Fig 1.10.

TABLE 6.1

Foz-do-Areia	Φ	h_r (m)	h_{os} (m)	Air duct Type	$\Delta p/\rho gh$	$\bar{u}$ (m/s)	h_3 (m)
Aerator I	7.12^0	0.2	0.5	Bell mouth	0.1 to 0.3	19 to 30	0.38 to 1.64
Aerator II	7.12^0	0.15	0.5	Bell mouth	0.1 to 0.3	19 to 32	0.39 to 1.48
Aerator III	7.12^0	0.1	0.5	Bell mouth	0.1 to 0.3	19 to 36	0.39 to 1.33

(ii) *McPhee Dam (USA)*

McPhee Dam is the main storage regulation reservoir in the Dolores Project in South West Colorado. The dam is an earthfill structure 82.3 m high and 396m wide crest. The chute spillway is 18.3m wide, 303m long and drops 90m in elevation. The bed slope of the spillway is 16.6^0. The jet length was calculated by Glasgow computer model. The details of aerator is given in Table 6.2 and shown in Fig 1.9.

TABLE 6.2

McPhee Dam Spillway	Φ	h_r (m)	h_{os} (m)	Air duct Type	$\Delta p/\rho gh$	$\bar{u}$ (m/s)	h_3 (m)
Aerator I	6.4°	0.914	0.0	Bell mouth	0.04 to 0.05	15.3 to 22.77	0.10 to 0.35

(iii) *Tarbel Dam (Pakistan)*

Tarbela dam was constructed on Upper Indus river of Pakistan in the period of 1965 – 1975. The dam is earth and rockfill structure 143m high and 2.74 km long. There are two tunnels and 5 outlet structures are for overflow and irrigation purpose. The outlet structures of Tunnel 3 and 4 are provided with aeration grooves. The bed slope of the outlet structures is horizontal. The jet length is calculated by Glasgow computer model. The details of the aerator is given in Table 6.3 and shown in Fig 1.7 and Fig 1.8.

TABLE 6.3

Tarbela Dam Spillway	Φ	h_r (m)	h_{os} (m)	Air duct Type	$\Delta p/\rho gh$	$\bar{u}$ (m/s)	h_3 (m)
Aerator I	7.12°	0.14	0.0	Bell mouth	0.02 to 0.08	28.0 to 47.0	2.44 to 7.35

(iv) *Colbun Dam*

Colbun dam has an open channel spillway of width varying from 50m to 71.1m. Two aeration grooves are provided in the design of spillway for the prevention of cavitation damage. The bed slope of the chute spillway is 27°. The jet length L is also calculated by Glasgow computer model.

TABLE 6.4

Colbun Dam Spillway	Φ	h_r (m)	h_{os} (m)	Air duct Type	$\Delta p/\rho gh$	$\bar{u}$ (m/s)	h_3 (m)
Aerator I	11.3°	0.39	0.25	Rectangular shape	0.1 to 0.4	15 to 25	0.3 to 2.2
Aerator II	11.3°	0.39	0.25	Rectangular shape	0.075 to 0.3	20 to 30	0.27 to 0.83

(v) *Emborcacao Dam*

Emborcacao dam has a chute spillway of total width of 58.5m being split into two by a central wall. The chute spillway has a bed slope of 10.2°. The jet length L was also calculated by Glasgow computer model. Detail of both aerators are given in Table 6.5 and shown in Fig 1.11.

TABLE 6.5

Emborcacao Spillway	Φ	h_r (m)	h_{os} (m)	Air duct Type	$\Delta p/\rho gh$	$\bar{u}$ (m/s)	h_3 (m)
Aerator I	7.12°	0.30	0.20	Bell mouth	0.02 to 0.22	17 to 30	0.44 to 1.66
Aerator II	7.12°	0.30	0.20	Bell mouth	0.02 to 0.25	17 to 33	0.44 to 1.48

It is important at this stage to compare the prototype data with the frame work developed in Chapter 6 for the result of this work. This frame work uses the shear velocity u_* rather than the mean velocity $\bar{u}$, and incorporates the minimum conditions to entrain air $w' = 0.3$ m/s or $u_* = 0.18$ m/s.

The result of the new frame work applied to prototype data is given in Figs 6.11 to 6.14, where $q_a / (u_* - 0.18)h$ is plotted against L/h and for each band of $\Delta h/h$ values (i.e $\Delta h/h = 0.0$, $0.0-0.2$, $0.2-0.4$ and 0.4 & above). Again $q_a / (u_* - 0.18)h_3$ is plotted in Fig 6.15 against L/h for all values of $\Delta h/h$ together with Glasgow model data. Figs 6.11 to 6.14 show in a clear way

(i) Good correlation between model and prototype data.

(ii) Confirm the validity of the chosen frame work for air entrainment.

(iii) Show the effect of L/h and underpressure $\Delta h/h$.

Having done this we may now proceed to our final correlation of air entrainment at aerators.

6.6 *FINAL CORRELATION FOR AERATION AT RAMPS*

A frame work for aeration uptake at a ramp aerator was proposed in section 6.3 and proved a reasonable correlation for the results of this work. Results of other model studies from around the world were investigated in section (6.4) and finally, comparison with prototype field data was carried out in section (6.5). The frame work for aeration is different from any previously proposed for the following reasons.

(i) It incorporates with the non−linear effect of jet length L/h.

(ii) It is based on knowledge of turbulence generation and decay.

(iii) It incorporates a scale effect term which appears to give reasonable correlation between model and prototype.

(iv) It also contains the influence of cavity underpressure $\Delta h/h$.

The starting position is Equation (5.35)

$$q_a = C_1 (w'_3 - 0.3) L \qquad (6.13)$$

where C_1 is a function of L/h as shown in Fig 5.17

Substituting for turbulent velocity

$$w'_3 \simeq 1.75\, u_*$$

we obtain

$$q_a = 1.75\, C_1 (u_* - 0.18) L \qquad (6.14)$$

$$q_a = C_2 \ (u_* - 0.18) \ L \qquad (6.15)$$

This relationship is valid for $\triangle h/h = 0.0$, only.

The value of C_2 for model and prototype data are shown in Fig (6.16) and show that when $L/h < 10$, then C_2 is constant around 1.8. For L/h values > 10, the value of C_2 is given approximately by the curve $C_2 = 9 \ (L/h)^{-0.7}$ as shown in Fig (6.16) and Table 6.6 below.

At this stage the picture can be completed by incorporating the effect of cavity underpressure by a new parameter, namely C_3 where,

$$q_a = C_2 \ C_3 \ (u_* - 0.18) \ L \qquad (6.16)$$

where $C_3 = f \ (\triangle h/h)$ and can be determined from

$$C_3 = \frac{q_a}{C_2 \ (u_* - 0.18) \ L} \qquad (6.17)$$

A plot of C_3 against $\triangle h/h$ is shown in Fig 6.17 for all Glasgow model studies and is shown in Fig 6.18 for all the known prototype data.

These are combined in one graph in Fig 6.19 showing that C_3 can be given approximately by,

$$C_3 \simeq e^{-4.81 \ (\triangle h/h)^{1.575}} \qquad (6.18)$$

This was determined by regression analysis, in which linear correlation coefficient $r = 0.9$.

TABLE 6.6

L/h values	$f_1(L/h)$ C_2	$f_2(\Delta h/h)$ C_3
0 → 10	1.8	$e^{-4.81\,(\Delta h/h)^{1.575}}$
11 → ∞	$9\,(L/h)^{-0.7}$	$e^{-4.81\,(\Delta h/h)^{1.575}}$

Equation (6.16) is the final correlation of this thesis. It is valid for any value of jet length ratio (L/h) and any value of underpressure $\Delta h/h$ for both model and prototype structures, for any scale of model and prototype.

Proof of this is given in Fig 6.20 for all known prototype data world wide, showing an extremely good correlation between measured and computed air flows.

This correlation means that the air uptake computed from $q_a = C_2\ C_3\ (u_* - 0.18)\ L$ is accurate to ± 10% and is suitable for use in computer programs such as that in Chapter 7. This equation is now being considered for inclusion in the computer programs of air slots at ETH Zurich, Switzerland.

6.7 *A new approach to aeration scale effects.*

An attampt is made in this section to produce a new method for quantifying the likely scale effects for air entrainment in ramp aerators and

chutes,. The idea is based on the ability to predict the turbulent energy or velocity spectrum for a prototype flow situation and for model situations at various scales. Procedures for estimationg more accurate turbulent spectrum are outlined in Hinze (1949) and Davies (1972) but the method used below is very rough approximation sufficient to give a first order approximation into likely scale effects.

A turbulent energy spectrum is schematised below showing the distribution of turbulent energy over a range of eddy lengths ranging from the full depth of the flow h to the Kolmogoroff micro scale, denoted by ℓ_k.

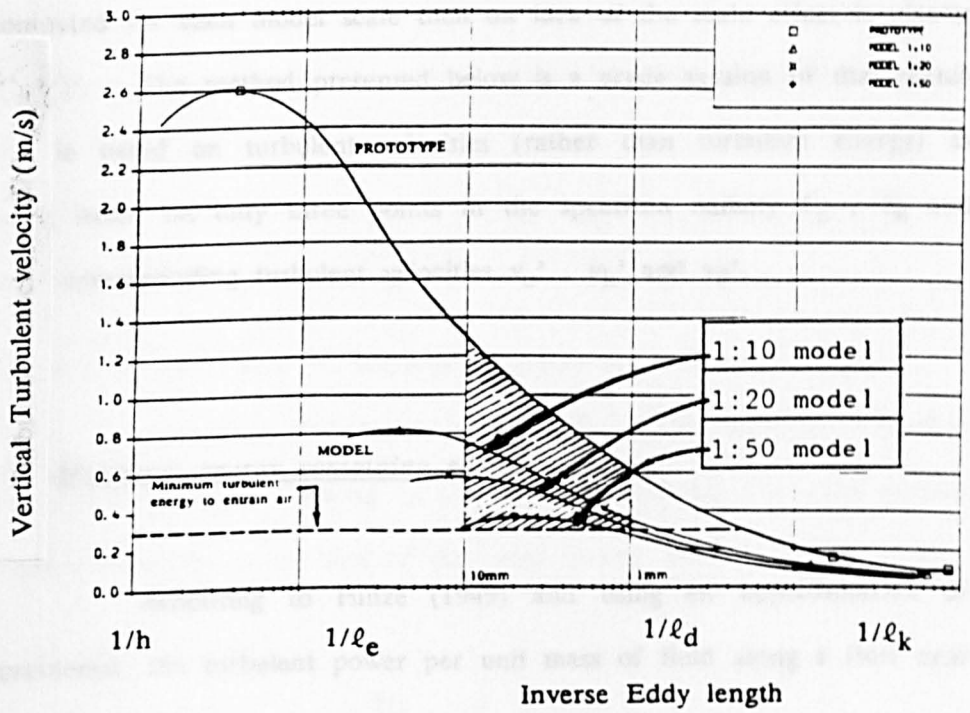

In the sketch above

h = flow depth and maximum eddy size

ℓ = Prandtl eddy length in $\tau = \rho \ell^2 (du/dy)^2$

ℓ_e = eddy length containing the maximum energy

ℓ_d = eddy length giving the maximum energy dissipation

ℓ_k = Kolmogoroff micro scale eddy length

Superimposed on the spectrum above is the range of eddy lengths where the air entrainment process occurs. This is given in the range 1mm to 10mm, simply because most entrained bubbles lie within that range.

Superimposed also is a horizontal line showing the minimum turbulent energy required to entrain an air bubble across the jet free surface in an aerator. This is equivalent to the minimum turbulent velocity (w' = 0.3m/s) required to entrain air.

Thus, the shaded area represents the turbulent energy available to entrain air bubbles into the flow across the jet free surface. In prototype this area is large and in models it may be small or zero. If this shaded area can be computed for each model scale then on idea of the scale effect is obtained.

The method presented below is a crude version of that sketched above and is based on turbulent velocities (rather than turbulent energy) as well as being based on only three points in the spectrum namely ℓ_e , ℓ_k and ℓ_d with their corresponding turbulent velocities v_e' , v_k' and v_d'.

(i) *Maximum energy containing eddies*

According to Hinze (1949) and using an approximation of isotropic turbulence, the turbulent power per unit mass of fluid along a flow near the base is given by

$$\text{Power / Unit mass} = (v_e')^3 / \ell_e \qquad (6.19)$$

Also Power = velocity x force

and hence considering a spillway flow of unit width and length dx

$$\text{Power} = \bar{u}\ \tau_0 \times 1 \times dx \tag{6.20}$$

or power per unit mass when the flow depth is h becames,

$$\text{Power / Unit mass} = \bar{u}\ \tau_0 / (\rho h) \tag{6.21}$$

and from D'arcy Wesibach $\tau_0 = \rho\ \bar{u}^2\ \lambda/8$, then

$$\text{Power / Unit mass} = (\bar{u})^3\ (\lambda/8h) = (v_e')^3 / \ell_e \tag{6.22}$$

This gives an estimate of the energy containing eddy length to be

$$\ell_e = \frac{8h}{\lambda} \left[\frac{v_e'}{\bar{u}} \right]^3 \tag{6.23}$$

where λ is the D'arcy – Weishbach friction factor for the flow.

According to Davies (1972), the RMS turbulent velocities can be substituted for v_e' , showing as an approximation that the eddy length containing maximum energy at the end of the ramp in this work can be given by

$$\ell_e \simeq \frac{8h}{\lambda} \left[\frac{w_3'}{\bar{u}} \right]^3 \tag{6.24}$$

where the actual value of w_3' has been measured (Chapter 4) and can be approximated to 1.75 u_*.

(ii) *Kolmogoroff micro scale*

The next point on the spectrum may be found by applying the standard definition of the Kolmogoroff micro scale namely,

$$v_k' \quad \ell_k \; / \; \nu \qquad = \; 1 \tag{6.25}$$

where ν is the kinematic eddy viscosity of the fluid. Davies (1972) combines this with the equal power per unit mass concept

$$(\; v_e' \;)^3 \; / \; \ell_e \qquad \simeq \qquad (\; v_k' \;)^3 \; / \; \ell_k \tag{6.26}$$

combining both equations

$$(\; v_e' \;)^3 \; / \; \ell_e \qquad = \qquad v_e' \; [\; \nu \; / \; v_k' \ell_e \;]^{1/3} \tag{6.27}$$

or from Equation (6.22),

$$v_k' \qquad = \; \bar{u} \left[\frac{\lambda}{8} \right]^{1/4} \left[\frac{1}{Re} \right]^{1/4} \tag{6.28}$$

where Re is defined as $\bar{u}\, h \; / \; \nu$.

Equation (6.28) gives an estimate for v_k' and the corresponding eddy length can be obtained from Equation (6.24).

In this research work as an example $\bar{u} = 7$m/s, $\lambda = 0.018$, $\nu = 1.1 \times 10^{-6}$ and $h = 50$mm, then $v_k' / \bar{u} \simeq 0.009$. In other words the turbulent intensity at the micro scale is around 10% of the turbulent intensity RMS measured, $w'/u \simeq 0.08 \rightarrow 0.1$.

Further more, this means that the turbulent energy per unit mass,

which is proportional to the turbulent velocity squared, $E \propto (v')^2$, is only one hundredth of the RMS value, at the micro scale.

(iii) *Eddy length for maximum energy dissipation*

This represent the third point on the turbulent velocity spectrum and has been approximated by Davies (1972) to

$$\ell_d \simeq 5\ \ell_k \tag{6.29}$$

and

$$v_d' \simeq 1.7\ v_k' \tag{6.30}$$

for the ideal case of isotropic turbulence.

(iv) *Application to experimental results and hypothetical example*

At this point it is possible to apply these ideas to a hypothetical prototype structure and various scale models of that structure.

The starting point is to assume that typical experimental data in this work represents a Froude model to scale 1:20 for example. This value is chosen because a typical velocity in this work is 7m/s and a typical depth of flow 50mm. Scaling up by Froude scaling to a prototype gives a prototype velocity of $7\sqrt{20} = 31.3$ m/s and depth $0.05\ (20) = 1$m, which is almost identical to some of prototype range of various structures discussed in section 6.5.

Thus, it is possible to used Equation (6.23), (6.25), (6.28), (6.29) and

(6.30) to obtain the turbulent velocity and eddy length for each of the three points along the spectrum. This will be done for a prototype, 1:10, 1:20 and 1:50 scale models.

The result is tabulated below for the case $v_e' = w_3' = 1.754$ and friction factor $\lambda = 0.018$ throughout. The hypothetical spectra are plotted for all four cases in Fig 6.21 where it appears that smaller scale models will entrain less air, or possibly no air entrainment if turbulence level fall below a certain value in the required range of eddy length.

	v_e'	$1/\ell_e$	v_d'	$1/\ell_d$	v_k'	$1/\ell_k$
Prototype	2.6	3.94	0.158	16960	0.093	84800
1:10 model	0.82	39.4	0.12	12727	0.07	63636
1:20 model	0.58	78.8	0.109	11636	0.064	58181
1:50 model	0.37	197	0.097	10360	0.057	51800

From Fig 6.21 it is proposed that the amount of air entrained is a function of the area above w' = 0.3m/s, and below the curve and bounded by ℓ = 1mm to 10mm or $1/\ell = 10^2$ to 10^3. As an approximation we may assume that because the width is constant (10^2 to 10^3) then the turbulence energy available is proportional to the distance from the curve to w' = 0.3m/s. i.e . the distance (w' − 0.3). The value of w' however relates not to w_3' (the RMS value), but rather the value of w' in the eddy length range 1mm to 10mm.

As a characteristic value of this range of eddy lengths it is proposed to use the air/water surface tension capillary length $\sqrt{\sigma/\rho g}$ which is 2.7mm (0.0027m) and deemed by Sene (1984) to be the median air bubble diameter.

Applying to the power law relationship

$$(v_e')^3 / \ell_e = (w_a')^3 / \ell_a \qquad (6.31)$$

Where ℓ_a is the air bubble eddy length (2.7mm) and v_a' the corresponding turbulent velocity at that eddy length. We may obtain the corresponding values of w_a' and use these as the real turbulent velocity in the air bubble eddy length range, rather than the $v_e' = w_3'$ value which relates to the maximum energy region in the spectrum.

The scale effect at 2.7mm eddy length may now be determined in the form $(w_a' - 0.3)/\bar{u}$. This is derived from the frame work for air flow, namely

$$\frac{q_a}{(w_3' - 0.3)h} = f_2\left[\frac{L}{h}\right] f_3\left[\frac{\Delta h}{h}\right] \qquad (6.32)$$

giving

$$\frac{q_a}{q_w} = \frac{q_a}{\bar{u}\,h} = \beta = \left[\frac{(w_3' - 0.3)}{\bar{u}}\right] f_2\left[\frac{L}{h}\right] f_3\left[\frac{\Delta h}{h}\right] \qquad (6.33)$$

Showing that the scale effect term is $(w_3' - 0.3) / \bar{u}$. (This is based on the assumption that 0.3m/s applies at all eddy length).

The scale effect for air entrainment for all four scales is plotted in Fig 6.22(a) for the cases of one eddy length 2.7mm the median bubble diameter. This predicts zero change in scale effect for air entrainment for velocities above 10m/s in this hypothetical scenario. The corresponds to a Reynolds Number $(\bar{u}\ h)/\nu > 10^6$ in this particular case.

Alternatively, if we use the RMS turbulent velocity v_e' (= w_3'), then the scale effect graph is as shown in Fig 6.22(b), revealing that some scale effects for air entrainment exist even at mean flow velocities of the order of 10m/s.

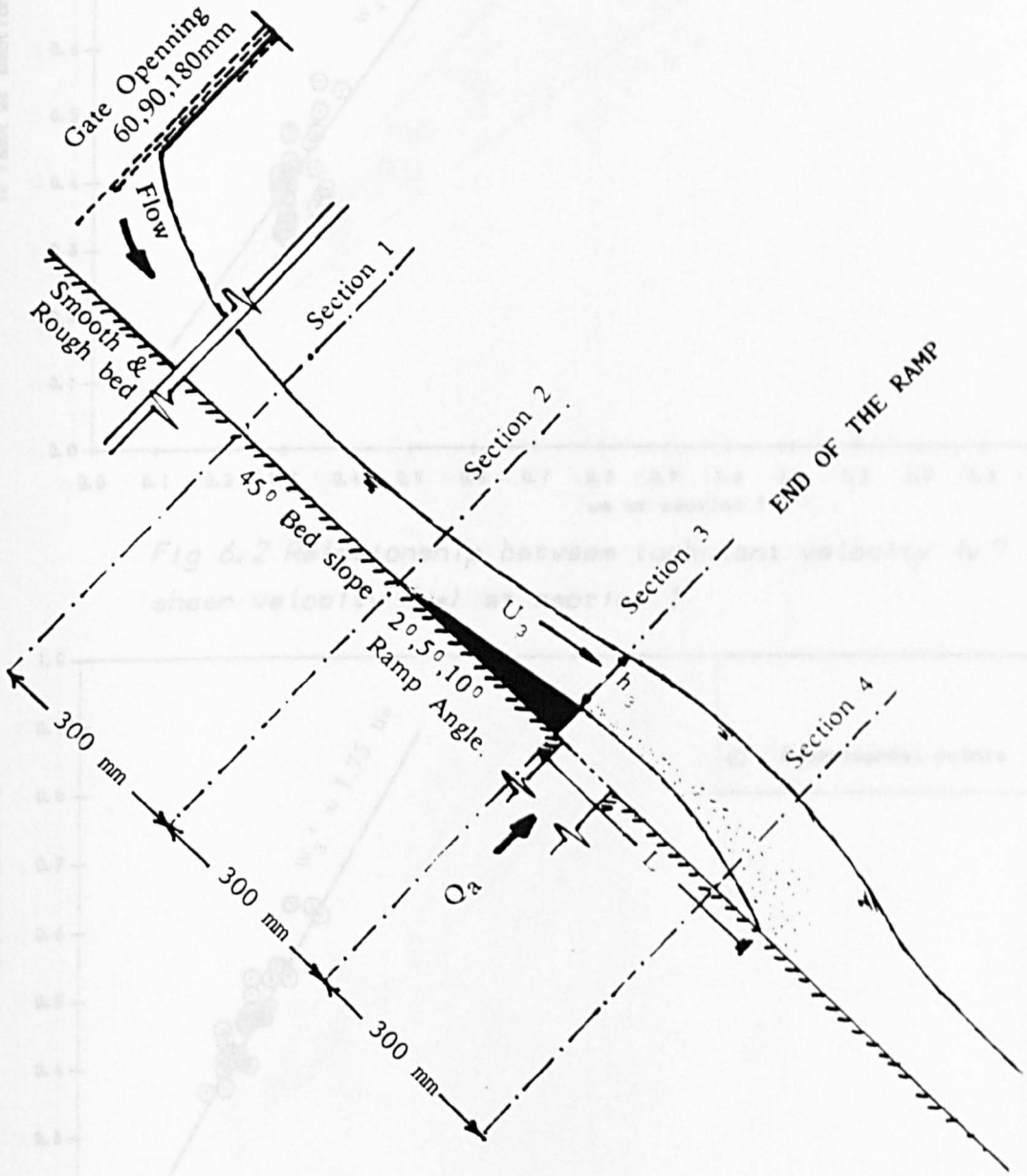

Fig 6.1 Sketch showing location of turbulence measurements

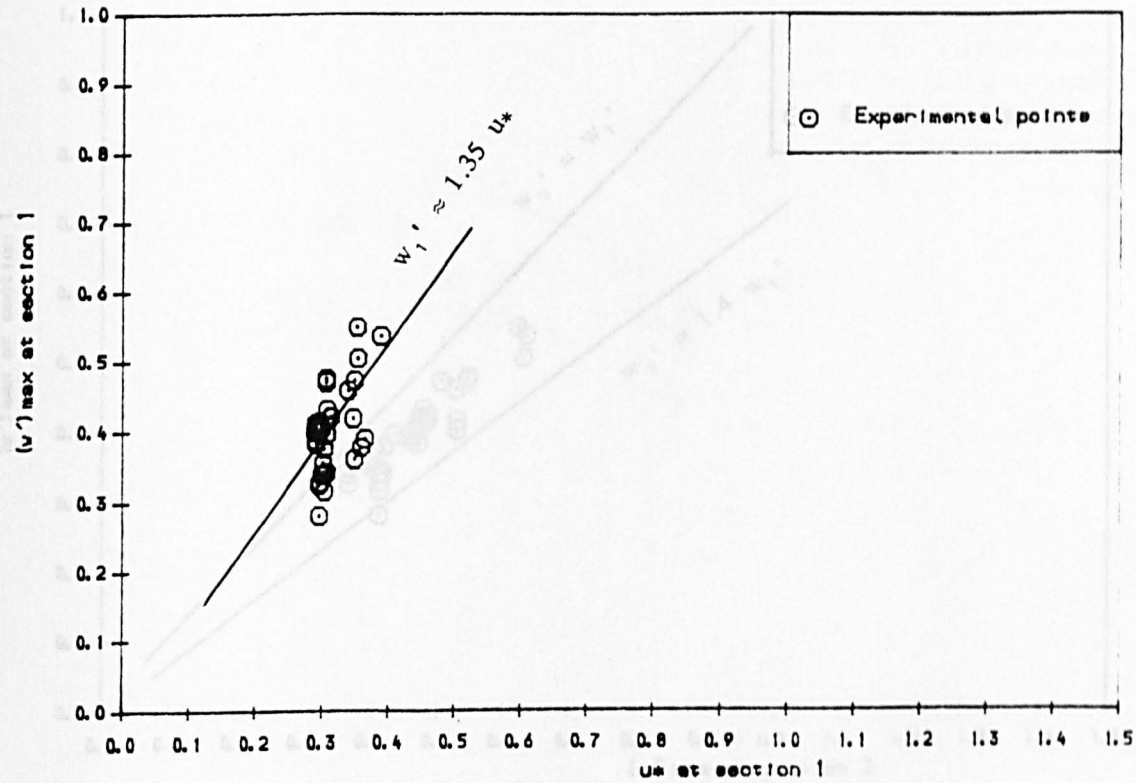

Fig 6.2 Relationship between turbulent velocity (w') and shear velocity (u) at section 1*

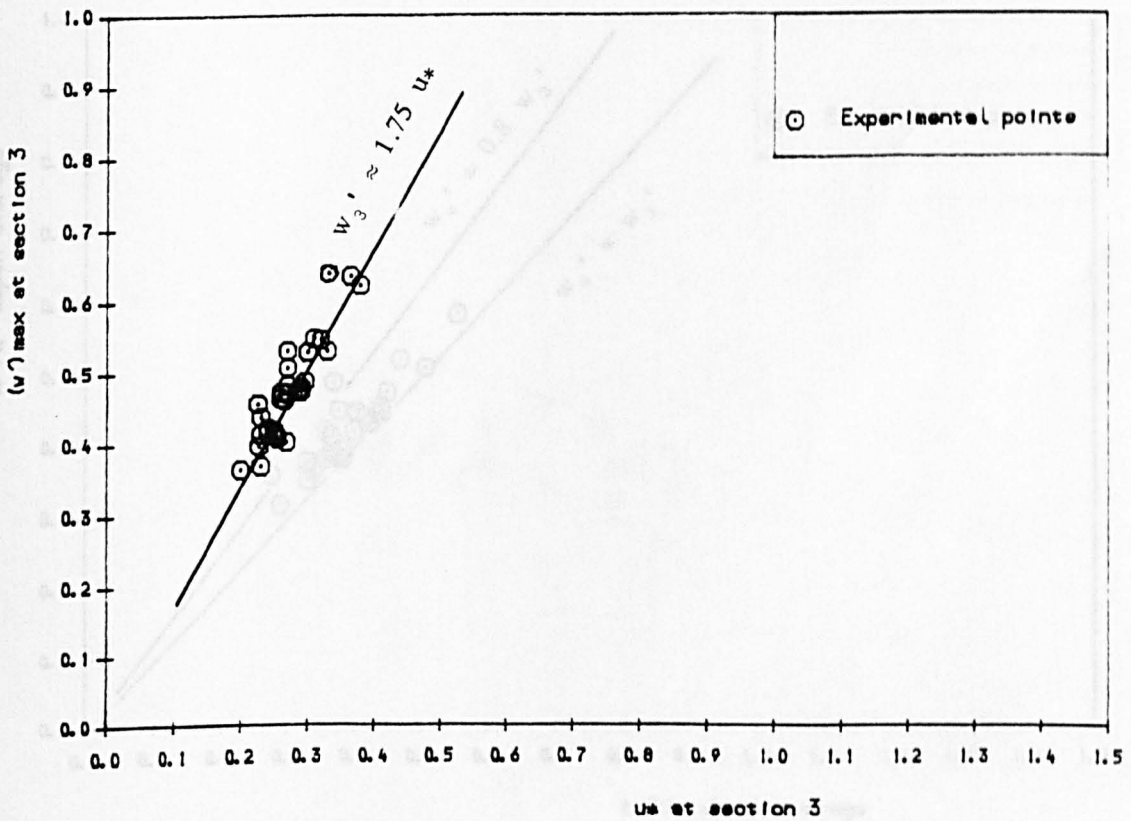

Fig 6.3 Relationship between turbulent velocity (w') and shear velocity (u) at section 3*

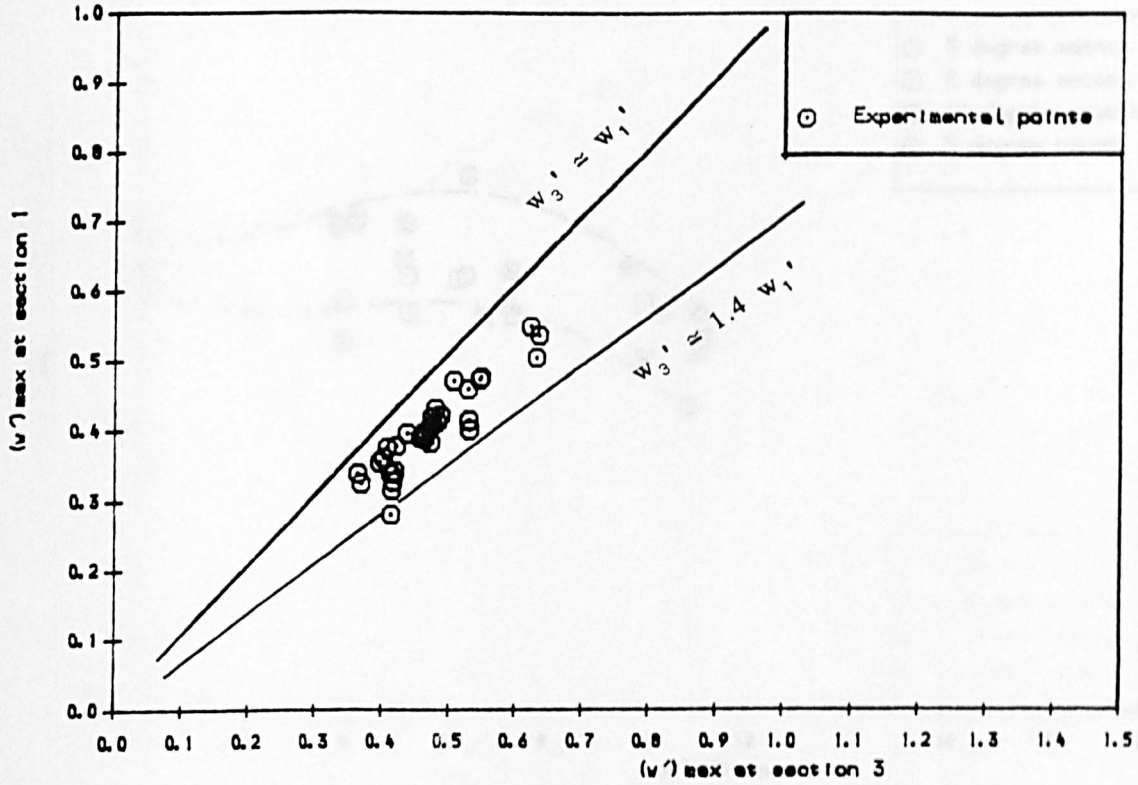

Fig 6.4 Variation of turbulent velocity (w')
from section 1 to section 3

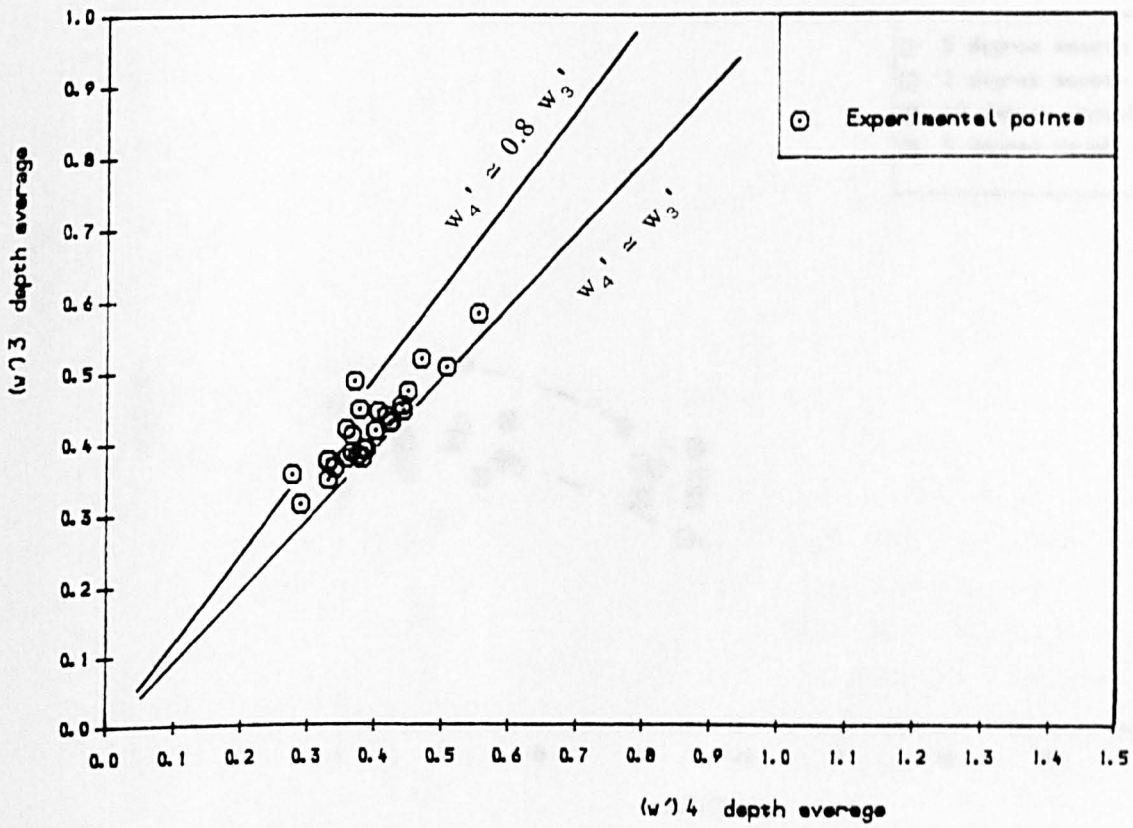

Fig 6.5 Variation of turbulent velocity (w')
from section 3 to section 4

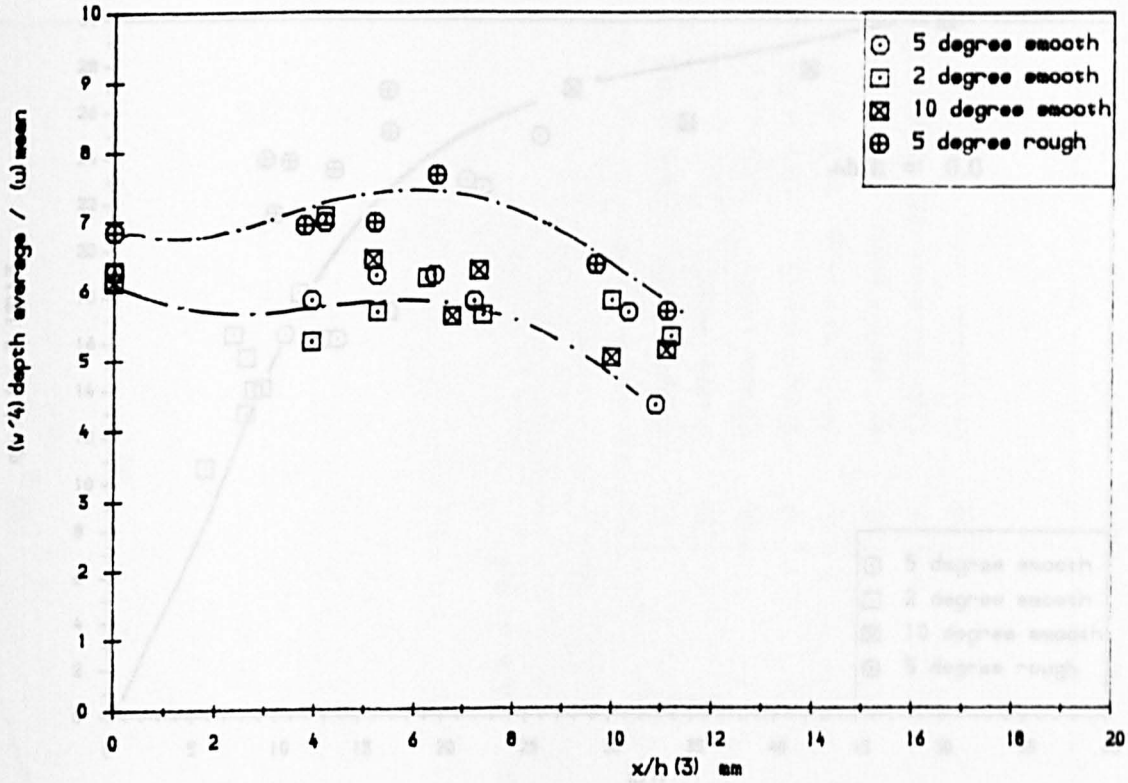

Fig 6.6 Variation of turbulent intensity (w')4/(u) mean along the jet length (depth average)

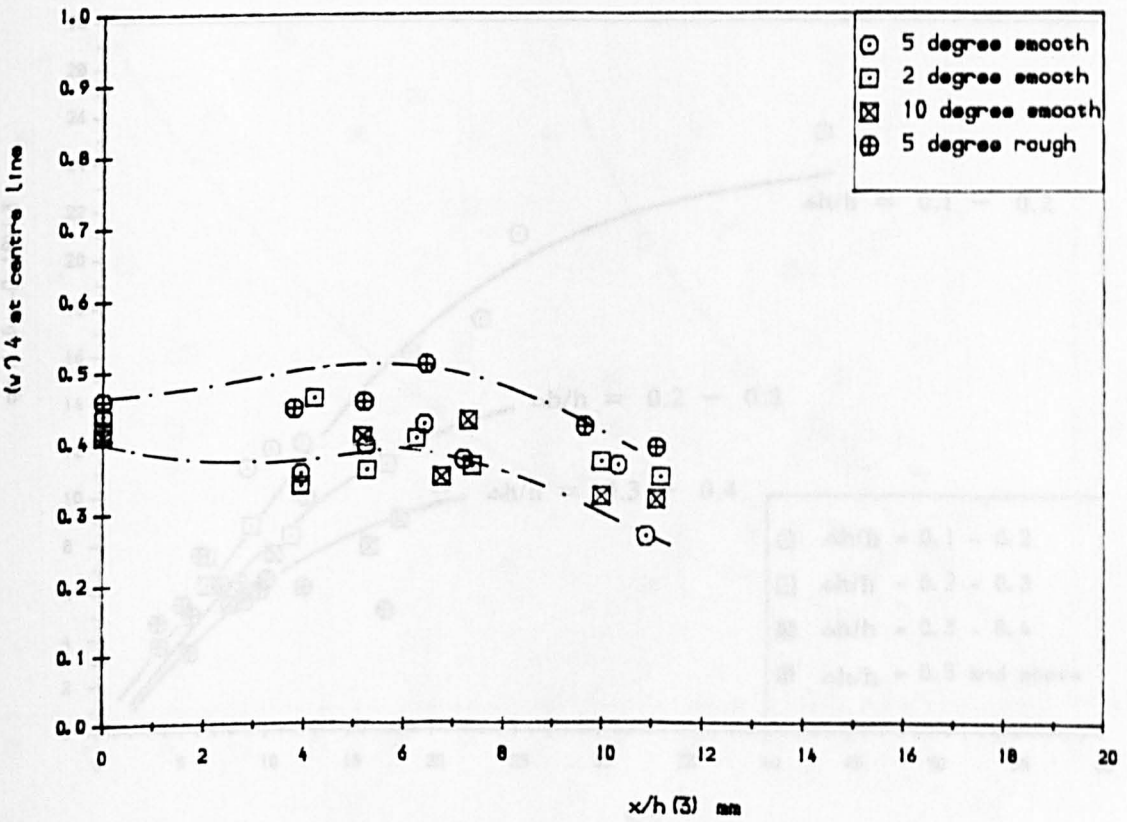

Fig 6.7 Variation of turbulent velocity (w')4 at centre line along the jet length

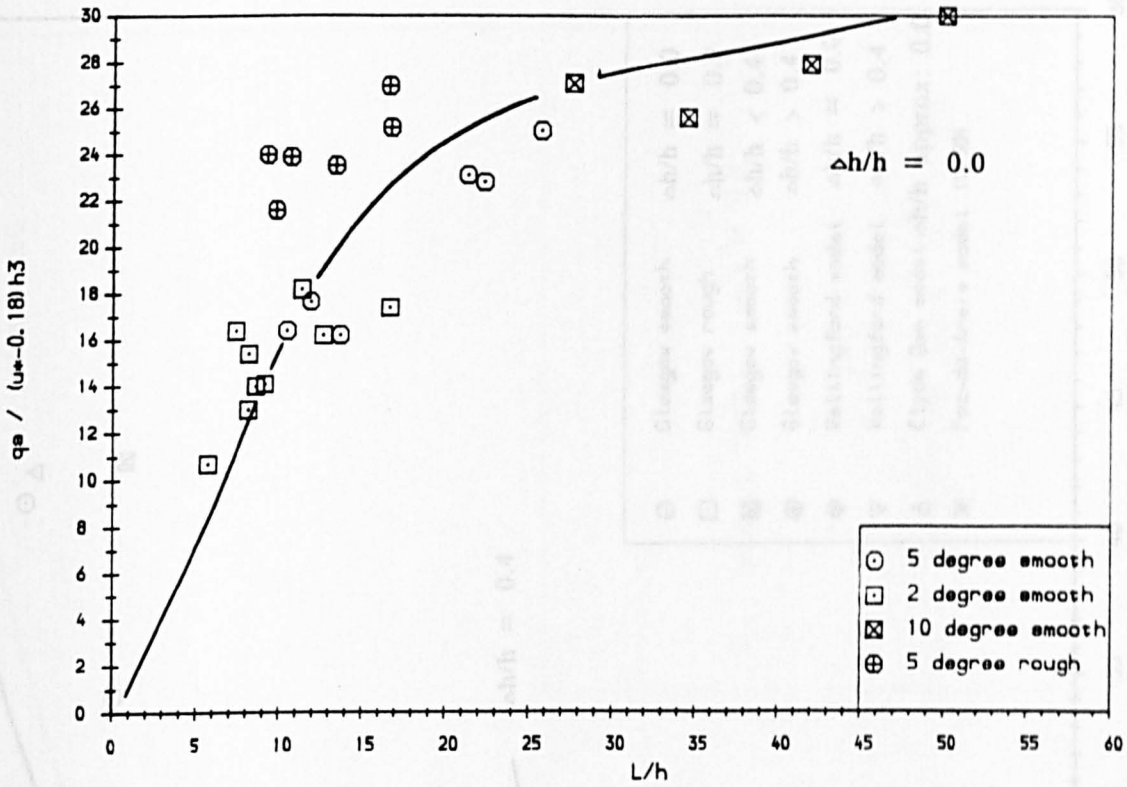

Fig 6.8 Variation of air entrainment with jet length at Δh/h = 0.0

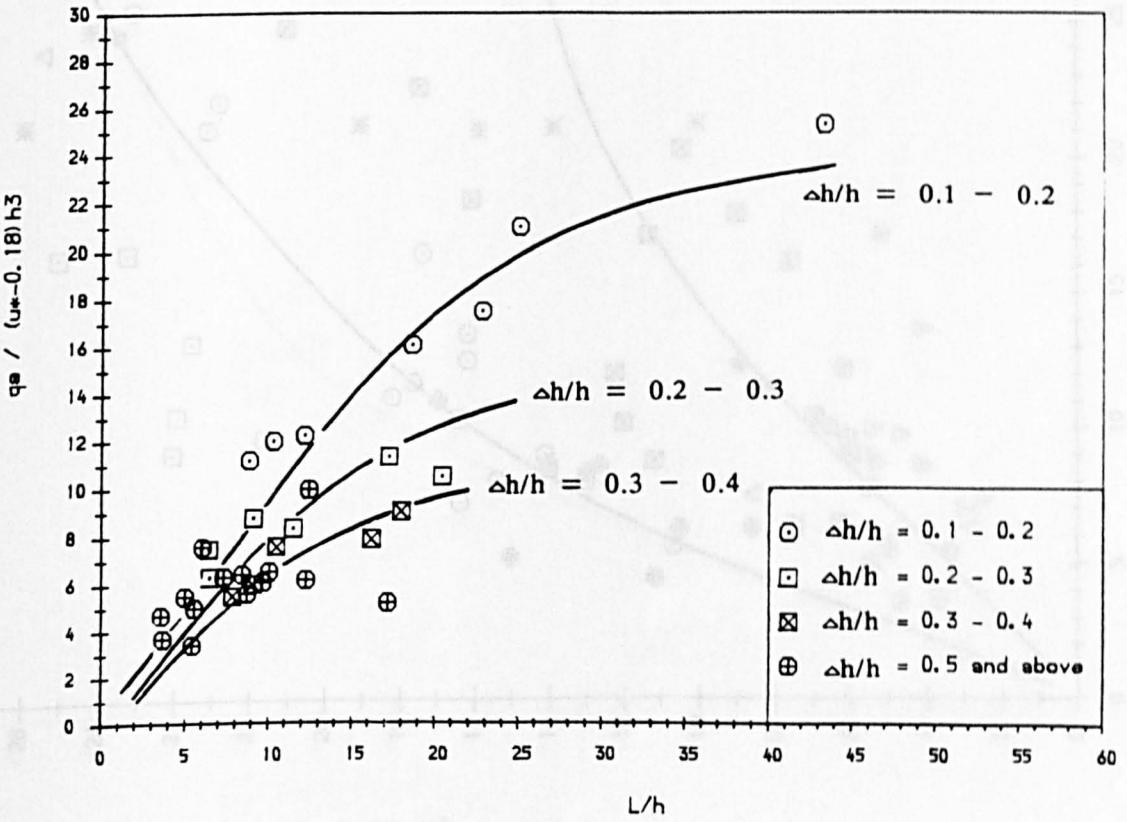

Fig 6.9 Variation of air entrainment with jet length at Δh/h > 0.0

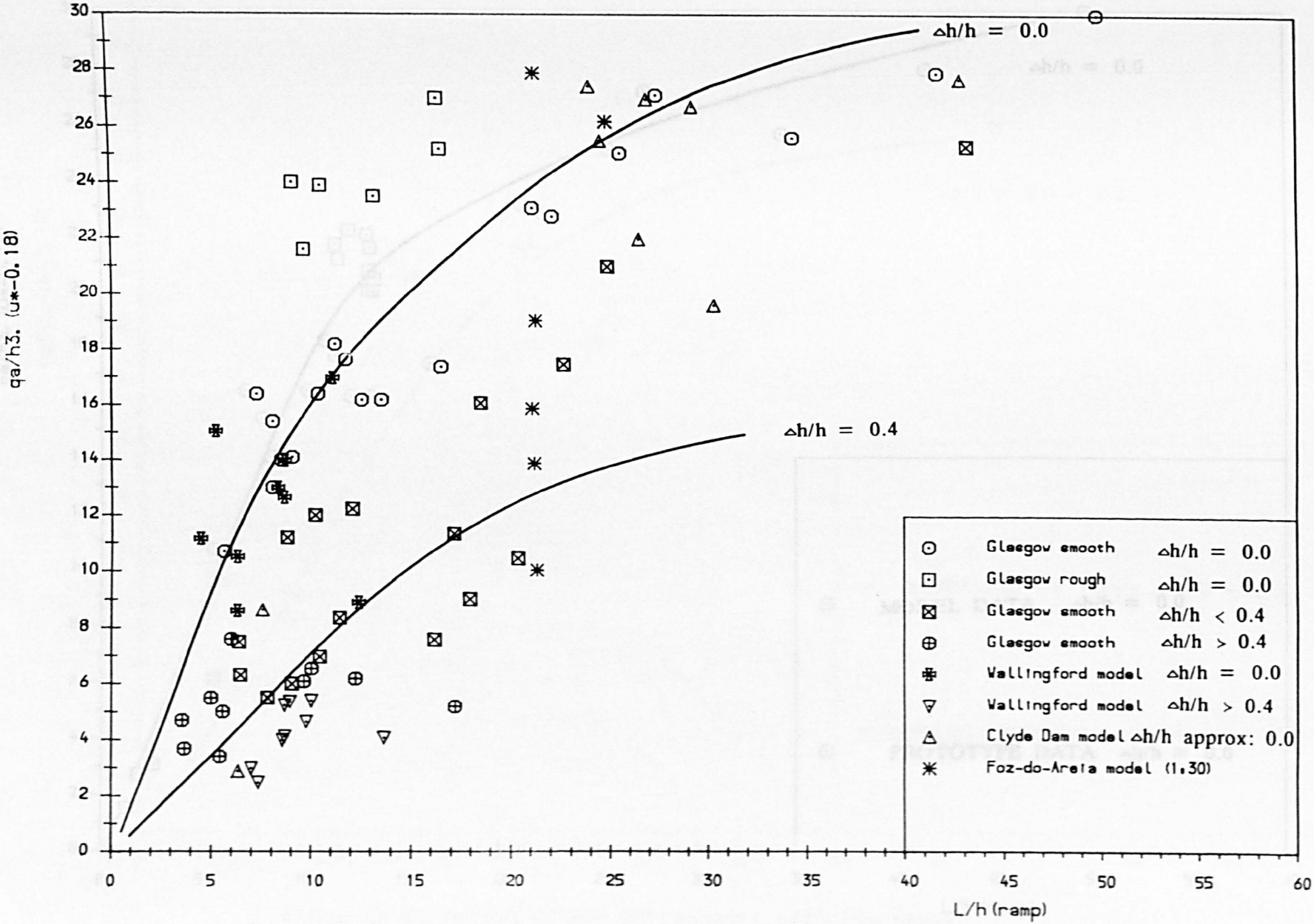

Fig 6.10 Variation of air entrainment with jet length in model studies

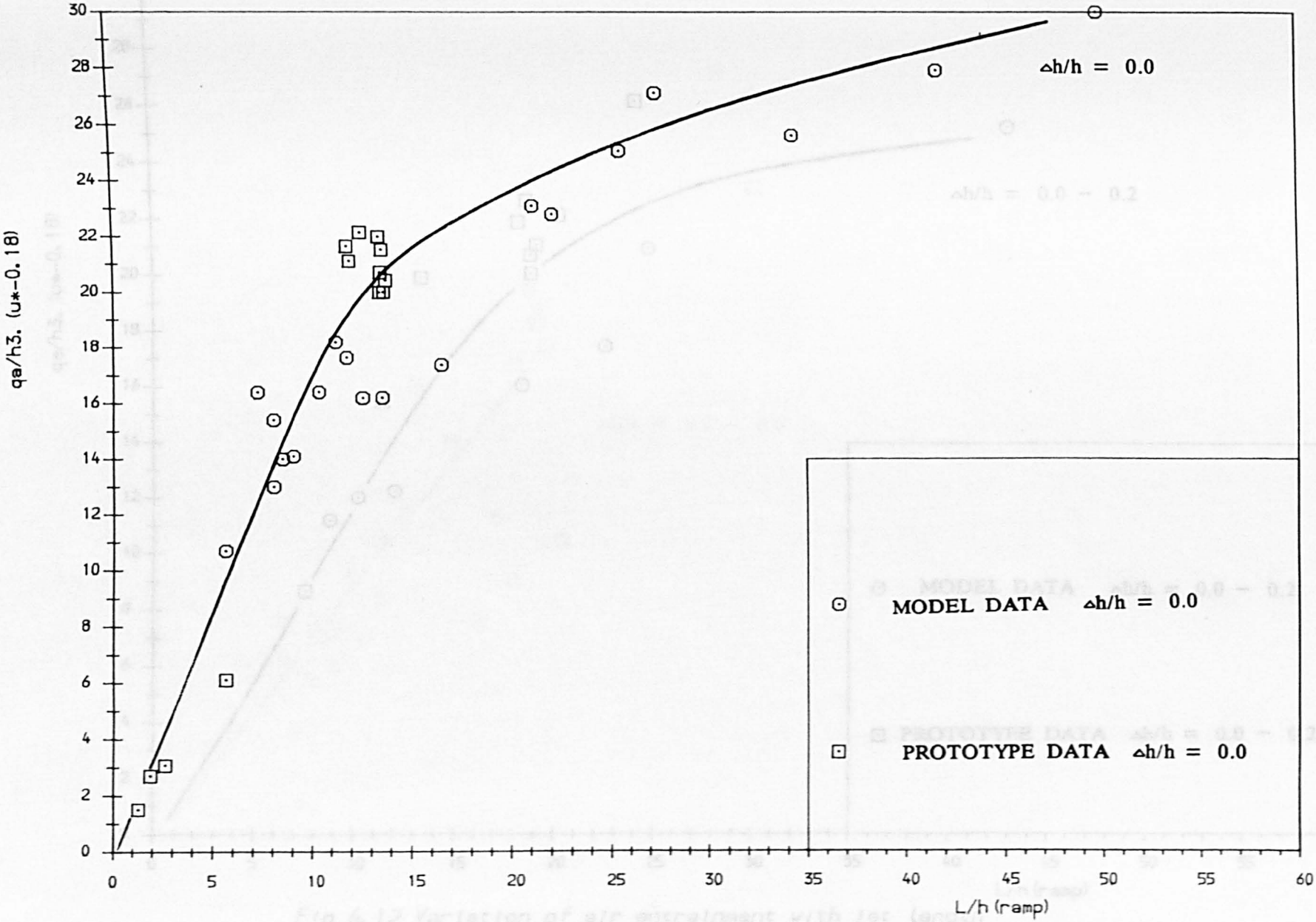

Fig 6.11 Variation of air entrainment with jet length in Model studies and Prototype structures

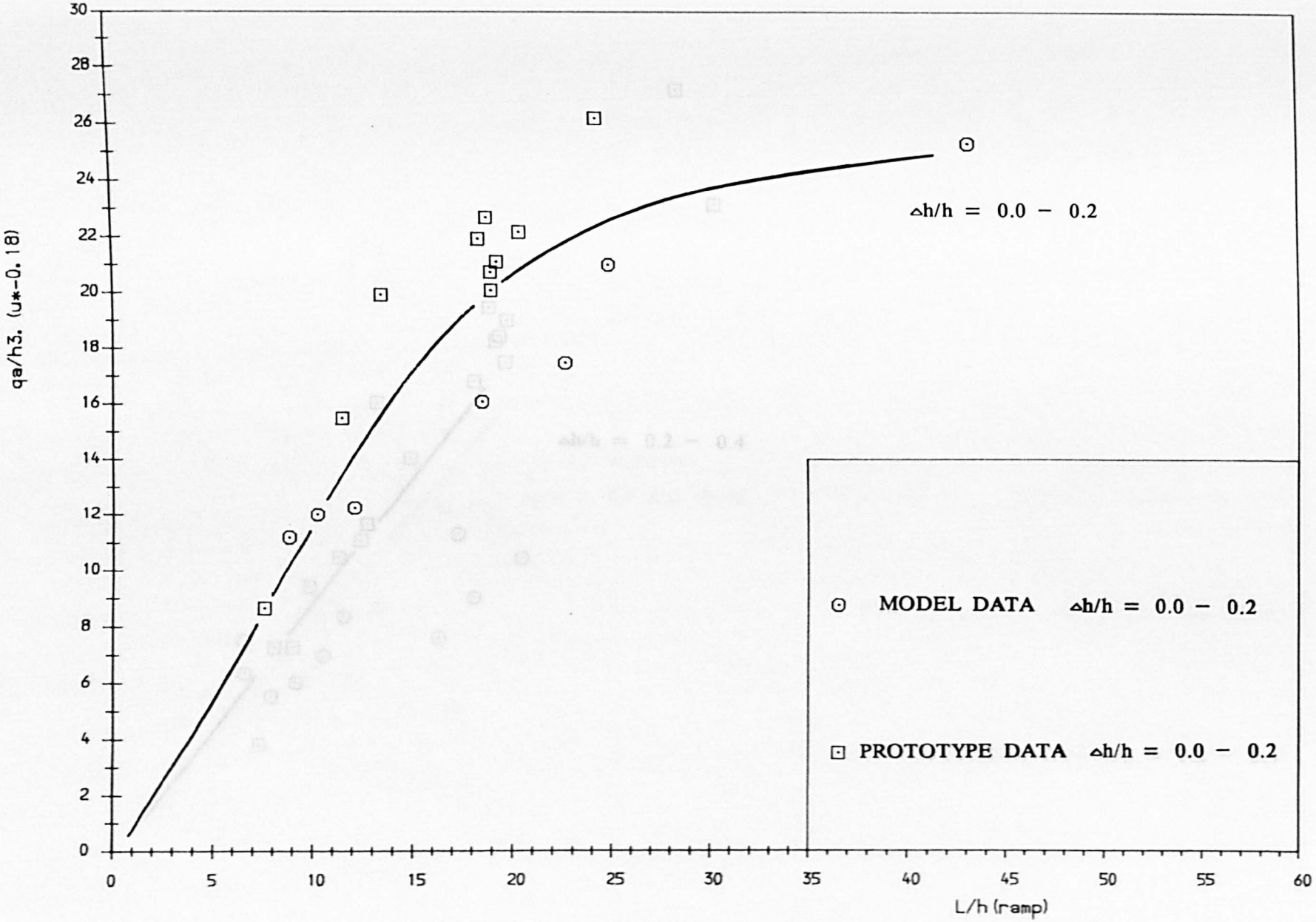

Fig 6.12 Variation of air entrainment with jet length in Model studies and Prototype structures

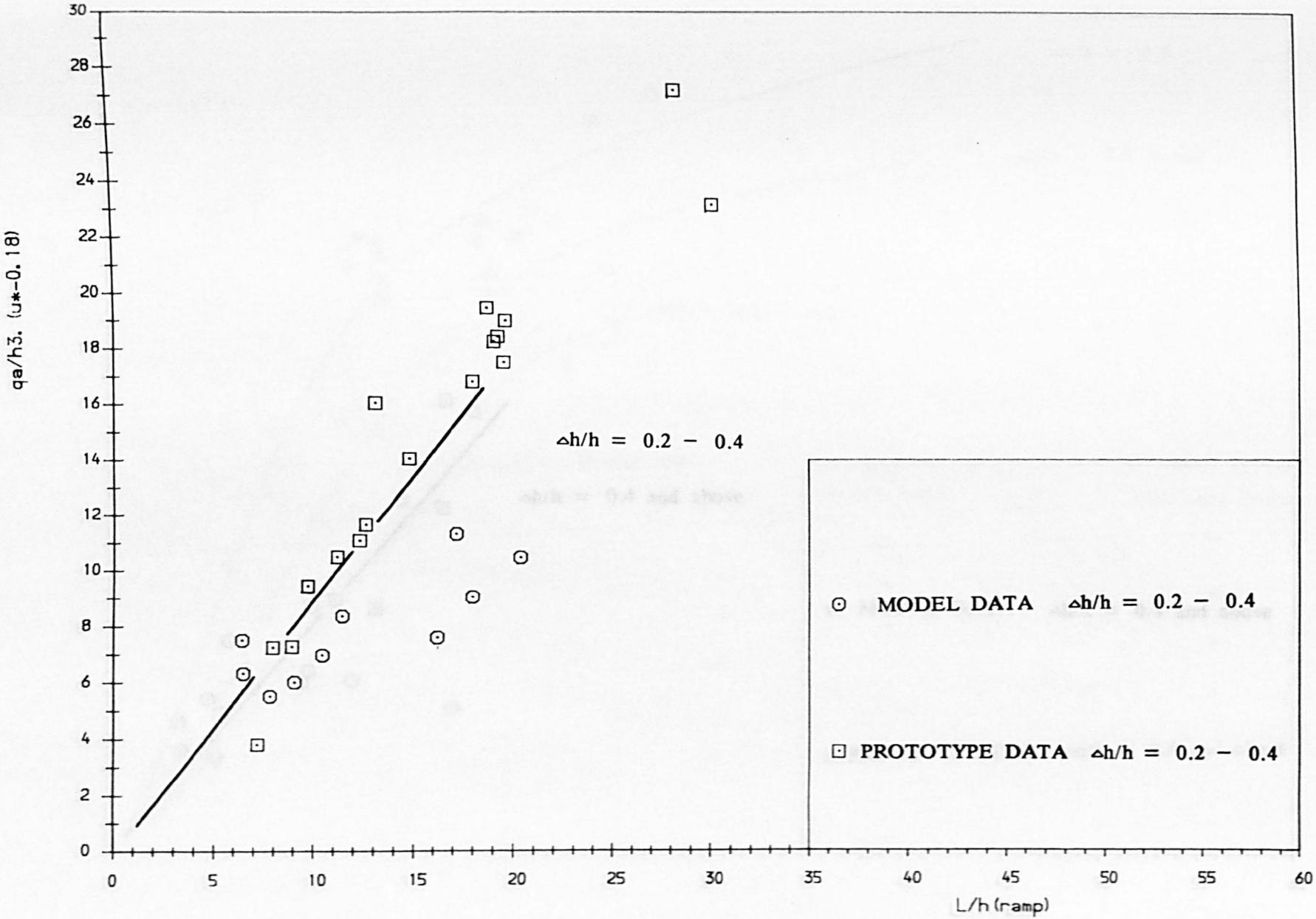

Fig 6.13 Variation of air entrainment with jet length in Model studies and Prototype structures

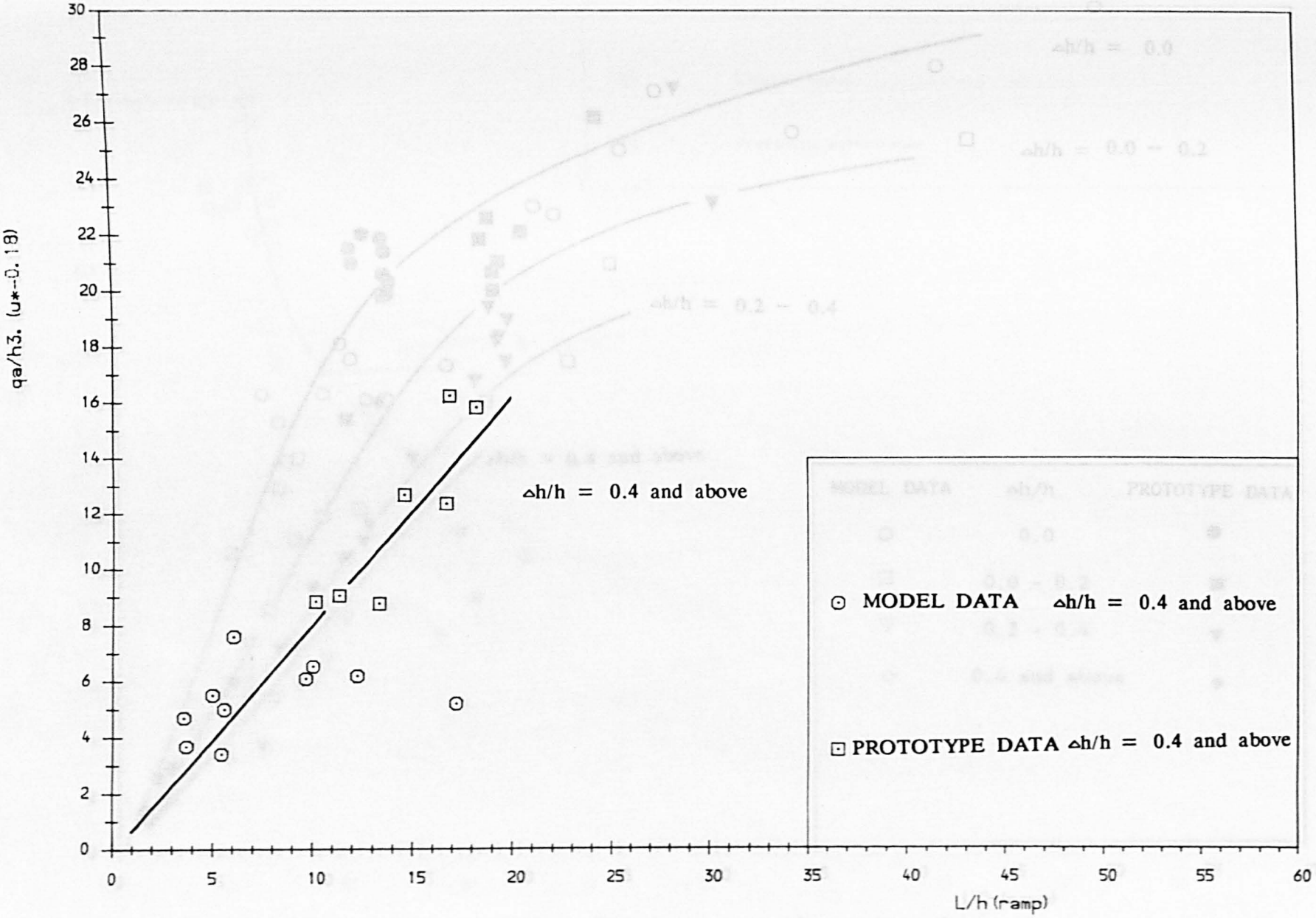

Fig 6.14 Variation of air entrainment with jet length in Model studies and Prototype structures

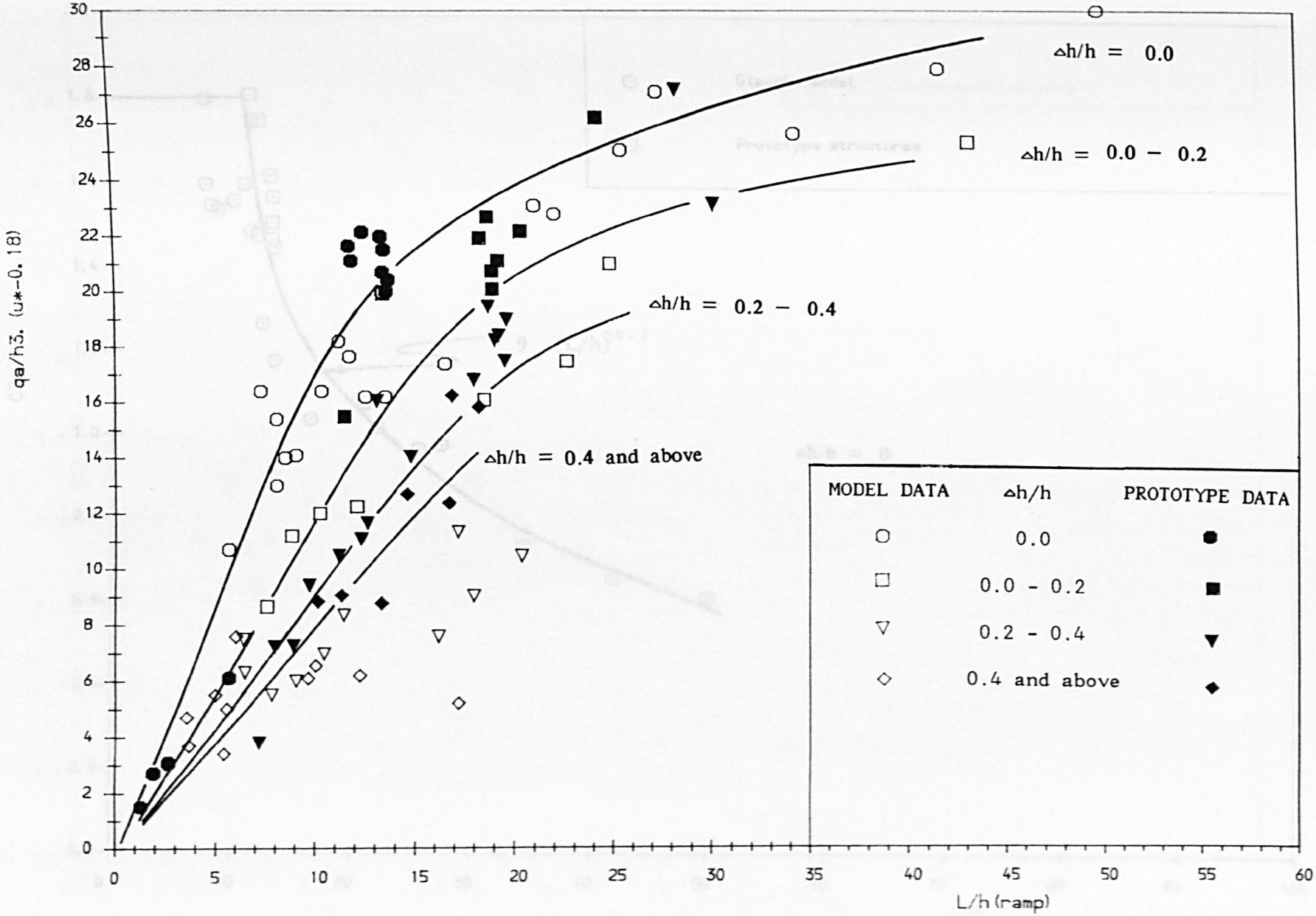

Fig 6.15 Variation of air entrainment with jet length in Model studies and Prototype structures

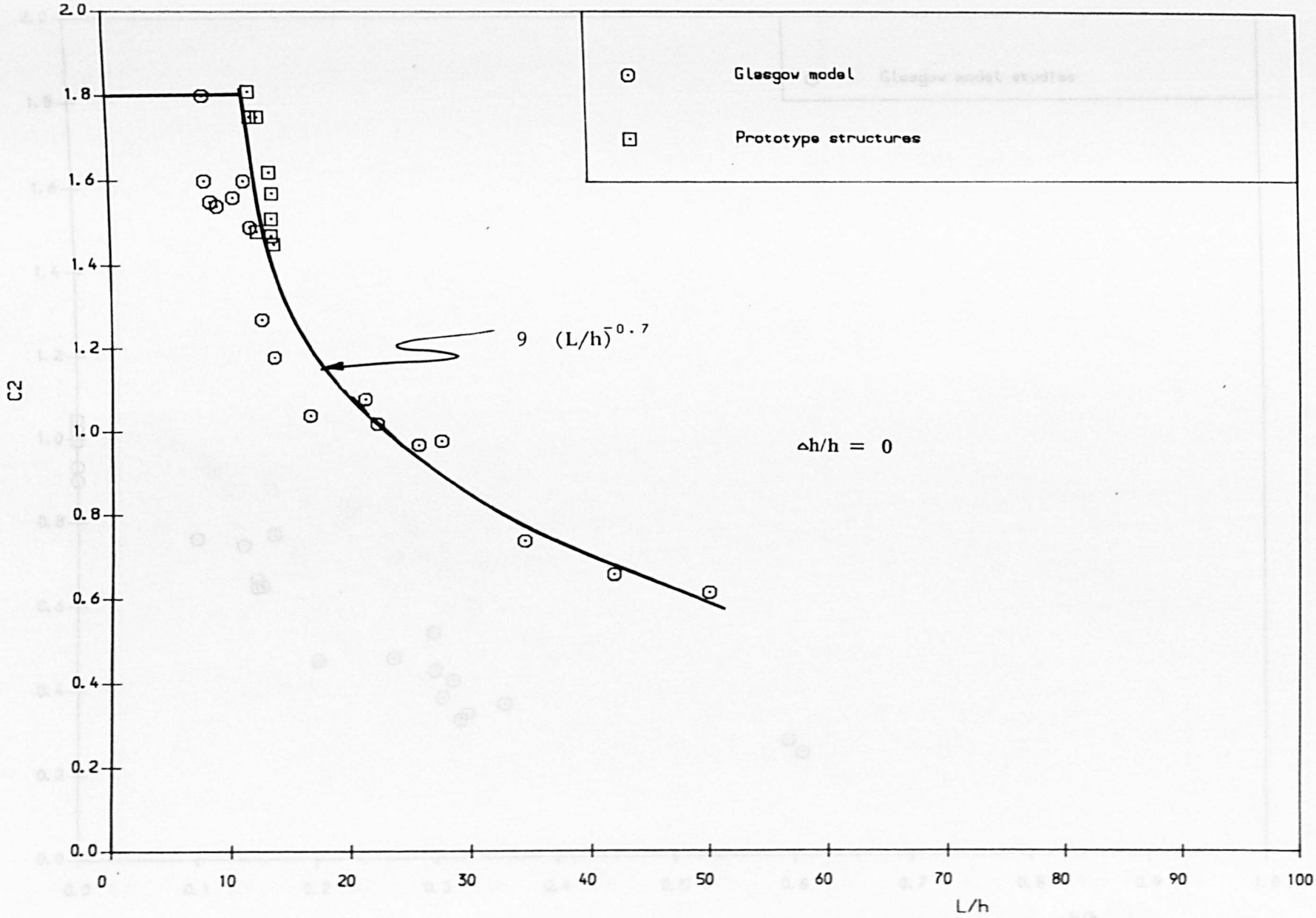

Fig 6.16 Variation of C2 with increasing jet length at $\Delta h/h = 0.0$ in model and prototype studies

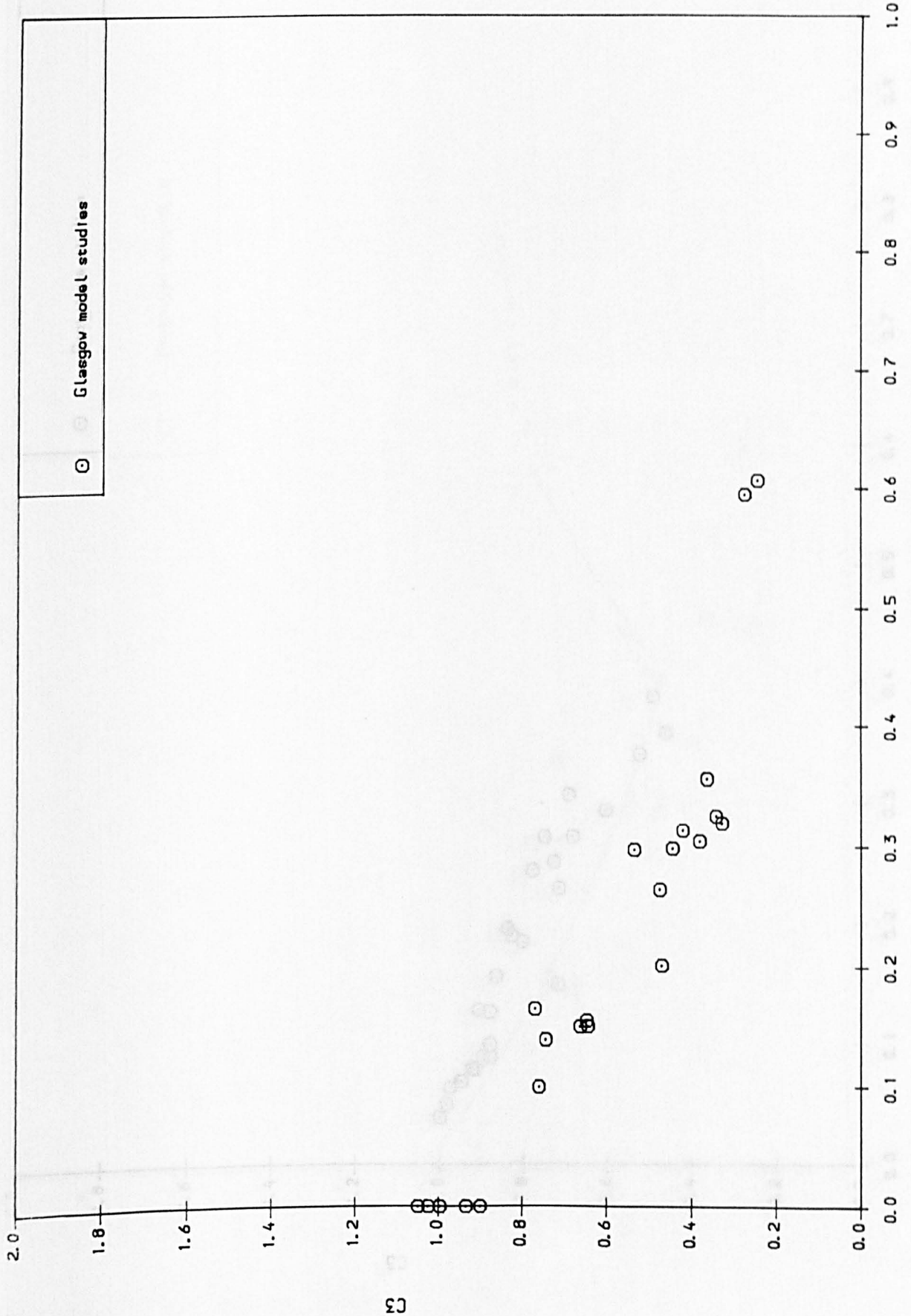

Fig 6.17 Variation in C3 with increasing underpressure in Glasgow model studies

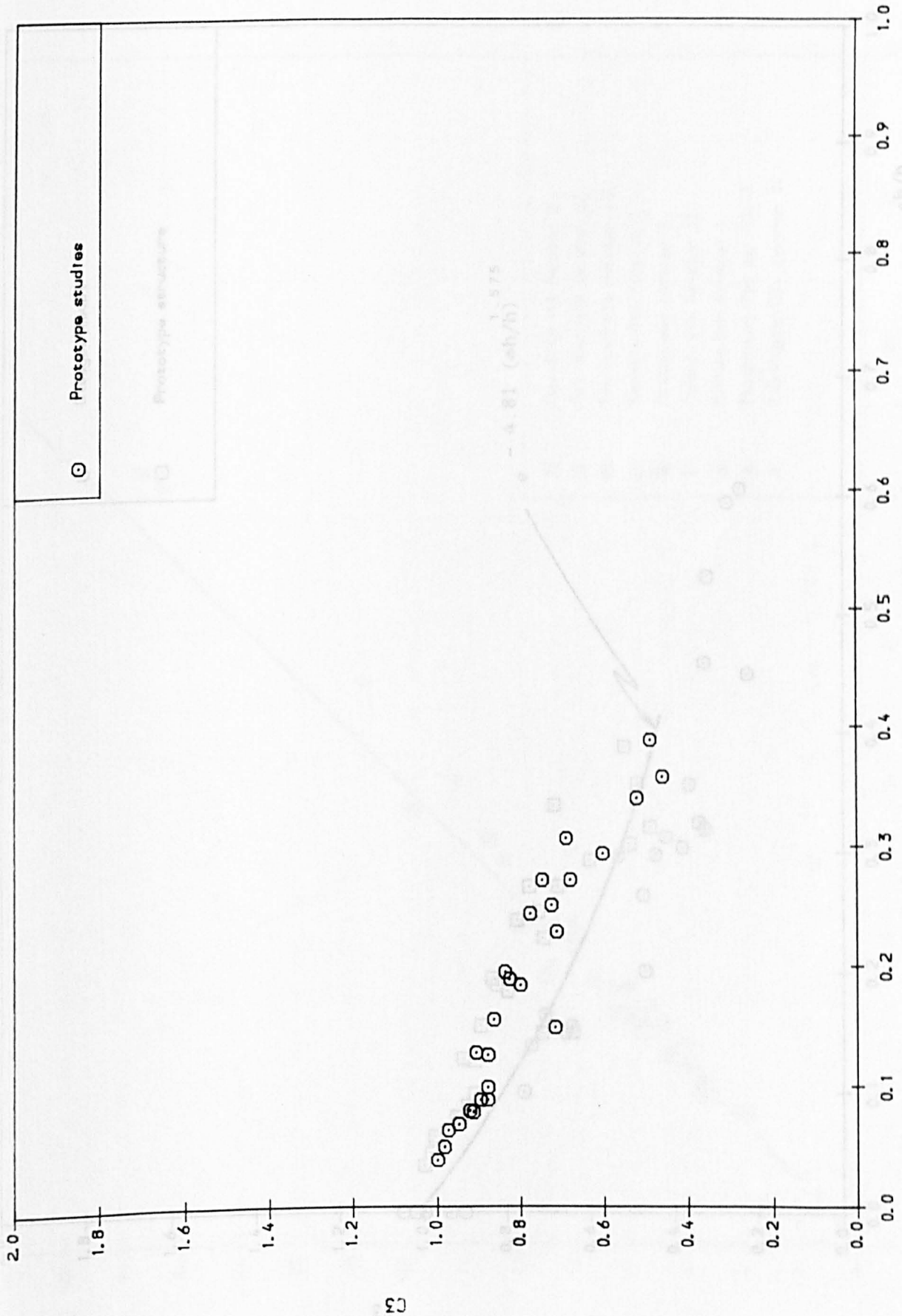

Fig 6.18 Variation in C3 with increasing underpressure in prototype studies

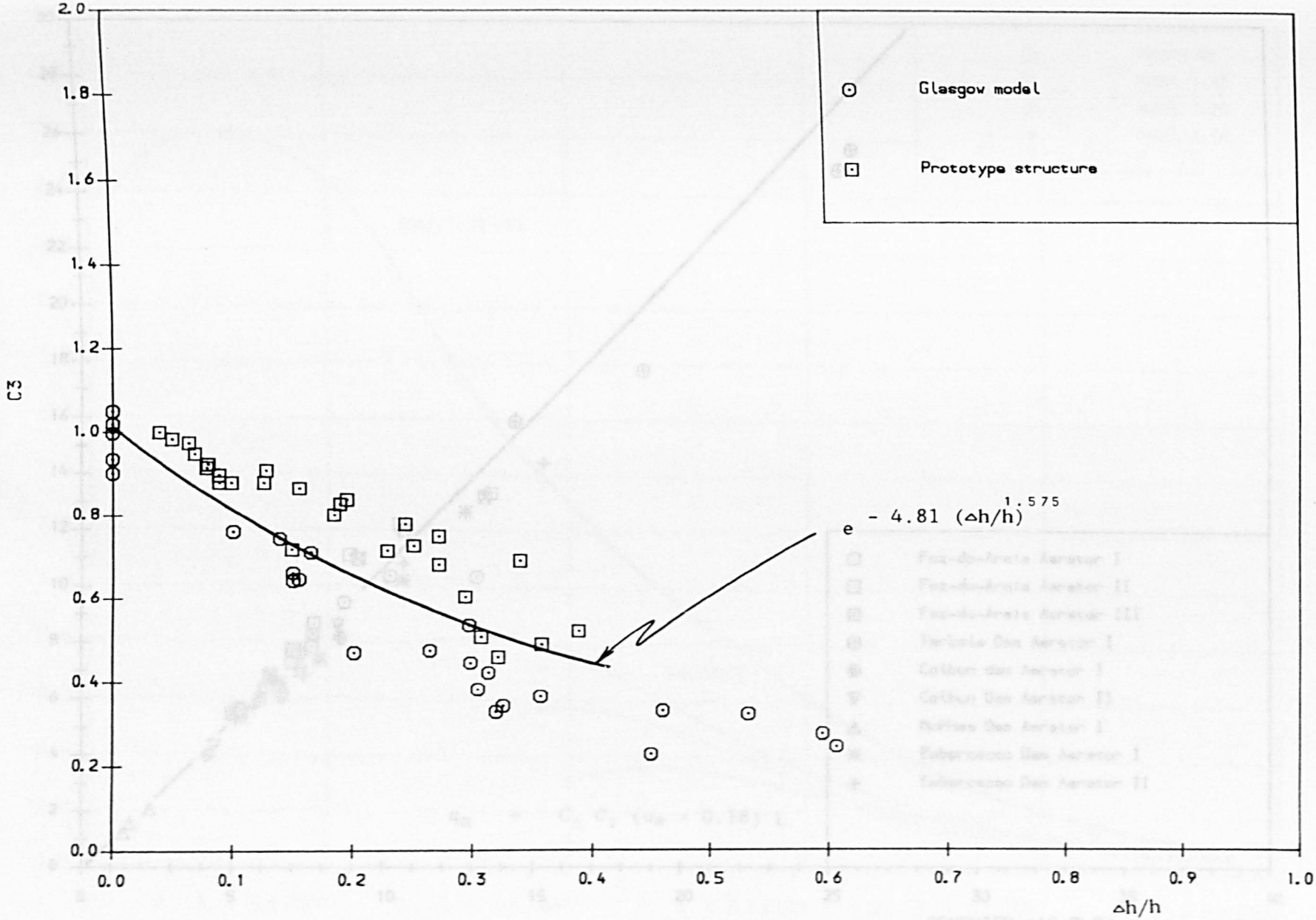

Fig 6.19 Variation of C3 with increasing underpressure in model and prototype structures all data.

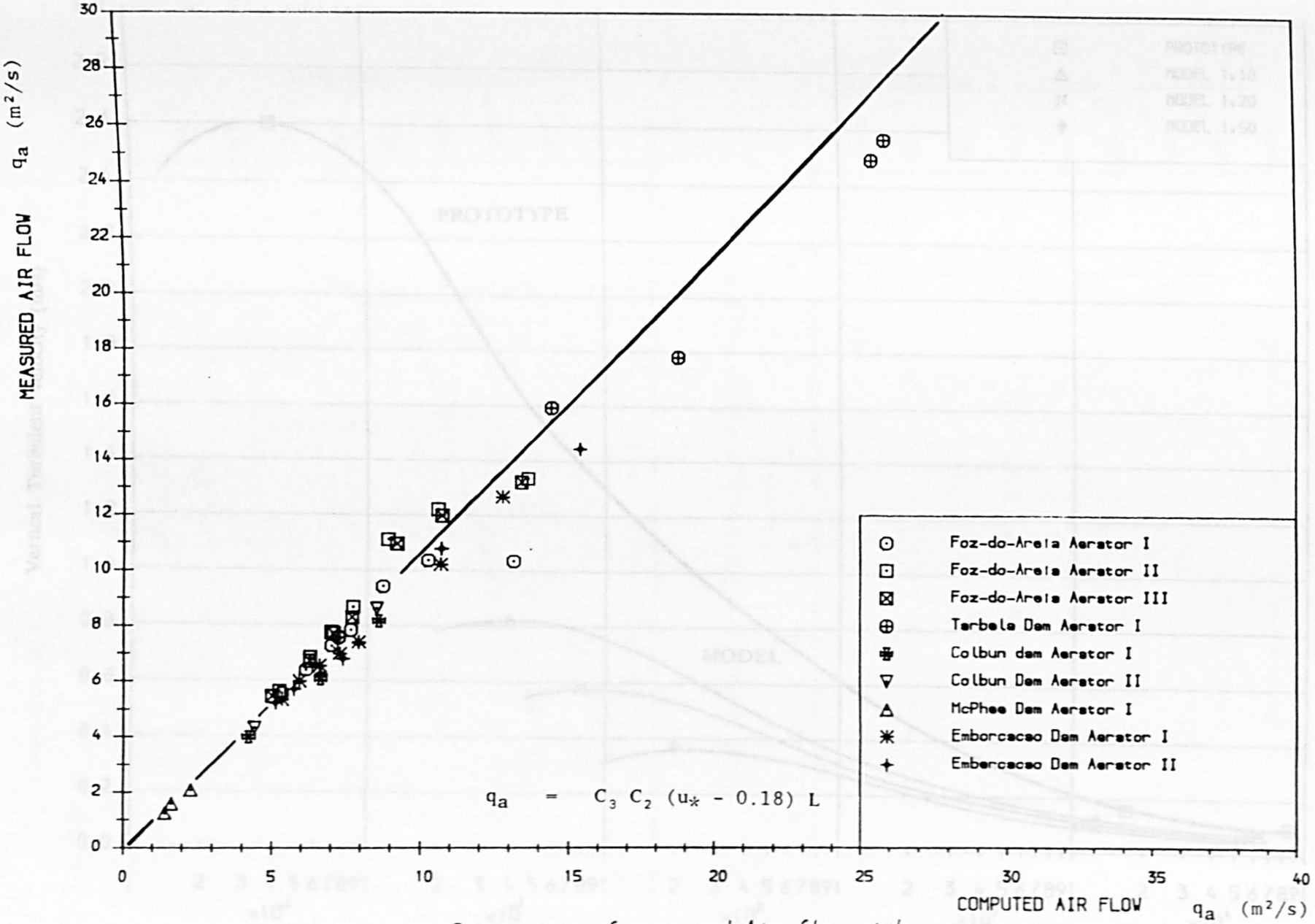

Fig 6.20 Comparison of computed Air flow with measured Air flow

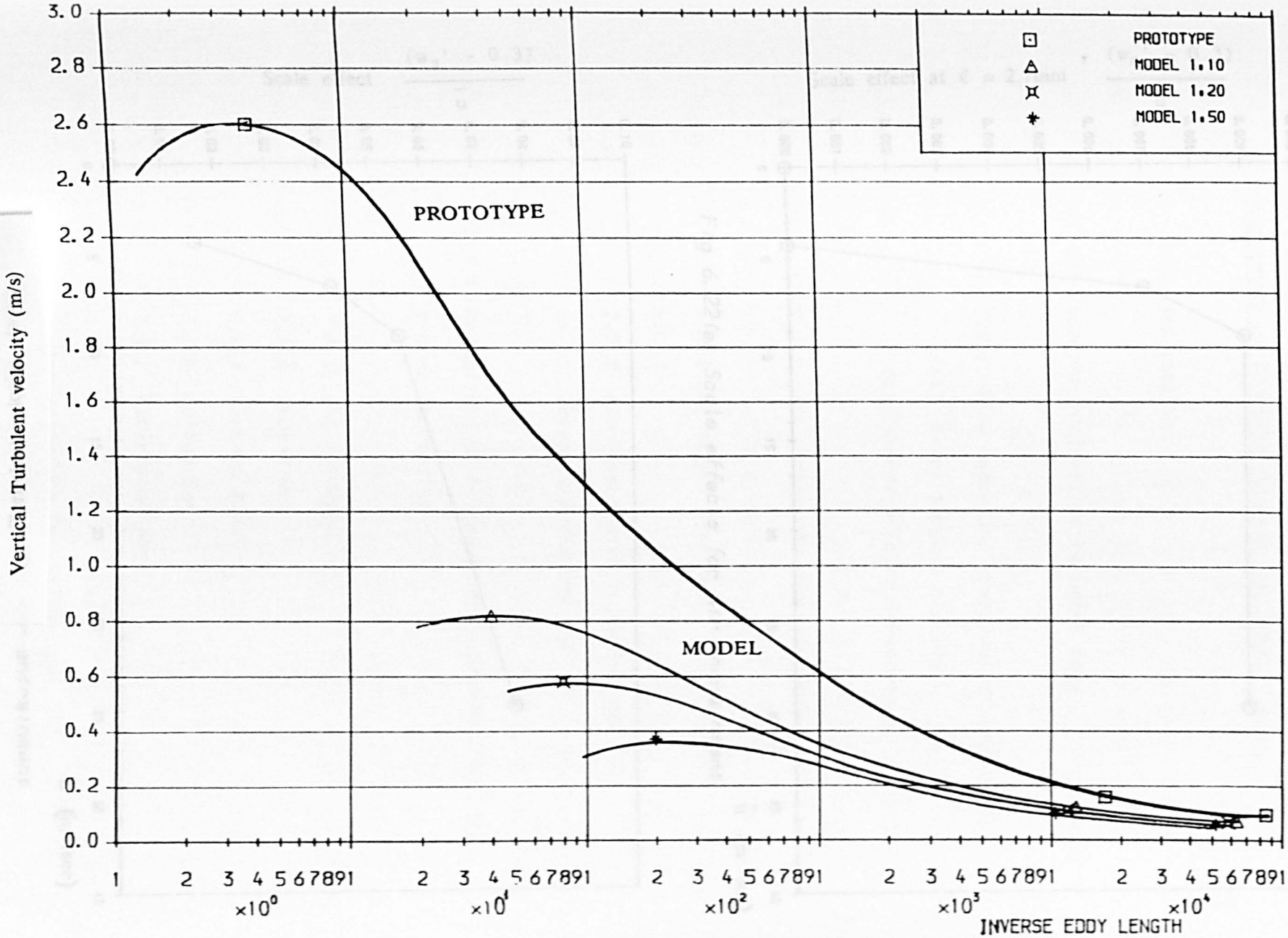

FIG 6.21 HYPOTHETICAL SPECTRA FOR MODEL AND PROTOTYPE STRUCTURES

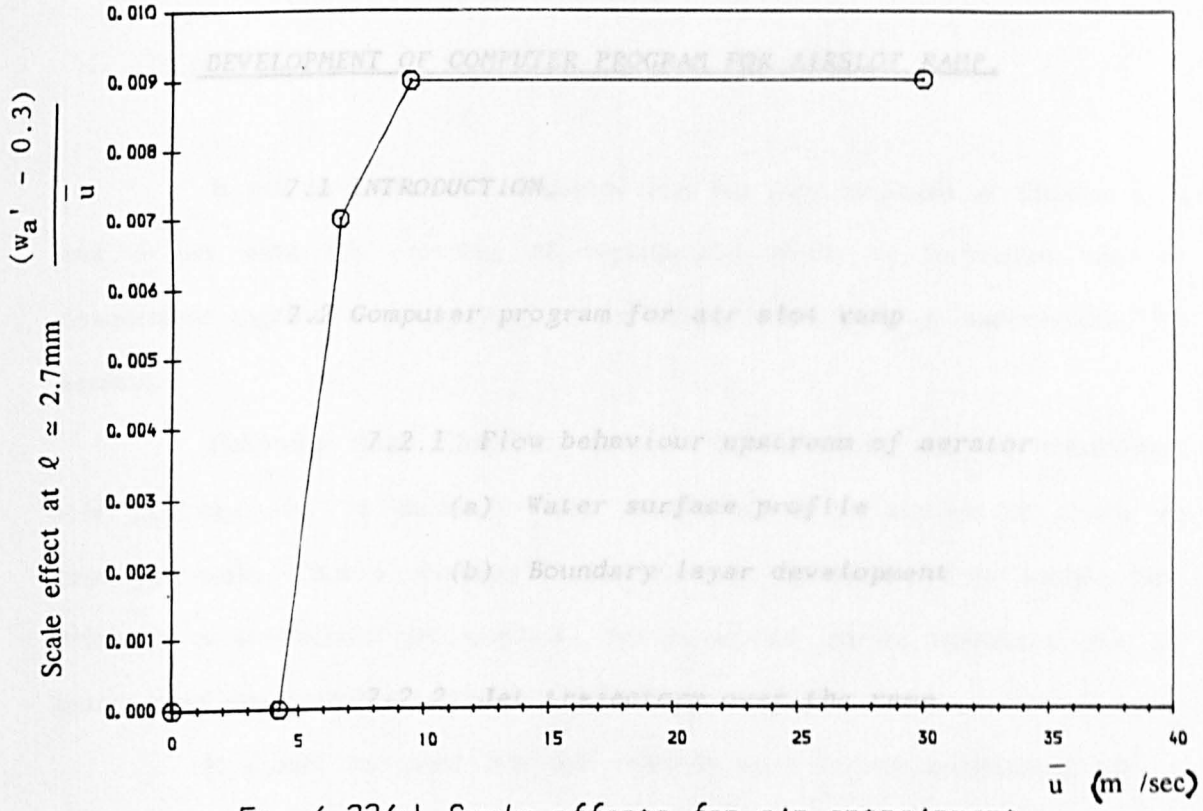

Fig 6.22(a) Scale effects for air entrainment

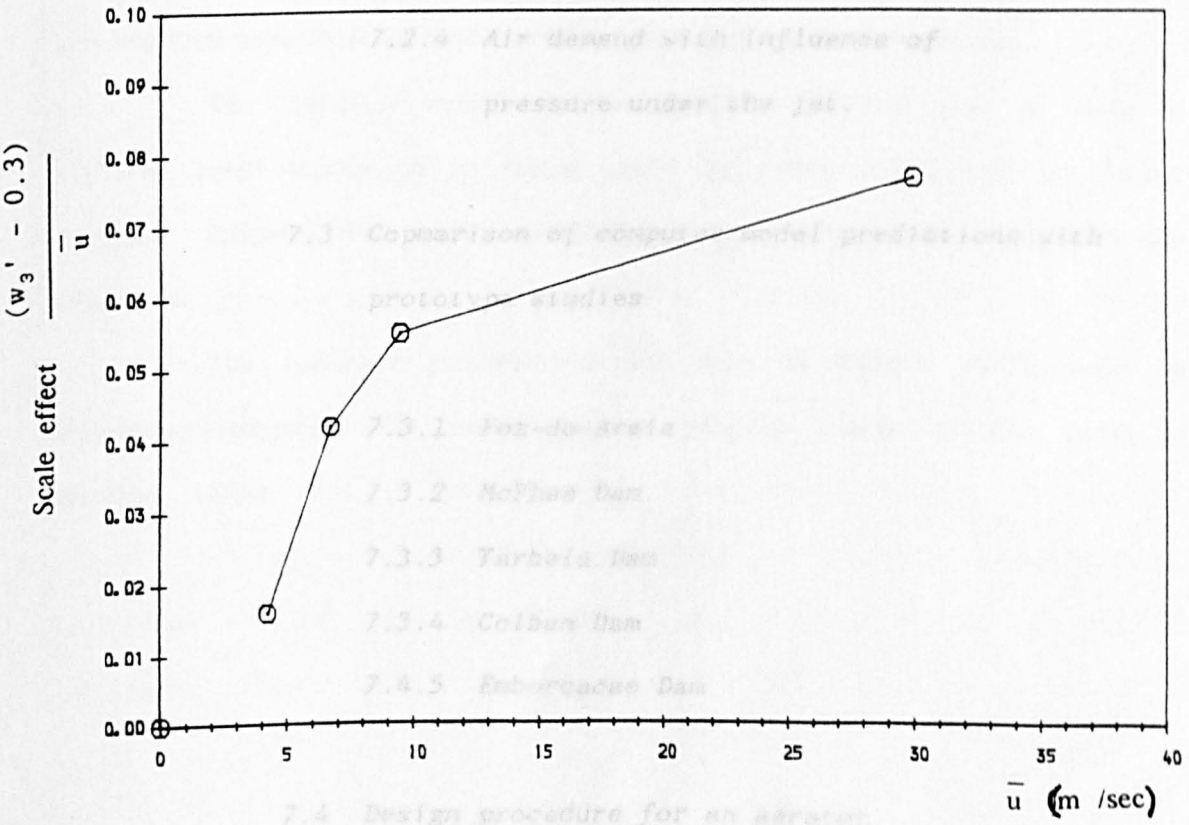

Fig 6.22(b) Scale effects for air entrainment

CHAPTER 7.

DEVELOPMENT OF COMPUTER PROGRAM FOR AIRSLOT RAMP.

7.1 INTRODUCTION.

7.2 Computer program for air slot ramp

7.2.1 Flow behaviour upstream of aerator

(a) Water surface profile

(b) Boundary layer development

7.2.2 Jet trajectory over the ramp

7.2.3 Air supply system

7.2.4 Air demand with influence of pressure under the jet.

7.3 Copmarison of computer model predictions with prototype studies

7.3.1 Foz-do-Areia

7.3.2 McPhee Dam

7.3.3 Tarbela Dam

7.3.4 Colbun Dam

7.4.5 Emborcacao Dam

7.4 Design procedure for an aerator

7.1 INTRODUCTION.

It will have been noted already that the main emphasis of Chapter 4, 5 and 6 has been the reporting of experimental results of turbulence and air entrainment together with analyses, to provide a frame work of understanding for aerators.

Following these Chapters, estimates of turbulence and air entrainment rate q_a, can now be made for any aerator geometry, whether at model or prototype scale. Thus a computer model can now be developed to analyse flow estimates of the aerator jet length L, the jet spread due to turbulence, the air entrainment rate, and the cavity underpressure $\triangle h$ or $(\triangle p)$.

It should be noted that this research work in fact commenced with a computer model of flow along a spillway and aerator ramp. However, there were various gaps in understanding of the flow behaviour over the ramp, which turned this research towards more experimental rather than computer modelling.

The computer model was developed in the first year of study in 1987–88 based loosely on an earlier model by Falvey (1988) and was further modified following the useful conclusions from Chapter 4, Chapter 5 and Chapter 6.

The computer programming was done in Fortran 77 langauge on mainframe computer. The main computer program consists of five stages as sketched below.

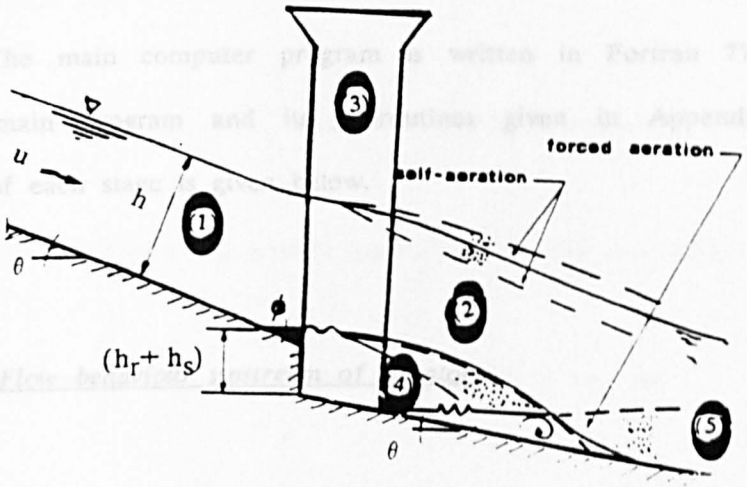

(1) Flow behaviour upstream of aerator.
(gradually varied flow and boundary layer development)

(2) Jet trajectory over the ramp aerator.(including jet spreading)

(3) Air Supply system

(4) Air demand with influence of pressure under the jet.

(5) Air distribution & concentration downstream of aerator

It should be noted the the one key area of aerator research was not attempted because of the time constraint. That was Stage (5) concerned with the air distribution and concentration downstream of the aerator which should be tackled in future research.

After giving a brief description of stages (1) to (4) above in the computer program, a comparison will be carried out for prototype studies of air entrainment rate and jet length estimation. Computed results will be compared with field measurements for five major dams around the world.

7.2 *Computer program for air slot ramp*

The main computer program is written in Fortran 77 language with details of main program and its subroutines given in Appendix A. A brief description of each stage is given below.

7.2.1 *Flow behaviour upstream of aerator*

(a) *Water surface profile*

The water surface profile upstream of the spillway ramp was computed using the standard step method as described below.

The principle of conservation of energy states that the total energy in the flow remains constant at each section.

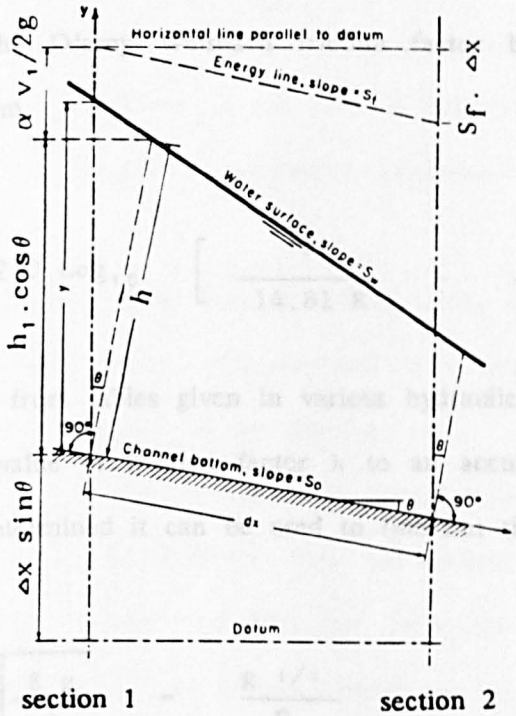

Consider sections (1) and (2) at a distance Δx apart. The principle of conservation of energy states, that Energy at section(1) = Energy at section(2) +

Losses between section(1) & (2).

Energy at section (1):

$$\text{Energy at section 1} = h_1.\cos\theta + \alpha_1 v_1/2g + \triangle x \sin\theta \qquad (7.1)$$

Energy at section (2) plus the energy losses between the two sections is given by:

$$\text{Energy at section 2} = h_2.\cos\theta + \alpha_2 v_2/2g + \bar{S}_f . \triangle x \qquad (7.2)$$

where $\bar{S}_f \triangle x$ represents the energy losses between section 1 and 2 with all the energy loss assumed to be due to bed friction. $\triangle x$ is the distance along the slope.

In principle, if h_1 and v_1 are known, then the total energy at section 1 is computed, which is then used to find the values of h_2 and v_2 from Equation (7.2). In order to solve Equation (7.2) iteratively, an expression for the friction head loss $S_f \triangle x$, must be found. This is done in subroutine called "ROGOUS" which computes the D'arcy Weisbach friction factor by using Colebrook White equation in the form

$$\frac{1}{\sqrt{\lambda}} = -2.0 \log_{10} \left[\frac{k_s}{14.81\, R} + \frac{2.51}{Re\sqrt{\lambda}} \right] \qquad (7.3)$$

By using k_s values from tables given in various hydraulic text books, the computer can find out the value of friction factor λ to an accuracy of $\pm$ 1%. Once the friction factor is determined it can be used to find out the Manning's 'n' from the linking equation:—

$$\sqrt{\frac{8g}{\lambda}} = \frac{R^{1/6}}{n} \qquad (7.4)$$

The Manning's n can be further used for determining the friction slope S_f for each section,

$$S_{f_1} = \frac{n_1^2 \; v_1^2}{R_1^{4/3}} \qquad (7.5)$$

and

$$S_{f_2} = \frac{n_2^2 \; v_2^2}{R_2^{4/3}} \qquad (7.6)$$

where R = hydraulic radius

The average friction slope is approximated to

$$\bar{S}_f = (S_{f_1} + S_{f_2}) \; / \; 2. \qquad (7.7)$$

The computer calculates the S_{f_1} and S_{f_2} for each trial depth 'h_2', and computes the energy at section 2 to compare with the energy at section 1, Equation (7.1). Once the energy at section 2 becomes equal to energy at section 1, the iterative process stops taking more trials and moves to the next section (3). This procedure is continues until the program reaches normal depth, or the ramp section, or at any other section as stated by the user.

The normal depth of the flow is determined by applying the Newton Raphson iterative technique to Manning's Equation with the bed slope given by $\sin\theta$.

The standard step method can be used, starting off at a known depth such as critical depth at the upstream end of a spillway, or from a known gate opening at the upstream end of the spillway.

The accuracy of the method is enhanced by choosing very small distance increments ($\triangle x$) along the spillway. Also the method is not applicable at control sections, and care is taken so that the computational procedure does not go through a control section, but in fact commences a short distance downstream of the critical depth point.

(b) Boundary layer development

Stage 1 of the computer program also computes the boundary layer development along the spillway flow.

When water enters an open channel, the velocity distribution over the channel section (owing to the presence of bottom boundary roughness), will vary with the distance over which the water travels in the channel as shown in Fig 7.1

Chow.V.T (1959) defined the effect of the boundary layer on the flow as equivalent to a fictitious upward displacement of the channel bottom to a virtual position by an amount equal to the so–called displacement thickness δ^* as shown in Fig 7.2

The boundary layer thickness is denoted by δ as shown in Fig 7.2. For the development of turbulent boundary layer in a wide open channel, an approximate but practical method of computation of δ has been proposed by Bauer (1954) for rough boundaries,

$$\frac{\delta}{x} = \frac{0.024}{[x/k_s]^{0.13}} \qquad (7.8)$$

where δ is the thickness of boundary layer, x is the distance along the channel slope and k_s the roughness size of the spillway surface. Equation (7.9) shows that the fully developed turbulent condition of the flow as a function of relative roughness. An estimate of boundary layer thickness δ on a smooth boundary can be given as

$$\frac{\delta}{x} = \frac{0.38}{[R_x]^{0.2}} \qquad (7.9)$$

where R_x is a distance Reynolds number ($v.x/\upsilon$) based on distance rather than depth. From the Eq (7.8) & Eq (7.9) it can be shown that the development of the

boundary layer in a fully developed turbulent flow condition is a function of,

i) the state of flow expressed by a distance Reynolds number.

ii) the relative roughness of the flow.

Toso (1986) showed that the effect of Reynolds number in a highly turbulent flow is much smaller, than the effect of relative roughness of the channel. His equation for boundary layer thickness is;

$$\delta = \frac{0.233\ x}{[\ x/k_s\ ]^{0.25}} \qquad (7.10)$$

where 'x' is the distance along the slope.

The computer program has a flexible option to use either Equation (7.9) or Equation (7.10) for the calculation of boundary layer growth, with Equation (7.9) preferred for smooth models with k_s values = 0.0.

A typical graph of computed water surface profile and boundary layer thickness using Toso's equation is shown in Fig 7.3

7.2.2 *Jet trajectory over the ramp aerator.*

Stage 2 of the computer program is to determine the trajectory of the jet after it leaves the ramp, including jet spreading due to turbulence.

Once the water surface profile is calculated in stage 1, one can find out the depth of flow at the end of the ramp h_3. The ramp angle Φ the depth of flow at the end of ramp h_3 the spillway angle θ, and the velocity at the ramp u_3, are the main parameters for calculating the jet trajectory.

As far as channel of steep slope is concerned, the exact line of the upper and lower jet surface trajectory would become a rather complicated task. To accomplish this, the spread of the jet is assumed to match its vertical turbulent

intensity w'/ u, this representing the line of the edge of the jet relative to the orignal line of the ramp, as sketched below.

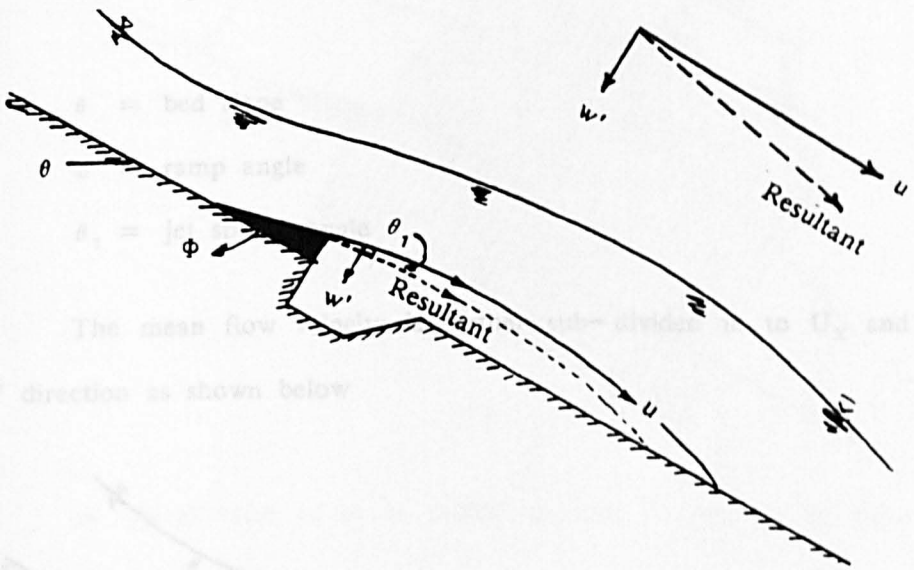

From Chapter 6 it can be concluded that the vertical turbulent velocity at the end of the ramp is a function of bed shear velocity

$$w'_3 = 1.75\ u_* \qquad (7.11)$$

Instead of using the vertical turbulent velocity the program is modified to use the bed shear velocity which can be calculated by using Colebrook–White equation, combined with the relation, $u_* = \bar{u} \surd (\lambda/8)$.

The jet spread angle θ_1 to be the same as turbulent intensity, Falvey (1991). Hence, the spread angle in the sketch above is,

$$\theta_1 = \tan^{-1} [(1.75\ u_*)/ \bar{u}\ ] \qquad (7.12)$$

$$= \tan^{-1} [\ 1.75 \surd (\lambda/8)] \qquad (7.13)$$

The angle θ_1 is now added to the net ramp angle for the lower nappe and substracted at the upper nappe for the trajectory calculation.

$$(\text{Theata})_{ramp} = (\theta - \Phi) + \theta_1 \quad \text{for Lower nappe} \qquad (7.14)$$

$$(\text{Theata})_{ramp} = (\theta - \Phi) - \theta_1 \quad \text{for upper nappe} \qquad (7.15)$$

where θ = bed slope

Φ = ramp angle

and θ_1 = jet spread angle

The mean flow velocity is further sub–divided in to U_x and U_y in X and Y direction as shown below

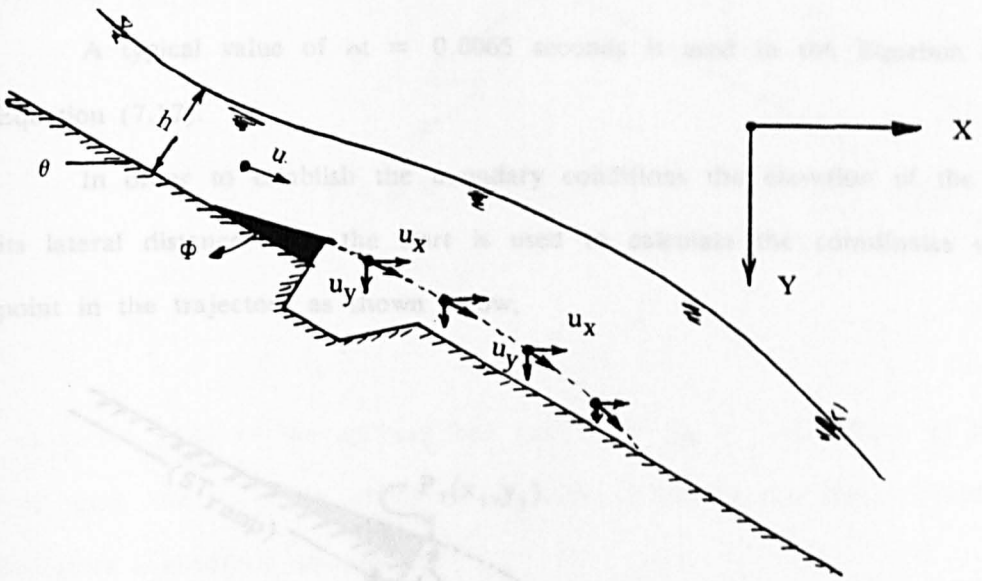

The coordintes of the jet trajectory are calculated by using Newton's laws of motion and basic projectile theory as in the equations below,

$$\triangle X = U_x \cdot \triangle t \qquad (7.16)$$

$$\triangle Y = U_y \triangle t + \tfrac{1}{2} g \triangle t^2 \qquad (7.17)$$

where $\triangle X$ and $\triangle Y$ are the change in coordinates of the jet trajectory in X and Y direction. In the computer program the time duration $\triangle t$ is made extremely small and assumed constant in order to estimate the smallest distance $\triangle x$, independent of

the variation of velocity for each increment Δx. This is sketched below,

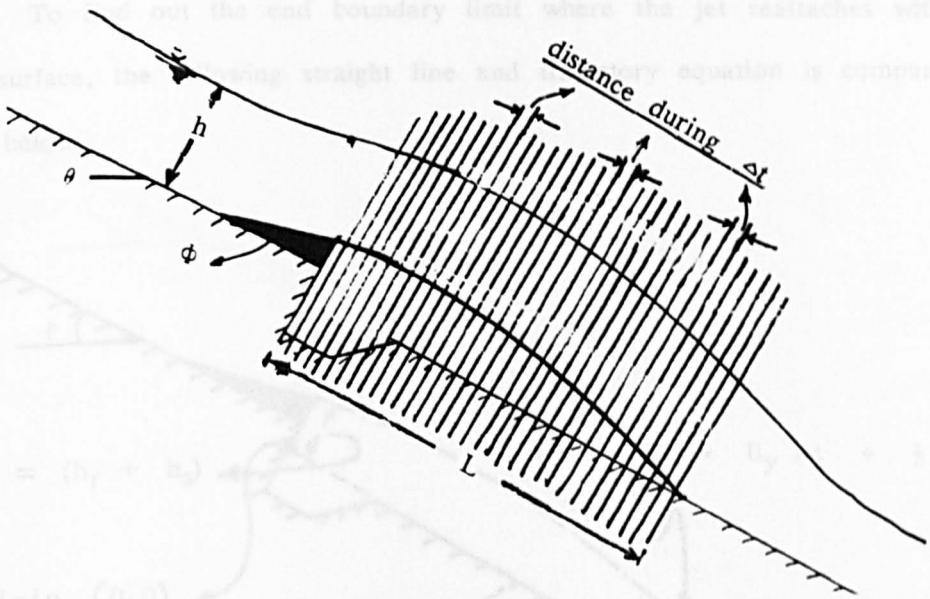

A typical value of $\Delta t = 0.0065$ seconds is used in the Equation (7.16) and Equation (7.17).

In order to establish the boundary conditions the elevation of the ramp and its lateral distance from the start is used to calculate the coordinates of the first point in the trajectory as shown below,

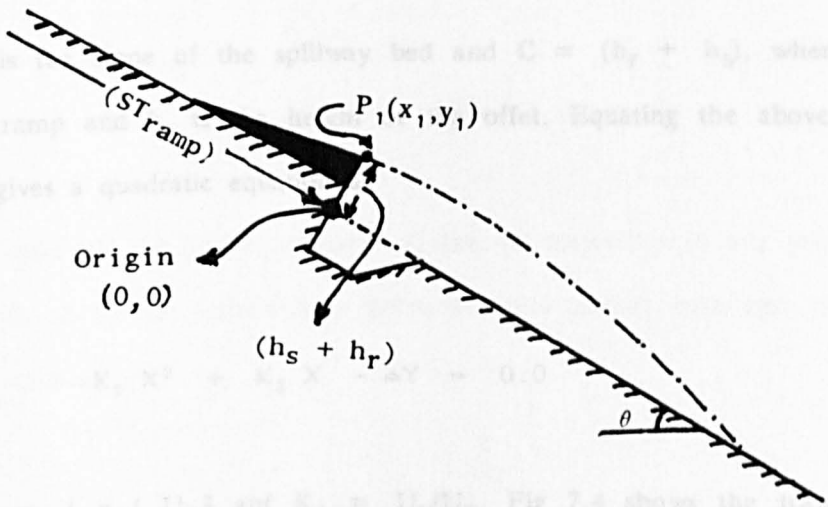

where $P_1(x_1,y_1)$ are the first coordinates of the jet trajectory as shown above,

$$x_1 = \text{Origin} + (h_s + h_r)\sin\theta \qquad (7.18)$$

$$y_1 = \text{Origin} + (h_s + h_r)\cos\theta \qquad (7.19)$$

where h_s and h_r are the offset and ramp heights.

To find out the end boundary limit where the jet reattaches with the spillway surface, the following straight line and trajectory equation is compared as sketched below.

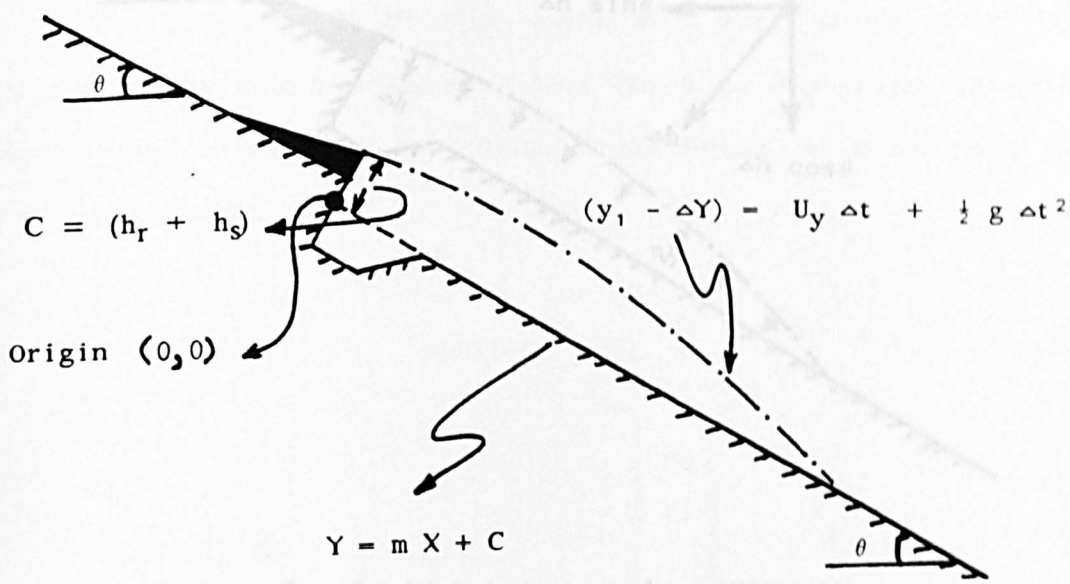

where m is the slope of the spillway bed and $C = (h_r + h_s)$, where h_r is the height of ramp and h_s is the height of the offet. Equating the above shown two equations gives a quadratic equation as

$$K_1 X^2 + K_2 X - \Delta Y = 0.0 \qquad (7.20)$$

where $K_1 = \frac{1}{2} g / U_x^2$ anf $K_2 = U_y/U_x$. Fig 7.4 shows the trajectory under atmospheric condition with no jet spread.

The computer program has the facility to predict the jet trajectory for any value of under pressure $\Delta h/h > 0$. The estimation of Δh (head loss in air duct) is described in detail in following section 7.2.3. The computer program uses

the following equation for simulating the effect of $\triangle h$ on the jet trajectory as sketched below,

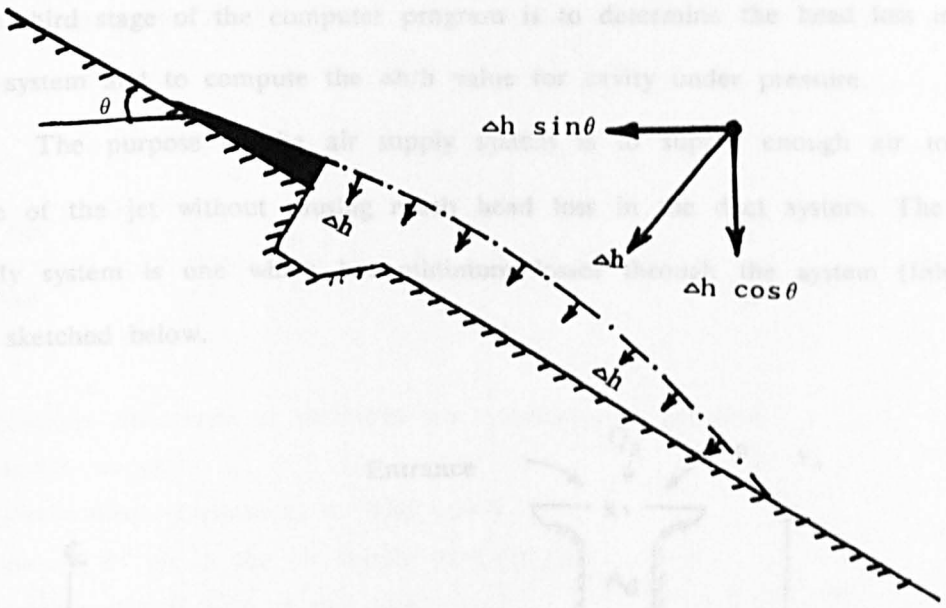

The final equations for jet trajectory can be written as:–

$$\triangle X = U_x \triangle t - \triangle h \sin\theta \qquad (7.21)$$

$$\triangle Y = U_y \triangle t + \tfrac{1}{2} g \triangle t^2 + \triangle h \cos\theta \qquad (7.22)$$

where $\triangle X$ and $\triangle Y$ are the coordinates of the jet trajectory at any point. Once the exact length of the jet trajectory is estimated it is further translated into jet length along the spillway as

$$L = \sum_{i=0}^{i=n} (\triangle X) \Big/ \cos\theta \qquad (7.23)$$

This length 'L' is used for calculating air demand for the jet. A typical example of a jet trajectory is shown in Fig 7.5 with allowance for underpressure $\triangle h$, and jet spread, included.

7.2.3 *Air supply system*

The third stage of the computer program is to determine the head loss in the air duct system and to compute the $\Delta h/h$ value for cavity under pressure.

The purpose of the air supply system is to supply enough air to the underside of the jet without causing much head loss in the duct system. The best air supply system is one which has minimum losses through the system (Inlet to Exit) as sketched below.

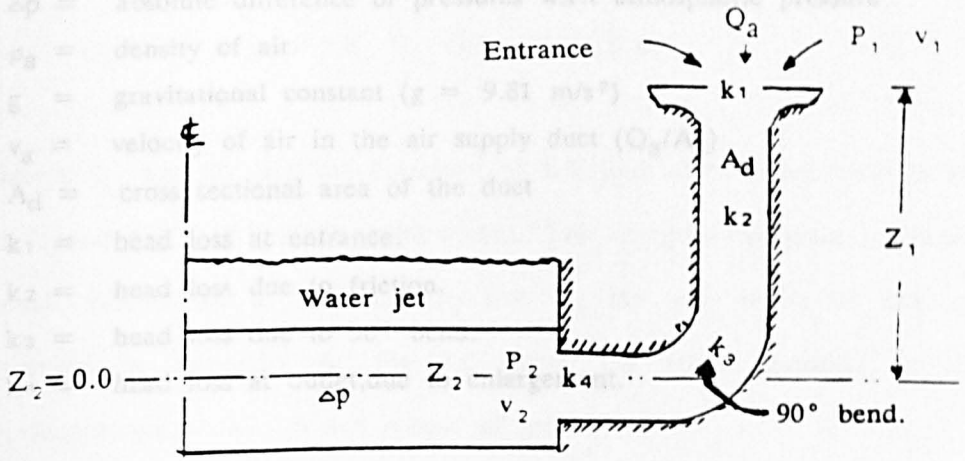

It should be noted that the final air flow occuring in an aerator depends on the balance between the air pumping capacity of the jet and the air supply characteristics as sketched below.

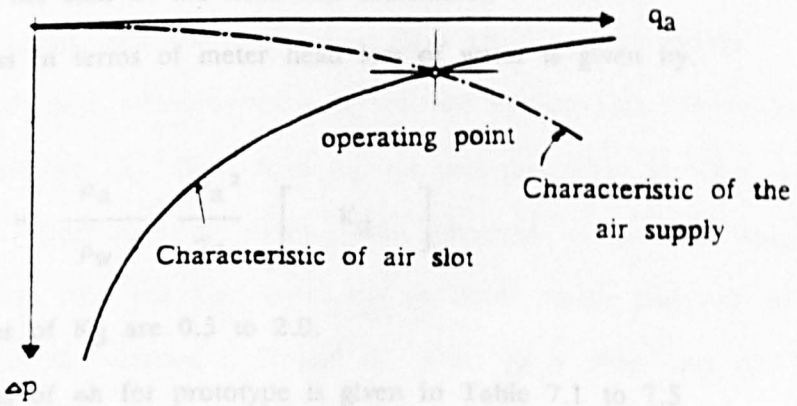

The air supply head loss $\triangle h$ can be estimated from the Bernoulli's Equation between inlet and exit of the system as described in detail in Chapter 2 in section 2.6.2. The computer program needs the proper dimensions of a given aerator air supply system. The head loss in terms pressure in the air duct can be written as

$$\frac{\triangle p}{\rho_a g} = \frac{1}{2g}\left[\left[k_1 + k_2 + k_3 + k_4 \right]\right] \frac{Q_a^2}{A_d^2} \qquad (7.24)$$

where

$\triangle p$ = absolute difference of pressures w.r.t atmospheric pressure

ρ_a = density of air

g = gravitational constant ($g = 9.81$ m/s^2)

v_a = velocity of air in the air supply duct (Q_a/A_d)

A_d = cross sectional area of the duct

k_1 = head loss at entrance.

k_2 = head loss due to friction.

k_3 = head loss due to 90° bend.

k_4 = head loss at outlet,due to enlargement.

$$\triangle p = \rho_a \frac{v_a^2}{2}\left[\left[1 + K_s \right]\right] \qquad (7.25)$$

$$\triangle p = \rho_a \frac{v_a^2}{2}\left[K_d \right] \qquad (7.26)$$

where K_d is the sum of the head loss coefficient.

The head loss in terms of meter head loss of water is given by,

$$\triangle h = \frac{\rho_a}{\rho_w}\frac{v_a^2}{2g}\left[K_d \right] \qquad (7.27)$$

Typical values of K_d are 0.5 to 2.0.

Typical values of $\triangle h$ for prototype is given in Table 7.1 to 7.5

7.2.4 *Air demand with influence of pressure under the jet.*

In stage 4 the computer program calculates the actual amount of air entrained into the jet. From Chapter 6, we concluded that the air entrainment is directly effected by two main parameters namely, jet length ratio (L/h) and jet under pressure ($\Delta h/h$). Equation (6.31) gives good estimate for the prediction of air flow under the jet. The computer program is modified to use the following equation for the prediction of air entrainment at an aerator jet.

$$q_a = C_2 C_3 (u_* - 0.18) L \qquad (7.28)$$

where C_2 and C_3 are the functions of L/h and $\Delta h/h$ respectively as shown in Fig 6.16 and Fig 6.19 and Equation (6.18). The computer program is furnished by two small subroutines to calculate C_2 and C_3 for any values of L/h and $\Delta h/h$ as detailed in Appendix A. Fig 7.5 shows the actual situation of the jet with underpressure $\Delta h/h > 0$ and spread of jet.

7.3 *Comparison of computer model predictions with prototype studies.*

After modification and finalising the computer program, stage 1 to 4, it was decided to apply the computer model to five key prototype structures world wide, where enough data was available to allow sensible computations.

Most field measurement data sets had considerable information on mean velocity $\bar{u}$, discharge Q_w, flow depth h_3, air vent geometry, air flow rate, etc. but practically no information on cavity under pressure Δh and jet length L. One exception to the rule was Foz–do–Areia in Brazil which had full range of data for all three of its aerators I, II and III. Most other field data did not include

prototype jet length measurements.

What follows below is a comparison of the computed values based on the research of this thesis, and field measurements at Foz–do–Areia, McPhee, Tarbela, Colbun and Emborcacao Dams.

7.3.1 Foz – do – Areia

The most comprehensive set of measurements made on prototype structures aerator were of Foz–do–Areia reported by Pinto et al (1982). The measurements were of the air flow through the side vents and pressure variation under the nappe. These measurements, including the authors computer predictions for jet length and air flow rate below for all three aerators.

Table 7.1

Aerator I

q_w (m^2/s)	h_3 (m)	v_w (m/s)	$\Delta h/h$ comp	L (m) (field)	q_a (m^2/s) data	L (m) computed	q_a (m^2/s)	β Pub:
7.58	0.38	19.94	0.08	8.2	5.59	9.07	5.36	0.74
9.77	0.46	21.25	0.11	9.5	6.42	9.52	6.19	0.66
12.04	0.52	23.15	0.14	10.1	7.29	10.32	7.07	0.61
14.16	0.59	24.01	0.16	11.1	7.85	11.07	7.73	0.55
20.82	0.81	25.71	0.22	12.6	9.43	12.65	8.84	0.45
29.60	1.08	27.41	0.25	12.8	10.37	13.26	10.35	0.35
46.74	1.64	28.5	0.23	14.0	10.34	13.64	13.23	0.22

Aerator II

q_w (m^2/s)	h_3 (m)	v_w (m/s)	$\Delta h/h$ comp	L (m) (field) data	q_a (m^2/s)	L (m) computed	q_a (m^2/s)	β Pub:
7.58	0.39	19.43	0.08	7.8	5.65	9.05	5.26	0.75
9.77	0.45	21.73	0.11	9.0	6.87	9.70	6.33	0.70
12.04	0.52	23.15	0.14	9.9	7.78	10.32	7.07	0.65
14.16	0.57	24.85	0.17	10.5	8.68	11.84	7.82	0.61
20.82	0.76	27.40	0.23	11.5	11.13	13.25	9.02	0.53
29.60	1.00	29.60	0.26	11.9	12.20	14.02	10.7	0.41
46.74	1.48	31.58	0.28	13.3	13.33	14.73	13.75	0.29

Aerator III

q_w (m^2/s)	h_3 (m)	v_w (m/s)	$\Delta h/h$ comp	L (m) (field) data	q_a (m^2/s)	L (m) computed	q_a (m^2/s)	β Pub:
7.58	0.39	19.43	0.10	7.4	5.47	8.87	5.03	0.72
9.77	0.45	21.73	0.11	8.7	6.74	9.70	6.33	0.69
12.04	0.51	23.61	0.15	9.7	7.73	10.70	7.15	0.64
14.16	0.56	25.29	0.18	11.0	8.31	12.19	7.78	0.59
20.82	0.73	28.52	0.23	11.9	10.98	13.64	9.31	0.53
29.60	0.93	31.83	0.27	12.5	11.98	14.82	10.83	0.40
46.74	1.33	35.14	0.30	14.3	13.20	14.76	13.52	0.28

The comparison between measured and computed jet lengths at Foz– do– Areia is shown in Fig 7.6. There is an excellent comparison for Aerator I geometry, with some discrepancy for geometries II and III.

The air flow comparisons are given in Fig 7.7 again showing reasonable correspondence for all three aerators.

The reason for discrepancy between measured and predicted jet lengths is not clear and may involve the accuracy of the underpressure ($\Delta h/h$) calculations in the computer model calculations. On the other hand, the field measurements of where the jet reattaches to the spillway must be subject to considerable error.

The main discrepancy in the air flow measurements in Fig 7.13 appears to be at high discharge rate, where computed rates increase significantly. The reason for this is not apparent as this phenomena did not occur in the other four prototype geometries.

(ii) *McPhee Dam*

The comparison for this aerator was a special interest because the McPhee aerator jets were much longer that most other prototype structures and appeared to give much lower air flow rates than that predicted by previous air entrainment formulae.

The McPhee data was reported by Frizzell & Pugh (1988) with aerator details are given in Table 6.2. The prototype aerator measurements contains air entrainment data only. The measured air flow and computer predictions for jet length and air flow are given in Table 7.2 below.

Table 7.2

q_w	h_3	v_w	$\Delta h/h$	q_a	L	q_a	β
(m^2/s)	(m)	(m/s)	comp	(m^2/s) (field)	(m)	(m^2/s) computed	Pub:
1.53	0.1	15.3	0.05	1.24	6.18	1.42	0.815
3.88	0.2	19.3	0.045	1.59	8.38	1.65	0.41
7.76	0.35	21.17	0.044	2.09	10.0	2.31	0.27

The Comparison is shown in Fig 7.8 and is remarkably good especially in the light of comments by Frizzell and Pugh who showed that the field air flow measurements appeared to be only about half of that predicted by previous air entrainment formulae. The reason for this is that previous formulae allowed only for linear variation between air flow β, and jet length L/h, whereas in the model in this thesis, this misconception has been corrected, to good effect. The long jet lengths at McPhee, L/h $\simeq$ 25 – 60, are subjected to correction by the C_2 factor as shown in Fig 6.20 in Chapter 6, and the result is an extremely good correlation.

7.3.3 Tarbela Dam

The comparison of Tarbela Dam was also of special interest as the author of this thesis worked there for 2 years.

In 1983 three ramp aerators were installed at the outlet tunnel 3 at Tarbela dam. Details of the geometry are shown in Fig 1.7. In June 1983, the tunnel was operated for the first time after introducing the aerators. S.Karaki et al (1983) reported the first few measurements at Tarbela dam. The data at aerator I is tabulated below in Table 7.3. The field data contains only air flow discharge measurements. The jet length was calculated by the Glasgow computer model.

Table 7.3

q_w (m^2/s)	h_3 (m)	v_w (m/s)	$\Delta h/h$ comp	q_a (m^2/s) (field)	L (m) computed	q_a (m^2/s) computed	β Pub:
69.2	2.44	32.7	0.08	15.89	8.3	14.54	0.23
84.2	2.44	39.8	0.023	23.53	11.0	26.0	0.28
99.64	2.44	47.1	0.052	34.86	13.2	36.5	0.35
168.67	7.33	23.6	0.08	7.59	6.5	7.3	0.045
208.5	7.33	29.2	0.027	17.7	12.0	18.85	0.085
248.5	7.33	34.8	0.07	24.8	14.0	25.53	0.10

Fig 7.9 shows the comparison of measured and computed air flow rates showing a very satisfactory correlation.

7.3.4 Colbun Dam

Pinto (1988) published some prototype data from Colbun and Emborcacao dam for air flow measurements. The measurements were carried out by the owners of the dam. The computed jet lengths from Glasgow computer model were used for air flow predictions. The measured and predicted air flow discharges for Colbun are given in Table 7.4 below

Table 7.4 Aerator I

q_w (m^2/s)	h_3 (m)	v_w (m/s)	$\Delta h/h$ comp	q_a (m^2/s) (field)	L (m) computed	q_a (m^2/s) computed	β Pub:
7.5	0.33	15.0	0.10	4.0	8.13	4.23	0.80
23.4	0.98	23.3	0.22	8.18	12.5	8.69	0.35
56.2	2.2	25.3	0.40	6.08	15.9	6.68	0.11

Aerator II

q_w (m^2/s)	h_3 (m)	v_w (m/s)	$\Delta h/h$ comp	q_a (m^2/s) (field)	L (m) computed	q_a (m^2/s) computed	β Pub:
5.0	0.27	20.0	0.075	4.34	8.9	4.43	0.87
23.4	0.83	30.2	0.28	8.63	12.0	8.62	0.37

Fig 7.10 shows the relationship between predicted and measured air flow, again showing a very good correlation, albeit with a slight tendency for the computed prediction to overestimate.

7.3.5 Emborcacao Dam

The field measurements for Emborcacao dam only includes the air flow measurements. The field measurements were carried out by the owner of the dam. Pinto (1988) published the data for Emborcacao dam with its aerator design as shown in Chapter 1. The detail of computer prediction for jet length and air flow rate is given in Table 7.5 below

Table 7.5 Aerator I

q_w (m^2/s)	h_3 (m)	v_w (m/s)	$\Delta h/h$ comp	q_a (m^2/s) (field)	L (m) computed	q_a (m^2/s) computed	β Pub:
7.92	0.44	17.6	0.04	5.36	5.57	5.35	0.68
8.84	0.46	18.7	0.02	6.01	6.24	5.96	0.68
9.75	0.48	19.8	0.026	6.57	6.58	6.66	0.67
10.77	0.51	20.6	0.027	7.0	6.95	7.35	0.65
11.78	0.54	21.3	0.03	7.43	7.33	8.0	0.63
21.26	0.83	24.9	0.15	10.22	9.63	10.77	0.48
49.5	1.66	29.1	0.22	12.65	12.66	12.87	0.26

Aerator II

q_w (m^2/s)	h_3 (m)	v_w (m/s)	$\Delta h/h$ comp	q_a (m^2/s) (field)	L (m) computed	q_a (m^2/s) computed	β Pub:
7.92	0.44	17.6	0.02	5.24	5.25	5.14	0.66
8.84	0.46	18.7	0.031	5.73	5.55	5.776	0.65
9.75	0.47	20.2	0.025	6.26	6.53	6.7	0.64
10.77	0.5	21.0	0.028	6.82	6.89	7.45	0.63
11.78	0.53	21.7	0.034	7.4	7.21	8.0	0.63
21.26	0.78	26.5	0.17	10.8	10.35	10.8	0.51
49.5	1.48	32.6	0.25	14.4	14.45	15.5	0.29

Fig 7.11 shows the comparison between computed and measured air flows with the computed values over-estimating by about 5% to 10%. It should be noted that Emborcacao Dam had most of its L/h values in the range of 10 to 15.

Most of its data comes under the changing limit of the constant C_2 from 1.8 to $9(L/h)^{-0.7}$ as seen in Fig 6.11. Hence, the data which lies under the

limit is calculated twice by using both relationships for C_2 with the mean value of C_2 taken for air flow discharge as shown in Fig 7.11.

Fig 7.12 shows the final picture of all prototype data in one graph. Fig 7.12 shows an excellent comparison for prototype structures except few points. The overall accuracy of this method of computing aerator air flows appears to be as low as ± 10%.

7.5 *Design Procedures for an aerator.*

The following steps are recommended in the design of a structure where cavitation is one of the overriding considerations:

(1). Decide upon preliminary design configuration of the spillway structure. Include the alignment and profile, the capacity of the structure required to pass the maximum flows, and the location of ancillary structures such as diversion tunnels, plunge pools, energy dissipators.

(2). Study the cavitation characteristics of structure through the use of the computer program written by H.T.Falvey (1991). The listing of the program is given in Appendix B. At least five increments of discharge encompassing the range of flows anticipated to pass through the structures should be simulated. This will ensure that the most critical flow condition is considered. This analysis will provide the cavitation index for each flow and each point along the spillway.

(3). Determine the required surface tolerances as a function of minimum value of cavitation index as given in Table A in Chapter 1. Table A will indicate if aeration is desirable or not. Aeration is usually provided for an index less than 0.25.

(4). If the flow cavitation index is less than 0.2, investigate the effect of change to the spillway geometry on the cavitation index. The computer program written by Falvey could be used to develop the optimum curvature in the case of vertical bends. If the invert profile is linear, then changes in the width or diameter of the structure can be investigated using the same computer program.

(5). If low values of cavitation indicies can not be ameliorated by change in geometry, than an aeration device can be designed using computer program in developed during this study and listed in Appendix A.

(6). For vary small values of cavitation indicies changes to design concept should be considered. For example replacing a tunnel spillway with a free jet that impinges into a plunge pool may be possible.

(7). Once aeration device and its location had been selected, the air entrainment rate and air flow characteristics can be calculated by using computer program in Apendix A. The choice of a ramp angle Φ is important so that the jet does not rise too high, or become broken–up because it is too long.

(8). The computer program in Apendix A gives a good estimate of jet length including its spread. The under nappe pressure calculated by this computer program leads to a suitable design of air duct. Head losses are minimised if the air duct is provided with bell mouth entrance and with large cross sectional area. The program will give a good estimate of air flow rate to an accuracy of ±10%.

(9). Future work is required for further addition in this program, to include air distribution and concentration downstream of aerator, which will help to locate the position of next aerator along the spillway.

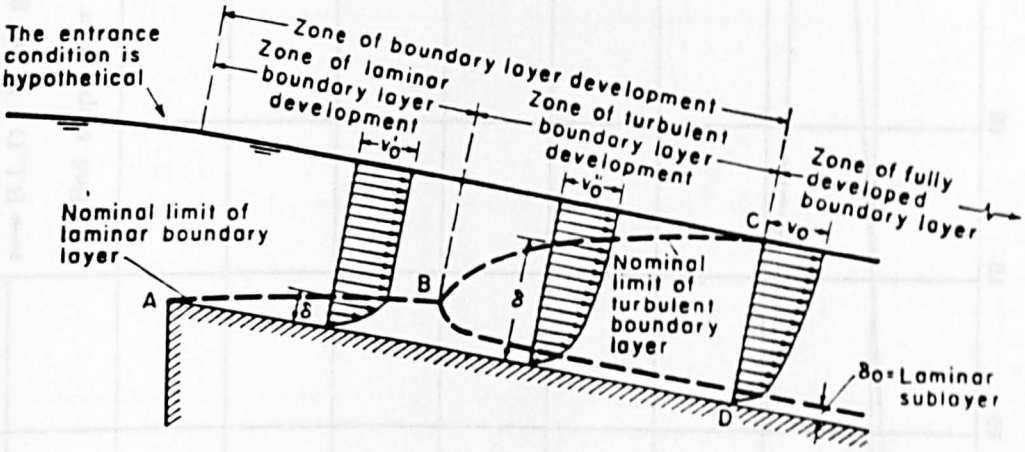

Fig 7.1 Development of boundary layer (V.T.Chow)

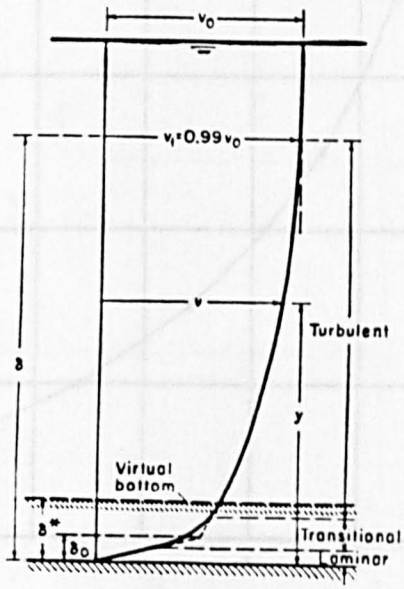

Fig 7.2 Distribution of velocity over smooth channel

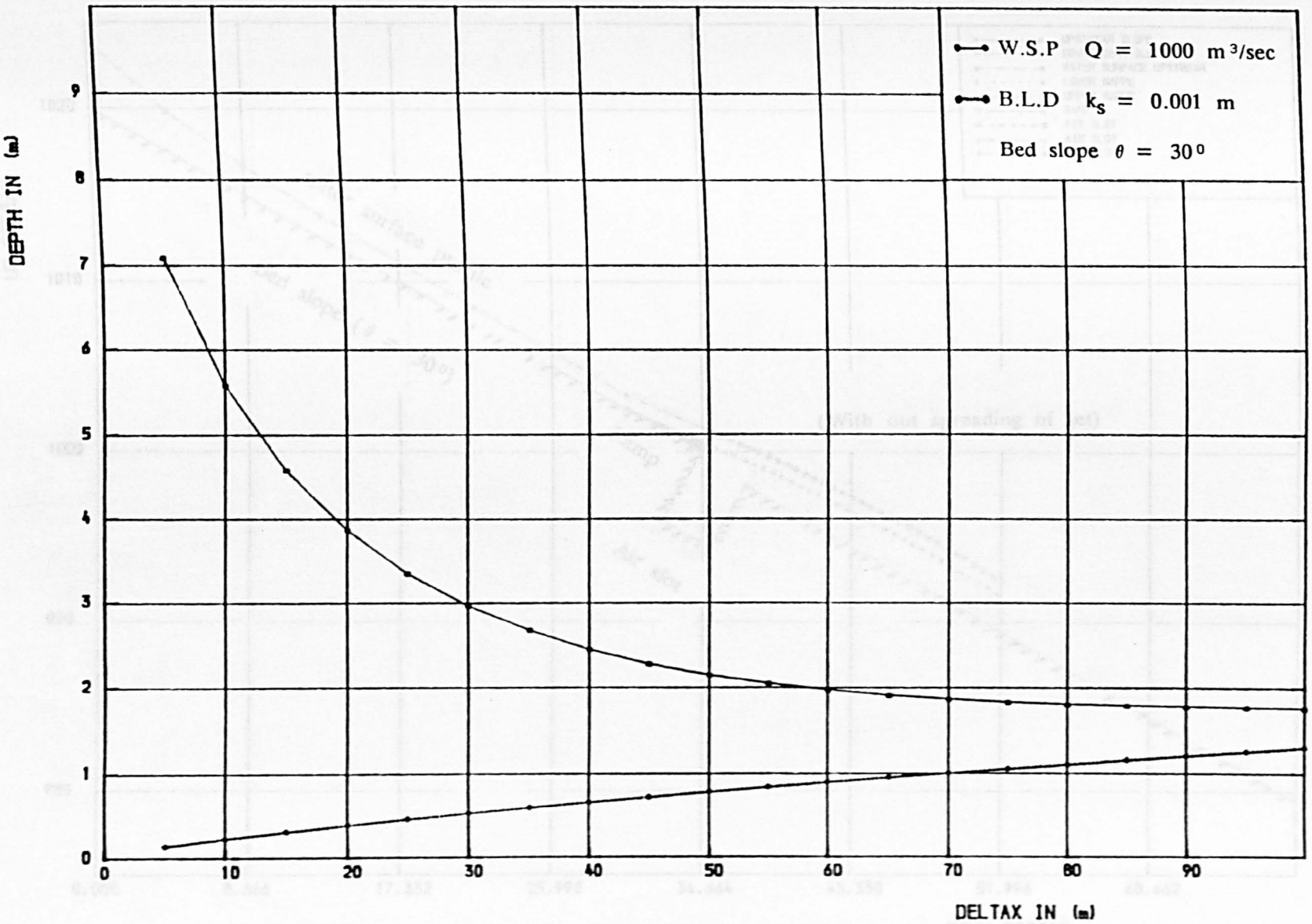

Fig 7.3 Water surface profile & boundary layer development

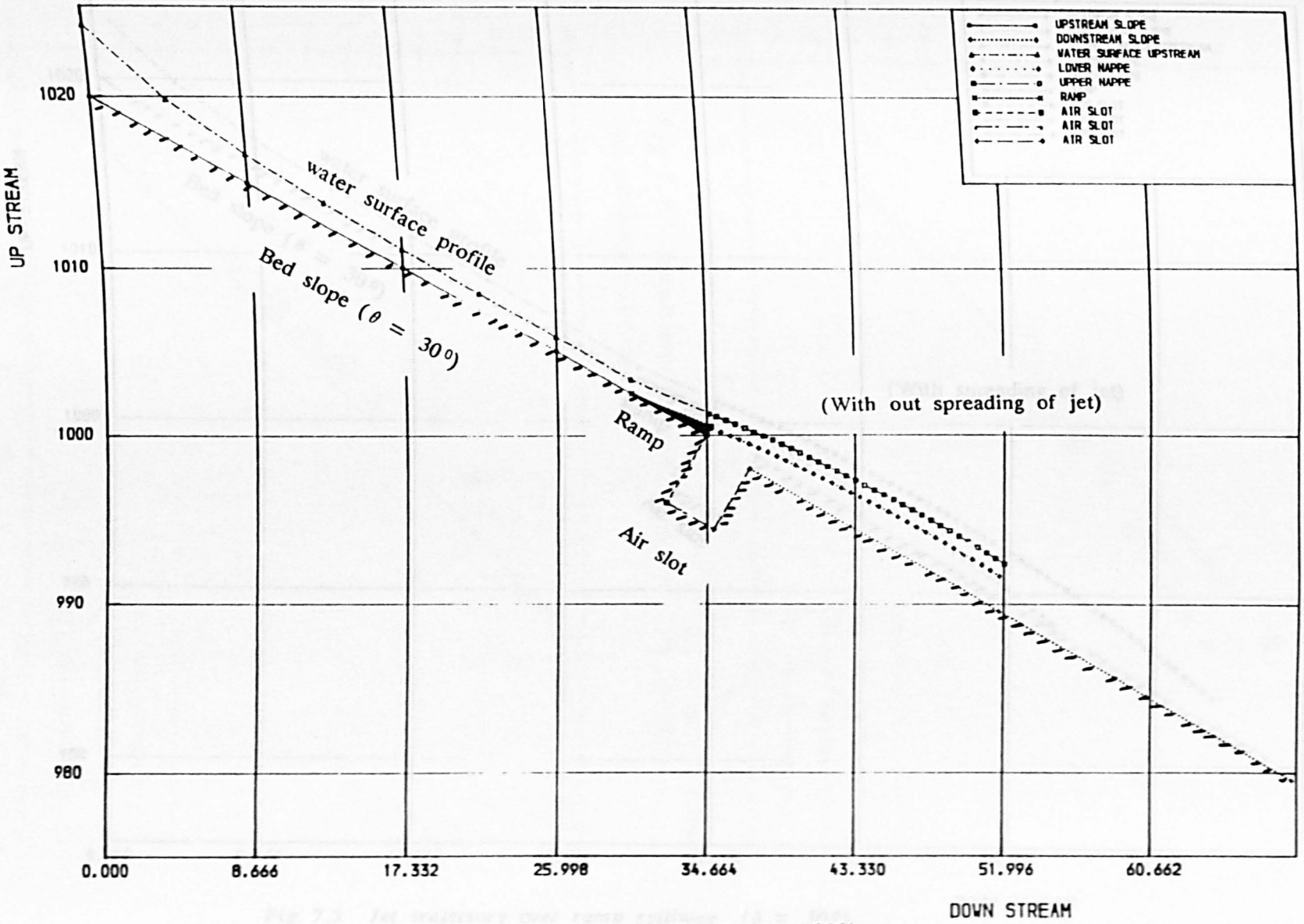

Fig 7.4 Jet trajectory over ramp spillway ($\theta = 30^0$)

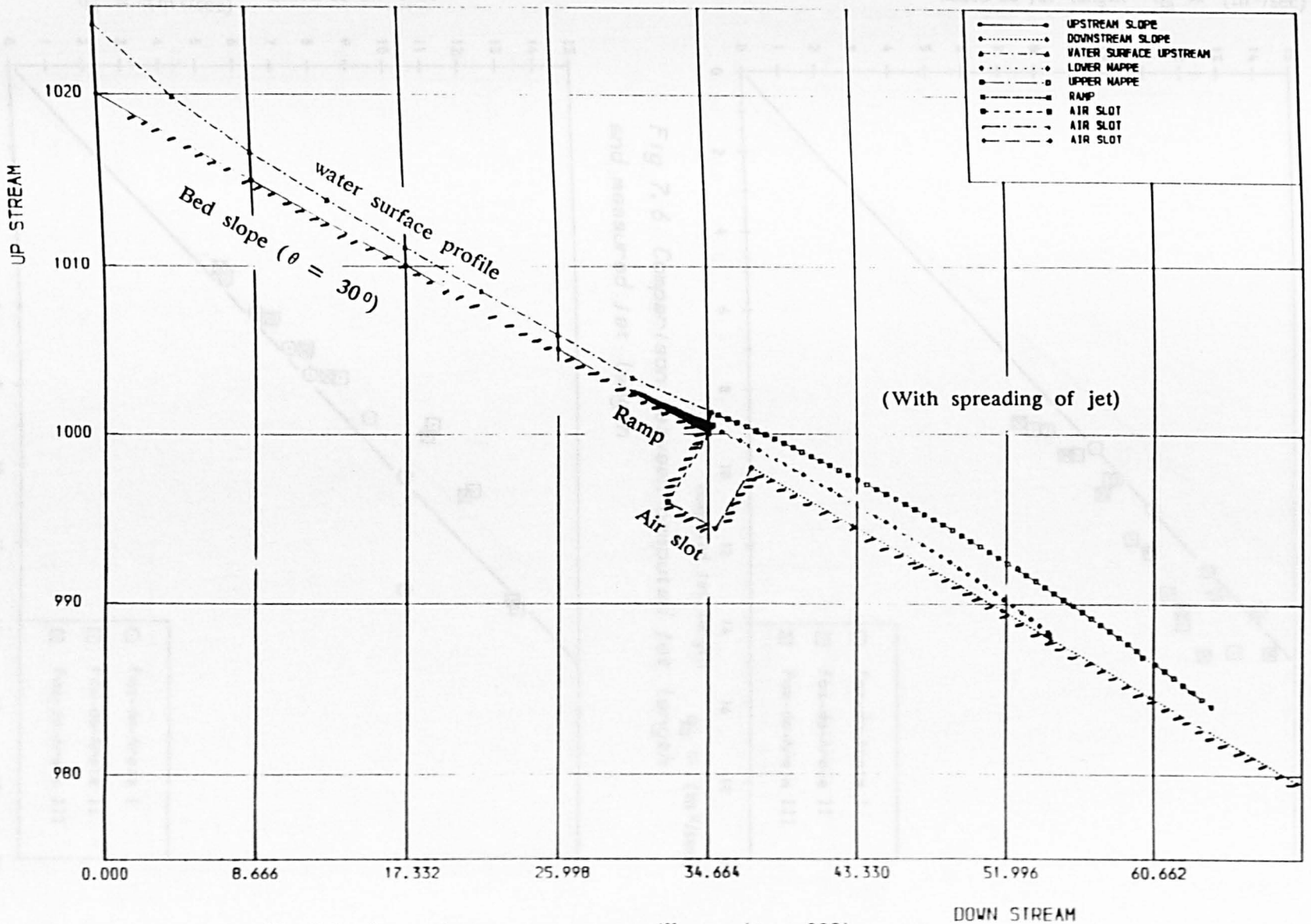

Fig 7.5 Jet trajectory over ramp spillway ($\theta = 30^0$)

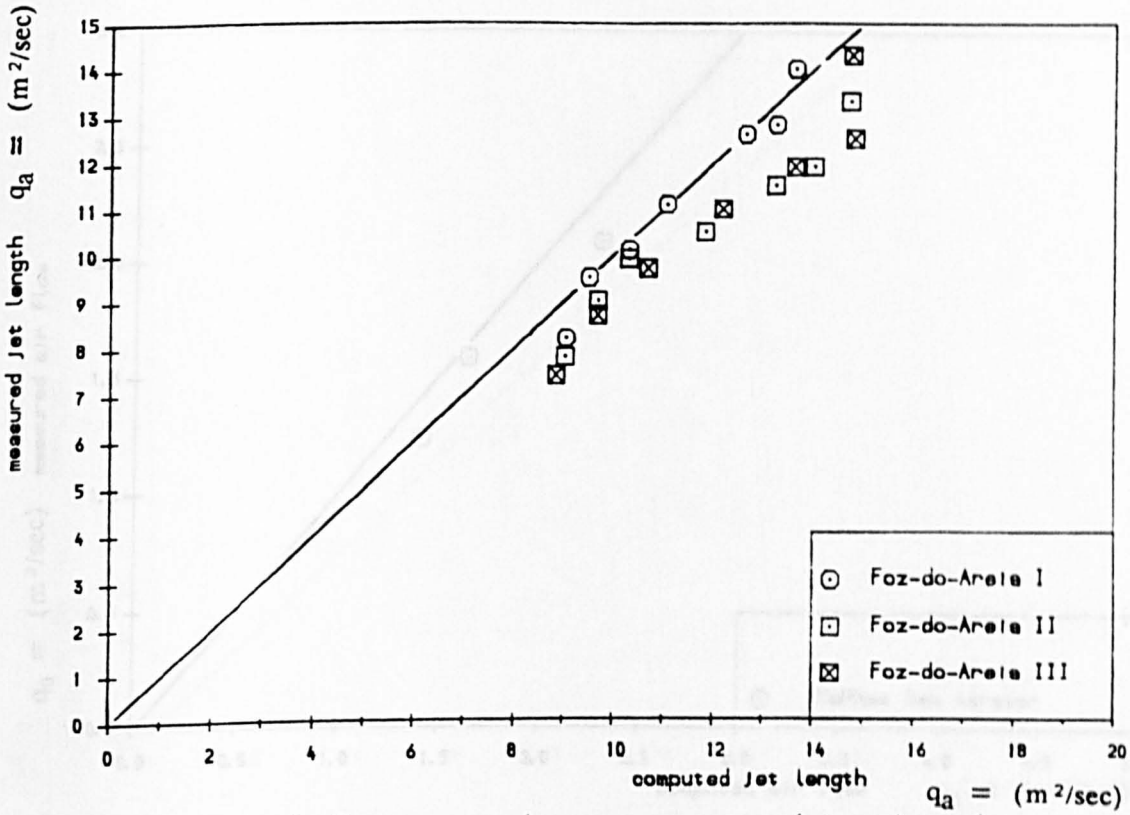

Fig 7.6 Comparison between computed jet length and measured jet length

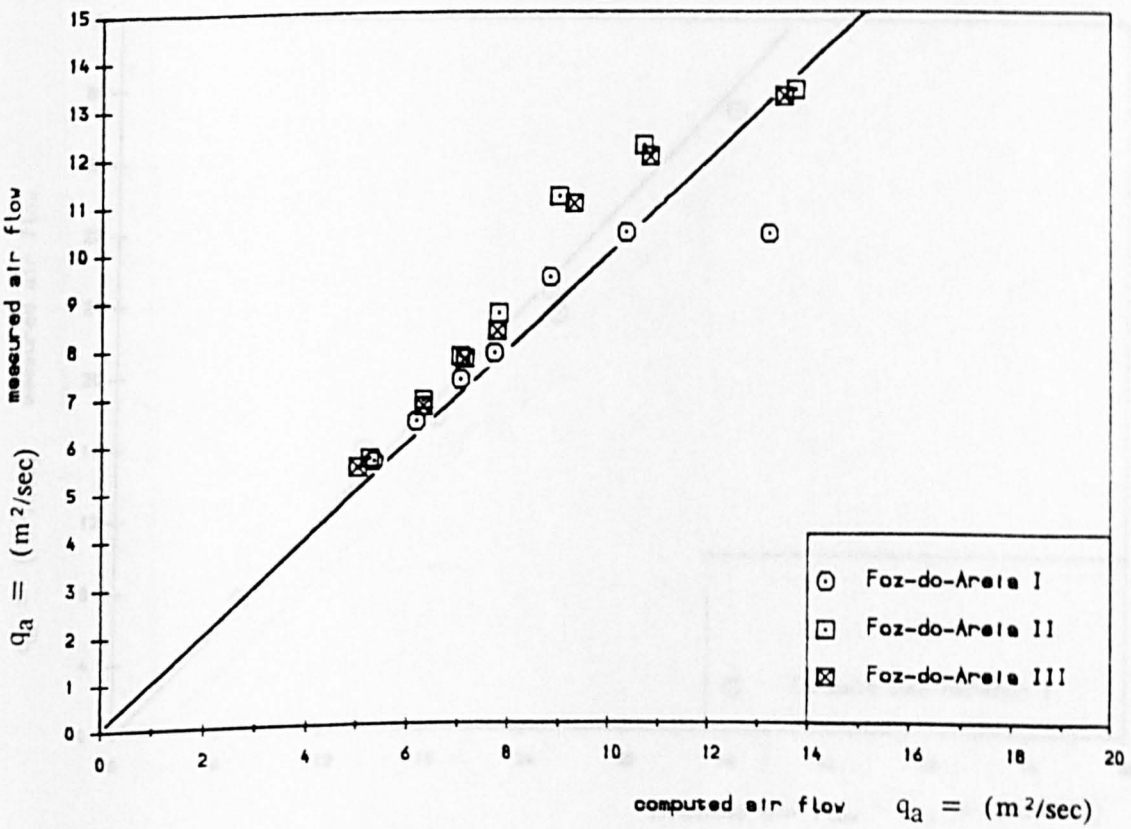

Fig 7.7 Comparison of computed Air flow with measured Air flow

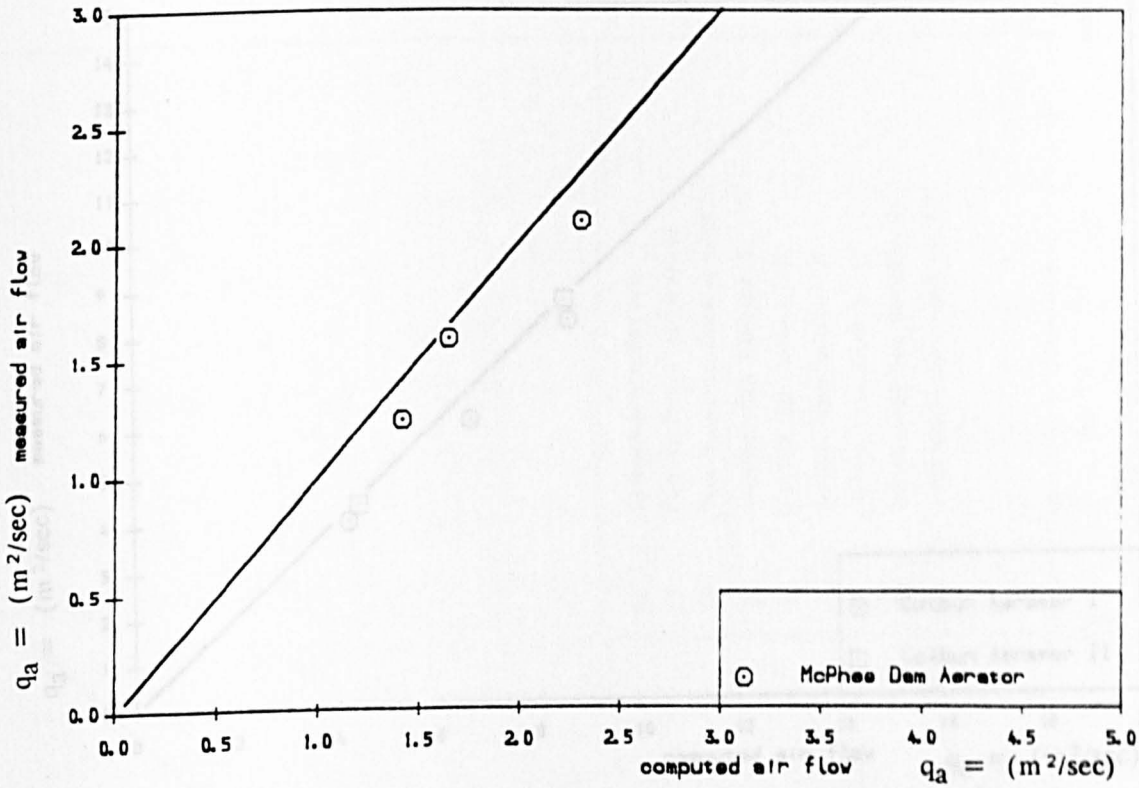

Fig 7.8 Comparison of computed Air flow with measured Air flow

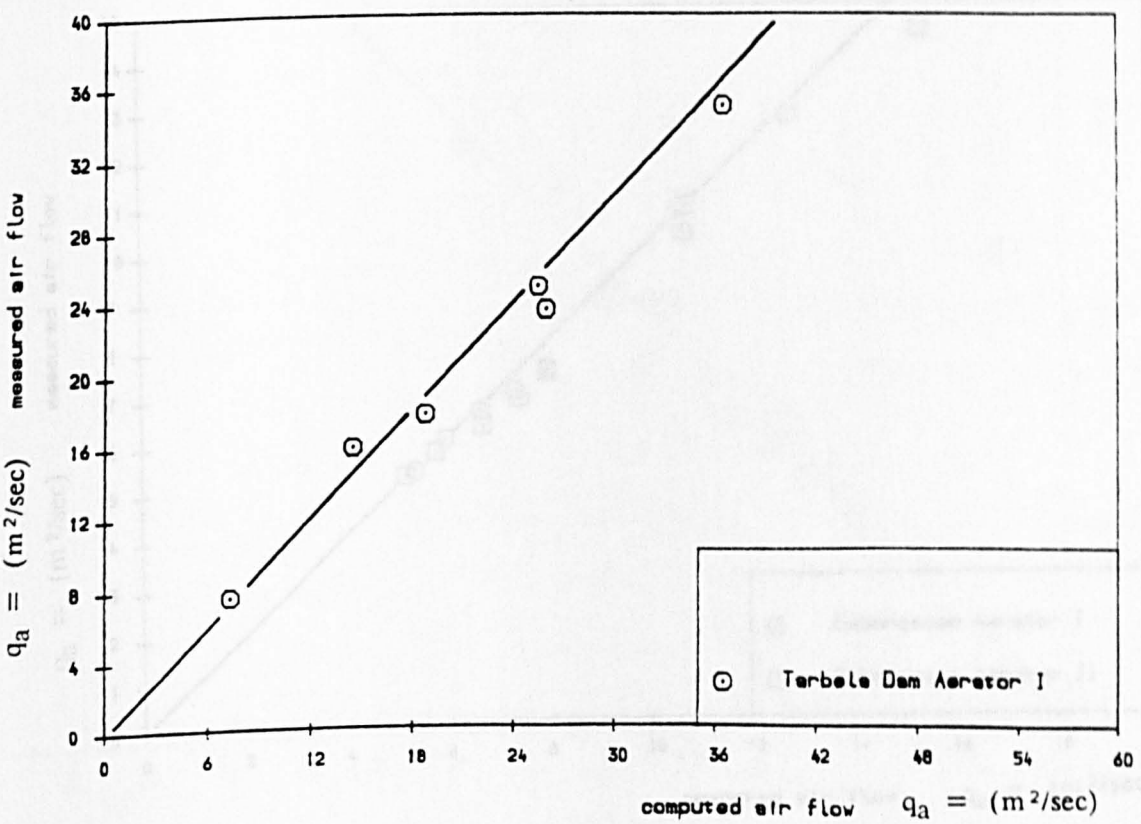

Fig 7.9 Comparison of computed Air flow with measured Air flow

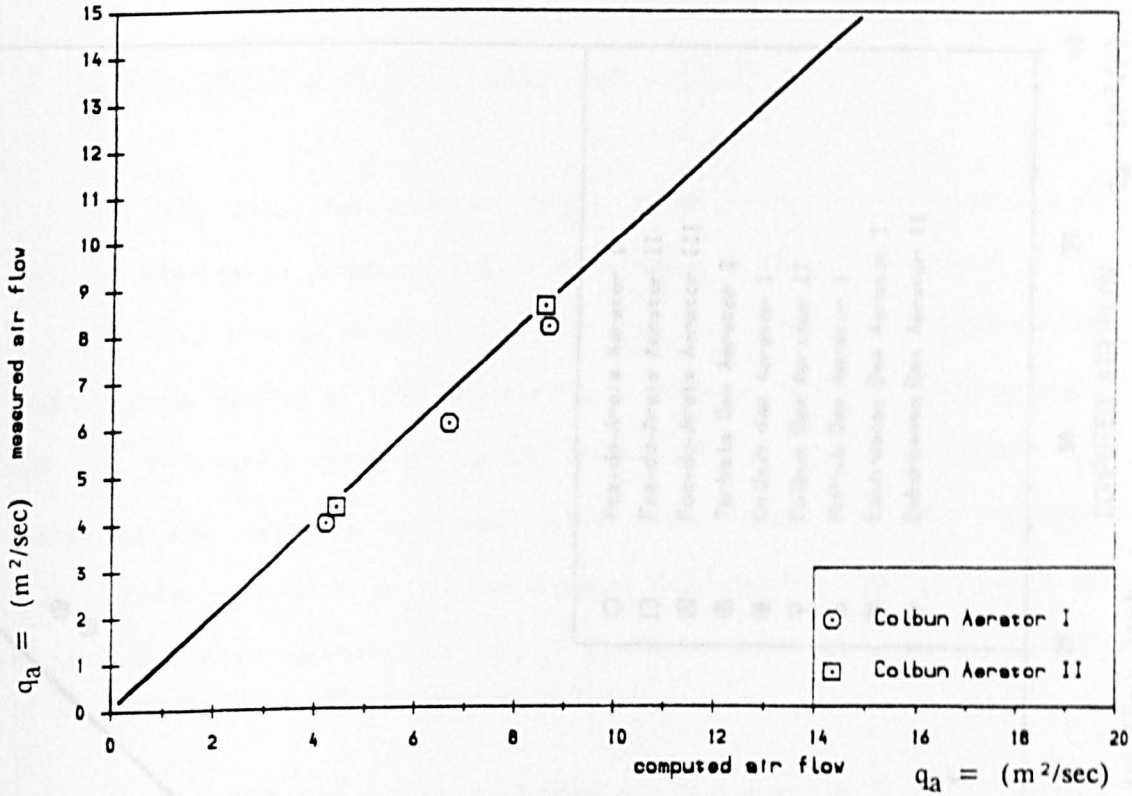

Fig 7.10 Comparison of computed Air flow with measured Air flow

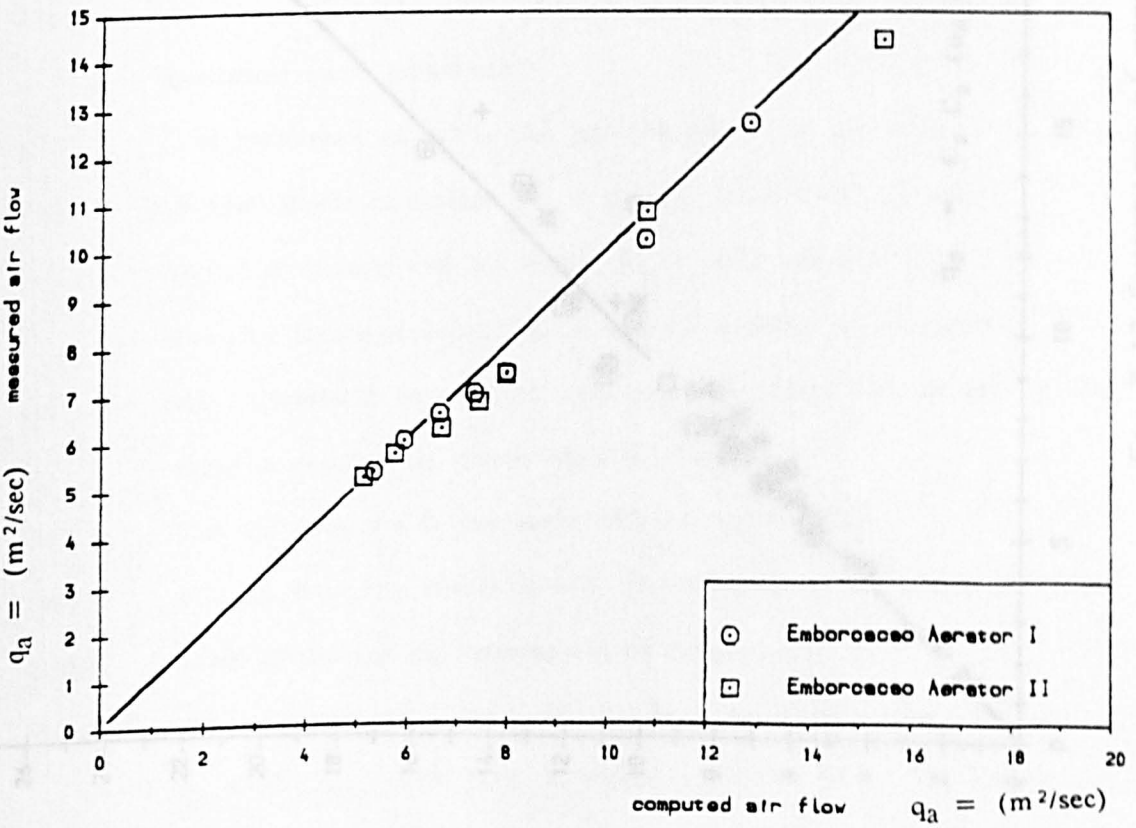

Fig 7.11 Comparison of computed Air flow with measured Air flow

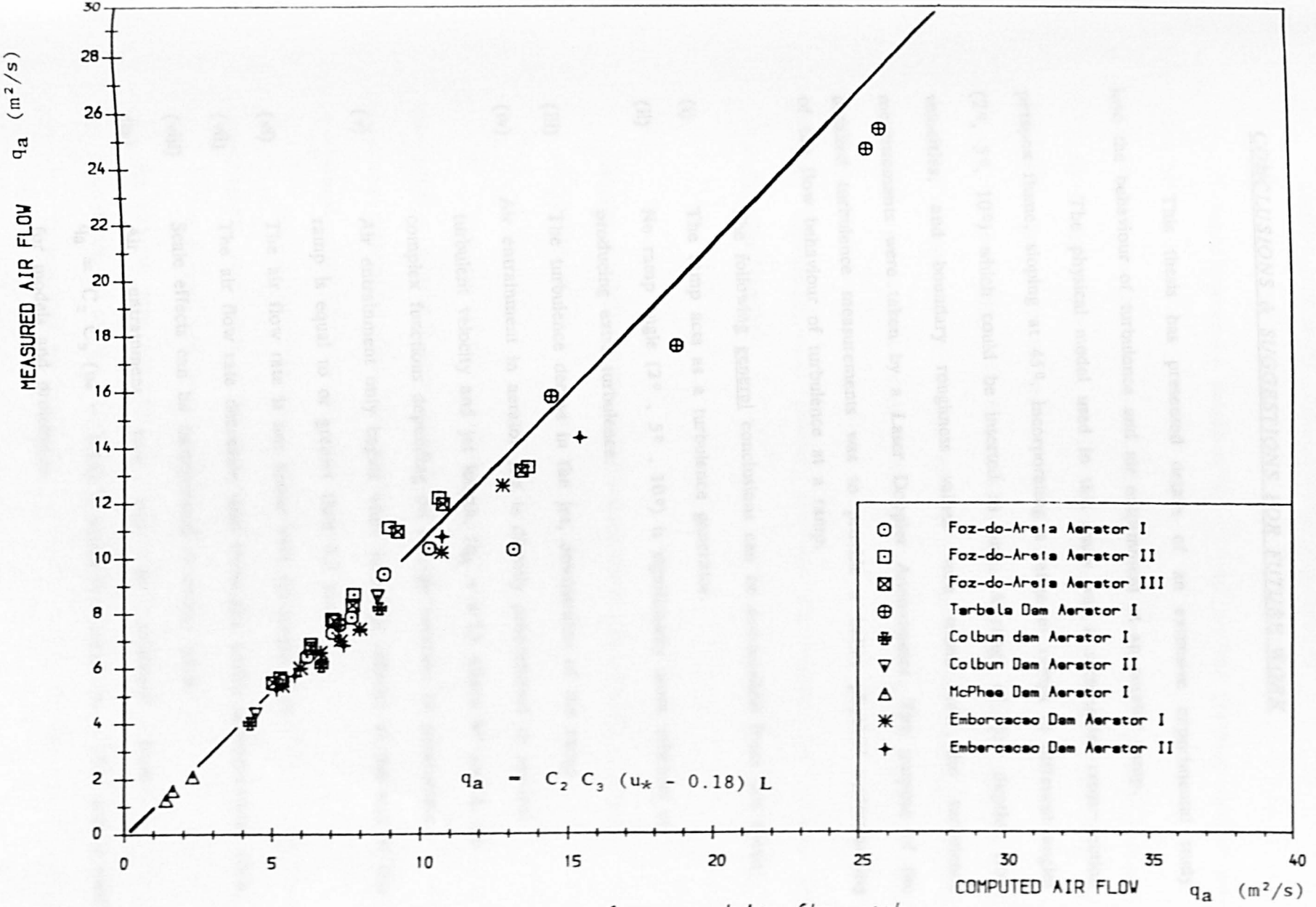

Fig 7.12 Comparison of computed Air flow with measured Air flow

CONCLUSIONS & SUGGESTIONS FOR FUTURE WORK

This thesis has presented details of an extensive experimental study into the behaviour of turbulence and air entrainment at an aerator ramp.

The physical model used in this study was a rectangular cross-section perspex flume, sloping at 45^0, incorporating a range of ramps at different angles (2^0, 5^0, 10^0) which could be inserted in turn. A range of flow depths, flow velocities, and boundary roughness values were tested and the turbulence measurements were taken by a Laser Doppler Anemometer. The purpose of the detailed turbulence measurements was to provide a better physical understanding of the flow behaviour of turbulence at a ramp.

The following general conclusions can be summarised from this thesis.

(i) The ramp acts as a turbulence generator.

(ii) No ramp angle (2^0 , 5^0 , 10^0) is significantly more efficient at producing extra turbulence.

(iii) The turbulence decays in the jet, downstream of the ramp.

(iv) Air entrainment in aerator jets is directly proportional to vertical turbulent velocity and jet length, ($q_a \propto w'L$) where w' and L are complex functions depending on a large numbers of parameters.

(v) Air entrainment only begins when turbulent velocity at the end of the ramp is equal to or greater than 0.3 m/s.

(vi) The air flow rate is not linear with jet length, L/h.

(vii) The air flow rate decreases with increasing cavity underpressure, $\Delta h/h$.

(viii) Scale effects can be incorporated at design stage.

(ix) Air entrainment rate can be predicted from $q_a = C_2\, C_3\, (u_* - 0.18)\, L$ which is accurate to ± 10% and is valid for models and prototypes.

Detailed conclusions from turbulence measurements.

Initial turbulence measurements on the vertical plunging circular jets reveal :–

(i) For the low turbulence nozzle jets, the centre line turbulence increases with jet plunge length. This is due to a redistribution of turbulence from the edge of the jet towards the centre.

(ii) For the higher turbulence orifice jet, the jet centre line turbulence increases initially with jet length, reaching a maximum and decaying thereafter. Atmospheric jet turbulence must eventually decay because velocity gradients decay to almost zero.

(iii) Turbulence values generally increases with velocity, jet diameter and hence Reynolds Number.

Detailed conclusions from turbulence measurements along the spillway, ramp and jet :–

(i) Variation of turbulence with height above the channel bed is flatter than previous subcritical open channel flow measurements. This is connected with turbulence transmitted from the upstream pressure box as well as the steep supercritical nature of the flow.

(ii) Values of turbulence are also higher than previous subcritical measurements, particularly in the case of u'/u more than w'/u.

(iii) The ramp acts as a turbulence generator with values of $w' \simeq 1.35\ u_*$ near the channel base upstream of the ramp, increasing to $w' \simeq 1.75\ u_*$ near the channel base at the end of the ramp.

(iv) Downstream of the ramp, turbulence decays in the jet, the decay

becoming significant at jet lengths (x/h_3) greater than 8 or 10.

(v) Turbulence measurements along the spillway increases with jet velocity, flow depth and Reynolds Number. (observation from circular jet measurements shows that turbulence does not increase significantly for jet velocities greater than 10 – 13 m/s).

(vi) The effect of varying the ramp slope Φ from 2^0 to 5^0 and to 10^0 produces negligible change in the turbulence values generated at the end of ramp.

(vii) Variation of aspect ratio (b/h) of the flow, shows an apparent decrease in turbulence as b/h increases from 1 to 5. This, for the most part, might simply reflect the reduction in flow depth h to produce an increase in b/h. A reducing flow depth h, reduces Reynolds Number and turbulence values.

(viii) Introducing a rougher boundary increases the values of turbulence intensity w'/u by around 15% – 20%, although the value of w'/u* remains largely unchanged.

Main conclusions from air flow measurements at the spillway ramp aerator.

The discussion of air flow data in Chapter 5 has produced a picture of the physical flow behaviour. The physical frame work for air entrainment rate used in this thesis is ($q_a \propto w'L$). This relationship seems deceptively simple, but hides a range of complex interactions. The simplest functional relationship which might be employed in this case would be, air/water ratio = $q_a/q_w = \beta = L/h_3 = f\{\theta, \Phi, Fr, \Delta h/h, w'/u, k_s/h, Re, x/h_3\}$.

The air flow measurements revealed that :–

(i) The jet length ratio L/h_3, varies linearly is with Froude Number at the end of the ramp (section 3).

(ii) A minimum Froude Number (i.e 2 – 4) is required to initiate air entrainment.

(iii) A reduction in jet length (L/h_3) occurs when the value of the cavity underpressure $\Delta h/h$ is increased.

(iv) The rough boundary produces slightly lower jet lengths than smooth boundary because of greater values of turbulent velocity w', and hence greater jet spread.

(v) The air entrainment per unit surface area (q_a/L) is high for short jet length ratios, $L/h < 10.0$, whilst long jets, $L/h > 20$, produce substantially less air entrainment.

(vi) The air entrainment rate reduces with increasing cavity underpressure, $\Delta h/h$.

(vii) Aeration in ramps occur only when certain minimum turbulent velocity is exceeded of the order $w'_{(min)} = 0.3m/s$. This value may be subjected to scale effects.

(viii) The 2^0 ramp angle is more efficient in entraining air, because it produces shorter jet length ratios (L/h).

(ix) The aerator can be made more efficient by introducing extra roughness on the channel bed upstream of the end of the ramp.

A new correlation for air entrainment rate at ramps.

A frame work for aeration uptake at a ramp aerator is proposed in section 6.3 and proved a reasonable correlation both for the results of this work and the results of other model studies from around the world [section (6.4)]. A comparison with prototype field data was carried out in section (6.5) giving an excellent correlation. The frame work for aeration is different from any previously proposed for the following reasons:–

(i) It incorporates the non– linear effect of jet length L/h.

(ii) It is based on knowledge of turbulence generation and decay at a ramp.

(iii) It incorporates a scale effect term which appears to give reasonable correlation between model and prototype.

(iv) It incorporates the effect of cavity underpressure $\triangle h/h$.

The new correlation is based on the equation

$$q_a = C_2 C_3 (u_* - 0.18) L$$

where C_2 represents the effect of jet length, whose value is given in Fig 6.16 and in the table below.

- C_3 represents the effect of cavity underpressure ($\triangle h/h$), and the value of C_3 is shown in Fig 6.19 and in the table below.
- $(u_* - 0.18)$ is based on a minimum turbulent velocity of $w_3' = 0.3$m/s for aeration to commence, hence it is based on the $(w_3' - 0.3)$ term, with a substitution for w_3' in the form $w_3' = 1.75\ u_*$.
- L is the jet length which is either measured by model study, or can now be computed, as described in Chapter 7.
- The computed value of L is based on projectile theory, with allowances for cavity underpressure and jet turbulence w'/u causing jet spread.
- The new correlation for air entrainment produced an accuracy of ± 10% for all prototype data world wide, and comparable order of magnitude for all model data world wide.

L/h values	$f_2(L/h)$ C_2	$f_3(\Delta h/h)$ C_3
0 → 10	1.8	$e^{-4.81\,(\Delta h/h)^{1.575}}$
11 → ∞	$9\,(L/h)^{-0.7}$	$e^{-4.81\,(\Delta h/h)^{1.575}}$

The author has also produced a new model for determining scale effects in aerators outlined in section 6.7. This is based on the ability to predict a synthetic turbulent velocity at each model scale including the prototype scale, and determining how much turbulent velocity above the minimum value of 0.3m/s exists at each scale. This produces a scaling term ($w_a' - 0.3$), when turbulent velocity is computed in the air bubble size range.

Suggestions for future research

(i) It should be noted that one key area of aerator research was not attempted because of the time constraint. That was, the behaviour of entrained air bubbles in the flow; the decrease in air concentration; (including diffusion– advection of air bubbles in the flow), the decrease in air concentration near the solid boundary downstream of an aerator; and what distance apart to place the next aerator. This work needs full physical and numerical modelling.

(ii) In this research only one spillway slope was used which produced a narrow range of velocities, aspect ratio and Reynolds Number. Further studies are required to extend the range of velocities $\bar{u}$, bed slope θ, and length of the channel up to the ramp L_{gr}.

(iii) Another key area is that of the influence of the free surface aeration which enters the flow from the upper free surface of the aerator jet. This process usually occurs due to turbulence from the ramp being transmitted to the free surface, which in turn entrain air, and may introduce as much air on the upper surface as the lower.

(iv) Further work is required to produce a comprehensive numerical modelling package which will analyse aerators in detail, including bubble dynamics, but will also fit into a general spillway numerical package generally used by Consulting Engineers.

(v) There would be some advantage in prototype turbulence measurements being done at one aerator with a view to comparing with turbulence in models at various model scales at the prototype, investigating the link between w' and air flow q_a at various scales, and looking at the value of $w'_{(min)} = 0.3$m/s at various scales including prototype.

REFERENCES

AHMED, A.A. (1981)
"Aeration in Hydraulic Structures" Int. Report: Department of Civil Engineering, University of GLASGOW. April 1981.

AHMED, A.A. ERVINE, D.A. & McKEOGH, E.J. (1984)
"The process of aeration in closed conduit hydraulic structures." Proc: Symp. of Scale Effects in Modelling Hydraulic Structures, Paper 4.13, Esslingen, Germany. Sept. 3–6.

ABELEV.A.S et al (1983)
"Methods de calcul de I'aeration d'un encoulenment dans les Projects de deversiors". Proc XXth IAHR Congress, Moscow, Vol 7, Sept. 5–9. pp 361 – 365.

ACKERS, P & PRIESTLEY, S.J (1985)
"Self aerated flow down a chute spillway" 2nd Int. Conf. on Hydraulics of Floods and Flood control, BHRA, Cambridge, England, pp 1–16.

ALBERTSON, M.L., DAI, Y.B., JENSEN, R.A., and ROUSE, H. (1948)
"Diffusion of Submerged Jets." Proc. A.S.C.E., Vol 74, pp 639 – 663

ANDERSON, A.G (1965)
"Influence of channel roughness on the aeration of high velocity, open–channel flow." Proc: XIth IAHR Congress Leningrad, Vol 1, paper 37.

ARNDT; R.E.A, HOLL,J.W, BOHN, J.C, BECHTEL, W.J (1979)
"Influence of surface irregularities on cavitation performance" Jnl of Ship Research, Vol 23, No 3, Sept. pp 157 – 170.

AVERY, S.& NOVAK. (1978)
"Oxygen transfer at hydraulic structures" Jnl of Hydraulics Division. American Society of Civil Engineers.November.

BABB, A.F et al. (1973)
"Air flow in a combined intake & shaft spillway" Proc of American Society of Engineers Vol.99. HY. 7, July.

BABB, A.F et al. (1981)
"Measurment of air in flowing water" Jnl of Hydraulics Division December. Proc. Paper 16742. HY12 pp.1615 to 1630.

BALL, J.W. (1976)
"Cavitation from surface irregularities in high velosity" Jnl of Hydraulics Division (A.S.C.E), Vol.102, HY9 Proc. Paper 12435.September, pp1283 to 1297.

BALL, J.W. (1963)
"Construction finishes & high–velocity Flow" Jnl of Construction Division (A.S.C.E) Vol.89, Proc. Paper

3646. September. pp 91 to 110

BALL, J.W. (1970)
"Hydraulic model studies spillway & high level outlet works" Mica Dam Canada, Report Western Canada Hydraulics Laboratory.April.

BARON, T. (1949)
"Technical Report" University od Illinois, No. 4 (Prepared under contract N–6–ORI–71, Task Order No.XI, ONR Navy Dept.)

BATCHELOR, G (1959)
"The theory of homogenous turbulence" Cambridge University Press London.

BALL, J.W, et al (1975)
" Predicting cavitation in sudden enlargements" Jnl of Hydraulics Division,(A.S.C.E) Proc. Paper 11442.July. pp 857 to 870.

BAUER, W.J. (1954)
"Turbulent boundry layer on steep slopes." Transaction American Society of Civil Engineers Vol.119, pp.1212–1233.

BAXTER, A.M. (1955)
"Air entrainment by fluid jets and stream." Ph.D. Thesis. University of GLASGOW. 1955.

BEICHLEY, G.L. (1973)
"Hydraulic Model Studies of Chute Offset,Airslots and Deflector from High Velocity Jet" United States Bureau of Reclamation.REC–ERC–73–5.1973.

BEICHLEY, G.L. & KING, D.L. (1975)
*"Cavitation control by aeration of high velocity jets."*Jnl of Hydraulics Division (A.S.C.E) Vol.101. Proc. Paper 11462 No.HY7. July, pp 829– 846.

BIN, A.K (1984)
"Air Entrainment by plunging liquid jets" Symposium on Scale Effects in Modelling Hydraulic Structures, Esslingen Germany. September 3–6. Edit (H.Kobus)

BLAISDELL, F.W. (1974)
"DISCUSSION" (On air flow in combined intake & shaft spillway.) Jnl of Hydraulics Division American Society of Civil Engineers,August, pp:1172 to 1175.

BRADLEY, J.N (1945)
"Study of air injection into the flow in the Boulder Dam spillway tunnel Boulder Canyon Project" Bureau of Reclamation Report No. HYD – 186.

BROWN, F.R. (1963)
"Cavitation in hydraulic structures: Problem created by cavitation phenomena." Jnl of Hydraulics Division. (A.S.C.E) Vol:89. Proc. Paper 3343. HY 1.pp: 99 to 112.

BRUSCHIN,J. (1984)
"Aeration offsets–for spillway chutes and bottom outlets" Symposium on Scale Effect in Modelling Hydraulic Structures. Editor (H.Kobus). Esslingen Germany. September 3–6.pp:4.3–1 to 4.3–4.

BRUSCHIN, J (1985)
"Hydraulic modelling at the Piedra del Aguila Dam " Water Power and Dam construction, Vol.37, Jan, pp 24–28.

BRUSCHIN, J. (1987)
"Froced aeration of high velocity flow." Jnl of Hydraulics Research, Vol.25. No:1.pp 5–14.

CAIN, P. &. WOOD, I. R. (1981)a
*"Instrumentation for measurment in self aerated flow on spillways."*Jnl of Hydraulics Division (A.S.C.E). Vol.107, HY11, November. pp 1404–1424.

CAIN, P. &. WOOD, I. R. (1981)b
"Measurment of self aerated flow on spillway." Jnl of Hydraulics Division.(A.S.C.E). Vol.107, HY11, November. pp:1425 – 1444

CAMPBELL, F.B. & ROBERT, G.C (1965)
"Boundary layer development and spillway energy losses." Jnl of Hydraulics Division,(A.S.C.E) Vol.91.Proc. Paper:4331.No:HY3 pp:149 to 163.

CASSIDY, J.J. & ELDER R.A (1983)
"Spillways of high dams" Developments in Hydraulics Engineering–2, Elsevier Applied Science Publishers, London. New York. pp:159 – 182.

CASTELEYN, J.A VAN GROEN, P & KOLKMAN, P.A. (1977)
"Air entrainment in siphons: Results of tests in two scale models and an attampt at extrapolation" 17th Congress of IAHR, Baden–Baden, Germany. Nov.15 –19.

CELIK, I and RODI, W (1984)
"Simulation of free surface effect in turbulent channel flows" PhysicoChemical Hydrodynamics, Vol 5 pp 217–227.

CHANSON, H (1988)
"Study of air entrainment and aeration devices on spillway model" Research Report 88–8, October University of Canterbury Christchurch, New Zealand.

CHEN, T.F and DAVIS, J.R (1964)
"Disintegration of a turbulent water jet" Journal of Hydraulics Division, A.S.C.E Vol 90, No. HY1, pp 175–206.

CHOW, V.T (1959)
"Open channel hydraulics" McGraw Hill Edition.

CLARK, J.A (1968)
"A study of incompressible turbulent boundary layer in channel flow" Transaction of ASME, Journal of Basic

Engineering pp 445– 468.

COLES, D. (1978)
"A model for flow in the viscous sublayer" Workshop on Coherent Structure of Turbulent Boundary Layers, Lehigh University Bethlehem. Pa.

COLGATE, D.M, ELDER, R. (1961)
"Design considerations regarding cavitation in hydraulic structures" 10th Hydraulics Division Conference A.S.C.E Urbana Illinois, August 16 – 18.

COLGATE, D.M (1971)
*"Hydraulic model studies of aeration devices for Yellow Tail Dam spillway tunnel Pick Sloan Missouri Basin Program, Montana."*U.S Bureau of Reclamation, Report:REC– ERC– 71– 47

COLGATE, D.M (1977)
"Cavitation damage in hydraulic structure" Intern Conf on Wear of Materials, St.Louis, MO, pp 433– 438.

COMOLET, R. (1979)
"ON the movement of a gas bubble in a liquid." La Houille Blanch, No:1. pp:31 to 42.

CUMMING, I.W (1975)
"The impact of falling liquids with liquid surfaces" Ph.D. Thesis, Loughborough University of Technology.

DAILY, J.W, JOHNSON, V.E. (1956)
"Turbulence and boundary layer effect on cavitation inception from gas nuclei" Trans: of American Society of Mech: Engg, Vol 78, pp 1695 – 1706.

DATTA, R.L, NAPIER, D.H & NEWITT, D.M (1950)
"The properties and behavior of gas bubble formed at a circular orifice." Trans of Chemical Engineers Vol:28.

DAVIES, J.T (1972)
"Turbulence Phenomena" Publisher Academic Press Inc. New York.

DeFAZIO, F.G & WEI, C.Y (1983)
"Design of aeration devices in hydraulic structures" Hydraulics Division Specialty Conf (A.S.C.E) Cambridge, MA. August.

ECCHER, L.&. SIEGENTHALER, A. (1982)
"Spillway Aeration of San Roque Project." Intern Water Power & Dam Construction, September. pp:37 to 41.

ELSAWY, E.M. &. McKEOGH, E.J (1977)
"Study of self aerated flow with regard to modelling criteria Proc. I.A.H.R 17th Congress, A60 Baden– Baden, August 15– 19

ERVINE, D.A. &. FALVEY, H.T (1987)
*"Behavior of turbulent water jet in the atmosphere and in plunge pools."*Proc. I.C.E, Part.2. Vol 83, March.

ERVINE, D.A. (1987)
DISCUSSION "On forced aeration of high velocity flow." by BRUSCHIN. (Unpublished).

ERVINE, D.A. &. ELSAWY, E.W (1975)
"The effect of a falling nappe on river aeration" Proc. 16th Congress I.A.H.R Sao Paulo, Brazil. July paper C45.

ERVINE, D.A. (1976)
"The entrainment of air in water." Intern Water Power & Dam Construction Dec. pp 27– 30.

ERVINE, D.A, McKEOGH, E.J, &. ELSAWAY, E.W (1980)
"Effect of turbulent intensity on the rate of air entrainment by plunging water jet." Proc:I.C.E part 2, Vol 69, June pp 425– 445.

ERVINE, D.A. (1980)
"A study of air ventring and cavitation in the M'Dez overflow spillway Morocco. Intern. Report S370, September. Delft Hyd Lab:

ERVINE, D.A. (1985)
"Two Phase Flow in Hydraulic Structures." A Lecture Series Presented to the Bureau of Reclamation, July.

ERVINE, D.A, McKEOGH, E.J & ELSAWY, E.M (1981)
"Model Prototype conformity in hydraulic structures involving aeration." Proc. 19th Intern Congress New Delhi India, Feb. Vol:5 pp. 65 – 72.

ERVINE, D.A. (1985)
*"A Review of Bubbly and Air Pocket Flow in Civil Engineering Hydraulic Structures."*A Series of Lectures Presented to the United States Bureau of Reclamation, Denver. July.

ERVINE, D.A & KHAN, A.R (1991)
"Turbulence measurements in an airslot ramp aerator" XXIV IAHR Congress 9 – 13 Sept: Madrid, Spain.

FALVEY, H.T & ERVINE, D.A (1988)
"Aeration in jets and high velocity flows" Model– Prototype Correlation of Hydraulic Structures, Proc. of Intern Symposium Colorado. August 9– 11.

FALVEY, H.T. (1990)
"Cavitation in chutes and spillways" United States Bureau of Reclamation, Engineering and Research Centre, Denver, Colorado. April "Monograph 42."

FALVEY, H.T (1980)
"Air–water flows in hydraulic structures" Bureau of Reclamation, Engineering Monograph No. 41, 143 pp. Dec.

FALVEY, H.T. (1982)
"Predicting cavitation in tunnel spillway" Intern Water Power & Dam Construction, Vol 34 August. pp 13 – 15.

FASSO, C. (1955)
"Experimental research on air entrainmen in gated outlet works. " Proc. I.A.H.R Proc. of General Meeting, The Hague. Vol 3.

FRIZELL, W (1988)
"Two dimensional air flows under an aerator nappe". Private communication to Dr D.A.Ervine.

FRIZELL & PUGH. (1988)
"Chutes spillway aerators McPhee Dam Model/ Prototype comparison" Symposium on Model– Prototype Correlation of Hydraulic Structures, ASCE August 9–11 pp 128 – 137.

GALPERIN et al (1977)
"Cavitation on hydraulic structures" Energia 10 Shiluzovaia Naberezhnaia, Moscow. M–114, 113114,(USBR translation)

GANGADHARAIAH,T.RAO, LAKSHMAN,N.S.& SEETHARAMIAH, K (1971)
"Inception and entrainment in self aerated flow." Journal of Hydraulics Division.(A.S.C.E) Vol:96 Proc. Paper 7427. No. HY 7 pp 1549 – 1564

GLAZOV,A.I. (1985)
"Calculation of the air capturing ability of a flow behind an aerator ledge." Hydrotechnical Construction, Plenum Publishing Corp., Vol18, No 11, pp 554 – 558.(Russian Translation).

GOLDRING, B.T (1979)
"The use of small–scale siphon models." Proc: I.C.E part 2, December pp 929 – 942.

GORTLER, H (1945)
"Berechnung von aufgaben der freien turbulenz auf grundeinez neuen Naherungsansatzes" Z.A.M.M. 22, pp 244 – 254

GRANT, R.P. &. MIDDLEMAN, S. (1966)
"Newtonian Jet Stability" American Institute of Chemical Engineering Journal, Vol 12 No. 4. pp 669 – 678.

HABERMAN, W.L.&. MORTON, R.K (1954)
"An experimental study of bubble moving in liquid " Proc: of A.S.C.E Vol:80, pp 379 – 427.

HAENLEIN, A. (1932)
"N.A.C.E. Technical Memo." No. 659. 1932.

HAINDL, K. (1984)
"Aeration of hydraulic structures." Chapter 3 Development in Hydraulic Engineering–2. Edited by P.Novak London, New York. pp 113 – 158.

HALL, L.S. (1943)
"Entrainment of air in flowing water." Open Channel Flow. Symposium Trans A.S.C.E, Vol:108. pp 1394 – 1434.

HAMILTON, W.S. (1983)
"Preventing cavitation damages to hydraulic structures." Intern Water Power & Dam Construction. November pp 40 – 43 Dec pp 48 – 50

HECKER, (1988)
"Private communication", Alden Laboratories Cambrigde MA, U.S.A

HENDERSON, J.B, McCARTHY, M.J, and MOLLOY, N.A. (1970)
"Entrainment by Plunging Jets" Proc. of Chemeca'70, Melbourne, Sec. 2. 1970, pp. 86 – 100.

HICKOX, G.H. (1939)
*"Air Entrainment on Spillway Faces."*Jour of Hydraulics Division, A.S.C.E Vol: 9 pp 89 – 96.

HINO,MIKIO. (1958)
"On the mechanism of self aerated flow on steep slopes channels. " Application of Statical theory of Turbulance. I.A.H.R, 9th Convention Dubrounik Yugoslavia, September pp 327 – 330.

HINZE, J.O et al (1949)
"Transfer of heat and matter in the turbulent mixing zone of an axiallry symmetrical jet". Journal Applied Science Research Al. pp 435 – 461.

HOLL, J.W. (1960)
"The inception of cavitation on isolated surface irregularities." Journal of Basic Engg: Transaction of American Society of Mechanical Engineering March pp 169 – 183.

HORENI, P. (1956)
"Disintegration of a free jet of water in air" Byzkumny ustav vodohospodarsky prace a studie, Sesit 93, Praha – Podbaba.

HOYT, J.W, and TAYLOR, J.J. (1977)
"Turbulence structure in a water jet discharging in air", The Physics of Fluids, Vol.20, No.10, Pt.11.

HUNT, J.C.R (1984)
"Turbulent structure and turbulent diffusion near glass liquid interface" Gas Transfer of water surface. pp 67–82 D.Reidel Publishing.

JEVDJEVICH, V. (1953)
"Entrainment of air in flowing water and technical problems connected with it." Proc. I.A.H.R Minieapolis, MN, pp 439 – 454.

JIN, T. LIU, C. LIU, X. (1980)
"Cavitation inception of gate slots." Department of Hydraulics Water Conservancy and Hydro electric Power, Scientific Research Institute, Beijing China.

KALINSKE, A.A & ROBERTSON, J.W (1943)
"Entrainment of air in flowing water–closed conduit flow"

Trans. A.S.C.E, Vol 108, pp 1435 – 1447

KARAKI, S. STEVENS, M.A. &. BRISBANE, T.E (1977)
"Air slots for end of gate chamber tunnel 3.&.4." Hydraulics Model studies, Colorado State University Fort Collins, Report No CER–76–77–SK–33.

KARAKI, S.et al. (1983)
"Performance of air slots in high velocity chutes at Tarbela tunnel outlet works." A separate paper Frontier in Hydraulics Engineering.(A.S.C.E) Massachuttus,(M.I.T) Boston Society of Engineers 9 – 12 August, Cambridge Massachuttus.

KATZ, J. (1984)
"Cavitation phenomena with in regions of flow separation" Journal of Fluid Mechanics, Vol 140, pp 397 – 436.

KELLER, R.J.&. RASTOGI, A.K (1977)
"Design chart for predicting critical point on spillways." Jnl of Hydraulics Division Proc A.S.C.E Vol 103, HY 12 December pp 1417 – 1429.

KENN, M.J.&. ZANKER, K.J (1967)
"Aspects of similarity for air entering water flows." Nature: Vol 213 (No 5071) January.

KENN, M.J.&. GARROD, A.D (1981)
"Cavitation damages and the Tarbela tunnel collapse of 1974." Proc. I.C.E, Part 1, Vol 70, Feb pp 65 – 89.

KNAPP, R.T. (1952)
"Cavitation mechanism and its relation to the design of hydraulic equipment" Proc Inst. Mech. Engrs, A Vol 166 pp 150 – 163.

KNAPP, R.T. DAILY, J.W. and HAMMILT, F.G (1970)
" Cavitation " McGrawhill Intern: New York. 1970

KOBUS, H.&. RAO, L. (1975)
"Characteristics of Self Aerated Flow." 1915. Ench Schmidt Verlay, Berlin & Bicleteld, Germany.

KOBUS, H. (1984)
"Local air entrainment & detainment." I.A.H.R Symposium on Scale Effects in Modelling Hydraulics Structures, Esslingen am Neckar, Germany Sept 3 – 6. paper 4.10 pp 1 – 10.

KOMORI, S. et al (1982)
"Turbulence structure and transport mechanism at the free surface in an open channel flow" Intern Journal Heat Mass Transfer, Vol 25 pp 513 – 522.

KOSCHITZKY, H.P. WESTRICH, B.&. KOBUS, H. (1984)
"Effects of model configuration flow conditions and scale in modelling spillway aeration grooves" I.A.H.R Symposium on Scale Effects in Modelling Hydraulic Structures, Esslingen am Neckar, Germany Sept 3 – 6. paper 4.4 pp 1 – 5.

LAI, K.K. (1971)
"Studies of air entrainment on steep open channel." M.Sc Thesis presented at the University of South Wales,at Sydney, Australia.

LAUFER, J. (1954)
"The structure of turbulence in fully developed pipe flow" Report 1174, U.S Nat. Adv. Com. Aerodynamics.

LEVIN, L (1965)
"Calcul hydraulique des conduits d'aeration des vidanges de fond et dispositifs d'eversants." La Houille Blanche, No 2 pp 121 – 126.

LESLEIGHTER, E.J. (1983)
"Prototype measurment and model simulation of cavitation in high head gated outlets." I.A.H.R Congress Moscow, Vol 1 part 1 September.5 – 9 .

LOCHER, F.A.
"Energy dessipation at high dams." Chapter 5 Development in Hydraulic Engineering–2.London. New York. Editor (P.Novak)

LOW, H.S (1986)
"Model studies of Clyde dam spillway aerator". M.Sc thesis submitted at the University of Canterbury, New Zealand.

LOWE, J. BANGASH, H.D.&. CHAO, D.C (1979)
"Some experience with high velocity flow at Tarbela Dam Project." 13th Intern Congress on large Dams New Delhi, India. Vol III paper Q50, R13. pp 215 – 247

LOWE, J. CHAO, P.C (1979)
"Tarbela service spillway plunge pool developments." Intern Water Power & Dam Construction.November, pp 85 – 90.

MARCANO, A.&. CASTILLEJO, N. (1984)
*"Model prototype comparison of aeration devices Guri Dam Spillway."*I.A.H.R Symposium on Scale Effects in Modelling Hydraulics Structures, Esslingen am Neckar, Germany Sept 3 – 6. paper 4.6 pp 1 – 5.

MAY, R.W.P. (1987)
"Cavitation in hydraulic structure" Research Report SR 79 River Engineering Dept, of Hydraulics Rearch Wallingford, U.K.

MAY, R.W.P. (1989)
"Performance of aerator dam spillway" Research Report SR198 River Engineering Dept, of Hydraulics Rearch Wallingford.

McCARTHY, M.J. and MOLLOY, N.A. (1974)
"Review of stability of liquid Jets and the influence of nozzle design". Chemical Engineering Journal, Vol 7 pp 1–20.

McKEOGH, E.J. (1978)
"Air Entrainment by plunging water Jets". Ph.D. Thesis.

The Queen's University Belfast, Oct.1978.

McKEOGH, E.J.&. ERVINE, D.A (1981)
"Air entrainment rate and diffusion patter of plunging liquid jets." Journal Science.Vol: 36.June pp 1661 to 1171.

MULLIN, T. (1989)
"Chaos in Turbulent flows" Research Report Deptarment of Physics, University of Oxford, 1989.

NAKAGAWA, H, NEZU, I. & UEDA, H. (1975)
"Turbulence of open channel flow over smooth and rough beds" Proc. Japan Society of Civil Engineers No 241, pp 155–168

NEZU, I. and RODI, W. (1986)
"Open channel flow measurements with Laser Doppler Anemometer". Journal of Hydraulics Engineering ASCE Vol 112 No.5, May pp 335 – 355.

PAN, S.&. SHAO, Y. (1984)
"Scale effect in modelling air demand by a ramp slot." I.A.H.R Symposium on Scale Effects in Modelling Hydraulic Structures, Esslingen am Neckar, Germany Sept 3 – 6. paper 4.7 pp 1 – 5.

PAN, SHUIBO, SHAO, YINGYING, XINGLIN. (1980)
"The self aeration capicity of water jet over aeration ramp." Jnl of Hydraulics Engineering No 5, Oct Beijing China.(in Chinese with English abstract)

PERTERKA, A.J. (1955)
"The effect of entrained air and cavitation pitting." Proc. of the Joint Meeting I.A.H.R 5th Congress Minnosota. U.S.A. August pp 507 – 518.

PHIRI, S. (1972)
"Velocity distribution down steep slopes." B.Sc Thesis Presented at the University of Liverpool England.

PINTO, N.L.des. (1984)
"Model evaluation of aerator in shooting f–low." I.A.H.R Symposium on Scale Effects in Modelling Hydraulic Structures, Esslingen am Neckar, Germany Sept 3 – 6. paper 4.2 pp 1 –6.

PINTO, N.L.des. (1982)
"Aeration at high velocity flow." Intern Water Power & Dam Construction. Part 1 February, pp: 34 to 38. Part 2 March, pp 42 – 44.

PINTO, N.L.des.&. NEIDERT, S.H. (1982)
"Model Prototype Confirmity in aerated spillway flow." Intern Conference on Hydraulics Modelling of Civil Engineering Structures, Coventry, England. September 22–24 pp 273 – 284.

PONCE, U.M. (1977)
"Shallow wave propagation in open channel flow." Jnl of

Hydraulics Division.(A.S.C.E)Proc. Paper:13392,HY12, December pp 1461 – 1476.

PRANDTL, L. (1925)
"Bericht uber unterschungen zur ausgebildeten Turbulenz." ZAMM 5, 136.

PRUSZA, V. et al (1983)
"Remedial measures against spillway cavitation". Proc: XXth IAHR Congress Moscow, Vol 3 pp 468 – 476.

QUINTELA, A.C. (1980)
"Flow aeration to prevent cavitation erosion." Intern Water Power & Dam Construction January pp 17 – 22.

RABBEN, L.&. ROUVE, G. (1984)
"Air demand of high head gates,model–family studies to quantity scale effect." Symposium on Scale Effects in Modelling Hydraulic Structures, Esslingen Germany. September 3–6. Edit (H.Kobus) paper 4.9 pp 1 – 3.

RAJAARATNAM, N (1976)
"Turbulent jets" Development in Water Science, Elsevier Scientific publishing company New York. 1976

RAO, P.V. MARTIN, C.S. RAO, B.C.S. RAO, N.S.L (1981)
"Estimation of cavitation erosion with incubation periods and materials properties". Journal of Testing and Evaluation, American Society of Testing and Materials pp 189 – 197.

RASHIDI, M et al (1987)
"Turbulence structure near gas liquid interface" Intern Association of Hydraulics Research Congress Lausanne Switzerland Vol 3 pp 80 – 85.

RENNER, J. (1975)
"Air entrainment in surface rollers" Symposium on the design and operation of Siphons and Siphon spillways BHRA. London.

REYNOLDS, A.J (1974)
"Turbulent flow in Engineering" Publisher John Wiley & sons London – New York.

REYNOLDS, O (1894)
"On the dynamical theory of Incompressible Fluids and the determination of the criterion". Philosophical Transactions of the Royal Society, Vol 186.

ROBERTSON, J. M.
" A Turbulence Primer." Engineering Experiment Station, Circular. No:79. Illinois Engineering Experiment Station Illinois. USA.

RUSSEL, S.O.&. SHEEHAN, G.J (1974)
"Effect of entrained air on cavitation damages." Canadian Jnl of Civil Engineers, Vol 1.

RUTSCHMANN, P .&. VOLKART, P. (1988)
"Calculation and optimum shape of spillway chute aerators" I.A.H.R Proc. of the Intern Symposium on Model– Prototype Correlation of Hydraulic Structures. A.S.C.E Colorado Spring Conference August pp 118 – 127.

SAKHUJA, V.S. PAUL, T.C.&. SINGH, S. (1984)
"Air entrainment distortion in free surface flow" Symposium on Scale Effects in Modelling Hydraulic Structures, Esslingen Germany. September 3–6. Edit (H.Kobus) paper 4.8 pp 1–4.

SCHLICHTING, H. (1968)
"Boundry Layer Theory" Publisher McGraw Hill Edition New York 6th Edition.

SCHUBAUER, G.B. (1935)
"A Turbulence indicator Utilizing the diffusion heat". NACA Report 524 1935.

SCHWARZ, H.I.&. NUTT, L.P. (1963)
"Projected nappes subject to transverse pressure". Proc: A.S.C.E, Journal of Hydraulics Division, Vol 89, HY 4, July Part 1, pp 97 – 104.

SEMENKOV, V.M.&. LENTJAEV, L.D. (1983)
"Spillway with Nappe Aeration." Hydrotechnical Construction. Gidroteknnicheshoe Stroitel'stvo, No 5 May, pp 16 – 20.

SEMENKOV, V.M.&. LENTYAVE, L.D. (1973)
"Spillway dams with aeration of flow over spillway." 9th ICOLD Congress Madrid, Separate paper.

SENE, K.J. (1984)
"Aspects of bubbly two–phase flow". Ph.D. Thesis, Trinity College, Cambridge, 1984.

SHARMA HARI, R. (1976)
"Air entrainment in high head gated condiuts." Jnl of Hydraulics Division Vol 102, HY11, November, pp 1629–1646.

SMUTEK, R. (1969)
"Discussion of Measurements of turbulence in Water" by E.V Richardson & R.S.McQuivey" Journal of Hydraulics Division A.S.C.E No HY1 pp 519 – 523.

STRAUB, L.G & ANDERSON, A.G (1958)
"Experiments on self aerated flow in open channel flow" Proc A.S.C.E Jornal of Hydraulics Division, Vol 84 HY7 Part 1 pp 1890/1–35.

TAYLOR, G.I (1932)
"The transport of vorticity and heat through fluids in turbulent motion" Proc Royal Society Vol A 135, pp 685–705.

TOSO, J.W.
"The magnitude and extent of extreem pressure fluctuations in the hydraulic jump." Ph.D Thesis submitted at the University of Minnesota, USA.

TOWNSEND, A.A. (1966)
"The mechanism of entrainment in free turbulent flows." Jnl of Fluid Mechanics.Vol: 26 Part 4, pp 689 – 775.

U.S.ARMY CROPS OF ENGINEERS. (1964)
"Hydraulic Design Criteria." Vol 1. Army Crops of Engineers Editor (Dr. Mayer,D.G)

VAN DE SANDE, E (1974)
"Air entrainment by plunging water jets". Ph.D. Thesis Technische Hogeschool Delft, 1974.

VAN DE DONK, J.A.C. (1981)
"Water aeration with plunging jets". Ph.D. Thesis, Technische Hogeschool Delft, 1981.

VEN DE SANDE, E. and SMITH, J.M (1976)
"Jet break–up and air entrainment by low velocity turbulent water Jets". Journal of Chemical Engineering Science, Vol.31 pp 219 – 224.

VERNET & LARREA, J.C (1985)
"Prototype and model aeration efficiency in a high head outlet for flood flows" 2nd Intern Conference on Hydraulic of Floods and Flood Control, BHRA, Cambridge England. pp 365 – 372.

VOLKART, P (1982)
"Self aerated flow in steep, partially filled pipes" Proc A.S.C.E, Journel Hydraulics Division Vol 108, HY9, September pp 1029 – 1046.

VISCHER, D. VOLKART.&. SIGENTHALER, A. (1982)
"Hydraulic modelling of air slots in open chute spillway." Intern Conference on Hydraulic Modelling of Civil Engineering Structures, BHRA Coventry, England. September, 22 – 24 pp 239 – 252.

VOLKART, P.&. CHERVET, A (1983)
"Air slots for flow aeration." Determination of shape, size & spacing of air slots for San Roque Dam spillway. Mitteilungen derversuchsanstalt fur wasserbau, Hydrologie und Glaziologie ETH, Zurich, Nr 66.

VOLKART, P.&. RUTSCHMANN, P (1984)
"Rapid flow in spillway chutes with and without deflector – A model prototype comparison." Symposium on Scale Effects in Modelling Hydraulic Structures, Esslingen Germany. September 3– 6. Edit (H.Kobus) paper 4.5 pp 1 – 8.

VOLKART, P.&. RUTSCHMANN, P (1986)
"Aerator on spillway chuts, fundamentals and applications." Advancement in Aerodynamics, Fluids Mechanics and Hydraulics Proc. of the specialty Conference A.S.C.E.Minneapolis MN, June, pp 163 – 177.

VON KARMAN, T.H (1936)
"The theory of homogenous turbulence" Journal Royal Aeronautical Society, December.

WANG, J.Y (1981)
"Comparison of depth formulae for high velocity aerated channel flows" Journal of Hydraulics Engineering, (Beijing) No 5, pp 48 – 52. (in Chinese)

WANG, S (1984)
"A formula for estimating air concentration of self–aerated flow in open channels" Jnl Hydr Engng (Beijing) No:7 pp 44–49 (in Chinese)

WAGNER, W.E (1967)
"Glen Canyon dam diversion tunnel outlets" Proc A.S.C.E Vol 93 No HY6 November.

WEBER, K. (1931)
" *Z. agnew. Math Mech."* Vol 11. p 136, 1931.

WEI, C.Y. DeFAZIO, F.G (1982)
"Simulation of free jet trajectories for design of aeration devices on hydraulic structures". 4th Intern Symposoium of Finit Elements on Hydraulic Structures, Hannover, Germany June pp 1 – 11.

WHITE, M.P (1943)
"DISCUSSION by W.L Moore," Energy loss at the base of free over fall" Trans A.S.C.E. Vol:108, pp 1343 – 1364.

WITHERS, W.J (1987)
"Pressure fluctuations in plunge pool basin due to impinging spillway jet." Research report 87, Dept. of Civil Engineering University of Glasgow.

WITHERS, W.J (1991)
"Pressure fluctuations in plunge pool basin due to impinging spillway jet." Ph.D Thesis 1991, Dept, of Civil Engineering University of Glasgow.

WOOD, I.R. (1983)
"Uniform region of self aerated flow." Proc A.S.C.E Journal of Hydraulics Division, Vol 109 January pp 447 – 461

WOOD, I.R. (1984)
"Air entrainment in high speed flows." Symposium on Scale Effects in Modelling Hydraulic Structures, Esslingen Germany. September 3–6. Edit (H.Kobus) paper 4.1 pp 1 – 7.

WOOD, I.R. (1985)
"Air water flows" Proc: XXIst IAHR Congress Melbourne Vol 6, pp 18 – 29.

YEVDJEVICH, V. & LEVIN, L. (1953)
"Entrainment of air in flowing water and technical problems connected with it." I.A.H.R Proc of the Vth Congress

Minnapolis, Minnesota pp 439 – 454.

ZAGUSTIN & CASTILLEJO (1983)
"Model prototype correlation for flow aeration in the Guri dam Spillway" Instituto de Mecanica de Fluidos, Universidad Central de Venezuela, Facaltad de Ingenieria, Boletin No:6

ZAGUSTIN, K. MANTELLIVI, T.&. CASTILLEJO, N (1982)
"Some experience on the relationship between a model and prototype for flow aeration in spillway." Intern Conference on the Hydraulics Modelling of Civil Engineering Structures, Coventry, England September 22 – 24.

ZHAROV, N.E. (1978)
"O melodike operedeleniia kriticheskikh chisel kavitatsii obtekanni nerovnostei". (Cavitation parameters of flow near surface irregularities) Izvestiia VNIIG im B.E.Vedeneeva, Sb.,nauchnykh trudov, Vol 126, Leningrad, pp 43– 48, 1978 (U.S.B.R translation book No.12, 245 paper No. 6)

ZHONG, LI XUE. (1983)
"Cavitation or Wear Erosion." Intern Water Power & Dam Construction.December, pp 43 – 50

APPENDICES

Appendix 'A'

Author's computer programs.

AI	Jet trajectory program (based on model of H.T.Falvey)
AII	Subroutine 'ROGOUS' calculates friction factor
AIII	Subroutine 'BOUND' calculates boundary layer development
AIV	Laser program for velocity & turbulence measurements (written in Asyst langauge)
AV	Frequency spectrum program (Asyst)
AVI	Calculation of shear velocity u_*.

Appendix 'B'

H.T.Falvey Cavitation program

Appendix 'C'

Detailed air flow measurement data (C1 – C12)

JET TRAJECTORY

```
      PROGRAM TRAJ
C     ****************************************************************
C      THIS PROGRAME ESTIMATE THE PRESSURE UNDER THE NAPPE
C     CALCULATE THE NAPPE TRAJECTORY
C     DETETMINE THE PRESSURE DROP ACCROSS THE VENT
C     ****************************************************************
      DIMENSION YAB(300),YAAB(300),XBB(300),YBB(300),XBT(300),YBT(300)
      DIMENSION XLN(300),YLN(300),XT(300),YT(300),XAB(300),XAAB(300)
      DIMENSION XB(300),YB1(300),XA(300),XAA(300),YA(300),YAA(300)
      DIMENSION AA(500),BB(500),XLD(300),YLD(300),XJET(300),BNAP(300)
      DIMENSION FYD(300),FYU(300),PHD(300),PHU(300),SLN(300),CLN(300)
      DIMENSION XLNN(300),YLNN(300),XLDD(300),YLDD(300),XNAP(300)
      DIMENSION XB1(300), YB(300),YNAP(300),Y(5000)
      COMMON/CONTR/DELPR
      READ(5,*)QD,B,YR,RANGLE,TURBI,BSLOPE,GS
      READ(5,*)D2,E2,DLT,BDT,ADLENG,CC,VENT
C
      TETA=(RANGLE*22.0)/(180.0*7.0)
      SS=(BSLOPE*22.0)/(180.0*7.0)
      C1=COS(SS)
      S1=TAN(SS)
      CO=COS(TETA)
      AR=YR*B
      VR=QD/AR
      C=0.2
      U=(C+YR)
      DT=0.02
      RO=1000.0
      G=9.81
      STR=D2
      ELR=E2
C
C     TO FIND THE LOWER LIMIT
C
      THR=TETA+ATAN(TURBI)
      VX=VR*COS(THR)
      VY=VR*SIN(THR)
      DO 10 J=1,150
      T=(DT*J)
C
      XB(J)=(VX*T)
      YB(J)=(VY*T)+(0.5*G*T*T)
C
      Y1=ELR-CC
      Y2=XB(J)*S1
      Y(J)=Y1-Y2
      XB1(J)=STR+XB(J)
      YB1(J)=ELR-YB(J)
      IF(YB1(J).LE.Y(J)) THEN
      GO TO 393
      ELSE
      GO TO 18
      END IF
```

Trajectory Program
(Continued)

```
C
   18 F1=(0.5*G)/(VX*VX)
      F2=(VY/VX)
      P=(F2-S1)
      Q=(F1*C)
C      Z1=(P*P+4.*Q)
C      IF(Z1.LT.0.0) THEN
C      Z=SQRT(ABS(Z1))
C      ELSE
C      Z=SQRT(Z1)
C      END IF
CC
C      XA(J)=(-P+Z)/(2.*F1)
C      XAA(J)=(-P-Z)/(2.*F1)
C      YA(J)=F1*XA(J)*XA(J)+F2*XA(J)
C      YAA(J)=F1*XAA(J)*XAA(J)+F2*XAA(J)
C      XBOT=XB(J)
C      YBOT=YB(J)
C      XBT(J)=STR+XBOT
CC      YBT(J)=ELR-YBOT
C
C
C      IF(YB(J).GT.YA(J)) THEN
C      GO TO 33
C      ELSE
C      GO TO 10
C      END IF
   10 CONTINUE
C
  393 MN=J
      N=1
      XLDD(N)=STR
      YLDD(N)=ELR
      SUM=0.0
      MM=MN
      DO 696 J=1,MM
      T=(DT*J)
      XLD(J+1)=(VX*T)
      YLD(J+1)=(((VY*T)+(0.5*G*T*T)))
      XLDD(J+1)=STR+XLD(J+1)
      YLDD(J+1)=ELR-YLD(J+1)
      AA(J)=(XLDD(J+1)-XLDD(J))**2
      BB(J)=(YLDD(J+1)-YLDD(J))**2
      PHD(J)=(YLDD(J)-YLDD(J+1))/(XLDD(J+1)-XLDD(J))
      FYD(J)=ATAN(PHD(J))
      XJET(J)=SQRT(AA(J)+BB(J))
      SUM=SUM+XJET(J)
  696 CONTINUE
      WRITE(6,424)
  424 FORMAT(2X,'JET LENGTH',5X)
      WRITE(6,*)  SUM
      QAIR=0.033*SUM*VR*B
C
      CALL  DELP(ELR,GS,DLT,BDT,ADLENG,QAIR,VENT)
C
```

Trajectory Program
(Continued)

```
C
C     FOR UPPER NAPPE
C
      DO 88 I=1,100
      T=(DT*I)
      XBB(I)=(VX*T)
      YBB(I)=(VY*T)+(0.5*G*T*T)
      F1=(0.5*G)/(VX*VX)
      F2=(VY/VX)
      P=(F2-S1)
      R=(F1*U)
      Z2=(P*P+4.0*R)
      IF(Z2.LT.0.0) THEN
      ZZ=SQRT(ABS(Z2))
      ELSE
      ZZ=SQRT(Z2)
      END IF
C
      XAB(I)=(-P+ZZ)/(2.*F1)
      XAAB(I)=(-P-ZZ)/(2.*F1)
C
      YAB(I)=F1*XAB(I)*XAB(I)+F2*XAB(I)
      YAAB(I)=F1*XAAB(I)*XAAB(I)+F2*XAAB(I)
C
      DDD=(YAB(I)+YR)
      IF(YBB(I).GT.DDD) THEN
      GO TO 44
      ELSE
      GO TO 88
      END IF
   88 CONTINUE
   44 L=I
C
C
C     TRAJECTORY FOR UPPER NAPPE
C
      THR=TETA-ATAN(TURBI)
      XOFF=YR*SIN(THR)

      YOFF=YR*COS(THR)
C
      VX=VR*COS(THR)
      VY=VR*SIN(THR)
      M=1
      XT(M)=STR+XOFF
      YT(M)=ELR+YOFF
C
      DO 303 I=1,L
      T=(DT*I)
      XXX=(VX*T)
      YYY=(VY*T)+(0.5*G*T*T)
      XX=XXX
      YY=YYY
      XT(I+1)=STR+XOFF+XX
      YT(I+1)=ELR+YOFF-YY
      PHU(I)=(YT(I)-YT(I+1))/(XT(I+1)-XT(I))
      FYU(I)=ATAN(PHU(I))
  303 CONTINUE
```

Trajectory Program
(Continued)

```
C
C     LOWER NAPPE CALCULATIONS WITH EFFECT OF UNDER PRESSURE.
C
      DO 17 I=1,50
      DELPR=(I/100.)
      MP=1
      XLNN(MP)=STR
      YLNN(MP)=ELR
      SUM=0.0
      XYZ=(G*RO*DELPR/(YR*RO))
C
      MM=MN
      DO 888 J=1,MM
      SLN(J)=SIN(FYD(J))
      CLN(J)=COS(FYD(J))
      T=(DT*J)
      XLN(J+1)=((VR*CLN(J))*T)-0.5*((XYZ*SLN(J))*T*T)
      YLN(J+1)=(((VR*SLN(J))*T)+0.5*((G+(XYZ*CLN(J)))*T*T))
      XLNN(J+1)=STR+(XLN(J+1))
      YLNN(J+1)=ELR-(YLN(J+1))
      ETT=ELR-CC
      ELR2=ETT-(S1*(XLNN(J+1)-STR))
      XNAP(J)=(XLNN(J+1)-XLNN(J))**2.
      YNAP(J)=(YLNN(J)-YLNN(J+1))**2.
      BNAP(J)=SQRT(XNAP(J)+YNAP(J))
      SUM=SUM+BNAP(J)
      IF(YLNN(J+1).LE.ELR2) THEN
      GO TO 808
      ELSE
      GO TO 888
      END IF
  888 CONTINUE
C
  808 SJET=(ETT-ELR2)/SIN(SS)
C      WRITE(6,858)
C  858 FORMAT(2X,'JET LENGTH ALONG THE BEDSLOPE W.E.F UNDER PRESSURE',2X)
C      WRITE(6,*) SJET
C      WRITE(6,848)
C  848 FORMAT(2X,'EXACT NAPPE LENGTH WITH EFFECT OF UNDER PRESSURE',3X)
      QAIR4=0.033*SUM*B*VR
      WRITE(6,*) I,J,DELPR,SUM,QAIR4
   17 CONTINUE
C
      WRITE(6,110)
  110 FORMAT(2X,'J E T   T R A J E C T O R Y   O V E R   R A M P',2X)
      WRITE(6,111)
  111 FORMAT(2X,'##################################################',2X)
      WRITE(6,112)
  112 FORMAT(5X,'     ',3X)
      WRITE(6,113)
  113 FORMAT(1X,'RAMP',10X,'DELTAX',5X,'ELEVATION',5X,'RAMP ANGLE',2X)
      WRITE(6,114) D2,E2,RANGLE
  114 FORMAT(10X,F10.2,3X,F10.2,3X,F10.2)
      WRITE(6,115)
  115 FORMAT(1X,'FLOW',10X,'DISCHARGE(W)',5X,'WIDTH',5X,'FLOW DEPTH
     +AT RAMP',5X,'TURB(I)',3X)
      WRITE(6,116) QD,B,YR,TURBI
  116 FORMAT(15X,F10.2,5X,F10.2,5X,F10.2,8X,F10.2,2X)
      WRITE(6,117)
```

Trajectory Program (Continued)

```
  117 FORMAT(2X,'    ',3X)
      WRITE(6,118)
  118 FORMAT(5X,'LOWER NAPPE',5X,'CENTRAL NAPPE',30X,'UPPER NAPPE',2X)
      WRITE(6,119)
  119 FORMAT(5X,'================================================',5X
     +,'=========================================',3X)
      WRITE(6,120)
  120 FORMAT(3X,'STATION',3X,'ELEVATION',3X,'STATION',3X,'ELEVATION'
     +,20X,'STATION',3X,'ELEVATION',4X)
C      WRITE(6,222)
C      DO 77 J=1,MN
C      WRITE(6,222) XBT(J),YBT(J),XT(J+1),YT(J+1)
C  222 FORMAT(3X,2F10.2,45X,2F10.2)
C   77 CONTINUE
C      WRITE(6,444)
C      DO 55 K=MN,L
C      WRITE(6,444) XT(K),YT(K)
C  444 FORMAT(66X,2F10.2)
C   55 CONTINUE
      STOP
      END
      SUBROUTINE DELP(ELR,GS,DLT,BDT,ADLENG,QAIR,VENT)
C     ****************************************************************
C     THIS SUBROUTINE CALCULATE THE PRESSURE HEAD LOSS IN THE AIR
C     SUPPLY DUCT.
C     ****************************************************************
      COMMON/CONTR/DELPR
C     A=SHARP END
C     B=RE-ENTRAINED
C     C=SLIGHTLY ROUNDED
C     D=BELLMOUTHED
C     E=FOOT VALUE & STAINER
C
C     IF(ET.EQ.A)  P1K=0.5
C     IF(ET.EQ.B)  P1K=0.8
C     IF(ET.EQ.C)  P1K=0.25
C     IF(ET.EQ.D)  P1K=0.05
C     IF(ET.EQ.E)  P1K=2.50
      P1K=0.05
C
      F=1/2
      G=1.0
      H=2.0
C
C      IF(BEND(R/D).EQ.F)  P2K=1.00
C      IF(BEND(R/D).EQ.G)  P2K=0.75
C      IF(BEND(R/D).EQ.H)  P2K=0.40
C
      P2K=0.55
C
C     FOR FRICTION FACTOR F
C
```

Trajectory Program
(Continued)

```
      ADUCT=(DLT*BDT)*VENT
      P=2.*(DLT+BDT)
      R=ADUCT/P
      VISC=0.000001
      VAIR=QAIR/ADUCT
      RE=(4*R*VAIR)/VISC
      WRITE(6,*) VAIR
      Y=GS/(14.8*R)
      Z=2.51/RE
      I1=0.001*1000000
      I2=1000000
      DO 121 I=I1,I2,100
      F=I/1000000.0
      FF=1./SQRT(F)
      S1=FF
      S22=(Y+(Z*FF))
      ST=ALOG10(S22)
      S2=(-2*ST)
      IF(ABS(S2-S1).LE.0.05) GO TO 89
  121 CONTINUE
   89 F=1./(FF*FF)
      WRITE(6,*) F
      TK=(F*ADLENG)/(4.*R)
      P3K=TK
C     EXIST LOSS  INLET/OUTLET DIAMETER
C
C      O=4/5
C      P=3/4
C      Q=2/3
C      RR=2/3
C      SS=1/3
C      TT=1/5
C      UU=1/1
C
C      IF(I/O.EQ.OO)  P4K=0.15
C      IF(I/O.EQ.PP)  P4K=0.20
C      IF(I/O.EQ.QQ)  P4K=0.35
C      IF(I/O.EQ.RR)  P4K=0.60
C      IF(I/O.EQ.SS)  P4K=0.80
C      IF(I/O.EQ.TT)  P4K=1.00
C      IF(I/O.EQ.UU)  P4K=0.00
C
      P4K=0.80
C
      TOTALK=(P1K+P2K+P3K+P4K)
      PA=10.33*(1-ELR/44303.)**5.255
      PABS=PA-0.12
C
      VVAIR=(VAIR*VAIR)/19.6
      DELPR=(TOTALK*VVAIR)*(1.23/1000.0)
      ELPR=(PABS-DELPR)
      WRITE(6,*) DELPR
C
      WRITE(6,434)
  434 FORMAT(2X,'ABS PRESSURE',2X,'DELTA PRESSURE',12X,'DELTA P',2X)
      WRITE(6,444) PABS,DELPR,ELPR
  444 FORMAT(2X,F10.3,10X,F10.3,8X,F10.3)
      RETURN
      END
```

FRICTION FACTOR

```
*** CONTENTS OF FILE :GNCV68.LAZ(1,*,1).A1(78) AT 17:01:15 ON 1991/09/13 ***

      PROGRAM ROGOUS
C     ******************************************************************
C     THIS SUBROUTINE CALCULATE THE MANNING'S 'N' BY USING
C     FACTOR 'F' IN ORDER TO ESTIMATE MORE ACCURATE VALUE.
C     ******************************************************************
      DIMENSION QD(300),YR(300),AJET(300)
      READ(5,*) N
      DO 11 I=1,N
      READ(5,*) QD(I),YR(I),AJET(I)
   11 CONTINUE
       READ(5,*) B,GS
      DO 39 K=1,N
      AD=B*YR(K)
      CG=QD(K)/B
      CGC=(CG**0.319)
      CGH=(CGC*6)
      RGH=(AJET(K)/CGH)
      PRINT*,'LB',CGH,'L/Lb',RGH
      VD=QD(K)/AD
      PD=(B+(2*YR(K)))
      R=AD/PD
      VISC=0.000001
      ROGG=(0.001)/(4*R)
      RE=(4.0*R*VD)/VISC
      T=GS/(14.8*R)
      VV=2.5/RE
      I1=.001*1000000
      I2=1000000
      DO 10 I=I1,I2,10
      F=I/1000000.0
      FF=1.0/SQRT(F)
      S1=FF
      S22=(T+(VV*F))
      ST=ALOG10(S22)
      S2=(-2*ST)
      IF(ABS(S1-S2).LE.0.05) GO TO 80
   10 CONTINUE
   80 F=1.0/(FF)
      FFF=(F*F)
      FSD=SQRT(FFF/8.)
       WW=(AJET(K))/(YR(K))
       BETA=(WW*FSD)
      WRITE(6,133)
  133 FORMAT(2X,'BETA',10X,'K/D',10X,'FF',10X,'L/H',2X)
      WRITE(6,*)BETA,ROGG,FFF,WW,RE
   39 CONTINUE
      STOP
      END
*** END OF FILE CONTENTS ***
-
-
-
-
```

BOUNDARY LAYER DEVELOPMENT

```
*** CONTENTS OF FILE :GNCV68.LAZ(1,*,1).BB(10) AT 17:01:34 ON 1991/09/13 ***
      PROGRAM BOUND
C     ************************************************************
C     THIS SUBROUTINE CALCULATES THE BOUNDRY LAYER
C     THICKNESS BY COMPAREING DIFFERENT FORMULE.
C     ************************************************************
C
      READ(5,*)XL,DELTA,GK
      WRITE(6,113)
      WRITE(6,115)
      N=XL/DELTA
      DO 9 I=1,N
      DELTAX=((DELTA)*I)
      BL=(DELTAX/GK)**(0.13)
      BLT1=(0.024*(DELTAX))/(BL)
      BL1=(DELTAX/GK)**(0.25)
      BLT2=(0.233)*(DELTAX)/(BL1)
      R2=1.0E+04
      R3=1.0E+05
      R4=1.0E+06
      R5=1.0E+07
      R6=1.0E+08
      BLT4=(0.38)*(DELTAX)/(R2**0.2)
      BLT5=(0.38)*(DELTAX)/(R3**0.2)
      BLT6=(0.38)*(DELTAX)/(R4**0.2)
      BLT7=(0.38)*(DELTAX)/(R5**0.2)
      BLT8=(0.38)*(DELTAX)/(R6**0.2)
      WRITE(6,111)DELTAX,BLT1,BLT2,BLT4,BLT5,BLT6,BLT7,BLT8
  111 FORMAT(//,1P8E12.4,/)
    9 CONTINUE
  113 FORMAT(2X,'DELTAX',7X,'BAUERS',5X,'MS.THESIS(USA)',
     +20X,'HANK FALVEY',2X)
  115 FORMAT(43X,'1.0E+04',5X,'1.0E+05',5X,'1.0E+06',5X,
     +'1.0E+07',5X,'1.0E+08',2X)
      STOP
      END
*** END OF FILE CONTENTS ***
```

ANALYSIS OF TURBULENCE DATA

```
\    PROGRAM : LASEP
\    THIS PROGRAM USED TO DETERMINE
\    VOLTAGE FROM LASER
\    SET BY (FREQUENCY LAZER COMMAND)

INTEGER SCALAR ERROR.CODE
INTEGER SCALAR SEGMT
INTEGER SCALAR CHN
INTEGER SCALAR GAIN
INTEGER SCALAR Z.CHN
INTEGER SCALAR RANGE
INTEGER SCALAR W
INTEGER SCALAR ADATA
REAL DIM[ 4096 ] ARRAY POSITIONO
\
\     DEFINE A GENERAL PURPOSE ERROR PROCESSING ROUTINE.
\
: ERROR?                          \ (STRING  _____)
   CALL[ PCI46S , ERR.SYS , ERROR.CODE ]
   ERROR.CODE O <> IF
      "TYPE ERROR.CODE . CR
   ELSE
      "DROP
   THEN
;
: LASER
CR ." SETTING ARRAYS TO ZERO"
O POSITIONO :=
\
\    INITIALIZE THE PCI-20046S-4 SYSTEM.  THIS SEQUENCE MUST BE
\    GIVEN PRIOR TO CALLING ANY OTHER PCI-20046S-4 INSTRUCTION.
CR
" 61"H SET.VECT
CALL[ PCI46S , SYSINIT ]
\
\    SEGMT, DEFINE BELOW,CONTAINS THE BASE ADDRESS OF THE CARRIER
\    WE USE " COOO"H, BUT YOU CAN SET IT ANY WHERE. REFER TO THE
\    CARRIER MANUAL FOR MORE INFORMATION.
\    [ PCI46S , INIT , SEGMT ] MUST BE CALLED ONCE FOR EACH CARRIER
\    IN THE SYSTEM, EACH WITH ITS OWN ADDRESS
\
" COOO"H SEGMT :=
CALL[ PCI46S , INIT , SEGMT ]
\
\    CHECK FOR A SYSTEM ERROR. DURING DEBUG, CALL ERR.SYS OFTEN,
\    POSSIBLY AFTER EVERY CALL TO THE PCI-20046S-4. IT IS A GOOD
\    IDEA TO LEAVE A FEW ERR.SYS CALL IN A FINISHED PROGRAME TO
\    MONITOR THE STATUS OF THE SYSTEM.
\
" ERROR FOUND DURING INIT" ERROR?

CR ." PROGRAM LASER"
```

Laser Program (Continued)

```
CR
CR ." SETTING GAIN AND RANGE"
0 CHN :=
1 GAIN :=
-1 Z.CHN :=
1 RANGE :=
\    W IS THE NUMBER OF READINGS +1 ON CHANNEL
4097 W :=
CR
CR ." CONFIGURING CHANNEL 0"
CALL[ PCI46S , CNF.AI , CHN , GAIN , Z.CHN , RANGE ]
" ERROR FOUND DURING CNF.AI" ERROR?
\
\    READ THE ANALOG INPUT CHANNEL
\
CR
CR ." READING CHANNEL"
\ SET FREQUENCY OF SAMPLING
SYNC.ERROR.ON
INV 1000. *
SYNC.PERIOD
CR ." DATA AQUISITION LOOP"
W 1 DO
SYNCHRONIZE
CALL[ PCI46S , READ.CH , AI.T , CHN , ADATA ]
\
\    GIVEN THE ADC READING, ADATA, TO ARRAY AND CONVERT
\
\    THE ASSUMPTION IS THAT THE PC1-20002M-1 MODULE IS SET
\    UP FOR +\- 10 VOLTS
\    THE PREVIOUS PROGRAME GIVES THE EQUATION TO BE USED IN PLACE
\    OF THE ABOVE LINE FOR OTHER THAN +\- 10 VOLTS
\
ADATA POSITIONO [ I ] :=
LOOP
CR ." DATA CONVERSION"
\
\    CONVERT ARRAY FROM ANALOG VOLTAGE TO DIGITAL VOLTAGE TO VELOC
\
POSITIONO 20.0 * 4096.0 / 10.0 - GAIN / POSITIONO :=
CR ." NUMBER OF READINGS ON CHANNEL 0 WAS" W 1 - .
CR
;

\ PRINT OUT DIMENSION OF EXPERIMENT
\ FROM PREVIOUSLY INPUTED DATA

\
REAL SCALAR VEL
REAL SCALAR RANGE2
20 STRING TESTRUN
20 STRING DATE
REAL SCALAR MAN
REAL SCALAR DEPTH
```

Laser Program (Continued)

```
\
: INPUTSO
CR ." CHANNAL 0 (LAZER DOPPLER)"
CR
CR DATE "TYPE
CR TESTRUN "TYPE

CR ." WATER DEPTH IN THE CHANNEL =" DEPTH . ." m"

CR ." MANOMETER READING(MERCURY) =" MAN . ." m"

MAN .494 **  1.164 * DEPTH / VEL :=

CR ." FREQUENCY RANGE (MAX) =" RANGE2 . ." Hz"

W 1 DO
POSITIONO [ I ] .000000632 * RANGE2 * 1.986395 / POSITIONO [ I ] :=
LOOP
;
\ DETERMINE STATICAL PROPERTIES AND RESULTS
REAL DIM[ 3 ] ARRAY TEMPO
: RESULTSO
  INPUTSO
CR
CR ." MEASURED VELOCITY BY MANOMETER (m/s) =" VEL . ." m/s"
\
CR ." LASER MEASUREMENTS (m/s)"
POSITIONO MEAN TEMPO [ 1 ] :=
POSITIONO VARIANCE SQRT TEMPO [ 2 ] :=
TEMPO [ 2 ] TEMPO [ 1 ] / 100 * TEMPO [ 3 ] :=
CR ." POINT VELOCITY IN THE CHANNEL=" TEMPO [ 1 ] . ." m/s"


CR ." TURBULENCE INTENSITY U` AT THE SAME POINT=" TEMPO [ 3 ] . ." %"
CR
CR ." TURN THE LASER AT 90 DEGREE FOR W`"
CR
;
```

POWER SPECTRUM

```
\   PROGRAM CONTAINING FREQUENCY SPECTRUM PLOTTING COMMANDS
\   SMOOTHED TIME SERIES COMMANDS, AND SOME ABREVIATED
\   COMMONLY USED ASYST COMMMANDS
\
\
\
\   PLOT FREQUENCY SPECTRUM
\
REAL DIM[ 4096 ] ARRAY POSITIONX
REAL DIM[ 4096 ] ARRAY FSPECTRUM
: FS
  VERTICAL LINEAR
  -1.2 0 5 LABEL.FORMAT
  HORIZONTAL LINEAR
  VERTICAL LINEAR
  -1.2 0 5 LABEL.FORMAT
  HORIZONTAL LINEAR
  -.5 -.8 4 LABEL.FORMAT
  -.5 -.8 4 LABEL.FORMAT
  FREQS SUB[ 2 , 2048 ]
  POSITIONX FFT ZMAG FSPECTRUM :=
  FSPECTRUM SUB[ 2 , 2048 ]
  XY.AUTO.PLOT
  NORMAL.COORDS
  0 LABEL.DIR 0 CHAR.DIR
  .5 .9 POSITION " FREQUENCY SPECTRUM" LABEL
  .7 .05 POSITION " FREQUENCY (Hz)" LABEL
  270 LABEL.DIR 0 CHAR.DIR
  .03 .90 POSITION " F.F.T. MAGNITUDE" LABEL
  OUTLINE
  CURSOR.OFF
  WORLD.COORDS
;

: P2
  VERTICAL LINEAR
  -1.2 0 5 LABEL.FORMAT
  HORIZONTAL LINEAR
  -.5 -.8 4 LABEL.FORMAT
  FREQS SUB[ 2 , 512 ]
  FSPECTRUM SUB[ 2 , 512 ]

  XY.AUTO.PLOT
;


: D
```

SHEAR VELOCITY

```
df exp.ww
*** CONTENTS OF FILE :GNCV68.EXP(1,*,1).WW(30) AT 11:14:42 ON 1991/09/18 ***

      PROGRAM SHEAR
C     ********************************************************************
      THIS PROGRAM CALCULATES THE BED SHEAR VELOCITY
      ********************************************************************
      DIMENSION DD(50),Y1(50),Y2(50),Y3(50),TUR1(50),TUR2(50),Q(50)
      READ(5,*) N
      DO 12 K = 1,N
      READ(5,*) Q(K),Y1(K),Y2(K),Y3(K),TUR1(K),TUR2(K)
   12 CONTINUE
      G = 9.8076
      B= 0.1
      DO 14 J = 1,N
      A=(Y1(J)*B)
      A1=(Y2(J)*B)
      A2=(Y3(J)*B)
      P=((2*Y1(J))+B)
      P1 = ((2*Y2(J))+B)
      P2 = ((2*Y3(J))+B)
      R=A/P
      R1=A1/P1
      R2=A2/P2
      RA=(R+R1)/2.
      RB=(R1+R2)/2.
      V=Q(J)/A
      V1=Q(J)/A1
      V2=Q(J)/A2
      VA=(V+V1)/2.
      VB=(V1+V2)/2.
      Y11= (Y2(J)-Y1(J))
C      Y11=(Y1(J)-Y2(J))
      V22 = ((V1*V1)-(V*V))/(2.*G)
      Y33= Y11*0.7071
      Y44= (Y33+V22)/0.3
      SFM = 0.7071 - Y44
      FF = (8*G*RA*SFM)/(VA*VA)
      UU1 = VA * SQRT(FF/8.)
      WRITE(6,133)
  133  FORMAT(2X,'FRIC',2X,'RE',2X,'SHEAR VELOCITY',2X)
      WRITE(6,*) FF,RE,UU1
   14 CONTINUE
      END
*** END OF FILE CONTENTS ***
-
```

FALVEY'S CAVITATION PROGRAM

```
*** CONTENTS OF FILE :GNCV68.LAZ(1,*,1).TRAJ(1) AT 17:02:35 ON 1991/09/13 ***

EQ.1)WRITE(3,112)Q,DNF,RUG,CNO
      IF(METRIC.EQ.1)WRITE (3,113)
      IF(METRIC.EQ.0)RUG= RUG*1000.
      IF(METRIC.EQ.0)WRITE(3,114)Q,DNF,RUG,CNO
      IF(METRIC.EQ.0)RUG= RUG/1000.
      IF(METRIC.EQ.0)WRITE (3,115)
      WRITE (3,116) STA,ELINV,SB,DN,V,D,TOTAL,BETA,AN,M,YN,YC,YB
      NL= NL+1
C
    6 IF(NL.LT.46)GO TO 7
      NL= 0
      WRITE(3,111)(TITL(ITIT),ITIT=1,60)
      IF(METRIC.EQ.1)WRITE(3,113)
      IF(METRIC.EQ.0)WRITE(3,115)
    7 READ (2,*,END=62) I,IS
      GO TO (8,9,10,12,14,11)I
C
C     RECTANGULAR OR TRAPEZOIDAL CHANNELS
    8 READ (2,*) STA,ELINV,W,SS,BENDR,RUGN
      IF(RUGN.GT.1.E-10)RUG= RUGN
      WRITE(1,117)STA,ELINV,W,SS,BENDR,RUG
      CALL TRAP(DN)
      TLF= 0.
      IF(ABS((WOLD-W)/W).GE.0.001)TLF= 0.1
      WOLD= W
      GO TO 17
C
C     CIRCULAR CONDUITS
    9 READ (2,*) STA,ELINV,R,BENDR,RUGN
      IF(RUGN.GT.1.E-10)RUG= RUGN
      WRITE(1,118)STA,ELINV,R,BENDR,RUG
      DIA= 1.99999*R
      IF(IS.EQ.1)DIA= DIA/SQRT(SB*SB+1.)
      CALL CIRC(DIA)
      TLF= 0.
      IF(ABS((ROLD-R)/R).GE.0.001)TLF= 0.1
      ROLD= R
      GO TO 17
C
C     EGG SHAPED SECTIONS
   10 READ(2,*)STA,ELINV,D,BENDR,RUGN
      IF(RUGN.GT.1.E-10)RUG= RUGN
      WRITE(1,118)STA,ELINV,D,BENDR,RUG
      R1= D/2.
      R2= D
      R3= (1.-SQRT(.32*.32+.5*.5))*D
      C1= D/2.
      C2= D/2.
      C3= 0.82*D
      GO TO 13
```

Cavitation Program
(Continued)

```
C
C       USER DEFINED CIRCULAR ARC SECTION
   11   READ(2,*)STA,ELINV,R1,R3,R2,C3,C2,BENDR,RUGN
        IF(RUGN.GT.1.E-10)RUG= RUGN
        WRITE(1,119)STA,ELINV,R2,R3,C3,R1,C2,BENDR,RUG
        C1= R1
        D= R2
        GO TO 13
C
C       HORSE SHOE SHAPED SECTIONS
   12   READ(2,*)STA,ELINV,D,BENDR,RUGN
        IF(RUGN.GT.1.E-10)RUG= RUGN
        WRITE(1,118)STA,ELINV,D,BENDR,RUG
        R1= D
        R2= D
        R3= D/2.
        C1= D
        C2= D/2.
        C3= D/2.
   13   CALL SECSOL
        DT=0.9999*(R3+C3)
        CALL ARCS(DT)
        TLF= 0.
        IF(ABS((ROLD-D)/D).GE.0.001)TLF= 0.1
        ROLD= D
        GO TO 17
C
C       COMPOSITE SECTIONS
   14   READ (2,*) STA,ELINV,W,R,RADCL,R1,T,BENDR,RUGN
        IF(RUGN.GT.1.E-10)RUG= RUGN
        WRITE(1,119)STA,ELINV,W,R,RADCL,R1,T,BENDR,RUG
        IF(RADCL.LT.0.)GO TO 15
        WMIN= (W-T)/2.
        IF(R.GE.WMIN)DT= 0.99999*(RADCL+SQRT(R*(W-T)-0.25*(W-T)*(W-T)))
        IF(R.LT.WMIN)DT= 0.99999*(RADCL+R)
        IF(IS.EQ.1)DT= DT/SQRT(SB*SB+1.)
        GO TO 16
C       IT= 1 IS THE CONDITION FOR A COMPOSITE SECTION WITH NO COVER
   15   DT= 100.*DN
        IT= 1
   16   CALL COMP(DT)
        TLF= 0.1
C
C       COMPUTATION OF REYNOLDS NUMBER
C
   17   REY= 4.*HR*(Q/A)/VISC
C
C       COMPUTATION OF ATMOSPHERIC PRESSURE
C
        PABS= 33.9*(1.-ELINV/145400.)**5.255-0.39
        IF(METRIC.EQ.0)PABS=10.33*(1.-ELINV/44303.)**5.255-0.13
C
```

Cavitation Program
(Continued)

```
C
C     CHECK TO ENSURE VERTICAL ACCELERATIONS OF FLOW DO NOT
C     INVALIDATE RESULTS.  HR/RUG MUST BE GREATER THAN 10.
C
      IF(ABS(HR/RUG).LT.10.)GO TO 64
C
C     COMPUTATION OF MANNINGS N FROM RUGOSITY
C
      CALL RUGOS(CN)
C
C     COMPUTATION OF BOTTOM SLOPE
C
C
C     .   NT= 1 IS THE CONDITION FOR THE FIRST STATION
C
      IF(NT.EQ.1)CNO= CN
      IF(NT.EQ.1)GO TO 18
      SBO= SB
      SB= (ELINV-STORE1)/ABS(SAVE-STA)
      IF(NCURV.EQ.1)SB= -SB
C
C     CHECK FOR MAXIMUM DISCHARGE IN CLOSED CONDUITS
C
   18 IF(I.EQ.1.OR.IT.EQ.1)GO TO 24
      QMAX= A*SQRT(ABS(SB))*(HR**0.66667)/CN
      IF(METRIC.EQ.1)QMAX= 1.49*QMAX
C
C     DETERMINATION OF DEPTH EQUIVALENT TO MAX FLOW IN CONDUIT
C
      IF(I.EQ.2)YBI= 0.8*DIA
      IF(I.EQ.3)YBI= C3
      IF(I.EQ.4.OR.I.EQ.6)YBI= C3+R3/2.
      IF(I.EQ.5)YBI= RADCL
C
C     IF Q<QMAX, USE THESE VALUES AS INITIAL DEPTHS FOR CRITICAL
C       AND NORMAL FLOW DEPTH COMPUTATIONS
      IF(ABS(SB).LE.1.E-6)GO TO 24
      IF(Q.LE.QMAX)GO TO 24
      IF(I.EQ.2)YTOP= 2.*DIA
      IF(I.EQ.3.OR.I.EQ.4)YTOP= C3+R3
      IF(I.EQ.5)YTOP= RADCL+R
      IF(I.EQ.6)YTOP= C3+R3
      CTE= SQRT(ABS(SB))/CN
      IF(METRIC.EQ.1)CTE= 1.49*CTE
      DO 23 NTL=1,20
C    .   IBY IS AN INDEX WHICH SHOWS THAT BISTABLE FLOW IS POSSIBLE
      IBY= 1
      GO TO (24,19,20,20,21,20)I
   19 CALL CIRC(YBI)
      GO TO 22
   20 CALL ARCS(YBI)
      GO TO 22
```

Cavitation Program
(Continued)

```
   21     CALL COMP(YBI)
   22     F= QMAX-A*CTE*HR**0.66667
          DFDY= -B*CTE*HR**0.66667-0.66667*CTE*A*DHRDY/(HR**0.33333)
          IF(ABS(F/QMAX).LE.0.0001)GO TO 24
          IF(ABS(DFDY).LE.1.E-8)GO TO 23
          YBO= YBI
          YBI= YBI-F/DFDY
          IF(YBI.GE.YTOP)YBI= YBO+(YTOP-YBO)/2.
   23   CONTINUE
C
C      COMPUTATION OF CRITICAL DEPTH
C
   24   DTRY= DN
        IF(IBY.EQ.1)DTRY= YBI
        IBY= 0
        CALL CRIT(YC,DTRY)
C
C      COMPUTATION OF NORMAL DEPTH
C
        IF(Q.LE.QMAX)GO TO 25
        IF(ABS(SB).LE.0.000001)GO TO 25
        IF(SB.GT.0.)YN= 1000.
        IF(SB.LT.0.)YN= -1000.
        GO TO 26
   25   CALL NORMAL(YN,DTRY)
C
C      DETERMINATION OF PROFILE TYPE
C
   26   IF(YN.LT.YC)GO TO 27
        IF(YN.EQ.YC)GO TO 28
        IF(SB.LT.(1.E-10).AND.SB.GT.(-1.E-10))GO TO 29
C
C      MILD SLOPE
C
        AN= 'M'
        IF(DN.GE.YN)M=1
        IF(DN.LT.YN.AND.DN.GT.YC)M=2
        IF(DN.LE.YC)M=3
        GO TO 31
C
C      STEEP SLOPE
C
   27   IF(SB.LT.(-1.E-10))GO TO 30
        AN='S'
        IF(DN.GE.YC)M=1
        IF(DN.GT.YN.AND.DN.LT.YC)M=2
        IF(DN.LE.YN)M=3
        GO TO 31
C
C      CRITICAL SLOPE
C
```

Cavitation Program
(Continued)

```
   28   AN= 'C'
        IF(DN.GE.YN)M=1
        IF(DN.LT.YN)M=3
        GO TO 31
C
C       HORIZONTAL
C
   29   AN= 'H'
        IF(DN.GE.YC)M=2
        IF(DN.LT.YC)M=3
        GO TO 31
C
C       ADVERSE
C
   30   AN= 'A'
        IF(DN.GE.YC)M=2
        IF(DN.LT.YC)M=3
C
C       COMPUTATIONAL LOOP TO DETERMINE WATER DEPTH
C
C
   31   DO 52 J=1,50
          NJ= J
C
C         COMPUTATION OF DEPTH BY STANDARD STEP METHOD
C
C
C         COMPUTATION OF HYDRAULIC PROPERTIES
C
          GO TO (32,33,34,34,35,34)I
C
C         HYDRAULIC PROPERTIES FOR RECTANGULAR SECTION
C
   32     CALL TRAP(DN)
          GO TO 36
C
C         HYDRAULIC PROPERTIES FOR CIRCULAR SECTION
C
   33     CALL CIRC(DN)
          IF(JIC.EQ.1)GO TO 61
          GO TO 36
C
C         HYDRAULIC PROPERTIES IN EGG OR HORSE SHOE SECTION
C
   34     CALL ARCS(DN)
          IF(JIC.EQ.1)GO TO 61
          GO TO 36
C
C         HYDRAULIC PROPERTIES IN COMPOSITE SECTION
C
   35     CALL COMP(DN)
          IF(JIC.EQ.1)GO TO 61
C
```

Cavitation Program
(Continued)

```
C       COMPUTATION OF FROUDE NUMBER
C       NOTE - THE FROUDE NUMBER IS CORRECTED FOR SLOPE, CURVATURE,
C       AND THE ENERGY CORRECTION FACTOR
C
   36   IF(NT.GT.1)GO TO 37
        RUN= ABS(STA-STAC)
        IF(RUN.LE.1.E-10)RUN= 0.1
        YB= 0.38*RUN/(RUN*(Q/A)/VISC)**0.2
        IF(YB.GE.DN)YB= DN
        ECF= 0.1*(YB/DN)*(YB/DN)+1.
   37   CF= SQRT(ECF)*(1.+SB*SB)**0.25
        IF(ABS(BENDR).LE.1.E-10)GO TO 38
        ROOT= 1.+2.*DN/BENDR-A/(B*BENDR)
        IF(ROOT.LE.0.)WRITE(3,131)
        IF(ROOT.LE.0.)GO TO 66
        CF= CF*SQRT(ROOT)
   38   F= (Q/A)/(SQRT(G*A/B))*CF
C
C       COMPUTATION OF VELOCITY HEAD
C
        V= Q/A
        HV= ECF*V*V/(2.*G)
        REY= 4.*HR*(Q/A)/VISC
C
C       COMPUTATION OF MANNINGS N FROM RUGOSITY
C
        CALL RUGOS(CN)
C
        HT= TLF*ABS(HV-HIDE1)
        S= (CN*CN*V*V)/(HR**1.3333)
        IF(METRIC.EQ.1)S=S/2.208
C
C       COMPUTATION OF PIEZOMETRIC HEAD
C
        IF(ABS(BENDR).GT.1.E-10)GO TO 39
        D= DN/SQRT(1.0+SB*SB)
        GO TO 40
   39   D= DN/SQRT(1.0+SB*SB)+2.0*HV*DN/BENDR
   40   IF(NT.GT.1)GO TO 41
        DYDX= (SB-S)/(1.-F*F)
        CHECK= ELINV+HV+D
        GO TO 55
C
   41   AVGS= (STORE+S)/2.0
C
C       COMPUTATION OF HEAD LOSS
C
        RUN= SQRT((STA-SAVE)*(STA-SAVE)+(STORE1-ELINV)*(STORE1-ELINV)
     +  )
        HF=RUN*AVGS
        SUM=HF+HT
        IF(D.LE.(-PABS))D= -PABS
C
```

Cavitation Program (Continued)

```
C       COMPUTATION OF ENERGY GRADE LINE
C
        TOTAL=ELINV+D+HV
        CHECK= EGL+SUM
        IF(NCURV.EQ.1)CHECK= EGL-SUM
C
C       CHECK ON THE ACCURACY OF COMPUTATIONS
C
        EGLCK= TOTAL-CHECK
        PCTEL= 100.*((EGLCK)/(ABS(STORE1-ELINV)+D+HV))
        IF(ABS(PCTEL).LT.0.001)GO TO 54
        IF(ABS(PCTEL).LT.0.1.AND.ABS((DN-YN)/YN).LE.0.0001)GO TO 54
        IF(ABS(PCTEL).GT.0.1.AND.ABS((DN-YN)/YN).LE.0.0001)GO TO 53
C
C       DETERMINATION OF FLOW DEPTH USING NEWTONS METHOD
C
        DTDY= 1./SQRT(1.+SB*SB)-2.*HV*B/A
        IF(ABS(BENDR).GT.1.E-10)DTDY= DTDY+2.*HV/BENDR-
     +  4.*DN*HV*B/(A*BENDR)
        DCDY= HF*((2./3.)*DHRDY/HR+B/A)+TLF*HV*B/A
        IF(NCURV.EQ.0)DCDY= -DCDY
        DEDY= DTDY-DCDY
        DINC= EGLCK/DEDY
C
C       CHECK TO ENSURE THAT NEWTONS METHOD DOES NOT CAUSE A
C       JUMP ACROSS NORMAL DEPTH OR CRITICAL DEPTH WITH A CONSTANT
C       BED SLOPE.
C
        IF(AN.EQ.'M')GO TO 42
        IF(AN.EQ.'S')GO TO 43
        IF(AN.EQ.'C')GO TO 44
        IF(AN.EQ.'H')GO TO 45
        IF(AN.EQ.'A')GO TO 46
        GO TO 49
C
C       MILD SLOPE
C
  42    IF(M.EQ.1.AND.NCURV.EQ.0)GO TO 47
        IF(M.EQ.1)GO TO 51
        IF(M.EQ.2.AND.NCURV.EQ.0)GO TO 47
        IF(M.EQ.2)GO TO 49
        IF(M.EQ.3.AND.NCURV.EQ.1)GO TO 49
        GO TO 51
C
C       STEEP SLOPES
C
  43    IF(M.EQ.1.AND.NCURV.EQ.0)GO TO 49
        IF(M.EQ.1)GO TO 51
        IF(M.EQ.2.AND.NCURV.EQ.0)GO TO 49
        IF(M.EQ.2)GO TO 47
        IF(M.EQ.3.AND.NCURV.EQ.1)GO TO 47
        GO TO 51
C
```

Cavitation Program
(Continued)

```
C         CRITICAL SLOPE
C
   44     IF(M.EQ.2)GO TO 51
          IF(M.EQ.1.AND.NCURV.EQ.0)GO TO 49
          IF(M.EQ.1)GO TO 51
          IF(M.EQ.3.AND.NCURV.EQ.1)GO TO 49
          GO TO 51
C
C         HORIZONTAL SLOPE
C
   45     IF(M.EQ.1)GO TO 51
          IF(M.EQ.2.AND.NCURV.EQ.1)GO TO 49
          IF(M.EQ.2)GO TO 51
          IF(M.EQ.3.AND.NCURV.EQ.1)GO TO 49
          GO TO 51
C
C         ADVERSE SLOPE
C
   46     IF(M.EQ.2)GO TO 51
          IF(M.EQ.2.AND.NCURV.EQ.1)GO TO 49
          IF(M.EQ.2)GO TO 51
          IF(M.EQ.3.AND.NCURV.EQ.1)GO TO 49
          GO TO 51
C
C         CHECK TO ENSURE THAT NEWTONS METHOD DOES NOT CAUSE A
C         JUMP ACROSS NORMAL DEPTH IF COMPUTATIONS ARE PROCEEDING
C         TOWARD NORMAL DEPTH. IF THE BED SLOPE IS NOT CONSTANT,
C         A JUMP ACROSS NORMAL DEPTH IS PERMITTED.
C
   47     IF(AN.EQ.'H')GO TO 51
          IF(ABS(SBO).LE.1.E-10)GO TO 51
          IF(ABS(1.-SB/SBO).GE.0.0001)GO TO 51
          IF(ABS(DINC).GT.ABS(DN-YN))GO TO 48
          GO TO 51
   48     DINC= ABS(DN-YN)*DINC/(ABS(DINC)*2.)
C
C         CHECK TO ENSURE THAT NEWTONS METHOD DOES NOT CAUSE A
C         JUMP ACROSS CRITICAL DEPTH IF COMPUTATIONS ARE PROCEEDING
C         TOWARD THE CRITICAL DEPTH.
C
   49     IF(ABS(DINC).GT.ABS(DN-YC))GO TO 50
          GO TO 51
   50     DINC= ABS(DN-YC)*DINC/(ABS(DINC)*2.)
C
C         INCREMENTAL DEPTH FOR NEXT TRIAL
C
   51     DN= DN-DINC
          IF(DN.LE.0.)DN= (DN+DINC)/2.
   52   CONTINUE
   53   DX=RUN/2.+SAVE
        IF(NCURV.EQ.0)DX= SAVE-RUN/2.
        WRITE(3,130)PCTEL
        NL= NL+2
C
```

Cavitation Program
(Continued)

```
C
C       CHECK FOR ZERO DEPTH WITH TYPE 3 CURVES
C
   54   N3= 0
        IF(DN.GT.DNO.AND.M.EQ.3.AND.NCURV.EQ.0)N3= 1
        IF(N3.EQ.1)WRITE(3,132)
        IF(N3.EQ.1)GO TO 66
C
C       COMPUTATION OF ENERGY GRADE LINE AT BEGINNING OF
C       BOUNDARY LAYER
C
        IF(NT.EQ.2)EGLBL= ((EGL-TOTAL)/(STA-SAVE))*(SAVE-STAC)+EGL
C
C       COMPUTATION OF BOUNDARY LAYER THICKNESS
C
   55   IF(NT.EQ.1)GO TO 57
        IF(NCURV.EQ.1)SUMRUN= SUMRUN+RUN
        IF(NCURV.EQ.0)SUMRUN= ABS(STA-STAC)
        IF(ABS(SUMRUN).LE.0.01)SUMRUN=0.01
        IF(NCURV.EQ.1)YB= YB+0.38*RUN/(SUMRUN*V/VISC)**0.2
        IF(NCURV.EQ.0)YB= 0.38*SUMRUN/(SUMRUN*V/VISC)**0.2
        IF(YB.GE.DN)YB= DN
        IF(YB.LE.1.E-10)YB= DN/100.
        ECF= 0.1*(YB/DN)*(YB/DN)+1.0
        IF(YB.GE.(0.95*DN))THEN
C
C       COMPUTATION OF AIR CONTENT WITH OPEN CHANNEL FLOW
C
          IF(SB.GE.0.)THEN
            ALPHA= ATAN(SB)
            YE= A/B
            E=(RHO*G*YE*YE)/SURFT
            C= 0.05*F-SQRT(SIN(ALPHA)*E)/63
            IF(C.LT.0.)C= 0.
            IF(C.GE.0.74)C= 0.74
          ELSE
            C= 0.
          ENDIF
          BETA= C/(1.-C)
        ELSE
          BETA= 0.
        ENDIF
C
C       WRITE OUTPUT
C
        WRITE (3,116) STA,ELINV,SB,DN,V,D,CHECK,BETA,AN,M,YN,YC,YB
        IF(I.EQ.1.OR.IT.EQ.1)GO TO 56
        IF(Q.LE.QMAX)GO TO 56
        IF(DN.GE.YBI)WRITE(3,120)
        IF(DN.GE.YBI)NL= NL+1
   56   NL= NL+1
C
```

Cavitation Program
(Continued)

```
C       CHECK ON SPACING OF STATIONS
C       (THIS KEEPS ERROR IN DEPTH TO LESS THAN 1-PERCENT)
C
        DYDX= (SB-S)/(1.-F*F)
        IF(DYDX.LE.1.E-10)GO TO 57
        ERRY= 100.*0.5*(RUN/DNO)*(RUN/DNO)*ABS((SB-STORE)/(
     +  (1.-FRUDO*FRUDO)*(1.-FRUDO*FRUDO))*(10./3.*STORE-3.*(SB-STORE)
     +  *FRUDO*FRUDO/(1.-FRUDO*FRUDO)))
        IF(ERRY.LT.1.0)GO TO 57
        DX= RUN/2.+SAVE
        IF(NCURV.EQ.0)DX= SAVE-RUN/2.
        WRITE(3,121)ERRY,DX
        NL= NL+2
C
C       CHECK ON CAVITATION FORMATION
C       YB=BOUNDARY LAYER THICKNESS
C       SIG= CAVITATION POTENTIAL OF FLOW
C       SIGR= CAVITATION POTENTIAL OF DISTRIBUTED ROUGHNESS
C       NSL= REQUIRED CHAMFER TO ELIMINATE CAVITATION
C
   57   DNO= DN
        FRUDO= F
        SIG= 2.*G*(PABS+D)/(V*V)
        IF(SIG.LE.1.E-10)SIG=1.E-10
        SIGR= 32.*G*CN*CN/HR**0.33333
        IF(METRIC.EQ.1)SIGR= SIGR/2.208
        IF(SIGR.GE.SIG)SIG= SIGR
C
C       COMPUTATION OF REQUIRED CHAMFER
        NSL= INT((1.8/SIG)**1.43)+1
C
C       DAMAGE POTENTIAL
C
        CALL DAMPOT(YB,V,D,SIG,PABS)
        IF(NJ.GE.50)GO TO 63
C
```

Cavitation Program
(Continued)

```
C
C       SAVING OF DATA IN ARRAYS FOR PLOT
        NDP= NT+NS*(NOPLT-1)
        IF(NOPLT.GT.1)GO TO 58
        YELEV(NDP)= ELINV
        XSTA(NDP)= STA
   58   YD(NDP)= D
        YBL(NDP)= YB
        YDN(NDP)= DN
        YSIG(NDP)= SIG
        RSIG(NDP)= SIGR
        NCMFR(NDP)= NSL
        YDP1(NDP)= DP1
        YDP2(NDP)= DP2
        YDP3(NDP)= DP3
        YDP4(NDP)= DP4
        YDP5(NDP)= DP5
        YDP6(NDP)= DP6
        QP(NOPLT)= Q
C       ENERGY BALANCE NOT REACHED
        IF(NJ.GE.50)GO TO 63
   59 CONTINUE
      WRITE(3,133)EGLBL
C     WRITE CAVITATION CHARACTERISTICS
C
      WRITE(3,111)(TITL(J),J=1,60)
      IF(METRIC.EQ.1)WRITE(3,112)Q,DNF,RUG,CNO
      IF(METRIC.EQ.0)RUG= 1000.*RUG
      IF(METRIC.EQ.0)WRITE(3,114)Q,DNF,RUG,CNO
      IF(METRIC.EQ.0)RUG=RUG/1000.
*** END OF FILE CONTENTS ***
-
-
-
-
-
-
```

GLASGOW AIR FLOW MEASUREMENT DATA

TABLE C.1 *5° smooth – 180mm gate opening*

Discharge Q_w (m^3/s)	Gate Openning Y_G (mm)	Ramp angle ‡	Froude No at ramp $V/\sqrt{gh_3}$	Velocity at ramp V (m/s)	Depth at ramp h_3 (mm)	Channel aspect ratio B/h_3	Jet Length L (mm)	Δh (mm)	Δh/h	Air flow rate Q_a (m^3/s)	Ratio of air/water $\beta = Q_a/Q_w$
0.02	180	5° smooth	12.7	6.89	29.0	3 44	620	0.0	0.0	0.0053	0.266
							540	4.33	0.14	0.00383	0.1916
							500	8.66	0.298	0.0027	0.135
0.038	180	5° smooth	8.89	6.66	57.2	1.74	680	0.0	0.0	0.00808	0.212
							590	8.66	0.151	0.0055	0.145
							520	18.66	0.326	0.00275	0.072
0.052	180	5° smooth	7.89	6.84	76.5	1.3	800	0.0	0.0	0.0088	0.169
							680	12.0	0.156	0.0060	0.115
							600	24.66	0.32	0.00295	0.056

TABLE C.2 *5° smooth – 90 mm gate opening*

Discharge Q_w (m^3/s)	Gate Openning Y_G (mm)	Ramp angle ‡	Froude No at ramp $V/\sqrt{gh_3}$	Velocity at ramp V (m/s)	Depth at ramp h_3 (mm)	Channel aspect ratio B/h_3	Jet Length L (mm)	Δh (mm)	Δh/h	Air flow rate Q_a (m^3/s)	Ratio of air/water $\beta = Q_a/Q_w$
0.018	90	5° smooth	14.09	7.05	25.5	3.92	410	16.66	0.62	No - Air	
							570	0.0	0.0	0.00525	0.291
							500	4.0	0.15	0.0033	0.183
							460	8.33	0.314	0.00208	0.1157
0.033	90	5° smooth	9.9	6.87	48.3	2.07	660	0.0	0.0	0.00705	0.213
							590	7.33	0.151	0.00533	0.161
							510	14.66	0.303	0.00303	0.091
0.048	90	5° smooth	8.35	6.9	69.5	1.43	800	21.33	0.299	0.0095	0.197
							700	12.0	0.607	0.00391	0.081
							600	86.67	1.18	0.00032	0.06

TABLE C.3 5^0 *smooth – 60 mm gate opening*

Discharge Q_w (m^3/s)	Gate Openning Y_C (mm)	Ramp angle Φ	Froude No at ramp $V/\sqrt{gh_3}$	Velocity at ramp V (m/s)	Depth at ramp h_3 (mm)	Channel aspect ratio B/h_3	Jet Length L (mm)	Δh (mm)	$\Delta h/h$	Air flow rate Q_a (m^3/s)	Ratio of air/water $\beta = Q_a/Q_w$
0.015	60	5^0 smooth	15.7	7.14	21.0	4.76	460	9.33	0.405	No - Air	
							540	0.0	0.0	0.0050	0.333
							480	2.33	0.101	0.003	0.2
							430	4.667	0.202	0.0021	0.14
0.028	60	5^0 smooth	11.17	7.0	40.0	2.5					
							470	35.3	0.861	No - Air	
							800	7.33	0.178	0.0045	0.16
							650	14.66	0.357	0.0028	0.1
0.037	60	5^0 smooth	11.59	7.87	47.0	2.12					
							500	70.0	1.48	No - Air	
							810	28.0	0.595	0.0022	0.042
							600	53.33	1.134	0.0009	0.027

TABLE C.4 2^0 *smooth – 180mm gate opening*

Discharge Q_w (m^3/s)	Gate Openning Y_C (mm)	Ramp angle Φ	Froude No at ramp $V/\sqrt{gh_3}$	Velocity at ramp V (m/s)	Depth at ramp h_3 (mm)	Channel aspect ratio B/h_3	Jet Length L (mm)	Δh (mm)	$\Delta h/h$	Air flow rate Q_a (m^3/s)	Ratio of air/water $\beta = Q_a/Q_w$
0.02	180	2^0 smooth	12.27	6.66	30.0	3.33	75	220	7.33	No - Air	
							340	0.0	0.0	0.00575	0.287
							210	55	0.14	0.0045	0.225
							185	110	0.298	0.00388	0.194
0.038	180	2^0 smooth	8.9	6.66	57.0	1.75					
							465	0.0	0.0	0.0088	0.232
							370	13.0	0.22	0.0036	0.094
							210	26.66	0.46	0.0021	0.055
0.052	180	2^0 smmoth	7.92	6.84	76.0	1.31					
							560	0.0	0.0	0.0121	0.232
							490	20.2	0.265	0.0055	0.105
							425	40.44	0.532	0.0037	0.071

TABLE C.5 2° *smooth – 90 mm gate opening*

Discharge Q_w (m^3/s)	Gate Openning Y_G (mm)	Ramp angle Φ	Froude No at ramp $V/\sqrt{gh_3}$	Velocity at ramp V (m/s)	Depth at ramp h_3 (mm)	Channel aspect ratio B/h_3	Jet Length L (mm)	Δh (mm)	$\Delta h/h$	Air flow rate Q_a (m^3/s)	Ratio of air/water $\beta = Q_a/Q_w$
0.018	90	2° smooth	13.08	6.71	26.8	.73	100	83.37	3.11	No - Air	
							340	0.0	0.0	0.0048	0.266
							260	21.667	0.808	0.00188	0.104
							230	41.667	1.555	0.00122	0.067
0.033	90	2° smooth	10.01	6.87	48.0	2.08	80	150	3.125	No - Air	
							390	0.0	0.0	0.00654	0.198
							240	38.33	0.79	0.0027	0.081
							200	76.667	1.59	0.00158	0.047
0.048	90	2° smooth	8.26	6.85	70.0	1.428	75	166.66	2.34	No Air	
							400	0.0	0.0	0.0071	0.047
							250	41.667	0.586	0.00308	0.064
							210	83.33	1.17	0.00157	0.0327

TABLE C.6 2° *smooth – 60 mm gate opening*

Discharge Q_w (m^3/s)	Gate Openning Y_G (mm)	Ramp angle Φ	Froude No at ramp $V/\sqrt{gh_3}$	Velocity at ramp V (m/s)	Depth at ramp h_3 (mm)	Channel aspect ratio B/h_3	Jet Length L (mm)	Δh (mm)	$\Delta h/h$	Air flow rate Q_a (m^3/s)	Ratio of air/water $\beta = Q_a/Q_w$
0.015	60	2° smooth	15.73	7.14	21.0	4.76	90	93.3	4.05	No - Air	
							350	0.0	0.0	0.0042	0.28
							260	23.3	1.01	0.0015	0.1
							220	46.67	2.03	0.0006	0.04
0.028	60	2° smooth	10.96	6.91	40.5	2.469	78	206.66	5.1	No - Air	
							370	0.0	0.0	0.00629	0.22
							220	51.66	1.27	0.0015	0.1
							190	103.33	2.55	0.00109	0.038
0.037	60	2° smooth	11.3	7.74	47.8	2.09					
							410	0.0	0.0	0.0071	0.19
							290	48.8	1.02	0.0038	0.102
							220	85.5	1.8	0.0028	0.075

TABLE C.7 *10° smooth – 180mm gate opening*

Discharge Q_w (m^3/s)	Gate Openning Y_G (mm)	Ramp angle Φ	Froude No at ramp $V/\sqrt{gh_3}$	Velocity at ramp V (m/s)	Depth at ramp h_3 (mm)	Channel aspect ratio B/h_3	Jet Length L (mm)	Δh (mm)	$\Delta h/h$	Air flow rate Q_a (m^3/s)	Ratio of air/water $\beta = Q_a/Q_w$
0.02	180	10° smooth	12.27	6.66	30.0	3.33					
							1150	8.66	0.28	No - Air	
							1500	0.0	0.0	0.01	0.50
							1300	4.33	0.143	0.0082	0.41
0.038	180	10° smooth	8.68	6.55	58.0	1.72					
							1250	21.33	0.267	No - Air	
							1600	0.0	0.0	0.011	0.29
							1450	10.66	0.132	0.00855	0.225

TABLE C.8 *10° smooth – 90 mm gate opening*

Discharge Q_w (m^3/s)	Gate Openning Y_G (mm)	Ramp angle Φ	Froude No at ramp $V/\sqrt{gh_3}$	Velocity at ramp V (m/s)	Depth at ramp h_3 (mm)	Channel aspect ratio B/h_3	Jet Length L (mm)	Δh (mm)	$\Delta h/h$	Air flow rate Q_a (m^3/s)	Ratio of air/water $\beta = Q_a/Q_w$
0.018	90	10° smooth	12.9	6.66	27.0	3.7	1100	7.333	0.27	No - Air	
							1550	0.0	0.0	0.0101	0.56
							1400	3.667	0.133	0.00894	0.497
0.033	90	10° smooth	9.6	6.7	49.2	2.03					
							1240	9.33		No - Air	
							1700	0.0	0.0	0.0101	0.489
							1550	4.667	0.094	0.0077	0.23
							1460	8.1	0.166	0.007	0.21

TABLE C.9 *10° smooth – 60 mm gate opening*

Discharge Q_w (m^3/s)	Gate Openning Y_C (mm)	Ramp angle Φ	Froude No at ramp $V/\sqrt{gh_3}$	Velocity at ramp V (m/s)	Depth at ramp h_3 (mm)	Channel aspect ratio B/h_3	Jet Length L (mm)	Δh (mm)	$\Delta h/h$	Air flow rate Q_a (m^3/s)	Ratio of air/water $\beta = Q_a/Q_w$
0.015	60	10° smooth	13.89	6.57	22.8	4.38	1300	6.0	0.263	No - Air	
							1600	0.0	0.0	0.0105	0.70
							1400	3.0	0.131	0.00782	0.52
0.028	60	10° smooth	10.75	6.82	41.0	2.44					
							1580	6.66	0.162	No - Air	
							1720	0.0	0.0	0.011	0.39

TABLE C.10 *5° rough – 180mm gate opening*

Discharge Q_w (m^3/s)	Gate Openning Y_C (mm)	Ramp angle Φ	Froude No at ramp $V/\sqrt{gh_3}$	Velocity at ramp V (m/s)	Depth at ramp h_3 (mm)	Channel aspect ratio B/h_3	Jet Length L (mm)	Δh (mm)	$\Delta h/h$	Air flow rate Q_a (m^3/s)	Ratio of air/water $\beta = Q_a/Q_w$
0.02	180	5° rough	10.99	6.19	32.3	3.09	300	80.66	2.57	No - Air	
							540	0.0	0.0	0.0106	0.531
							460	20.0	0.638	0.0066	0.33
							350	40.0	1.27	0.00444	0.222
0.038	180	5° rough	8.51	6.48	59.0	1.38					
							630	0.0	0.0	0.0148	0.392
							540	13.33	0.225	0.0055	0.144
							500	32.0	0.542	0.00398	0.104
0.052	180	5° rough	7.47	6.58	79.0	1.26					
							730	0.0	0.0	0.0191	0.368
							610	23.33	0.295	0.0145	0.28
							580	46.66	0.59	0.005	0.096

TABLE C.11 5° rough – 90 mm gate opening

Discharge Q_w (m^3/s)	Gate Openning Y_C (mm)	Ramp angle Φ	Froude No at ramp $V/\sqrt{gh_3}$	Velocity at ramp V (m/s)	Depth at ramp h_3 (mm)	Channel aspect ratio B/h_3	Jet Length L (mm)	Δh (mm)	$\Delta h/h$	Air flow rate Q_a (m^3/s)	Ratio of air/water $\beta = Q_a/Q_w$
0.018	90	5° rough	12.07	6.36	28.3	3.53	370	18.66	0.67	No - Air	
							470	0.0	0.0	0.011	0.61
							450	4.0	0.146	0.0094	0.52
							430	8.33	0.305	0.0071	0.394
0.033	90	5° rough	9.8	6.73	49.0	2.04	400	51.33	1.04	No - Air	
							480	0.0	0.0	0.012	0.363
							450	16.66	0.34	0.0045	0.136
							430	25.0	0.51	0.0032	0.0969
0.048	90	5° rough	8.09	6.76	71.0	1.408	410	120.0	1.64	No - Air	
							510	0.0	0.0	0.0188	0.39
							480	40.0	0.54	0.0105	0.21
							460	60.0	0.82	0.009	0.180

TABLE C.12 5° rough – 60 mm gate opening

Discharge Q_w (m^3/s)	Gate Openning Y_C (mm)	Ramp angle Φ	Froude No at ramp $V/\sqrt{gh_3}$	Velocity at ramp V (m/s)	Depth at ramp h_3 (mm)	Channel aspect ratio B/h_3	Jet Length L (mm)	Δh (mm)	$\Delta h/h$	Air flow rate Q_a (m^3/s)	Ratio of air/water $\beta = Q_a/Q_w$
0.015	60	5° rough	13.43	6.25	24.0	4.16	370	13.33	0.555	No - Air	
							470	0.0	0.0	0.01133	0.75
							440	4.00	0.166	0.011	0.73
							410	6.667	0.277	0.0082	0.544
0.028	60	5° rough	10.49	6.71	41.7	2.39	400	44.6	1.04	No - Air	
							560	0.0	0.0	0.01177	0.42
							520	25.33	0.59	0.0051	0.182
							460	33.33	0.78	0.0041	0.146
0.037	60	5° rough	10.88	7.55	49.0	2.04	330	33.33	1.98	No - Air	
							520	0.0	0.0	0.01183	0.32
							420	66.66	0.595	0.0064	0.17
							400	76.67	1.134	0.0057	0.15